No 2.

LIGHT SCATTERING SPECTROSCOPY

Studies of Electronic Excitations

and

Atomic Vibrations in Matter

DAVID J. LOCKWOOD

Doctor of Science

University of Edinburgh

January 1978

Abstract

This thesis comprises a compendium of forty-two publications on various research topics unified by a common theme, light scattering spectroscopy. The research work presented ranges from experimental studies of the dynamics of atoms in various phases of matter through to theoretical investigations of the light scattering process. The topics discussed are the dynamics of structural phase transitions in proper and improper ferroelectrics, and in antiferroelectrics, for both ordered and disordered systems; the magnetic phase transitions in ordered and disordered compounds; the electronic properties of divalent transition metal ions in pure and dilute systems; the lattice vibrations of ionic, covalent and molecular crystals; the selection rules governing higher-order light scattering processes; the weak interactions occurring between chemical species in both aqueous and non-aqueous solvents; and the use of automation techniques in light scattering spectroscopy.

Statement

I declare that all of the following work is my own, except in the case of collaborative publications where my contributions are as follows. I have made major contributions in all phases of the work for publications with J.H. Christie, J.D. Riddell, J. Scott, J.W. Arthur, T.J. Hosea and A.F. Murray, as in these cases my collaborators were post-graduate students working under my instruction for higher degrees. For the other publications, my contribution has been at least one-half of the work except for papers 21, 26, 30 and 35, where I was responsible for the light scattering work alone. The work reported in section 2 of paper 9 was previously submitted as part of a thesis for the degree of Doctor of Philosophy of the University of Canterbury, New Zealand in 1969.

Prologue

Fifty years ago, in March 1928, Sir C.V. Raman announced[1,2] the discovery of an effect which now bears his name and was to win him the Nobel Prize. His discovery was simply made, using primitive equipment, but it has had far reaching consequences in modern physics and chemistry. Raman observed that matter, when irradiated with monochromatic light, produced scattered light of a different frequency, albeit but weakly. He further discovered that each material produced its own unique spectrum of scattered light, the Raman spectrum. Other discoveries and theories followed and the basics of light scattering spectroscopy were well understood by 1934 when G. Placzek wrote his masterly review.[3] The Raman spectrum comprises structure, which may arise from first- or higher-order scattering processes, where the difference in energy between the incident radiation and a feature in the structure corresponds to the energy of some elementary excitation of the scattering medium. Raman scattering characteristically probes atomic vibrations and low energy electronic excitations in gases, liquids and solids. After the initial flurry of activity, up into the 1930's, light scattering lost appeal as a research activity, mainly because of the extreme experimental difficulties, and was used predominently as a tool for structural work in physical chemistry. But the discovery of the laser changed everything. Here at last was the ideal source for light scattering experiments, i.e. a well-defined intense monochromatic source of variable frequency. Once again there was intense activity in the field, with numerous new discoveries and concomitant theories dating from the early 1960's. Nowadays laser light scattering techniques are common place in physics, chemistry and

biology laboratories. Another plateau region has been reached where technique development has slowed and applications as a laboratory tool are paramount.

The author was fortunate to join the light scattering field in the early stages of the post-laser revival and, after some experience of the old ways (i.e. mercury lamp light source, prism monochromator, and photographic plate detection), participated in some of the first argon-laser light scattering work. Early in this work it was apparent to the author that computers and automation would play an increasingly important role in Raman spectroscopy. In 1967 he devised what was probably the first "on-line" computer controlled data collection system for Raman spectroscopy. These days, computer control of the experiment and computerised data analysis are standard features and figure prominently in the publications in this thesis. These publications cover a period of eight years' research and show the increasing sophistication of light scattering experiments following improvements in equipment performance as the technique is applied to more and more difficult problems.

The work reported in this thesis is more concerned with solving problems using light scattering spectroscopy than with the technique itself. However, two papers are presented that are technique oriented. Paper 2 gives group-theoretically determined selection rules for Raman scattering involving three and four photons as well as the usual two-photon scattering. Paper 9 is concerned with automated spectroscopy and reviews, with examples, the various methods of automation ranging from a simple dedicated control box to full computer control in time-shared mode.

Papers 5, 12 and 14 also stand apart, being chemical in nature as opposed to the majority interest in solid state physics. These papers are directed at a problem of long standing interest in chemistry: how do molecular species interact in solution? In general, the interactions between solute and solvent are weak, but papers 5 and 12 show that these interactions can be detected via Raman spectroscopy and, furthermore, the nature of the interaction can also be inferred. Paper 14 deals with, dut does not solve, the interesting problem of why degenerate vibrational bands of the NO_3^- ion are split when the ion is in solution.

The remaining publications all deal with problems in solid state physics and can be classified under one of three headings; magnetic and electronic properties, lattice vibrations, and structural phase transitions.

Some of the first and last publications in the list deal with problems that have long interested the author. Crystals with the $CdCl_2$ and CdI_2 structures have trigonal symmetry, and this low symmetry, together with the layered nature of the crystal structures, produces materials with unusual physical properties. Papers 1, 3, 4, 31, 41 and 42 are the result of a lengthy study of some of these properties. Phonons and electronic excitations have been studied in $CoCl_2$, $FeCl_2$, $FeBr_2$, $CdCl_2$: Co^{2+}, $CdBr_2$: Co^{2+} and $MnCl_2$: Co^{2+}. Papers 17 and 27 also deal with electronic properties, being concerned with Raman scattering from magnons in $KMnF_3$ and $KNi_xMn_{1-x}F_3$.

The lattice vibrations of solids containing diverse bonding forces have been examined. The ionic crystals $ZrSiO_4$ and $ThSiO_4$ (paper 28) and $Zn_4O(BO_2)_6$ (paper 22) are of interest because they

contain SiO_4^{4-} and BO_4^{5-} tetrahedra, respectively, which are not found in a "free" state. An analysis of the respective Raman spectra allowed an assignment of internal mode frequencies in a first approximation. The Raman spectrum of zinc metaborate contained an unusual resonance interference feature between phonons (papers 24 and 33). In semiconductors, valency bonding forces play a significant role. The Raman spectrum of the widely-studied ternary semiconductor $AgGaS_2$ was examined (papers 13 and 15) to try and resolve conflicting and incomplete results from earlier measurements, and to provide zone-centre frequencies for lattice dynamical calculations. Several unique experimental difficulties had to be overcome because of the peculiar optical properties and low symmetry of $AgGaS_2$, but eventually all Raman active modes were determined. A temperature dependent study (paper 29) was needed to assist the assignment. The unusual ordered vacancy compounds, $HgIn_2\square Te_4$ and $Hg_3In_2\square Te_6$, proved even more difficult to study experimentally. These ternary compounds are opaque in the visible and a Brewster-angle scattering technique had to be applied. Even though the Raman signal was extremely weak, the experiments gave interesting results bearing on the role of the vacancies in crystal structures (papers 21, 26 and 30). The final example in this section on lattice vibrations is SnI_4, a molecular crystal exhibiting pronounced anharmonic properties. A detailed temperature and pressure dependent study was made of the lattice dynamics of this high symmetry compound using Raman spectroscopy (papers 32 and 35).

Structural phase transitions of various types have been examined in light scattering experiments. Measurements on NH_4HSO_4 (paper 6) classified the ferroelectric transition as

being largely order-disorder in character, with the presence of a temperature-dependent Debye-like wing feature in the Raman spectrum. At the other extreme is $KMnF_3$, where the anti-ferroelectric transition at 186 K is largely displacive in character. Here, Raman studies gave details of the soft mode temperature dependence, which showed non-classical behaviour for temperatures close to the transition (papers 8 and 10). The intensity of a hard mode that disappears near the phase transition was found to be proportional to the soft-mode frequency squared (paper 7). Another structural transition in $KMnF_3$ that occurs at 91.5 K was also investigated (paper 10). The ferroelectric phase transition in $Pb_5Ge_3O_{11}$ exhibits classical behaviour because of its uniaxial symmetry, and interest has centred on the statics and dynamics of this material at temperatures close to the transition. Raman and Brillouin studies of lead germanate (paper 23) have revealed an unresolved central peak, whose temperature dependence may be explained on the basis of a static defect model. Other features in the Raman spectrum, including the ferroelectric soft mode, have also been investigated (papers 19 and 25). Replacing a small percentage of the lead atoms with barium dramatically lowers the Curie temperature of lead germanate. A Raman investigation (paper 38) showed that the damping of all normal modes is greatly increased by the addition of barium, and that the relative intensity of the low frequency response near T_c is much weaker for the doped material suggestive of a more diffuse transition. Improper ferroelectrics form the last example of materials with structural phase transitions to be considered here. Boracites, $M_3B_7O_{13}X$ where M is a divalent metal and X a halogen, exhibit an

improper transition from a cubic paraelectric phase to the low temperature orthorhombic ferroelectric phase. The lattice dynamics of the paraelectric and ferroelectric phases of various boracites have been characterised by Raman scattering (papers 11, 16, 18, 20, 34, 36, 37, 39 and 40). Two soft modes were discovered in the ferroelectric phase (papers 18 and 36), verifying a microscopic theory of the transition. A Debye-like wing was found (papers 16 and 20) whose temperature dependence indicated that the transition has order-disorder character as well as a displacive nature demonstrated by the mode softening. In nickel-iodine boracite, an anomalous temperature dependent behaviour of lattice modes was observed at about 128 K (papers 34 and 40), consistent with a curious and unexplained expansion of the lattice at around that temperature. Anomalous mode softening was found in the cubic and orthorhombic phases of nickel-iodine boracite (papers 37 and 40). The light scattering experiments on boracites have produced results that have raised more problems than have been solved. They are, indeed, most puzzling materials, exhibiting temperature dependent behaviour of extreme complexity and variety.

References

1. C.V. Raman, Indian J. Phys. 2, 387 (1928).

2. C.V. Raman and R.S. Krishnan, Nature 121, 501 (1928).

3. G. Placzek, "Marx Handbuch der Radiologie", 2nd ed., vol. VI, part 2, p.209 (1934).

List of Publications

1. J.H. Christie and D.J. Lockwood,
   Chem. Phys. Letters 8, 120 (1971),
   "Electronic Raman Spectrum of Co^{2+} in $CoCl_2$".

2. J.H. Christie and D.J. Lockwood,
   J. Chem. Phys. 54, 1141 (1971),
   "Selection Rules for Three- and Four-Photon Raman Interactions".

3. D.J. Lockwood and J.H. Christie,
   Chem. Phys. Letters 9, 559 (1971),
   "Electronic Raman Spectra of Co^{2+} in $CdCl_2$, $CdBr_2$ and $MnCl_2$".

4. J.H. Christie and D.J. Lockwood,
   Light Scattering in Solids, M. Balkanski Ed.
   (Flammarion, Paris, 1971), p. 145,
   "Electronic Raman Scattering in $CoCl_2$".

5. J.D. Riddell, D.J. Lockwood and D.E. Irish,
   Can. J. Chem. 50, 2951 (1972),
   "Ion Pair Formation in $NaNO_3/D_2O$ Solutions:
   Raman and Infrared Spectra, Partial Molal Volumes,
   Conductance and Viscosity".

6. J.W. Arthur, D.J. Lockwood and W. Taylor,
   Advances in Raman Spectroscopy, J.P. Mathieu Ed.
   (Heyden, London, 1972), Vol. 1, p. 144,
   "The Raman Spectrum of Ammonium Bisulphate".

7. D.J. Lockwood and B.H. Torrie,
Anharmonic Lattices, Structural Transitions and Melting,
T. Riste Ed. (Noordhoff, Leyden, 1974), p. 147,
"Raman Spectral Study of the Upper Phase Transition in $KMnF_3$".

8. B.H. Torrie and D.J. Lockwood,
Ferroelectrics, 8, 583 (1974),
"Raman Spectral Study of $KMnF_3$".

9. J.W. Arthur and D.J. Lockwood,
J. Raman Spectroscopy 2, 53 (1974),
"Automation Techniques for Raman Spectroscopy".

10. D.J. Lockwood and B.H. Torrie,
J. Phys. C; Solid State Phys. 7, 2729 (1974),
"Raman Scattering Study of the Three Structural Phases of $KMnF_3$".

11. D.J. Lockwood,
J. Raman Spectroscopy 2, 555 (1974),
"Isolating the Totally Symmetric Raman Spectrum of Cubic Crystals".

12. D.J. Lockwood, J. Scott, W.L. Elsdon and D.E. Irish,
J. Raman Spectroscopy 2, 593 (1974),
"Raman Spectral Studies of Cis-2-Butene-Benzene-Mixtures".

13. D.J. Lockwood and H. Montgomery,
J. de Physique 36, C3-183 (1975),
"Raman Spectrum of $AgGaS_2$".

14. D.J. Lockwood,

J. Chem. Soc. Faraday II 71, 1440 (1975),

"Effect of Rotations on Degenerate Vibrations of the Nitrate Ion".

15. D.J. Lockwood and H. Montgomery,

J. Phys. C: Solid State Phys. 8, 3241 (1975),

"Raman Spectrum of $AgGaS_2$".

16. D.J. Lockwood,

Light Scattering in Solids, M. Balkanski, R.C.C. Leite and S.P.S. Porto Eds.

(Flammarion, Paris, 1975), p.933,

"A Raman Study of the Ferroelectric Phase Transition in Chromium Chlorine Boracite".

17. D.J. Lockwood and G.J. Coombs,

J. Phys. C: Solid State Phys. 8, 4062 (1975),

"Two-magnon Raman Scattering in $KMnF_3$".

18. D.J. Lockwood,

Solid State Commun. 18, 115 (1976),

"Observation of Soft Modes in the Raman Spectrum of Ferroelectric $Cr_3B_7O_{13}C\ell$".

19. W. Taylor, D.J. Lockwood, J.W. Arthur and T.J. Hosea,

Ferroelectrics 12, 113 (1976).

"The Raman Spectrum of Lead Germanate".

20. D.J. Lockwood,
Ferroelectrics 13, 353 (1976),
"Raman Spectral Study of the Ferroelectric Phase Transition in Boracites".

21. A. Miller, A. MacKinnon, D. Weaire and D.J. Lockwood,
J. Phys. C: Solid State Phys. 9, 2997 (1976),
"Lattice Dynamics of the Ordered Vacancy Compound $HgIn_2\square Te_4$".

22. A.F. Murray and D.J. Lockwood,
J. Phys. C: Solid State Phys. 9, 3691 (1976),
"Raman Spectrum of $Zn_4O(BO_2)_6$".

23. D.J. Lockwood, J.W. Arthur, W. Taylor and T.J. Hosea,
Solid State Commun. 20, 703 (1976),
"Observation of a Central Peak in Lead Germanate by Light Scattering".

24. A.F. Murray and D.J. Lockwood,
Proc. 5th Int. Conf. on Raman Spectroscopy, E.D. Schmid, J. Branmuller, W. Kiefer, B. Schrader and H.W. Schrotter Eds. (Hans Ferdinand Schulz Verlag, Freiburg, 1976) p.636,
"Phonon Coupling in Zinc Metaborate".

25. T.J. Hosea, D.J. Lockwood, W. Taylor and J.W. Arthur,
Proc. 5th Int. Conf. on Raman Spectroscopy, E.D. Schmid et al. Eds. (Schulz Verlag, Freiburg, 1976) p.610.
"Analysis of the Ferroelectric Soft Mode in Lead Germanate".

26. A. Miller, A. MacKinnon, D. Weaire, C.R. Pidgeon, D. Lockwood and G.A. Saunders,
Physics of Semiconductors, F.G. Fumi Ed. (Tipografia Marves, Rome, 1976), p.509,
"Investigation of Electronic and Lattice Properties of the Ordered Vacancy Compound $HgIn_2\square Te_4$".

27. G.J. Coombs and D.J. Lockwood,
Physica 86B, 710 (1977),
"Two-Magnon Raman Scattering in $KNi_xMn_{1-x}F_3$".

28. R.W.G. Syme, D.J. Lockwood and H.J. Kerr,
J. Phys. C: Solid State Phys. 10, 1335 (1977),
"Raman Spectrum of Synthetic Zircon ($ZrSiO_4$) and Thorite ($ThSiO_4$)".

29. D.J. Lockwood, Ternary Compounds,
G.D. Holah Ed. (Inst. of Physics, Bristol, 1977), p. 97,
"Raman Spectrum of $AgGaS_2$ Revisited: temperature dependence of the degenerate modes".

30. A. MacKinnon, A. Miller, G. Ross, G.D. Holah and D.J. Lockwood,
Ternary Compounds, G.D. Holah Ed. (Inst. of Physics, Bristol, 1977), p. 119,
"Structure and Lattice Dynamics of the Complex Ordered Vacancy Compound $Hg_3In_2\square Te_6$".

31. D.J. Lockwood, I.W. Johnstone, G. Mischler and P. Carrara,
Solid State Commun., in press,
"Raman Scattering from Magnons in $CoC\ell_2$ and $FeC\ell_2$".

32. I.U. Heilmann, D.J. Lockwood and G.S. Pawley,
J. Phys. C: Solid State Phys., in press,
"Raman Spectrum of Tin-tetraiodide: Temperature and Pressure Measurements and Lattice Dynamical Calculations".

33. A.F. Murray and D.J. Lockwood,
J. Phys. C: Solid State Phys. 11, 387 (1978),
"Phonon Coupling in $Zn_4O(BO_2)_6$ Studied by Raman Spectroscopy".

34. A.F. Murray and D.J. Lockwood,
Proceedings of Lattice Dynamics Conference, Paris 1977,
to be published,
"Raman Spectral Study of Cubic Nickel-Iodine Boracite".

35. I.U. Heilmann, N.B. Olsen, D.J. Lockwood, G.A. Mackenzie and G.S. Pawley,
Proceedings of Lattice Dynamics Conference, Paris 1977,
to be published,
"Dynamics of the Molecular Solid SnI_4".

36. D.J. Lockwood and R.W.G. Syme,
Ferroelectrics, to be published,
"Raman Study of the Ferroelectric Phase Transition in Copper-Chlorine Boracite".

37. D.J. Lockwood and A.F. Murray,
Ferroelectrics, to be published,
"Lattice Dynamics of Nickel-Iodine Boracite".

38. T.J. Hosea, W. Taylor and D.J. Lockwood,
Ferroelectrics, to be published,
"The Raman Spectrum of Pure and Barium Doped Lead Germanate".

39. D.J. Lockwood,
Indian J. Pure Appl. Phys., to be published,
"Raman Spectrum of the Orthorhombic Phase of the Improper Ferroelectric Manganese - Chlorine Boracite".

40. A.F. Murray and D.J. Lockwood,
J. Phys. C: Solid State Phys., to be published,
"Raman Spectrum of the Puzzling Paraelectric Phase of Nickel-Iodine Boracite".

41. I.W. Johnstone, D.J. Lockwood and G. Mischler,
J. Phys. C: Solid State Phys., submitted,
"Temperature-Dependent Electron-Phonon Coupling in $FeCl_2$ Observed by Raman Scattering".

42. I.W. Johnstone, D.J. Lockwood and G. Mischler,
J. Phys. C: Solid State Phys., submitted,
"Examples of a Dynamic Jahn-Teller System: Raman Scattering from Electronic Excitations and Phonons in Paramagnetic and Antiferromagnetic $FeCl_2$ and $FeBr_2$".

Reprinted from:

CHEMICAL PHYSICS LETTERS

Volume 8, number 1, 1 January 1971

ELECTRONIC RAMAN SPECTRUM OF Co^{2+} IN $CoCl_2$ *

J. H. CHRISTIE ** and D. J. LOCKWOOD ***
Department of Physics, University of Canterbury, Christchurch, New Zealand

pp. 120 – 122

NORTH-HOLLAND PUBLISHING COMPANY — AMSTERDAM

ELECTRONIC RAMAN SPECTRUM OF Co^{2+} IN $CoCl_2$ *

J. H. CHRISTIE ** and D. J. LOCKWOOD ***
Department of Physics, University of Canterbury, Christchurch, New Zealand

Received 9 November 1970

The low-lying electronic energy levels of the Co^{2+} ion in $CoCl_2$ have been measured at low temperatures by means of Raman spectroscopy. The observed energies at 233, 551, 962, 984 and 1014 cm^{-1} are not in total agreement with values deduced from crystal-field theory calculations. Discrepancies between the Raman results and earlier infrared absorption measurements are discussed.

Ever since the first observation in 1963 [1], studies of the electronic Raman effect of ions in crystals have been restricted to the lanthanides [2]. This letter reports what we believe to be the first observation of electronic Raman scattering by a transition-metal ion †.

The cobaltous ion was chosen for study because it possesses several low-lying energy levels, and because its optical absorption is compatible with argon laser excitation of the Raman spectrum. Cobalt chloride, which crystallizes with the cadmium chloride structure (space group D_{3d}^5) [4], was chosen as the host material for two reasons. Firstly, the intensity of the electronic transitions is at a maximum because of the high cobalt concentration. Secondly, the cobaltous ion experiences a crystal field that is only a slight trigonal distortion from cubic symmetry. Therefore in $CoCl_2$ we have the interesting case of a trigonal field that can raise degeneracies but remains small enough to be treated by normal perturbation theory.

The Raman spectrum was excited with argon laser radiation at 4880Å, analyzed with a double monochromator, and detected photoelectrically. Single-crystal samples of $CoCl_2$, cleaved along planes perpendicular to the crystal c axis, were mounted on the cold finger of a liquid helium cryostat such that the laser beam travelled through the crystal parallel to the cleavage plane, and the scattered light was collected in the c axis direction. It was found that there was considerable absorption of the laser light. The sample absorption was reduced on cooling, but was still sufficiently high to require surface scattering experiments even at 4.2°K. The electronic Raman spectrum could not be observed at room temperature, presumably because the lines are too wide. On cooling the sample, five electronic lines were seen. Fig. 1 shows typical spectra recorded under similar conditions at both liquid air and liquid helium temperatures. The intensities of these electronic Raman lines are comparable to that of the first-order phonon line at 253 cm^{-1} shown in fig. 1. Details of this phonon spectrum will be reported elsewhere [5]. The electronic frequencies measured at 4.2°K are given in table 1. As shown by fig. 1, the electronic lines sharpen appreciably on lowering the temperature from 83°K to 4.2°K, and shift about 10 cm^{-1} to higher frequencies. The 551 cm^{-1} line has associated with it what appears to be a broader, weaker line on its high-frequency side, and this feature is being further investigated. Temperature dependence studies indicate that its appearance is correlated with the onset of antiferromagnetic ordering.

The energy levels of Co^{2+} in $CoCl_2$ are given by crystal field theory [6-8], and the cumulative effect of different perturbations on the Co^{2+} free-ion ground state is shown in fig. 2. Following the method of Griffith [6], the energy levels of the $^4T_1$ multiplet may be expressed in terms of the

* Research sponsored in part by the Air Force Office of Scientific Research, Office of Aerospace Research, United States Air Force, under AFOSR Grant No. 1275-67 and by the N.Z. University Grants Committee under URG Grant No. 66-241.

** N.Z. University Grants Committee post-graduate scholar.

*** Present address: Department of Chemistry, University of Waterloo, Waterloo, Ontario, Canada.

† An unsuccessful attempt to measure such spectra has been reported by Lockwood [3].

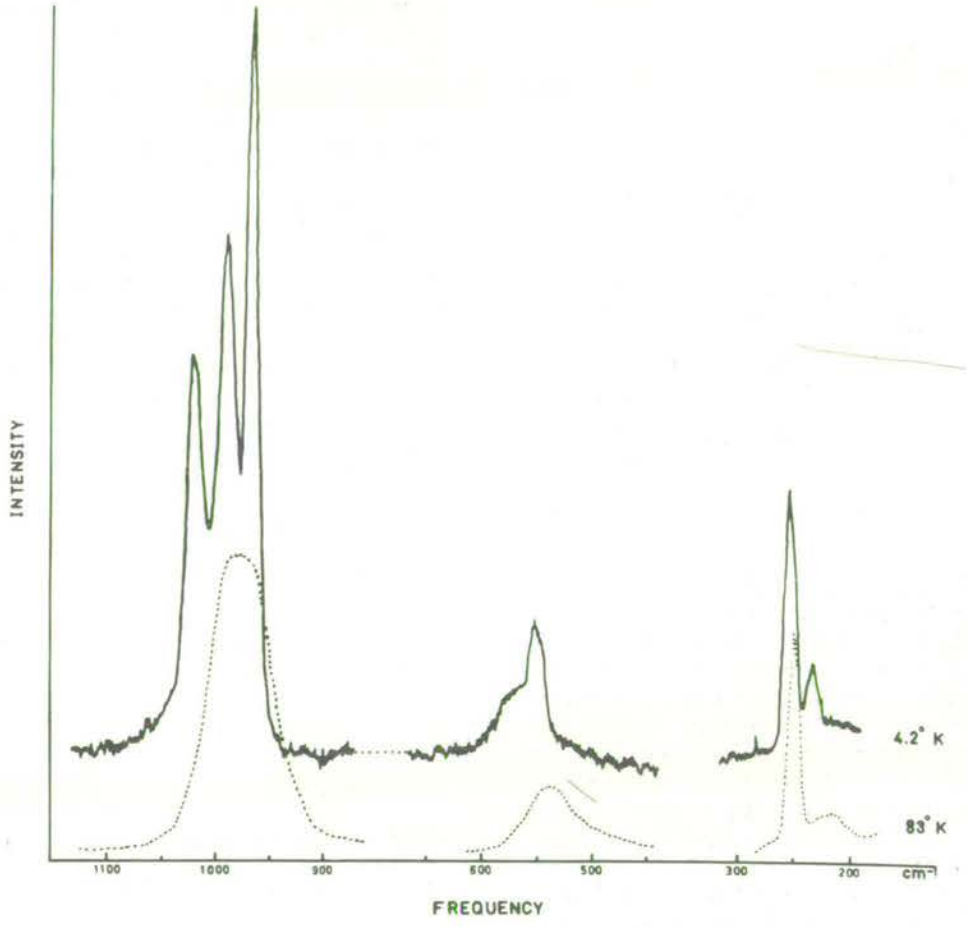

Fig. 1. Electronic Raman spectrum of Co^{2+} in $CoCl_2$.

Table 1
Observed frequencies, assignments and calculated frequencies for the electronic Raman lines in $CoCl_2$ at 4.2°K

Observed frequency (cm^{-1}) ± 1 cm^{-1}	Assignment	Calculated frequencies (cm^{-1})	
		$\delta/\zeta = -0.20$	$\delta/\zeta = -0.97$
233	$^4T_{1,1/2} \rightarrow {}^4T_{1,3/2}$ (±3/2)	340	235
551	$^4T_{1,3/2}$ (±1/2)	394	560
962	$^4T_{1,5/2}$ (±1/2)	958	982
984	$^4T_{1,5/2}$ (±3/2)	986	1081
1014	$^4T_{1,5/2}$ (±5/2)	1012	1202

spin-orbit coupling constant ζ and the parameter δ/ζ [9], where δ is the trigonal field parameter. The resulting energy level scheme is characterised by three groups of levels: a Kramers' doublet lowest, a pair, and a triplet of levels. The experimental data reflects this pattern in showing a pair of lines at 233 and 551 cm^{-1} and a triplet at 962, 984 and 1014 cm^{-1}. However, one

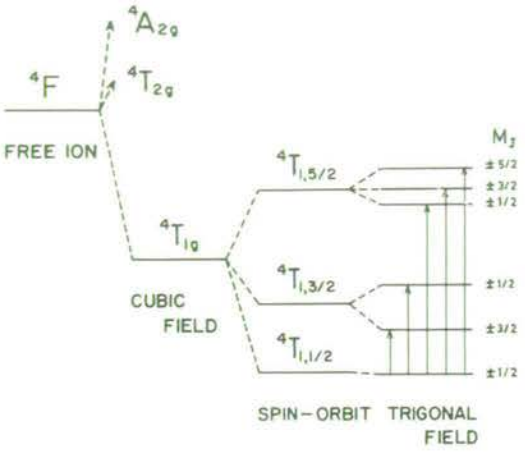

Fig. 2. Ground state energy-level splittings for Co^{2+} in $CoCl_2$.

value of δ/ζ could not give a fit for the pair of lines and for the triplet simultaneously. Table 1 gives the calculated energies for two values of δ/ζ chosen to fit each group separately. The inability to obtain a better fit demonstrates the inadequacy of the crystal field theory for calculating the energy levels. This discrepancy could be a manifestation of the dynamic Jahn-Teller effect operating on the cobalt $^4T_1$ level [10]. The value of 490 cm^{-1} obtained for ζ, which is appropriate for both the triplet and the doublet, is consistent with the previous estimates of 420 cm^{-1} and 528 cm^{-1} made by Ferguson et al. [11] and Lines [8] respectively, and is 9% less than the free-ion value [7].

The infrared absorption spectrum of $CoCl_2$ in the 700 - 1500 cm^{-1} region has been measured by several workers. Newman and Chrenko [12] report absorption peaks at 1195, 985, 905 and 735 cm^{-1} measured at 77°K, while Zvyagin et al. [13] give frequencies of 1188, 1120 and 980 cm^{-1}. We have also measured the infrared spectrum of $CoCl_2$ in this region at 77°K, and like Zvyagin et al. we found no trace of the narrow absorption band at 735 cm^{-1}. This absorption band is produced by a local-mode vibration of an impurity in the crystal [5]. The 905 cm^{-1} band also appears to be impurity induced. Apart from this, the infrared results agree, and there appears to be a coincidence with the Raman band at 984 cm^{-1}. However, Zvyagin et al. give the temperature dependence of the frequency of their 980 cm^{-1} band, which shifts in frequency to 1015 cm^{-1} at 10°K. This suggests that the infrared 980 cm^{-1} band is equivalent to the 1014 cm^{-1} Raman band and is in no way connected with the 984 cm^{-1} Raman band. It is suggested that the remaining higher-frequency infrared bands are vibronic sidebands of the 980 cm^{-1} line, because the energy separations between peaks at ≈ 210 and ≈ 140 cm^{-1} are of the same order as $k = 0$ phonon energies at 190 cm^{-1} and 156 cm^{-1} in $CoCl_2$ [5]. This view is supported by the fact that the 1188 and 1120 cm^{-1} bands are much broader and more intense than the 980 cm^{-1} line [12, 13]. The phonon sideband effectively masks the presence of other electronic lines. This comparison of infrared and Raman spectra serves to emphasize the great advantages of electronic Raman scattering over far infrared absorption in crystals [14]. The electronic Raman spectrum is seldom confused by the crystal phonon energies, whereas the phonons can affect the infrared results in the form of strong lattice absorptions and as vibronic sidebands to "forbidden" electronic lines.

We wish to acknowledge many helpful discussions with Dr. G. D. Jones.

REFERENCES

[1] J. T. Hougen and S. Singh, Phys. Rev. Letters 10 (1963) 406.
[2] J. A. Koningstein and O. S. Mortensen, in: Proceedings of the International Conference on Light Scattering Spectra of Solids, ed. G. B. Wright (Springer, New York, 1969) p. 239.
[3] D. J. Lockwood, in: Proceedings of the International Conference on Light Scattering Spectra of Solids, ed. G. B. Wright (Springer, New York, 1969) p. 75.
[4] R. W. G. Wyckoff, Crystal structures, Vol. 1 (Interscience, New York, 1964).
[5] D. J. Lockwood, to be published
[6] J. S. Griffith, The theory of transition metal ions (Cambridge Univ. Press, London, 1961) p. 360.
[7] A. Abragam and M. H. L. Pryce, Proc. Roy. Soc. A206 (1951) 173.
[8] M. E. Lines, Phys. Rev. 131 (1963) 546.
[9] A. B. Robson, private communication.
[10] M. D. Sturge, in: Solid state physics, Vol. 20, eds. F. Seitz and D. Turnbull (Academic Press, New York, 1967) p. 154.
[11] J. Ferguson, D. L. Wood and K. Knox, J. Chem. Phys. 39 (1963) 881.
[12] R. Newman and R. M. Chrenko, Phys. Rev. 115 (1959) 1147.
[13] A. I. Zvyagin, V. V. Eremenko and I. V. Skorobogatova, Ukrayin. Fiz. Zh. 11 (1966) 520.
[14] A. Kiel, in: Proceedings of the International Conference on Light Scattering Spectra of Solids, ed. G. B. Wright (Springer, New York, 1969) p. 245.

Reprinted from:

THE JOURNAL OF CHEMICAL PHYSICS VOLUME 54, NUMBER 3 1 FEBRUARY 1971

Selection Rules for Three- and Four-Photon Raman Interactions*

J. H. CHRISTIE AND D. J. LOCKWOOD†

Department of Physics, University of Canterbury, Christchurch, New Zealand

(Received 5 March 1970)

The dipole moment induced by a radiation field may be expanded in terms of the electric field vector. The third- and fourth-rank tensors in this expansion, β and γ, respectively, correspond to three- and four-photon Raman effects. Diagrammatic perturbation theory is used to obtain explicit quantum-mechanical expressions for the β and γ tensors. Selection rules for the symmetric γ tensor and for the nonsymmetric β and γ tensors are then calculated for the important molecular point groups. The results are compared with those for the ordinary Raman effect, and conditions necessary for the observation of nonlinear effects are discussed.

I. INTRODUCTION

When a system of nuclei and electrons is subjected to an external electric field, a dipole moment is produced. This induced moment μ may be expanded as a power series in the applied field E:

$$\mu(E)=\alpha E+\beta E^2+\gamma E^3+\cdots. \quad (1)$$

The linear term adequately describes the induced moment for moderate field strengths, but when intense fields are used, the β and γ terms may become significant. At optical frequencies, high-powered lasers have been used to produce nonlinear effects such as second- and third-harmonic generation and frequency mixing. The polarizability expression (1) also relates to Raman processes where the final state of the system after the scattering process differs from the initial state. The field strengths required to produce two-photon stimulated Raman scattering are sufficiently intense to produce observable higher-order Raman scattering.

Selection rules for the Raman process described by β were calculated by Cyvin *et al.*[1] following the first observation of three-photon Raman scattering.[2] In 1965 Dumartin *et al.*[3] observed the ν_7 line of benzene in an inverse Raman experiment carried out near threshold for stimulated Raman emission; these authors attributed the relaxation of selection rules to the high value of the laser field. This view was subsequently confirmed by Ievelva and Karagodova[4] who calculated the transformation properties of the γ tensor for the group D_{6h}, and showed that the ν_7 line, forbidden by the α selection rules, was allowed by those for γ. More recently, three-photon electronic Raman scattering has been observed in K and Rb vapors[5,6] under near-resonance conditions.

In Sec. II of this work diagrammatic perturbation theory[7,8] is used to investigate the explicit form of the Raman tensors for the β and γ terms in the polarizability expansion. Both of the earlier selection rule papers[1,4] assumed tensors β and γ to be totally symmetric with respect to interchange of the component indices, whereas by definition these tensors do not possess this symmetry. On examining the symmetry properties of β and γ we find that in cases favorable for observation of the higher-order effects which they describe, the nonsymmetric components cannot be neglected. Accordingly, in Sec. III we have calculated selection rules for nonsymmetric β and γ terms as well as for the symmetric γ terms for the important molecular point groups including the 32 crystallographic point groups. In Sec. IV, the significance of the selection rules is discussed, and optimum experimental conditions for observation of the three- and four-photon Raman effects are postulated.

II. THEORY

In the electric dipole approximation, the total radiated intensity per unit time of a spontaneous transition from state i to state f of an atomic system is given by[9]

$$I_{if}=(4\omega_0^4/3c^3)\,|\,\mu_{if}\,|^2, \quad (2)$$

where ω_0 is the frequency of the emitted light, c the velocity of light, and μ_{if} the transition moment matrix element derived from the associated dipole moment. For Raman and Rayleigh scattering, the appropriate

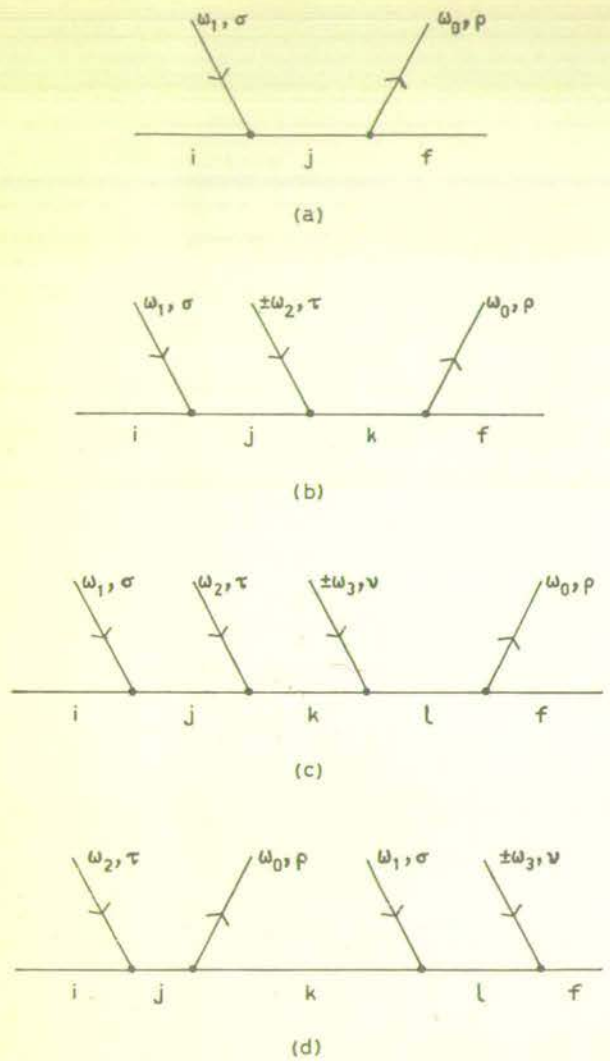

FIG. 1. Perturbation diagrams describing terms contributing to (a) α, (b) β, and (c)–(d) γ Raman tensor components.

moment is given by Eq. (1), which may be written in Cartesian component form as

$$\mu_\rho=\sum_\sigma \alpha_{\rho\sigma}E_\sigma+\sum_{\sigma,\tau}\beta_{\rho\sigma\tau}E_\sigma E_\tau+\sum_{\sigma,\tau,\nu}\gamma_{\rho\sigma\tau\nu}E_\sigma E_\tau E_\nu+\cdots, \quad (3)$$

with $\rho, \sigma, \tau, \nu = x, y,$ or z. The linear term in the expansion (3) gives rise to the well-known two-photon Raman effect in which the emitted light has frequency $\omega_0=\omega_1+\omega_{if}$, where ω_1 is the frequency of the incident light, and $\hbar\omega_{if}$ is the energy difference (E_i-E_f) between states i and f. The quantum mechanical expression for the first-order polarizability is found from second-order time-dependent perturbation theory to be[10]

$$\alpha_{\rho\sigma}{}^{if}=\hbar^{-1}\times\sum_j\left(\frac{\langle f\,|\,M_\rho\,|\,j\rangle\langle j\,|\,M_\sigma\,|\,i\rangle}{\omega_{ji}-\omega_1}+\frac{\langle f\,|\,M_\sigma\,|\,j\rangle\langle j|\,M_\rho\,|\,i\rangle}{\omega_{ji}+\omega_0}\right), \quad (4)$$

provided that ω_0 does not coincide with a resonance frequency of the system. Note that $\alpha_{\rho\sigma}$ is an unsymmetric tensor.

The result (4) can also be obtained using a diagrammatic perturbation technique.[7,8] As Ward has shown, this technique is very useful in describing higher-order effects. It is instructive to consider the diagrams relating to the more familiar α tensor before applying the technique to the hyper-Raman effect. The diagram corresponding to the first term inside the summation in Eq. (4) is given in Fig. 1(a). The second α diagram corresponding to the other term in Eq. (4) is obtained by interchanging the order of the interaction vertices of Fig. 1(a). The diagrams are constructed and interpreted according to the rules given in Refs. 7 and 8.

The β term in the expansion (3) produces several nonlinear effects including three-photon Raman scattering and electric-field induced emission and absorption. We are concerned here only with those phenomena in which the initial and final states of the system differ after the scattering process. The quantum-mechanical expression for the β tensor is

$$\begin{aligned}\beta_{\rho\sigma\tau}{}^{if}=\frac{1}{\hbar^2}\sum_{j,k}\Bigg(&\frac{\langle f\,|\,M_\rho\,|\,k\rangle\langle k\,|\,M_\tau\,|\,j\rangle\langle j\,|\,M_\sigma\,|\,i\rangle}{(\omega_{ji}-\omega_1)(\omega_{kf}-\omega_0)}\\&+\frac{\langle f\,|\,M_\rho\,|\,k\rangle\langle k\,|\,M_\sigma\,|\,j\rangle\langle j\,|\,M_\tau\,|\,i\rangle}{(\omega_{ji}\mp\omega_2)(\omega_{kf}-\omega_0)}\\&+\frac{\langle f\,|\,M_\tau\,|\,k\rangle\langle k\,|\,M_\rho\,|\,j\rangle\langle j\,|\,M_\sigma\,|\,i\rangle}{(\omega_{ji}-\omega_1)(\omega_{kf}\pm\omega_2)}\\&+\frac{\langle f\,|\,M_\tau\,|\,k\rangle\langle k\,|\,M_\sigma\,|\,j\rangle\langle j\,|\,M_\rho\,|\,i\rangle}{(\omega_{ji}+\omega_0)(\omega_{kf}\pm\omega_2)}\\&+\frac{\langle f\,|\,M_\sigma\,|\,k\rangle\langle k\,|\,M_\rho\,|\,j\rangle\langle j\,|\,M_\tau\,|\,i\rangle}{(\omega_{ji}\mp\omega_2)(\omega_{kf}+\omega_1)}\\&+\frac{\langle f\,|\,M_\sigma\,|\,k\rangle\langle k\,|\,M_\tau\,|\,j\rangle\langle j\,|\,M_\rho\,|\,i\rangle}{(\omega_{ji}+\omega_0)(\omega_{kf}+\omega_1)}\Bigg). \quad (5)\end{aligned}$$

This equation was obtained using diagrammatic perturbation theory; it agrees with expressions for β given by Li,[11] and Akhmanov and Klyshko.[12] The diagram corresponding to the first term inside the large parentheses is given in Fig. 1(b). The other five diagrams are obtained by permuting the order of the interaction vertices in this figure.

If we take the incident photon frequencies ω_1 and ω_2 to be equal, as is usually the case, then with the plus sign Eq. (5) describes the hyper-Raman effect with emitted frequency $\omega_0=2\omega_1+\omega_{if}$. With the minus sign, the incident radiation interferes to produce a dc field, and Eq. (5) describes induced electric-dipole emission of frequency $\omega_0=\omega_{if}$. For induced emission we must add another equivalent set of terms to Eq. (5), as the two processes described by $\beta_{\rho\sigma\tau}{}^{if}(\omega_0, -\omega_1, \omega_1)$ and $\beta_{\rho\sigma\tau}{}^{if}(\omega_0, \omega_1, -\omega_1)$ are inseparable. The induced emission

process involves a transition from state i to state f. The tensor for the corresponding absorption process involving a transition from state f to state i is merely the complex conjugate of that for the emission process. When $\omega_1 \neq \omega_2$, the three-photon Raman emission occurs at a frequency given by $\omega_0 = \omega_1 \pm \omega_2 + \omega_{if}$.

Inspection of Eq. (5) shows that when $\omega_1 = \omega_2$ the β tensor is symmetric in the indices σ, τ. That is, $\beta_{\rho\sigma\tau}{}^{if}(\omega_0, \omega_1, \omega_1) = \beta_{\rho\tau\sigma}{}^{if}(\omega_0, \omega_1, \omega_1)$. This is also true for the higher-order emission and absorption processes because of the indistinguishability of the tensors $\beta(\omega_0, -\omega_1, \omega_1)$ and $\beta(\omega_0, \omega_1, -\omega_1)$. If $\omega_1 \neq \omega_2$, then, as in the case of the α tensor, the β tensor does not exhibit any symmetry.

The fourth-order process involving three incident photons of frequency ω_1, ω_2, and ω_3, respectively, is described by the γ term in Eq. (3). The diagrams Fig. 1(c) and Fig. 1(d) illustrate this interaction. From these diagrams, and the other twenty-two similar diagrams, the quantum-mechanical expression for tensor component $\gamma_{\rho\sigma\tau\nu}{}^{if}$ is found from diagrammatic perturbation theory to be

$$
\begin{aligned}
\gamma_{\rho\sigma\tau\nu}{}^{if} = \frac{1}{\hbar^3} \sum_{j,k,l} \Bigg(& \frac{\langle f|M_\rho|l\rangle\langle l|M_\nu|k\rangle\langle k|M_\tau|j\rangle\langle j|M_\sigma|i\rangle}{(\omega_{ji}-\omega_1)(\omega_{ki}-\omega_1-\omega_2)(\omega_{lf}-\omega_0)} + \frac{\langle f|M_\rho|l\rangle\langle l|M_\tau|k\rangle\langle k|M_\nu|j\rangle\langle j|M_\sigma|i\rangle}{(\omega_{ji}-\omega_1)(\omega_{ki}-\omega_1\mp\omega_3)(\omega_{lf}-\omega_0)} \\
& + \frac{\langle f|M_\rho|l\rangle\langle l|M_\nu|k\rangle\langle k|M_\sigma|j\rangle\langle j|M_\tau|i\rangle}{(\omega_{ji}-\omega_2)(\omega_{ki}-\omega_1-\omega_2)(\omega_{lf}-\omega_0)} + \frac{\langle f|M_\rho|l\rangle\langle l|M_\tau|k\rangle\langle k|M_\sigma|j\rangle\langle j|M_\nu|i\rangle}{(\omega_{ji}\mp\omega_3)(\omega_{ki}-\omega_1\mp\omega_3)(\omega_{lf}-\omega_0)} \\
& + \frac{\langle f|M_\rho|l\rangle\langle l|M_\sigma|k\rangle\langle k|M_\nu|j\rangle\langle j|M_\tau|i\rangle}{(\omega_{ji}-\omega_2)(\omega_{ki}-\omega_2\mp\omega_3)(\omega_{lf}-\omega_0)} + \frac{\langle f|M_\rho|l\rangle\langle l|M_\sigma|k\rangle\langle k|M_\tau|j\rangle\langle j|M_\nu|i\rangle}{(\omega_{ji}\mp\omega_3)(\omega_{ki}-\omega_2\mp\omega_3)(\omega_{lf}-\omega_0)} \\
& + \frac{\langle f|M_\nu|l\rangle\langle l|M_\rho|k\rangle\langle k|M_\tau|j\rangle\langle j|M_\sigma|i\rangle}{(\omega_{ji}-\omega_1)(\omega_{ki}-\omega_1-\omega_2)(\omega_{lf}\pm\omega_3)} + \frac{\langle f|M_\tau|l\rangle\langle l|M_\rho|k\rangle\langle k|M_\nu|j\rangle\langle j|M_\sigma|i\rangle}{(\omega_{ji}-\omega_1)(\omega_{ki}-\omega_1\mp\omega_3)(\omega_{lf}+\omega_2)} \\
& + \frac{\langle f|M_\nu|l\rangle\langle l|M_\rho|k\rangle\langle k|M_\sigma|j\rangle\langle j|M_\tau|i\rangle}{(\omega_{ji}-\omega_2)(\omega_{ki}-\omega_1-\omega_2)(\omega_{lf}\pm\omega_3)} + \frac{\langle f|M_\tau|l\rangle\langle l|M_\rho|k\rangle\langle k|M_\sigma|j\rangle\langle j|M_\nu|i\rangle}{(\omega_{ji}\mp\omega_3)(\omega_{ki}-\omega_1\mp\omega_3)(\omega_{lf}+\omega_2)} \\
& + \frac{\langle f|M_\sigma|l\rangle\langle l|M_\rho|k\rangle\langle k|M_\nu|j\rangle\langle j|M_\tau|i\rangle}{(\omega_{ji}-\omega_2)(\omega_{ki}-\omega_1\mp\omega_3)(\omega_{lf}+\omega_1)} + \frac{\langle f|M_\sigma|l\rangle\langle l|M_\rho|k\rangle\langle k|M_\tau|j\rangle\langle j|M_\nu|i\rangle}{(\omega_{ji}\mp\omega_3)(\omega_{ki}-\omega_2\mp\omega_3)(\omega_{lf}+\omega_1)} \\
& + \frac{\langle f|M_\nu|l\rangle\langle l|M_\tau|k\rangle\langle k|M_\rho|j\rangle\langle j|M_\sigma|i\rangle}{(\omega_{ji}-\omega_1)(\omega_{kf}+\omega_2\pm\omega_3)(\omega_{lf}\pm\omega_3)} + \frac{\langle f|M_\tau|l\rangle\langle l|M_\nu|k\rangle\langle k|M_\rho|j\rangle\langle j|M_\sigma|i\rangle}{(\omega_{ji}-\omega_1)(\omega_{kf}+\omega_2\pm\omega_3)(\omega_{lf}+\omega_2)} \\
& + \frac{\langle f|M_\nu|l\rangle\langle l|M_\sigma|k\rangle\langle k|M_\rho|j\rangle\langle j|M_\tau|i\rangle}{(\omega_{ji}-\omega_2)(\omega_{kf}+\omega_1\pm\omega_3)(\omega_{lf}\pm\omega_3)} + \frac{\langle f|M_\tau|l\rangle\langle l|M_\sigma|k\rangle\langle k|M_\rho|j\rangle\langle j|M_\nu|i\rangle}{(\omega_{ji}\mp\omega_3)(\omega_{kf}+\omega_1+\omega_2)(\omega_{lf}+\omega_2)} \\
& + \frac{\langle f|M_\sigma|l\rangle\langle l|M_\nu|k\rangle\langle k|M_\rho|j\rangle\langle j|M_\tau|i\rangle}{(\omega_{ji}-\omega_2)(\omega_{kf}+\omega_1\pm\omega_3)(\omega_{lf}+\omega_1)} + \frac{\langle f|M_\sigma|l\rangle\langle l|M_\tau|k\rangle\langle k|M_\rho|j\rangle\langle j|M_\nu|i\rangle}{(\omega_{ji}\mp\omega_3)(\omega_{kf}+\omega_1+\omega_2)(\omega_{lf}+\omega_1)} \\
& + \frac{\langle f|M_\nu|l\rangle\langle l|M_\tau|k\rangle\langle k|M_\sigma|j\rangle\langle j|M_\rho|i\rangle}{(\omega_{ji}+\omega_0)(\omega_{kf}+\omega_2\pm\omega_3)(\omega_{lf}\pm\omega_3)} + \frac{\langle f|M_\tau|l\rangle\langle l|M_\nu|k\rangle\langle k|M_\sigma|j\rangle\langle j|M_\rho|i\rangle}{(\omega_{ji}+\omega_0)(\omega_{kf}+\omega_2\pm\omega_3)(\omega_{lf}+\omega_2)} \\
& + \frac{\langle f|M_\nu|l\rangle\langle l|M_\sigma|k\rangle\langle k|M_\tau|j\rangle\langle j|M_\rho|i\rangle}{(\omega_{ji}+\omega_0)(\omega_{kf}+\omega_1\pm\omega_3)(\omega_{lf}\pm\omega_3)} + \frac{\langle f|M_\tau|l\rangle\langle l|M_\sigma|k\rangle\langle k|M_\nu|j\rangle\langle j|M_\rho|i\rangle}{(\omega_{ji}+\omega_0)(\omega_{kf}+\omega_1+\omega_2)(\omega_{lf}+\omega_2)} \\
& + \frac{\langle f|M_\sigma|l\rangle\langle l|M_\nu|k\rangle\langle k|M_\tau|j\rangle\langle j|M_\rho|i\rangle}{(\omega_{ji}+\omega_0)(\omega_{kf}+\omega_1\pm\omega_3)(\omega_{lf}+\omega_1)} + \frac{\langle f|M_\sigma|l\rangle\langle l|M_\tau|k\rangle\langle k|M_\nu|j\rangle\langle j|M_\rho|i\rangle}{(\omega_{ji}+\omega_0)(\omega_{kf}+\omega_1+\omega_2)(\omega_{lf}+\omega_1)} \Bigg). \qquad (6)
\end{aligned}
$$

The first and fifteenth terms inside the summation in Eq. (6) correspond to Fig. 1(c) and Fig. 1(d), respectively.

The tensor $\gamma(\omega_0, \omega_1, \omega_2, \pm\omega_3)$ gives rise to four-photon Raman scattering with emitted frequency $\omega_0 = \omega_1 + \omega_2 \pm \omega_3 + \omega_{if}$. If $\omega_1 \neq \omega_2 \neq \omega_3$, then γ is completely unsymmetric. If any two of ω_1, ω_2, and ω_3 are equal, then the tensor is symmetric in the indices with which these frequencies are associated. For example,

$$\gamma_{\rho\sigma\tau\nu}{}^{if}(\omega_0, \omega_1, \omega_1, \omega_3) = \gamma_{\rho\tau\sigma\nu}{}^{if}(\omega_0, \omega_1, \omega_1, \omega_3).$$

However, if we choose $|\omega_3| = \omega_1$ or ω_2 and take the minus sign with ω_3, then we must add two tensors as in the case of β. Therefore, the resultant tensor retains the

symmetry in the appropriate indices. For example, if $\omega_3=\omega_2$ and the minus sign is taken, then the combined tensor element

$$\gamma_{\rho\sigma\tau\nu}{}^{if}=\gamma_{\rho\sigma\tau\nu}{}^{if}(\omega_0,\omega_1,\omega_2,-\omega_2)+\gamma_{\rho\sigma\tau\nu}{}^{if}(\omega_0,\omega_1,-\omega_2,\omega_2)$$

is symmetric with respect to τ and ν. The experimentally interesting case is where $\omega_1=\omega_2=\omega_3$. Choosing the plus sign associated with frequency ω_3 gives four-photon Raman scattering of frequency $\omega_0=3\omega_1+\omega_{if}$, and the γ tensor is symmetric in σ, τ, and ν. If the minus sign is chosen, it is still symmetric in σ, τ, and ν, because the physically observable tensor comprises three equivalent parts $\gamma(\omega_0,\omega_1,\omega_1,-\omega_1)$, $\gamma(\omega_0,\omega_1,-\omega_1,\omega_1)$, and $\gamma(\omega_0,-\omega_1,\omega_1,\omega_1)$. Here the four-photon scattered frequency is $\omega_0=\omega_1+\omega_{if}$, which represents a fourth-order contribution to ordinary Raman scattering.

In their present forms, the α, β, and γ tensors may be used to describe all Raman-type processes. We will now restrict our attention to the vibrational Raman effect.

We have noted that in its general form the α tensor is unsymmetric. Placzek[10] applied a series of approximations to α in the case of the vibrational Raman effect, the result being a symmetric tensor of the form

$$\alpha_{\rho\sigma}=\hbar^{-1}\sum_{nj\neq n0}\left(\frac{(M_\rho)_{0j}(M_\sigma)_{j0}}{\omega_{njn0}+\omega_0}+\frac{(M_\sigma)_{0j}(M_\rho)_{j0}}{\omega_{njn0}-\omega_0}\right), \quad (7)$$

with

$$(M_\rho)_{0j}=\langle n_0\mid M_\rho\mid n_j\rangle,$$

such that

$$\alpha_{\rho\sigma}{}^{if}=\langle v_f\mid\alpha_{\rho\sigma}\mid v_i\rangle.$$

The n's and v's label the electronic and vibrational states, respectively. The approximations used are valid under the condition that the electronic ground state is not degenerate, and that $\omega_0\gg\omega_{v_iv_f}$ and $(\omega_{njn0}-\omega_0)\gg\omega_{v_iv_f}$.

Li[11] applied the same approximations to $\beta_{\rho\sigma\tau}{}^{if}(\omega_0,\omega_1,\omega_2)$ and found that the simplified tensor elements $\beta_{\rho\sigma\tau}(\omega_0,\omega_1,\omega_2)$, defined in an anlogous manner to $\alpha_{\rho\sigma}(\omega_0,\omega_1)$, possess no symmetry in any coordinates, and that $\beta_{\rho\sigma\tau}(\omega_0,\omega_1,\omega_1)$ is symmetric in σ and τ only. Thus the symmetry of β is not altered under Placzek's approximation.

We have investigated in the same manner as Li the tensors describing the various fourth-order processes. It is a simple matter to prove that the simplified γ tensors do not possess any extra symmetry. For example, the term

$$\frac{1}{\hbar^3}\sum_{nj\neq0,nk\neq0,nl\neq0}\frac{(M_\rho)_{0l}(M_\nu)_{lk}(M_\tau)_{kj}(M_\sigma)_{j0}}{(\omega_{njn0}-\omega_1)(\omega_{nkn0}-\omega_1-\omega_2)(\omega_{nln0}-\omega_0)}$$

in the expansion of $\gamma_{\rho\sigma\tau\nu}(\omega_0,\omega_1,\omega_2,\omega_3)$ is totally unsymmetric, and there are no other terms with the same denominator.

Therefore, at first glance it appears unnecessary to distinguish between the symmetric and nonsymmetric parts of β and γ. However, Zhu[13] has pointed out that $\beta_{\rho\sigma\tau}(\omega_0,\omega_1,\omega_2)$ becomes symmetric under the condition that $(\omega_{0,1,2}/\omega_{njn0})\ll1$. Similarly, when $(\omega_{0,1,2,3}/\omega_{njn0})\ll1$, γ becomes a symmetric tensor. This behavior demonstrates the different frequency dependence of the magnitudes of the symmetric and nonsymmetric parts of the β and γ tensors. For both β and γ, the nonsymmetric part of the tensor becomes less significant as the photon energies become smaller. This statement also holds for α, as has been demonstrated by Placzek.[14] It thus becomes necessary to distinguish between those transitions involving the symmetric parts of the tensors from those involving the nonsymmetric parts. This is achieved by listing separately the transformation properties of the symmetric and nonsymmetric parts of the tensors. This procedure has the added advantage of enabling correlation with tables already published[1,4,11] which list the symmetric parts only. Strictly speaking, this other work is not correct, as the true selection rules are given by the properties of the complete tensor. When the incident radiation is of low frequency and far away from resonance, it may be that only the symmetric part is important in the vibrational Raman effect; but under practical conditions with excitation at optical frequencies the frequency dependence indicates that this is not so, as here $(\omega_{0,1,2,3}/\omega_{njn0})\sim0.3$. Thus even though the α tensor becomes symmetric in the vibrational Raman effect, there is no justification for ignoring asymmetric parts in the β and γ tensors.

For Raman scattering by excitations other than vibrations, such as in the electronic Raman effect, the general Raman tensor applies, and the symmetric and nonsymmetric selection rules must both be considered.

III. SELECTION RULES

In Sec. II the symmetries of the β and γ tensors were discussed, and it was shown that in the case of single-frequency excitation $\beta_{\rho\sigma\tau}{}^{if}$ is symmetric with respect to permutation of the indices σ and τ, and $\gamma_{\rho\sigma\tau\nu}{}^{if}$ is symmetric in the indices σ, τ, and ν. In order to analyze these symmetries we make use of the permutation group associated with each tensor. These groups are defined as the set of permutation operators which, when operating on a tensor component, yield every independent component that may be produced by permuting the indices of that component. For an nth-rank tensor possessing no symmetry the appropriate group is merely the symmetric group S_n; but if the tensor does have some symmetry, the required group is a subgroup of S_n. For example, consider a nonsymmetric second-rank tensor such as the α tensor used in describing the electronic Raman effect. The associated permutation group is $S_2=\{E,(12)\}$. If α is symmetric, the appropriate subgroup is the trivial group $\{E\}$. Examination of tables of subgroups of the symmetric groups shows that the groups associated with $\beta(\omega_0,\omega_1,\omega_1)$ and $\gamma(\omega_0,\omega_1,\omega_1,\omega_1)$ are the subgroups H_4 and H_5 of S_4, respectively.[15] The character tables for these groups are readily obtained from those of the parent group.[16] They are,

or α:

S_2	E	(12)	n
	1	1	6
	1	−1	3

or β:

H_4	E	(123)	(132)	n
	1	1	1	10
	1	ϵ	ϵ^*	4
	1	ϵ^*	ϵ	4

where $\epsilon=\exp(2\pi i/3)$; and for γ:

H_5	E	(1234)	$(13)(24)$	(1432)	n
	1	1	1	1	15
	1	1	−1	−1	5
	1	−1	1	−1	5
	1	−1	−1	1	5

The number n associated with each representation is the number of components of the appropriate tensor which transform according to that representation.[17] The tensors transforming as each representation may be obtained by operating on the general tensor with the projection operator of each representation.[18] In the cases we are considering, the tensors transforming according to the nonsymmetric representations do not possess any mutual distinction, but each of them is clearly distinguishable from the corresponding totally symmetric tensor. Furthermore, it is evident from Sec. I that the relative magnitudes of the symmetric and nonsymmetric tensors is variable, depending on the physical constants of a particular experiment. Therefore, we shall tabulate separately the selection rules for the symmetric and the nonsymmetric β and γ tensors. Selection rules for the general tensors may be obtained by addition of the symmetric and nonsymmetric components transforming under each representation. It should be noted that since the selection rules depend only on the rank and symmetry of the β and γ tensors, they are applicable to any process described by such tensors.

In order to calculate the nonsymmetric part of each tensor we add together all tensors transforming according to the nonsymmetric irreducible representations of H_4 and H_5. Thus for β we have

$$\bar{\beta}_{\rho\sigma\tau}=P_{R_2}\beta_{\rho\sigma\tau}+P_{R_3}\beta_{\rho\sigma\tau}=(P_{R_2}+P_{R_3})\beta_{\rho\sigma\tau},$$

where P_{R_i} is the projection operator constructed on the ith representation of H_4; and similarly for $\bar{\gamma}$. The resulting nonsymmetric tensors have the following forms:

$$\bar{\beta}_{\rho\sigma\tau}=\tfrac{1}{3}(2\beta_{\rho\sigma\tau}-\beta_{\tau\rho\sigma}-\beta_{\sigma\tau\rho})$$

and

$$\bar{\gamma}_{\rho\sigma\tau\nu}=\tfrac{1}{4}(3\gamma_{\rho\sigma\tau\nu}-\gamma_{\nu\rho\sigma\tau}-\gamma_{\tau\nu\rho\sigma}-\gamma_{\sigma\tau\nu\rho}).$$

The corresponding expression for $\bar{\alpha}$ is $\bar{\alpha}_{\rho\sigma}=\frac{1}{2}(\alpha_{\rho\sigma}-\alpha_{\sigma\rho})$. The symmetry of $\bar{\beta}$ and $\bar{\gamma}$ is described by the two equations

$$\bar{\beta}_{\rho\sigma\tau}+\bar{\beta}_{\tau\rho\sigma}+\bar{\beta}_{\sigma\tau\rho}=0$$

and

$$\bar{\gamma}_{\rho\sigma\tau\nu}+\bar{\gamma}_{\nu\rho\sigma\tau}+\bar{\gamma}_{\tau\nu\rho\sigma}+\bar{\gamma}_{\sigma\tau\nu\rho}=0.$$

These relations are an expression of the fact that neither tensor contains a totally symmetric part. The equations can be used to find detailed relations between the elements of the tensors. For example, $\bar{\beta}_{iij}+2\bar{\beta}_{jii}=0$ and $\bar{\beta}_{iii}=0$. Similar relations hold for $\bar{\gamma}$. Both $\bar{\beta}$ and $\bar{\gamma}$ retain any symmetry possessed by the general tensor; these tensors can be recovered from $\bar{\beta}$ and $\bar{\gamma}$ by adding in the corresponding totally symmetric tensor. We have used the symbols $\bar{\alpha}$, $\bar{\beta}$, and $\bar{\gamma}$ to represent, respectively, the antisymmetric part of the α tensor and the nonsymmetric parts of the β and γ tensors; from now on, the symbols α, β, and γ will be used to denote the totally symmetric tensors.

The transformation properties of β, $\bar{\beta}$, γ, and $\bar{\gamma}$ have been calculated for the important molecular point groups by the method of projection operators using an IBM 360/44 computer. The results are listed in Table I together with the selection rules for α and $\bar{\alpha}$. In order to simplify the tables, the various linear combinations which appear are represented by numerically subscripted symbols. Table II gives the correspondence between these two representations. Groups which contain inversion symmetry have been omitted from the tables, as these are always equal to the direct product of the group C_i and some other point group. Selection rules for groups containing inversion may be obtained from the parent point group by applying the following rules: (1) The α, $\bar{\alpha}$, γ, and $\bar{\gamma}$ tensors always transform as the even representations, and the β and $\bar{\beta}$ tensors as the odd representations: (2) the distribution of the tensor components among the odd or even representations is identical with the distribution among the representations of the parent group. As an example we give some of the selection rules for the group $C_{2h}=C_2\times C_i$:

C_{2h}	
A_g	$\alpha_{xx}, \alpha_{yy}, \alpha_{zz}, \alpha_{xy}$
B_g	α_{yz}, α_{zx}
A_u	$\bar{\beta}_2, \bar{\beta}_4, \bar{\beta}_7, \bar{\beta}_8$
B_u	$\bar{\beta}_1, \bar{\beta}_3, \bar{\beta}_5, \bar{\beta}_6$

There exists a simple control method for checking the results in Table I. The method consists of first forming a reducible representation of each group using the components of the tensor under investigation as a basis, and then analyzing it using the formula[19]

$$n_i=N^{-1}\sum_R \chi(R)\chi_i(R), \qquad (8)$$

where N is the order of the group, $\chi(R)$ the character of the reducible representation corresponding to the element R of the group, $\chi_i(R)$ the corresponding character of the ith irreducible representation of the group,

TABLE I. Selection rules for single-frequency excitation of two-, three-, and four-photon Raman effects.

A. The groups C_s and C_n ($n=2, 3, 4, 5, 6$)

C_s	A'	$\alpha_{xx}, \alpha_{yy}, \alpha_{zz}, \alpha_{xy}$	$\bar{\alpha}_{xy}$	$\beta_1, \beta_2, \beta_4, \beta_6, \beta_8, \beta_9$	$\bar{\beta}_1, \bar{\beta}_3, \bar{\beta}_5, \bar{\beta}_6$	$\gamma_1, \gamma_2, \gamma_3, \gamma_4, \gamma_5, \gamma_6, \gamma_7, \gamma_9, \gamma_{15}$	$\bar{\gamma}_1, \bar{\gamma}_3, \bar{\gamma}_7, \bar{\gamma}_8, \bar{\gamma}_9, \bar{\gamma}_{10}, \bar{\gamma}_{11}$
	A''	α_{yz}, α_{zx}	$\bar{\alpha}_{yz}, \bar{\alpha}_{zx}$	$\beta_3, \beta_5, \beta_7, \beta_{10}$	$\bar{\beta}_2, \bar{\beta}_4, \bar{\beta}_7, \bar{\beta}_8$	$\gamma_8, \gamma_{10}, \gamma_{11}, \gamma_{12}, \gamma_{13}, \gamma_{14}$	$\bar{\gamma}_2, \bar{\gamma}_4, \bar{\gamma}_5, \bar{\gamma}_6, \bar{\gamma}_{12}, \bar{\gamma}_{13}, \bar{\gamma}_{14}, \bar{\gamma}_{15}$
C_2	A	$\alpha_{xx}, \alpha_{yy}, \alpha_{zz}, \alpha_{xy}$	$\bar{\alpha}_{xy}$	$\beta_3, \beta_5, \beta_7, \beta_{10}$	$\bar{\beta}_2, \bar{\beta}_4, \bar{\beta}_7, \bar{\beta}_8$	$\gamma_1, \gamma_2, \gamma_3, \gamma_4, \gamma_5, \gamma_6, \gamma_7, \gamma_9, \gamma_{15}$	$\bar{\gamma}_1, \bar{\gamma}_3, \bar{\gamma}_7, \bar{\gamma}_8, \bar{\gamma}_9, \bar{\gamma}_{10}, \bar{\gamma}_{11}$
	B	α_{yz}, α_{zx}	$\bar{\alpha}_{yz}, \bar{\alpha}_{zx}$	$\beta_1, \beta_2, \beta_4, \beta_6, \beta_8, \beta_9$	$\bar{\beta}_1, \bar{\beta}_3, \bar{\beta}_5, \bar{\beta}_6$	$\gamma_8, \gamma_{10}, \gamma_{11}, \gamma_{12}, \gamma_{13}, \gamma_{14}$	$\bar{\gamma}_2, \bar{\gamma}_4, \bar{\gamma}_5, \bar{\gamma}_6, \bar{\gamma}_{12}, \bar{\gamma}_{13}, \bar{\gamma}_{14}, \bar{\gamma}_{15}$
C_3	A	$\alpha_{xx}+\alpha_{yy}, \alpha_{zz}$	$\bar{\alpha}_{xy}$	$\beta_3, \beta_{13}, \beta_{19}, \beta_{20}$	$\bar{\beta}_{11}, \bar{\beta}_{16}$	$\gamma_3, \gamma_{20}, \gamma_{22}, \gamma_{34}, \gamma_{35}$	$\bar{\gamma}_{19}, \bar{\gamma}_{23}, \bar{\gamma}_{29}, \bar{\gamma}_{34}, \bar{\gamma}_{35}$
	E	$(\alpha_{xx}-\alpha_{yy}, \alpha_{xy})$, $(\alpha_{yz}, \alpha_{zx})$	$(\bar{\alpha}_{yz}, \bar{\alpha}_{zx})$	(β_8, β_9), (β_{10}, β_{16}), (β_{17}, β_{18})	$(\bar{\beta}_1, \bar{\beta}_3)$, $(\bar{\beta}_5, \bar{\beta}_6)$, $(\bar{\beta}_{14}, \bar{\beta}_{15})$	$(\gamma_{11}, \gamma_{12})$, $(\gamma_{15}, \gamma_{23})$, $(\gamma_{17}, \gamma_{26})$, $(\gamma_{21}, \gamma_{29})$, $(\gamma_{32}, \gamma_{33})$	$(\bar{\gamma}_5, \bar{\gamma}_6)$, $(\bar{\gamma}_7, \bar{\gamma}_{16})$, $(\bar{\gamma}_{12}, \bar{\gamma}_{15})$, $(\bar{\gamma}_{22}, \bar{\gamma}_{26})$, $(\bar{\gamma}_{32}, \bar{\gamma}_{33})$
C_4	A	$\alpha_{xx}+\alpha_{yy}, \alpha_{zz}$	$\bar{\alpha}_{xy}$	β_3, β_{13}	$\bar{\beta}_{11}, \bar{\beta}_{16}$	$\gamma_3, \gamma_4, \gamma_{16}, \gamma_{22}, \gamma_{29}$	$\bar{\gamma}_{19}, \bar{\gamma}_{23}, \bar{\gamma}_{29}$
	B	$\alpha_{xx}-\alpha_{yy}, \alpha_{xy}$		β_{10}, β_{16}	$\bar{\beta}_{14}, \bar{\beta}_{15}$	$\gamma_{15}, \gamma_{17}, \gamma_{23}, \gamma_{26}$	$\bar{\gamma}_7, \bar{\gamma}_{16}, \bar{\gamma}_{22}, \bar{\gamma}_{26}$
	E	$(\alpha_{yz}, \alpha_{zx})$	$(\bar{\alpha}_{yz}, \bar{\alpha}_{zx})$	(β_1, β_2), (β_4, β_6), (β_8, β_9)	$(\bar{\beta}_1, \bar{\beta}_3)$, $(\bar{\beta}_5, \bar{\beta}_6)$	(γ_8, γ_{10}), $(\gamma_{11}, \gamma_{12})$, $(\gamma_{13}, \gamma_{14})$	$(\bar{\gamma}_2, \bar{\gamma}_4)$, $(\bar{\gamma}_5, \bar{\gamma}_6)$, $(\bar{\gamma}_{12}, \bar{\gamma}_{15})$, $(\bar{\gamma}_{13}, \bar{\gamma}_{14})$
C_5	A	$\alpha_{xx}+\alpha_{yy}, \alpha_{zz}$	$\bar{\alpha}_{xy}$	β_3, β_{13}	$\bar{\beta}_{11}, \bar{\beta}_{16}$	$\gamma_3, \gamma_{20}, \gamma_{22}$	$\bar{\gamma}_{19}, \bar{\gamma}_{23}, \bar{\gamma}_{29}$
	E_1	$(\alpha_{yz}, \alpha_{zx})$	$(\bar{\alpha}_{yz}, \bar{\alpha}_{zx})$	(β_8, β_9), (β_{17}, β_{18})	$(\bar{\beta}_1, \bar{\beta}_3)$, $(\bar{\beta}_5, \bar{\beta}_6)$	$(\gamma_{11}, \gamma_{12})$, $(\gamma_{21}, \gamma_{29})$, $(\gamma_{32}, \gamma_{33})$	$(\bar{\gamma}_5, \bar{\gamma}_6)$, $(\bar{\gamma}_{12}, \bar{\gamma}_{15})$, $(\bar{\gamma}_{32}, \bar{\gamma}_{33})$
	E_2	$(\alpha_{xx}-\alpha_{yy}, \alpha_{xy})$		(β_{10}, β_{16}), (β_{19}, β_{20})	$(\bar{\beta}_{14}, \bar{\beta}_{15})$	$(\gamma_{15}, \gamma_{23})$, $(\gamma_{17}, \gamma_{26})$, $(\gamma_{34}, \gamma_{35})$	$(\bar{\gamma}_7, \bar{\gamma}_{16})$, $(\bar{\gamma}_{22}, \bar{\gamma}_{26})$, $(\bar{\gamma}_{34}, \bar{\gamma}_{35})$
C_6	A	$\alpha_{xx}+\alpha_{yy}, \alpha_{zz}$	$\bar{\alpha}_{xy}$	β_3, β_{13}	$\bar{\beta}_{11}, \bar{\beta}_{16}$	$\gamma_3, \gamma_{20}, \gamma_{22}$	$\bar{\gamma}_{19}, \bar{\gamma}_{23}, \bar{\gamma}_{29}$
	B			β_{19}, β_{20}		γ_{34}, γ_{35}	$\bar{\gamma}_{34}, \bar{\gamma}_{35}$
	E_1	$(\alpha_{yz}, \alpha_{zx})$	$(\bar{\alpha}_{yz}, \bar{\alpha}_{zx})$	(β_8, β_9), (β_{17}, β_{18})	$(\bar{\beta}_1, \bar{\beta}_3)$, $(\bar{\beta}_5, \bar{\beta}_6)$	$(\gamma_{11}, \gamma_{12})$, $(\gamma_{32}, \gamma_{33})$	$(\bar{\gamma}_5, \bar{\gamma}_6)$, $(\bar{\gamma}_{12}, \bar{\gamma}_{15})$, $(\bar{\gamma}_{32}, \bar{\gamma}_{33})$
	E_2	$(\alpha_{xx}-\alpha_{yy}, \alpha_{xy})$		(β_{10}, β_{16})	$(\bar{\beta}_{14}, \bar{\beta}_{15})$	$(\gamma_{15}, \gamma_{23})$, $(\gamma_{17}, \gamma_{26})$, $(\gamma_{21}, \gamma_{29})$	$(\bar{\gamma}_7, \bar{\gamma}_{16})$, $(\bar{\gamma}_{22}, \bar{\gamma}_{26})$

B. The groups D_n ($n=2, 3, 4, 5, 6$)

D_2	A	$\alpha_{xx}, \alpha_{yy}, \alpha_{zz}$		β_{10}	$\bar{\beta}_7, \bar{\beta}_8$	$\gamma_1, \gamma_2, \gamma_3, \gamma_4, \gamma_5, \gamma_6$	$\bar{\gamma}_7, \bar{\gamma}_8, \bar{\gamma}_9$
	B_1	α_{xy}	$\bar{\alpha}_{xy}$	$\beta_3, \beta_5, \beta_7$	$\bar{\beta}_2, \bar{\beta}_4$	$\gamma_7, \gamma_9, \gamma_{15}$	$\bar{\gamma}_1, \bar{\gamma}_3, \bar{\gamma}_{10}, \bar{\gamma}_{11}$
	B_2	α_{zx}	$\bar{\alpha}_{zx}$	$\beta_2, \beta_4, \beta_9$	$\bar{\beta}_1, \bar{\beta}_6$	$\gamma_8, \gamma_{11}, \gamma_{14}$	$\bar{\gamma}_2, \bar{\gamma}_5, \bar{\gamma}_{14}, \bar{\gamma}_{15}$
	B_3	α_{yz}	$\bar{\alpha}_{yz}$	$\beta_1, \beta_6, \beta_8$	$\bar{\beta}_3, \bar{\beta}_5$	$\gamma_{10}, \gamma_{12}, \gamma_{13}$	$\bar{\gamma}_4, \bar{\gamma}_6, \bar{\gamma}_{12}, \bar{\gamma}_{13}$
D_3	A_1[a]	$\alpha_{xx}+\alpha_{yy}, \alpha_{zz}$		β_{19}	$\bar{\beta}_{16}$	$\gamma_3, \gamma_{20}, \gamma_{22}, \gamma_{35}$	$\bar{\gamma}_{23}, \bar{\gamma}_{35}$
	A_2[a]		$\bar{\alpha}_{xy}$	$\beta_3, \beta_{13}, \beta_{20}$	$\bar{\beta}_{11}$	γ_{34}	$\bar{\gamma}_{19}, \bar{\gamma}_{29}, \bar{\gamma}_{34}$
	E	$(\alpha_{xx}-\alpha_{yy}, \alpha_{xy})$, $(\alpha_{yz}, \alpha_{zx})$	$(\bar{\alpha}_{yz}, \bar{\alpha}_{zx})$	(β_8, β_9), (β_{10}, β_{16}), (β_{17}, β_{18})	$(\bar{\beta}_1, \bar{\beta}_3)$, $(\bar{\beta}_5, \bar{\beta}_6)$, $(\bar{\beta}_{14}, \bar{\beta}_{15})$	$(\gamma_{11}, \gamma_{12})$, $(\gamma_{15}, \gamma_{23})$, $(\gamma_{17}, \gamma_{26})$, $(\gamma_{21}, \gamma_{29})$, $(\gamma_{32}, \gamma_{33})$	$(\bar{\gamma}_5, \bar{\gamma}_6)$, $(\bar{\gamma}_7, \bar{\gamma}_{16})$, $(\bar{\gamma}_{12}, \bar{\gamma}_{15})$, $(\bar{\gamma}_{22}, \bar{\gamma}_{26})$, $(\bar{\gamma}_{32}, \bar{\gamma}_{33})$
D_4	A_1	$\alpha_{xx}+\alpha_{yy}, \alpha_{zz}$			$\bar{\beta}_{16}$	$\gamma_3, \gamma_4, \gamma_{16}, \gamma_{22}$	$\bar{\gamma}_{23}$
	A_2		$\bar{\alpha}_{xy}$	β_3, β_{13}	$\bar{\beta}_{11}$	γ_{29}	$\bar{\gamma}_{19}, \bar{\gamma}_{29}$
	B_1	$\alpha_{xx}-\alpha_{yy}$		β_{10}	$\bar{\beta}_{15}$	γ_{17}, γ_{23}	$\bar{\gamma}_7, \bar{\gamma}_{22}$
	B_2	α_{xy}		β_{16}	$\bar{\beta}_{14}$	γ_{15}, γ_{26}	$\bar{\gamma}_{16}, \bar{\gamma}_{26}$
	E	$(\alpha_{yz}, \alpha_{zx})$	$(\bar{\alpha}_{yz}, \bar{\alpha}_{zx})$	(β_1, β_2), (β_4, β_6), (β_8, β_9)	$(\bar{\beta}_1, \bar{\beta}_3)$, $(\bar{\beta}_5, \bar{\beta}_6)$	(γ_8, γ_{10}), $(\gamma_{11}, \gamma_{12})$, $(\gamma_{13}, \gamma_{14})$	$(\bar{\gamma}_2, \bar{\gamma}_4)$, $(\bar{\gamma}_5, \bar{\gamma}_6)$, $(\bar{\gamma}_{12}, \bar{\gamma}_{15})$, $(\bar{\gamma}_{13}, \bar{\gamma}_{14})$
D_5	A_1	$\alpha_{xx}+\alpha_{yy}, \alpha_{zz}$			$\bar{\beta}_{16}$	$\gamma_3, \gamma_{20}, \gamma_{22}$	$\bar{\gamma}_{23}$
	A_2		$\bar{\alpha}_{xy}$	β_3, β_{13}	$\bar{\beta}_{11}$		$\bar{\gamma}_{19}, \bar{\gamma}_{29}$
	E_1	$(\alpha_{yz}, \alpha_{zx})$	$(\bar{\alpha}_{yz}, \bar{\alpha}_{zx})$	(β_8, β_9), (β_{17}, β_{18})	$(\bar{\beta}_1, \bar{\beta}_3)$, $(\bar{\beta}_5, \bar{\beta}_6)$	$(\gamma_{11}, \gamma_{12})$, $(\gamma_{21}, \gamma_{29})$, $(\gamma_{32}, \gamma_{33})$	$(\bar{\gamma}_5, \bar{\gamma}_6)$, $(\bar{\gamma}_{12}, \bar{\gamma}_{15})$, $(\bar{\gamma}_{32}, \bar{\gamma}_{33})$
	E_2	$(\alpha_{xx}-\alpha_{yy}, \alpha_{xy})$		(β_{10}, β_{16}), (β_{19}, β_{20})	$(\bar{\beta}_{14}, \bar{\beta}_{15})$	$(\gamma_{15}, \gamma_{23})$, $(\gamma_{17}, \gamma_{26})$, $(\gamma_{34}, \gamma_{35})$	$(\bar{\gamma}_7, \bar{\gamma}_{16})$, $(\bar{\gamma}_{22}, \bar{\gamma}_{26})$, $(\bar{\gamma}_{34}, \bar{\gamma}_{35})$

TABLE I (*Continued*)

D_6	A_1	$\alpha_{xx}+\alpha_{yy}, \alpha_{zz}$			$\bar{\beta}_{16}$	$\gamma_3, \gamma_{20}, \gamma_{22}$	$\bar{\gamma}_{23}$
	A_2		$\bar{\alpha}_{xy}$	β_3, β_{13}	$\bar{\beta}_{11}$		$\bar{\gamma}_{19}, \bar{\gamma}_{29}$
	B_1[b]			β_{19}		γ_{35}	$\bar{\gamma}_{35}$
	B_2[b]			β_{20}		γ_{34}	$\bar{\gamma}_{34}$
	E_1	$(\alpha_{yz}, \alpha_{zx})$	$(\bar{\alpha}_{yz}, \bar{\alpha}_{zx})$	$(\beta_8, \beta_9), (\beta_{17}, \beta_{18})$	$(\bar{\beta}_1, \bar{\beta}_3), (\bar{\beta}_5, \bar{\beta}_6)$	$(\gamma_{11}, \gamma_{12}), (\gamma_{32}, \gamma_{33})$	$(\bar{\gamma}_5, \bar{\gamma}_6), (\bar{\gamma}_{12}, \bar{\gamma}_{15}), (\bar{\gamma}_{32}, \bar{\gamma}_{33})$
	E_2	$(\alpha_{xx}-\alpha_{yy}, \alpha_{xy})$		(β_{10}, β_{16})	$(\bar{\beta}_{14}, \bar{\beta}_{15})$	$(\gamma_{15}, \gamma_{23}), (\gamma_{17}, \gamma_{26}), (\gamma_{21}, \gamma_{29})$	$(\bar{\gamma}_7, \bar{\gamma}_{16}), (\bar{\gamma}_{22}, \bar{\gamma}_{26})$

C. The groups C_{nv} ($n=2, 3, 4, 5, 6$)

C_{2v}	A_1	$\alpha_{xx}, \alpha_{yy}, \alpha_{zz}$		$\beta_2, \beta_5, \beta_7$	$\bar{\beta}_2, \bar{\beta}_4$	$\gamma_1, \gamma_2, \gamma_3, \gamma_4, \gamma_5, \gamma_6$	$\bar{\gamma}_7, \bar{\gamma}_8, \bar{\gamma}_9$
	A_2	α_{xy}	$\bar{\alpha}_{xy}$	β_{10}	$\bar{\beta}_7, \bar{\beta}_8$	$\gamma_7, \gamma_9, \gamma_{15}$	$\bar{\gamma}_1, \bar{\gamma}_3, \bar{\gamma}_{10}, \bar{\gamma}_{11}$
	B_1	α_{zx}	$\bar{\alpha}_{zx}$	$\beta_1, \beta_6, \beta_8$	$\bar{\beta}_3, \bar{\beta}_5$	$\gamma_8, \gamma_{11}, \gamma_{14}$	$\bar{\gamma}_2, \bar{\gamma}_5, \bar{\gamma}_{14}, \bar{\gamma}_{15}$
	B_2	α_{yz}	$\bar{\alpha}_{yz}$	$\beta_2, \beta_4, \beta_9$	$\bar{\beta}_1, \bar{\beta}_6$	$\gamma_{10}, \gamma_{12}, \gamma_{13}$	$\bar{\gamma}_4, \bar{\gamma}_6, \bar{\gamma}_{12}, \bar{\gamma}_{13}$
C_{3v}	A_1[c]	$\alpha_{xx}+\alpha_{yy}, \alpha_{zz}$		$\beta_3, \beta_{13}, \beta_{19}$	$\bar{\beta}_{11}$	$\gamma_3, \gamma_{20}, \gamma_{22}, \gamma_{34}$	$\bar{\gamma}_{23}, \bar{\gamma}_{34}$
	A_2[c]		$\bar{\alpha}_{xy}$	β_{20}	$\bar{\beta}_{16}$	γ_{35}	$\bar{\gamma}_{19}, \bar{\gamma}_{29}, \bar{\gamma}_{35}$
	E	$(\alpha_{xx}-\alpha_{yy}, \alpha_{xy}),$ $(\alpha_{yz}, \alpha_{zx})$	$(\bar{\alpha}_{yz}, \bar{\alpha}_{zx})$	$(\beta_8, \beta_9), (\beta_{10}, \beta_{16}),$ (β_{17}, β_{18})	$(\bar{\beta}_1, \bar{\beta}_3), (\bar{\beta}_5, \bar{\beta}_6),$ $(\bar{\beta}_{14}, \bar{\beta}_{15})$	$(\gamma_{11}, \gamma_{12}), (\gamma_{15}, \gamma_{23}), (\gamma_{17}, \gamma_{26}),$ $(\gamma_{21}, \gamma_{29}), (\gamma_{32}, \gamma_{33})$	$(\bar{\gamma}_5, \bar{\gamma}_6), (\bar{\gamma}_7, \bar{\gamma}_{16}), (\bar{\gamma}_{12}, \bar{\gamma}_{15}),$ $(\bar{\gamma}_{22}, \bar{\gamma}_{26}), (\bar{\gamma}_{32}, \bar{\gamma}_{33})$
C_{4v}	A_1	$\alpha_{xx}+\alpha_{yy}, \alpha_{zz}$		β_3, β_{13}	$\bar{\beta}_{11}$	$\gamma_3, \gamma_4, \gamma_{16}, \gamma_{22}$	$\bar{\gamma}_{23}$
	A_2		$\bar{\alpha}_{xy}$		$\bar{\beta}_{16}$	γ_{29}	$\bar{\gamma}_{19}, \bar{\gamma}_{29}$
	B_1	$\alpha_{xx}-\alpha_{yy}$		β_{16}	$\bar{\beta}_{14}$	γ_{17}, γ_{23}	$\bar{\gamma}_7, \bar{\gamma}_{22}$
	B_2	α_{xy}		β_{10}	$\bar{\beta}_{15}$	γ_{15}, γ_{26}	$\bar{\gamma}_{16}, \bar{\gamma}_{26}$
	E	$(\alpha_{yz}, \alpha_{zx})$	$(\bar{\alpha}_{yz}, \bar{\alpha}_{zx})$	$(\beta_1, \beta_2), (\beta_4, \beta_6), (\beta_8, \beta_9)$	$(\bar{\beta}_1, \bar{\beta}_3), (\bar{\beta}_5, \bar{\beta}_6)$	$(\gamma_8, \gamma_{10}), (\gamma_{11}, \gamma_{12}), (\gamma_{13}, \gamma_{14})$	$(\bar{\gamma}_2, \bar{\gamma}_4), (\bar{\gamma}_5, \bar{\gamma}_6), (\bar{\gamma}_{12}, \bar{\gamma}_{15}),$ $(\bar{\gamma}_{13}, \bar{\gamma}_{14})$
C_{5v}	A_1	$\alpha_{xx}+\alpha_{yy}, \alpha_{zz}$		β_3, β_{13}	$\bar{\beta}_{11}$	$\gamma_3, \gamma_{20}, \gamma_{22}$	$\bar{\gamma}_{23}$
	A_2		$\bar{\alpha}_{xy}$		$\bar{\beta}_{16}$		$\bar{\gamma}_{19}, \bar{\gamma}_{29}$
	E_1	$(\alpha_{yz}, \alpha_{zx})$	$(\bar{\alpha}_{yz}, \bar{\alpha}_{zx})$	$(\beta_8, \beta_9), (\beta_{17}, \beta_{18})$	$(\bar{\beta}_1, \bar{\beta}_3), (\bar{\beta}_5, \bar{\beta}_6)$	$(\gamma_{11}, \gamma_{12}), (\gamma_{21}, \gamma_{29}), (\gamma_{32}, \gamma_{33})$	$(\bar{\gamma}_5, \bar{\gamma}_6), (\bar{\gamma}_{12}, \bar{\gamma}_{15}), (\bar{\gamma}_{32}, \bar{\gamma}_{33})$
	E_2	$(\alpha_{xx}-\alpha_{yy}, \alpha_{xy})$		$(\beta_{10}, \beta_{16}), (\beta_{19}, \beta_{20})$	$(\bar{\beta}_{14}, \bar{\beta}_{15})$	$(\gamma_{15}, \gamma_{23}), (\gamma_{17}, \gamma_{26}), (\gamma_{34}, \gamma_{35})$	$(\bar{\gamma}_7, \bar{\gamma}_{16}), (\bar{\gamma}_{22}, \bar{\gamma}_{26}), (\bar{\gamma}_{34}, \bar{\gamma}_{35})$
C_{6v}	A_1	$\alpha_{xx}+\alpha_{yy}, \alpha_{zz}$		β_3, β_{13}	$\bar{\beta}_{11}$	$\gamma_3, \gamma_{20}, \gamma_{22}$	$\bar{\gamma}_{23}$
	A_2		$\bar{\alpha}_{xy}$		$\bar{\beta}_{16}$		$\bar{\gamma}_{19}, \bar{\gamma}_{29}$
	B_1[c]			β_{19}		γ_{34}	$\bar{\gamma}_{34}$
	B_2[c]			β_{20}		γ_{35}	$\bar{\gamma}_{35}$
	E_1	$(\alpha_{yz}, \alpha_{zx})$	$(\bar{\alpha}_{yz}, \bar{\alpha}_{zx})$	$(\beta_8, \beta_9), (\beta_{17}, \beta_{18})$	$(\bar{\beta}_1, \bar{\beta}_3), (\bar{\beta}_5, \bar{\beta}_6)$	$(\gamma_{11}, \gamma_{12}), (\gamma_{32}, \gamma_{33})$	$(\bar{\gamma}_5, \bar{\gamma}_6), (\bar{\gamma}_{12}, \bar{\gamma}_{15}), (\bar{\gamma}_{32}, \bar{\gamma}_{33})$
	E_2	$(\alpha_{xx}-\alpha_{yy}, \alpha_{xy})$		(β_{10}, β_{16})	$(\bar{\beta}_{14}, \bar{\beta}_{15})$	$(\gamma_{15}, \gamma_{23}), (\gamma_{17}, \gamma_{26}), (\gamma_{21}, \gamma_{29})$	$(\bar{\gamma}_7, \bar{\gamma}_{16}), (\bar{\gamma}_{22}, \bar{\gamma}_{26})$

D. The groups C_{nh} ($n=3, 5$)

C_{3h}	A'	$\alpha_{xx}+\alpha_{yy}, \alpha_{zz}$	$\bar{\alpha}_{xy}$	β_{19}, β_{20}		$\gamma_3, \gamma_{20}, \gamma_{22}$	$\bar{\gamma}_{19}, \bar{\gamma}_{23}, \bar{\gamma}_{29}$
	E'	$(\alpha_{xx}-\alpha_{yy}, \alpha_{xy})$		$(\beta_8, \beta_9), (\beta_{17}, \beta_{18})$	$(\bar{\beta}_1, \bar{\beta}_3), (\bar{\beta}_5, \bar{\beta}_6)$	$(\gamma_{15}, \gamma_{23}), (\gamma_{17}, \gamma_{26}), (\gamma_{21}, \gamma_{29})$	$(\bar{\gamma}_7, \bar{\gamma}_{16}), (\bar{\gamma}_{22}, \bar{\gamma}_{26})$
	A''			β_3, β_{13}	$\bar{\beta}_{11}, \bar{\beta}_{16}$	γ_{34}, γ_{35}	$\bar{\gamma}_{34}, \bar{\gamma}_{35}$
	E''	$(\alpha_{yz}, \alpha_{zx})$	$(\bar{\alpha}_{yz}, \bar{\alpha}_{zx})$	(β_{10}, β_{16})	$(\bar{\beta}_{14}, \bar{\beta}_{15})$	$(\gamma_{11}, \gamma_{12}), (\gamma_{32}, \gamma_{33})$	$(\bar{\gamma}_5, \bar{\gamma}_6), (\bar{\gamma}_{12}, \bar{\gamma}_{15}), (\bar{\gamma}_{32}, \bar{\gamma}_{33})$
C_{5h}	A'	$\alpha_{xx}+\alpha_{yy}, \alpha_{zz}$	$\bar{\alpha}_{xy}$			$\gamma_3, \gamma_{20}, \gamma_{22}$	$\bar{\gamma}_{19}, \bar{\gamma}_{23}, \bar{\gamma}_{29}$
	E_1'			$(\beta_8, \beta_9), (\beta_{17}, \beta_{18})$	$(\bar{\beta}_1, \bar{\beta}_3), (\bar{\beta}_5, \bar{\beta}_6)$	$(\gamma_{21}, \gamma_{29})$	
	E_2'	$(\alpha_{xx}-\alpha_{yy}, \alpha_{xy})$		(β_{19}, β_{20})		$(\gamma_{15}, \gamma_{23}), (\gamma_{17}, \gamma_{26})$	$(\bar{\gamma}_7, \bar{\gamma}_{16}), (\bar{\gamma}_{22}, \bar{\gamma}_{26})$

TABLE I (*Continued*)

	A''		β_3, β_{13}	$\bar{\beta}_{11}, \bar{\beta}_{16}$		
	E_1''	$(\alpha_{yz}, \alpha_{zz})$	$(\bar{\alpha}_{yz}, \bar{\alpha}_{zz})$		$(\gamma_{11}, \gamma_{12}), (\gamma_{32}, \gamma_{33})$	$(\bar{\gamma}_5, \bar{\gamma}_6), (\bar{\gamma}_{12}, \bar{\gamma}_{15}), (\bar{\gamma}_{32}, \bar{\gamma}_{33})$
	E_2''		(β_{10}, β_{16})	$(\bar{\beta}_{14}, \bar{\beta}_{15})$	$(\gamma_{34}, \gamma_{35})$	$(\bar{\gamma}_{34}, \bar{\gamma}_{35})$

E. The groups D_{nh} ($n=3, 5$)

D_{3h}	A_1' a	$\alpha_{xx}+\alpha_{yy}, \alpha_{zz}$		β_{19}		$\gamma_3, \gamma_{20}, \gamma_{22}$	$\bar{\gamma}_{23}$
	A_2' a		$\bar{\alpha}_{xy}$	β_{20}			$\bar{\gamma}_{19}, \bar{\gamma}_{29}$
	E'	$(\alpha_{xx}-\alpha_{yy}, \alpha_{xy})$		$(\beta_8, \beta_9), (\beta_{17}, \beta_{18})$	$(\bar{\beta}_1, \bar{\beta}_3), (\bar{\beta}_5, \bar{\beta}_6)$	$(\gamma_{15}, \gamma_{23}), (\gamma_{17}, \gamma_{26}), (\gamma_{21}, \gamma_{29})$	$(\bar{\gamma}_7, \bar{\gamma}_{16}), (\bar{\gamma}_{22}, \bar{\gamma}_{26})$
	A_1''				$\bar{\beta}_{16}$	γ_{35}	$\bar{\gamma}_{35}$
	A_2''			β_3, β_{13}	$\bar{\beta}_{11}$	γ_{34}	$\bar{\gamma}_{34}$
	E''	$(\alpha_{yz}, \alpha_{zz})$	$(\bar{\alpha}_{yz}, \bar{\alpha}_{zz})$	(β_{10}, β_{16})	$(\bar{\beta}_{14}, \bar{\beta}_{15})$	$(\gamma_{11}, \gamma_{12}), (\gamma_{32}, \gamma_{33})$	$(\bar{\gamma}_5, \bar{\gamma}_6), (\bar{\gamma}_{12}, \bar{\gamma}_{15}), (\bar{\gamma}_{32}, \bar{\gamma}_{33})$
D_{5h}	A_1'	$\alpha_{xx}+\alpha_{yy}, \alpha_{zz}$				$\gamma_3, \gamma_{20}, \gamma_{22}$	$\bar{\gamma}_{23}$
	A_2'		$\bar{\alpha}_{xy}$				$\bar{\gamma}_{19}, \bar{\gamma}_{29}$
	E_1'			$(\beta_8, \beta_9), (\beta_{17}, \beta_{18})$	$(\bar{\beta}_1, \bar{\beta}_3), (\bar{\beta}_5, \bar{\beta}_6)$	$(\gamma_{21}, \gamma_{29})$	
	E_2'	$(\alpha_{xx}-\alpha_{yy}, \alpha_{xy})$		(β_{19}, β_{20})		$(\gamma_{15}, \gamma_{23}), (\gamma_{17}, \gamma_{26})$	$(\bar{\gamma}_7, \bar{\gamma}_{16}), (\bar{\gamma}_{22}, \bar{\gamma}_{26})$
	A_1''				$\bar{\beta}_{16}$		
	A_2''			β_3, β_{13}	$\bar{\beta}_{11}$		
	E_1''	$(\alpha_{yz}, \alpha_{zz})$	$(\bar{\alpha}_{yz}, \bar{\alpha}_{zz})$			$(\gamma_{11}, \gamma_{12}), (\gamma_{32}, \gamma_{33})$	$(\bar{\gamma}_5, \bar{\gamma}_6), (\bar{\gamma}_{12}, \bar{\gamma}_{15}), (\bar{\gamma}_{32}, \bar{\gamma}_{33})$
	E_2''			(β_{10}, β_{16})	$(\bar{\beta}_{14}, \bar{\beta}_{15})$	$(\gamma_{34}, \gamma_{35})$	$(\bar{\gamma}_{34}, \bar{\gamma}_{35})$

F. The groups D_{nd} ($n=2, 4, 6$)

D_{2d}	A_1	$\alpha_{xx}+\alpha_{yy}, \alpha_{zz}$		β_{10}	$\bar{\beta}_{15}$	$\gamma_3, \gamma_4, \gamma_{16}, \gamma_{22}$	$\bar{\gamma}_{23}$
	A_2		$\bar{\alpha}_{xy}$	β_{16}	$\bar{\beta}_{14}$	γ_{29}	$\bar{\gamma}_{19}, \bar{\gamma}_{29}$
	B_1	$\alpha_{xx}-\alpha_{yy}$			$\bar{\beta}_{16}$	γ_{17}, γ_{23}	$\bar{\gamma}_7, \bar{\gamma}_{22}$
	B_2	α_{xy}		β_3, β_{13}	$\bar{\beta}_{11}$	γ_{15}, γ_{26}	$\bar{\gamma}_{16}, \bar{\gamma}_{26}$
	E	$(\alpha_{yz}, \alpha_{zz})$	$(\bar{\alpha}_{yz}, \bar{\alpha}_{zz})$	$(\beta_1, \beta_2), (\beta_4, \beta_6), (\beta_8, \beta_9)$	$(\bar{\beta}_1, \bar{\beta}_2), (\bar{\beta}_5, \bar{\beta}_6)$	$(\gamma_8, \gamma_{10}), (\gamma_{11}, \gamma_{12}), (\gamma_{13}, \gamma_{14})$	$(\bar{\gamma}_2, \bar{\gamma}_4), (\bar{\gamma}_5, \bar{\gamma}_6), (\bar{\gamma}_{12}, \bar{\gamma}_{15}), (\bar{\gamma}_{13}, \bar{\gamma}_{14})$
D_{4d}	A_1	$\alpha_{xx}+\alpha_{yy}, \alpha_{zz}$				$\gamma_3, \gamma_{20}, \gamma_{22}$	$\bar{\gamma}_{23}$
	A_2		$\bar{\alpha}_{xy}$				$\bar{\gamma}_{19}, \bar{\gamma}_{29}$
	B_1				$\bar{\beta}_{16}$	γ_{21}	
	B_2			β_3, β_{13}	$\bar{\beta}_{11}$	γ_{29}	
	E_1			$(\beta_8, \beta_9), (\beta_{17}, \beta_{18})$	$(\bar{\beta}_1, \bar{\beta}_3), (\bar{\beta}_5, \bar{\beta}_6)$	$(\gamma_{34}, \gamma_{35})$	$(\bar{\gamma}_{34}, \bar{\gamma}_{35})$
	E_2	$(\alpha_{xx}-\alpha_{yy}, \alpha_{xy})$		(β_{10}, β_{16})	$(\bar{\beta}_{14}, \bar{\beta}_{15})$	$(\gamma_{15}, \gamma_{23}), (\gamma_{17}, \gamma_{26})$	$(\bar{\gamma}_7, \bar{\gamma}_{16}), (\bar{\gamma}_{22}, \bar{\gamma}_{26})$
	E_3	$(\alpha_{yz}, \alpha_{zz})$	$(\bar{\alpha}_{yz}, \bar{\alpha}_{zz})$	(β_{19}, β_{20})		$(\gamma_{11}, \gamma_{12}), (\gamma_{32}, \gamma_{33})$	$(\bar{\gamma}_5, \bar{\gamma}_6), (\bar{\gamma}_{12}, \bar{\gamma}_{15}), (\bar{\gamma}_{32}, \bar{\gamma}_{33})$
D_{6d}	A_1	$\alpha_{xx}+\alpha_{yy}, \alpha_{zz}$				$\gamma_3, \gamma_{20}, \gamma_{22}$	$\bar{\gamma}_{23}$
	A_2		$\bar{\alpha}_{xy}$				$\bar{\gamma}_{19}, \bar{\gamma}_{29}$
	B_1				$\bar{\beta}_{16}$		
	B_2			β_3, β_{13}	$\bar{\beta}_{11}$		
	E_1			$(\beta_8, \beta_9), (\beta_{17}, \beta_{18})$	$(\bar{\beta}_1, \bar{\beta}_3), (\bar{\beta}_5, \bar{\beta}_6)$		
	E_2	$(\alpha_{xx}-\alpha_{yy}, \alpha_{xy})$				$(\gamma_{15}, \gamma_{23}), (\gamma_{17}, \gamma_{26})$	$(\bar{\gamma}_7, \bar{\gamma}_{16}), (\bar{\gamma}_{22}, \bar{\gamma}_{26})$
	E_3			(β_{19}, β_{20})		$(\gamma_{34}, \gamma_{35})$	$(\bar{\gamma}_{34}, \bar{\gamma}_{35})$

TABLE I (*Continued*)

	E_4			(β_{10}, β_{16})	$(\bar{\beta}_{14}, \bar{\beta}_{15})$	$(\gamma_{21}, \gamma_{29})$	
	E_5	$(\alpha_{yz}, \alpha_{zz})$	$(\bar{\alpha}_{yz}, \bar{\alpha}_{zz})$			$(\gamma_{11}, \gamma_{12})$, $(\gamma_{32}, \gamma_{33})$	$(\bar{\gamma}_5, \bar{\gamma}_6)$, $(\bar{\gamma}_{12}, \bar{\gamma}_{15})$, $(\bar{\gamma}_{32}, \bar{\gamma}_{33})$

G. The groups S_n $(n=4, 8)$

S_4	A	$\alpha_{xx}+\alpha_{yy}, \alpha_{zz}$	$\bar{\alpha}_{xy}$	β_{10}, β_{16}	$\bar{\beta}_{14}, \bar{\beta}_{15}$	$\gamma_3, \gamma_4, \gamma_{16}, \gamma_{22}, \gamma_{29}$	$\bar{\gamma}_{19}, \bar{\gamma}_{23}, \bar{\gamma}_{29}$
	B	$\alpha_{xx}-\alpha_{yy}, \alpha_{xy}$		β_3, β_{13}	$\bar{\beta}_{11}, \bar{\beta}_{16}$	$\gamma_{15}, \gamma_{17}, \gamma_{23}, \gamma_{26}$	$\bar{\gamma}_7, \bar{\gamma}_{16}, \bar{\gamma}_{22}, \bar{\gamma}_{26}$
	E	$(\alpha_{yz}, \alpha_{xz})$	$(\bar{\alpha}_{yz}, \bar{\alpha}_{xz})$	(β_1, β_2), (β_4, β_6), (β_8, β_9)	$(\bar{\beta}_1, \bar{\beta}_3)$, $(\bar{\beta}_5, \bar{\beta}_6)$	(γ_8, γ_{10}), $(\gamma_{11}, \gamma_{12})$, $(\gamma_{13}, \gamma_{14})$	$(\bar{\gamma}_2, \bar{\gamma}_7)$, $(\bar{\gamma}_5, \bar{\gamma}_6)$, $(\bar{\gamma}_{12}, \bar{\gamma}_{15})$, $(\bar{\gamma}_{13}, \bar{\gamma}_{14})$
S_8	A	$\alpha_{xx}+\alpha_{yy}, \alpha_{zz}$	$\bar{\alpha}_{xy}$			$\gamma_3, \gamma_{20}, \gamma_{22}$	$\bar{\gamma}_{19}, \bar{\gamma}_{23}, \bar{\gamma}_{29}$
	B			β_3, β_{13}	$\bar{\beta}_{11}, \bar{\beta}_{16}$	γ_{21}, γ_{29}	
	E_1			(β_8, β_9), (β_{17}, β_{18})	$(\bar{\beta}_1, \bar{\beta}_3)$, $(\bar{\beta}_5, \bar{\beta}_6)$	$(\gamma_{34}, \gamma_{35})$	$(\bar{\gamma}_{34}, \bar{\gamma}_{35})$
	E_2	$(\alpha_{xx}-\alpha_{yy}, \alpha_{xy})$		(β_{10}, β_{16})	$(\bar{\beta}_{14}, \bar{\beta}_{15})$	$(\gamma_{15}, \gamma_{23})$, (γ_1, γ_{26})	$(\bar{\gamma}_7, \bar{\gamma}_{16})$, $(\bar{\gamma}_{22}, \bar{\gamma}_{26})$
	E_3	$(\alpha_{yz}, \alpha_{xz})$	$(\bar{\alpha}_{yz}, \bar{\alpha}_{xz})$	(β_{19}, β_{20})		$(\gamma_{11}, \gamma_{12})$, $(\gamma_{32}, \gamma_{33})$	$(\bar{\gamma}_5, \bar{\gamma}_6)$, $(\bar{\gamma}_{12}, \bar{\gamma}_{15})$, $(\bar{\gamma}_{32}, \bar{\gamma}_{33})$

H. The groups T, T_d and O

T	A	$\alpha_{xx}+\alpha_{yy}+\alpha_{zz}$		β_{10}		γ_{18}, γ_{24}	$\bar{\gamma}_{24}$
	E	$(\alpha_{xx}+\alpha_{yy}-2\alpha_{zz}, \alpha_{xx}-\alpha_{yy})$			$(\bar{\beta}_{15}, \bar{\beta}_{16})$	$(\gamma_{17}, \gamma_{19})$, $(\gamma_{23}, \gamma_{25})$	$(\bar{\gamma}_{23}, \bar{\gamma}_{25})$
	F	$(\alpha_{xy}, \alpha_{yz}, \alpha_{zx})$	$(\bar{\alpha}_{xy}, \bar{\alpha}_{yz}, \bar{\alpha}_{zx})$	$(\beta_1, \beta_2, \beta_3)$, $(\beta_5, \beta_6, \beta_9)$, $(\beta_4, \beta_7, \beta_8)$	$(\bar{\beta}_2, \bar{\beta}_3, \bar{\beta}_6)$, $(\bar{\beta}_1, \bar{\beta}_4, \bar{\beta}_5)$	$(\gamma_7, \gamma_{16}, \gamma_{11})$, $(\gamma_8, \gamma_9, \gamma_{12})$, $(\gamma_{13}, \gamma_{14}, \gamma_{15})$	$(\bar{\gamma}_1, \bar{\gamma}_4, \bar{\gamma}_6)$, $(\bar{\gamma}_2, \bar{\gamma}_3, \bar{\gamma}_6)$, $(\bar{\gamma}_{10}, \bar{\gamma}_{12}, \bar{\gamma}_{14})$, $(\bar{\gamma}_{11}, \bar{\gamma}_{13}, \bar{\gamma}_{15})$
T_d	A_1	$\alpha_{xx}+\alpha_{yy}+\alpha_{zz}$		β_{10}		γ_{18}, γ_{24}	
	A_2						$\bar{\gamma}_{24}$
	E	$(\alpha_{xx}+\alpha_{yy}-2\alpha_{zz}, \alpha_{xx}-\alpha_{yy})$			$(\bar{\beta}_{15}, \bar{\beta}_{16})$	$(\gamma_{17}, \gamma_{19})$, $(\gamma_{23}, \gamma_{25})$	$(\bar{\gamma}_{23}, \bar{\gamma}_{25})$
	F_1		$(\bar{\alpha}_{xy}, \bar{\alpha}_{yz}, \bar{\alpha}_{zx})$	$(\beta_{14}, \beta_{15}, \beta_{16})$	$(\bar{\beta}_{12}, \bar{\beta}_{13}, \bar{\beta}_{14})$	$(\gamma_{29}, \gamma_{30}, \gamma_{31})$	$(\bar{\gamma}_{19}, \bar{\gamma}_{20}, \bar{\gamma}_{21})$, $(\bar{\gamma}_{29}, \bar{\gamma}_{30}, \bar{\gamma}_{31})$
	F_2	$(\alpha_{xy}, \alpha_{yz}, \alpha_{zx})$		$(\beta_1, \beta_2, \beta_3)$, $(\beta_{11}, \beta_{12}, \beta_{13})$	$(\bar{\beta}_9, \bar{\beta}_{10}, \bar{\beta}_{11})$	$(\gamma_{13}, \gamma_{14}, \gamma_{15})$, $(\gamma_{26}, \gamma_{27}, \gamma_{28})$	$(\bar{\gamma}_{16}, \bar{\gamma}_{17}, \bar{\gamma}_{18})$, $(\bar{\gamma}_{26}, \bar{\gamma}_{27}, \bar{\gamma}_{28})$
O	A_1	$\alpha_{xx}+\alpha_{yy}+\alpha_{zz}$				γ_{18}, γ_{24}	
	A_2			β_{10}			$\bar{\gamma}_{24}$
	E	$(\alpha_{xx}+\alpha_{yy}-2\alpha_{zz}, \alpha_{xx}-\alpha_{yy})$			$(\bar{\beta}_{15}, \bar{\beta}_{16})$	$(\gamma_{17}, \gamma_{19})$, $(\gamma_{23}, \gamma_{25})$	$(\bar{\gamma}_{23}, \bar{\gamma}_{25})$
	F_1		$(\bar{\alpha}_{xy}, \bar{\alpha}_{yz}, \bar{\alpha}_{zx})$	$(\beta_1, \beta_2, \beta_3)$, $(\beta_{11}, \beta_{12}, \beta_{13})$	$(\bar{\beta}_9, \bar{\beta}_{10}, \bar{\beta}_{11})$	$(\gamma_{29}, \gamma_{30}, \gamma_{31})$	$(\bar{\gamma}_{19}, \bar{\gamma}_{20}, \bar{\gamma}_{21})$, $(\bar{\gamma}_{29}, \bar{\gamma}_{30}, \bar{\gamma}_{31})$
	F_2	$(\alpha_{xy}, \alpha_{yz}, \alpha_{zx})$		$(\beta_{14}, \beta_{15}, \beta_{16})$	$(\bar{\beta}_{12}, \bar{\beta}_{13}, \bar{\beta}_{14})$	$(\gamma_{13}, \gamma_{14}, \gamma_{15})$, $(\gamma_{26}, \gamma_{27}, \gamma_{28})$	$(\bar{\gamma}_{16}, \bar{\gamma}_{17}, \bar{\gamma}_{18})$, $(\bar{\gamma}_{26}, \bar{\gamma}_{27}, \bar{\gamma}_{28})$

I. The group $C_{\infty v}$

$C_{\infty v}$	A_1	$\alpha_{xx}+\alpha_{yy}, \alpha_{zz}$		β_3, β_{13}	$\bar{\beta}_{11}$	$\gamma_3, \gamma_{20}, \gamma_{22}$	$\bar{\gamma}_{23}$
	A_2		$\bar{\alpha}_{xy}$		$\bar{\beta}_{16}$		$\bar{\gamma}_{19}, \bar{\gamma}_{29}$
	E_1	$(\alpha_{yz}, \alpha_{xz})$	$(\bar{\alpha}_{yz}, \bar{\alpha}_{xz})$	(β_8, β_9), (β_{17}, β_{18})	$(\bar{\beta}_1, \bar{\beta}_3)$, $(\bar{\beta}_5, \bar{\beta}_6)$	$(\gamma_{11}, \gamma_{12})$, $(\gamma_{32}, \gamma_{33})$	$(\bar{\gamma}_5, \bar{\gamma}_6)$, $(\bar{\gamma}_{12}, \bar{\gamma}_{15})$, $(\bar{\gamma}_{32}, \bar{\gamma}_{33})$
	E_2	$(\alpha_{xx}-\alpha_{yy}, \alpha_{xy})$		(β_{10}, β_{16})	$(\bar{\beta}_{14}, \bar{\beta}_{15})$	$(\gamma_{15}, \gamma_{23})$, $(\gamma_{17}, \gamma_{26})$	$(\bar{\gamma}_7, \bar{\gamma}_{16})$, $(\bar{\gamma}_{22}, \bar{\gamma}_{26})$
	E_3			(β_{19}, β_{20})		$(\gamma_{34}, \gamma_{35})$	$(\bar{\gamma}_{34}, \bar{\gamma}_{35})$
	E_4					$(\gamma_{21}, \gamma_{29})$	

[a] x axis along C_2. [b] x axis along C_2' [illegible] axis in σ_v.

TABLE II. Definition of symbols used in selection rule tables.

$\beta_1=\beta_{xxx}$	$\bar{\beta}_1=\bar{\beta}_{xxy}$
$\beta_2=\beta_{yyy}$	$\bar{\beta}_2=\bar{\beta}_{xxz}$
$\beta_3=\beta_{zzz}$	$\bar{\beta}_3=\bar{\beta}_{yyz}$
$\beta_4=\beta_{xxy}$	$\bar{\beta}_4=\bar{\beta}_{yyx}$
$\beta_5=\beta_{xzz}$	$\bar{\beta}_5=\bar{\beta}_{zzx}$
$\beta_6=\beta_{xyy}$	$\bar{\beta}_6=\bar{\beta}_{zzy}$
$\beta_7=\beta_{yyz}$	$\bar{\beta}_7=\bar{\beta}_{xyz}$
$\beta_8=\beta_{xzz}$	$\bar{\beta}_8=\bar{\beta}_{yzz}$
$\beta_9=\beta_{yzz}$	$\bar{\beta}_9=\bar{\beta}_{yyz}+\bar{\beta}_{xzz}$
$\beta_{10}=\beta_{xyz}$	$\bar{\beta}_{10}=\bar{\beta}_{xzy}+\bar{\beta}_{xzy}$
$\beta_{11}=\beta_{xyy}+\beta_{xzz}$	$\bar{\beta}_{11}=\bar{\beta}_{xzz}+\bar{\beta}_{yyz}$
$\beta_{12}=\beta_{xxy}+\beta_{yzz}$	$\bar{\beta}_{12}=\bar{\beta}_{yyz}-\bar{\beta}_{xzz}$
$\beta_{13}=\beta_{xzz}+\beta_{yyz}$	$\bar{\beta}_{13}=\bar{\beta}_{xzy}-\bar{\beta}_{xzy}$
$\beta_{14}=\beta_{xyy}-\beta_{xzz}$	$\bar{\beta}_{14}=\bar{\beta}_{xzz}-\bar{\beta}_{yyz}$
$\beta_{15}=\beta_{xxy}-\beta_{yzz}$	$\bar{\beta}_{15}=\bar{\beta}_{xyz}+\bar{\beta}_{yzz}$
$\beta_{16}=\beta_{xzz}-\beta_{yyz}$	$\bar{\beta}_{16}=\bar{\beta}_{xyz}-\bar{\beta}_{yzz}$
$\beta_{17}=\beta_{xxz}+\beta_{xyy}$	
$\beta_{18}=\beta_{yyy}+\beta_{xxy}$	
$\beta_{19}=\beta_{xxz}-3\beta_{xyy}$	
$\beta_{20}=\beta_{yyy}-3\beta_{xxy}$	

$\gamma_1=\gamma_{xxxx}$	$\bar{\gamma}_1=\bar{\gamma}_{xxxy}$
$\gamma_2=\gamma_{yyyy}$	$\bar{\gamma}_2=\bar{\gamma}_{xxxz}$
$\gamma_3=\gamma_{zzzz}$	$\bar{\gamma}_3=\bar{\gamma}_{yyyx}$
$\gamma_4=\gamma_{xxyy}$	$\bar{\gamma}_4=\bar{\gamma}_{yyyz}$
$\gamma_5=\gamma_{yyzz}$	$\bar{\gamma}_5=\bar{\gamma}_{zzzx}$
$\gamma_6=\gamma_{xxzz}$	$\bar{\gamma}_6=\bar{\gamma}_{zzzy}$
$\gamma_7=\gamma_{xxxy}$	$\bar{\gamma}_7=\bar{\gamma}_{xxyy}$
$\gamma_8=\gamma_{xxxz}$	$\bar{\gamma}_8=\bar{\gamma}_{yyzz}$
$\gamma_9=\gamma_{yyyx}$	$\bar{\gamma}_9=\bar{\gamma}_{zzzx}$
$\gamma_{10}=\gamma_{yyyz}$	$\bar{\gamma}_{10}=\bar{\gamma}_{xyzz}$
$\gamma_{11}=\gamma_{zzzx}$	$\bar{\gamma}_{11}=\bar{\gamma}_{yzzz}$
$\gamma_{12}=\gamma_{zzzy}$	$\bar{\gamma}_{12}=\bar{\gamma}_{yzzz}$
$\gamma_{13}=\gamma_{xxyz}$	$\bar{\gamma}_{13}=\bar{\gamma}_{xyzz}$
$\gamma_{14}=\gamma_{yyzx}$	$\bar{\gamma}_{14}=\bar{\gamma}_{zzxy}$
$\gamma_{15}=\gamma_{xxzy}$	$\bar{\gamma}_{15}=\bar{\gamma}_{xzyy}$
$\gamma_{16}=\gamma_{xxxx}+\gamma_{yyyy}$	$\bar{\gamma}_{16}=\bar{\gamma}_{xxxy}+\bar{\gamma}_{yyyx}$
$\gamma_{17}=\gamma_{xxxx}-\gamma_{yyyy}$	$\bar{\gamma}_{17}=\bar{\gamma}_{yyyz}+\bar{\gamma}_{zzzy}$
$\gamma_{18}=\gamma_{xxxx}+\gamma_{yyyy}+\gamma_{zzzz}$	$\bar{\gamma}_{18}=\bar{\gamma}_{zzzx}+\bar{\gamma}_{xxxz}$
$\gamma_{19}=\gamma_{xxxx}+\gamma_{yyyy}-2\gamma_{zzzz}$	$\bar{\gamma}_{19}=\bar{\gamma}_{xxxy}-\bar{\gamma}_{yyyx}$
$\gamma_{20}=\gamma_{xxxx}+2\gamma_{xxyy}+\gamma_{zzzz}$	$\bar{\gamma}_{20}=\bar{\gamma}_{yyyz}-\bar{\gamma}_{zzzy}$
$\gamma_{21}=\gamma_{xxxx}-6\gamma_{xxyy}+\gamma_{yyyy}$	$\bar{\gamma}_{21}=\bar{\gamma}_{zzzx}-\bar{\gamma}_{xxxz}$
$\gamma_{22}=\gamma_{yyzz}+\gamma_{zzzz}$	$\bar{\gamma}_{22}=\bar{\gamma}_{yyzz}+\bar{\gamma}_{zzzz}$
$\gamma_{23}=\gamma_{yyzz}-\gamma_{zzzz}$	$\bar{\gamma}_{23}=\bar{\gamma}_{yyzz}-\bar{\gamma}_{zzzz}$
$\gamma_{24}=\gamma_{xxyy}+\gamma_{yyzz}+\gamma_{zzzz}$	$\bar{\gamma}_{24}=\bar{\gamma}_{xxyy}+\bar{\gamma}_{yyzz}+\bar{\gamma}_{zzzz}$
$\gamma_{25}=\gamma_{yyzz}+\gamma_{zzzz}-2\gamma_{xxyy}$	$\bar{\gamma}_{25}=\bar{\gamma}_{yyzz}+\bar{\gamma}_{zzzz}-2\bar{\gamma}_{xxyy}$
$\gamma_{26}=\gamma_{xxxy}+\gamma_{yyyx}$	$\bar{\gamma}_{26}=\bar{\gamma}_{xyzz}+\bar{\gamma}_{yxzz}$
$\gamma_{27}=\gamma_{yyyz}+\gamma_{zzzy}$	$\bar{\gamma}_{27}=\bar{\gamma}_{yzzx}+\bar{\gamma}_{zyxz}$
$\gamma_{28}=\gamma_{zzzx}+\gamma_{xxxz}$	$\bar{\gamma}_{28}=\bar{\gamma}_{xzyy}+\bar{\gamma}_{xzyy}$
$\gamma_{29}=\gamma_{xxxy}-\gamma_{yyyx}$	$\bar{\gamma}_{29}=\bar{\gamma}_{xyzz}-\bar{\gamma}_{yxzz}$
$\gamma_{30}=\gamma_{yyyz}-\gamma_{zzzy}$	$\bar{\gamma}_{30}=\bar{\gamma}_{yzzx}-\bar{\gamma}_{zyxz}$
$\gamma_{31}=\gamma_{zzzx}-\gamma_{xxxz}$	$\bar{\gamma}_{31}=\bar{\gamma}_{xzyy}-\bar{\gamma}_{xzyy}$
$\gamma_{32}=\gamma_{xxxz}+\gamma_{yyzz}$	$\bar{\gamma}_{32}=\bar{\gamma}_{xxxz}-\bar{\gamma}_{zzyy}$
$\gamma_{33}=\gamma_{yyyz}+\gamma_{zzyz}$	$\bar{\gamma}_{33}=\bar{\gamma}_{yyyz}-\bar{\gamma}_{zyxz}$
$\gamma_{34}=\gamma_{xxxz}-3\gamma_{yyzz}$	$\bar{\gamma}_{34}=\bar{\gamma}_{xxxz}+3\bar{\gamma}_{zzyy}-\bar{\gamma}_{zzyy}$
$\gamma_{35}=\gamma_{yyyz}-3\gamma_{zzyz}$	$\bar{\gamma}_{35}=\bar{\gamma}_{yyyz}+3\bar{\gamma}_{zyxz}-\bar{\gamma}_{yzzz}$

and n_i is the number of times the ith representation is contained in the reducible representation. The value obtained for n_i should equal the number of tensor elements listed in Table I for the ith irreducible representation. We have checked all our results by this method. Expressions for $\chi(R)$ are obtained by considering a general transformation S, of the type[19]

$$Sx=x\cos\theta+y\sin\theta,$$
$$Sy=-x\sin\theta+y\cos\theta,$$
$$Sz=\pm z, \tag{9}$$

where θ denotes the angle of rotation about the z axis, and the upper and lower signs refer to proper and improper rotations, respectively. Using Eq. (9) we have obtained the following characters of the transformation matrices of the β, $\bar{\beta}$, γ, and $\bar{\gamma}$ tensors:

$$\chi_\beta(R)=8\cos^3\theta\pm4\cos^2\theta-2\cos\theta,$$
$$\chi_{\bar{\beta}}(R)=\pm4\cos^2\theta+4\cos\theta,$$
$$\chi_\gamma(R)=16\cos^4\theta\pm8\cos^3\theta-8\cos^2\theta\pm(-2\cos\theta)+1,$$
$$\chi_{\bar{\gamma}}(R)=\pm8\cos^3\theta+8\cos^2\theta-1.$$

The value of the character for a particular operation may be obtained by substituting in the value of θ for the operation and choosing the plus or minus sign depending on whether the operation is a proper or improper rotation. A reflection is treated as an improper rotation of zero radians, and inversion as one of π radians.

As the projection operator method is not readily applicable to the infinite groups, the selection rules for these groups were calculated using the above control method in conjunction with correlation tables giving the relations between the representations of the infinite group and those of its finite subgroups.

As a final check, we have compared some of our results with earlier calculations. We find that our (symmetric) β selection rules are in agreement with those given in Refs. 1 and 11, and that our $D_{6h}=D_6\times C_i$ selection rules on γ agree with those listed in Ref. 4.

In the Appendix we list the number of tensor components transforming according to each representation of the point groups for the more general tensors $\beta'(\omega_0,\omega_1,\omega_2)$, $\gamma'(\omega_0,\omega_1,\omega_2,\omega_3)$, and $\gamma''(\omega_0,\omega_1,\omega_2,\omega_2)$. The dashes are used to distinguish these *asymmetric* tensors from the previously defined β, $\bar{\beta}$, γ, and $\bar{\gamma}$ tensors.

IV. DISCUSSION

In this section we will discuss the nature and significance of the selection rule table and the phenomena to which the selection rules are applicable. There are some general observations that can be made:

(1) The selection rules are a function of the rank and symmetry of the tensors only and thus do not distinguish between the various phenomena associated with each tensor. We will therefore refer to modes allowed by the β selection rules, for example, as being β active, and similarly for modes allowed by the other tensors.

(2) All normal modes active in two-photon Raman scattering are active in four-photon Raman scattering, and all infrared active modes are β active.

(3) In systems containing a center of symmetry all β-active modes belong to the odd species, and all γ-active modes to the even species.

(4) The most important and obvious feature of the tables is the large number of modes, inactive in two-photon Raman scattering and infrared absorption, which are active in either three- or four-photon Raman scattering.

Benzene provides a convenient example with which to illustrate the above characteristics of the table. The benzene molecule possesses D_{6h} symmetry and has 20 fundamental frequencies distributed as follows: $2A_{1g}+A_{2g}+A_{2u}+2B_{1u}+2B_{2g}+2B_{2u}+E_{1g}+3E_{1u}+4E_{2g}+2E_{2u}$. Following the procedure described in Sec. III, we use the group D_6 to obtain the D_{6h} selection rules given in Table III. The A_{2u} and E_{1u} modes are infrared active, and it will be noted that these modes are all β active also; rule (2) is similarly obeyed by the α- and γ-active modes. The six frequencies distributed as $2B_{1u}+B_{2u}+2E_{2u}$ are active in the β-type processes only, the B_{2g} modes are active in four-photon Raman scattering, and the A_{2g} is active in $\bar{\alpha}$ and $\bar{\gamma}$. One of the B_{2g} modes has been observed[3,4] in the inverse Raman effect. It may be possible to observe the A_{2g} mode in the two-photon Raman effect under resonance conditions, when Placzek's approximation is no longer valid. Reference 1 gives other examples of modes active in three-photon Raman scattering only, and the reader will without difficulty find many other examples of modes active only in the higher-order processes.

As has been pointed out previously, both the β and γ terms in the expansion of the induced dipole moment describe two processes. The β term represents three-photon Raman scattering, and induced emission and absorption, which are illustrated in Fig. 1(b). In a practical experiment using a pulsed laser as a light source, ω_1 will equal ω_2, and the Raman spectrum will be observed as sidebands to $2\omega_L$, where ω_L is the laser frequency. If a ruby laser is used as an exciting source, the spectrum origin will be at 3471 Å. In this case then, observation of three-photon Raman scattering is restricted to those materials which are transparent in this region. If the sample to be investigated has an absorption band in the near ultraviolet, there are several infrared lasers, notably the neodymium laser, which may be used instead, though one loses some scattering intensity due to its fourth-power dependancy on the emission frequency. One other advantage of observing spectra in the near ultraviolet is that photomultipliers have a high-quantum efficiency and low noise in this region.

TABLE III. Selection rules for benzene.

Tensor	Active modes
α	A_{1g}, E_{1g}, E_{2g}
$\bar{\alpha}$	A_{2g}, E_{1g}
β	$A_{2u}, B_{1u}, B_{2u}, E_{1u}, E_{2u}$
$\bar{\beta}$	A_{2u}, E_{1u}, E_{2u}
γ	$A_{1g}, B_{2g}, E_{1g}, E_{2g}$
$\bar{\gamma}$	$A_{1g}, A_{2g}, B_{2g}, E_{1g}, E_{2g}$

An important difference between two- and three-photon Raman scattering is that in the higher-order process, an absorption at the spectral origin does not effect the intensity of light scattered at different frequencies; in two-photon scattering, such an absorption effects a lowering of the intensity of the exciting light. This enables full advantage to be taken of the $2\omega_L$ resonance, i.e., we have resonance enhancement without absorption retardation. It should be noted that three-photon Rayleigh scattering (second-harmonic generation) is forbidden in systems possessing a center of symmetry, so that the three-photon Raman spectrum will be the only structure visible in the vicinity of the frequency $2\omega_L$ in such cases.

Induced emission and absorption represent third-order contributions to ordinary or first-order emission and absorption. Of the two, the absorption process is of the most interest as it is much simpler to observe experimentally. If the excitation frequency ω is chosen to be near one of the absorption frequencies of the system being investigated, benefit is gained from resonant enhancement of the absorption intensities as well as from the possibility of observing transitions involving the nonsymmetric components of the absorption tensor. The exciting light should consist preferably of a sharp single frequency, together with the continuum in which the absorption spectrum is to be observed; if instead of a single frequency continuous frequencies are used, the third-order spectrum will also be continuous. For this reason, third-order absorption will not be observed in conventional absorption experiments in which the broad-band source radiation is incident on the sample before passing through the spectrometer.

The two sets of phenomena represented by the γ term in (1) may both be termed four-photon Raman scattering, but for clarity we shall use this to refer to the process in which the emitted frequencies have as their origin the tripled-laser frequency, $3\omega_L$. The other process is analogous to the higher-order emission/absorption process, and we will thus refer to it as "induced Raman scattering."

Four-photon Raman scattering is similar in form to the three-photon scattering, and most of the comments made about the latter are applicable here, with suitable adjustments. This time three, instead of two, photons are absorbed, and the Raman spectrum is centered at $3\omega_L$ [see Fig. 1(c)]. There are three resonances, one each at ω_L, $2\omega_L$, and $3\omega_L$, the $2\omega_L$ being the most useful as it enables a broad-band absorption to give resonant enhancement without any accompanying losses.

TABLE IV. The symmetric structure of the β', γ', and γ'' tensor components.

Group	Rep.	Number of tensor components β'	γ'	γ''
C_s	A'	14	41	28
	A''	13	40	26
C_2	A	13	41	28
	B	14	40	26
C_3	A	9	27	18
	E	9	27	18
C_4	A	7	21	14
	B	6	20	14
	E	7	20	13
C_5	A	7	19	12
	E_1	6	17	11
	E_2	4	14	10
C_6	A	7	19	12
	B	2	8	6
	E_1	6	16	10
	E_2	3	11	8
D_2	A	6	21	15
	B_1	7	20	13
	B_2	7	20	13
	B_3	7	20	13
D_3	A_1	4	14	10
	A_2	5	13	8
	E	9	27	18
D_4	A_1	3	11	8
	A_2	4	10	6
	B_1	3	10	7
	B_2	3	10	7
	E	7	20	13
D_5	A_1	3	10	7
	A_2	4	9	5
	E_1	6	17	11
	E_2	4	14	10
D_6	A_1	3	10	7
	A_2	4	9	5
	B_1	1	4	3
	B_2	1	4	3
	E_1	6	16	10
	E_2	3	11	8
C_{2v}	A_1	7	21	15
	A_2	6	20	13
	B_1	7	20	13
	B_2	7	20	13
C_{3v}	A_1	5	14	10
	A_2	4	13	8
	E	9	27	18
C_{4v}	A_1	4	11	8
	A_2	3	10	6
	B_1	3	10	7
	B_2	3	10	7
	E	7	20	13
C_{5v}	A_1	4	10	7
	A_2	3	9	5
	E_1	6	17	11
	E_2	4	14	10
C_{6v}	A_1	4	10	7
	A_2	3	9	5
	B_1	1	4	3
	B_2	1	4	3
	E_1	6	16	10
	E_2	3	11	8
C_{3h}	A'	2	19	12
	E'	6	11	8
	A''	7	8	6
	E''	3	16	10
C_{5h}	A'	0	19	12
	E_1'	6	1	1
	E_2'	1	10	7
	A''	7	0	0
	E_1''	0	16	10
	E_2''	3	4	3
D_{3h}	A_1'	1	10	7
	A_2'	1	9	5
	E'	6	11	8
	A_1''	3	4	3
	A_2''	4	4	3
	E''	3	16	10
D_{5h}	A_1'	0	10	7
	A_2'	0	9	5
	E_1'	6	1	1
	E_2'	1	10	7
	A_1''	3	0	0
	A_2''	4	0	0
	E_1''	0	16	10
	E_2''	3	4	3
D_{2d}	A_1	3	11	8
	A_2	3	10	6
	B_1	3	10	7
	B_2	4	10	7
	E	7	20	13
D_{4d}	A_1	0	10	7
	A_2	0	9	5
	B_1	3	1	1
	B_2	4	1	1
	E_1	6	4	3
	E_2	3	10	7
	E_3	1	16	10
D_{6d}	A_1	0	10	7
	A_2	0	9	5
	B_1	3	0	0

TABLE IV (*Continued*)

Group	Rep.	Number of tensor components β'	γ'	γ''
	B_2	4	0	0
	E_1	6	0	0
	E_2	0	10	7
	E_3	1	4	3
	E_4	3	1	1
	E_5	0	16	10
S_4	A	6	21	14
	B	7	20	14
	E	7	20	13
S_8	A	0	19 21	12
	B	7	2 0	2
	E_1	6	4	3
	E_2	3	10	7
	E_3	1	16	10
T	A	2	7	5
	E	2	7	5
	F	7	20	13
T_d	A_1	1	4	3
	A_2	1	3	2
	E	2	7	5
	F_1	3	10	6
	F_2	4	10	7
O	A_1	1	4	3
	A_2	1	3	2
	E	2	7	5
	F_1	4	10	6
	F_2	3	10	7
$C_{\infty v}$	A_1	4	10	7
	A_2	3	9	5
	E_1	6	16	10
	E_2	3	10	7
	E_3	1	4	3
	E_4	0	1	1

Induced Raman scattering represents a higher-order contribution to the first-order Raman spectrum in which three, instead of one, photons are absorbed [Fig. 1(d)]. The spectrum is centered about the laser frequency ω_L, and is thus accessible to existing Raman spectrometers. Increased difficulties arise, however, because the higher-order spectrum may be obscured by the fundamental lines in the two-photon Raman spectrum or confused with two-phonon effects. It should be pointed out that neither of these difficulties arise when observing four-photon Raman spectra. Induced Raman scattering has resonances at ω_L and $2\omega_L$, the latter once again being of the most potential value.

In all experiments designed to observe these higher-order phenomena, the dominating characteristic which has to be considered is the extreme weakness of the effects. Various authors[4,11–13] have given estimates of the radiated power in the three- and four-photon Raman effects. According to Ref. 4, the ratio of the intensities of the two-, three, and four-photon Raman spectra at a field intensity of 10^6 cgs units are given by $(\alpha E/\beta E^2)\sim 10^{-2}$ and $(\alpha E/\gamma E^3)\sim 10^{-4}$. The third-order spectra should therefore be readily obtainable, provided field strengths of sufficient magnitude can be used. It will be more difficult to observe the fourth-order spectra, and it may be that this is possible only under resonance conditions. It should be noted that not only will the scattered intensities be relatively large at resonance, but that the nonsymmetric tensors should also be significant, so that many extra modes will be active.

The weakness of the spectra demand that the most intense possible source of excitation be used. In practice, the limiting factor may not be the laser power available, but breakdown of the subject material, which occurs when the strength of the laser electric field reaches that of the fields present in the atomic structure. These fields are typically of the order of 10^6 cgs units. In some cases also it may be necessary to remain below the threshold for stimulated emission in order to obtain the maximum effective field.

As well as giving Raman selection rules, Table I may also be used to find the forms of irreducible tensors transforming according to the one-dimensional repretions of the point groups. The technique consists of extracting from each element of the reducible tensor the part which transforms under the representation in which we are interested. The remainder of the element is zero, so that if two tensor elements project out the same linear combination, the corresponding elements in the irreducible tensor will be equal. As an example, we take a fourth-rank totally symmetric tensor which is required to have D_6 symmetry. The A_1 representation contains three linear combinations $\gamma_3=\gamma_{zzzz}$, $\gamma_{20}=\gamma_{xxxx}+2\gamma_{xxyy}+\gamma_{yyyy}$, and $\gamma_{22}=\gamma_{yyzz}+\gamma_{zzxx}$, from which we deduce that the required tensor has only three independent elements. γ_{xxxx} and γ_{yyyy} will both project out γ_{20} and hence the $xxxx$ and $yyyy$ elements of the irreducible tensor will be equal. The element γ_{xxyy} will project out $\frac{1}{2}\gamma_{20}$, so that the $xxyy$ element will equal one-half of the $xxxx$ element. Application of this procedure to the other elements gives the following result for the irreducible tensor: $\gamma_{xxxx}=\gamma_{yyyy}=\alpha$, $\gamma_{xxyy}=\frac{1}{2}a$, $\gamma_{yyzz}=\gamma_{zzxx}=b$, $\gamma_{zzzz}=c$. All other elements are zero. Using Table I, similar result may be obtained for second-,

third-, and fourth-rank tensors possessing the same initial symmetries as the α, $\bar{\alpha}$, β, $\bar{\beta}$, γ, and $\bar{\gamma}$ tensors, as well as for tensors possessing the symmetry properties of the $\alpha+\bar{\alpha}$, $\beta+\bar{\beta}$, and $\gamma+\bar{\gamma}$ tensors. The above procedure is also applicable to tensors transforming according to two- and three-dimensional representations, but knowledge of normalization constants is required. These constants are not given, though the projection operator method can provide the information.

The higher-order Raman effects represent a rich field for study with high-powered lasers. The spectra may be observed at $\omega_L \pm \omega_{fi}$, $2\omega_L \pm \omega_{fi}$, $3\omega_L \pm \omega_{fi}$, and in the infrared, and in the case of the Raman processes, in either emission or absorption. The relaxation of selection rules implies that a large number of modes unobservable directly in lower-order processes can be measured.

ACKNOWLEDGMENTS

We wish to acknowledge helpful discussions with Professor A. G. McLellan and Professor B. G. Wybourne. One of us (J.H.C.) is the holder of a New Zealand University Grants Committee post-graduate scholarship.

APPENDIX

In Table IV we list the distribution of the components of the β', γ', and γ'' tensors among the various irreducible representations of the important molecular point groups. These tensors have rank three, four, and four, respectively; the first two possess no symmetry, but the third is symmetric in the last two indices. The symmetric structure of the γ'' tensor components is in fact identical with that for a fourth-rank tensor possessing symmetry in any pair of indices. The numbers were obtained using the group-theoretical method of Bhagavantam and Suryanarayana[19] which was described in Sec. III. The characters of the transformation matrices are

$$\chi_{\beta'}(R) = 8\cos^3\theta \pm 12\cos^2\theta + 6\cos\theta \pm 1,$$

$$\chi_{\gamma'}(R) = 16\cos^4\theta \pm 32\cos^3\theta + 24\cos^2\theta \pm 8\cos\theta + 1,$$

and

$$\chi_{\gamma''}(R) = 16\cos^4\theta \pm 24\cos^3\theta + 12\cos^2\theta \pm 2\cos\theta.$$

Equivalent information for the β, $\bar{\beta}$, γ, and $\bar{\gamma}$ tensors, whose symmetry properties are described in Sec. III, may be obtained from Table I.

* Research sponsored in part by the Air Force Office of Scientific Research, Office of Aerospace Research, United States Air Force, under AFOSR Grant 1275-67.

† Present address: Department of Chemistry, University of Waterloo, Waterloo, Ontario, Canada.

[1] S. J. Cyvin, J. E. Rauch, and J. C. Decius, J. Chem. Phys. **43**, 4083 (1965).

[2] R. W. Terhune, P. D. Maker, and C. M. Savage, Phys. Rev. Letters **14**, 681 (1965); P. D. Maker, in *Physics of Quantum Electronics*, edited by P. L. Kelley *et al.* (McGraw-Hill, New York, 1966), p. 60; P. D. Maker and C. M. Savage, 22nd Symposium on Molecular Structure and Spectroscopy, Ohio State University, Columbus, Ohio, September 1969.

[3] S. Dumartin, B. Oksengorn, and B. Vodar, Compt. Rend **261**, 3767 (1965).

[4] L. D. Ievleva and T. Ya. Karagodova, Opt. Spektrosk. **23**, 991 (1967) [Opt. Spectrosc. **23**, 541 (1967)].

[5] S. Yatsiv, M. Rokni, and S. Barak, IEEE J. Quantum Electron. **4**, 900 (1968).

[6] N. N. Badalyan, V. A. Iradyan, and M. E. Movsesyan, ZhETF Pis. Red. **8**, 518 (1968) [JETP Letters **8**, 316 (1968)].

[7] J. F. Ward, Rev. Mod. Phys. **37**, 1 (1965).

[8] R. Wallace, Mol. Phys. **11**, 457 (1966).

[9] W. Heitler, *The Quantum Theory of Radiation* (Oxford U. P., London, 1954), 3rd ed., p. 178.

[10] G. Placzek, *Handbuch der Radiologie* (Akademische Verlagsgesellschaft, Leipzig, 1934), Vol. 6, Pt. 2, p. 205 [English transl.: Lawrence Radiation Laboratory, University of Californa, Translation 526 (L), 1959].

[11] Y.-Y. Li, Acta Physica Sinica **20**, 164 (1964).

[12] S. A. Akhmanov and D. N. Klyshko, ZhETF Pis. Red. **2**, 171 (1965) [JETP Letters **2**, 108 (1965)].

[13] Z.-H. Zhu, Acta Physica Sinica **21**, 1587 (1965).

[14] Reference 10, English translation, p. 38.

[15] G. de B. Robinson, *Representation Theory of the Symmetric Group* (Edinburgh U. P., Edinburgh, 1961), p. 5.

[16] D. E. Littlewood, *The Theory of Group Characters* (Oxford U. P., London, 1958), 2nd ed., Chap. 9, p. 150.

[17] These numbers may be obtained using Eq. (8), or by empirically calculating the numbers of components in the totally symmetric tensors.

[18] M. Tinkham, *Group Theory and Quantum Mechanics* (McGraw-Hill, New York, 1964), Chap. 3, p. 39.

[19] S. Bhagavantam and D. Suryanarayana, Acta Cryst. **2**, 21 (1949).

Reprinted from:

CHEMICAL PHYSICS LETTERS

Volume 9, No. 6, 15 June 1971

ELECTRONIC RAMAN SPECTRA OF Co^{2+} IN $CdCl_2$, $CdBr_2$ AND $MnCl_2$ *†

D. J. LOCKWOOD
Department of Chemistry, University of Waterloo, Waterloo, Ontario, Canada

and

J. H. CHRISTIE ‡
Department of Physics, University of Canterbury, Christchurch, New Zealand

pp. 559 – 563

NORTH-HOLLAND PUBLISHING COMPANY — AMSTERDAM

ELECTRONIC RAMAN SPECTRA OF Co^{2+} IN $CdCl_2$, $CdBr_2$ AND $MnCl_2$ *†

D. J. LOCKWOOD
Department of Chemistry, University of Waterloo, Waterloo, Ontario, Canada

and

J. H. CHRISTIE ‡
Department of Physics, University of Canterbury, Christchurch, New Zealand

Received 22 April 1971

The low-lying electronic energy levels of the divalent cobalt ion in doped isomorphic single crystals of $CdCl_2$, $CdBr_2$ and $MnCl_2$ have been measured at low temperatures by means of the Raman effect. The observed energies, which are markedly concentration dependent, are assigned to transitions within the ^4F ground-state manifold of Co^{2+} with the aid of crystal-field theory.

The electronic Raman effect has proved to be very useful in determining the low-lying energy levels of ions in crystals [1] and, in so doing, has provided additional tests for crystal-field theory. Almost all previous electronic Raman studies of ions in crystals have been limited to the lanthanides, the exceptions being studies of the Co^{2+} ion in $CoCl_2$ [2], CoF_2 [3] and $Co(NH_4)_2SO_4.6H_2O$ [4]. Here, we report the first observations of electronic Raman scattering by a transition metal ion in dilute systems.

The cobaltous ion was chosen for this study because it possesses low-lying energy levels that are suitable for electronic Raman effect measurements. The blue-green window in the Co^{2+} visible absorption spectrum dictates the use of argon laser excitation of the Raman spectrum. In certain cases, this could lead to resonance enhancement of the spectrum, because of the close proximity of argon laser lines to cobalt absorption bands. A series of crystals with the $CdCl_2$ structure were chosen as host materials. Crystals such as $CdCl_2$, $MnCl_2$ and $CdBr_2$ are readily doped with cobalt to high concentrations, since their structure is isomorphic with that of $CoCl_2$ [5]. The $CdCl_2$ structure is trigonal, space group D^5_{3d}, with one molecular unit to the primitive cell [5]. The crystal is made up of layers of anions, which are nearly cubic close-packed, with cations sandwiched between alternate anion layers. Each cation is surrounded by a trigonally distorted octahedron of anions. The cobalt ion, when dissolved in these crystals, substitutes for the cation, and so experiences a crystal field of D_{3d} symmetry. This field effectively reduces Co^{2+} energy-level degeneracies, which makes this crystal system more interesting than the usual cubic environment. The ^4F ground-state energy-level splitting for Co^{2+} in a trigonal field has been described in detail in ref. [2]. The six Kramers-degenerate energy levels in the $^4T_{1g}$ ground-state multiplet can be characterized by their $|J, M_J\rangle$ quantum numbers. The $|1/2, \pm 1/2\rangle$ state is lowest, followed by the pair $|3/2, \pm 3/2\rangle$, $|3/2, \pm 1/2\rangle$ and the trio $|5/2, \pm 1/2\rangle$, $|5/2, \pm 3/2\rangle$, $|5/2, \pm 5/2\rangle$, in order of increasing energy. Therefore theory predicts five electronic transition energies in the form of a doublet and a triplet with all transitions allowed in the electronic Raman effect, according to ΔJ selection rules.

Single-crystal samples of $CdCl_2$, $MnCl_2$ and $CdBr_2$ doped with cobalt at different concentrations ranging from 1 to 50 wt. % were grown in

* Presented in part at the Second International Conference on Raman Spectroscopy, Oxford, England (1970).

† Research supported by the U.S. Air Force Office of Scientific Research under AFOSR Grant No. 1275-67 and by the N. Z. University Grants Committee under URG Grant No. 66-241.

‡ N. Z. University Grants Committee post-graduate scholar.

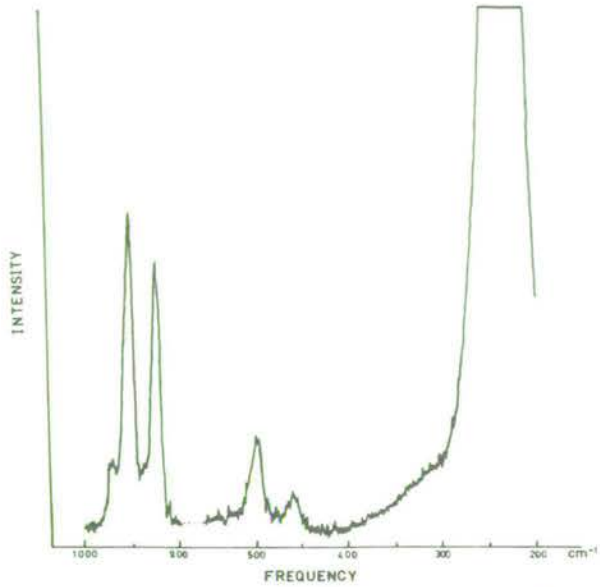

Fig. 1. Raman spectrum of $CdCl_2$:Co (3%) at 4.2°K.

our laboratory for use in this study. The Raman spectra were excited with argon laser radiation at 4880 Å. The scattered light was analyzed with a double monochromator, detected photoelectrically, and the Raman signal processed with either a lock-in amplifier or an on-line computer-controlled photon counting system. Raman spectra were recorded at sample temperatures of 4.2, 83 and 300°K. However, detailed studies were carried out at 4.2°K only, because the electronic lines are most prominent at this low temperature. Each sample was mounted so that the direction of propagation of the laser beam was perpendicular to the crystal *c*-axis, and the scattered light was observed in the *c*-axis direction. Typical electronic Raman spectra were recorded with a spectral slit width of 6 cm^{-1} are shown in figs. 1, 2 and 3. Fig. 1 depicts a $CdCl_2$: Co (3%) Raman spectrum. The Co^{2+} electronic Raman lines are distinguishable from the $CdCl_2$ phonon bands by their different temperature dependence, and by comparison with a pure $CdCl_2$ Raman spectrum. Such evidence indicates that the lines at 500, 923 and 953 cm^{-1}, and the sideband at 969 cm^{-1}, in fig. 1 are electronic in origin. The strong Raman band at 235 cm^{-1} is a $CdCl_2$ phonon line of A_{1g} symmetry, and the weak band at 460 cm^{-1} is assigned to the overtone of the A_{1g} fundamental [6, 7]. The structure in fig. 1 between these two bands arises from two-phonon scattering. The electronic lines are approximately 25 times weaker in intensity than the phonon line at 235 cm^{-1}. This is to be compared with $CoCl_2$, where the electronic line intensities are comparable to that of the phonons [2]. The reduced electronic line intensity in $CdCl_2$: Co (3%) is in accordance with the reduction in cobalt concentration as compared with $CoCl_2$. The $MnCl_2$: Co (3%) spectrum shown in fig. 2 exhibits features similar to those seen in

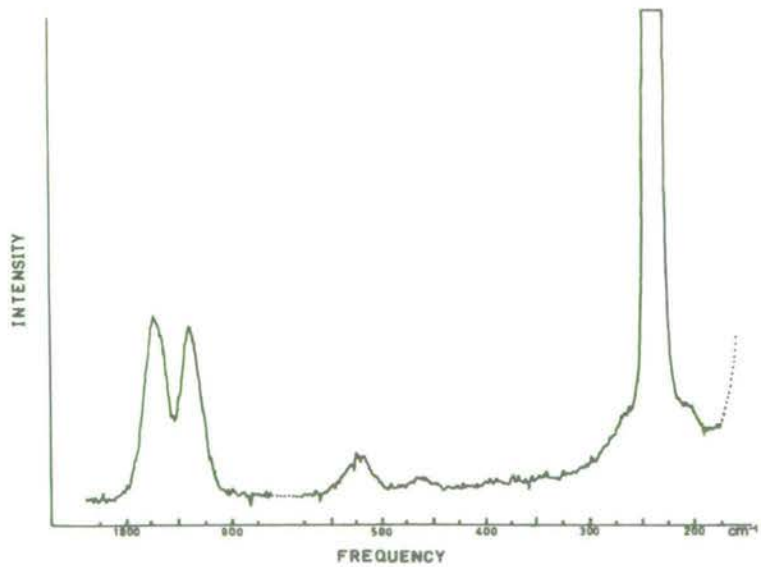

Fig. 2. Raman spectrum of $MnCl_2$:Co (3%) at 83°K.

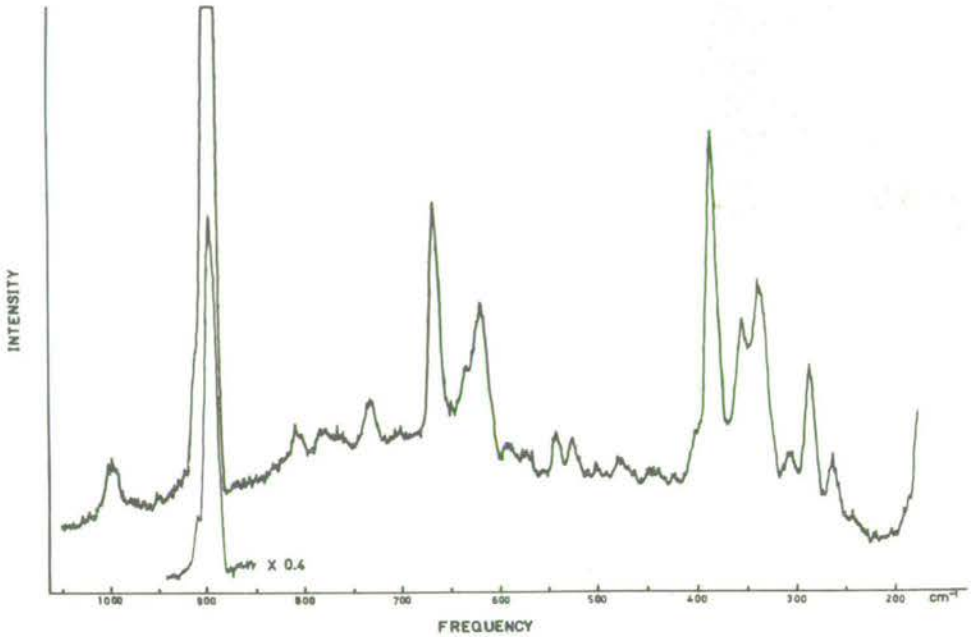

Fig. 3. Raman spectrum of $CdBr_2$:Co (3%) at 4.2°K.

$CdCl_2$: Co. Electronic lines are evident at 206, 529, 936 and 967 cm^{-1}. The 206 cm^{-1} line is partially masked by the $MnCl_2$ A_{1g} phonon line at 241 cm^{-1} [7]. The line at 463 cm^{-1} in fig. 2 is the counterpart of the 460 cm^{-1} line in $CdCl_2$. It can be seen from figs. 1 and 2 that the electronic Raman spectra of $CdCl_2$: Co and $MnCl_2$: Co are very similar, particularly in the 950 cm^{-1} region. $CdBr_2$: Co, however, is different. A 3%-cobalt spectrum is shown in fig. 3. There is a large number of lines in the low frequency region above the $CdBr_2$ A_{1g} phonon line at 151 cm^{-1} [6,7]. Only the strong 894 cm^{-1} and weak 995 cm^{-1} lines together with a weak line at 284 cm^{-1}, have been determined to be electronic Raman lines. Cobalt doped $CdBr_2$ is a green-coloured crystal, which means that the argon laser frequencies are much closer to Co^{2+} absorption lines than in the blue-coloured chlorides. This would lead to an enhancement of resonance effects, so that some of the $CdBr_2$: Co low-frequency bands are probably due to fluorescence. However, *pure* $CdBr_2$ exhibits some low-frequency structure also, which indicates an impurity problem [7] as well as fluorescence. The identity of the electronic lines in $CdBr_2$: Co was verified by running numerous samples with different cobalt concentrations. The fluorescence structure varied from crystal to crystal, even between different samples with the same nominal cobalt concentration, whereas the electronic features were comparatively insensitive to such changes.

The frequencies of electronic Raman lines seen in $CoCl_2$, $CdCl_2$: Co (3%), $MnCl_2$: Co (3%) and $CdBr_2$: Co (3%) are compared in table 1. All five predicted electronic transitions have been observed in $CoCl_2$ only, but the results obtained

Table 1
Co^{2+} electronic Raman frequencies in cm^{-1} (± 2 cm^{-1}) recorded at 4.2°K

$CoCl_2$ [a]	$CdCl_2$:Co (3%)	$MnCl_2$:Co (3%)	$CdBr_2$:Co (3%)
223	-	206	284
551	500	529	-
962	923	936	894
984	953	967	995
1014	969	-	-

[a] Ref. [2].

Table 2
A comparison between infrared and Raman Co^{2+} electronic frequencies (in cm^{-1}) at 4.2°K for various cobalt concentrations in $CdCl_2$

Raman		Infrared	
$CdCl_2$:Co (3%)	$CdCl_2$:Co(10%)	$CdCl_2$:Co (3%)	$CdCl_2$:Co(10%)
923	917	923.8	915.0
	929		
953	942	952.4	941.0
969	960	966.0	959.5
		996.0	988.5
		1011.6	
		1026.8	1016.5

for the different crystal hosts do show some correlation. A general pattern of two lines at $\approx 250\ cm^{-1}$ and $\approx 530\ cm^{-1}$ together with a group at $\approx 950\ cm^{-1}$ is evident. This agrees with theory. The low frequency electronic line has not yet been observed in the $CdCl_2$: Co system, most probably because it is hidden beneath the intense phonon line at 235 cm^{-1}. Crystal-field theory has been used in an attempt to predict the experimentally observed frequencies. It was reported for $CoCl_2$ [2] that the crystal-field parameters could not be adjusted to give a good fit for the doublet ($J = 1/2 \rightarrow J = 3/2$ transitions) and triplet ($J = 1/2 \rightarrow J = 5/2$) simultaneously. Theoretical calculations for lightly doped $CdCl_2$, $MnCl_2$ and $CdBr_2$ produced a similar result. For example, in $MnCl_2$: Co (3%), using the reasonable assignments of $|1/2, \pm 1/2\rangle \rightarrow |3/2, \pm 3/2\rangle$, $|1/2, \pm 1/2\rangle \rightarrow |3/2, \pm 1/2\rangle$, $|1/2, \pm 1/2\rangle \rightarrow |5/2, \pm 1/2\rangle$ and $|1/2, \pm 1/2\rangle \rightarrow |5/2, \pm 3/2\rangle$ for the lines at 206, 529, 936 and 967 cm^{-1} respectively, the following results were obtained. The pair of lines at 206 and 529 cm^{-1} produced a spin-orbit coupling constant ζ of 447 cm^{-1} and a δ/ζ of -1.04, where δ is the trigonal field parameter. In contrast to this result, the 936 and 967 cm^{-1} lines produced the values $\zeta = 481\ cm^{-1}$ and $\delta/\zeta = -0.30$. Despite the lack of success in fitting parameters, the crystal-field calculations did show that $CdCl_2$: Co and $MnCl_2$: Co have a similar δ/ζ ratio, and that δ is smaller in $CdBr_2$ in comparison with the chlorides.

In the doped crystals, the number, strength and position of the electronic lines in the 950 cm^{-1} region was found to be very dependent on the cobalt concentration. In table 2, Raman frequencies obtained for $CdCl_2$: Co at 3 and 10 wt. % concentrations are compared. Note the shift in frequency of the lines as the concentration of cobalt increases, and the appearance of a new line at 929 cm^{-1}. This behaviour is typical of all the crystal hosts studied here. The appearance of additional bands in the Raman spectra as the cobalt concentration increases indicates that cobalt exchange interactions are taking place. The concentration dependence of the electronic spectra is being further investigated in detail to characterise these interactions. The frequencies of the host lattice vibrations were also found to be dependent on the cobalt concentration. The cobalt-doped systems exhibit *one-mode* behaviour [8]. Details of the phonon behaviour will be reported elsewhere.

Our cobalt-doped crystals have also been examined in the infrared by G. D. Jones and coworkers. The spectral features obtained by infrared absorption in the 950 cm^{-1} region for $CdCl_2$: Co (3 and 10%) are listed in table 2 for comparison with the Raman results. The agreement between infrared and Raman results is excellent. The infrared spectra are complicated by the presence of additional peaks (see table 2) and vibronic sidebands on the high-frequency side of the electronic lines. The Raman spectra are free of such confusion. This fact gives Raman spectroscopy a definite superiority over infrared techniques when it comes to interpretting electronic spectra of the type described above.

We wish to acknowledge useful discussions with Dr. G. D. Jones and thank him for providing the infrared results prior to publication.

REFERENCES

[1] A. Kiel, in: Proc. Intern. Conf. Light Scattering Spectra of Solids, ed. G. B. Wright (Springer, New York, 1969) p. 245.
[2] J. H. Christie and D. J. Lockwood, Chem. Phys. Letters 8 (1971) 120.
[3] R. M. Macfarlane, Phys. Rev. Letters 25 (1970) 1454.
[4] A. Azima, P. Grunberg, J. Hoff, J. A. Koningstein and J. Preudhomme, Chem. Phys. Letters 7 (1970) 565.
[5] R. W. G. Wyckoff, Crystal structures, Vol. 1 (Interscience, New York, 1964) p. 270.

[6] D.J. Lockwood, in: Proc. Intern. Conf. Light Scattering Spectra of Solids, ed. G.B. Wright (Springer, New York, 1969) p. 75.
[7] D.J. Lockwood, to be published.
[8] I.F. Chang and S.S. Mitra, Phys. Rev. 172 (1968) 924.

4

Reprinted from

PROCEEDINGS OF THE SECOND INTERNATIONAL CONFERENCE

on

LIGHT SCATTERING IN SOLIDS

(Paris, July 19-23, 1971)

edited by

M. BALKANSKI

FLAMMARION SCIENCES
20 rue de Vaugirard, Paris 6e

theory than the case of low energy excitations. A detailed calculation would have to be performed : it would probably explain that some excitations show intensities so small that they are not observed.

In addition, we recently got experimental data concerning Raman scattering in $KCoF_3$[23], which, when combined with our previous[7] and planned work in $RbMnF_3$–Co^{2+}, as well as with neutron scattering studies on $KMnF_3$–Co^{2+} [10] and $KCoF_3$[11], will contribute to provide a large set of results important to understand exchange in Co^{2+} compounds.

ACKNOWLEDGEMENTS

The MnF_2–Co^{2+} crystals were kindly furnished by W. J. L. Buyers and H. J. Guggenheim and we wish to thank them very much. We benefited of enlightening discussions with S. J. Allen and, concerning MnF_2–Co^{2+}, with R. E. Dietz and G. Parisot. We had the opportunity to work with the help of preprints sent by various cited authors (ref.[1, 2, 6, 11b]).

REFERENCES

[1] A. Ishikawa and T. Moriya, J. Phys. Soc. Japan **30,** 117 (1971).
[2] S. J. Allen Jr and H. J. Guggenheim, to be published.
[3] R. Weber, J. Appl. Phys. **40,** 995 (1969).
[4] *a*) G. Parisot, S. J. Allen, R. E. Dietz and H. J. Guggenheim, R. Moyal, P. Moch and C. Dugautier, J. Appl. Phys. **41,** 890 (1970).
b) R. Moyal. Thèse 3e cycle, Paris (1970).
[5] P. Moch, R. Moyal, C. Dugautier and H. J. Guggenheim, J. Physique **32,** p. C1 806 (1971).
[6] R. M. Macfarlane, Phys. Rev. Letters **25,** 1454 (1970).
[7] P. Moch et al. Laboratoire de Physique des solides. Rapport d'activité n° 7 (Paris 1971), p. 152.
[8] W. J. L. Buyers, R. A. Cowley, T. M. Holden and R. W. H. Stevenson 5 Appl. Phys. **39,** 1118 (1968).
[9] P. Martel, R. A. Cowley and R. W. H. Stevenson, Canad. J. Phys. **46,** 1355 (1968).
[10] F. C. Svensson, W. J. L. Buyers, T. M. Holden, R. A. Cowley and R. W. H. Stevenson, Canadian J. Phys. **47,** 1983 (1969).
[11a] W. J. L. Buyers, R. A. Cowley, T. M. Holden, E. C. Svensson, M. T. Hutchkings, D. Hukin and R. W. H. Stevenson : Proc of 11th international conference of low temperature Physics, St Andrews, Scotland, 1968 (Univ. of St Andrews) p. 1330.
[11b] W. J. L. Buyers, T. M. Holden, E. C. Svensson, R. A. Cowley and M. T. Hutchkings : to be published.
[12a] H. M. Gladney, Phys. Rev. **146,** 253 (1966).
[12b] H. Kamimura and Y. Tanabe, J. Appl. Physics **34,** 1239 (1963).
[13a] M. E. Lines, Phys. Rev. **137,** A982 (1965).
[13b] H. Kamimura, J. Appl. Phys. **35,** 844 (1964).
[14] R. A. Erickson, Phys. Rev. **90,** 779 (1953).
[15] F. Hartmann-Boutron, Journal de Physique **29,** 212 (1968).
[16] R. J. Elliot and M. F. Thorpe, J. Appl. Phys. **39,** 802 (1968).
[17] G. M. Copland and P. M. Levy, Phys. Rev. B **1,** 3043 (1970).
[18] P. Moch, G. Parisot, R. E. Dietz and H. J. Guggenheim, Proceedings of the international conference on light scattering of solids (Springer Verlag, New York, 1969) p. 231.
[19a] P. A. Fleury and R. Loudon, Phys. Rev. **166,** 514 (1968).
[19b] A. P. Cracknell, J. Phys. C **2,** 500, 1969.
[20] J. Cipriani, S. Racine and R. Dupeyrat, Physics letters, **34** A, 187 (1971).
[21] *a*) R. M. Macfarlane and S. Ushioda, Sol. state Comm. **8,** 1081 (1970).
b) R. M. Macfarlane and H. Morawitz, Bull. Am. Phys. Soc. **15,** 1604 (1970).
[22] L. F. Johnson, R. E. Dietz and H. J. Guggenheim, Appl. Phys. Letters **5,** 21 (1964).
[23] P. Moch and C. Dugautier to be published.

ELECTRONIC RAMAN SCATTERING IN $CoCl_2$

J. H. CHRISTIE
Department of Physics, University of Canterbury, Christchurch, New Zealand
AND D. J. LOCKWOOD
Department of Chemistry, University of Waterloo,
Waterloo, Ontario, Canada.

ABSTRACT

Crystal field theory shows that the Co^{2+} ion in $CoCl_2$ possesses six doubly-degenerate low-lying energy levels with a total splitting of about 1000 cm^{-1}. We have measured the Raman scattering spectrum of the Co^{2+} ion in $CoCl_2$ at room, liquid nitrogen and liquid helium temperatures. Bands have been seen in the room temperature spectrum that disappear at lower temperatures. These features are assigned to electronic hot bands. At liquid helium temperatures, electronic transitions with energies of 234, 549, 962, 984 and 1015 cm^{-1} were observed. An attempt to fit these values to an energy level scheme derived from crystal field theory gave poor results. Below 25 K, $CoCl_2$ is antiferromagnetic, and attempts have been made to measure the $k = 0$ magnon energy with, as yet, no success. However, a magnetic effect has been observed in association with the 549 cm^{-1} electronic line. When the crystal temperature is lowered below T_N, an exciton sideband appears at 577 cm^{-1}.

Electronic Raman scattering by transition metal ions has been given scant attention in comparison with the rare earth ions. This neglect is underserving; there is much to be learnt about the electronic and magnetic properties of transition metal ions from a Raman study of their low-lying energy levels. There have been a few publications reporting elec-

tronic Raman studies of the Co^{2+} ion in various crystalline materials[1-4]. In this paper we present further results from our Raman investigations of the cobaltous ion in $CoCl_2$[1].

THEORY

The crystal structure of $CoCl_2$ is trigonal, space group D_{3d}^5, with one molecular unit in the primitive cell[5]. The Co^{2+} ion experiences a crystal field that is only a slight trigonal distortion from octahedral symmetry. The crystalline field and spin-orbit interaction act on the Co^{2+} ^4F free-ion ground state to produce six lowest-lying energy levels, each of which is Kramers degenerate[1]. Therefore, crystal field theory predicts five electronic transition energies that are expected[6,7] to appear in the region 100-1000 cm^{-1}. Fig. 1 illustrates qualitatively the energy level splittings. The levels of this ground-state multiplet are conveniently distinguished by their $|J, M_J\rangle$ quantum numbers. Each of the states within the manifold transforms according to even representations of the double group D_{3d}. Using[8] the full rotation group compatibility table for D_{3d}, the specific representations to which each level belongs have been determined. The results are depicted in Fig. 1, using the notation of Koster *et al.*[8].

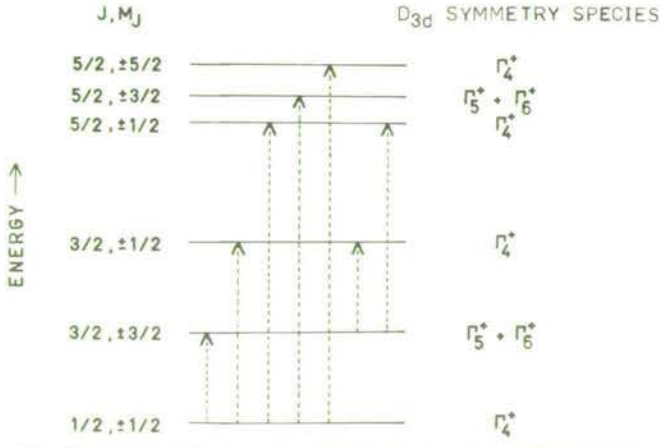

FIG. 1. — Ground state energy level splittings for Co^{2+} in $CoCl_2$. The arrows denote experimentally observed electronic Raman transitions, and the energy levels are labelled with their quantum numbers and corresponding symmetry.

Raman transitions are allowed between two electronic states if the direct product of the representations to which they belong contains the $\Gamma_1^+(A_{1g})$, $\Gamma_2^+(A_{2g})$ or $\Gamma_3^+(E_g)$ representations, or any sum of them. In electronic Raman scattering, there is no requirement that the Raman tensor be symmetric[9]. In fact, the Raman tensor for the Γ_2^+ representation is completely antisymmetric[10]. Therefore, in general, the tensor element $\alpha_{\rho\sigma} \neq \alpha_{\sigma\rho}$ for $\rho \neq \sigma$. For the group D_{3d}, the Raman tensors have the following non-zero elements.

$$\Gamma_1^+ \quad \alpha_{xx} = \alpha_{yy} = a; \quad \alpha_{zz} = b$$

$$\Gamma_2^+ \quad \alpha_{xy} = -\alpha_{yx} = c$$

$$\Gamma_3^+ \quad \alpha_{xx} = -\alpha_{yy} = \alpha_{xy} = \alpha_{yx} = d$$

$$\alpha_{yz} = -\alpha_{xz} = e; \quad \alpha_{zy} = -\alpha_{xz} = f$$

The z axis is chosen to be parallel to the crystal c axis. The Γ_3^+ tensor is asymmetric in the off-diagonal z components because the tensor is an admixture of symmetric and antisymmetric parts[10]. For electronic transitions in $CoCl_2$, the relevant portions of the multiplication table for representations of the double group D_{3d} are

$$\Gamma_4^+ \times \Gamma_4^+ = \Gamma_1^+ + \Gamma_2^+ + \Gamma_3^+,$$

$$\Gamma_4^+ \times (\Gamma_5^+ + \Gamma_6^+) = 2\Gamma_3^+,$$

$$\text{and } (\Gamma_5^+ + \Gamma_6^+) \times (\Gamma_5^+ + \Gamma_6^+) = 2\Gamma_1^+ + 2\Gamma_2^+.$$

The direct product $\Gamma_4^+ \times \Gamma_4^+$ reduces into the sum of all three Raman-active representations. Therefore Raman transitions between two Γ_4^+ states will in general be visible in all polarizations, the only symmetry restrictions being that $|\alpha_{yz}| = |\alpha_{xz}|$ and $|\alpha_{zy}| = |\alpha_{zx}|$. Γ_4^+ to $(\Gamma_5^+ + \Gamma_6^+)$ transitions will be characterised by a zero α_{zz} component, as well as the equal intensities specified under the Γ_3^+ list above. In both the previous cases, a non-zero antisymmetric tensor will be manifest as a difference in scattered intensity of the α_{zx} and α_{yz} components as compared with the intensities of the α_{xz} and α_{zy} components respectively. For transitions between Γ_4^+ states, there is also the possibility of asymmetry in the α_{xy} and α_{yx} components. The other possible transition is from a $(\Gamma_5^+ + \Gamma_6^+)$ state to another $(\Gamma_5^+ + \Gamma_6^+)$ state, and this transition will be characterised by zero α_{yz}, α_{zx}, α_{zy} and α_{xz} components. The antisymmetric $\alpha_{xy} - \alpha_{yx}$ component arising from Γ_2^+ may result in visible and equal intensity scattering in the xy and yx polarizations.

Below 24.7 K, $CoCl_2$ is antiferromagnetic, with a magnetic unit cell twice as large in the c-axis direction as the crystallographic one[11,12]. A $CoCl_2$ crystal is made up of layers of chlorine ions with a layer of cobalt ions sandwiched between alternate chlorine layers. The layers are perpendicular to the crystal c-axis direction. In the antiferromagnetic state, the atomic moments in $CoCl_2$ are directed parallel to the plane of the layers and are parallel to one another within a given layer. The moment directions in adjacent cobalt layers are antiparallel, and thus the crystal as a whole is antiferromagnetic[12]. The anisotropy and exchange fields associated with the ferromagnetic ordering lift the Kramers degeneracy of the Co^{2+} electronic levels. Therefore at temperatures below T_N, each of the energy levels shown in Fig. 1 is split in two. Exciton states with wavevector dependence are formed by considering all single-ion transitions on different sites[13]. The interaction between the two magnetic sublattices can result in further Davydov splittings of exciton levels possessing the appropriate symmetry and wavevector.

EXPERIMENTAL

Cobalt chloride exhibits strong optical absorption in all except the blue region, and is therefore suitable for investigation with the high frequency lines of the argon ion laser. Raman spectra were excited with radiation at wavelengths of 4880, 4765 and 4579 Å produced by a 2 watt Spacerays Model 5600 argon laser. Individual laser lines were selected with the aid of an intra-cavity prism. The scattered light was

analysed with a Jarrell-Ash Model 25-103 double 1-*m* spectrometer, and detected photoelectrically with a thermoelectrically cooled EMI 6255 SA photomultiplier. The Raman signal was processed with a photon-counting system controlled by an on-line DEC PDP-8 computer. The polarization of the Raman lines was determined by fixing the incident light polarization with a half-wavelength plate and Glan-Thompson prism, and analyzing the scattered light with a Nicol prism.

The $CoCl_2$ crystals were grown from the melt using the Stockbarger technique. Analar grade powders of the hydrated salt were first dehydrated by heating in vacuum for several days, further treated with dry HCl gas, and then sealed into quartz ampoules. The crystals were grown by slowly lowering the ampoules through a sharp temperature gradient. In this way clear single crystals of $CoCl_2$ were obtained with boule dimensions of about 1 cm in diameter and 2 cm in length. The crystal orientation was determined from the direction of the cleavage planes, as $CoCl_2$ will cleave readily along covalent-bonded chlorine planes perpendicular to the *c* axis, but not in any other direction. The *c*-axis direction varied from crystal to crystal, and was usually inclined to the axis of the quartz tube. Crystals of $CoCl_2$ are hygroscopic, and therefore dry nitrogen atmospheres were used when Raman samples were being prepared to prevent rehydration from atmospheric moisture. The Raman sample was cleaved from the crystal boule just prior to mounting on the cold finger of a Hoffman low-temperature Dewar. The sample was mounted such that the laser beam travelled through the crystal parallel to the cleavage plane, and the scattered light was viewed in the *c*-axis direction.

Even though $CoCl_2$ exhibits[14] a minimum optical absorption at $\sim 21{,}000\ cm^{-1}$, there is still sufficient absorption to require surface scattering experiments. The laser beam was directed onto the face of the crystal, and the light scattered from or near the surface was observed. In the low temperature experiments, the crystal is not in direct contact with the liquid coolant and is absorbing a significant proportion of the laser light. Therefore the actual crystal temperature is higher than that of the refrigerant. For example, with 4579 Å excitation, the crystal temperature was of the order of 15 K during liquid helium runs. Some features of the spectra in fact depend on which laser frequency is being used. The laser line intensities are ordered as follows, $I_{4880} \gg I_{4765} \gg I_{4579}$, whereas the sample absorption decreases with decreasing wavelength in this region[14], and thus the absorbed laser power is much lower at 4579 Å compared with 4880 Å. This means that the sample temperature during liquid helium experiments is lower when using the 4579 Å laser line than when exciting with 4880 Å, and the spectral features of

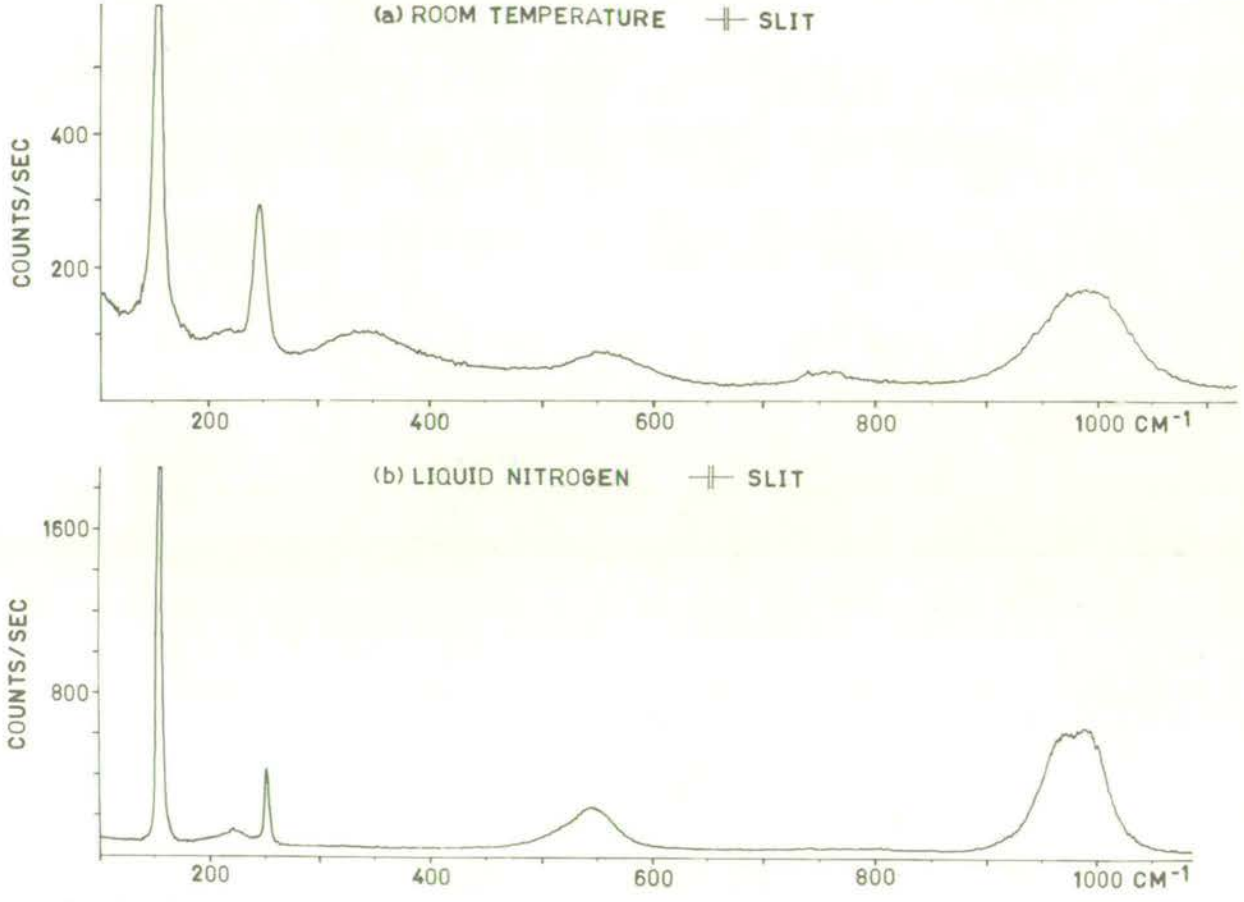

FIG. 2. — Raman spectrum of $CoCl_2$ recorded at room and liquid nitrogen temperatures using the 4880 Å laser line.

magnetic origin are very temperature dependent in the 4.2 to 25 K temperature range. Despite the fact that there is comparatively little power in the 4579 Å laser line, it was found that this line gave the strongest Raman spectrum in terms of absolute intensities. The change in crystal absorption between 4880 Å and 4579 Å is too small to account for the large increase in scattered intensity, especially with the great difference in laser powers at these two wavelengths. The Raman spectrum is resonance enhanced under excitation at 4579 Å (21,838 cm^{-1}). This laser line is coupling to two weak spinforbidden bands[14] at 21,790 ± 30 cm^{-1} and 21,900 ± 30 cm^{-1}. Because of the desirable conditions of low sample heating and high Raman scattering intensity,

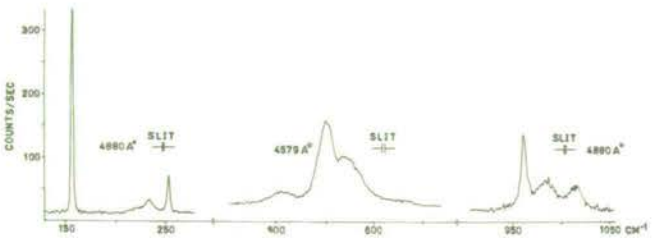

FIG. 3. — Raman spectrum of $CoCl_2$ recorded at liquid helium temperature using the 4579 and 4880 Å laser lines.

the 4579 Å laser line was favoured in this investigation. However, the laser lines at 4880 and 4765 Å were used to verify spectral information obtained with the 4579 Å line.

Typical spectra obtained at room and liquid nitrogen temperatures are shown in Fig. 2. The spectra are plotted directly by computer using digitised intensity and frequency data recorded permanently on tape by the PDP-8 computer. Fig. 3 shows a Raman spectrum obtained at liquid helium temperature. A comparison of the spectra in Figs. 2 and 3 reveals the strong temperature dependence of the Raman line widths. The frequencies and widths of the observed Raman lines are given in Table I.

It should be noted that the Co^{2+} electronic lines are visible in the room temperature Raman spectrum. We believe this to be first observation of electronic Raman scattering by ions in solids at room temperature. Such scattering was not observed in our earlier work[1]. Improvements since then in crystal quality, and changing the signal processor from a PAR HR-8 lock-in amplifier to the photon counting system, resulted in an increased signal-to-noise ratio that enabled us to pick out these lines.

DISCUSSION OF RESULTS

The intense sharp lines at 152 and 250 cm^{-1} in the room temperature spectrum are the two Raman-active first-order $k = 0$ phonons of $CoCl_2$[15]. The spectrum also shows a series of broad bands at 344, 559, 755 and 986 cm^{-1}, with a fifth line barely visible at 220 cm^{-1}. These bands are assigned to Co^{2+} electronic transitions. On cooling the sample, the 344 and 755 cm^{-1} lines disappear, as can be seen in Fig. 2. Also, if these frequencies are added to that of the 220 cm^{-1} line, the following frequencies are obtained.

$$(344 \pm 5) + (220 \pm 3) = 564 \pm 8\ cm^{-1}$$

$$(755 \pm 5) + (220 \pm 3) = 975 \pm 8\ cm^{-1}$$

These frequencies agree with those of the Raman lines at 559 and 986 cm^{-1} respectively, when the total uncertainty of ± 11 cm^{-1} is taken into account. Therefore the 344 and 755 cm^{-1} bands can be assigned to transitions from a thermally populated energy level 220 cm^{-1} above the ground state to higher states represented by the 559 and 986 cm^{-1} bands. At 300 K, $kT \approx 210\ cm^{-1}$, indicating an appreciable population of a 220 cm^{-1} excited state, which is consistent with the experimentally observed intensities. The appearance, of these hot bands is, in itself, confirmation of the electronic nature of the 220, 559 and 986 cm^{-1} Raman transitions. On the basis of the energy level scheme given in Fig. 1, and knowing the expected pattern of the electronic lines[1,16], the observed energies have been assigned to transitions within

TABLE I. — Frequencies (cm^{-1}), linewidths (cm^{-1}) and assignments of Raman lines observed in $CoCl_2$ at room, liquid nitrogen and liquid helium temperatures

Assignment	Room Temperature Frequency	Room Temperature Width	Liquid Nitrogen Frequency	Liquid Nitrogen Width	Liquid Helium Frequency	Liquid Helium Width
E_g phonon	152.0 ± 0.5	10 ± 1	155.5 ± 0.5	< 3	156.6 ± 0.3	< 1.2
A_{1g} phonon	250 ± 1	< 14	253.0 ± 0.5	< 3	253 ± 0.5	< 3.5
$\|1/2, \pm 1/2\rangle \rightarrow \|3/2, \pm 3/2\rangle$	220 ± 3	?	221 ± 2	20 ± 3	233.7 ± 0.5	10 ± 1
$\|3/2, \pm 3/2\rangle \rightarrow \|3/2, \pm 1/2\rangle$	344 ± 5	75 ± 5	—		—	
$2 \times A_{1g}$ phonon	—		—		510 ± 2	35 ± 3
$\|1/2, \pm 1/2\rangle \rightarrow \|3/2, \pm 1/2\rangle$	559 ± 3	70 ± 5	545 ± 1	51 ± 2	549 ± 0.5	20 ± 1
Exciton sideband	—		—		577 ± 2	28 ± 3[a]
$\|3/2, \pm 3/2\rangle \rightarrow \|5/2, ?\rangle$	755 ± 5	65 ± 15	—		—	
$\|1/2, \pm 1/2\rangle \rightarrow \|5/2, ?\rangle$	986 ± 3	90 ± 5	—		—	
$\|1/2, \pm 1/2\rangle \rightarrow \|5/2, \pm 1/2\rangle$	—		968 ± 5	50 ± 10	961.5 ± 0.5	6 ± 1
$\|1/2, \pm 1/2\rangle \rightarrow \|5/2, \pm 3/2\rangle$	—		987 ± 2	50 ± 10	983.5 ± 1	20 ± 3
$\|1/2, \pm 1/2\rangle \rightarrow \|5/2, \pm 5/2\rangle$	—		—		1014.5 ± 1	18 ± 3

[a] Strongly dependent on temperature.

the ground-state multiplet, as indicated in Table I. The triplet structure of the 986 cm^{-1} band is not resolved at room temperature, and consequently the M_J value can not be stated.

At liquid nitrogen temperature, the two phonon lines have become sharper and have increased in frequency. Lowering the temperature to liquid helium temperature produces only a slight increase in frequency and further narrowing of the lines. The temperature dependence of the electronic lines is much more marked, and will be discussed in detail.

The $|1/2, \pm 1/2\rangle \rightarrow |3/2, \pm 3/2\rangle$ transition changes only slightly in frequency with a change in temperature from room to liquid nitrogen temperature. But at liquid helium temperature, the frequency of this band has increased by 14 cm^{-1}. The band sharpens appreciably as the temperature is lowered, and this is characteristic of all the observed electronic bands. The $CoCl_2$ crystal is in the antiferromagnetic state at liquid helium temperature, and therefore the observed electronic energies now correspond to transitions between exciton states at $k = 0$. The sudden change in the frequency of the $|1/2, \pm 1/2\rangle \rightarrow |3/2, \pm 3/2\rangle$ transition on cooling through the Néel point is indicative of a change from single-ion to exciton scattering. Theory predicts two exciton energies in the 230 cm^{-1} region, but only the one at 234 cm^{-1} has been observed. The other band may be hidden by the intense phonon line at 253 cm^{-1}. Also, because of the close proximity in energy and similarity in symmetry, there could be strong coupling between the excitons and this vibrational mode. The temperature dependence of the phonon linewidth around T_N is being investigated to find evidence for this coupling. The separation between exciton pairs can be estimated from a knowledge of the $CoCl_2$ magnon energy, which corresponds to a transition between the exciton states associated with the $|1/2, \pm 1/2\rangle$ ground state. We have attempted to observe the $k = 0$ magnon by Raman scattering, but as yet have had no success. However, the magnon energy has been measured by infrared absorption, and is 19.2 cm^{-1} at 4.2 K[17]. The separation between the exciton at 234 cm^{-1} and the phonon at 253 cm^{-1} is 19 cm^{-1}, which is consistent with the point of view that the other exciton and the phonon are accidentally degenerate.

In the 550 cm^{-1} region, the single broad band evident at room temperature is resolveable into three lines at liquid helium temperature. The frequency of the central, and strongest line has an unusual temperature dependence. Between room and liquid nitrogen temperatures, the frequency falls from 559 to 545 cm^{-1}, but, as the temperature is further lowered, the frequency *increases* by 4 cm^{-1}. This abrupt change in the general trend is again characteristic of the existence of exciton states at liquid helium temperature. The overall smooth temperature dependence (above T_N) of the frequencies of all the electronic transitions can be attributed to the variation in crystal field parameters with temperature. The trigonal field parameter, which governs the ground state splittings, is sensitive to temperature-induced changes in the lattice constants.

The 550 cm^{-1} band contour at liquid helium temperature has been fitted with three Lorentzian lines by the method of least squares using an IBM 360/44 computer, and the results are shown in Fig. 4. The frequencies and line widths calculated by this method are those given in Table I. The relative intensities of these lines is 1 : 7 : 3 in order of increasing frequency. The high-frequency sideband of the 549 cm^{-1} line is not present at temperatures above 30 K, and within the temperature range below T_N that we have so far explored, its intensity shows a strong inverse dependence on temperature. Also, the line width of the 577 cm^{-1} band decreases markedly as the crystal temperature is lowered from T_N. The difference in energies of the central peak and the sideband is 28 cm^{-1},

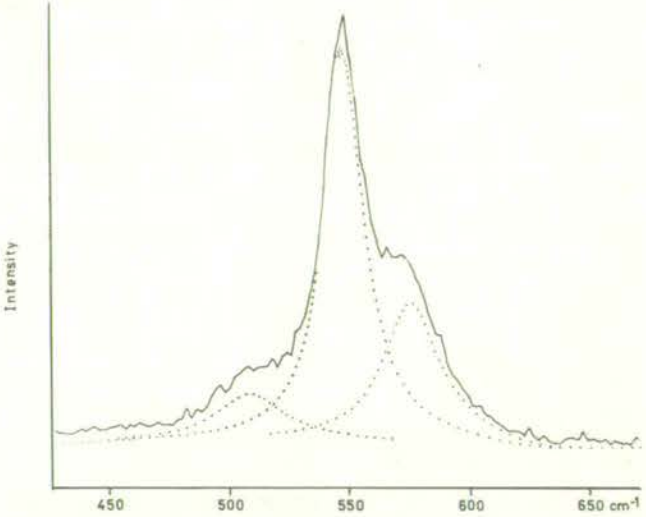

FIG. 4. — Curve-resolved Raman contour for the 550 cm^{-1} region of $CoCl_2$ recorded at liquid helium temperature using the 4579 Å laser line.

which is of the order expected for exciton-pair splittings within the ground state multiplet. The 577 cm^{-1} line is thus definitely associated with the onset of antiferromagnetic ordering, and can be positively assigned to the companion exciton state to the 549 cm^{-1} line associated with the $|1/2, \pm 1/2\rangle \rightarrow |3/2, \pm 1/2\rangle$ transition. The 510 cm^{-1} line is clearly visible only at temperatures below 30 K. However, its frequency, which is twice that of the A_{1g} phonon, and its relative broadness even at very low temperatures characterize this line as the overtone of the A_{1g} phonon, although not necessarily arising from $k = 0$. The band shape of the 545 cm^{-1} line at liquid nitrogen temperature, which is well above T_N, supports this assignment. There is a definite asymmetry in the band on the low frequency side. Furthermore, similar overtone bands have been observed in $CdCl_2$ and $MnCl_2$ at 83 and 4.2 K[4].

The three lines in the 985 cm^{-1} region shown in Fig. 3 have been assigned to transitions from the ground state to the $J = 5/2$ triplet. As with the 550 cm^{-1} band, the band splitting does not become distinct until low temperatures are reached. However, a relationship between the number of lines in the 985 cm^{-1} region and the antiferromagnetic ordering cannot be as definitely established. The 985 cm^{-1} band is broader and more intense than the 550 cm^{-1} band at both room and liquid nitrogen temperature, thus indicating the presence of more than one line. The presence of at least two lines is evident in the liquid nitrogen spectrum shown in

Fig. 2. Thus the splitting of the 985 cm^{-1} band appears at higher temperatures, and is more pronounced than in the 550 cm^{-1} region. All the lines are sharper than the 577 cm^{-1} line, the widest being equal in width to the 549 cm^{-1} line. In addition, dilute systems of Co^{2+} ions, in which antiferromagnetic ordering involving Co^{2+} ions does not occur, give Raman spectra showing at least two lines in the 900-1000 cm^{-1} region that can be assigned to Co^{2+} transitions[4]. Theory predicts three lines in the 985 cm^{-1} region, so the assignments given in Table I are reasonable. The expected resolution at liquid helium temperature of each electronic transition into two excitons is not directly obvious in the spectrum given in Fig. 3. However, the lines at 984 and 1015 cm^{-1} are much broader than the 962 cm^{-1} exciton, possibly indicating the presence of further lines beneath the band contour. The temperature dependence of the 985 cm^{-1} band shape is being further investigated for evidence of other exciton states.

A polarization study of the Raman lines would enable the assignments to be confirmed. For temperatures greater then T_N, the selection rules given earlier apply. The $M_J = 1/2$ to $M_J = 1/2$, 5/2 transitions will be visible in all polarizations, whereas the $M_J = 1/2$ to $M_J = 3/2$ transition will be of zero intensity in ZZ polarization, and visible in all others. The 510 cm^{-1} line will have zero off-diagonal tensor elements if it is the $2 \times A_{1g}$ phonon. The polarization measurements we have attempted have not yielded many results for the following reasons :

(1) The crystals do not cleave parallel to the c axis, and cannot be cut in this direction because of the « soft » nature of these crystals. This has prevented the ZZ polarization component from being measured and thereby distinguishing $1/2 \rightarrow 1/2$, 5/2 and $1/2 \rightarrow 3/2$ M_J transitions.

(2) High quality crystal faces are difficult to obtain, due mainly to the chemical and physical properties of the crystals. Our samples are now superior to those used in the earlier study[1], as evidenced by a much lower intensity of the A_{1g} phonon in comparison with the E_g phonon in polarization conditions where the A_{1g} phonon is forbidden. Improvements in sample quality and experimental conditions are still needed, as the A_{1g} band is still being observed in forbidden polarizations. (See Fig. 3 for example.)

(3) These optically-active crystals can depolarize the laser light and the scattered light. Despite these difficulties, some information was obtained. The polarization properties of the 253 cm^{-1} phonon support the A_{1g} symmetry assignment. At liquid helium temperature, the intensities of the ZX and ZY polarization components of the 984 cm^{-1} line are at variance. This behaviour contradicts the theoretical prediction of equal intensity. Theory is obeyed by the companion lines at 962 and 1015 cm^{-1}, which do have ZX and ZY components of equal intensity. We can not explain this result at present, but anticipate that the answer will come from a study of the selection rules for electronic transitions in antiferromagnetic $CoCl_2$.

It is interesting to note that the Co^{2+} $\Delta J = 1$ transitions are consistently lower in intensity than $\Delta J = 2$ transitions, both in $CoCl_2$ and in cobalt doped isomorphous halides[4].

The splittings of energy levels described above are associated with crystal-field and ferromagnetic-ordering effects. We have not observed any Davydov splitting of the exciton states. The ferromagnetic interaction within a Co^{2+} layer is much stronger than the antiferromagnetic interaction between layers[12], and therefore the Davydov splittings could be too small to be detected.

Using crystal field theory, an attempt was made to theoretically predict the observed electronic transition energies, with poor results[1]. The adjustable field and spin-orbit parameters could not be chosen to give a good fit to both the doublet, corresponding to the transitions $J = 1/2 \rightarrow J = 3/2$, and the triplet ($J = 1/2 \rightarrow J = 5/2$) simultaneously. The expected splitting of the triplet is much larger than that actually observed. We believe that this could be a consequence of the operation of the dynamic Jahn-Teller effect in this trigonally distorted cubic system[18]. The $CoCl_2$ electronic structure is worthy of a detailed theoretical study with regard to both the Jahn-Teller effect and the effects of magnetic ordering.

ACKNOWLEDGEMENTS

This work was supported by the N. Z. University Grants Committee through URG Grant No. 66-241, and through the award of a post-graduate scholarship to one of us (J.H.C). The authors are grateful to Dr. G. D. Jones for helpful discussions, to R. W. Tyree and R. Ritchie for technical assistance, and to Professors A. G. McLellan and B. G. Wybourne for their interest and support.

REFERENCES

[1] J. H. Christie and D. J. Lockwood, Chem. Phys. Letters **8**, 120 (1971).
[2] R. M. Macfarlane, Phys. Rev. Letters **25**, 1454 (1970).
[3] A. Azima, P. Grunberg, J. Hoff, J. A. Koningstein and J. Preudhomme, Chem. Phys. Letters **7**, 565 (1970).
[4] D. J. Lockwood and J. H. Christie, Chem. Phys. Letters to be published.
[5] R. W. G. Wyckoff, Crystal Structures Vol. 1 (Interscience, New York, 1964), p. 270.
[6] W. Low, Phys. Rev. **109**, 256 (1958).
[7] R. Newman and R. M. Chrenko, Phys. Rev. **115**, 1147 (1959).
[8] G. F. Koster, J. O. Dimmock, R. G. Wheeler and H. Statz, Properties of the Thirty-Two Point Groups (M.I.T. Press, Cambridge, Mass., 1963).
[9] O. S. Mortensen and J. A. Koningstein, J. Chem. Phys. **48**, 3971 (1968).
[10] J. H. Christie and D. J. Lockwood, J. Chem. Phys. **54**, 1141 (1971).
[11] R. C. Chisholm and J. W. Stout, J. Chem. Phys. **36**, 972 (1962).
[12] M. K. Wilkinson, J. W. Cable, E. O. Wollan and W. C. Koehler, Phys. Rev. **113**, 497 (1959).
[13] R. London, Advan. Phys. **17**, 243 (1968).
[14] J. Ferguson, D. L. Wood and K. Knox, J. Chem. Phys. **39**, 881 (1963).
[15] D. J. Lockwood, to be published.
[16] M. E. Lines, Phys. Rev. **131**, 546 (1963).
[17] I. S. Jacobs, S. Roberts and P. E. Lawrence, J. Appl. Phys. **36**, 1197 (1965).
[18] P. J. Stephens, J. Chem. Phys. **51**, 1995 (1969).

Reprinted from

Canadian Journal of Chemistry

Ion Pair Formation in $NaNO_3/D_2O$ Solutions: Raman and Infrared Spectra, Partial Molal Volumes, Conductance, and Viscosity

J. D. Riddell, D. J. Lockwood, and D. E. Irish

Volume 50 • Number 18 • 1972
Pages 2951–2962

Published by The National Research Council of Canada

Ion Pair Formation in $NaNO_3/D_2O$ Solutions: Raman and Infrared Spectra, Partial Molal Volumes, Conductance, and Viscosity[1]

J. D. RIDDELL, D. J. LOCKWOOD,[2] AND D. E. IRISH[3]

Department of Chemistry, University of Waterloo, Waterloo, Ontario

Received February 2, 1972

Laser Raman and infrared vibrational spectra of solutions of $NaNO_3$ in deuterium oxide reveal the presence of both $Na^+NO_3^-$ ion pairs and solvated nitrate ions. The degree of association has been measured. The concentration quotients are remarkably independent of concentration and almost equal to the thermodynamic association constant, 0.060 ± 0.006 kg mol^{-1} at 25.0 °C. The latter quantity was obtained by an extrapolation procedure, taking account of the activity coefficients. Values are reported for the activity coefficient of the ion pair. Interpretation is also considered in terms of a place-exchange equilibrium involving the solvent. Vibrational assignments are made to the two forms of nitrate ion present. Density, partial molal volume, conductance, and viscosity data are also presented and discussed in terms of the reported constitution.

Les spectres vibrationnels infrarouge et Raman au laser de solutions de $NaNO_3$ dans l'oxyde de deutérium révèlent la présence de paires d'ions $Na^+NO_3^-$ et d'ions nitrate solvatés. Nous avons mesuré le degré d'association. Les quotients de concentration sont indépendants de façon remarquable de la concentration et presqu'égaux à la constante d'association thermodynamique, 0.060 ± 0.006 kg mol^{-1} à 25.0 °C. Nous obtenons cette dernière quantité par extrapolation, en tenant compte des coëfficients d'activité. Nous rapportons des valeurs pour le coëfficient d'activité de la paire d'ions. L'interprétation est faite en termes d'un équilibre d'échange impliquant le solvant. Les assignations vibrationnelles sont faites pour les deux formes d'ions nitrate présentes. Nous présentons aussi la densité, le volume molal partiel, la conductance et la viscosité et en discutons en termes de la structure proposée. [Traduit par le journal]

Canadian Journal of Chemistry, **50**, 2951 (1972)

An extensive study of the vibrational frequencies, half-widths, intensities, and line shapes of aqueous solutions of lithium, sodium, potassium, and cesium nitrate was previously reported (1). Solutions of $LiNO_3$ received the greatest attention and studies were possible over the greatest concentration range at 25 °C. It was shown that, for solutions more concentrated than 7 *M*, nitrate ion exists in two types of environment. In one environment vibrational lines are generated which resemble crystal frequencies and nitrate can be considered to be bound directly to lithium. In the other environment nitrate is free of such a direct linkage to the cation. The comparisons were later extended and interpreted in terms of a quasi-lattice model (2). A place-exchange equilibrium constant was tentatively estimated as 0.24 at 25 °C for the process

$$Li^+(H_2O)_3 + NO_3^- \rightleftarrows Li^+(H_2O)_2NO_3^- + H_2O$$

The early study suggested that $NaNO_3$ solutions were similar to $LiNO_3$ solutions; however, the spectral features of the ion pair were more difficult to detect. In particular an infrared line at about 740 cm^{-1} was detected, as for $LiNO_3$, and it was believed that the lower solubility was the chief factor preventing detection of the Raman counterpart (1). Subsequently Raman experiments were carried out at elevated temperatures on liquids with as little as two moles water per mole salt but, using 435.8 nm mercury excitation, no asymmetry in the shape of the 718 cm^{-1} Raman line could be detected (3). This observation was apparently at variance with the earlier work and thus an extensive study was in order.

D_2O was chosen as solvent because the 700–800 cm^{-1} infrared region is less obscured than with H_2O. Also the 689 cm^{-1} feature (1) is not present in the Raman spectrum of the D_2O solutions and thus it becomes easier to detect asymmetry on the high frequency side of the 718 cm^{-1} line. Furthermore, knowledge of the infrared and Raman frequencies for the same solvent, D_2O, is desirable in case the extent of interaction is different in H_2O and

[1]Presented in part at the 54th Canadian Chemical Conference of the Chemical Institute of Canada, Halifax, Nova Scotia, May 31 – June 2, 1971.

[2]Present address: Department of Physics, The University, Edinburgh, Scotland.

[3]To whom correspondence should be addressed.

D_2O. (In previous work i.r. spectra were obtained with D_2O solvent and Raman spectra with H_2O in the 700 cm^{-1} region (1).) Using the 488.0 nm line of an argon ion laser it has been possible to detect the high frequency Raman component. As noted previously (1), the 740 cm^{-1} i.r. component is inherently more intense and thus can be detected when the Raman counterpart is virtually absent. A quantitative Raman intensity study has been made and the results of this study and the implications concerning the constitution of concentrated aqueous $NaNO_3$ solutions are described below. Conductance, viscosity, and density have also been measured to ascertain to what extent the existence of ion pairs is revealed by these macroscopic properties.

Experimental

Thirty solutions were prepared in a nitrogen-purged dry box from dried $NaNO_3$ (Fisher certified reagent) and D_2O. Solutions were filtered through a 0.45 μ Millipore filter prior to spectral measurements. Raman spectra were recorded on a Cary 81 spectrophotometer specially adapted for the use of a Coherent Radiation Model 54 Argon ion laser. The laser beam was directed down the length of a cylindrical glass cell 5 mm in diameter which terminated in a blackened horn to reduce stray light. The cell was positioned parallel to the horizontal slit of the Cary 81 monochromator by means of a specially built adjustable platform. The Raman radiation was focused onto the slit by a cylindrical lens. Thus all of the fore optics of the Cary 81 were bypassed. The gain, slit width, scan speed, and time constant were varied in preliminary studies to determine the combination which would insure no introduction of band distortion. The laser was operated at 488.0 nm and 250 mW. After a 1 h warm up excellent laser power stability was achieved and a yellowish-green fluorescence seen on first introducing the sample had disappeared.

No carbon tetrachloride external standard was used in this laser work because of the difficulty in reproducing the sample cell position relative to the laser beam. Instead, an internal standard was used; namely, the integrated intensity of the 1050 cm^{-1} band of the aqueous $NaNO_3$ solutions. We have assumed a direct proportionality between the integrated intensity of this band and the stoichiometric concentration of the $NaNO_3/D_2O$ solution, based on the work of Davis (4) and Sze (5). Both of these workers employed carbon tetrachloride as an external standard for intensity measurements in their studies. Relative integrated intensities were effectively obtained in this work by dividing the integrated intensity of a given band by that of the 1050 cm^{-1} line of a 1 mol l^{-1} solution of $NaNO_3/D_2O$.

Infrared spectra were obtained on a Beckman IR-9 spectrophotometer operated with the slit program at three times standard and the gain control at 0.8%. In order to eliminate water vapor interference, the instrument was continuously purged by a stream of dry nitrogen. The solutions were contained in a thermostated (25 ± 0.05 °C) R.I.I.C. cell fitted with silver bromide windows that were separated by a 0.012 mm Teflon spacer. Band areas, designated as "integrated absorbances" were measured with a polar planimeter. Since the cell was dismantled and cleaned between solutions, band areas are relative only within a given spectrum, and the infrared spectra are generally of qualitative value. The infrared spectra were run concurrently with the laser Raman spectra of the $NaNO_3/D_2O$ solutions.

The curve resolving of spectral envelopes into component bands was accomplished by means of the CURVER program of the 360/44 IBM computer. This facility is given a more detailed description elsewhere (6), but in essence the program employs one of three distribution functions to fit the Raman bands by an operator-controlled, visual procedure. These model band shapes come from the Lorentzian, Gaussian, and the Lorentz–Gaussian product function. The program provides a measure of the goodness-of-fit.

Soon after the first laser Raman spectra were analyzed, however, it became clear that none of these mathematical functions satisfactorily fitted a single, symmetrical band shape excited by the 488.0 nm laser line. A new model band shape was developed, therefore, specifically for the laser Raman spectra of the $NaNO_3/D_2O$ system. This band shape is a mathematical copy of the 1050 cm^{-1} symmetric stretch of nitrate ion obtained from a spectrum of 4.2 M $NaNO_3/D_2O$. Frequencies and half-widths of band components were maintained at approximately constant values for all spectra of a series of solutions.

Viscosity measurements were taken for a series of $NaNO_3/D_2O$ solutions at 25 ± 0.05 °C using a Cannon–Ubbelohde viscometer. All viscosity efflux times were greater than 100 s and within 0.1 s for at least three repetitions for a given solution. Conductance measurements were performed concurrently with the viscosity measurements at the same temperature using a 1 kHz Industrial Instruments Inc. conductivity bridge with the cell and variable decade resistance in adjacent arms of the Wheatstone bridge arrangement. The cell electrodes were separated by about 15.0 cm of 3 mm i.d. capillary tubing. After a thorough cleaning with dilute HCl and a fresh electrode coating of platinum black, the conductance cell had a cell constant of 319.7 cm^{-1}. This constant was checked periodically using a 0.1000 and a 1.000 mol l^{-1} aqueous solution of KCl. All solutions were allowed at least 20 min to come to temperature equilibrium before measurements were made. Densities were measured at 25 ± 0.05 °C, either with a calibrated pycnometer or in volumetric flasks. The accuracy of the latter method was sufficient for concentrative properties and agreed well with the more accurate measurements.

Results and Discussion

The Degree of Dissociation

The measurement of α, the degree of dissociation of $NaNO_3$, is possible because two Raman lines are observed in the ν_4 region of the Raman spectrum; one at 718 cm^{-1} assignable to the solvated nitrate ion and a second at 728 cm^{-1}

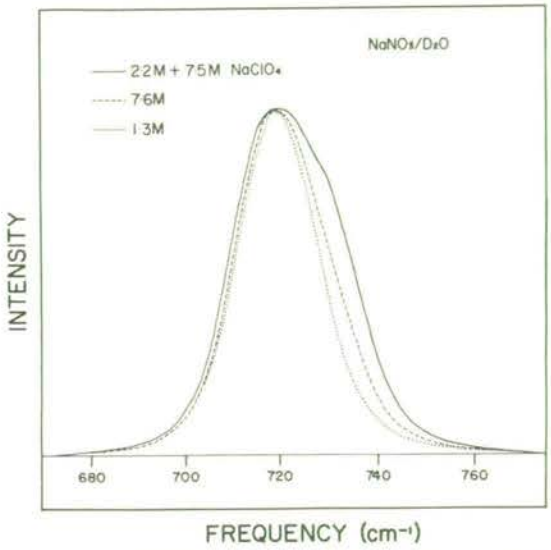

FIG. 1. Comparison of the Raman 720 cm^{-1} regions of ···, 1.3 *M* $NaNO_3/D_2O$; ---, 7.6 *M* $NaNO_3/D_2O$; —, 7.5 *M* $NaClO_4$ + 2.2 *M* $NaNO_3/D_2O$.

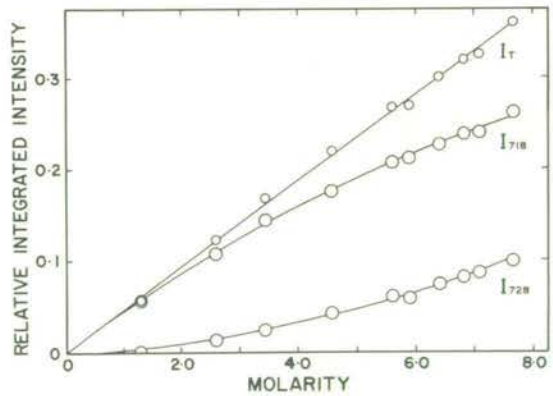

FIG. 2. Relative integrated intensity *vs.* molarity for the 720 cm^{-1} region of the Raman spectrum of $NaNO_3/D_2O$.

assignable to an ion pair (7). The latter frequency is close to that observed for anhydrous sodium nitrate crystal (8). In dilute solution ($C < 1$ mol l^{-1}) the 718 cm^{-1} band is a single symmetrical line. At a concentration of 7.67 mol l^{-1} a small but significant amount of intensity distorts the high frequency side of this band. Increasing the sodium : nitrate concentration ratio to 4.48:1 (a "common ion" effect obtained by mixing $NaClO_4$ and $NaNO_3$) increases the intensity of the 728 cm^{-1} shoulder as expected if an equilibrium was displaced

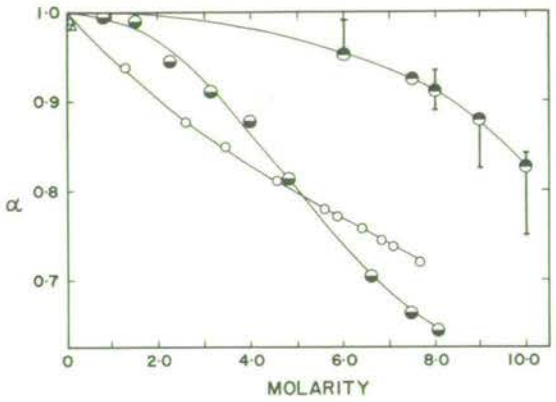

FIG. 3. The degree of ionization, α, *vs.* molarity of nitrate at 25 °C: ◓, $LiNO_3/H_2O$; ◒, HNO_3/H_2O; ○, $NaNO_3/D_2O$; △, Davies' values for $NaNO_3/H_2O$.

to favor a higher concentration of ion-pair (728 cm^{-1}) and a lower concentration of free ion (718 cm^{-1}) (Fig. 1). Using the computer procedure it was possible to fit two bands to the intensity envelope in this spectral region, each with constant half-width and frequency. The relative integrated intensities of the total contour and the components are plotted against concentration in Fig. 2.

The total integrated intensity (I_T) is directly proportional to the stoichiometric concentration. Dividing this concentration into that of ion pairs C_B and that of free ions C_F, one has

$$[1] \qquad I_T = I_{718} + I_{728} = J_B C_B + J_F C_F$$

where J is the molar intensity of the bound (B) or the free (F) forms of nitrate ion. If $J_B = J_F$, eq. 1 will reduce to

$$I_T = J_B(C_B + C_F) = J_B C_T$$

a linear equation with zero intercept consistent with experiment. Thus J_B can be obtained from the slope of I_T *vs.* C_T in Fig. 2. The implication is that although ion association changes the force constant and hence frequency associated with the deformation mode of the nitrate ion, it does not change the molar intensity of the mode. It now follows that

$$[2] \quad C_B = I_{728}/J_B \quad \text{and} \quad \alpha = 1 - C_B/C = C_F/C$$

α is plotted against molarity in Fig. 3. Two data obtained from conductance studies of dilute solutions by Davies (9) are also shown. For comparison the more scattered data (2)

TABLE 1. Data for the calculation of the thermodynamic association constant

m (mol kg^{-1})	$(1-\alpha)$ Expt.	$(1-\alpha)$ Smoothed	$(\gamma_\pm)^2_{ST}$	${}^TK_A \cdot \gamma_u^{-1}$	$Q_C = m_B \cdot m_F^{-2}$	γ_u
9.35	0.279	0.279	0.110	0.271	0.057	0.222
8.43	0.262	0.262	0.114	0.274	0.057	0.220
8.01	0.255	0.254	0.116	0.274	0.057	0.219
7.37	0.242	0.242	0.120	0.274	0.057	0.219
6.63	0.228	0.228	0.125	0.274	0.058	0.219
6.24	0.220	0.220	0.128	0.275	0.058	0.218
4.88	0.188	0.189	0.143	0.271	0.059	0.221
3.52	0.151	0.152	0.167	0.258	0.060	0.232
2.58	0.123	0.120	0.194	0.239	0.060	0.251
2.00*		0.098	0.218	0.224		0.268
1.23	0.062	0.064	0.268	0.194	0.059	0.311
0.50*		0.028	0.367	0.153		0.393
0.25*		0.014	0.454	0.123		0.487
0.10*		0.0057	0.568	0.100		0.600
0.07*		0.0040	0.612	0.093		0.643
0.05*		0.0029	0.648	0.090		0.668
0.02*		0.0012	0.746	0.080		0.747
0.01*		0.00058	0.796	0.073		0.822
0.0	0.0	0.0	1.000	0.060		1.000

*Interpolated values.

for $LiNO_3/H_2O$ and the values for HNO_3/H_2O obtained by Krawetz from Raman intensity measurements (10) are shown.

The equilibrium process is formulated as

$$Na^+_{(aq)} + NO_{3(aq)}^- \rightleftarrows Na^+ \cdot NO_{3(aq)}^-$$

The thermodynamic equilibrium constant for the association can be written as the product of a concentration quotient Q_C and an activity coefficient quotient Q_γ

$$[3] \quad {}^TK_A = \frac{a_u}{a_{Na^+} \cdot a_{NO_3^-}} = \frac{m_u}{m_{Na^+} \cdot m_{NO_3^-}} \cdot \frac{\gamma_u}{\gamma_{Na^+} \cdot \gamma_{NO_3^-}} = Q_C \cdot Q_\gamma$$

where a, m, and γ refer to activity, molality, and activity coefficient, respectively. Solution concentrations are converted from molarity to molality units, through the measured densities, for convenience when using activity coefficients described below.

Considering first $Q_C = (1-\alpha)/\alpha^2 m$ we find that the concentration quotient is remarkably constant, changing from 0.057 to 0.059 kg mol^{-1} for a concentration change from 9.35 to 1.23 m (Table 1). The system's behavior is surprisingly ideal. Such constant Q_C's obtained for salt solutions by Raman spectroscopy have been noted before (11, 12). The same is not true for acid solutions however (13).

It is possible to incorporate values for $\gamma_{Na^+} \cdot \gamma_{NO_3^-}$ and thus explore the concentration dependence of ${}^TK_A\gamma_u^{-1}$. In terms of the mean ionic activity coefficients, $\gamma_{Na^+} \cdot \gamma_{NO_3^-}$ equals $\gamma_\pm^2$ for the free ions. Following the treatment given by Robinson and Stokes (ref. 14, pp. 37, 38)

$$\gamma_\pm^2 = (\gamma_\pm^2)_{ST}\alpha^{-2}$$

$(\gamma_\pm^2)_{ST}$, the mean stoichiometric activity coefficients, are reported by Robinson and Stokes (ref. 14, p. 492) for the $NaNO_3/H_2O$ system. In order to use these values a correction has been applied for the fact that the D_2O solutions contain fewer moles of solvent than the H_2O solutions of the same molality. Values of $\gamma_\pm$ were chosen corresponding to the molality of the D_2O solution multiplied by the factor 55.51/49.93. These values are consistent with the trends presented by Bonner (15) for activity coefficients of other salts dissolved in D_2O.

Thus ${}^TK_A\gamma_u^{-1}$ equals $[(1-\alpha)/m] \cdot (1/(\gamma_\pm)^2_{ST})$. Figure 4 is a plot of both ${}^TK_A\gamma_u^{-1}$ and Q_C *vs.* molality. Data are presented in Table 1. $(1-\alpha)$ is zero at zero concentration and thus the experimental values of $(1-\alpha)$ can be expressed

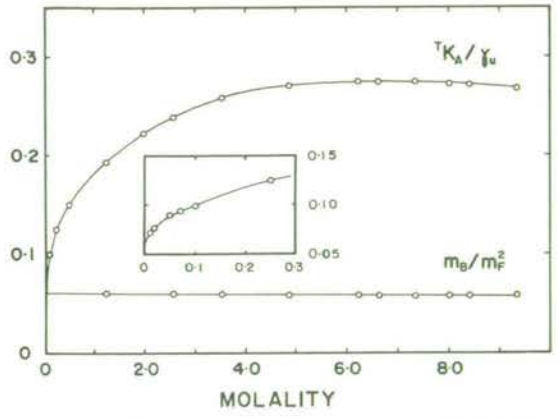

FIG. 4. $^TK_A/\gamma_u$ and m_B/m_F^2 *vs.* molality for $NaNO_3/D_2O$ at 25 °C. The inset shows the horizontal scale expanded and the extrapolation of $^TK_A/\gamma_u$ to zero concentration.

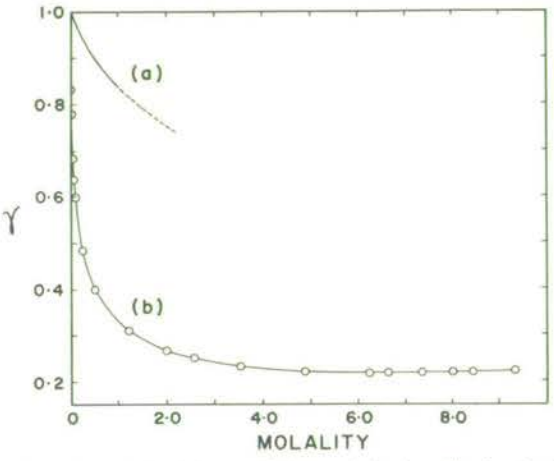

FIG. 5. (*a*) Activity coefficient of glycine (dipolar ion) *vs.* molality of KCl at 25 °C; (*b*) activity coefficient of the $Na^+ \cdot NO_3^-$ ion-pair *vs.* molality of $NaNO_3/D_2O$ at 25 °C.

as a polynomial in m with a required zero intercept:

$$(1-\alpha) = 0.05762_6 m - 0.004827 m^2 + 0.0001989_4 m^3$$

The plot of $^TK_A\gamma_u^{-1}$ has been extrapolated by interpolations using the above polynomial. In the limit of infinite dilution, γ_u is unity and ^TK_A is 0.060 ± 0.006 kg mol^{-1}. As the concentration increases, $^TK_A\gamma_u^{-1}$ rises smoothly and then levels off (Fig. 4). This can be attributed to a decrease of γ_u, as shown in Fig. 5. There are few examples where γ_u is known for an ion pair over such a wide concentration range. Roberts and Kirkwood measured the activity coefficient of glycine in aqueous solutions of KCl (16). Glycine forms a dipolar ion of large electric moment in solvents with a high dielectric constant. Figure 5 shows γ_u for glycine plotted against molality of KCl. The trend is similar to that of γ_u for $NaNO_3$. On the other hand, for HNO_3, γ_u calculated from the data of Krawetz rises continuously from unity.

Davies (9) obtained a value of 0.26 for the association constant of $NaNO_3$ in water at 18 °C. His approach, $\alpha = \Lambda/\Lambda_x$, necessitates questionable assumptions about the form of Λ_x. It is worth noting, however, that Davies' value of α for 0.1 M is 0.985 and ours is 0.995 while at 0.05 M Davies' value is 0.991 and ours is 0.997. The value of $^TK_A\gamma_u^{-1}$ changes by a factor of about four when α changes by only 6 parts in 1000. This comparison serves to point out the extreme sensitivity of $^TK_A\gamma_u^{-1}$ to small differences in α in dilute solutions for an electrolyte as strong as $NaNO_3$. Robinson (17) combined Davies' conductance data and activity coefficient data to obtain a value of 0.38 for K_A.

The near constancy of Q_C implies that Q_γ is almost constant over most of the concentration range. To a good approximation $\gamma_u\gamma_\pm^{-2}$ equals 1.04 when $0.01 < m < 9.35$ but γ_u approaches unity faster than $\gamma_\pm^2$, accounting for the sharp change of slope in Fig. 4 as m approaches zero.

With reference to Fig. 3, the strength of the electrolytes decreases in the order $LiNO_3 > HNO_3 > NaNO_3$ for $C < 5$ M. In keeping with this trend Krawetz reports ^TK_A of HNO_3 equal to 0.042 kg mol^{-1} (10), smaller than our value of 0.060 kg mol^{-1} for $NaNO_3$. The trend of increasing values of ^TK_A with increasing alkali metal radius seems probable (18).

Reliability

In the above analysis an uncertainty of 10% in the value of K has been implied. This is a realistic estimate. When D_2O is used as solvent the spectral base lines are straight. The noise level was less than 1% of the maximum peak height except for the most dilute solutions for which it did not exceed 1.5%. The 1050 cm^{-1} line is an ideal internal standard because it is intense and isolated. Its use also circumvents intensity corrections which may arise because of a changing refractive index.

The principle source of uncertainty is the partition of the signal into two components. This problem is common to many types of experimentation and is often more severe than that encountered here. The precision obtainable in this work is a consequence of the singular features of the computer procedure *viz.* an exactly reproduceable, defined line shape and a criterion for the goodness-of-fit (6). Because of this severe overlap, however, an estimated 10% uncertainty may exist in each ratio I_{728}/I_{718}, which leads to an uncertainty of about 8% in individual values of $(1 - \alpha)$. Once the equality of J_F and J_B is established or assumed the results are independent of the intensity of the 1050 cm^{-1} line because $(1 - \alpha)$ can be expressed as $(I_{728}/I_{718})(1 + I_{728}/I_{718})^{-1}$, from which the 8% estimate is derived. To some extent this uncertainty is reduced by the averaging procedure which was used to fit all the points to a smooth curve. Thus 10% reliability is believed to be a reasonable upper limit. The values in Table 1 imply greater precision; the three significant figures quoted there are in fact an indication of our internal consistency. The trends and conclusions are not changed by rounding off.

The Place-Exchange Equilibrium Constant

An alternative way of considering the association process is in terms of a competition between water molecules and nitrate ions for sites in the first coordination sphere of the cation. A place-exchange equilibrium constant for this quasi-lattice model (19) can be expressed in terms of the process

$$Na^+(D_2O)_x + NO_3^- \rightleftarrows Na^+ \cdot NO_3^-(D_2O)_{x-1} + D_2O.$$

The constant (a concentration quotient) is defined as

$$^cK_A = \frac{C_B C_W}{(C - C_B)^2}$$

where C_B is the concentration of bound nitrate and C_W the concentration of free solvent molecules. C_W is calculated from density and weight percent data such that $C_W = [D_2O]_T - x(C - C_B) - (x - 1)C_B$. The constant has been evaluated for $1 \leqslant x \leqslant 6$ (Fig. 6). At infinite dilution ^cK_A has a value of 2.98_3, independent of x. With increasing concentration the values decrease.

The less certain data for $LiNO_3/H_2O$ were

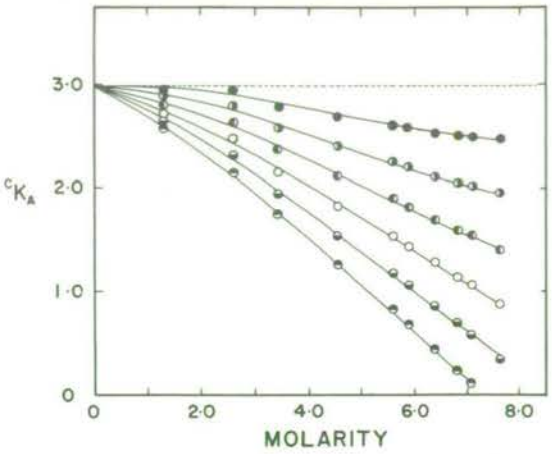

FIG. 6. ^cK_A *vs.* molarity of $NaNO_3/D_2O$ at 25 °C: ●, $x = 1$; ◑, $x = 2$; ◐, $x = 3$; ○, $x = 4$; ◒, $x = 5$; ◓, $x = 6$.

consistent with the almost constant value for ^cK_A of 0.24 when x is 3. The smaller value is consistent with the view that Li^+ binds waters more strongly than Na^+ and thus nitrate ion competes less successfully with the solvent molecules for a position in the primary solvation sphere of the smaller cation. The sodium ion appears to display little or no preference for a fixed value of x, unlike lithium, magnesium, or zinc for example. The value probably decreases as concentration increases.

Spectral Properties of the Ion-Pair

The normal modes of vibration of an isolated nitrate ion with D_{3h} symmetry and their approximate frequencies are: $\nu_1(A_1')$ 1050 cm^{-1}; $\nu_2(A_2'')$ 825 cm^{-1}; $\nu_3(E')$ 1385 cm^{-1}; and $\nu_4(E')$ 720 cm^{-1}. Solvation in water causes the $\nu_3(E')$ mode to split into a doublet with maxima about 1356 and 1410 cm^{-1}, the separation also depending on the concentration and cation (12). Attachment of a cation subjects nitrate ion to a larger perturbation and the symmetry is lowered to C_{2v}, C_s or C_1. It is probable that the cation and anion will be oriented in a number of different ways to each other such that no single symmetry designation will be applicable to all ion pairs. This will cause the vibrational lines to broaden. But, for all symmetries above, the effect is to remove the degeneracy of the E' modes. For simplicity we will describe the vibrations of the ion pair in terms of C_{2v} symmetry. Thus the correlations will be: $A_1' \rightarrow A_1$;

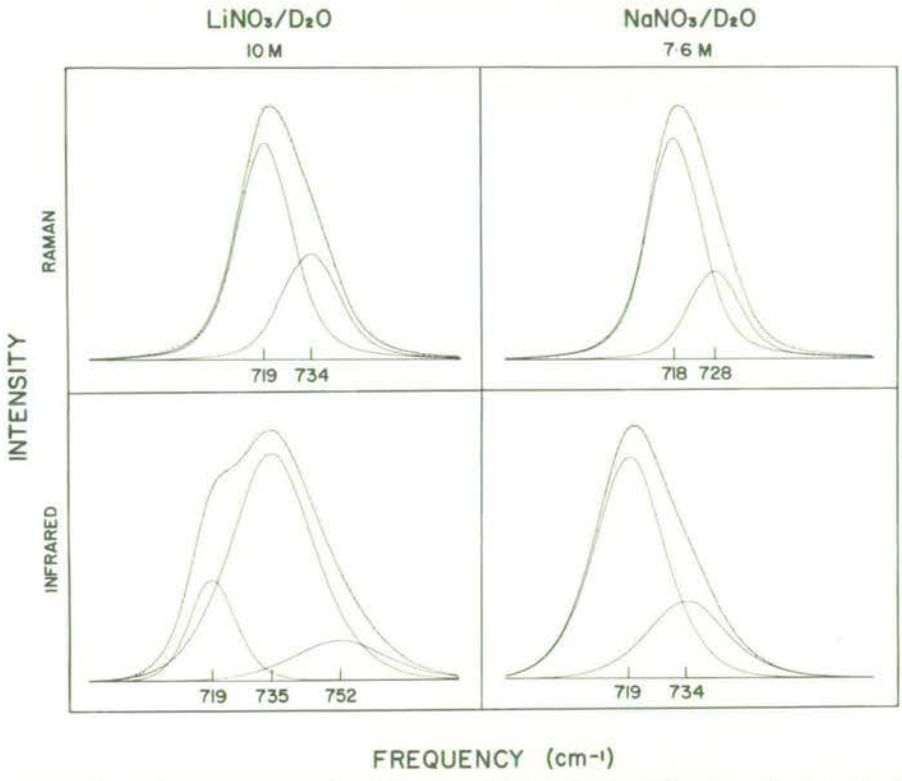

FIG. 7. Comparison of the computer-analyzed Raman and infrared 720 cm^{-1} regions of saturated solutions of $LiNO_3/D_2O$ and $NaNO_3/D_2O$. The 752 cm^{-1} infrared band is due to water in the $LiNO_3$ salt.

$E' \rightarrow A_1 + B_2$ and $A_2'' \rightarrow B_1$. All six modes are allowed in both infrared and Raman.

No lines were detected which could be attributed to a Na^+–nitrate vibration. This suggests that the interaction is largely electrostatic. The ion pair exhibits a Raman line at 728 cm^{-1} as already discussed which is assigned to an A_1 mode; the observed polarization of this line is weak but probably genuine. The infrared contour has two components, the 719 cm^{-1} line of free nitrate and an intense line at about 734 cm^{-1}. This line is ascribed to the B_2 mode of the ion pair. It is assumed that the Raman counterpart is of inherently low intensity. (The observations contrast sharply with those for $LiNO_3$ where infrared and Raman lines are almost identical in frequency at 734 cm^{-1} (see Fig. 7).)

A low intensity band at 831 cm^{-1} is detectable in Raman spectra of solutions more concentrated than 2 mol l^{-1}. The integrated intensity of this band appears to vary directly with the integrated intensity of the 1050 cm^{-1} band which is proportional to total nitrate concentration. It was not detected in the spectrum of the mixture containing $NaNO_3$ and $NaClO_4$ in D_2O where ion–ion contact is forced. This band is therefore assigned to solvated nitrate, perturbed by the solvent such that the normally Raman inactive $\nu_2(A_2'')$ vibration is allowed. The overtone was a single, somewhat more intense symmetric band at 1660 cm^{-1}. The greater intensity is consistent with the fact that it is Raman allowed under D_{3h} selection rules. The 831 cm^{-1} vibration is a single intense line in the infrared spectrum and is assigned to both bound and free nitrate ions.

The line shape of the intense Raman line at 1050 cm^{-1} was studied carefully with 1 cm^{-1} slit width. It is symmetrical. This does not entirely preclude the possibility that more than one band is present under the contour, however. There is a small increase of frequency with increasing concentration and a slight broad-

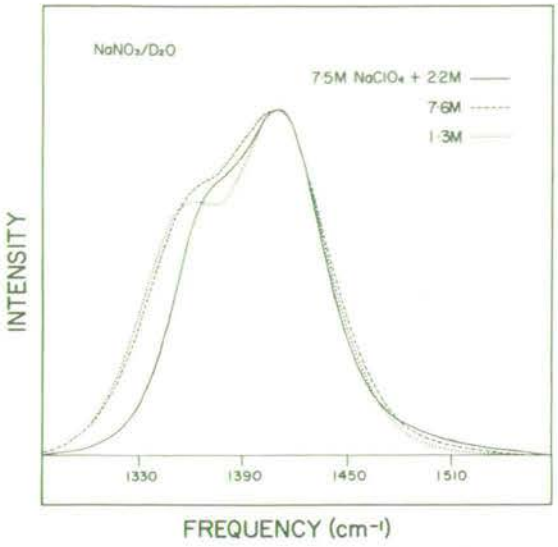

FIG. 8. Comparison of the Raman 1400 cm^{-1} regions of ···, 1.3 *M* $NaNO_3/D_2O$; ---, 7.6 *M* $NaNO_3/D_2O$; —, 7.5 *M* $NaClO_4$ + 2.2 *M* $NaNO_3/D_2O$.

ening. A weak infrared counterpart is observed about 2 cm^{-1} lower in frequency. We believe the ion pair and solvated nitrate ion both contribute to this line (*cf.* ref. 12).

A broad envelope extends from approximately 1300 to 1500 cm^{-1} in the Raman spectrum. For dilute solutions ($C < 1$ mol l^{-1}) this region can be resolved into two components by computer techniques, *viz.* 1355 and 1415 cm^{-1}. At higher concentrations subtle changes in the contour of the band envelope become apparent. As ion pairing is enhanced the intensity *between* the two maxima is enhanced and the overall width of the envelope decreases (Fig. 8). Attempts were made to fit the envelope with two, three, and four bands. Although a two and three band fit can be achieved, it is obtained only by allowing the positions and half-widths to continually change in an inconsistent manner. A four band fit which allows the retention of the frequencies, half-widths, and intensity ratio of the 1355 and 1415 cm^{-1} bands over the entire concentration range is most acceptable. Two new bands, located at 1368 and 1417 cm^{-1}, and assigned to the A_1 and B_2 modes of the ion-pair, respectively, have almost constant line parameters over the concentration range and account for the overall narrowing of the contour. The concentration dependence of the intensities is similar to that observed for the 719–740

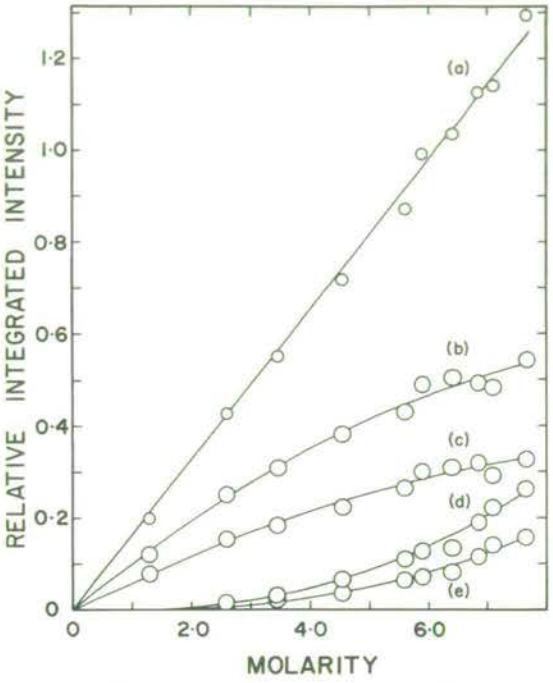

FIG. 9. Relative integrated intensity *vs.* molarity for the 1400 cm^{-1} region of the Raman spectrum of $NaNO_3/D_2O$: (*a*) I_T; (*b*) I_{1415}; (*c*) I_{1355}; (*d*) I_{1417}; (*e*) I_{1368}.

cm^{-1} region (Fig. 9). The infrared contours in this region have very high absorbance and are not amenable to study. The assignments are summarized in Table 2.

Density and Partial Molal Volumes

The concentrative properties of the $NaNO_3/D_2O$ system are given in Table 3. The density of D_2O at 25 °C has been taken from Millero *et al.* (20). Smooth values of the density are given by the polynomial, obtained from a least-squares analysis of the data,

$$D = 1.1043_5 + 0.0523_9C - 0.0007_0C^2$$

where C is measured in mol l^{-1}. Similarly, weight percent is given by

$$\text{Wt. percent} = 7.6778C - 0.3574C^2 + 0.02031C^3 - 0.000743C^4$$

The values in Table 3 are for the unsmoothed experimental data.

To a good approximation direct proportionality exists between density and molarity, specific volume and weight percent, and mean molal volume and mole fraction over the con-

TABLE 2. Vibrational assignments*

	Solvated nitrate ion					$Na^+NO_3^-$ ion pair			
	Raman			Infrared		Raman			Infrared
D_{3h}	$\bar{\nu}$ (cm^{-1})	W (cm^{-1})†	I_R‡	$\bar{\nu}$ (cm^{-1})	C_{2v}	$\bar{\nu}$ (cm^{-1})	W (cm^{-1})	I_R	$\bar{\nu}$ (cm^{-1})
$\nu_1(A_1')$	1051	13.9	100	1050	$\nu_2(A_1)$	1051	13.9	100	1050
$\nu_2(A_2'')$	831	14	0.1	831	$\nu_4(B_1)$	831	14	0.1	831
$\nu_3(E')$	1355	61	4.1	§	$\nu_1(A_1)$	1368	51	2.0	§
	1417	62	6.8	§	$\nu_5(B_2)$	1415	66	3.2	§
$\nu_4(E')$	718	18	3.4	719	$\nu_3(A_1)$	728	17	1.2	‖
					$\nu_6(B_2)$	‖			734
$2\nu_2(A_1')$	1660	16	1.3	§	$2\nu_4(A_1)$	1660	16	1.3	§

*Data are taken for 7.09 M $NaNO_3$ in D_2O. There are small changes with concentration.
†Full width at half-height; for cases of double assignment the value of W does not indicate the value of the component. Spectral slit width ~8 cm^{-1}.
‡Integrated intensity relative to that of the 1052 cm^{-1} line.
§Region not studied because of the high infrared absorbance.
‖Line required by selection rules but obscured or weak.

centration range studied. Similar linearities also exist for comparable plots of the $LiNO_3/H_2O$ data (21).

The partial molal volumes were obtained from apparent molal volumes by an analytical procedure (22). Values of ϕV_2, the apparent molal volume, were computed from the smoothed density, concentration data and fitted to a polynomial in molality, m

$$\phi V_2 = 29.538 + 0.69772m - 0.01975m^2 - 0.00149m^3 + 0.00049m^4$$

The expression for $\bar{V}_2$ is then obtained by differentiation. The partial molal volume of the solvent, $\bar{V}_1$, was obtained from

$$\bar{V}_1 = \frac{20.028}{1000}\left[\frac{1000 + mM_2}{D} - m\bar{V}_2\right]$$

where 20.028 is the molecular weight of the solvent, M_2 is the molecular weight of the solute, m is the concentration in mol kg^{-1}, and D is the density. The linearity of the mean molal volume against mole fraction plot arises because the partial molal volumes balance each other, superficially indicating ideal behavior. This feature can be compared with the ideality revealed by the constancy of Q_C in the previous section.

Conductance and Viscosity

It has long been recognized that the degree of dissociation, α, should be obtainable from conductance measurements. One approach is to adopt the relation $\Lambda/\Lambda_x = \alpha$ where Λ is the observed equivalent conductance and Λ_x is the hypothetical conductance the electrolyte would have if it were completely dissociated into ions and at a concentration αC (23, 24). Much uncertainty exists concerning the appropriate expression for Λ_x which in general is a function of Λ_0, viscosity, concentration, charge type, temperature, and solvent. Considerable effort has been expended on this problem (23) since the interpretation of Davies (9), referred to in the first section of this discussion, was advanced. It is of interest to be able to correlate constitution, a microscopic property measured by Raman spectroscopy, and conductance, a macroscopic property, for this 1:1 electrolyte with a relatively small degree of ion association. The experiments were conducted with this objective in mind.

The Λ_0 value for the $NaNO_3/D_2O$ system is obtainable from Walden's Rule, using the known values for the $NaNO_3/H_2O$ system, because the solvents are comparable (25). Thus

$$\Lambda_0 = \frac{(\eta_0\Lambda_0)_{H_2O}}{(\eta_0)_{D_2O}} = \frac{0.8903 \times 121.56}{1.096_6} = 98.69 \text{ ohm}^{-1} \text{ cm}^2 \text{ equiv}^{-1}$$

The experimental data for specific conductance, κ, equivalent conductance, Λ, and viscosity, η, are presented in Table 4. The viscosity and specific conductance data have also been smoothed by means of a least squares computer

TABLE 3. Concentrative properties of $NaNO_3/D_2O$ at 25 °C

Wt. %	D_{25} (g ml^{-1})	C (mol l^{-1})	m (mol kg^{-1})	C_{D_2O} (mol l^{-1})	Sp. Vol (ml g^{-1})	$\bar{V}_2$(cm^3)	$\bar{V}_1$ (cm^3)
0.000	1.1044	0.000	0.000	55.14	0.9055	29.54	18.14
1.010	1.110	0.132	0.120	54.89	0.9005	29.70	18.14
1.652	1.112	0.216	0.198	54.58	0.8996	29.81	18.14
7.410	1.158	1.01	0.941	53.52	0.8637	30.80	18.12
9.312	1.174	1.29	1.21	52.91	0.8518	31.15	18.12
12.31	1.196	1.73	1.65	52.36	0.8361	31.68	18.10
14.11	1.206	2.00	1.93	51.70	0.8295	32.01	18.09
20.36	1.2568	3.01	3.01	49.98	0.7957	33.20	18.03
20.50	1.257	3.03	3.03	49.91	0.7954	33.23	18.03
25.38	1.295	3.87	4.00	48.24	0.7723	34.17	17.96
26.94	1.309	4.15	4.34	47.74	0.7641	34.48	17.94
31.54	1.349	5.01	5.42	46.10	0.7414	35.36	17.85
34.52	1.379	5.60	6.20	45.09	0.7252	35.93	17.78
36.04	1.388	5.88	6.63	44.28	0.7206	36.18	17.75
36.52	1.385	5.95	6.77	43.90	0.7221	36.24	17.74
39.00	1.4146	6.49	7.52	43.08	0.7069	36.68	17.68
40.56	1.430	6.83	8.03	42.53	0.6990	36.93	17.64
41.94	1.437	7.09	8.50	42.06	0.6959	37.10	17.62
42.83	1.455	7.33	8.81	41.53	0.6873	37.25	17.59
44.48	1.466	7.67	9.42	40.94	0.6821	37.43	17.56

TABLE 4. Viscosity and conductivity data for $NaNO_3/D_2O$ at 25.0 °C

C (mol l^{-1})	η (cP)	κ (Ω^{-1} cm^{-1})	Λ (Ω^{-1} cm^2 equiv^{-1}) Observed	Calculated
0.0	1.100	0.001	98.69*	98.66†
0.132		0.01083	82.38	80.87
0.216	1.108	0.01703	78.95	77.59
1.009	1.162	0.06383	63.26	64.17
2.002	1.266	0.1059	52.93	54.81
3.033	1.429	0.1357	44.75	46.49
3.866	1.602	0.1520	39.32	40.23
5.006	1.912	0.1654	33.03	32.42
5.951	2.246	0.1706	28.68	26.78
7.332	2.914	0.1704	23.23	20.02

*From Walden's Rule (see text).
†From equation with $C = 10^{-6}$ mol l^{-1} and $\mathring{a} = 4.10$ Å.

program and the smoothed data are given by the polynomials in C (mol l^{-1}):

$$\eta = 1.096_2 + 0.05671C + 0.01077C^2 + 0.00208C^3$$

$$\kappa = 0.00209 + 0.06899C - 0.00941C^2 + 0.00043C^3$$

We anticipate that the ion pairing in $NaNO_3/D_2O$ will be similar to that in $NaNO_3/H_2O$ although some Raman evidence has been accumulated which suggests that the degree of association may be somewhat larger in D_2O. A plot of $\kappa\eta$ against concentration was compared for the two systems. For $NaNO_3/H_2O$ the conductance data of Nelson were used (3) and the viscosity data were measured in our laboratory by Walker (*cf.* Janz *et al.* (26)). The polynomials for these quantities are:

$$\kappa = 0.00062 + 0.09245C - 0.02120C^2 + 0.00332C^3$$

$$\eta = 0.8904 + 0.05234C + 0.009883C^2 + 0.00166C^3$$

The two $\kappa\eta$ curves exhibit the same trends and inflections. Since $\kappa\eta$ is sensitive to solution constitution, such as ion-pair formation, differences are probably not large.

An empirical expression for Λ_x was obtained by dividing the observed conductance by the observed α. The expression

$$\Lambda_x = \Lambda_0 - 50.146C^{1/2} + 30.781C - 14.476C^{3/2} + 3.059C^2 - 0.226C^{5/2}$$

fits the data to within 0.1%. The two conductance curves are shown in Fig. 10. Efforts to develop an equation for Λ_x whose coefficients have real physical meaning for the system at moderate to high concentrations have so far been unsuccessful. Such a theoretical equation, together with measured values of Λ, would allow the computation of α for any concentration.

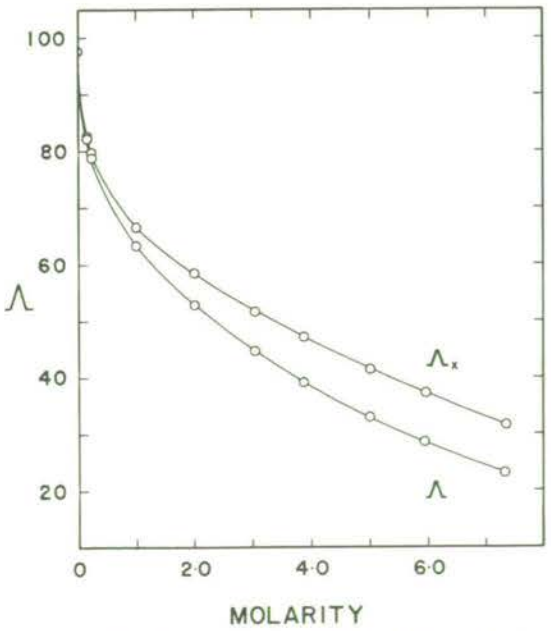

FIG. 10. Λ and Λ_x *vs.* molarity of $NaNO_3/D_2O$ at 25 °C.

Wishaw and Stokes (27) obtained satisfactory agreement between experimental data and conductance calculated from the equation

$$\Lambda = \left(\Lambda_0 - \frac{B_2\sqrt{C}}{1 + B\mathring{a}\sqrt{C}}\right)\left(1 - \frac{B_1\sqrt{C}}{1 + B\mathring{a}\sqrt{C}}F\right)\frac{\eta_0}{\eta}$$

for NH_4Cl/H_2O when $\mathring{a} = 4.35$ Å. This equation also fits the $NaNO_3$ data fairly well when $\mathring{a}$ is given the reasonable value 4.10 Å (Table 4). The constants used are: $B = 0.32999$; $B_1 = 0.23167$; $B_2 = 49.366$; $F = (e^x - 1)x^{-1}$ where $x = 0.09667\sqrt{c}\,\mathring{a}$ (*cf.* 28). There is no reason to believe that the difference between measured and calculated values should be attributed to ion association; rather it reflects the limitations of the equation; *i.e.*, the equation, with no allowance for ion association, does not give values which differ from the experimental values in any systematic way attributable to the known ion-pair formation.

Aspects of this work were supported by the Department of the Environment, the National Research Council of Canada, and the University of Waterloo Research Grant Programme. We are also grateful to Atomic Energy of Canada, Ltd., for deuterium oxide. Particular appreciation is extended to Dr. W. L. Elsdon for many helpful discussions. D.E.I. also expresses his thanks to Professor R. A. Robinson for his suggestions. J.D.R. acknowledges with thanks an Ontario Graduate Fellowship (1970–1971). We also thank Mr. John Walker for measuring the viscosity of the $NaNO_3/H_2O$ system.

1. D. E. Irish and A. R. Davis. Can. J. Chem. **46**, 943 (1968).
2. D. E. Irish, D. L. Nelson, and M. H. Brooker. J. Chem. Phys. **54**, 654 (1971).
3. D. L. Nelson. Ph.D. Thesis. University of Waterloo, Waterloo, Ontario, 1969.
4. A. R. Davis. Ph.D. Thesis. University of Waterloo, Waterloo, Ontario, 1967.
5. Y.-K. Sze. M.Sc. Thesis. University of Waterloo, Waterloo, Ontario, 1970.
6. A. R. Davis, D. E. Irish, R. B. Roden, and A. J. Weerheim. Appl. Spectrosc. In press.
7. D. E. Irish, G. Chang, and D. L. Nelson. Inorg. Chem. **9**, 425 (1970).
8. M. H. Brooker and D. E. Irish. Can. J. Chem. **48**, 1183 (1970).
9. C. W. Davies. Discuss. Faraday Soc. **23**, 351 (1927).
10. A. A. Krawetz. Ph.D. Thesis, University of Chicago, Chicago, Illinois, 1955. *Summarized by* T. F. Young, L. F. Maranville, and H. M. Smith. *In* The structure of electrolytic solutions. *Edited by* W. J. Hamer. John Wiley and Sons Inc., New York. 1959. p. 35.
11. J. Nixon and R. A. Plane. J. Am. Chem. Soc. **84**, 4445 (1962).
12. D. L. Nelson and D. E. Irish. J. Chem. Phys. **54**, 4479 (1971).
13. H. Chen and D. E. Irish. J. Phys. Chem. **75**, 2672 (1971).
14. R. A. Robinson and R. H. Stokes. Electrolyte solutions. 2nd ed. Butterworths, London. 1968.
15. O. D. Bonner. J. Chem. Thermodyn. **3**, 837 (1971).
16. R. M. Roberts and J. G. Kirkwood. J. Am. Chem. Soc. **63**, 1373 (1941).
17. R. A. Robinson. J. Am. Chem. Soc. **59**, 84 (1937).
18. C. W. Davies. Ion association. Butterworths, London. 1962. p. 77.
19. J. Braunstein. *In* Ionic interactions. Vol. 2. *Edited by* S. Petrucci. Academic Press, N.Y. 1971. p. 243.
20. F. J. Millero, R. Dexter, and E. Hoff. J. Chem. Eng. Data, **16**, 85 (1971).
21. A. N. Campbell, G. H. Debus, and E. M. Kartzmark. Can. J. Chem. **33**, 1508 (1955).
22. I. M. Klotz. Chemical thermodynamics. Prentice-Hall, Inc., Englewood Cliffs, N.J. 1957. p. 200.
23. E. M. Hanna, A. D. Pethybridge, and J. E. Prue. Electrochim. Acta, **16**, 677 (1971).
24. E. M. Hanna, A. D. Pethybridge, and J. E. Prue. J. Phys. Chem. **75**, 291 (1971).
25. R. L. Kay and D. F. Evans. J. Phys. Chem. **69**, 4216 (1965).
26. G. J. Janz, B. G. Oliver, G. R. Lakshminarayanan, and G. E. Mayer. J. Phys. Chem. **74**, 1285 (1970).
27. B. F. Wishaw and R. H. Stokes. J. Am. Chem. Soc. **76**, 2065 (1954).
28. R. A. Robinson and R. H. Stokes. J. Am. Chem. Soc. **76**, 1991 (1954).

Reprinted from

ADVANCES IN RAMAN SPECTROSCOPY, VOLUME 1

(Proceedings of Third International Conference on Raman Spectroscopy, Reims, France, September 1972)

Heyden & Son Ltd., London

17. THE RAMAN SPECTRUM OF AMMONIUM BISULPHATE

J. W. Arthur, D. J. Lockwood and W. Taylor
Department of Physics, University of Edinburgh, Edinburgh, Scotland

INTRODUCTION

Ammonium bisulphate (NH_4HSO_4 or AHS) has three crystalline phases. At room temperature the space group is $P2_1/c$, but at 270 K there is a second-order phase transition to P_c and below this at 154 K there is a first-order transition to P_1. At the upper transition there is a sharp dielectric anomaly, below which the crystal becomes ferroelectric.[1] This anomaly, however, is much smaller than in the classic ferroelectrics KDP and $BaTiO_3$ where strong low frequency Raman scattering in the form of temperature dependent 'Rayleigh wings' has been observed[2] and interpreted variously in terms of an overdamped phonon, which in KDP is coupled with a hydrogen bond order-disorder mechanism.

The aim of the present work was to determine if scattering from a similar mechanism might be observed in AHS. It would appear that the NH_4^+ ions are not involved in the upper transition, since a similar transition exists in RHS ($RbHSO_4$) at 258 K; but there is evidence that they have a high degree of rotational freedom and take part in the lower transition.[3] Recent structural work on AHS by Nelmes[4] indicates large thermal parameters for one of the symmetrically inequivalent types of sulphate ion in the room temperature structure. Nelmes has fitted this to a model in which these ions are disordered between two orientations.[5] In passing to the ferroelectric phase the centre of inversion is lost, and the disordered ions become ordered.[6] It is possible that this ordering mechanism is associated with a ferroelectric mode as postulated by Cochran in his lattice dynamical theory of ferroelectrics.[7] It is difficult, however, to regard the sulphate order-disorder motion as a phonon, and it may be more appropriate to interpret the spectra in terms of molecular dipole reorientation.

The positions of the H^+ ions with respect to the SO_4^{2-} ions have not been determined in the ferroelectric phase, but it is clear that they are already ordered at room temperature.[4,5] In addition to this, deuteration does not appreciably affect the transition temperatures.[8] Although this seems to indicate that the hydrogens play no direct part in the transition, there may be some involvement, as suggested by infrared[9] and NMR[3] via H bonding between sulphate groups along the *b* axis.

Earlier Raman work on AHS has been carried out by Bazhulin *et al.*[10] using mercury lamp excitation, but no low frequency or extensive polarization data were reported.

GROUP THEORY

AHS has eight formula units in the primitive cell giving 264 normal modes at $q = 0$. Considering the internal molecular vibrations of NH_4^+ and HSO_4^- separately, there are 93 external lattice modes, excluding acoustic modes. In the room temperature phase the modes are classified according to the irreducible representations of the point group $C_{2h}(2/m)$

$$\begin{aligned} &\text{Translatory modes:} && 12A_g + 12B_g + 11A_u + 10B_u \\ &\text{Rotatory modes:} && 12A_g + 12B_g + 12A_u + 12B_u \end{aligned}$$

The remaining internal modes transform as:

$$42A_g + 42B_g + 42A_u + 42B_u$$

The 'g' modes are Raman active, whereas the 'u' modes are infrared active. If the Y axis is oriented along the crystallographic b axis, the Raman tensor has the form:

$$\begin{pmatrix} a & & d \\ & b & \\ d & & c \end{pmatrix} \sim A_g \qquad \begin{pmatrix} & e & \\ e & & f \\ & f & \end{pmatrix} \sim B_g$$

For infrared polarizations, $P_y \sim A_u$, and $P_x, P_z \sim B_u$.

In the ferroelectric phase, the modes transform under the irreducible representations of C_s, and the compatibility relations are

$$\begin{aligned} C_{2h}(A_g, B_u) &\longrightarrow C_s(A') \\ C_{2h}(A_u, B_g) &\longrightarrow C_s(A'') \end{aligned}$$

The centre of inversion is no longer present and all modes are simultaneously Raman and infrared active.

The 9 internal modes of the NH_4^+ ion and the 12 internal modes of the HSO_4^- ion give rise to 72 and 96 modes respectively in the crystal. In the room temperature phase these modes transform as

$$\begin{aligned} NH_4^+ &: \quad 18A_g + 18B_g + 18A_u + 18B_u \\ HSO_4^- &: \quad 24A_g + 24B_g + 24A_u + 24B_g \end{aligned}$$

The compatibility relations can be applied to give the results for the ferroelectric phase.

A rotatory motion of the SO_4^{2-} ions, as associated with the upper phase transition, transforms as B_u above, and A' below the transition. It is therefore to be expected that a related soft ferroelectric mode, if it exists, would appear in the Raman spectrum only below the transition in the xx, yy, zz or xz polarizations, unless there is a relaxing of selection rules above the transition caused by the disorder situation in the lattice.

RESULTS AND DISCUSSION

The Raman spectra of AHS were recorded using conventional techniques. The

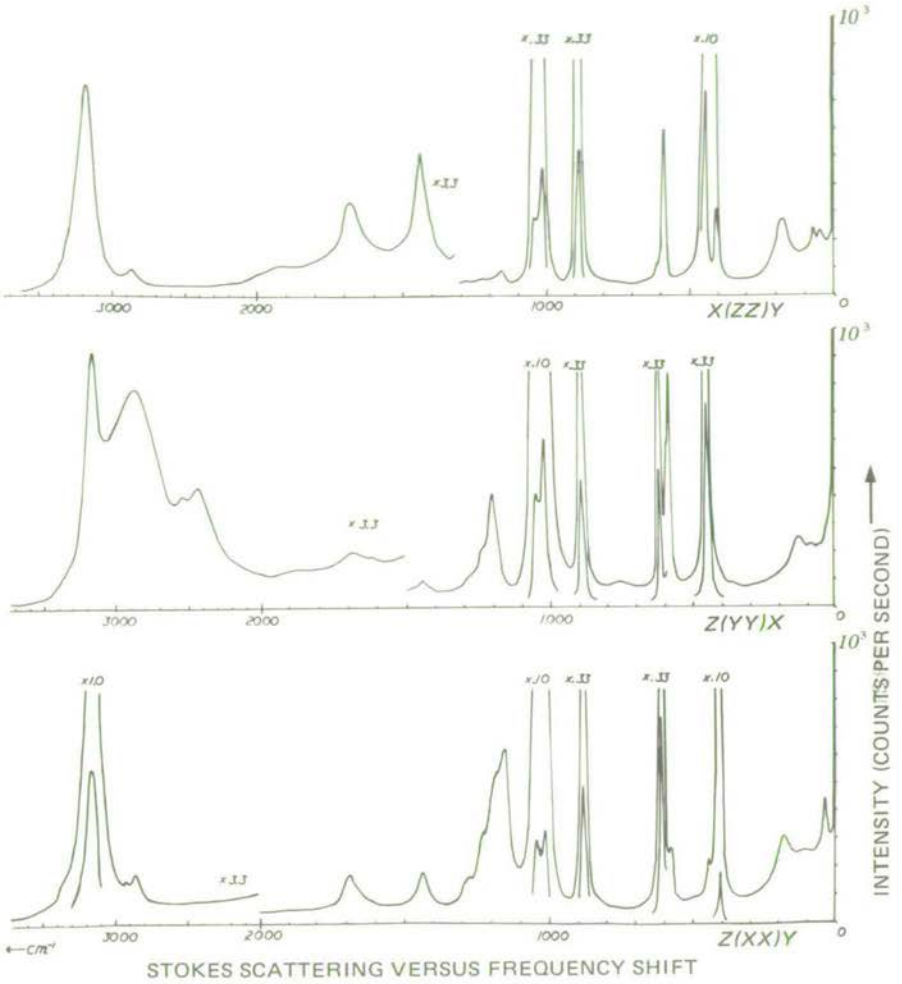

Fig. 1. Stokes scattering at room temperature.

excitation used was the 488 nm line of the argon-ion laser, and the spectrometer slit width was about 3 cm^{-1}. The sample was a single crystal of approximate dimensions 4 mm × 5 mm × 6 mm, with *X*, *Y* and *Z* directed along the *a*, *b* and *c* axes of the pseudo orthorhombic cell. The spectra are displayed in Figs. 1–3, and the frequencies and assignments are presented in Tables 1 and 2. All the internal frequencies of the SO_4^{2-} ion reported by Bazhulin *et al.*[10] were observed, but the frequencies obtained here are higher by as much as 9 cm^{-1}. The assignments were based on free-ion frequencies and the results of other works.[9,11]

Although group theory predicts a doubling in the number of Raman active lattice modes, no significant change takes place on passing through the 270 K transition. It is possible that, as in $BaTiO_3$, the disordered nature of the lattice breaks the expected symmetry requirements.[12] On the other hand, comparison of the Raman spectra with the infrared spectra of Schutte and van Rensburg[9] shows that the frequencies of the internal vibrations are apparently exclusive, still consistent with a centre of inversion. In

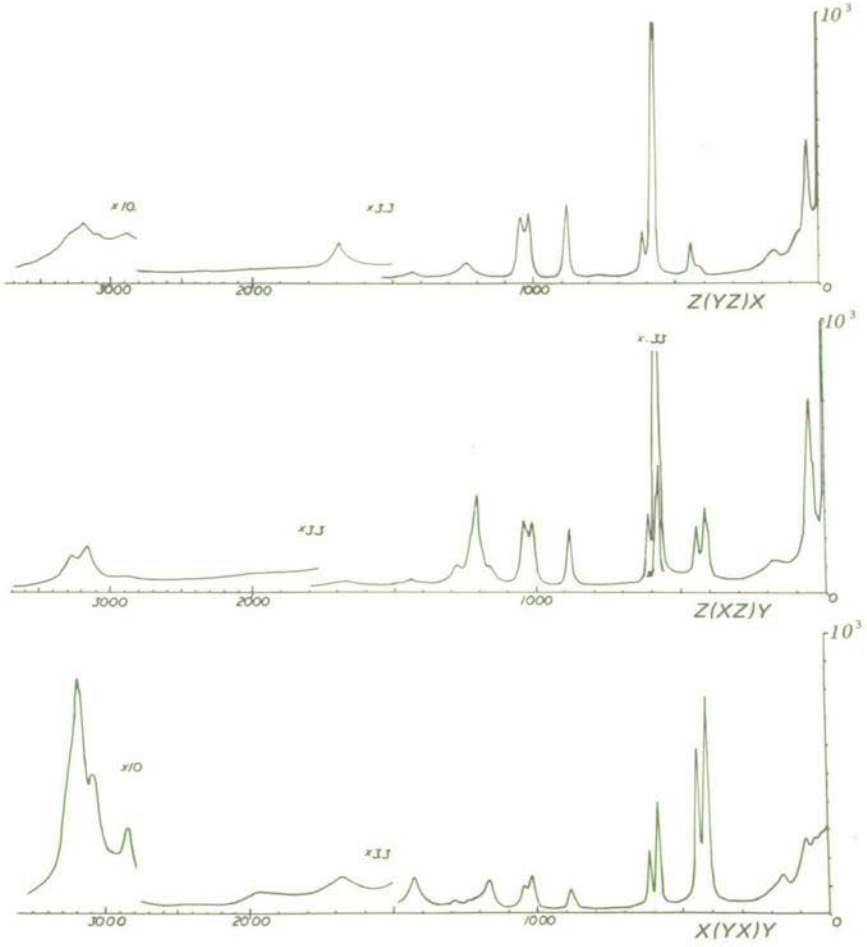

ig. 2. Stokes scattering at room temperature.

he ferroelectric phase, the deviation of the structure from one having a centre of inversion quite small, suggesting that most of the modes which are infrared active at room emperature become only weakly Raman active in the ferroelectric phase and are not asily seen.

In the low frequency region, principal features of interest are the prominent Rayleigh wings', especially obvious in the *yy* and *xy* spectra. These Rayleigh wings xhibit some temperature dependence; between 290 K and 170 K the *xy* wing loses ntensity in an approximately linear fashion, but, perhaps more interestingly, the *yy* wing ppears to change its profile, losing intensity and simultaneously revealing a small tempera- ure dependent peak around 40 cm^{-1}. The *yy* spectrum is compatible with modes of A' ymmetry, this being the expected symmetry of a ferroelectric mode involving SO_4^{2-} otatory motions as mentioned above. It is possible, however, that the Rayleigh wings esult from nearly-free NH_4^+ rotations, but some distortion of the ion from T_d symmetry ould then be necessary to allow Raman activity. It is not clear that these wings can be ccounted for by a soft mode at the upper transition, particularly as they change little

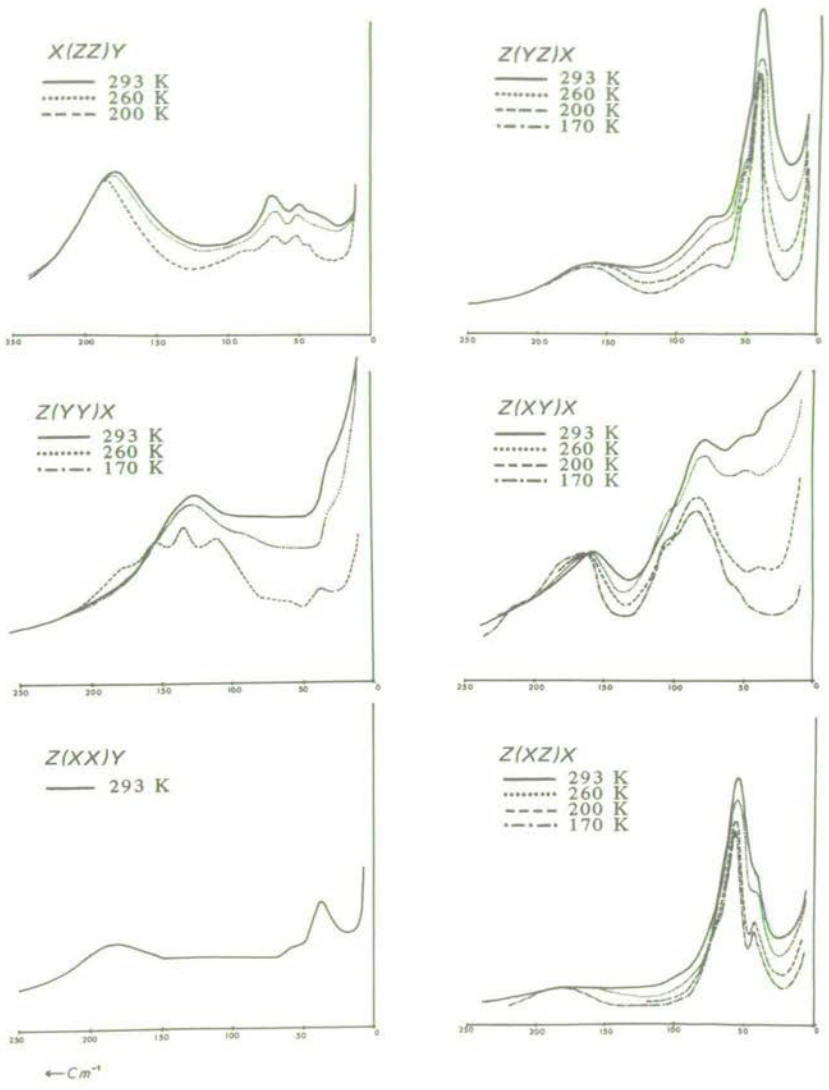

Fig. 3. Low frequency scattering.

at this point. Some additional temperature dependence is found in the frequency of some strong, low-frequency peaks. In the *yz* spectrum, for example, a peak shifts out from 40 cm^{-1} at 290 K to 45 cm^{-1} at 170 K.

In the high frequency region, a feature of interest is the very broad 2870 cm^{-1} peak in the *yy* spectrum ($\Delta\nu \approx 600$ cm^{-1}). This is presumably the O–H stretch band. Some broadening might be expected in this band because of the role played by the hydrogens in the O–H – – – O bonding which couples the SO_4^{2-} ions along the *b* axis. Unfortunately, the behaviour of this 2870 cm^{-1} peak could not be clearly observed in the ferroelectric phase because it is obscured by intensity from a strong background which appeared in the region 300–3500 cm^{-1}

Table 1. Internal molecular frequencies at room temperature, cm^{-1}.

XX		*YY*		*ZZ*		*XZ*		*XY*		*YZ*		
ν	$\Delta\nu$	ν	$\Delta\nu$	ν	$\Delta\nu$	ν	$\Delta\nu$	ν	$\Delta\nu$	ν	$\Delta\nu$	
404 s	13			404 s	16	410 sh						
						419		419	18	418		$\nu_2\ SO_4^{2-}$
445		446 s		443 vs	15	448		449	14	446	16	
578		575				576 s				575 s		
		582		586	16	583 sh		585		583 s		$\nu_4\ SO_4^{2-}$
609 s	10	611 s	11	612 wsh		611		615		615	19	
		750 vw										S-O-H torsion
881 s	18	887 s	18	883 s		880	17	883 w		882	19	$\nu_1\ SO_4^{2-}$
1014 vs		1017 vs		1014 s		1017		1017		1018		
1043 vs		1046 vs		1043 s		1044		1047		1046		$\nu_3\ SO_4^{2-}$
1155				1160 w		1160 w		1168				$\nu_4\ SO_4^{2-}$
1188 sh		1188				1213						
1230 sh		1235 sh		1220 sh		1230 sh		1230 wsh		1235 w		S-O-H bend
1275 sh		1280 sh		1275 wsh		1281 w		1280 w				
1438		1445 w		1438	95	1435 w		1435		1430 w		$\nu_4 NH_4^+$
1630 w		1630 vw		1630 vw						1635 vw		
1685		1680 w		1680		1685 w		1685 w		1680 w		$\nu_2 NH_4^+$
1900 vw,b		1860 vw,b		1900 vw,b				1900 vw,b				$\nu_1 + \nu_3 SO_4^{2-}$
		2423 w						1420 vw				
		2540 w										
2856 w		2870 ~ 600		2860 vw		1870 vw		2855 w	80	2890 vw		O-H str. and
2920 vw								3095 wsh				$2\ \nu_4 NH_4^+$
3160	~ 95	3160 ~ 100		3175	~ 140	3180 w		3210 w		3190 vw		ν_1 and $\nu_3\ NH_4^+$
						3280 w				3260 w		
				3360 wsh								$2\ \nu_2 NH_4^+$

s: strong. w: weak. vw: very weak. b: broad. sh: shoulder.

Table 2. Lattice vibrational frequencies (cm^{-1}).

XX	*YY*			*ZZ*			*XZ*				*XY*				*YZ*			
Temperature 293	293	260	170	293	260	200	293	260	200	170	293	260	200	170	293	260	200	170
		20 sh	21 sh															
	31 sh	32 sh	38 w	33 w														
37											36 w	36 w	30 w	40 w				
						42 w	40 sh	40 sh	41	42					40 ns	41 ns	44 ns	45 ns
				48 w	48 w	51 w					51 w	50 w	57 w	57 w		54 sh	54 sh	55 sh
							54 ns	55 ns	56 ns	58 ns								
59 w			63 w															
				68	68	67			70 sh	75 sh								
															75	75	75	74
						90 w					80	78	84	87				
		112	109									110 sh	110 sh	106 sh				
	130 b	130	133															
		150	155															
											158 b	163 b	163 b	163 b	163 b	163 b	165 b	166 b
182 b			180 sh	179 bs	180 bs	184 bs	175 b	175 b	*	185 b				178 sh				

w: weak. s: strong. n: narrow. b: broad. sh: shoulder.

* not measured

When the temperature is reduced from 290 K to 160 K, the profile of the ν_3 SO_4^{2-} band changes distinctly as the high frequency component shifts out in frequency and becomes clearly resolved into an unusually sharp intense peak. This feature was also reported by Bazhulin *et al.*,[10] and as they suggest, it is likely evidence of increasing distortion in the sulphate ions. No similar feature is apparent in other bands.

Although much of interest has been seen in the present work, more detailed temperature studies and work on isomorphous materials are required before a precise understanding of the relation between the ferroelectric properties of AHS and its Raman spectra can be reached.

ACKNOWLEDGEMENTS

The authors wish to acknowledge helpful discussions with Dr. Richard Nelmes. The work was supported by the Science Research Council.

REFERENCES

1 R. Pepinsky, K. Vedam, S. Hoshino and Y. Okaya, *Phys. Rev.* **111**, 1508 (1958).
2 I. P. Kaminow and T. C. Damen, *Phys. Rev. Letters* **20**, 1105 (1968). A. Pinczuk, W. Taylor, E. Burstein and I. Lefkowitz, *Solid State Commun.* **5**, 429 (1967). M. Didomenico, S. Wemple, S. P. S. Porto and R. P. Bauman, *Phys. Rev.* **174**, 522 (1968).
3 S. R. Miller, R. Blinc, M. Brenman and J. S. Waugh, *Phys. Rev.* **126**, 528 (1962).
4 R. J. Nelmes, *Acta Cryst.* B27, 272 (1971).
5 R. J. Nelmes, *Acta Cryst.* (to be published).
6 R. J. Nelmes, *Ferroelectrics* (to be published).
7 W. Cochran, *Advan. Phys.* **9**, 387 (1960); **10**, 401 (1961).
8 M. Kasahara and I. Tatzusaki, *J. Phys. Soc. Japan* **29**, 1392 (1970).
9 C. J. H. Schutte and D. J. J. Van Rensburg, *J. Mol. Structure* **9**, 77 (1971).
10 P. A. Bazhulin, T. P. Myasnikova and A. V. Rakov, *Sov. Phys.–Solid State* **5**, 1299 (1964).
11 B. H. Torrie, C. C. Lin, O. S. Binbrek and A. Anderson, *J. Phys. Chem. Solids* **33**, 697 (1972).
12 M. P. Fontana and M. Lambert, *Solid State Commun.* **10**, 1 (1972).

RAMAN SPECTRAL STUDY OF THE UPPER PHASE TRANSITION IN $KMnF_3$

D.J. Lockwood and B.H. Torrie

Department of Physics, University of Edinburgh,
Edinburgh, Scotland

INTRODUCTION

Crystals with the perovskite structure, of which $KMnF_3$ is an example, undergo phase transitions as a result of rotations of the anion octahedra about the four-fold axes of the high-temperature cubic phase. The archetype of such transitions is the second order cubic to tetragonal transition in $SrTiO_3$ that results from the condensation of one of the modes associated with the zone boundary R $(\frac{1}{2}, \frac{1}{2}, \frac{1}{2})$ point. Considerable theoretical and experimental effort has been expended in developing a detailed understanding of this phase transition, as is evident from other papers presented here. $KMnF_3$ undergoes a similar phase transition at T_c = 186K except that in this case the transition is slightly first order in nature, with a hysteresis of a degree or less. In spite of this difference, experimental work to date indicates that the phase transitions in the two crystals can both be described by the same basic theory (1).

We have measured the Raman scattering from a sample of $KMnF_3$ with emphasis on the temperature dependence of both the soft and hard modes in the tetragonal phase. The sample was grown for us by Dr. D.A. Jones of Aberdeen University, and although the sample did show considerable scattering from defects, its quality appears to be better than that of many of the other $KMnF_3$ crystals that have been examined (2).

EXPERIMENT

The Raman spectrum was excited with argon laser light at 476.5 nm so as to avoid fluorescence problems: the laser power

was 400 mW. The light scattered at 90° was analysed using a double monochromator with a spectral slit width of 1.7 cm^{-1} for all but the hard mode intensity measurements, where it was 7 cm^{-1}. A digitised data collection system enabled direct computer processing of the results. The $KMnF_3$ crystal was mounted on the cold finger of a continuous-flow cryostat: the crystal temperature could be controlled to within 0.1 K. After changing the sample temperature, a period of at least 15 mins. was spent waiting for thermal equilibrium to be established before running the new spectrum: this period was determined experimentally to be satisfactory. Cycling the temperature below T_c did not affect the results of soft mode measurements. In the hard mode intensity measurements, waiting for an hour at a temperature within 5 K of T_c did not result in any change in the measured intensity. Our experience in this respect agrees with observations made from measurements of the specific heat of $KMnF_3$ (3).

Typical Raman spectra for $T<T_c$ are shown in Fig. 1.

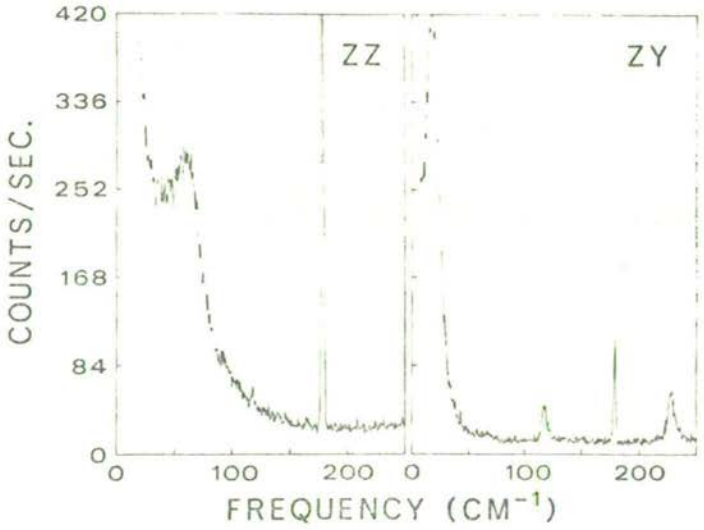

Figure 1. Polarized Raman spectra of $KMnF_3$ at 125 K. The sharp feature at 178 cm^{-1} is a plasma line.

The spectrum with (ZZ) polarization exhibits a soft mode of A_{1g} symmetry and the (ZY) spectrum shows the other soft mode of E_g symmetry. Five other Raman active modes are predicted for the tetragonal phase and these have all been observed. Full details of the group theory and observations for both the tetragonal and

orthorhombic (T<92 K) phases will be published elsewhere.

SOFT MODE TEMPERATURE DEPENDENCE

The soft-mode spectra were analysed with a computer using a least-squares routine. The E_g mode was fitted to a damped simple harmonic oscillator (DSHO) model of the form

$$\left[S\omega_o^2\gamma^2\omega(\bar{n}(\omega)+1)\right]/\left[(\omega_o^2-\omega^2)^2+\gamma^2\omega^2\right],$$

where S is the strength, ω_o the frequency, and γ the width of the oscillator; $\bar{n}(\omega)$ is the usual Bose population factor. Because of the clean background spectrum, good fits were obtained to within 8 cm^{-1} of the exciting line. The values of ω_o and γ obtained for the E_g mode at various temperatures are shown in Fig. 2. According to this data, the line becomes overdamped at a frequency $\omega_o = \gamma/\sqrt{2} \approx 16$ cm^{-1}. For an overdamped mode, the parameters S, ω_o and γ are highly correlated, and this is reflected in the large standard deviations near T_c indicated by the error bars in Fig. 2. At low temperatures, the standard deviations are less than the size of the symbols used in the figure. The A_{1g} mode was also fitted to a DSHO model, but this time the fitting procedure was more complicated because the (ZZ) spectrum contains a background component that goes as ω^{-2} approximately, and which is of comparable intensity to the soft mode. Good fits could not be obtained for temperatures greater than about 160 K. The A_{1g}-mode ω_o and γ show a temperature dependence of the same form as the E_g soft mode, and at 105 K $\omega_o = 71$ cm^{-1} and $\gamma = 17$ cm^{-1}. It is interesting to note that in the low-temperature limit the anisotropy in the soft mode frequencies for $KMnF_3$ is the same as that for $SrTiO_3$ (4).

INTENSITIES OF THE HARD MODES

The temperature dependent parts of the Raman cross-section are $(\bar{n}+1)\,|P_{\alpha\beta}|^2$, where $P_{\alpha\beta}$ is a component of the polarizability tensor. Expanding $P_{\alpha\beta}$ in terms of normal mode coordinates A(qj) gives

$$P_{\alpha\beta} = P^o_{\alpha\beta} + \sum_{qj} P_{\alpha\beta}\begin{pmatrix} q \\ j \end{pmatrix} A(qj) + \sum_{\substack{q_1 j_1 \\ q_2 j_2}} P_{\alpha\beta}\begin{pmatrix} q_1 q_2 \\ j_1 j_2 \end{pmatrix} A(q_1 j_1) A(q_2 j_2) + \ldots .$$

Normal first order scattering is associated with the second term in this expansion and second order scattering with the third term. If the crystal has inversion symmetry and is cubic, then there is no first order scattering. For T close to T_c the main contribution to the second order scattering will come from the

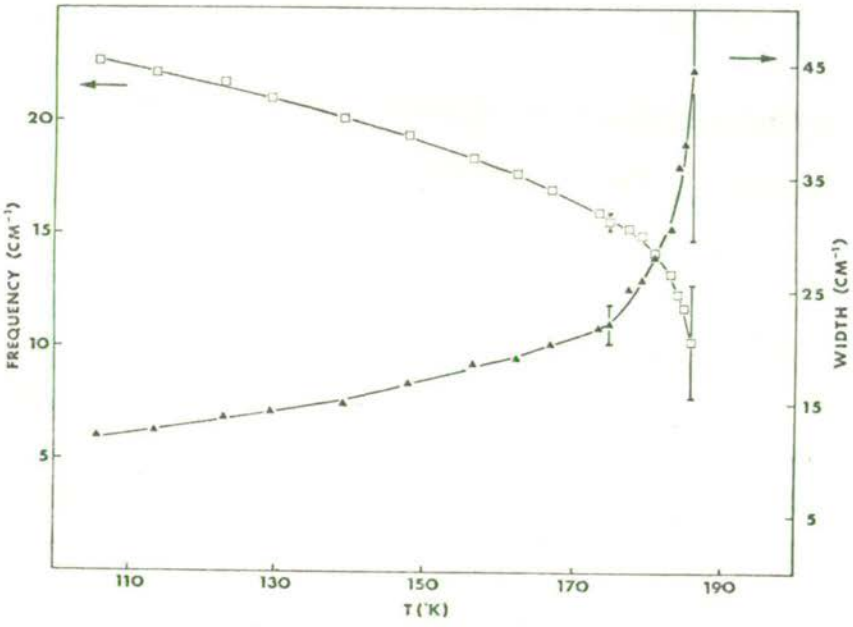

Figure 2. E_g soft mode frequency and width versus temperature.

soft mode because of its low frequency, so that

$$P_{\alpha\beta} \simeq \sum_{q_1 j_1} P_{\alpha\beta}\begin{pmatrix} q_1 q_s \\ j_1 j_s \end{pmatrix} A(q_1 j_1) A(q_s j_s),$$

where $A(q_s j_s)$ can be divided up into a static part and a dynamic part. The static part is proportional to the order parameter ϕ and gives rise to scattering which could be regarded as first order for T below T_c. When the static part is much larger than the dynamic part, the intensity of the hard modes should be proportional to ϕ^2 and hence to ω_o^2. As $(T_c-T)\to 0$, the dynamic part will become more important, and above T_c there is no static displacement so that the total contribution to the intensity will come from the dynamic part of $A(q_s j_s)$.

We have measured the intensities of several hard modes, but here we concentrate on the intensity of the E_g mode at 227 cm^{-1}, which has a good signal to noise ratio. Scans of this peak were made at several temperatures and the integrated intensities of the observed peaks are shown in Fig. 3. Note that there is a discontinuity in the curve in Fig. 3 at T_c as expected for a first order transition and that the integrated intensity does not go to zero for $T>T_c$; the residual weak peak disappears gradually as T is increased until it is lost in the background for T>230 K.

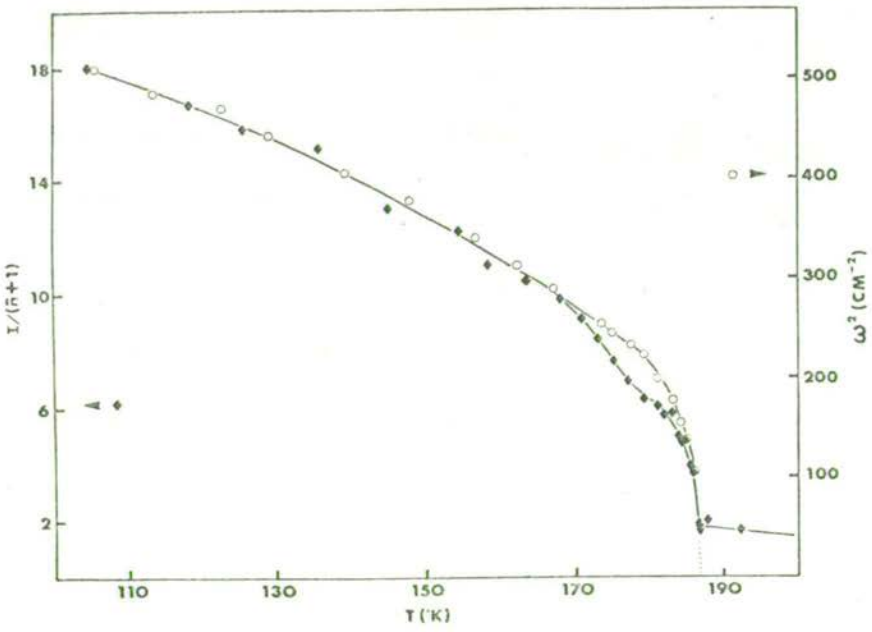

Figure 3. The temperature dependence of the E_g (227 cm^{-1}) mode intensity and the E_g soft mode frequency squared.

This observation is in qualitative agreement with the theory given above and indicates that dynamic effects are important in the range T_c to T_c + 40 K.

Below T_c, the results are again in qualitative agreement with the theory, but the accuracy is not good enough to justify the extraction of temperature exponents. Suffice it to say that a straight line, I versus $(T-T_c')$, can be fitted to short regions of the curve provided that an appropriate choice of $T_c'>T_c$ is made. The dip shown in Fig. 3 between 175 and 180 K is reproducible and may be partially caused by the difficulty in separating the static and dynamic parts of the scattering. The dynamic scattering could add to the observed peak near T_c and increase its intensity, which would leave an apparent dip in the intensity at lower temperatures. Note that a similar, but smaller dip, is also found in the birefringence and NMR results (5,6). In Fig. 3, the intensity measurements have been scaled to fit ω_o^2 for the E_g mode. There is general agreement between the intensity and ω_o^2 values for T away from T_c, as predicted above, and the disagreement for T close to T_c is not significant because of the uncertainties in ω_o and I discussed earlier.

CENTRAL MODE

As yet, we have no direct evidence for a quasi-elastic peak. Measurements of the integrated intensity from ~ 6 cm^{-1} on either side of the central peak were carried out, but the high stray light intensity (3×10^9 counts/sec. at 0 cm^{-1} in (ZZ)) swamped any temperature dependent effect. Indirect evidence for a quasi-elastic peak comes from two results. The fact that the hard E_g mode exists for $T>T_c$ at almost the same frequency as that observed below T_c illustrates the importance of dynamic effects and indicates the presence of a central mode. Also, the A_{1g} and E_g soft mode frequencies and widths show a similar temperature dependence to that observed in lead germanate by Hisano and Ryan (7). These authors showed that the Cowley-Coombs model (8) fitted their data, thereby producing a central mode and a width that no longer diverged. Similar results could be expected for $KMnF_3$.

CONCLUSIONS

The results discussed here illustrate the difficulties in obtaining critical exponents from Raman data when T is close to T_c. In the case of $KMnF_3$ the difficulties are accentuated by the first order nature of the transition, which limits the range over which temperature dependences can be measured and makes it impossible to obtain two decades of temperature dependent behaviour. Our results show that the intensity of a hard mode is proportional to the square of the soft mode frequency for temperatures away from T_c. Indirect evidence was found for the existence of a central component.

We wish to acknowledge helpful discussions with R.A. Cowley and A.D. Bruce, and thank D.A. Jones for providing the crystal.

REFERENCES

1. S.M. Shapiro, J.D. Axe, G. Shirane and T. Riste, Phys. Rev. B6, 4332 (1972) and references therein.
2. Yu.A. Popkov, V.V. Eremenko and V.I. Fomin, Sov. Phys. Solid State 13, 1701 (1972) and also private communications.
3. V.G. Khlyustov, I.N. Flerov, A.T. Silin and A.N. Sal'nikov, Sov. Phys. Solid State 14, 139 (1972).
4. J.M. Worlock and D.H. Olson, in Light Scattering in Solids, edited by M. Balkanski (Flammarion, Paris, 1971), p.410.
5. S. Hirotsu and S. Sawada, Solid State Comm. 12, 1003 (1973).
6. F. Borsa, Phys. Rev. B7, 913 (1973).
7. K. Hisano and J.F. Ryan, Solid State Comm. 11, 1745 (1972).
8. R.A. Cowley and G.J. Coombs, J. Phys. C. 6, 143 (1973).

Ferroelectrics
1974, Vol. 8, pp. 583–584

RAMAN SPECTRAL STUDY OF $KMnF_3$

B. H. TORRIE and D. J. LOCKWOOD

Department of Physics, Edinburgh University, Scotland

(Received September 10, 1973)

The temperature dependence of the E_g soft mode in the tetragonal phase of $KMnF_3$ was recorded and analysed using a spectral response function of the form

$$\chi^{-1}(\omega) = (\omega_\infty^2 - \omega^2 + i\gamma\omega - \delta^2/(1 + i\omega\tau))$$

The soft mode frequencies were found to be consistent with the power law $\omega_0^2 \alpha (T_c - T)^{2/3}$. $\gamma = 22\ \text{cm}^{-1}$ and $\delta^2 = 60\text{–}70\ \text{cm}^{-2}$ at T_c.

$KMnF_3$ undergoes a cubic to tetragonal phase transition at $T_1 = 186$K as a result of the condensation of one of the modes associated with the zone boundary $R(\frac{1}{2}\ \frac{1}{2}\ \frac{1}{2})$ point. This phase transition is similar to the one in $SrTiO_3$ except that the soft mode is much more heavily damped[1] and the transition is slightly first order in nature, with a hysteresis of a degree or less. In spite of these differences, experimental work to date[1–3] indicates that the phase transitions in the two crystals can both be described by the same basic theory.

We have measured the Raman scattering from a sample of $KMnF_3$ with emphasis on the temperature dependence of both the soft and hard modes, but we wish to report here only our work on the E_g soft mode in the tetragonal phase. The Raman spectrum was excited with 400 mW of argon laser light at 476.5 nm and the light scattered at 90° was analysed using a double monochromator with a spectral slit width of 1.7 cm^{-1}. A digitized data collection system enabled direct processing of the results. Sample temperature was controlled to within 0.1K and at least 15 minutes was allowed between runs for thermal equilibrium to be established; a time which was determined experimentally to be satisfactory.

The intensity of Raman light scattering per unit frequency interval is given by

$$I(\omega) = A(\bar{n} + 1)\langle Q\rangle^2 \chi''(\omega)$$

where A is a constant, $\bar{n}$ is the population factor for bosons, Q is the order parameter and $\chi''(\omega)$ is the imaginary part of a response function. Previously[4] we took χ to be of the damped simple harmonic oscillator (DSHO) form so that

$$\chi^{-1}(\omega) = (\omega_s^2 - \omega^2 + i\gamma\omega)$$

where ω_s is the characteristic frequency of the soft mode which is proportional to $\langle Q\rangle$ and γ is the damping constant. Cowley and Coombs[5] have proposed a low frequency channel for decay which gives rise to an additional term in the response function so that

$$\chi^{-1}(\omega) = (\omega_\infty^2 - \omega^2 + i\gamma\omega - \delta^2/(1 + i\omega\tau))$$

where δ^2 is a temperature dependent coupling constant and τ is an average phonon lifetime. With this model a distinction must be made between the mode frequency ω_0 in the limit $\omega \to 0$ and the mode frequency ω_∞ in the limit $\omega \to \infty$. These two frequencies are related by

$$\omega_0^2(T) = \omega_\infty^2(T) - \delta^2(T)$$

and ω_0 is proportional to $\langle Q\rangle$. Use of this extended response function improves the fit, but the parameters are so highly correlated that constraints must be applied in order to obtain values which vary smoothly with temperature. Preliminary least-squares fits were made over the range 7 to 50 cm^{-1} and all parameters were allowed to vary. The background scattering was taken to be the residual scattering seen above T_1 which was almost independent of temperature over the range T_1 to 200K. It was found that the quality of the fits was not very sensitive to the value of τ so it was fixed at 1 cm. γ was well behaved as long as the soft mode was underdamped but it varied irregularly over the

range 18 to 40 when the mode was overdamped ($T > 170$K). A linear extrapolation of γ from the underdamped region up to T_c was used for subsequent calculations (see Figure 1). Finally the scaling parameter A was fixed at three values 100, 120, 140 which covered the range of values found for A. Values

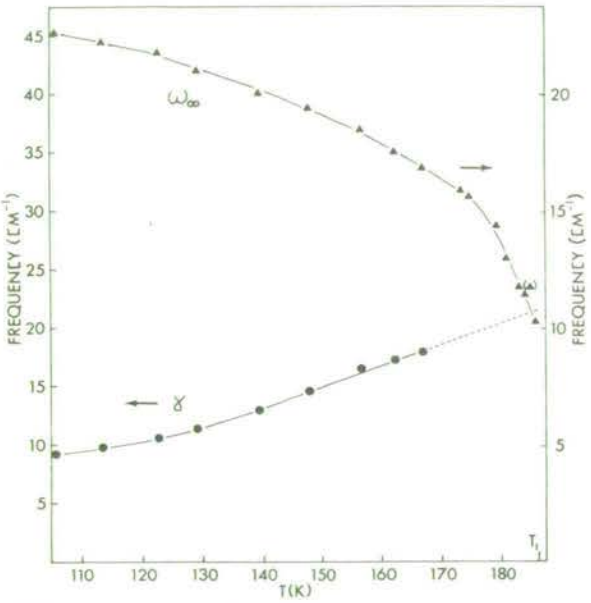

FIGURE 1 $\omega_\infty = (\omega_0^2 + \delta^2)^{1/2}$ and γ as a function of temperature. The quality of the least-squares fits was almost constant except for the fits associated with the point in brackets and the two lowest temperature points which gave poorer fits.

of ω_0^2 and δ^2 were then determined and were found to be well behaved in the overdamped region. At lower temperatures only the sum $\omega_0^2 + \delta^2$ varies smoothly with temperature and this sum is both independent of A and in good agreement with the values of ω_s^2 found earlier.

In Figure 2 we have plotted ω_0^2 versus $(T_c - T)^{2/3}$ for $T_c = 187$K. The lines through the points were drawn to connect the origin to the uppermost point; the justification for this choice being that the correlation between ω_0^2 and δ^2 is lowest about 20K below T_1. A plot of ω_0^2 versus $(T_c - T)$ for the same T_c has a pronounced curvature to it so the results are definitely not in agreement with the prediction of a linear theory. A least-squares fit to the points using a constant weighting factor gives $T_c = 186.4 \pm 0.1$K and an exponent of 0.60 ± 0.05 for all three values of A; again the exponent is less than one. Values of δ^2 can now be found from the differences between the curves in Figure 2. The temperature dependence of δ^2 is similar to that found in $SrTiO_3$ above T_c but

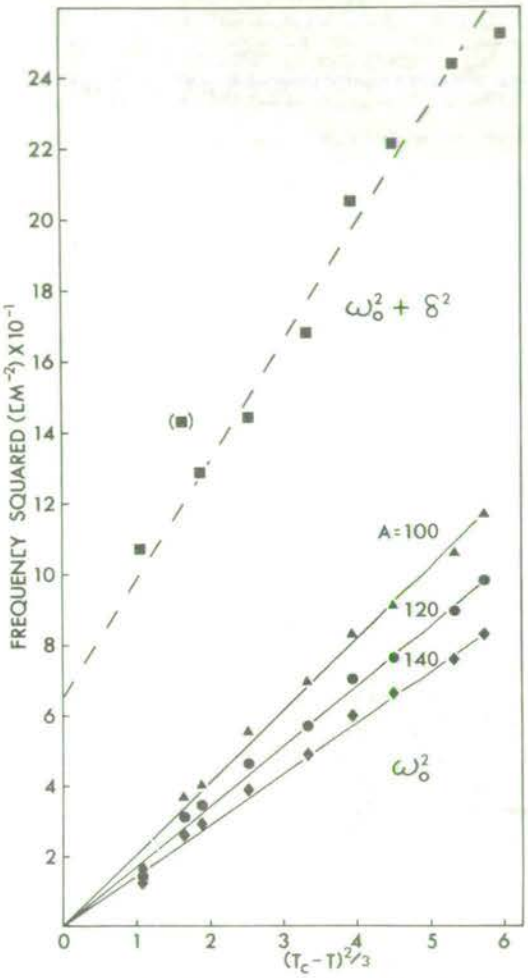

FIGURE 2 $\omega_0^2 + \delta^2$ and ω_0^2 as a function of temperature. $\omega_0^2 + \delta^2$ was independent of the value of the scaling parameter A.

its magnitude is larger (60–70 cm^{-2} compared to 20 cm^{-2} at T_c). This does not seem unreasonable when one considers that γ is also larger in $KMnF_3$ (22 cm^{-1} compared to 7 cm^{-1} at T_c).[1] Note that a linear theory gives $\delta^2 = 0$ at T_c.[5]

We wish to acknowledge helpful discussions with A.D. Bruce and R. A. Cowley, and to thank D. A. Jones for providing the crystal.

REFERENCES

1. S. M. Shapiro, J. D. Axe, G. Shirane and T. Riste, *Phys. Rev.* **B6**, 4332 (1972).
2. F. Borsa, *Phys. Rev.* **B7**, 913 (1973).
3. S. Hirotsu and S. Sawada, *Solid State Comm.* **12**, 1003 (1973).
4. D. J. Lockwood and B. H. Torrie, *Proc. NATO Advanced Study Institute*, "Anharmonic lattices, structural transitions and melting", Ustaoset, Norway (1973).
5. R. A. Cowley and G. J. Coombs, *J. Phys. C.* **6**, 143 (1973).

AUTOMATION TECHNIQUES FOR RAMAN SPECTROSCOPY

J. W. ARTHUR and D. J. LOCKWOOD
Dept. of Physics, University of Edinburgh, Edinburgh, U.K.

(Received 12 November, 1973)

Abstract. This paper is concerned with the automation and control of grating spectrometers by digital techniques. The methods outlined include: a simple manually operated digital control; a dedicated logic system with data storage; data acquisition and control systems run by a computer in real-time and time-sharing modes. The performance of these methods is evaluated. A basic spectrometer control unit is described; this unit forms a module around which more general spectrometer control systems may be constructed.

1. Introduction

Computers are increasingly being applied to problems in spectroscopy. The possibility of performing routine data reduction and calculations with spectroscopic data on a large scale poses the problem of providing data in a form readily assimilated by a computer. Chart recorder output is not a suitable medium for computers. One solution to the problem is to have a device which produces digital output from a spectrum as it is recorded and punches it on paper tape. The paper tape is read by a computer and the spectrum reconstructed from an implied relationship with the numbers on the tape. Another solution is to link the spectrometer directly to the computer through an interface. The data is actually collected in the computer so that no intermediate storage medium need exist. But having raised the question of data acquisition by computer it is as well to consider the possibility of the computer controlling the spectrometer so that a dialogue is established between the two.

This paper outlines four general methods of approaching the problem of digitisation and computerisation. Specific systems are described, the first of which uses an on-line computer for data-acquisition; different modes of operation are considered which illustrate the possibilities. The second has no direct link with a computer but instead a specially constructed control unit links the spectrometer with a multi-channel scaler which acts as an intermediate data storage device. The third method is the simplest and is a very basic circuit for collecting data on paper tape. The last shows how the basic circuit used in the previous method can be used in a full-blown computer control system suitable for time-sharing operation.

Thus it is intended to give a reasonably general survey of the possibilities as well as reporting recent developments in the problem of computer-spectrometer linkage. The descriptions apply to wavenumber scanned instruments and Raman spectroscopy in particular but there is no reason why they should not be put to use elsewhere.

2. Systems With Direct Computer Linkage

The most common digitisation requirement in spectroscopy is a simple data-logging

Journal of Raman Spectroscopy **2** (1974) 53–69.

operation, where the operator retains control of the spectrometer and ancilliary equipment, but the spectral information is obtained in a form suitable for computer analysis. The systems described in this section perform this function through the use of a small on-line computer. If such a computer is available then these systems are readily put into operation, for the computer itself provides the interface to the experiment and little additional electronic equipment is needed.

The systems are based on a DEC PDP-8 computer used as an active information processor which can operate under the control of three different programs. For each program the computer performs a function that could be carried out by an independent set of electronic equipment: the advantage is that one instrument performs the work of many, and each function can be easily modified by rewriting the control program. The modes of operation are (1) digitise, (2) photon-count, and (3) signal-average. Although the details given here relate to a particular installation the principles involved in each mode are quite general, and are separate examples of the different ways of tying an experiment into a computer. Time-shared use of the computer is possible for modes (2) and (3) but here this type of operation is inefficient, and can lead to difficulties through priority conflicts with other computer functions. The reason for this is that the sequence of operations within the computer is controlled by external devices rather than the other way round.

The three modes of operation have been in operation since 1968 [1], and examples of Raman spectra recorded with the PDP-8 operating in the photon-count mode, for example, can be found in Reference 2.

2.1. Digitise mode

In the digitise mode, the spectrometer operates in the normal manner. The computer converts an analogue signal from the photomultiplier (PM) current amplifier into digital form and punches the result on paper tape. Wavenumber information is also recorded from a marker pulse.

The experimental arrangement is outlined in the block diagram of Figure 1. Signals from the current amplifier are fed into the computer via its analogue-to-digital converter (ADC). Spectrometer wavenumber-marker pulses are processed by means of the computer skip line facility [3]. The computer recognises a marker pulse via hard-wired circuitry, and encodes the information on the output tape via the software. The connection between hardware and software is achieved by means of a device address code, which is 6412 in this case. A remote control switch is used to start or stop the program allowing the PDP-8 to be some distance away from the spectrometer. The switch also operates through the skip line. The ADC unit has provision for a multiplexer which would enable other analogue inputs to be fed to the computer. For example, the laser power can be monitored, and the Raman spectrum corrected for variations in the source intensity by performing a ratio calculation in the computer. The standard low-speed Teletype paper tape punch (10 characters/s) limits the output data rate to approximately one point every 0.2 s.

For the digitise mode the main computer program is designed to cycle in a fixed

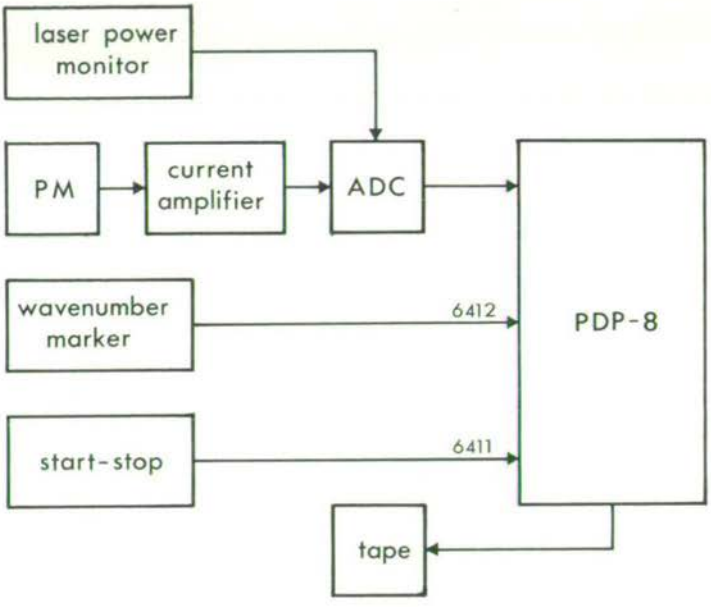

Fig. 1. Block diagram of the digitise mode of operation.

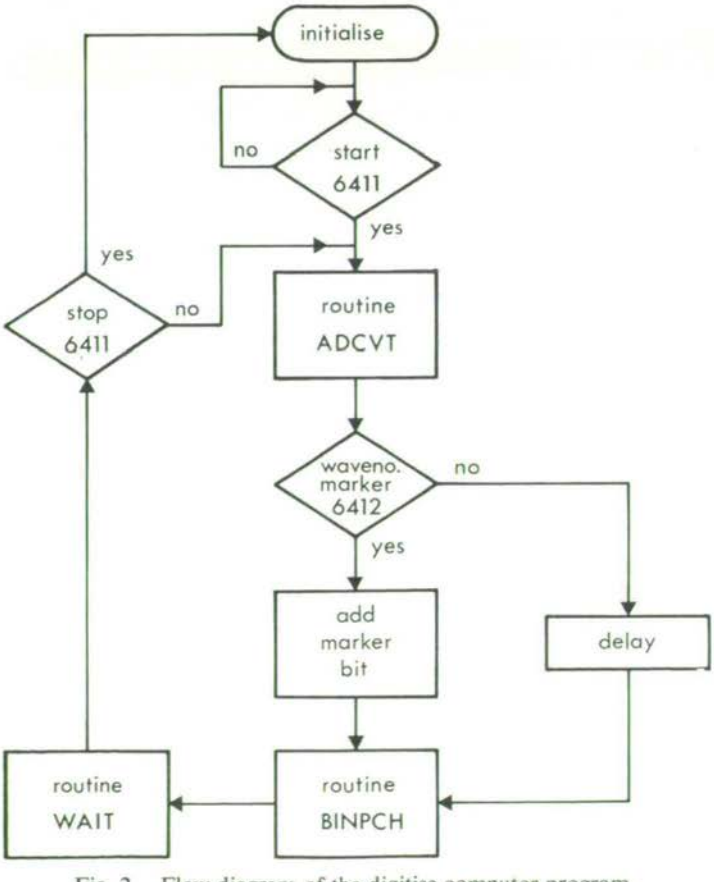

Fig. 2. Flow diagram of the digitise computer program.

time so that each data point can be related to wavenumber via the scan-rate of the spectrometer. The method relies on the fact that the spectrometer is scanning continuously. As the simplified flow diagram of Figure 2 shows, the control program consists of a number of subroutines. The ADCVT subroutine digitises the analogue signal presented to the ADC and the digital value is punched on tape by means of subroutine BINPCH. If a wavenumber marker pulse occurs an additional information bit is also punched. The computer waits – in subroutine WAIT – while the punching takes place.

The digitise mode is a case where the computer is being used as a real-time clock. The fixed cycle time of the main program defines a unit of time, and the aquisition of information from external sources is based on that time scale. The computer can not operate in a time-shared mode under such conditions, and this is a disadvantage. Another disadvantage is the limit imposed on the output data rate by the slow-speed punch, but this limitation can be overcome by using a high-speed device such as a fast punch or magnetic-tape drive.

2.2. Photon-count mode

Conventional current-amplification techniques used for recording PM signals work satisfactorily at moderate signal levels, but for the weaker signals often encountered in Raman spectroscopy the pulse-counting technique inherently possesses a superior signal-to-noise ratio [4]. The photon-count mode of operation has been designed specifically to deal with low signal levels. In the photon-count mode the computer counts PM pulses for fixed time intervals while the spectrum is scanned, and punches the totals on paper tape. Wavenumber information is recorded as in the digitise program. The total count is also produced as an analogue signal for chart recording purposes.

The experimental arrangement is outlined in Figure 3. All input information is processed by means of the PDP-8 program interrupt facility [3]. In this mode of operation, information arriving at the computer interrupts the main computer program and is then processed via the program interrupt subroutine. A crystal controlled clock provides timing pulses, and these pulses are used to determine the integration time as specified in the control program. The wavenumber marker and start-stop controls are the same as those described earlier, and again there is provision for other analogue inputs such as for laser power monitoring. One of the computer's digital-to-analogue converters (DAC) provides a chart recorder signal from the integrated PM pulses.

The operation of the main computer program is indicated in the flow diagram Figure 4(a). Subroutine DSPLY provides the analogue signal for chart recording purposes; the DSPLY subroutine is used frequently so that the comparatively long time constant of the chart recorder makes the displayed signal seem continuous. The program interupt subroutine is outlined in the flow diagram Figure 4(b). Each interrupt device is tested sequentially and, depending on its state, appropriate action is taken. In order to shorten the program interrupt cycle time some short cuts are

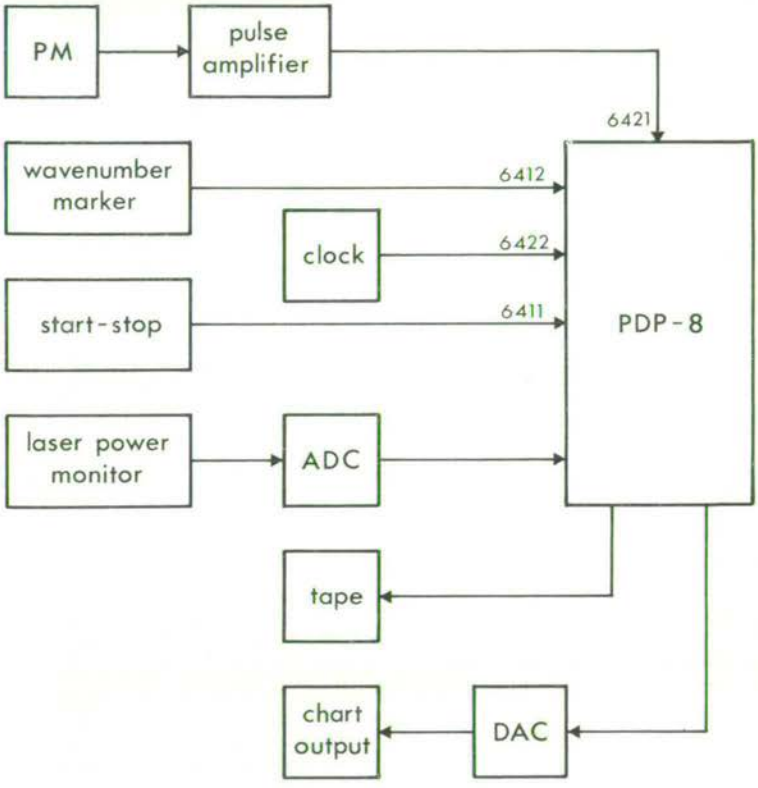

Fig. 3. Block diagram of the photon-count mode of operation.

made. PM pulses occur most frequently and these are tested first, while the low frequency clock pulses are tested last. This arrangement ensures that no clock pulses are missed and gives the lowest possible photon-count dead time. Note that an interrupt can not occur whilst the computer is running under the control of the interrupt subroutine until the 'interrupt ON' instruction is given. The photon-counting section of the program has a total computer-instruction cycle time of 15 μs, which results in a linear response for count rates $\lesssim$6 kHz.

In the photon-count mode the real-time clock is external to the computer, but, as in the digitise mode, the cycle of operations in the computer is closely controlled through the software. This leads to some disadvantages. Any change in the details of the running of the experiment, such as changing the integration time, requires an alteration in the computer program and this is not a rapid procedure; and time-shared use of the computer is only possible for the simplest of additional tasks. The use of the program interrupt line for photon counting is an inefficient method of operation: a better method would be to count pulses external to the computer for the integration period and then transfer the total count from a buffer using the data break facility [3].

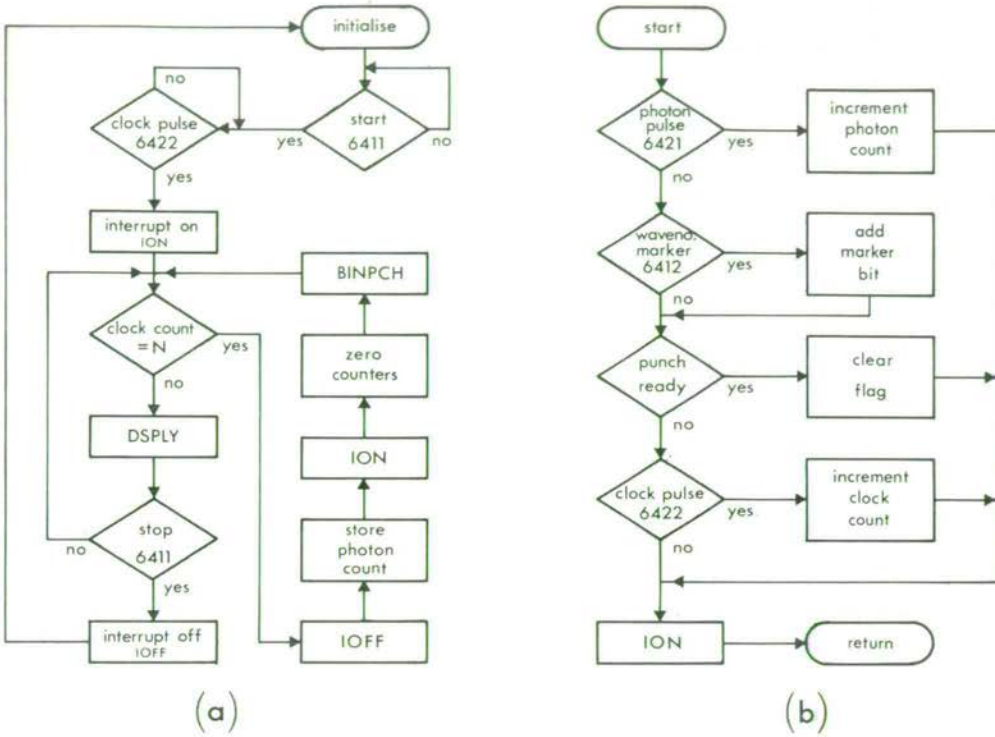

Fig. 4. Flow diagram of (a) the photon-count main computer program and (b) the program interrupt subroutine.

2.3. Signal-average mode

By repeatedly scanning a spectrum and adding the results it is possible to improve the signal-to-noise ratio (S/N). The signal increases in strength in direct proportion to the number of scans n whereas the noise increases as $\sqrt{n}$. In theory, the S/N can be improved without limit, provided the noise is completely random: non-random noise can also be reduced if it is not synchronised with the scan repetition rate.

In optical spectroscopy, the usual averaging technique is to scan through a part of the spectrum in the normal manner by rotating the grating, to repeat the process several times, and then average the spectra. It is much simpler to keep the dispersive element stationary and scan the spectrum via a rotating refractor plate. In this arrangement a parallel plate of transparent refractive material is placed behind the entrance slit of the spectrometer and the plate is rotated about an axis parallel to the length of the slit. The spectrometer experiences at the focal curve a translation of wavelength proportional to the sine of the angle of rotation.

This section describes a signal averaging technique based on the rotating refractor plate method and at the same time shows how the normal operation of a spectrometer can be extended by the use of a computer. The scanning system is built around a quartz refractor plate that is driven by a variable-speed motor. One revolution of

the refractor plate drive shaft produces two spectral scans and each scan is divided into 512 channels by a digital shaft-position encoder. Thus the refractor position – and hence wavenumber – is related to a definite channel number. Successive sweeps are synchronized by a start-scan pulse produced by another shaft-locked encoder. The repetitively scanned spectra are integrated by the PDP-8 computer operating in the signal-average mode.

A block diagram of the experimental arrangement is given in Figure 5. The PM signal and refractor plate position information is processed by the data break facility. This facility operates entirely through hardware, and so is independent of the control program. Starting at channel zero, the computer adds up the number of photomultiplier pulses received on data-break line DB1 by counting them into a switch-specified location in the computer's memory. Data-break operations occur almost instantaneously on request, but the maximum linear count rate is limited to ~60 kHz by the 1.5 μs data break cycle time. Higher count rates can be accommodated by using a buffered scaler between the pulse amplifier and the computer. On receipt of a channel increment pulse (DB2) the computer adds the signal pulses into the next consecutive memory location. This latter process is repeated until a start-scan pulse (DB3) is received, at which time the computer returns to the memory address corre-

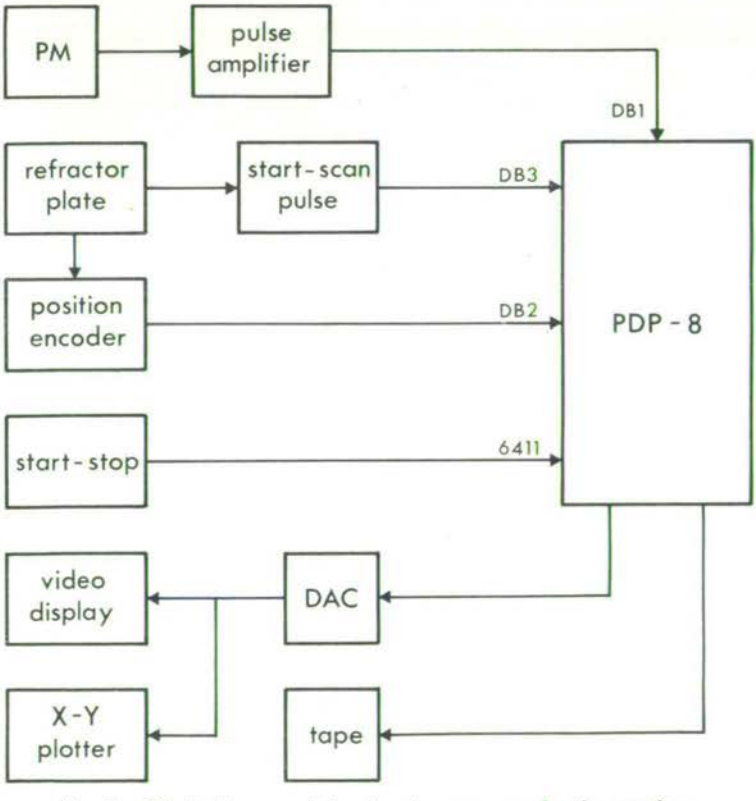

Fig. 5. Block diagram of the signal-average mode of operation.

sponding to channel zero. In this way the computer integrates the spectrum by automatically adding the signal pulses from each successive sweep. A remote stop-start switch is used to halt the computer at the end of a run. Throughout the run the computer produces an oscilloscope display of the integrated spectrum so that the improvement in the S/N can be observed. At the conclusion of the run the computer punches the spectral information on paper tape, and can also plot the data on an $X-Y$ recorder.

Time-sharing operations are possible in the signal-average mode as during a run the computer software performs the background task of providing an oscilloscope display from the data fed into the computer. The data transfer from external devices is independent of the software. However the basic operation is still real-time, since data transfers command immediate action by the computer.

The system described here has been based on the refractor plate technique for signal averaging. However, the computer linkage section is quite general and can be applied to other techniques for rapid scanning of spectra.

3. Hard-Wired System

The approach described here is to build a 'hard-wired' logic system for the specific task of controlling the spectrometer and linking it to a data storage device such as a multi-channel scaler (MCS). The logic system allows only a fixed set of scan parameters to be programmed; for example, start of scan in cm^{-1}, end of can, scan rate, number of scans, and channel width. The programme of the logic system can be made to suit any particular purpose, but once built it cannot easily be altered. This kind of system is therefore a compromise where the 'on-line' use of a computer is not possible. It does however have the advantages of a high degree of reliability, low cost, relative simplicity and independence.

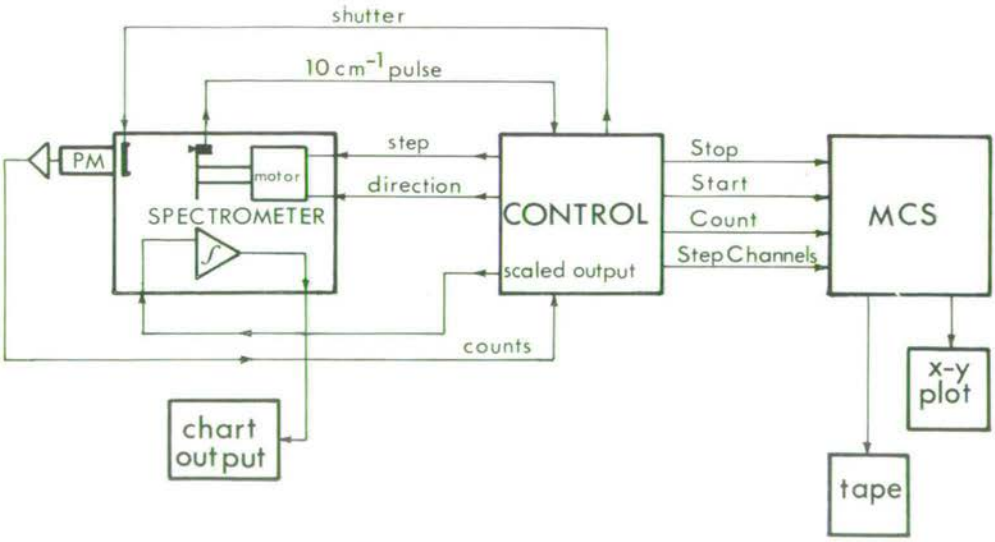

Fig. 6. Configuration of conventional spectrometer with MCS control unit.

Figure 6 shows the configuration of this type of system for a particular spectrometer and MCS. In this case as much use as possible has been made of built-in spectrometer (Spex Ramalab) equipment and functions so that the small details may vary from one instrument to another. Figure 7 shows more detail of the control system, the basic operation of which is as follows.

3.1. Motor drive

Stepping pulses for the motor are derived from the system clock. A presettable divider brings the clock frequency down to the rate required for scanning ($200/M$ Hz where M can be set from 1 to 99 on digital switches). A further divider provides a pulse for every N motor steps and N is set so that this pulse advances channels in the desired wavenumber step sizes (channel width, CW). For purposes other than actual scanning, full clock frequency is selected to drive the motor at high speed.

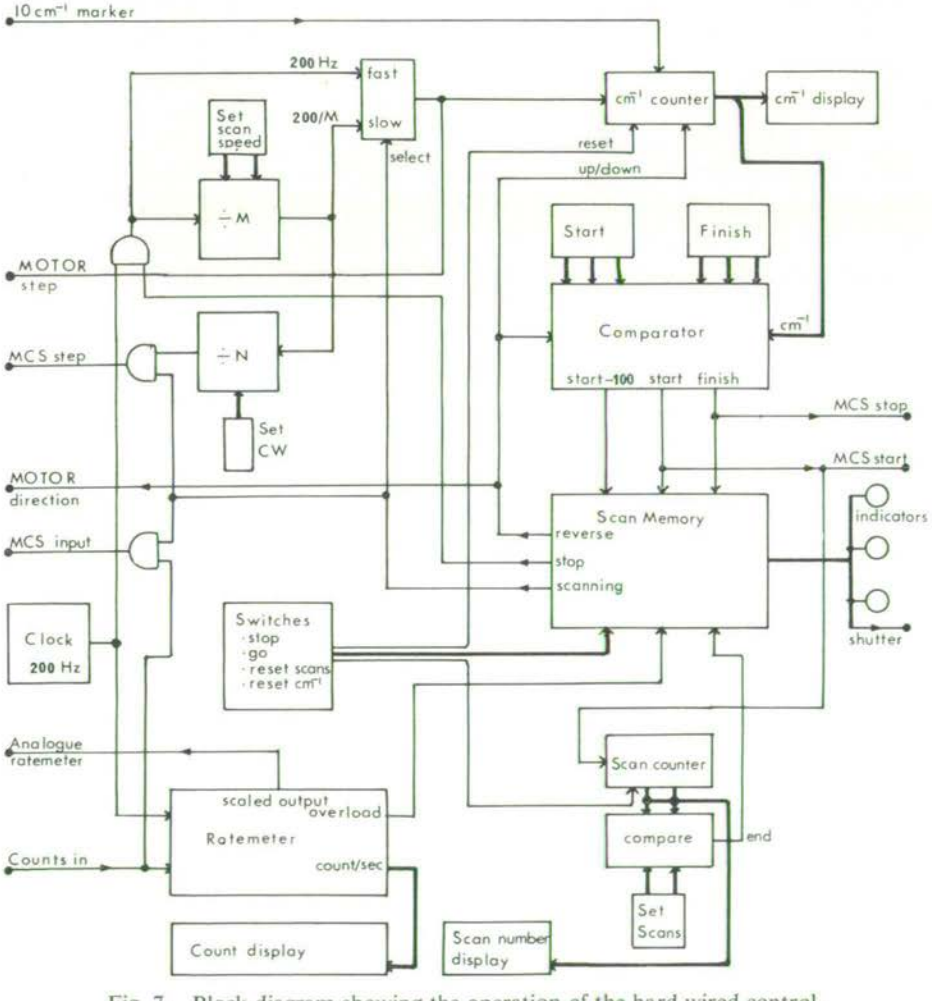

Fig. 7. Block diagram showing the operation of the hard-wired control.

3.2. Wavenumber counter

A reversible counter keeps track of motor steps and presents a readout of the wavenumber shift of the spectrometer with respect to some reference position chosen when the counter is manually reset to zero. A 10 cm^{-1} marker pulse from the spectrometer is used to synchronise the counter. The contents of this counter are compared with scan limits set on digital switches to give three possible signals: at 100 cm^{-1} below the start position, 'start − 100', at the start position, 'start', and at the finish position, 'finish'. Scanning takes place between the limits and these signals change the phases of operation of the control unit.

3.3. Count rate

The photon counts are fed to the MCS scaling input and in addition they are continuously monitored by a six decade ratemeter with display. The ratemeter is a buffered scaler which is updated once a second with the count for the previous one second period. An overflow condition is used to signal an overload on the photomultiplier. Also available from the ratemeter is an automatically scaled frequency output. This represents the input count frequency divided by a power of ten selected by the most significant digit in the buffer store. The powers of ten are readily available at the outputs along the divider chain of the scaler. The output, normally in the range 10–100 Hz, is quite useful for display on a chart recorder through an analogue ratemeter since scale changes are performed automatically.

3.4. Phases of operation

The control will scan the spectrometer over the selected frequency range, reverse to 100 cm^{-1} below the start position and stop if the selected number of scans has been completed. Otherwise another scan is carried out and the scan counter incremented. The 100 cm^{-1} difference allows backlash to be taken up after a change in direction; the amount required is machine dependent but 100 is a number which is easy to incorporate in the comparator logic! While the machine is not actually scanning a shutter is switched into place to protect the photomultiplier from accidental exposure to out-of-range sources. But even in the case of accidental exposure during scanning the overload signal from the ratemeter trips the shutter and halts the machine. Table I below shows the phases of operation with relevant signals and transitions. The scan memory is a set of flip-flops which have their states altered in changing from one phase to another. Indicator lights show the status of the control at any time.

Once the control has been initialised, running a spectrum simply requires that the scan parameters be entered on sets of digital switches and the 'go' switch is pushed. Thereafter the control does all the work until the data for the spectrum has been accumulated in the MCS. The MCS oscilloscope display allows immediate inspection of the results; more scans can be done if this is necessary to improve the signal to noise ratio, otherwise the data is committed to permanent storage on paper tape, or graphically on an $X-Y$ plotter.

TABLE I

Signals and transitions during the various phases of operation

Signal	Stop	Reverse	Fast forward	Scan
Motor step	0	Full speed	Full speed	Scan speed
MCS step	0	0	0	After N steps
Motor direction	X	0	1	1
MCS input	0	0	0	Count in
Shutter	1	1	1	0
Start-100		○——→		
Start (MCS start)			○——→	
Finish (MCS stop)		←——————————○		
End	←——○ (at Start-100 after last scan)			

0 = Off; 1 = On; X = Irrelevant; ○→ = at this transition.

This system, built basically from series 7400 TTL integrated circuits, has been in use for one year at the time of writing and has proved both useful and reliable. It has been found possible to run spectra routinely with a degree of reproducibility that would have only been painstakingly achieved in manual operation. Published results, using computer analysis of the data tapes, are found in References 5 and 6.

4. Simple Control

While the control system described in Section 3 has its merits it suffers from the disadvantage that any further expansion and sophistication would mean reconstruction. Being built for a specific task it does not lend easily to radical modification. A 'modular approach' may therefore be more appealing. The problem, therefore, is to build a basic control of little complexity which can be used both as a simple manually operated control and as a module in the more complete and automated system. Such a control has been built, Figure 8, and is described here. A different approach to the scanning problem has been adopted which has several advantages. Most spectrometers in the past have relied on high precision constant velocity motors to scan the gratings while the signal is simultaneously recorded on a chart recorder. This procedure is not necessary when a stepper motor drive is used, instead the gratings can be stepped and the function of the control is a succession of cycles of increment wavenumber, wait and count. Not only does this remove the problem of synchronising other devices such as a chart recorder or real-time computer to the scan rate, it also effectively increases the resolution because the gratings are stationary during the integration time of the counter.

The operation of the control is as follows. Individual motor steps are generated by the oscillator OSC, the frequency of which is not very important but gives a good stepping speed. The flip-flops STEP, INT and ON provide independent means of arresting the motor steps at MOTOR GATE. When steps are allowed through the gate they are counted by the stepsize counter. N individual steps make a complete

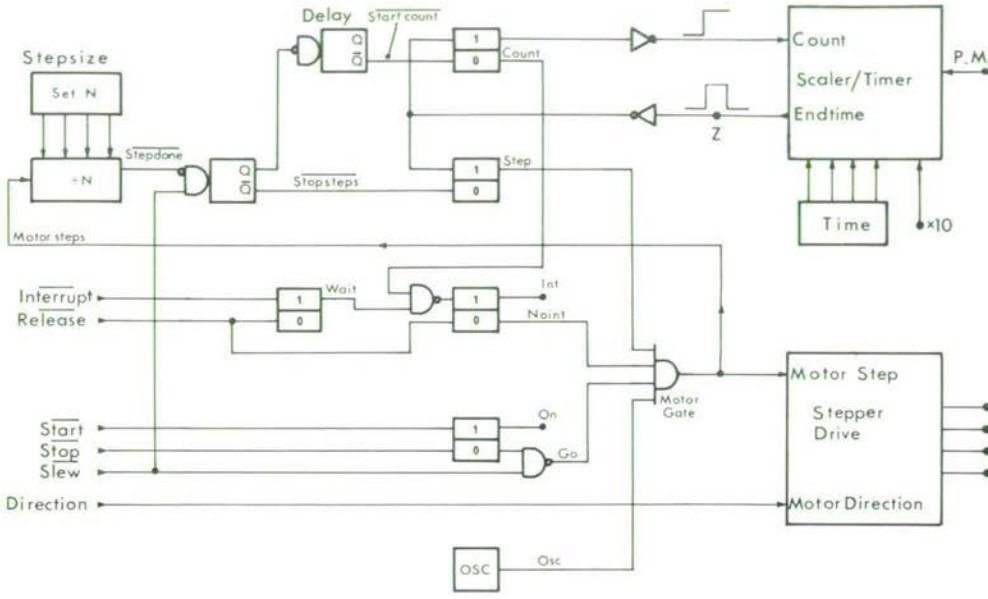

Fig. 8. Circuit of the basic step-count control.

scan step and produce a '0' level at the output, $\overline{\text{STEPDONE}}$. This signal does two things: it inhibits any more motor steps by resetting the STEP flip-flop to a '0' state, and it sets the COUNT flip-flop to a '1' state, after a short delay to allow for the lag in response of the motor. The COUNT flag initiates a scaler cycle lasting for a preset period, TIME, and terminated by a pulse ENDTIME. This pulse resets the flip flops to their former statuses allowing another cycle to proceed. Thus the operation consists of a sequence... STEP, COUNT, STEP, COUNT... which can only be terminated by the action of one of the flip-flops INT or ON.

The flip-flop ON starts or stops the operation through push-button switches. SLEW overrides the stopped condition; count cycles are inhibited so that the motor runs continuously. A separate flip-flop INT can also be used to halt operation. But here the operation is more subtle. Two flip-flops are used, the first captures the momentary signal $\overline{\text{INTERRUPT}}$ and produces a signal WAIT. When the next count cycle appears the INT condition is set preventing the control starting up at the following step cycle. RELEASE cancels this condition and the next step proceeds. This gives a means of temporarily stopping a scan without interfering with the count in progress or upsetting the calibration by stopping in the middle of a step. It is well to have these as separate means of stopping the scan, bearing in mind the uses to which they might be put in a modular system. A version of this control has been built to operate a Spex 1400 instrument adapted to take a stepper motor drive. The scan parameters stepsize and count time are programmed conveniently by digital switches with bcd outputs. In this version a step counter was included to automatically halt

the scan after a selected number of steps. The photon-count scaler outputs its data, six digits, to a Teletype, and a built-in analogue to digital converter gives graphic output on a chart recorder. It is convenient to have a chart recorder with a stepper drive operating on the same pulses that drive the spectrometer. There is no facility for repeated scans but this is not essential in the majority of experiments. Long scans however are readily done because there is no limitation of a fixed memory size.

5. A Complete System

The simple control used on its own provides a neat and effective way of programming the basic functions of the spectrometer but it has few of the luxuries of automation. Before trying to elaborate on it however, it becomes worthwhile to review the nature of the experimental problem to ascertain the general suitability of the step-count technique.

Measuring a spectrum means recording intensities $I(\nu)$ over a range of frequencies ν. I is more precisely proportional to the photon count rate than the photo-current at a given ν. Scanning at a constant rate over the required frequency range is not essential to the technique. Recording a set of intensities, or photon counts, $I(\nu_i)$ over a set of frequencies ν_i gives the information required if the steps $\delta\nu_i = \nu_{i+1} - \nu_i$ can be made reasonably small. On careful reflection it is apparent that even in the continuously scanning case there is always some window $\delta\nu$ around which the data is smeared. The magnitude of $\delta\nu$ depends on the time constant of the recording apparatus and on the scan rate. Nothing is lost, therefore, when discrete data points are taken and in fact as much information can be obtained as by any other technique.

Returning to the operation of the basic control unit, which operates in a stepping manner giving discrete points, it can be seen that the essential control parameters stepsize, count time, direction, stop and start can be collected together and represented by a logical word (string of binary bits) 12 bits long. The control unit translates this word into action by the spectrometer.

If this control word, as it may be called, is specified for each step-count cycle then any action can be accomplished. The control word can be set by some other logic system or by a computer in which case the control word is virtually an extension of the computer's commands. Figure 9 shows how this may be accomplished. The operation of the control is the same as described in Section 4 but here the step-count cycle is interrupted by the computer at point Z in Figure 8. The computer provides a control word from its output section and signals its availability to the control. The control accepts the word, translates it into action by the spectrometer and starts a scaler count cycle. When the count is complete the scaler signals the presence of data to the computer. Not until this data has been accepted and processed can a new control word be set and another cycle activated. The complete cycle time depends on the individual cycle times for control, scaler and computer but its duration is of no importance to the operation of the system. External interrupts and waits have no adverse effect because the spectrometer is forced to wait as well as the computer. This system is at once suitable for use in a time-sharing environment.

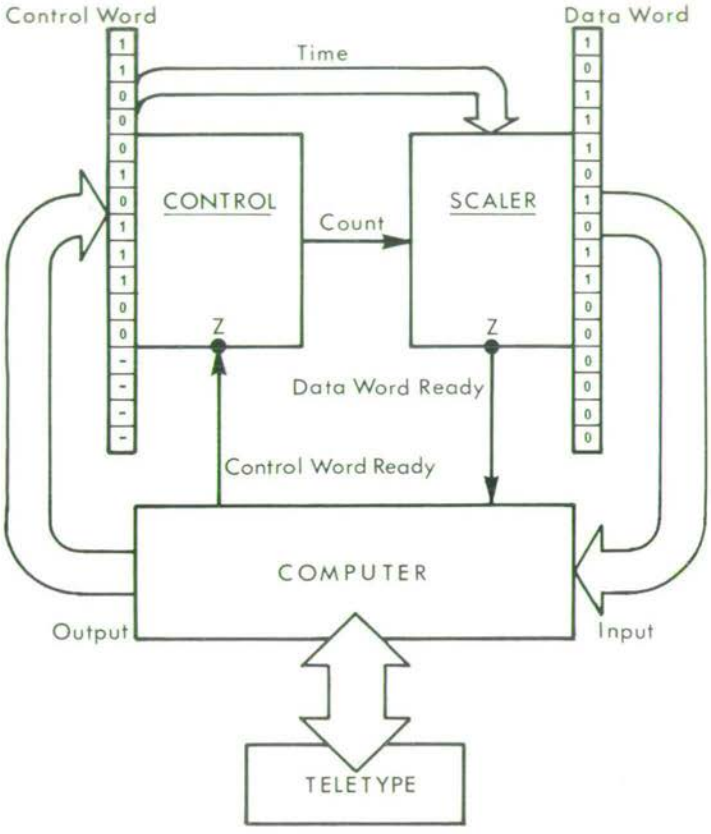

Fig. 9. Flow of data for the computer operated control.

Control of the spectrometer is by a programme initiated in the computer from the Teletype. Input of data and output of control word appear to the computer the same as input-output from normal channels (e.g. paper tape reader and punch), so that there is no reason why normal programming techniques in a high level language may not be used. The correct binary pattern for the control word can be set by an expression such as:

$$\text{CONTROL} = \text{STOP} + 2*\text{GO} + 4*\text{TX10} + 8*\text{TIME} + 128*\text{DIR} + \\ + 256*\text{STEP}.$$

At this stage the system has a great deal of flexibility and information contained in the spectrum can be recorded optimally. It is possible to multiscan, to do automatic calibration, to hunt for bands using variable stepsizes and count-times – the scope is bounded only by the limiting capabilities of spectrometer and computer. But it is a pity to have such flexibility in the spectrometer part of the experiment alone. The concept of operating through a control word and data word, however allows

immediate extensions to be made. Translator circuits may be built for other experimental equipment so that it is possible to set and record such parameters as sample temperature, light polarisation and laser power. The digital voltmeter can act directly as a translator for a thermocouple or laser power monitor. It is also possible to operate an $X-Y$ plotter and other displays all on the same basis. The control and data words for individual translators together form extended control and data words for the computer to handle. Multiplexing techniques are necessary when the sizes of these words become too large for a single input-output transfer. Such a system would be readily built along the lines of CAMAC [7].

Work on such a system is already in progress and it should be possible to report on it in the near future.

6. Conclusion

The adoption of a particular system depends on the type of computer available. There are three major categories of computer system to consider, These are: full use of a small computer ('mini-computer') to perform one task, of limited scope, at a time; time-sharing on a medium sized computer with several users running independent tasks; and computation facilities only on a large job-processing computer.

In the first category almost all of the interfacing may be provided by the computer which can be housed in the same laboratory as the spectrometer. Programming is done at a very basic level and small memory size and long instruction cycle times restrict the scope of both real-time control and off-line data reduction. No doubt most of these difficulties would be overcome by an enterprising programmer, but the experimentalist may neither have the time or desire to do so. The advantage of having the full use of even a small computer is that there are no external users or programmes to interfere with the experiment and, as a result, the user is free to use the computer as a clock to send motor pulses or set count times. Section 2 above describes examples of this type where the small computer is a PDP-8 with 4K words of store. Commercially available spectrometer-plus-small-computer systems may, however, be an attractive proposition since it falls to the manufacturer to provide a working system with software.

The category at the other extreme is the large scale computer system which is completely reserved for off-line computation. There is no reason, however, why a small computer should not be used as a control and pre-processor device. But where this is not possible the systems of Section 3 and 4 produce spectroscopic data in a form which can be processed directly on the large computer as a normal 'job'. The hard-wired logic system is intended to replicate some of the programming facilities that would otherwise be possible only under direct computer control. Multiscanning, for example, is a well proven technique for weak signals and its implementation usefully extends the capability of any system. The construction of such a control system requires a deal of constructional effort and expertise with logic systems. The operation is quite flexible but only within the bounds of the facilities provided in

the programming switches – and multichannel scalers tend to have more restricted memory capacities than computers. This type of system, however, can be justified where there is a large amount of routine work to be done, or where multiscanning is a necessity. It can be operated by personnel having no special experience with computers.

The simpler control unit of Section 4 is truly basic in its operation but its design purpose is well fulfilled. Even this simple control, without data collection on paper tape, offers an alternative mode of operating a spectrometer manually which is neat and effective. By its own nature it is suitable for use as a component in more complex circuits or in modular systems. The latter aspect is to be emphasised both as it is good constructional practice and because of compatibility with systems making use of the large range of commercially available plug-in units, e.g. NIM and CAMAC.

Many research groups have shared access for a medium sized computer such as a DEC PDP-11. A typical system would have software, an operating system for time sharing, and some mass storage devices such as disk or magnetic tape. The computer services the users tasks in a manner which preserves their independence of each other. It is not possible for a user to know that his demands for service will be met immediately on request. A special technique is required because the experiment may be forced to wait, even if only for a short while. The complete control system described in Section 5 fits the requirements of this type of computer environment. Here the situation for the experimenter is quite ideal. The computer is large enough to do both control and processing of many tasks. System programming already exists and the user can take full advantage of a powerful programming language such as FORTRAN. Expansion to a larger experimental work-load is, in principle, no problem. This type of system then, allows more possibilities than any other at a level which is easy for the experimenter to come to grips with. It should certainly find application now that the sharing of computer resources has become commonplace.

Other systems have been reported which are in some ways similar to the examples given here. Manfait *et al.* [8] describe a system using a MCS, and Schmid *et al.* [9] describe a PDP-8 system. A larger system, also controlling an infrared spectrometer, has been reported by Scherer and Kint [10]. These are specific systems and a less general approach has been taken. A novel system in which an electronic calculator is interfaced to a spectrometer is described by Warren and Ramaley [11], but this is a very specific system requiring a deal of circuitry.

Finally we wish to acknowledge the support of the New Zealand University Grants Committee for the work of Section 2 and of the Science Research Council for Sections 3–5.

References

1. Lockwood, D. J.: Ph. D. Thesis, University of Canterbury, N.Z., 1969.
2. Christie, J. H. and Lockwood, D. J.: in M. Balkanski (ed.), *Light Scattering in Solids*, Flammarion, Paris, 1971, p. 145.

3. *The PDP-8 Users Handbook*, Digital Equipment Corporation, Massachusetts, U.S.A.
4. Tull, R. G.: *Appl. Optics* **7**, 2023 (1968); Alfano, R. R. and Ockman, N.: *J. Opt. Soc. Am.* **58**, 90 (1968).
5. Arthur, J. W. and Taylor, W.: *Ferroelectrics*, to be published.
6. Lockwood, D. J. and Torrie, B. H.: in T. Riste (ed.) *Anharmonic Lattices, Structural Transitions and Melting*, Noordhoff, Leyden, 1973.
7. Barnes, R. C. M. and Hooton, I. N.: *IEEE Trans. Nucl. Sci.* NS-16, No. 5, 76 (1969).
8. Manfait, M., Beaudoin, J. L., and Bernard, L.: in J. P. Mathieu (ed.), *Advances in Raman Spectroscopy*, Heyden, London, Vol. 1, 1973, p. 76.
9. Schmid, E. D., Berthold, G., Berthold, H., and Brosa, B.: in J. P. Mathieu (ed.), *Advances in Raman Spectroscopy*, Heyden, London, Vol. 1, 1973, p. 87.
10. Scherer, J. R. and Kint, S.: *Appl. Optics* **9**, 1615 (1970).
11. Warren, L. H. and Ramaley, L.: *Appl. Optics* **12**, 1976 (1973).

J. Phys. C: Solid State Phys., Vol. 7, 1974. Printed in Great Britain.

10

Raman scattering study of the three structural phases of $KMnF_3$

D J Lockwood and B H Torrie†

Department of Physics, University of Edinburgh, Edinburgh EH9 3JZ, Scotland

Received 14 March 1974

Abstract. The Raman spectra of the three phases of $KMnF_3$ have been measured and a detailed group theoretical analysis has been carried out in order to identify the observed peaks. The results for the intermediate temperature phase are consistent with a tetragonal structure of D_{4h}^{18} symmetry but the results for the low-temperature phase do not unambiguously determine the crystal structure. Particular attention was paid to the temperature-dependent modes. The soft modes associated with the upper phase transition were fitted to the response functions for a damped simple harmonic oscillator and for a model including damping by phonon density fluctuations. The results favour the latter model and suggest that non-classical critical fluctuations play an important rôle near the upper phase transition.

1. Introduction

Perovskite type crystals ABC_3 (space group O_h^1), of which $KMnF_3$ is an example, undergo phase transitions as a result of rotations of the BC_6 octahedra about one of the major crystallographic axes of the high-temperature phase (Cochran and Zia 1968). The archetype of such transitions is the one in $SrTiO_3$ which undergoes a second-order phase transition as a result of the condensation of one of the vibrational modes associated with the Brillouin zone boundary R point of the cubic structure. Considerable theoretical and experimental effort has been expended in developing a detailed understanding of this phase transition (see Riste 1974). $KMnF_3$ undergoes a similar transition to a tetragonal phase (space group D_{4h}^{18}) at 186 K except that in this case the transition is slightly first order in nature with a hysteresis of about 0·5 K (Gesi *et al* 1972 and references therein). In spite of this difference, experimental work to date indicates that the phase transitions in the two crystals can both be described by the same basic theory (Shapiro *et al* 1972, Borsa 1973, Hirotsu and Sawada 1973).

$KMnF_3$ also undergoes a second phase transition at 91·5 K which is believed to be caused by the condensation of a mode associated with the cubic zone boundary M point (Gesi *et al* 1972 and references therein). This is a first-order transition with a hysteresis of several degrees (Beckman and Knox 1961, Shirane *et al* 1970, Khlyustov *et al* 1972).

† Permanent address: Department of Physics, University of Waterloo, Waterloo, Ontario, Canada

In this paper we present results of measurements of the Raman spectrum for all three structural phases of $KMnF_3$. Preliminary reports of the temperature dependence of phonons in the tetragonal phase appear elsewhere (Lockwood and Torrie 1974, Torrie and Lockwood 1974). The Raman spectrum of $KMnF_3$ has also been reported by Popkov *et al* (1972) but their results are not as detailed or as comprehensive as the ones presented here.

2. Experiment

The $KMnF_3$ crystal was grown by the Bridgeman method and samples of approximate size $5 \times 5 \times 5$ mm with faces perpendicular to the cubic axes were cleaved from the boule. The samples showed visible signs of growth strains, which could not be relieved by annealing the crystals, and these produced intense scattering of the laser beam. Thus intense plasma lines appeared in the weak Raman spectrum. The $KMnF_3$ sample was mounted on the cold finger of an Oxford Instruments flow cryostat for the low-temperature studies. An Au/Fe–chromel thermocouple mounted on the sample monitored the crystal temperature, which was controlled to within 0·1 K.

The Raman measurements were performed using conventional techniques. The spectra were excited with 400 mW of argon laser light at 476·5 nm; this line was chosen in order to optimize signal conditions for the pink-coloured crystal. The 90° scattered light was analysed with a Spex Ramalab spectrometer, and the photomultiplier detector pulses were processed with a digitized data collection system linked to a multichannel analyser (Arthur and Lockwood 1974). The Raman spectrum was stored on paper tape in a form suitable for direct processing on a large computer. The polarization of the scattered light was analysed with Polaroid film, and a polarization scrambler was placed between the analyser and the spectrometer. The directions X, Y and Z that are used to denote the various polarizations refer to the crystal cubic axes unless otherwise indicated.

In some experiments a DC electric field was applied to the crystal via two circular aluminium electrodes deposited on opposite faces of the sample. The sample was placed in a glass cryostat such that the laser beam and scattered light directions were orthogonal to the electric-field gradient. The crystal was cooled by a flow of cold nitrogen gas and a thermocouple was used to measure the sample temperature.

3. Group theory

Using group theory it is possible to predict the number and symmetry of the Raman-active modes in each phase and to correlate these with equivalent modes of different species in other phases. This is done in table 1 which starts with the irreducible representations for the fifteen normal modes associated with each of the R, M, X and Γ symmetry points of the cubic phase Brillouin zone (Cowley 1964) and follows them through the other phases. The R, M and X points are the ones that become zone-centre points at one or the other of the phase transitions. In the table, the representations for the orthorhombic phase refer to the group D_{2h}. Cowley (1964) gave the irreducible representations corresponding to a choice of origin at the K atom: we prefer to use the Mn atom as our origin since the rotating fluorine octahedron is centred on the Mn atom. The character labelling system follows that of Koster (1957) to be consistent with previous work.

Table 1. Branching rules for symmetry species of phonons at high-symmetry points in the Brillouin zone of $KMnF_3$.

Cubic R point	
Crystal phase	Phonon symmetries
Cubic	
K origin	$R_2' + R_{12}' + R_{25} + R_{25}' + 2R_{15}$
Mn origin	$R_1 + R_{12} + R_{15}' + R_{15} + 2R_{25}'$
Tetragonal	$\Gamma_2 + (\Gamma_4 + \Gamma_2) + (\Gamma_1 + \Gamma_5) + (\Gamma_1' + \Gamma_5') + 2(\Gamma_3 + \Gamma_5)$
Orthorhombic	$\Gamma_2 + (\Gamma_2 + \Gamma_2) + (\Gamma_1 + \Gamma_3 + \Gamma_4) + (\Gamma_1' + \Gamma_3' + \Gamma_4') + 2(\Gamma_1 + \Gamma_3 + \Gamma_4)$
Cubic M point	
Crystal phase	Phonon symmetries
Cubic	
K origin	$M_1 + M_2 + M_2' + M_3 + 2M_3' + M_4 + M_5 + 3M_5'$
Mn origin	$M_4 + M_3 + M_3' + M_2 + 2M_2' + M_1 + M_5 + 3M_5'$
Tetragonal	$M_3 + M_1 + M_1' + M_3 + 2M_3' + M_1 + (M_2 + M_4) + 3(M_2' + M_4')$
Orthorhombic	$\Gamma_1 + \Gamma_3 + \Gamma_3' + \Gamma_1 + 2\Gamma_1' + \Gamma_3 + (\Gamma_4 + \Gamma_2) + 3(\Gamma_4' + \Gamma_2')$
Cubic X point	
Crystal phase	
Cubic	Phonon symmetries
K origin	$2X_1 + 2X_2' + X_3 + 3X_5 + 2X_5'$
Mn origin	$2X_2' + 2X_1 + X_4' + 3X_5' + 2X_5$
Tetragonal	$2X_4' + 2X_2 + X_4' + 3(X_1' + X_3') + 2(X_1 + X_3)$
Orthorhombic	$2\Gamma_2' + 2\Gamma_4 + \Gamma_2' + 3(\Gamma_3' + \Gamma_1') + 2(\Gamma_3 + \Gamma_1)$
Cubic Γ point	
Crystal phase	Phonon symmetries
Cubic	$\Gamma_{25} + 4\Gamma_{15}$
Tetragonal	$(\Gamma_4' + \Gamma_5') + 4(\Gamma_2' + \Gamma_5')$
Orthorhombic	$(\Gamma_2' + \Gamma_3' + \Gamma_4') + 4(\Gamma_2' + \Gamma_3' + \Gamma_4')$

4. Results and discussion

4.1. Cubic phase

4.1.1. Second-order spectrum. There is no first-order Raman spectrum in the cubic phase (see table 1), but a weak second-order spectrum was observed as shown in figure 1. Measurements were made both with the incident-light electric vector parallel to the cubic axes and at 45° to the cubic axes in order to separate the Γ_{12} spectrum from the Γ_1 spectrum. Peak frequencies at room temperature are listed in table 2. Two low-frequency peaks had a noticeable temperature dependence as shown in figure 2. As the temperature was reduced from room temperature to the temperature of the first phase transition, the peak at 210 cm^{-1} increased in frequency whereas the peak at 280 cm^{-1} decreased in frequency. The temperature dependence indicates the involvement of the R_{15}' and M_2 soft modes. The peaks can be identified by making use of the inelastic neutron measurements (Gesi *et al* 1972), which give the low-frequency dispersion curves, and the rigid-ion model calculations of Stirling (private communication) for higher frequencies. The temperature dependence of the 210 cm^{-1} peak indicates that it is a difference band and $R_{25}' - R_{15}'$ and $M_3 - M_2$ are the only Raman-active combinations with approximately the correct frequency. Similarly, the temperature dependence of

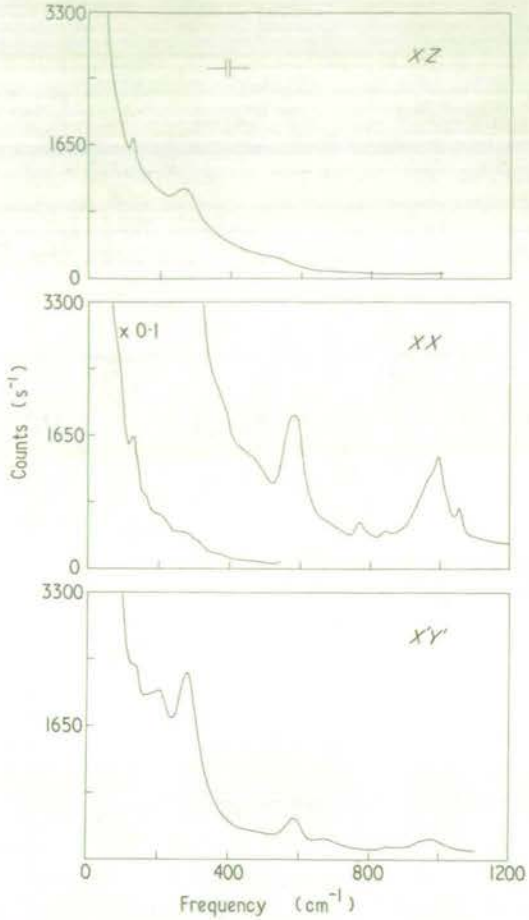

Figure 1. Polarized Raman spectra of $KMnF_3$ at room temperature. X, Y and Z refer to the cubic axes, and X' and Y' are at 45° to X and Y in the XY plane.

Table 2. Peak frequencies (cm^{-1}) for the second-order spectra at room temperature.

$XX(\Gamma_1 + \Gamma_{12})$	$XZ(\Gamma'_{25})$	$X'Y'(\Gamma_{12})$†
	125	
		136
163		
211		206
278	274	282
384		
	531	
582		590
		676
769		
846		850
		974
994		
1055		

† X' and Y' are at 45° to X and Y in the XY plane.

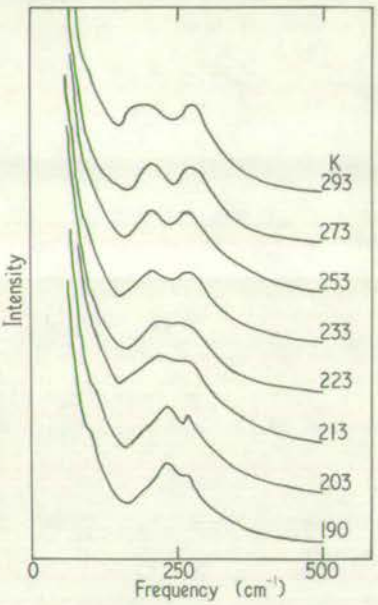

Figure 2. Temperature dependence of the low-frequency part of the second-order spectrum. The spectra were recorded without an analyser.

the 280 cm^{-1} peak indicates that it is a sum band: $R'_{25} + R'_{15}$ and $M_3 + M_2$ are the only possibilities. The combinations $R'_{25} \pm R'_{15}$ and $M_3 \pm M_2$ transform as the $\Gamma_{12} + \Gamma'_{25}$ and Γ_{12} polarizability tensors respectively. The frequency difference $280 - 210 = 70$ cm^{-1} is too large for either the M- or R-point modes alone to be involved, as $2R'_{15} \simeq 2M_2 \simeq 50$ cm^{-1} at room temperature. The polarization measurements in table 2 would indicate that the 210 and 280 cm^{-1} peaks can be assigned to the combinations $M_3 - M_2$ and $R'_{25} + R'_{15}$ respectively, but there must also be contributions to the Raman intensity from the remaining combinations. The observed temperature dependence, then, is associated with softening of the M_2 and R'_{15} modes with decreasing temperature.

4.1.2. Electric-field experiments. In an attempt to parallel the work of Fleury and Worlock (1968) on $SrTiO_3$, an electric field was applied to one sample of $KMnF_3$ in the cubic phase so that the temperature dependence of the normally Raman-inactive modes at the zone centre (see table 1) could be studied. Fields up to 27 kV cm^{-1} were applied both at room temperature and 200 K to record difference spectra (field on − field off) but no effect was observed. This can likely be attributed to a combination of high background, the high frequencies of the zone centre modes, and the low polarizability.

4.2. Low-temperature phases

4.2.1. Upper phase transition (186 K). The upper phase transition is produced by the softening of the R'_{15} (Mn origin) modes. Below the transition, a static displacement is associated with one of these modes to give a tetragonal phase with D_{4h}^{18} symmetry. The primitive unit cell for this new phase is $\sqrt{2}a \times \sqrt{2}a \times a$, that is, twice as large as the original cube, and the two axes of length $\sqrt{2}a$ are oriented at 45° to two of the cubic

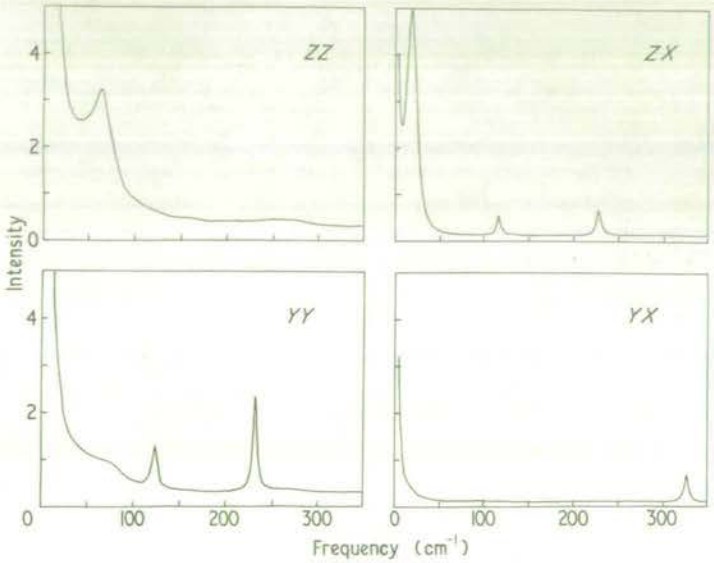

Figure 3. Raman spectra for the intermediate phase at 100 K. Z is the unique axis, and the slit width was 1·7 cm.$^{-1}$

axes. There are three possible orientations for the tetragonal unit cell relative to the cubic unit cell but our sample had a preferred orientation, most likely as a result of the growth strains. From table 1, the Raman-active modes in the new phase are $\Gamma_1 + 2\Gamma_3 + \Gamma_4 + 3\Gamma_5$. All seven of these modes were observed and are shown in figure 3; their frequencies and assignments are listed in table 3. Note that the polarizability tensors for Γ_3 and Γ_4 are interchanged because of the 45° rotation of the tetragonal a, b axes relative to the cubic axes (see below). Comparisons are made in the table with the previous work of Popkov *et al* (1972) and with the zone boundary R-point frequencies calculated by Stirling (private communication) using a rigid-ion model.

4.2.2. Lower phase transition (91·5 K). Analysis of the spectra for the lowest-temperature phase is more complicated because less is known about this phase. Neutron scattering measurements by Minkiewicz and Shirane (1969) have established that the phase transition occurs as a result of condensation of a cubic phase M_2 (Mn origin) mode.

Table 3. Assignments and peak frequencies (cm^{-1}) of the Raman-active modes in the intermediate temperature phase.

Assignment	This work (100 K)	Previous Raman work†	Rigid-ion model
Γ_5 (E_g)	20·5 (ZX)		soft modes
Γ_1 (A_{1g})	62 (ZZ)		
Γ_5 (E_g)	116 (ZX)	117	113 (R'_{25})
Γ_3 (B_{2g})	124 (YY)		
Γ_5 (E_g)	227·5 (ZX)		282 (R'_{25})
Γ_3 (B_{2g})	231 (YY)	230	
Γ_4 (B_{1g})	327·5 (YX)		293 (R_{12})

† Popkov *et al* (1972)

The M points of the cubic phase are split into a M′ point and two M″ points in the tetragonal phase. Condensation of the M′ (M_2) mode corresponds to a further rotation of the fluorine octahedra about the same axis associated with the condensation of the R'_{15} mode at the upper transition. This condensation gives a tetragonal structure of D^5_{4h} symmetry with a primitive unit cell $\sqrt{2}a \times \sqrt{2}a \times 2a$, that is, twice as long in the c direction as the equivalent cell in this tetragonal phase above 91·5 K. There are two other possible condensations since either one or both of the M″ (M_2) modes could condense. In the first case an orthorhombic structure of symmetry D^{17}_{2h} is produced which again has a primitive unit cell $\sqrt{2}a \times \sqrt{2}a \times 2a$. In the second case another orthorhombic structure is produced with symmetry D^{13}_{2h} and primitive unit cell $2a \times 2a \times 2a$. From an experimental point of view, Beckman and Knox (1961) on the basis of their x-ray data have proposed that at low temperatures the crystal has D^{16}_{2h} symmetry with a primitive unit cell of size $\sqrt{2}a \times \sqrt{2}a \times 2a$ containing four molecules. More recent x-ray work by Hidaka (1974) suggests that the low-temperature structure has D^5_{4h} symmetry, as described above. These two structures agree as to the size of the primitive unit cell and the number of molecules it contains.

Condensation of the M′(M_2) mode brings the M′ and one X point into the zone centre in addition to the R point which remains there from the tetragonal phase along with the original cubic Γ point. The M′ point and the relevant X point retain their cubic phase (tetragonal) symmetry in all three phases, so the Raman-active modes can be found from table 1 by selecting the appropriate representations from R (tetragonal) + M (cubic) + X (cubic) to give $4\Gamma_1 + 3\Gamma_3 + 2\Gamma_4 + 6\Gamma_5$. For the X-point representations, X is simply relabelled Γ, but for the M point representations $M_1 \rightarrow \Gamma_2$, $M_2 \rightarrow \Gamma_1$, $M_3 \rightarrow \Gamma_4$, $M_4 \rightarrow \Gamma_3$ and $M_5 \rightarrow \Gamma_5$. The cubic Γ-point modes remain Raman inactive, and this is true for all crystal structures considered here.

Condensation of one M″ (M_2) mode brings one M″ and one X point into the zone centre so that the expected Raman active modes are $15\Gamma_1 + 6\Gamma_2 + 15\Gamma_3 + 12\Gamma_4$. These from the representations R (ortho) + M (ortho) + X (ortho) to be $7\Gamma_1 + 4\Gamma_2 + 7\Gamma_3 + 6\Gamma_4$. Condensation of two M″ (M_2) modes brings all of the M and X points into the zone centre so that the expected Raman active modes are $15\Gamma_1 + 6\Gamma_2 + 15\Gamma_3 + 12\Gamma_4$. These modes can be obtained from table 1 by examining the representations R (ortho) + 3M (ortho) + 3X (ortho).

Finally, the Raman-active modes for the structure proposed by Beckman and Knox (1961) can be determined from the site symmetries of the atoms in the usual way. This gives $7\Gamma_1 + 7\Gamma_2 + 5\Gamma_3 + 5\Gamma_4$.

The experimental conditions used require some modification of the above predictions. The laser beam enters along what was originally one of the cubic axes and scattered light is collected along another 'cubic' axis. Three of the unit cells described above are rotated by 45° about the c axis with respect to the cubic axes so the corresponding Raman tensors must also be rotated through 45°. This has the effect of interchanging polarizability tensors Γ_3 $(xx - yy)$ and Γ_4 (xy) for the point group D_{4h}, and for D_{2h} the rotation produces the following changes.

$$\Gamma_1 \begin{pmatrix} a & & \\ & b & \\ & & c \end{pmatrix} \rightarrow \begin{pmatrix} A & B & \\ B & A & \\ & & c \end{pmatrix}$$

$$\Gamma_2 \begin{pmatrix} \cdot & d & \\ d & \cdot & \\ & & \cdot \end{pmatrix} \rightarrow \begin{pmatrix} -d & & \\ & d & \\ & & \cdot \end{pmatrix}$$

and Γ_3 (xz) and Γ_4 (yz) produce identical spectra (xz, yz). We have measured four spectra ZZ, ZX, YX and YZ using one orientation of the sample and two polarizations of the incident beam.

One additional complication must be allowed for. It is impossible to go into the lowest-temperature phase without inducing strains in the samples. These strains depolarize the beams so that the spectrum of one polarization may contain an admixture of the spectra for other polarizations. We have used the ratio of the intensities of the central peaks ($\omega = 0$) for the ZZ and ZX spectra as a measure of this depolarization. When this ratio was one the ZZ and ZX spectra were identical. Every time the sample was taken through the transition a different ratio was obtained in the range 1 to 18. The spectra shown in figure 4 were obtained when the ratio was 18. Weak features that could

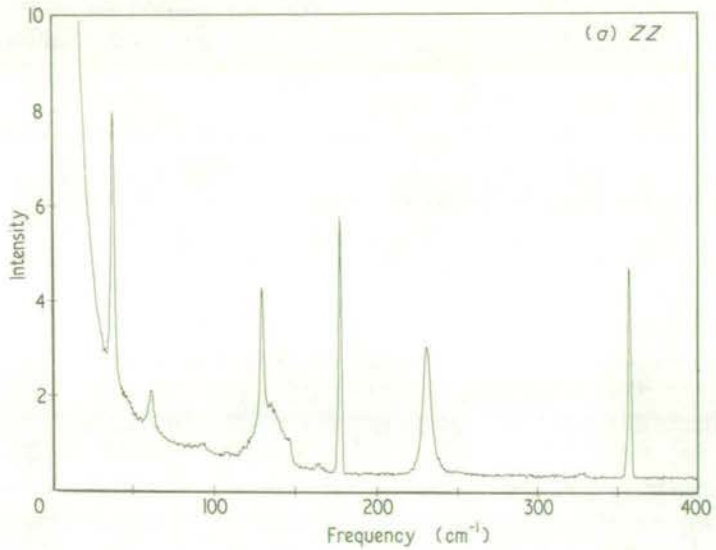

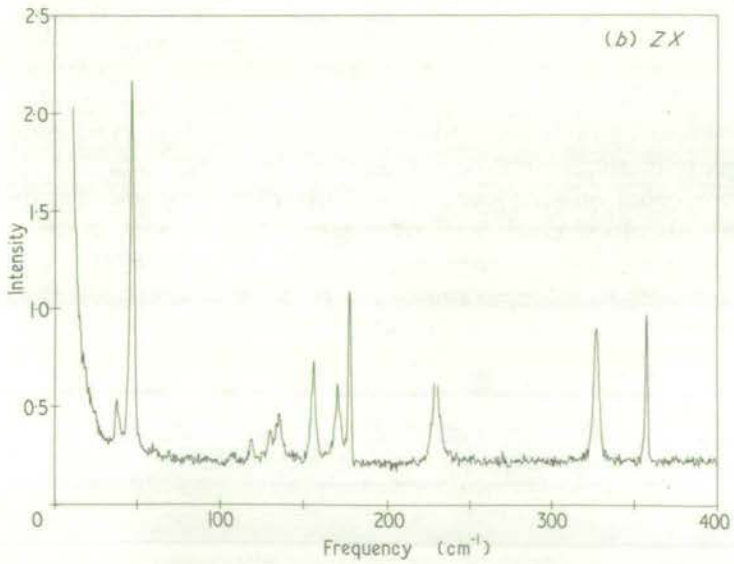

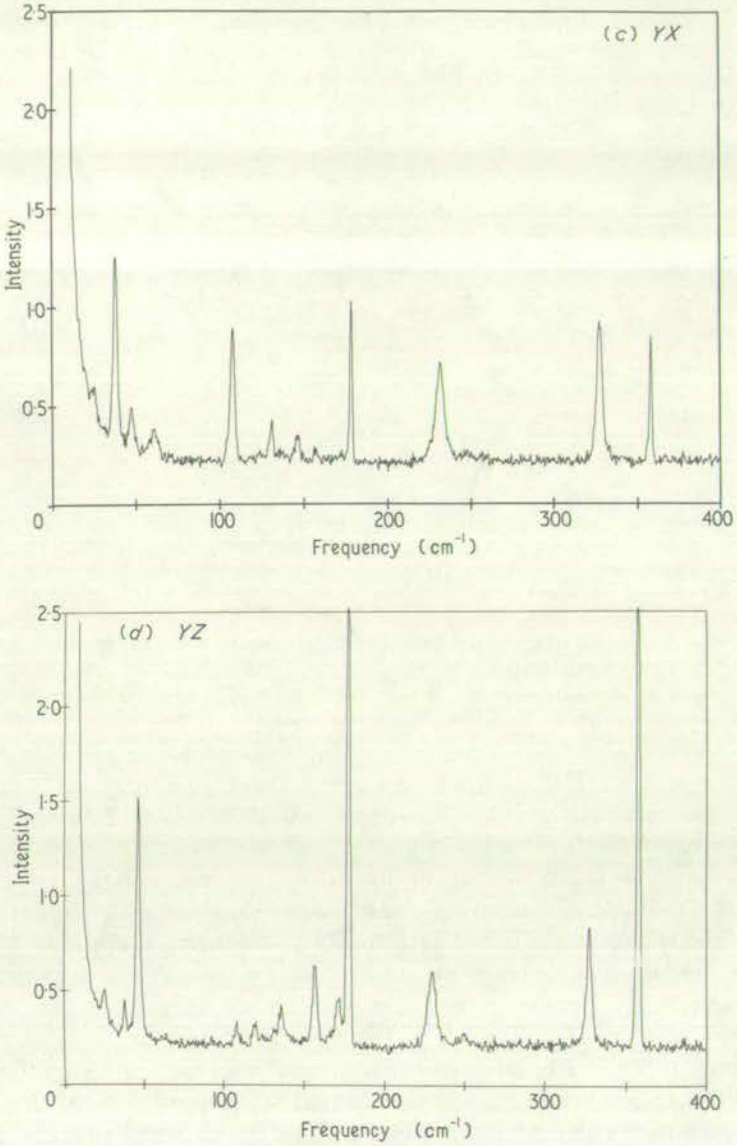

Figure 4. Raman spectra for the lowest-temperature phase at 45 K recorded with a slit width of 1·7 cm.$^{-1}$ The sharp features at 178 and 358 cm^{-1} are plasma lines.

be explained on the basis of a depolarization effect have been ignored in the frequency list given in table 4. An attempt was made to obtain spectra from a crystal cut at 45° to the cubic axes in order to eliminate the mixing of certain elements of the Raman tensors as mentioned above. This sample always gave central peak ratios of 1 to 3 and therefore the attempt was abandoned.

From figure 4 and table 4 we see that the ZX and YZ spectra are identical if the weak features at 25 and 250 cm^{-1} are ignored. Also the ZZ and YX spectra have five features in common and produce a total of ten peaks between them. The ZZ spectrum has no

Table 4. Peak frequencies (cm^{-1}) in the lowest-temperature phase at 45 K.

ZZ†	*YX*†	*ZX*†	*YZ*†
	25		25
38	38		
		47	47
61	61		
92·5			
	108		
		119·5	119·5
130·5	130·5		
136‡		136	136
146	146		
		157	157
165			
		171	171
		229·5	229·5
231	231		
			250·5
	327·5	327·5	327·5
		442§	442§

† *X*, *Y* and *Z* refer to cubic axes. *Z* is the unique axis in the intermediate temperature phase.
‡ Two-magnon feature.
§ A weak band, not shown in figure 4.

features in common with the *ZX* and *YZ* spectra, and the bands at 25 and 327 cm^{-1} are the only features common to the *YX* spectrum and the other off-diagonal spectra. The similarities between the *ZX* and *YZ* spectra and the differences between the *ZZ* and *YX* spectra could be taken to indicate tetragonal symmetry, but there are too many peaks in the *ZZ* and *YZ* spectra for these results to fit the D_{4h}^5 structure mentioned previously. The results could fit the D_{2h}^{17} and D_{2h}^{16} structures, and the D_{2h}^{13} structure fits by virtue of the fact that many more modes of all symmetries are predicted than are actually observed.

A further check was made by taking the rigid-ion model calculations of Stirling for the frequencies at the R, M and X points in the cubic phase and using the correlations given in table 1 to predict frequencies of Raman-active modes in the low-temperature phase. By allowing for the mixing of polarizations it was found that the predicted frequencies based on the D_{2h}^{17} structure were in reasonable agreement with the experimental results. The D_{2h}^{13} structure also gave a good fit because of the great multiplicity of modes, but the D_{4h}^5 structure produced few correlations and did not predict all of the low-frequency modes. The D_{2h}^{16} structure does not fit into the framework of table 1.

It therefore appears that both the D_{2h}^{17} and D_{2h}^{16} structures will fit the Raman results, and at this point it is not possible to differentiate between them although it must be remembered that the M_2 soft-mode mechanism favours the D_{2h}^{17} structure. It should also be noted that these structures may only be first approximations to the low-temperature structure. There is strong evidence that the structure is not of D_{4h}^5 symmetry, although some distortion of this structure (probably orthorhombic) might fit the Raman results. The D_{2h}^{13} structure is not tenable on two counts: one, because too few Raman peaks are seen, and two, because the x-ray work of Beckman and Knox (1961) and Hidaka (1974) indicates a smaller unit cell.

4.3. Temperature-dependent modes in the lowest-temperature phase

Four low-frequency modes have a slight temperature dependence below 91·5 K as shown in figure 5. None of these behaves like a soft mode. This is not unexpected since the lower phase transition is much more first order in nature. The lattice parameters show a much larger discontinuity at this transition compared with the upper one (Beckman and Knox 1961) and the hysteresis of the lower transition temperature is ~ 7 K as determined from our Raman measurements.

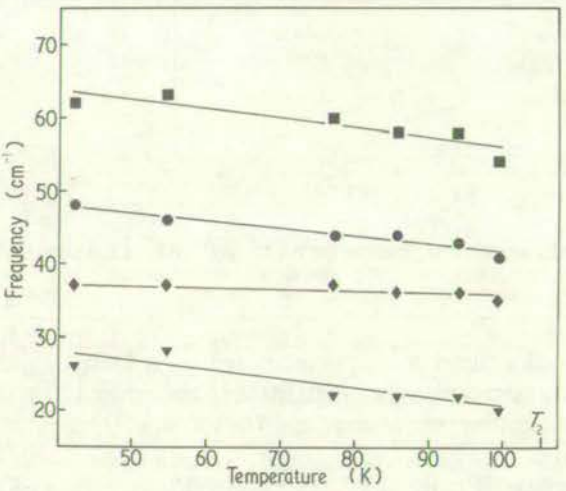

Figure 5. Temperature dependence of the low-frequency modes in the lowest-temperature phase.

4.4. Temperature-dependent modes in the intermediate phase

Below the cubic to tetragonal phase transition at 186 K, the R'_{15} mode which condensed to produce the transition splits into one soft mode of Γ_1 (A_{1g}) symmetry and another of Γ_5 (E_g) symmetry. These low-frequency modes are depicted in figure 3 and their peak frequencies are 62 and 20·5 cm^{-1} respectively at 100 K.

The intensity of Raman light scattering per unit frequency interval is given by

$$I(\omega) = A(\bar{n} + 1)\langle Q\rangle^2 \chi''(\omega)$$

where A is a constant, $\bar{n}$ is the population factor for bosons, Q is the order parameter and $\chi''(\omega)$ is the imaginary part of the response function. If χ is taken to be of the damped simple harmonic oscillator form then

$$\chi^{-1}(\omega) = (\omega_s^2 - \omega^2 + i\gamma\omega)$$

where ω_s is the characteristic frequency of the soft mode which is proportional to $\langle Q\rangle$ and γ is the damping constant.

The greatest care must be taken in separating the low-frequency scattering associated with the soft mode and that associated with second-order scattering and impurity-induced first-order scattering. This was particularly difficult in the case of the $\Gamma_1(ZZ)$ spectrum which contained a background component that was of comparable intensity

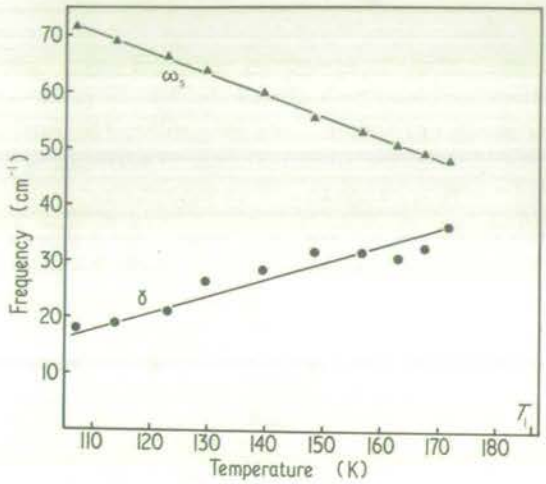

Figure 6. ω_s and γ against temperature for the Γ_1 soft mode in the intermediate phase.

to the soft mode. This background was approximated by a Debye function fitted to the range 10–35 cm^{-1} plus a constant component fitted to the range 120–170 cm^{-1}. Final fits to the ZZ spectrum were then made over the 10–100 cm^{-1} range with this background held fixed. This procedure gave reasonable fits up to 170 K, that is as long as the soft mode was clearly separated from the background. Final values of ω_s and γ are plotted in figure 6.

In the case of the Γ_5 mode, the background was much smaller and calculations were made both with and without a frequency-dependent background in order to estimate the effect of background on the final parameters. The background scattering was taken to be residual scattering seen above T_1 (186 K) (shown in figure 7) which was almost independent of temperature over the range T_1 to 200 K. ω_s and γ are plotted in figures

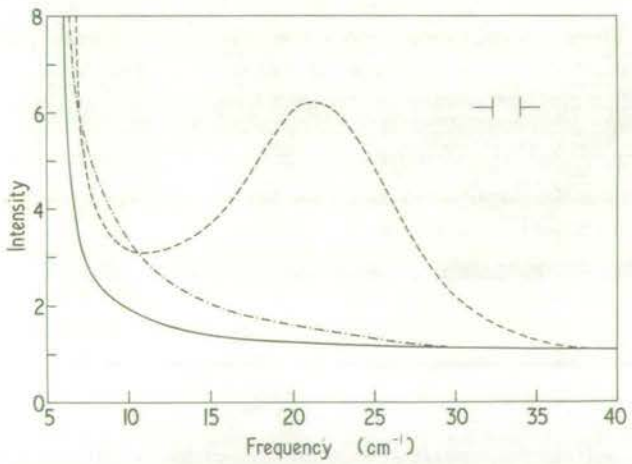

Figure 7. The low-frequency ZX spectrum at temperatures above (200·7 K, full curve) and below (105·8 K, broken curve and 185·9 K, chain curve) T_1.

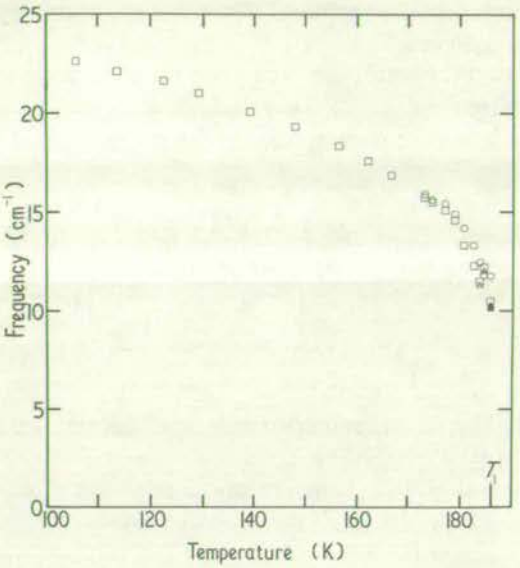

Figure 8. ω_s and ω_∞ against temperature for the Γ_5 soft mode. □ω_s, background subtracted; ○ω_s, background not subtracted; ▲ω_∞, background subtracted, $A = 120$; △ω_∞, background not subtracted, $A = 120$: ○, ▲ and △ have the same value as □ unless otherwise indicated.

8 and 9 as determined from least-square fits with A, ω_s and γ as variables. If A is held fixed at its average value then the quality of the fits is not as good and γ is not a smooth function of temperature in the overdamped region near T_1. It can be seen from the figures that

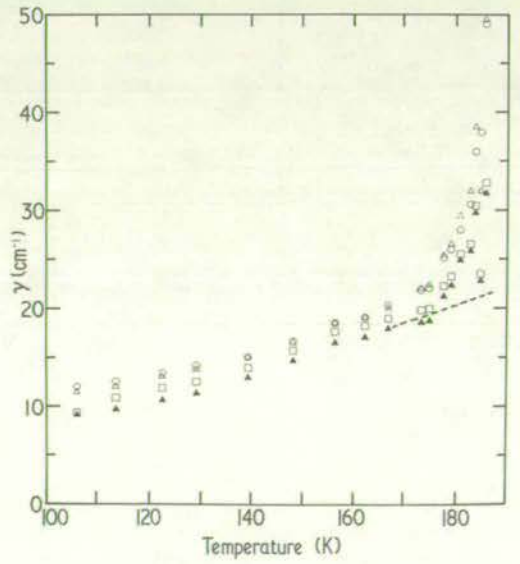

Figure 9. γ against temperature for the Γ_5 soft mode. □ simple harmonic oscillator model, background subtracted; ○ simple harmonic oscillator model, background not subtracted; ▲ Cowley–Coombs model, background subtracted, $A = 120$; △ Cowley–Coombs model, background not subtracted, $A = 120$; ——— linear extrapolation.

inclusion of the frequency-dependent background decreases ω_s and γ by $\sim 30\%$ near T_1 and by smaller amounts away from T_1.

For the Γ_5 mode we also fitted the results to a response function proposed by Cowley and Coombs (1973) and Shapiro *et al* (1972). They included an additional term in the response function to allow for a low-frequency channel for decay so that

$$\chi^{-1}(\omega) = (\omega_\infty^2 - \omega^2 + i\gamma\omega - \delta^2/(1 + i\omega\tau))$$

where δ^2 is a temperature-dependent coupling constant and τ is an average phonon lifetime. With this model a distinction must be made between the mode frequency ω_0 in the limit $\omega \to 0$ and the mode frequency ω_∞ in the limit $\omega \to \infty$. These two frequencies are related by

$$\omega_0^2(T) = \omega_\infty^2(T) - \delta^2(T)$$

and ω_0 is proportional to $\langle Q \rangle$. Use of this extended response function improves the fits, but the parameters are so highly correlated that constraints must be applied in order to obtain values which vary smoothly with temperature. Preliminary least-squares fits were made over the range 7 to 50 cm^{-1} and all parameters were allowed to vary. It was found that the quality of the fits was not very sensitive to the value of τ so it was fixed at 1 cm. γ was well behaved as long as the soft mode was underdamped but it diverged as shown in figure 9 when the mode was overdamped ($T > 170$ K). A linear extrapolation of γ from the underdamped region up to T_1 was used for subsequent calculations (see figure 9). Our extrapolated value of 22 cm^{-1} for γ at T_1 compares well with the value of

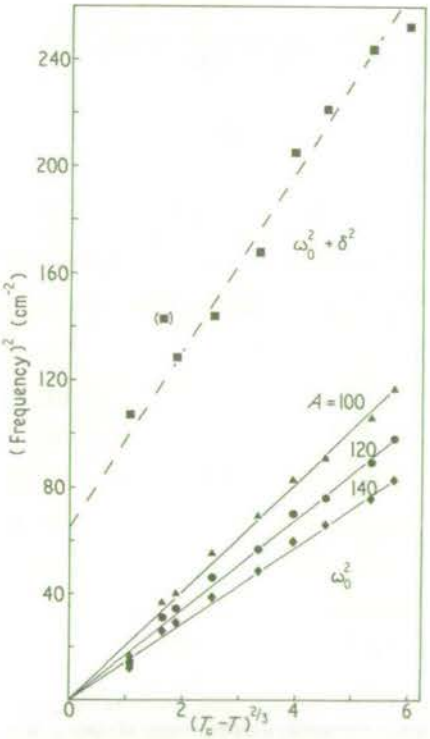

Figure 10. ω_0^2 and $\omega_\infty^2 = \omega_0^2 + \delta^2$ against $(T_c - T)^{2/3}$ for $T_c = 187$ K.

25 cm^{-1} obtained by linearly extrapolating γ for $T > T_1$ as determined from the neutron measurements of Gesi *et al* (1972). Finally, the scaling parameter A was fixed at three values, 100, 120, 140 which covered the range of values found for A. Values of ω_0^2 and δ^2 were then determined and were found to be well behaved in the overdamped region. At lower temperatures only the sum $\omega_0^2 + \delta^2$ varies smoothly with temperature and this sum is both independent of A and in good agreement with the values of ω_s^2 found earlier (see figure 8).

The temperature dependence of ω_0^2 was examined in the temperature range $T_1 - 15$ to T_1. In figure 10 we have plotted ω_0^2 against $(T_c - T)^{2/3}$ for $T_c = 187$ K. The lines through the points were drawn to connect the origin to the uppermost point; the justification for this choice being that the correlation between ω_0^2 and δ^2 is lowest about 20 K below T_1. A plot of ω_0^2 against $(T_c - T)$ for the same T_c has a pronounced curvature to it. A least-squares fit to the points using a constant weighting factor gives $T_c = 186{\cdot}4 \pm 0{\cdot}1$ K and an exponent of $0{\cdot}60 \pm 0{\cdot}05$ for all three values of A; again the exponent is less than one. Similar results were obtained by Steigmeier and Auderset (1973) from a Raman study of the temperature dependence of the Γ_1 soft mode in $SrTiO_3$; they found an exponent of 0·66 for $T/T_c > 0{\cdot}9$.

Values of δ^2 can now be found from the differences between the curves in figure 10. The temperature dependence of δ^2 is similar to that found in $SrTiO_3$ above T_c but its magnitude is larger: 60–70 cm^{-2} compared to 20 cm^{-2} (Shapiro *et al* 1972) at T_c. This does not seem unreasonable when one considers that γ is also larger in $KMnF_3$: 22 cm^{-1} compared with 7 cm^{-1} (Shapiro *et al* 1972) at T_c. From their neutron studies of $KMnF_3$ Shapiro *et al* (1972) obtained a value of 18 cm^{-2} for δ^2 at 210 K; this is somewhat lower than our estimate of δ^2 for $T \leqslant T_1$, but it is of the same order, and there is no reason for close agreement in these quite separate cases. Our results, then, indicate that $\omega_0^2 \propto (T_c - T)^n$ where $n < 1$ and that $\delta^2 > 0$ at T_c. These results are in agreement with a theory which includes critical fluctuations but not with linear theories which give $n = 1$ and $\delta^2 = 0$ at T_c.

The temperature dependence of the intensity of the Γ_5 (227 cm^{-1}) hard mode was studied, and the intensity was found to be proportional to the Γ_5 soft-mode frequency squared over a wide temperature range. Details are given in Lockwood and Torrie (1974).

Acknowledgments

We wish to acknowledge helpful discussions with A D Bruce, R A Cowley and H Montgomery and to thank J W Arthur for technical and computational assistance. We are grateful to D A Jones for providing the crystal and to W G Stirling for the use of his lattice dynamics calculations for $KMnF_3$. This work was supported by the Science Research Council.

References

Arthur J W and Lockwood D J 1974 *J. Raman Spectrosc.* **2** 53–69
Beckman O and Knox K 1961 *Phys. Rev.* **121** 376–80
Borsa F 1973 *Phys. Rev.* B **7** 913–7
Cochran W and Zia A 1968 *Phys. Stat. Solidi* **25** 273–83
Cowley R A 1964 *Phys. Rev.* **134** A981–97

Cowley R A and Coombs G J 1973 *J. Phys.* C: *Solid St. Phys.* **6** 143–57
Fleury P A and Worlock J M 1968 *Phys. Rev.* **174** 613–23
Gesi K, Axe J D, Shirane G and Linz A 1972 *Phys. Rev.* B **5** 1933–41
Hidaka M 1974 *J. Phys. Soc. Japan* to be published
Hirotsu S and Sawada S 1973 *Solid St. Commun.* **12** 1003–5
Khlyustov V G, Flerov I N, Silin A T and Sal'nikov A N 1972 *Sov. Phys.–Solid St.* **14** 139–41
Koster G F 1957 *Solid St. Phys.* **5** 174–256 (New York: Academic Press)
Lockwood D J and Torrie B H 1974 *Anharmonic Lattices, Structural Transitions and Melting* (Leiden: Noordhoff) pp147–52
Minkiewicz V J and Shirane G 1969 *J. Phys. Soc. Japan* **26** 674–80
Popkov Yu A, Eremenko V V and Fomin V I 1972 *Sov. Phys.–Solid St.* **13** 1701–8
Riste T 1974 *Anharmonic Lattices, Structural Transitions and Melting* (Leiden: Noordhoff)
Shapiro S M, Axe J D, Shirane G and Riste T 1972 *Phys. Rev.* B **6** 4332–41
Shirane G, Minkiewicz V J and Linz A 1970 *Solid St. Commun.* **8** 1941–4
Steigmeier E F and Auderset H 1973 *Solid St. Commun.* **12** 565–8
Torrie B H and Lockwood D J 1974 *Ferroelectrics* **8** ~~to be published~~ 583–4

ISOLATING THE TOTALLY SYMMETRIC RAMAN SPECTRUM OF CUBIC CRYSTALS: THE A_1 SPECTRUM OF $Cr_3B_7O_{13}Cl$

D. J. LOCKWOOD

Dept. of Physics, University of Edinburgh, Edinburgh EH9 3JZ, Scotland

(Received 6 August, 1974)

Abstract. It is shown that by measuring the appropriate diagonal and off-diagonal tensor components of the Raman spectrum of a cubic crystal and then carrying out a simple subtraction process in a computer it is possible to isolate the totally symmetric Raman spectrum from the other components. The method relies on obtaining the data in digital form using automated spectrometry. The technique is applied to cubic $Cr_3B_7O_{13}Cl$, whose Raman spectrum is reported here for the first time. The A_1 spectrum at 300 K comprises four bands at 176, 209, 375 and 657 cm^{-1} in agreement with group theoretical predictions. In addition, the spectrum contains a prominent wing feature extending to 250 cm^{-1} that is most likely associated with the ferroelectric phase transition at 263 K.

1. Introduction

For crystals with cubic symmetry the Raman tensors have the following form [1]

$$\underset{A}{\begin{bmatrix} a & & \\ & a & \\ & & a \end{bmatrix}}, \underset{E}{\begin{bmatrix} b & & \\ & b & \\ & & -2b \end{bmatrix}} \begin{bmatrix} -\sqrt{3}b & & \\ & \sqrt{3}b & \\ & & \cdot \end{bmatrix}, \quad \text{and}$$

$$\underset{F}{\begin{bmatrix} \cdot & & \\ & \cdot & d \\ & d & \cdot \end{bmatrix}} \begin{bmatrix} \cdot & & d \\ & \cdot & \\ d & & \cdot \end{bmatrix} \begin{bmatrix} \cdot & d & \\ d & \cdot & \\ & & \cdot \end{bmatrix},$$

where the symmetry labels A, E and F refer to the appropriate irreducible representations of the different cubic classes. The Raman tensor components α_{ij} have been chosen such that i and j take on the values x, y and z used to denote the cubic axes. It is apparent from the form of the tensors that in a conventional Raman experiment, where the directions of the incident and scattered light are along principal axes, one can not distinguish between scattering of A and E symmetry. But if the crystal is rotated by 45° about the z axis say, and the incident-light electric vector is at 45° to the cubic x and y axes, along x' say, and the scattered light is observed along y' orthogonal to x', then it is possible to determine the E component. The Raman tensors for the rotated coordinate system x', y' and z are

Journal of Raman Spectroscopy **2** (1974) 555–562.

$$\overset{A}{\begin{bmatrix} a & & \\ & a & \\ & & a \end{bmatrix}}, \overset{E}{\begin{bmatrix} b & & \\ & b & \\ & & -2b \end{bmatrix}} \begin{bmatrix} \cdot & \sqrt{3}b & \\ \sqrt{3}b & \cdot & \\ & & \cdot \end{bmatrix}, \text{ and}$$

$$\overset{F}{\begin{bmatrix} \cdot & & d/\sqrt{2} \\ & \cdot & d/\sqrt{2} \\ d/\sqrt{2} & d/\sqrt{2} & \cdot \end{bmatrix}} \begin{bmatrix} \cdot & & d/\sqrt{2} \\ & \cdot & -d/\sqrt{2} \\ d/\sqrt{2} & -d/\sqrt{2} & \cdot \end{bmatrix} \begin{bmatrix} d & & \\ & -d & \\ & & \cdot \end{bmatrix}$$

and the E spectrum is obtained by measuring the $\alpha_{x'y'}$ tensor element. This is a well known result. The A component remains mixed with other symmetry components and there is no experimental scattering geometry that will extricate it alone.

From a theoretician's viewpoint, this is unsatisfactory. The A spectrum often contains features of interest, notably in materials exhibiting phase transitions. Furthermore, cubic crystals are, of all crystals, the ones most amenable to a lattice dynamical calculation. Such calculations can be verified and further tested by computing the Raman spectrum of the crystal. The theoretical calculations determine the properties of different symmetries independently and these are then compared with experiment. The process giving rise to the A spectrum can be parametrically different from that of other symmetries [2]. It is more difficult to check the results of such calculations when the experimental A spectrum is combined with other symmetry components.

It is possible to isolate the A spectrum from the E spectrum by manual subtraction, but this is difficult, inaccurate and time consuming and has seldom been done in the past [3]. However, now that automation and digital techniques are freely available to Raman spectroscopy, such a subtraction can be easily and routinely performed. The A plus E and E spectra are first recorded in digital form and then, after appropriate scaling, the E spectrum is subtracted to leave the A spectrum. As an example of this technique, and to show how digitisation has rendered previously complicated processes simple, we give here the A_1 spectrum of chromium chlorine boracite (Cr—Cl—B), $Cr_3B_7O_{13}Cl$.

Cr—Cl—B is cubic at room temperature, space group $F\bar{4}3c$ (T_d^5), with two formula units in the primitive cell [4]. A factor group analysis of the normal modes at $q=0$ gives the following symmetry reduction:

$$\Gamma_{144} = 4A_1 + 6A_2 + 10E + 18F_1 + 20F_2 .$$

The complete Raman spectrum is therefore expected to comprise $4A_1 + 10E + 19F_2$ modes. Boracites, in general, undergo at some temperature a transition from the cubic phase to a ferroelectric phase of orthorhombic symmetry: the transition is of the 'improper' type involving more than one order parameter [5]. In Cr—Cl—B the transition occurs at 263 K [6]. The dynamics of this coupled ferroelectric phase transition are of some interest [5], and this Raman study is being carried out in order to provide

nformation that could lead to a better understanding of the nature of the transition. The isolated spectrum of A_1 symmetry is important to this study.

2. Experiment

Two crystals of Cr—Cl—B were obtained through the generosity of Dr H. Schmid of he Battelle Institute, Geneva. The crystals were grown by the vapour transport meth-od [7]. Two samples of approximate size 1 mm × 1 mm × 1 mm were cut from the crystals and the faces were polished with 1 μ diamond powder. The finished faces were obtained by reference to natural growth faces and were accurate to better than 0.5°. The faces of one sample were perpendicular to the principal cubic axes; the other sample was cut with faces perpendicular to [001], [110] and [1$\bar{1}$0].

The Raman spectra were recorded at 300 K using the conventional 90° scattering geometry. The spectra were excited with 600 mW of argon laser light at 488.0 nm and analysed with a Spex Ramalab spectrometer. A spectral slit width of 3 cm^{-1} was used for all measurements. The polarisation of the scattered light was analysed with Polaroid film and a polarisation scrambler was placed between the analyser and the spectrometer. The directions X, Y and Z which are used to denote the various polarisations refer to the crystal cubic axes: X' and Y' denote the [110] and [1$\bar{1}$0] directions.

A 'hard-wired' logic system was used to control the experiment and to store the spectrum in digital form in a multi-channel scaler [8]. The recorded spectrum could be examined at leisure using the oscilloscope display of the multi-channel scaler, and was later punched out on paper tape for the subsequent computer analysis.

Spectra with polarisations $Z(YY)X$ and $Z(X'Y')X'$ were measured in separate experiments on the two crystals. Precise positioning of the small samples was necessary in order to obtain the correct scattering geometry, and therefore a goniometer mount was used. Even so, some polarisation leak-through was seen from strong A_1 modes in the E spectrum and this was principally due to the wide collection angle of the lens used to gather the scattered light.

3. Results and Discussion

The YY spectrum, which contains the A_1 plus E spectral features, and the $X'Y'$ spectrum are shown in Figures 1 to 3.

The polarisability tensors given earlier indicate that the E modes have intensity factors $4b^2$ and $3b^2$ in the YY and $X'Y'$ spectra respectively. Thus if the experiment was perfect the $X'Y'$ spectrum is to be multiplied by $\frac{4}{3}$ and subtracted from the YY spectrum to expose the A_1 spectral component. Unfortunately, this is not the case and the intensity scaling factor needs to be determined in each case. Also, the frequency calibration may require a slight correction due to shifts between runs. Here, the frequency calibration could be in error by one channel width (0.5 cm^{-1} in this case), because of the nature of the logic control system. With the spectra in digital form,

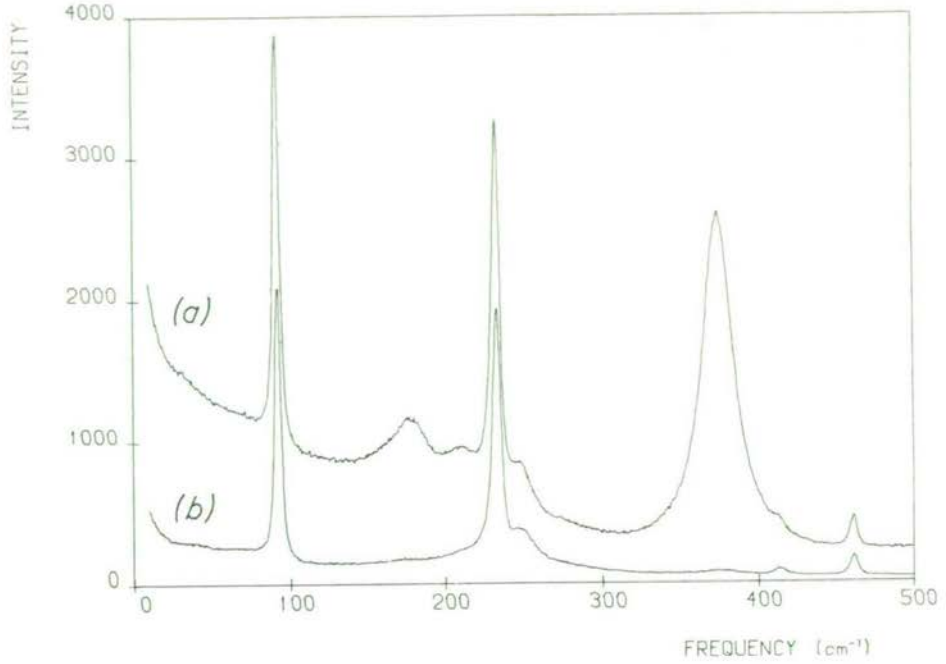

Figs. 1a–c. The (a) YY, (b) $X'Y'$ and (c) A_1 Raman spectrum of Cr—Cl—B recorded at 300 K from 0–500 cm^{-1}.

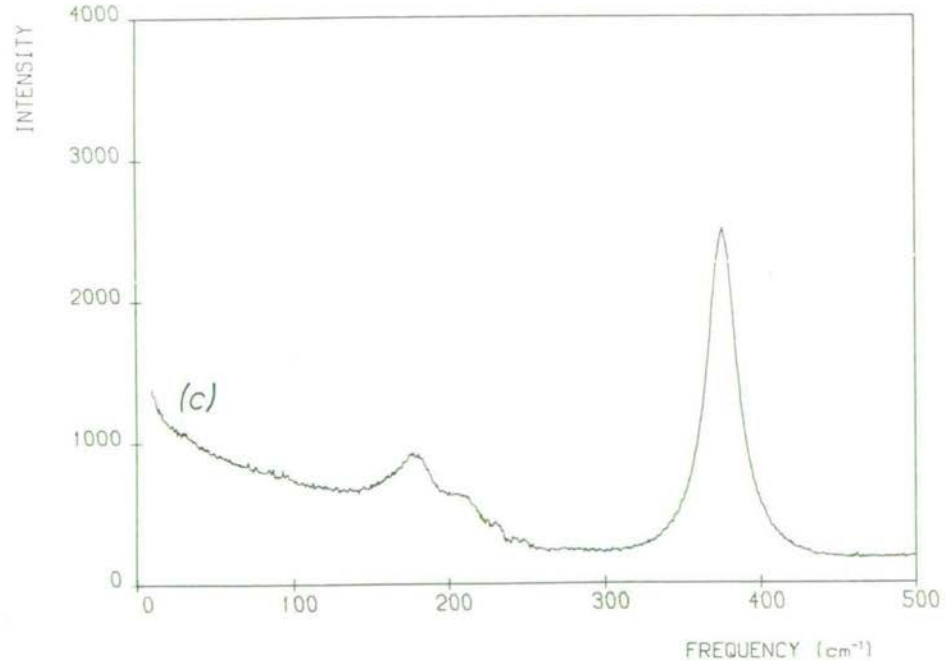

Fig. 1c.

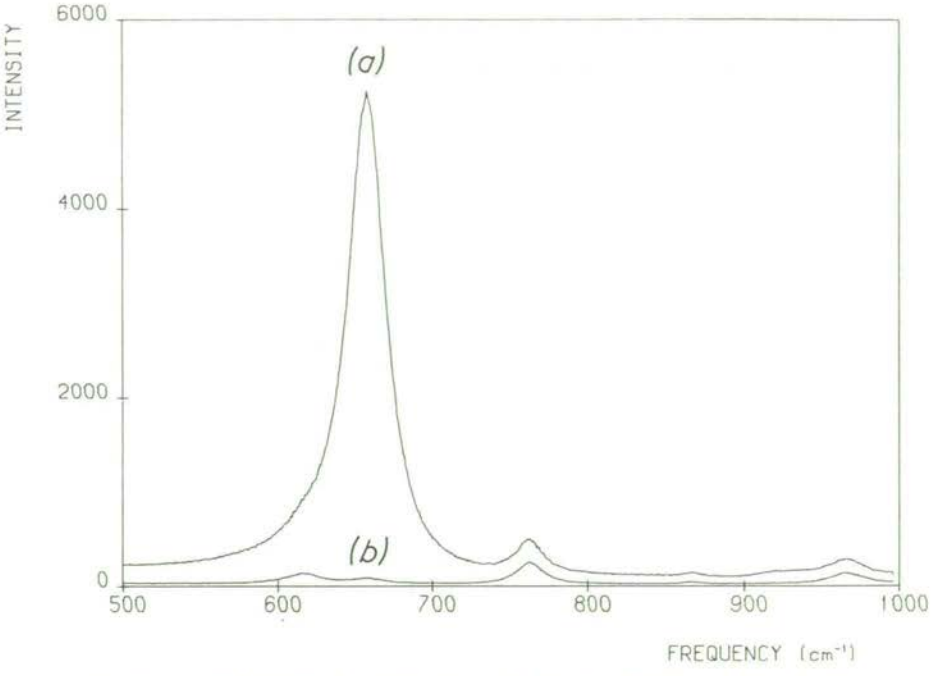

Figs. 2a–c. The (a) YY, (b) $X'Y'$ and (c) A_1 Raman spectrum of Cr—Cl—B recorded at 300 K from 500–1000 cm^{-1}.

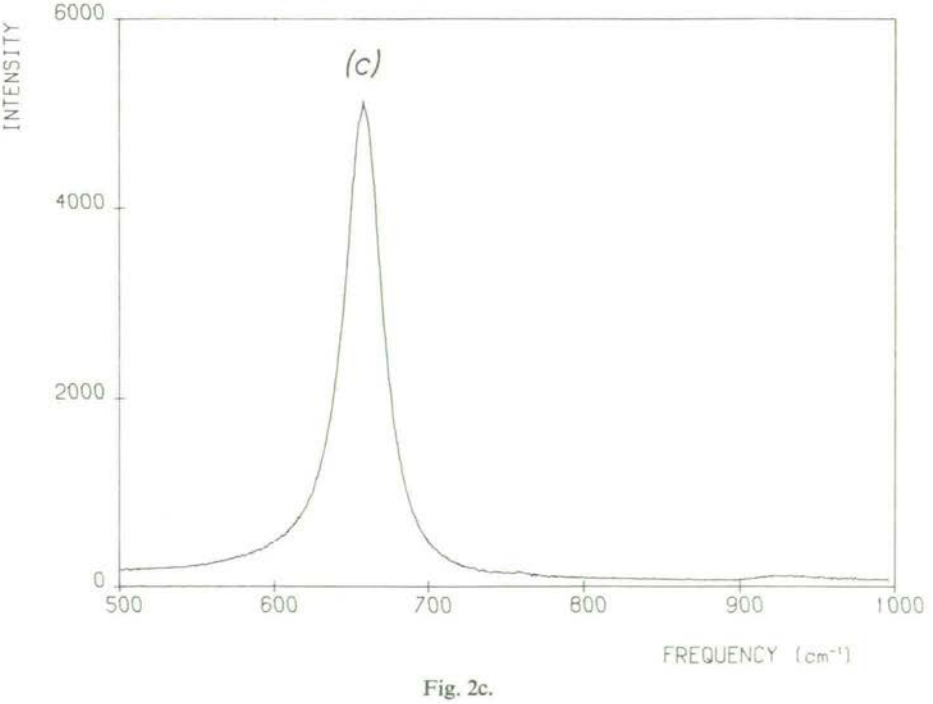

Fig. 2c.

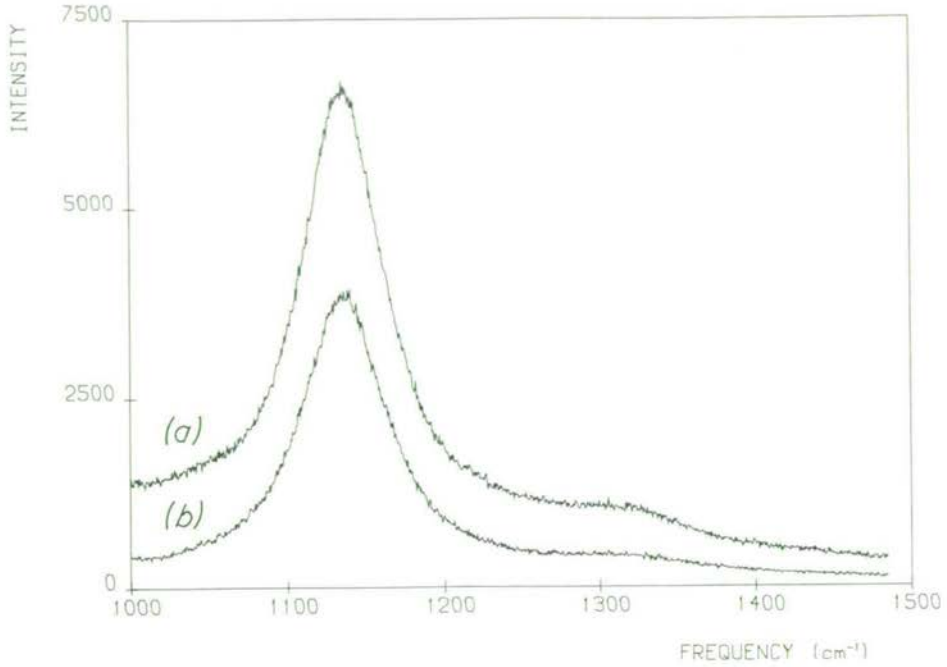

Figs. 3a–c. The (a) YY, (b) $X'Y'$ and (c) A_1 Raman spectrum of Cr–Cl–B recorded at 300 K from 1000–1500 cm^{-1}. The intensity scale is magnified 10 times compared with the scales used in Figures 1 and 2.

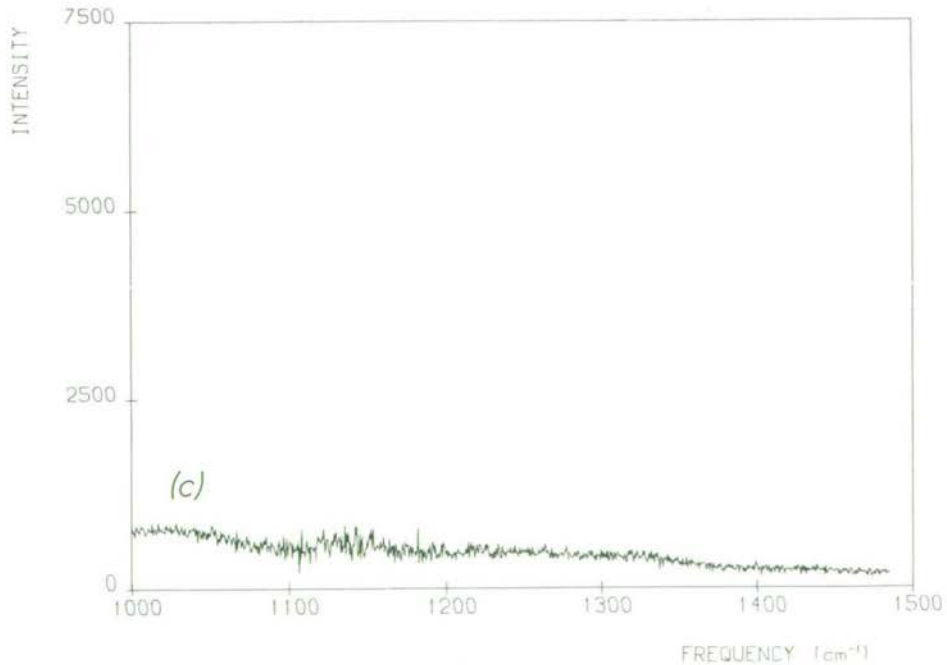

Fig. 3c.

these corrections are readily carried out in a computer. A first approximation to the scaling factor was found by integrating the areas under distinct E peaks in the spectra, allowing for the background, and then adjusting the factor until cancellation was achieved. The frequency shift was easily effected by first determining the peak frequencies and then shifting appropriately. Any small error in this operation will produce additional features in the A spectrum that appear as derivatives of the E features. The calculations were carried out in an interactive manner on a time-sharing multi-access computer using a set of basic routines for data file handling, peak finding, integration, intensity measuring and graphing [9]. This real time interaction between the experimenter and his data was a decisive advantage in carrying out this kind of analysis.

The isolated A_1 spectrum is shown in Figures 1 to 3. The actual scale factors required ranged from 1.4 to 1.55 as compared with the theoretical value of 1.33, but this difference is not unexpected considering that the different 500-cm^{-1} blocks of the YY and $X'Y'$ spectra were run on different days or under different conditions. Constant laser power throughout a given run and reproducible scans are sufficient to enable a clean subtraction. It can now be seen that the $X'Y'$ spectrum contains weak A_1 modes, as mentioned previously. This leak-through was not intense enough to upset the subtraction process.

The A_1 spectrum, as revealed, contains four peaks at 176, 209, 375 and 657 cm^{-1} in agreement with theoretical predictions. These peaks are all clearly distinguishable, which was not the case with the YY spectrum. There is one additional feature present in the A_1 spectrum that was not predicted – a prominent wing extending to 250 cm^{-1} – it is anticipated that this wing is associated with the phase transition at 263 K. The diffuse X-ray scattering found in Cr—Cl—B by Felix [10] can be interpreted in terms of a low frequency optic mode branch along the $\langle 100 \rangle$ directions [4,5], and the wing feature may arise from higher order scattering from this branch. The temperature dependence of the low-frequency A_1 spectrum is being investigated in an effort to clarify the origins of this feature.

4. Conclusion

The totally symmetric component of the Raman spectrum of cubic crystals can be easily obtained by a simple subtraction process using digitised data and a computer. Automation techniques play an essential role in obtaining spectra in the required form. Two spectra are required, ZZ and $X'Y'$, and these may be obtained from just one crystal, although two crystals were used here. Because of experimental imperfections, the scaling factor between spectra may differ from the theoretical value of 1.33, and in this case there must be a clear spectral feature of E symmetry which can be used to obtain an appropriate scaling value. Difficulties could arise in dealing with second-order spectra where there is usually no clear peak, and the A spectrum may in any case dominate, as in the cubic alkali halides.

The scaling and subtraction technique is also useful where a spectrum of one

polarisation is contaminated by spectra of other polarisations. This is often the case for uniaxial and biaxial crystals, particularly if they are optically active. The admixture of other polarisations can be removed by the subtraction technique. A successful example of this is in some recent work on sulphur where the A_g (ZZ) and B_{1g} spectra have been clarified by removing the scattering belonging to other polarisations [11].

The A_1 spectrum of cubic Cr—Cl—B has been successfully isolated and found to contain the four expected bands plus additional scattering in the form of a wing feature.

Acknowledgements

Special thanks are due to Dr H. Schmid for providing the crystals and for valuable advice based on his wide knowledge of the properties of boracites. The financial assistance of the Science Research Council and of the Battelle Research Centre, Geneva is gratefully acknowledged.

References

1. Loudon, R.: *Advan. Phys.* **13**, 423 (1964).
2. See for example Bruce, A. D.: *J. Phys. C: Solid State Phys.* **5**, 2909 (1972).
3. A point by point subtraction has been carried out, for example, by M. Krauzman (*Compt. Rend. Acad. Sci. Paris* **265B**, 689 (1967)) but no spectrum was given.
4. Nelmes, R. J. and Thornley, F. R.: *J. Phys. C: Solid State Phys.* **7**, 3855 (1974).
5. Nelmes, R. J.: *J. Phys. C: Solid State Phys.* **7**, 3840 (1974).
6. Schmid, H: private communication.
7. Schmid, H: *J. Phys. Chem. Solids* **26**, 973 (1965).
8. Arthur, J. W. and Lockwood, D. J.: *J. Raman Spectrosc.* **2**, 53 (1974).
9. Arthur, J. W.: Ph.D. Thesis, University of Edinburgh, 1974.
10. Felix, P.: Thesis l'Université de Paris-Sud, 1973.
11. Arthur, J. W. and Mackenzie, G. A.: *J. Raman Spectrosc.* **2**, 199 (1974).

RAMAN SPECTRAL STUDIES OF *CIS*-2-BUTENE-BENZENE MIXTURES

D. J. LOCKWOOD*, J. SCOTT**, W. L. ELSDON, and D. E. IRISH‡
Dept. of Chemistry, University of Waterloo, Waterloo, Ontario, Canada

(Received 21 February; in revised form 1 October, 1974)

Abstract. Raman spectra of neat liquid *cis*-2-butene and *cis*-2-butene-benzene mixtures, covering the accessible composition range at 20 °C and atmospheric pressure, have been obtained. Parameters of the benzene bands at 605.6, 1178 and 991.6 cm^{-1} and *cis*-2-butene bands at 395.5, 871.5 and 1660 cm^{-1} are reported. Changes in the parameters as a function of concentration are interpreted in terms of a weak dipole-induced dipole interaction and the consequent effect on rotational motions and resonance energy transfer.

1. Introduction

The gas *cis*-2-butene is very soluble in benzene. At 20 °C and ~1 atm pressure a mole fraction of 0.502 is attainable. Isothermal studies of vapour-liquid equilibria, involving measurement of the total pressure and the composition of both the liquid and vapour phases, revealed small positive deviations from ideality [1]. During the past decade the use of Raman spectroscopy in the study of molecular interactions in non-electrolyte solutions has increased greatly. Recognition that reorientational motions of molecules contribute to the lineshape of vibrational Raman bands resulted in a number of qualitative or semi-quantitative interpretations for change in the half-widths of both depolarized [2–4] and polarized [5–10] Raman bands and the scattering power [11–13]. The problem has been placed on a more rigorous theoretical base [14] and considerable information concerning molecular dynamics has recently been extracted, especially for pure liquids [15–21]. Systems in which strong molecular interactions such as hydrogen bonding occur, may exhibit large changes in the measurable line parameters (half-width, frequency, intensity). Weak interactions, such as van der Waals forces, give rise to less pronounced changes in the above parameters. Raman studies of *cis*-2-butene-benzene mixtures were carried out in anticipation that the data would further the understanding of the molecular causes of the departure from thermodynamic ideality.

2. Experimental

Raman spectra were excited with the 488.0 nm line from a Coherent Radiation Laboratories model 54 argon laser operating at approximately 250 mw light power and recorded using a Cary 81 spectrometer. The Cary 81 was especially adapted for

* Present address: Department of Physics, University of Edinburgh, Edinburgh, Scotland.
** Present address: Conestoga College of Applied Arts and Technology, 299 Doon Valley Drive, Kitchener, Ontario, Canada.
‡ To whom correspondence should be addressed.

Journal of Raman Spectroscopy **2** (1974) 593–607.

use with a laser exciting source [22]. Spectra were recorded at room temperature and with a spectral slit width of 5.8 cm^{-1} at 488.0 nm. The amplifier integration time and spectrometer scanning speed were adjusted so that Schubert's rule [23] for minimum recording distortion was obeyed. For polarization studies, HN-38 Polaroid sheets and a quartz polarization scrambler were placed before the entrance slit.

Fisher Spectroanalysed Grade benzene and Phillips Research Quality 99.91 mole % pure *cis*-2-butene were purified and mixed on a vacuum rack in a specially designed thermostated cell. The assembly was designed to permit subsequent gas chromatographic analysis of liquid and vapour phases and pressure measurements [1]. The maximum total pressure above the mixtures, as determined by the vacuum apparatus, was slightly in excess of one atmosphere; hence the highest concentration of *cis*-2-butene in benzene was limited to a mole fraction of 0.502 at 20 °C. Samples of about 70 μl volume, consisting of the portion remaining after the gas chromatographic analysis, were frozen into vials made from 5 mm o.d. Pyrex glass which were sealed under vacuum.

A vertical sample holder (Figure 1) was constructed with a base plug and locating pin such that it could be removed and then replaced in the sample compartment of the spectrometer with precision. The inner diameter of the holder was machined to provide a tight sliding fit for the sample vials. Raman intensities were found to be relatively independent of small displacements of the beam position in the sample either through imperfections in the glass tubing or the sample holder. This was because the majority of the scattered light comes from the small region in the sample where the laser beam is concentrated due to the lens effect of the curved glass-air interface.

The technique used in recording Raman intensities of a given line in the mixtures was to run alternately the pure component, which was used as the standard, and two or three mixtures until all of the mixtures had been examined. The areas of the selected lines were measured with a polar planimeter. The integrated intensity of a Raman line in a given mixture, relative to the intensity of the pure component, designated I_R, could be reproduced within 5% at any time.

All Raman frequencies were measured relative to the 488.0 nm laser line, which was used as a frequency standard. The Cary 81 frequency specifications are absolute frequency accurate to $\pm 0.5\ cm^{-1}$, and repeatability accurate to $\pm 0.1\ cm^{-1}$. Our frequency measurements of Raman lines confirm these specifications. Even though the absolute frequency is accurate only to $\pm 0.5\ cm^{-1}$, frequency differences and half-widths can be measured to higher accuracies due to the $\pm 0.1\ cm^{-1}$ repeatability. In addition, the measurements were repeated a number of times and the average value was used, resulting in a reduction of the uncertainty.

The spectra for benzene and *cis*-2-butene were recorded from 300 cm^{-1} to 3200 cm^{-1} and the resulting traces studied to select peaks which were of sufficient intensity and were clear of interference in the mixtures. In general the region above 1700 cm^{-1} did not produce these clear single peaks and thus it was not considered in any detail. For the peaks that were clear of interference, the parameters of width at half height

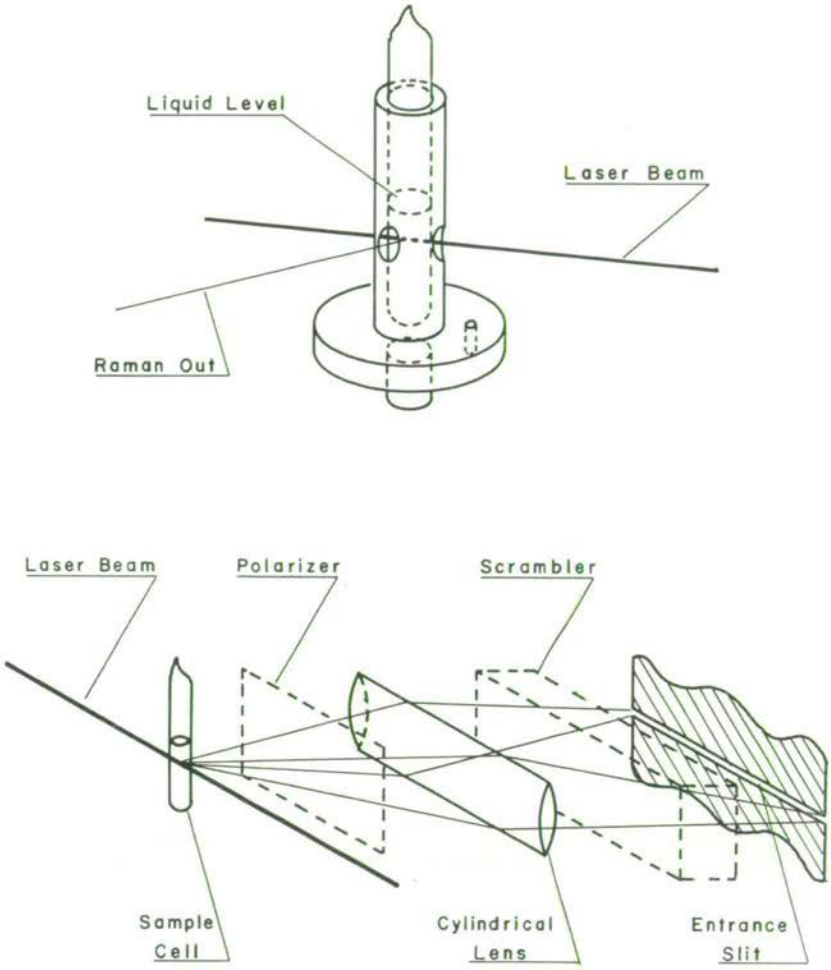

Fig. 1. Sample holder and experimental configuration.

$\bar{\nu}_{1/2}$(FWHH), frequency and in some cases area could be measured directly. Observed half-widths were greater than twice the spectral slit width in all but two cases and no slit correction was applied. Changes in the measured half-width are considered to be a result of changes in the half-width of the line. Two of the three *cis*-2-butene lines which were studied in detail were in regions in which some interference from benzene occurred. In order to separate the information it was necessary to use a curve resolving technique [24]. A Lorentzian-Gaussian product function was used to fit the band envelopes.

It is well known that the integrated Raman intensity is directly proportional to the number of molecules per unit volume and thus the molarity. In order to convert from mole fractions to molarity, densities of the solutions were measured with an accuracy of 1% [1].

3. Results

Representative spectra of a purified sample of *cis*-2-butene contained in a pyrex glass vial under its own vapour pressure are presented in Figure 2. Measured frequencies are listed in Table I. Assignments are made with reference to the normal coordinate analysis of Kilpatrick and Pitzer [25] and the studies of Richards and Nielsen [26] and Durig *et al.* [27]. The strong bands at 872 and 1660 cm^{-1} and a band of medium intensity at 395 cm^{-1} are relatively clear of interference and their line parameters were studied in more detail.

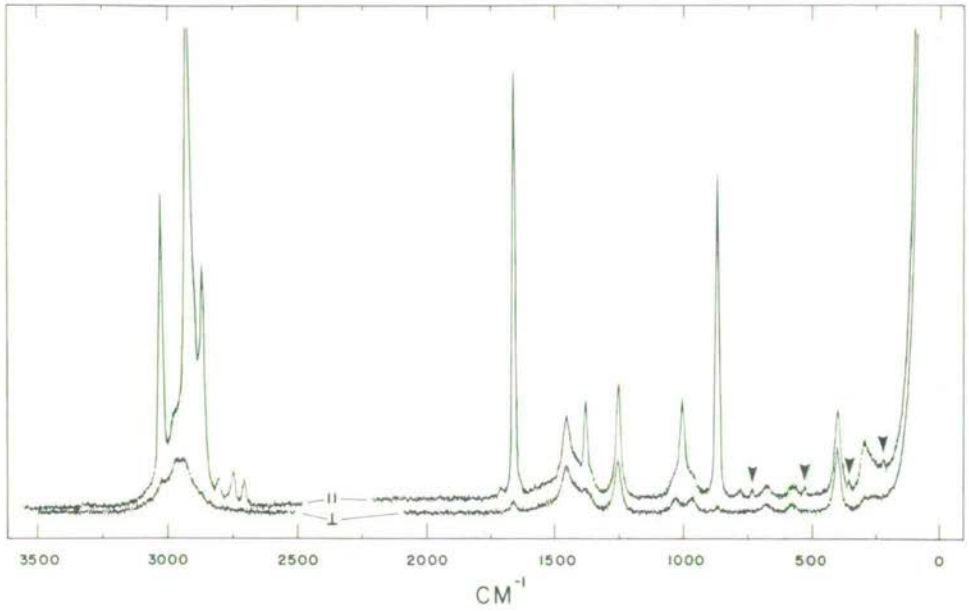

Fig. 2. The parallel (||) and perpendicular (⊥) Raman spectra of *cis*-2-butene. An ↓ denotes a plasma line.

Frequencies and assignments of the benzene bands are listed by Herzberg [28]. The only bands which met the criteria of high intensity and freedom from interference occur at 605.6, 991.6 and 1178.0 cm^{-1}.*

3.1. Benzene bands

The depolarized 605.6 cm^{-1} band has been assigned to the $\nu_{18}(E_{2g})$, C—C—C in plane bending mode [28]. Half-widths and frequencies are presented in Figure 3. The data are from a single spectrum unless indicated otherwise by a small number on

* Bands are identified by the literature values although these do not necessarily correspond exactly with the observed values.

TABLE I

Cis-2-Butene Raman bands

Frequency (cm^{-1})	Intensity [b]	Polarization	Assignment
263	0.2		
292	0.8	P	skeletal δ
395	1.54	dP $\varrho=0.75$	skeletal δ
570	0.2	dP	skeletal δ
677	0.2	dP	CH wag
783	0.1	P	possible overtone
872	6.3	P $\varrho=0.01$	C—C sym. stretch
972 [a]	0.4	dP	C—C stretch
1009	1.86	P	CH_3 wag
1030	0.4	dP	CH_3 wag
1254	2.2	P $\varrho=0.5$	CH wag
1374 [a]		dP?	CH_3 δ
1382	1.9	P	CH_3 δ sym.
1467	1.6	P $\varrho=0.6$	CH_3 δ
1660	8.4	P $\varrho=0.03$	C=C sym. stretch
1700	0.1	P	possible combination
2704	0.5	P	possible combination
2745	0.6	P	possible overtone
2905	4.6	P	C—H methyl sym. stretch
2922	10.0	P	C—H methyl sym. stretch
2950 [a]	1.8	dP	C—H methyl stretch
3024	6.1	P	C—H ethylenic sym. stretch

[a] Frequency measured from $\perp$ spectrum.
[b] Peak intensity measured from $\parallel$ spectrum relative to I_{2922}.

the figure. The results for the pure component are average values from four spectra with a standard deviation of 0.2 cm^{-1} for the half-width and 0.3 cm^{-1} for the frequency.

The depolarized 1178 cm^{-1} band has been assigned to the $\nu_{17}(E_{2g})$, C—H in plane bending mode [28]. Data are presented in Figure 4. Standard deviations obtained from results of four spectra for the pure component were 0.2 cm^{-1} for $\bar{\nu}_{1/2}$ and 0.4 cm^{-1} for $\bar{\nu}$.

The strongly polarized 991.6 cm^{-1} band is the $\nu_2(A_{1g})$, C—C stretching mode [28]. Data for half-width and frequency obtained from four spectra for each mixture are presented in Figure 5. Standard deviations obtained from results for thirteen spectra were 0.03 cm^{-1} and 0.04 cm^{-1} respectively. Relative intensity measurements were also obtained for this band and are plotted against mole fraction of solute in Figure 6. The results indicate that the relative intensity is proportional to the mole fraction of benzene (i.e. $1-X_2$). The molar relative intensity, defined in terms of the molar concentration C as

$$J_{991.6} = I_R/C,$$

is given in Table II and is also constant.

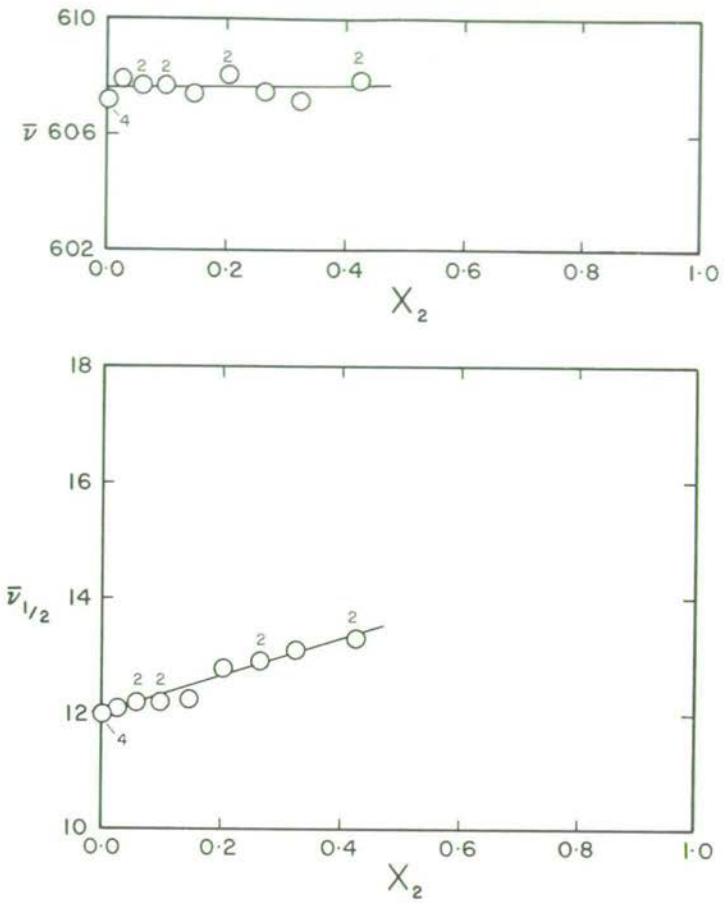

Fig. 3. The benzene 605.6 cm^{-1} band in *cis*-2-butene solutions: frequency ($\bar{\nu}$) and half-width ($\bar{\nu}_{1/2}$) in cm^{-1} against mole fraction of *cis*-2-butene, X_2.

TABLE II

Molar relative intensity of the benzene 991.6 cm^{-1} line

X_1	D	C_1	I_R	$J_{991.6}$	J/J°
1.000	0.887	11.4	1.0	$J^\circ=0.088$	1.00
0.976	0.881	11.1	0.977	0.088	1.00
0.901	0.864	10.3	0.907	0.088	1.00
0.856	0.853	9.76	0.831	0.085	0.97
0.797	0.849	9.20	0.807	0.088	1.00
0.735	0.825	8.40	0.740	0.088	1.00
0.675	0.809	7.71	0.674	0.087	0.99
0.574	0.783	6.55	0.578	0.088	1.00

X_1 mole fraction of benzene.
D density of solution, g cm^{-3}.
C_1 molarity of benzene, mol l^{-1}.

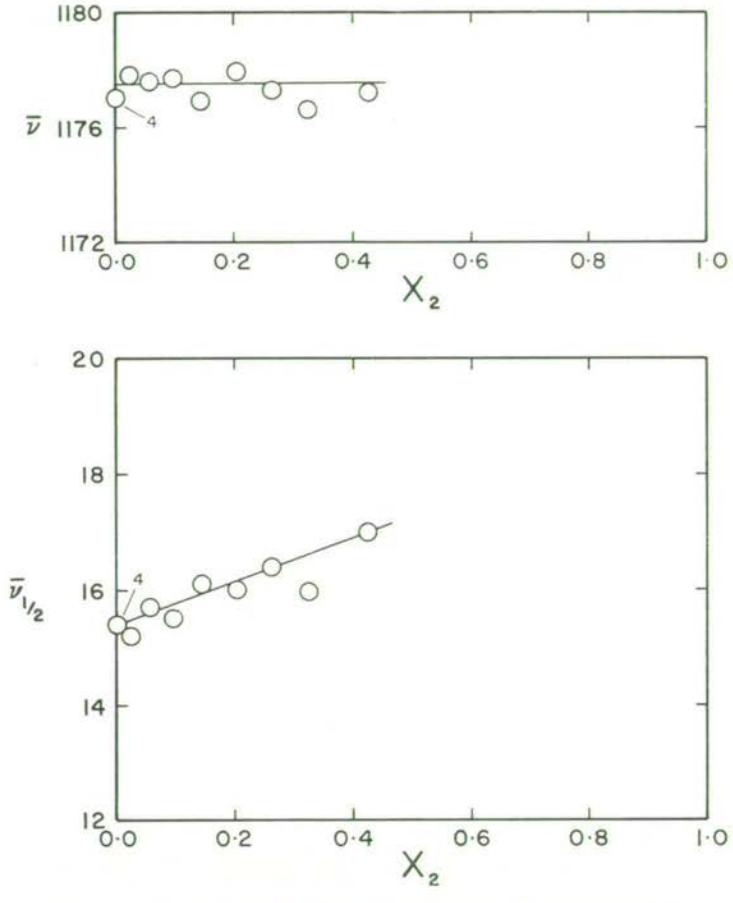

Fig. 4. The benzene 1178 cm^{-1} band in *cis*-2-butene solutions: frequency and half-width against mole fraction.

3.2. *Cis*-2-BUTENE BANDS

The 395.5 cm^{-1} depolarized band is the A_2 twisting skeletal deformation [25]. A large change in $\bar{\nu}_{1/2}$ detected during preliminary studies aroused interest in this relatively broad, medium strength band. Much of the change in $\bar{\nu}_{1/2}$ was found to be due to interference from a forbidden but weakly observed benzene band at 404 cm^{-1} [28]. The curve resolving technique described earlier was employed to remove the effect of this band. Results are plotted in Figure 7. Each value represents the average of five curve fittings with a standard deviation of 0.6 cm^{-1}.

The 871.5 cm^{-1} polarized band is the A_1 C—C stretching mode [25]. This band is intense and sharp but there is some interference from the 849 cm^{-1} benzene line [28] which becomes significant at the lower concentrations. Therefore it was necessary to separate the bands by applying the curve resolving procedure. Results are presented in Figure 8.

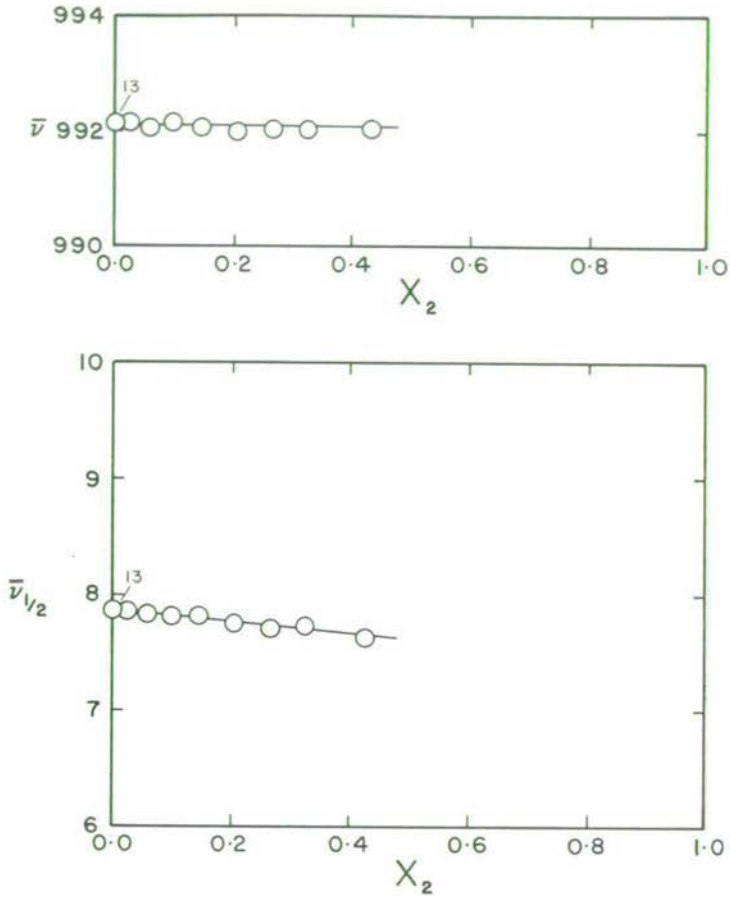

Fig. 5. The benzene 991.6 cm^{-1} band in *cis* 2-butene solutions: frequency and half-width against mole fraction.

TABLE III

Molar relative intensity of the *cis*-2-butene 1660 cm^{-1} line

X_2	D	C_2	I_R	J_{1660}	J/J°
1.0	0.623	11.1	1.00	$J^\circ=0.090$	1.00
0.426	0.783	4.86	0.472	0.097	1.08
0.325	0.809	3.71	0.359	0.097	1.08
0.265	0.825	3.03	0.303	0.100	1.11
0.203	0.849	2.34	0.239	0.102	1.14
0.144	0.853	1.64	0.154	0.094	1.05
0.099	0.864	1.13	0.110	0.097	1.08
0.024	0.881	0.27	0.033	0.122	1.36

The 1660 cm^{-1} polarized, intense sharp line is the A_1 C=C symmetric stretch [25]. The frequencies and half-widths presented in Figure 9 are averages of two spectra unless otherwise indicated. At $X_2 = 0.024$ standard deviations were 0.4 cm^{-1} and 0.6 cm^{-1} respectively. Relative intensities are plotted against mole fraction in Figure 6 and are listed as a function of molarity in Table III.

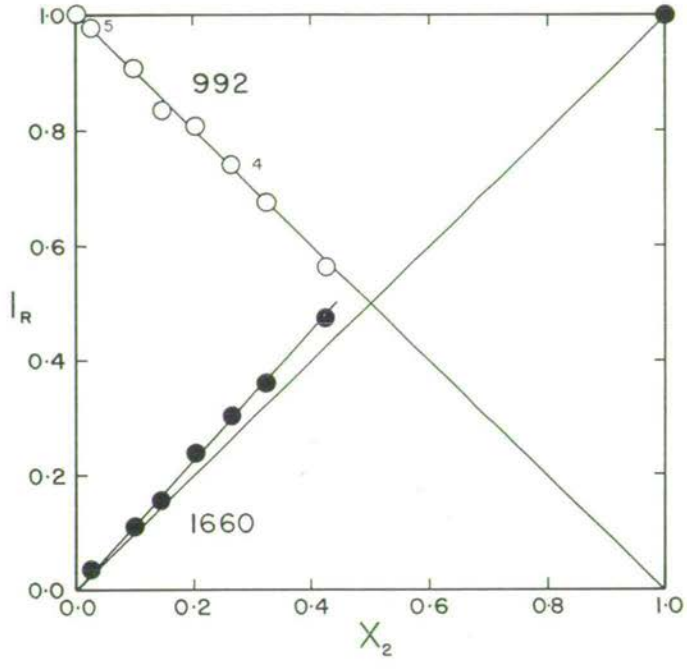

Fig. 6. The benzene 991.6 cm^{-1} and *cis*-2-butene 1660 cm^{-1} bands: relative integrated intensities against mole fraction. ○ Average of 3 spectra, except where noted. ● Single spectra.

4. Discussion

The frequencies of the 605.6, 1178 and 991.6 cm^{-1} bands of benzene and the 871.5 cm^{-1} band of *cis*-2-butene are concentration independent. The slight upward shift of the 395.5 cm^{-1} band position and decrease of the 1660 cm^{-1} band may not be significant. Thus intermolecular forces do not appear to be perturbing the vibrational energy states.

The relative intensity of the 992 cm^{-1} benzene band conforms to ideal 'Beer's Law' behaviour up to $X_2 = 0.43$. The concentration dependence of the relative intensity of the 1660 cm^{-1} line of *cis*-2-butene departs in a positive sense from ideality although an approximately linear dependence is observed. It appears fortuitous that also over the same composition range the partial pressure of *cis*-2-butene exhibits positive deviations from ideality whereas the partial pressure of benzene is virtually following Raoult's Law. In another system which exhibits positive departure from thermo-

dynamic ideality, *cis*-2-butene in 2-propanol, we observed that whereas the intensity of the 817 cm^{-1} line of 2-propanol (the solvent) conformed to ideal behaviour the intensity-composition plots of the 1660 and 872 cm^{-1} lines of *cis*-2-butene depart in a negative sense from ideality [1]. Kalashnikova and Sidorov [12] advanced some evidence for the general rule that when the scattering power of one component of a

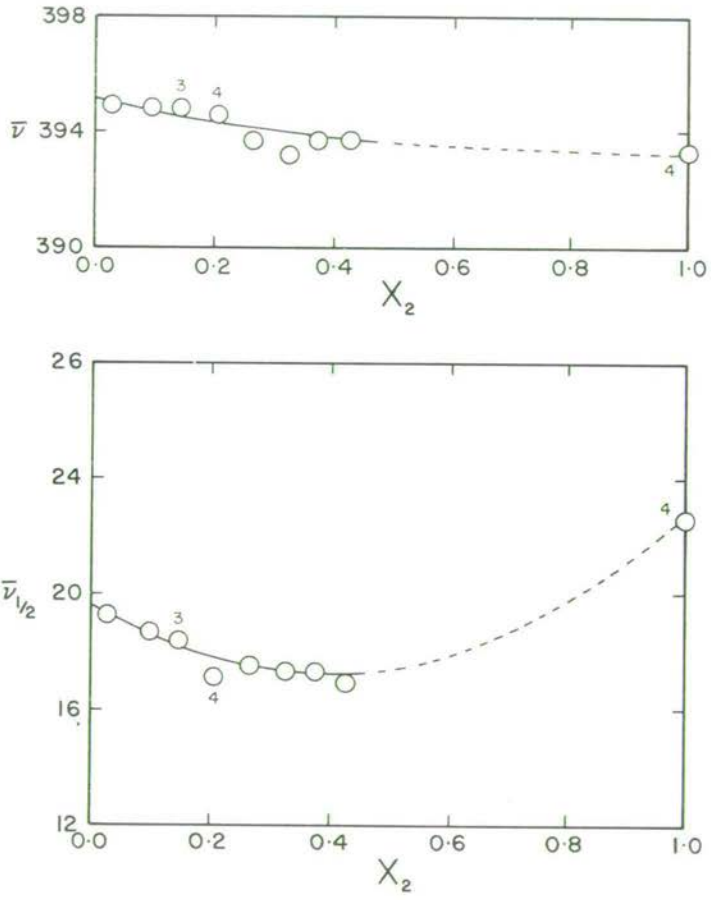

Fig. 7. The *cis*-2-butene 395 cm^{-1} band in benzene solutions: frequency and half-width against mole fraction.

binary liquid mixture increases with concentration the scattering power of the other component decreases; but they also documented several exceptions and speculated on specific interactions as a rational for these. Bahnick and Person [29] reported that the molar intensities of the 314 and 459 cm^{-1} lines of CCl_4 are increased by complexation to donors.

A specific interaction between *cis*-2-butene and benzene is also inferred. A model in which the plane of the *cis*-2-butene is oriented perpendicular to the plane of the

benzene molecule with the methyl groups adjacent to the benzene plane is proposed. Electron density in the C=C bond (the negative end of the dipole) would be increased through polarization by the oriented benzene molecule and thus a polarizability change on extension and contraction greater than that for the pure liquid is expected. Because intensity is proportional to $(\delta\alpha/\delta Q)^2$, where α is the polarizability and Q the normal coordinate under consideration, a molar intensity of the 1660 cm^{-1}

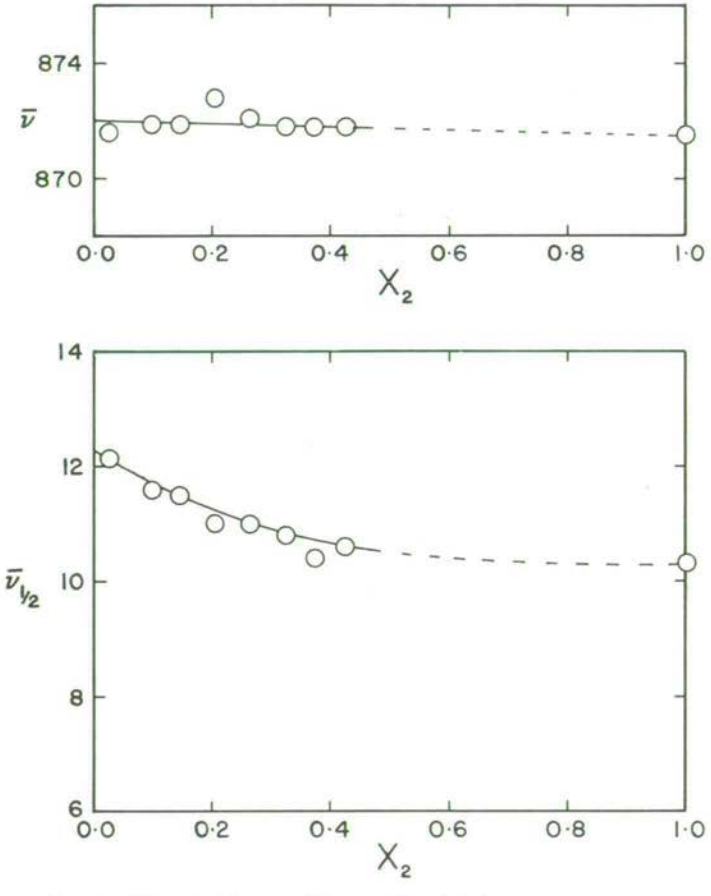

Fig. 8. The *cis*-2-butene 872 cm^{-1} band in benzene solutions: frequency and half-width against mole fraction.

line that is larger when the species is dissolved in benzene than for a neat liquid is consistent with the model. The 1660 cm^{-1} line is the only one which exhibited a frequency change which could be significant. The frequency marginally decreases when the polarizability is increased. The implied weakening of the C=C bond is attributed to a greater partial negative charge on each of the carbon atoms and hence greater C=C repulsion, resulting from the enhanced bond dipole moments in the C—C directions.

The 992 cm^{-1} vibration of benzene occurs in the plane of the benzene ring and th line parameters are almost insensitive to the presence of *cis*-2-butene. The sligh decrease in half-width with decreasing concentration has been noted before fo strongly polarized bands [6, 7, 21]. It indicated an increase in the life time for th excited vibrational state which occurs because the separation of benzene molecule by *cis*-2-butene molecules reduces the probability of transfer of energy of excitation

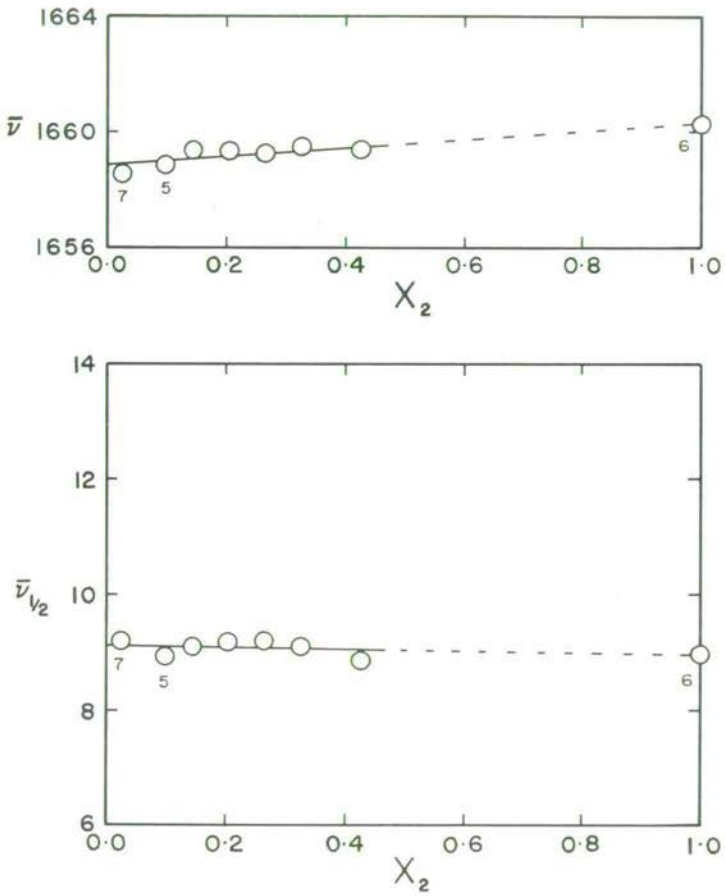

Fig. 9. The *cis*-2-butene 1660 cm^{-1} band in benzene solutions: frequency and half-width against mole fraction.

Griffiths *et al.* [21] have studied the half-width of the 992 cm^{-1} band as a functio of concentration for benzene dissolved in C_6D_6. Their half-width for this band i pure benzene is 2.24 cm^{-1}: our uncorrected value is 7.9 cm^{-1}, but if we assume tha both the 992 cm^{-1} band and the slit function have identical band profiles (e.g Lorentzian), then subtracting the slit width gives a corrected half-width of 2.1 cm^{-1}. Th small difference suggests that the assumption is a reasonable one. More importantly

the changes in the measured half-width with concentration do indeed represent the changes in the true half-width. Using 2.24 cm^{-1} for the half-width in pure benzene, the half-width has decreased by 11% when $X_2 = 0.43$. For the same composition of benzene in C_6D_6, the decrease in half-width is 14% [21]. Therefore it is probable that the same near-resonance energy transfer between benzene molecules takes place in both systems.

Transfer of energy between *cis*-2-butene and benzene may also occur through the interaction of the dipole of the *cis*-2-butene and any dipole which may be induced in the benzene. Such a path for the energy transfer would become more likely as the concentration of the benzene increased because *cis*-2-butene will encounter more frequently benzene molecules with the orientation proposed in the model above. The transfer of energy from the *cis*-2-butene to the benzene in this manner would involve those vibrations which change the dipole moment. Results for the 872 cm^{-1} line are consistent with this hypothesis since this polarized line increases in width in the benzene rich solutions and the vibration is largely parallel to the dipole moment. The ν_{11} line of benzene (849 cm^{-1}) is an out-of-plane mode sufficiently close in frequency to admit the process. The apparent insensitivity of the half-width of the 1660 cm^{-1} polarized *cis*-2-butene band is consistent with the facts that this vibration does not change the dipole moment, the process is less probable for a high frequency vibration [30], and no frequency of benzene is sufficiently close. The 992 cm^{-1} strongly polarized benzene vibration occurs in the plane of the benzene ring and thus is not sensitive to the presence of *cis*-2-butene. This is consistent with our conclusion above, which attributed changes in the half-width of this line to benzene-benzene interactions.

The depolarized benzene lines (606 and 1178 cm^{-1}) both increase in width, whereas the half-width of the low frequency depolarized line of *cis*-2-butene (395.5 cm^{-1}) decreases with increasing *cis*-2-butene concentration, passes through a minimum at approximately $X_2 = 0.4$ and then must increase again to attain the value for the pure component. The tendency for the half-width to decrease from that for pure *cis*-2-butene as the concentration decreases is in agreement with the observations of Kalashnikova and Sidorov [3] who pointed out that for all cases studied the broadening of a depolarized line for one component as the concentration is changed (i.e. 606 and 1178 cm^{-1} in this case) is accompanied by a narrowing or no change at all in the depolarized lines of the other component.

The fact that *cis*-2-butene is a gas at room temperature and pressure suggests that the intermolecular forces are weaker than those between benzene molecules, despite the presence of a small permanent dipole moment. One possible explanation for the spectral results follows: as the benzene is added to the *cis*-2-butene, the rotation of *cis*-2-butene is further hindered because of stronger *cis*-2-butene-benzene attractive forces. The concept that solvent-solute attractive forces are likely to be stronger than the solute-solute attractive forces is consistent with the high solubility of the solute. The decreased re-orientation rate causes the 395 cm^{-1} line to sharpen as benzene is added. Conversely benzene-benzene interactive forces are the strongest in this system.

As benzene molecules are separated by *cis*-2-butene (X_2 increasing) the molecules of benzene become more free to execute Brownian rotational motions and the depolarized 607 and 1178 cm^{-1} lines broaden.

For the 395 cm^{-1} line, another competing process becomes apparent when the half-width of the line passes through a minimum and then increases as X_2 decreases (Figure 7). The increase is tentatively ascribed to the transfer of energy from *cis*-2-butene to benzene. This process would occur at all compositions but becomes dominant when the benzene concentration is high. The 404 cm^{-1} E_{2u} out of plane ring deformation mode of benzene is sufficiently close in frequency to the 395 cm^{-1} deformation mode of *cis*-2-butene to permit this process.

It is now recognized that molecular reorientation affects only the bandshape of the anisotropic part of the scattered light [17–21]. At the time the present measurements were made (1970–71) the need for determining the depolarized component of polarized lines was not appreciated. The polarized lines discussed here are *strongly* polarized and therefore changes in reorientation rate will not be discernable in our measurements [21]. A more quantitative treatment of the data is not possible.

5. Conclusion

The Raman spectral data for the benzene and *cis*-2-butene system have been rationalized in terms of an attraction between *cis*-2-butene and benzene which is probably greater than that attributable to only London type forces. This attractive force is considered to be due to a weak dipole – induced dipole type of interaction. Since the Regular Solution theory of Hildebrand and Scott [31] is based on attractive forces of only the London type it is worthwhile to compare the results obtained in this work with those predicted by the Regular Solution theory. Calculations [1] reveal that the experimental values of the activity coefficients are smaller than those predicted by the Regular Solution theory. This difference would cause the total pressure, predicted by the Regular Solution method, to be larger than the observed values. The difference between calculated and empirical values is consistent with the interpretation that forces, such as dipole – induced dipole attractions, exist between *cis*-2-butene and benzene in addition to the London type forces accommodated by Regular Solution theory. Another system, carbon tetrachloride-benzene, also exhibits lower values for the total pressure than those predicted by Regular Solution theory [31]. A 'specific interaction' between molecules of carbon tetrachloride and benzene has been postulated by Rastogi *et al.* [32] providing additional support for the interpretation.

The attractive forces between the two different molecules, $A-B$, of binary systems which approach 'regular solutions' in behaviour (such as benzene – *cis*-2-butene) must have magnitudes, which are intermediate between those forces which exist in the pure components, $A-A$ and $B-B$. In fact the $A-B$ attractive force in a regular solution is considered to be the geometric mean of the $A-A$ and $B-B$ attractive forces. For such systems, one of the components should 'see' a weakening of the attractive forces acting on it as it is diluted, while the other component will 'see' an

increase in the attractive forces acting on it as it is diluted. This may account for the observation by Kalashnikova and Sidorov [3]: viz. for depolarized lines in solution, broadening of the lines for one component as it is diluted is generally accompanied by narrowing, or no change, of the lines for the other component as it is diluted. Since changes in the attractive forces should have some effect on the rotatory motions in solution the two ideas appear related.

Acknowledgements

The support of the National Research Council of Canada is gratefully acknowledged. J.S. also gratefully acknowledges the support of the Province of Ontario in the form of Ontario Graduate Fellowships for 1967–1969.

References

1. Scott, J.: Ph.D. Thesis, University of Waterloo, Waterloo, Ontario, Canada, 1972.
2. Rakov, A. V.: *Tr. Fiz. Inst. Akad. Nauk. S.S.S.R.* **27**, 111 (1964).
3. Kalashnikova, L. P. and Sidorov, N. K.: *Opt. Spec.* **28**, 603 (1970).
4. Kalashnikova, L. P. and Sidorov, N. K.: *Ibid.* **30**, 236 (1971).
5. Rezaev, N. I. and Schepanyak, K.: *Ibid.* **16**, 238 (1964).
6. Kondilenko, I. I., Pogorelov, V. E., and Khue, K.: *Ibid.* **26**, 518 (1969).
7. Kondilenko, I. I., Pogorelov, V. E., and Khue, K.: *Ibid.* **28**, 367 (1970).
8. Zubova, N. V., Shalomeyeva, N. E., Gorelik, V. S., and Sushchinskii, M. M.: *Ibid.* **27**, 508 (1969).
9. Boldeskul, A. E., Kondilenko, I. I., Pogorelev, V. E., and Khue, K.: *Ibid.* **29**, 142 (1970).
10. Buyan, G. P., Kondilenko, I. I., and Pogorelov, V. E.: *Ibid.* **27**, 132 (1969).
11. Babich, I. L. and Kondilenko, I. I.: *Ibid.* **23**, 395 (1967).
12. Kalashnikova, L. P. and Sidorov, N. K.: *Ibid.* **28**, 141 (1970).
13. Kalashnikova, L. P. and Sidorov, N. K.: *Ibid.* **29**, 225 (1970).
14. Gordon, R. G.: *J. Chem. Phys.* **42**, 1307 (1965).
15. McClintock, M., Jennings, D. A., and Mizushima, M.: *Phys. Rev. Letters* **21**, 276 (1968).
16. Perchard, J. P., Murphy, W. F., and Bernstein, H. J.: *Mol. Phys.* **23**, 499, 519, and 535 (1972).
17. Bartoli, F. J. and Litovitz, T. A.: *J. Chem. Phys.* **56**, 404 and 413 (1972).
18. Clarke, J. H. R. and Miller, S.: *Chem. Phys. Letters* **13**, 97 (1972).
19. Gillen, T. and Griffiths, J. E.: *Chem. Phys. Letters* **17**, 359 (1972).
20. Johnson, E. F. and Drago, R. S.: *J. Am. Chem. Soc.* **95**, 1391 (1973).
21. Griffiths, J. E., Clerc, M., and Rentzepis, P. M.: *J. Chem. Phys.* **60**, 3824 (1974).
22. Riddell, J. D., Lockwood, D. J., and Irish, D. E.: *Can. J. Chem.* **50**, 2951 (1972).
23. Schubert, M.: *Exptl. Tech. Physik* **5**, 203 (1958).
24. Davis, A. R., Irish, D. E., Roden, R. B., and Weerheim, A. J.: *Appl. Spectrosc.* **26**, 384 (1972).
25. Kilpatrick, J. E. and Pitzer, K. S.: *J. Res. U.S. Nat. Bur. Stds.* **38**, 191 (1947).
26. Richards, C. M. and Nielsen, J. R.: *J. Opt. Soc. Am.* **40**, 442 (1950).
27. Durig, J. R., Hawley, C. W., and Bragin, J.: *J. Chem. Phys.* **57**, 1426 (1972).
28. Herzberg, G.: *Molecular Spectra and Molecular Structure*, Vol. II, Van Nostrand, New York, 1945, p. 364.
29. Bahnick, D. A. and Person, W. B.: *J. Chem. Phys.* **48**, 1251 (1968).
30. Valiev, K. A.: *Opt. Spec.* **11**, 253 (1961).
31. Hildebrand, J. H. and Scott, R. L.: *Regular Solutions*, Prentice Hall, New York, 1962.
32. Rastogi, R. P., Nath, J., and Misra, J.: *J. Phys. Chem.* **71**, 2524 (1967).

RAMAN SPECTRUM OF $AgGaS_2$

D. J. LOCKWOOD and H. MONTGOMERY

Physics Department, Edinburgh University, Scotland

Résumé. — De nouvelles mesures des fréquences des modes optiques dans $AgGaS_2$ sont présentées ; plusieurs raisons expliquant pourquoi les déterminations précédentes sont erronées sont suggérées. Nos résultats indiquent que la structure de $AgGaS_2$ ne peut être considérée comme une perturbation faible de la structure blende, mais ils sont en accord avec les prédictions d'un modèle calculé récemment par Bettini.

Abstract. — We present new measurements of the optical mode frequencies in $AgGaS_2$, and suggest reasons why previous determinations are in error. The results indicate that $AgGaS_2$ cannot be regarded as a small perturbation of a zincblende structure, but they are in accord with the predictions of a recent model calculation by Bettini.

Recently two papers have appeared reporting Raman measurements of optic mode frequencies in $AgGaS_2$ [1, 2]. There is good agreement between the two determinations of the A_1 and E modes, but serious disagreement in the case of the B_1 and B_2 modes. This suggests that the discrepancies arise from errors in the measurements rather than from imperfections in the crystals, and the sample used in reference [2] has now been re-examined under greatly improved experimental conditions. We believe that the true B_1 modes have been observed for the first time, and that *both* the previous investigations gave erroneous values for their frequencies.

The new measurements were performed on two automated instruments, a Spex 1400 double monochromator and a Coderg T800 triple monochromator [3] ; all spectra were obtained using 5 145 Å light from an argon laser, because effects due to the optical activity of $AgGaS_2$ are negligible at this wavelength [4]. The interpretation of the spectra was complicated by two effects, the depolarisation of the scattered light [5], and the background produced by the second order scattering. The latter was fairly weak for off diagonal spectra in which the incident and scattered beams had different polarisations, and the B_2 and E modes could be identified without much difficulty. But for diagonal spectra the second order background was found to be much stronger, and it completely obscured the B_1 peaks in the usual $z(xx)\,y$ scattering geometry. However, when the crystal was rotated about the z axis the B_1 modes appeared in the off diagonal geometry $z(y'\,x')\,y'$, and the genuine peaks could be distinguished clearly by the fact that they rose to maximum height as the angle of rotation passed through 45°. The final results for all the modes are listed below.

Optic mode frequencies (cm^{-1}) in $AgGaS_2$

A_1	295
B_1	54, 190.5, 333.5
B_2	64, (212-237.5), (364-398.5)
E	84.5, 94.5, (159.5-160), (224-229.5), (321.5-346), (368-391).

These measurements cast considerable doubt on the validity of the *zincblende approximation* which was used to interpret the earlier data [2]. According to this approximation the highest B_1 mode should have a similar frequency to the second highest B_2 mode, because the corresponding modes in the zincblende structure are symmetry related. The discrepancy can be ascribed to the large mass difference between the two cations Ag and Ga ; but it is very surprising that in $CuAlS_2$, where the cation mass difference is even greater, the zincblende approximation seems to be much more successful [6].

The solution of this problem is probably contained in the recent model calculation by Bettini, which he has applied to the lattice dynamics of II-IV-V_2 compounds [7]. The present results on $AgGaS_2$ show the same detailed structure as earlier data on the analogous compound $CdGeP_2$ [8], and the only important difference between them is that the Coulomb splittings are larger for the sulphide than for the phosphide. Bettini's model implies that in $CdGeP_2$ the mass and force constant differences are too great for the zincblende approximation to be valid, and the same is clearly true for $AgGaS_2$. A corresponding analogy can be drawn between $CuAlS_2$ and $CdSiP_2$; the measured phonon spectra are in fact very similar, and in both cases one of the three B_1 modes has escaped observation [6, 9]. Bettini's model predicts that the missing mode in

$CdSiP_2$ is the highest B_1 mode, and its frequency shows a very large deviation from the zincblende approximation. The same argument could well apply to $CuAlS_2$, and the apparent success of the zincblende approximation in these compounds probably arises from an incorrect classification of the observed B_1 modes. It would be very interesting to search for the predicted high frequency B_1 mode in $CuAlS_2$ and $CdSiP_2$, using the technique described above ; discovery of this mode would add strong support to Bettini's model.

References

[1] Van der Ziel, J. P., Meixner, A. E., Kasper, H. M. and Ditzenberger, J. A., *Phys. Rev.* **B 9** (1974) 4286.

[2] Holah, G. D., Webb, J. S. and Montgomery, H., *J. Phys. C* (Solid State Physics) **7** (1974) 3875.

[3] Arthur, J. W. and Lockwood, D. J., *J. Raman Spectros.* **2** (1974) 53.

[4] Hobden, M. V., *Acta Crystallogr.* **A 24** (1968) 676.

[5] Porto, S. P. S., Giordmaine, J. A. and Damen, T. C., *Phys. Rev.* **147** (1966) 608.

[6] Koschel, W. H., Hohler, V., Rauber, A. and Baars, J., *Solid State Commun.* **13** (1973) 1011.

[7] Bettini, M., *Phys. Stat. Sol.*, to be published.

[8] Bettini, M. and Miller, A., *Phys. Stat. Sol.* (b) **66** (1974) 579.

[9] Bettini, M., Bauhofer, W., Cardona, M. and Nitsche, R., *Phys. Stat. Sol.* (b) **63** (1974) 641.

Offprinted from the *Journal of The Chemical Society, Faraday Transactions II*, 1975, vol. 71.

Effect of Rotations on Degenerate Vibrations of the Nitrate Ion

By David J. Lockwood

Department of Physics, Edinburgh University, Edinburgh EH9 3JZ

Received 3rd *February*, 1975

Rotational-vibrational infrared and Raman spectra have been calculated for the degenerate modes of a hypothetical free nitrate ion. Comparison of the computed spectra with results obtained for the nitrate ion in aqueous solution indicates that rotational motions are not the primary cause of the doublet structure of the $\nu_3(E')$ band.

In aqueous solutions the $\nu_3(E')$ vibrational mode of NO_3^- occurs as a broad doublet.[1, 2] For alkali metal nitrates the two components are centred at about 1348 and 1406 cm^{-1} in the Raman spectrum, as shown in fig. 1. A similar doublet is apparent in the infrared spectrum, but here the components are at approximately

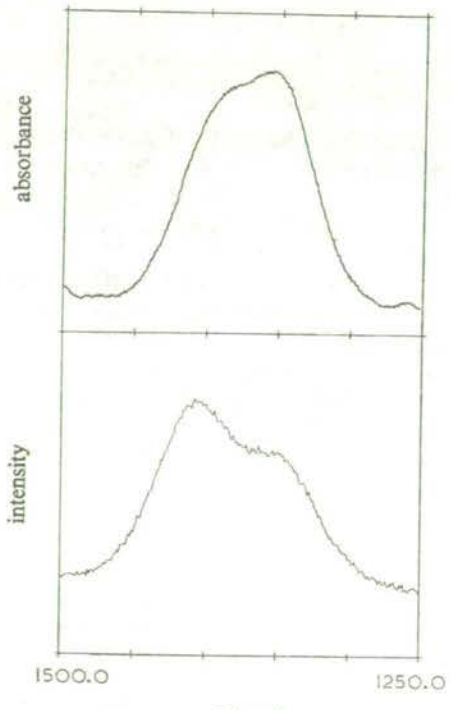

FIG. 1.—The ν_3 band of nitrate ion from 0.50 mol dm^{-3} $NaNO_3$. Upper: infrared band scanned with a PE-180 using the 0.025 mm pathlength and the Wilks Mini-Cell with AgCl windows. Spectral slit width is 3 cm^{-1}. Lower: the Raman band after 36 scans (total of 5 h) using the Jarrell–Ash model 25-100 interfaced to a PDP-11 as described elsewhere.[12] Spectral slit width 6 cm^{-1}.

1347 and 1395 cm^{-1} and there is a reversal of intensity in the peaks as compared with the Raman spectrum (fig. 1). The splitting is apparent even for dilute solutions where no cation-nitrate ion direct interaction is present and where the $\nu_4(E')$ mode does not appear to be split.[1]

The origin of the ν_3 splitting has been tentatively ascribed to librational motions of the nitrate ion within a solvent cage.[3] The lack of infrared–Raman coincidence particularly suggested rotating motions as a contributing pertubation rather than just anion distortion by the environment.[3] To test this model the Raman and infrared ν_3 band contours of a hypothetical gaseous nitrate ion have been calculated. Two cases are considered : an undistorted D_{3h} nitrate ion, and an ion with C_{3v} symmetry. The calculations and the resulting rotational-vibrational spectra for the E' modes are described in the next section. In the final section the computed spectra are compared with the experimental results and conclusions are drawn with regard to the model of the solvated nitrate ion.

CALCULATION AND RESULTS

Ignoring higher order effects, the ground state rotational energy levels of a gaseous symmetric top molecule are given by [4]

$$G_0 = B_0 J(J+1)+(A_0-B_0)K^2, \tag{1}$$

where A_0 and B_0 are the rotational constants of the molecule and J and K are the quantum numbers for the total angular momentum and for angular momentum about the symmetry axis of the molecule. The constants are found from

$$A_0 = \hbar/4\pi c\, I_{A_0}$$

and

$$B_0 = \hbar/4\pi c\, I_{B_0}, \tag{2}$$

where I_{A_0} is the moment of inertia about the molecular symmetry axis and I_{B_0} is the moment about an axis perpendicular to this axis. The energy levels for the first excited state of a doubly-degenerate molecular vibration are obtained from [4]

$$G_1 = \nu_i + B_1 J(J+1)+(A_1-B_1)K^2 \mp 2A_1\zeta_i K \tag{3}$$

again ignoring higher order effects such as centrifugal distortion. In eqn (3) ν_i denotes the band origin and ζ_i is the Coriolis constant for the ith vibrational mode. The Coriolis force produces a first-order splitting of the degenerate vibrational levels, and the splitting is linear in K as can be seen from eqn (3). The minus (or plus) sign is taken when the vibrational angular momentum has the same (or opposite) direction as the rotational angular momentum. The Coriolis constant takes some value in the range $0 \leqslant |\zeta_i| \leqslant 1$, and for an XY_3 molecule such as NO_3^-

$$\zeta_3+\zeta_4 = B/2A-1. \tag{4}$$

A "free" nitrate ion has D_{3h} symmetry and therefore the selection rules for transitions between the A_1' ground state, G_0, and G_1 are

infrared	Raman
$\Delta K = \pm 1$	$\Delta K = \pm 2$
$\Delta J = 0, \pm 1$	$\Delta J = 0, \pm 1, \pm 2.$

The statistical weights of the ground-state levels are $2J+1$ for $K = 0$ and $2(2J+1)$ for $K \neq 0$ and because the nuclear spin of oxygen is zero the allowed K values are 0, 3, 6, 9, . . . only, and for $K = 0$ levels, J can only be an even number.

For the planar nitrate ion, $I_{A_0} = 3m_O r_{N-O}^2$ and $I_{B_0} = \frac{1}{2}I_{A_0}$, where m_O is the oxygen

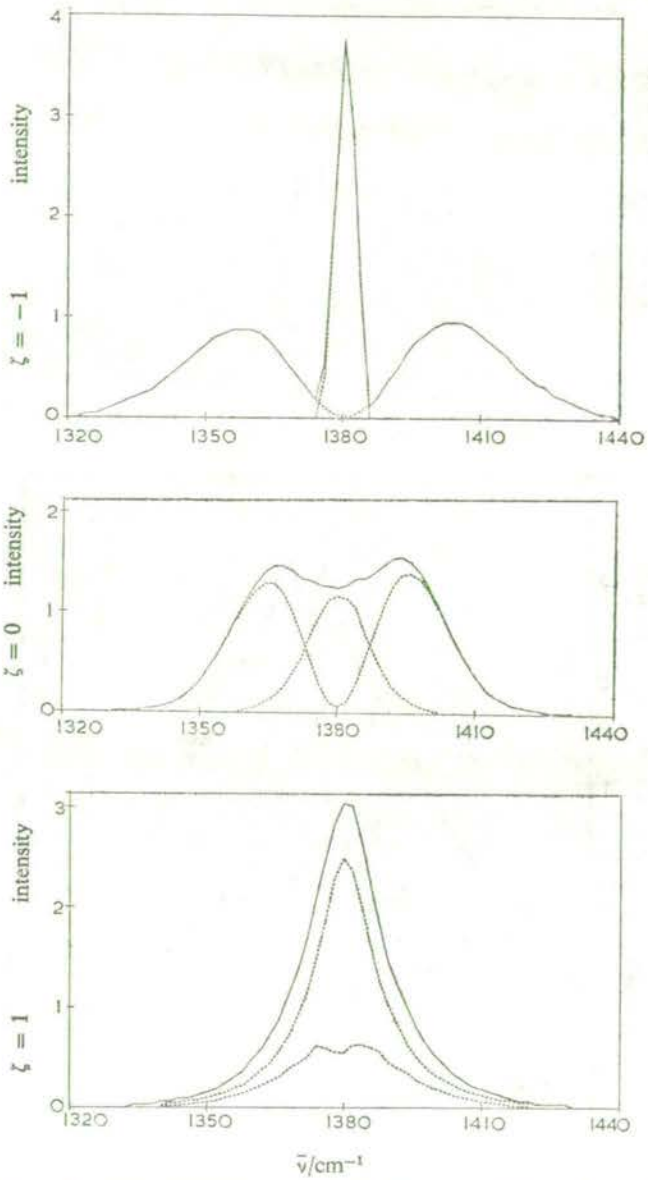

FIG. 2.—The $\Delta K = \pm 1$ infrared spectrum of the planar NO_3^- ion computed for different values of the Coriolis coupling constant ζ. The solid line is the complete spectrum and the dashed lines comprise the Q and P and R branches. The P and R branches are the outer bands for $\zeta = -1$.

mass and r_{N-O} the N—O separation. Thus the nitrate ion affords an example of an oblate symmetric top where $B_0 = 2A_0$, and it follows from eqn (4) that $\zeta_3 = -\zeta_4$. A reasonable value for r_{N-O} is 1.22 Å [5] and this gives $A_0 = 0.235\ cm^{-1}$. The Coriolis splitting can now be estimated from $2A_0\zeta_i K$ to be of the order of $15\ cm^{-1}$ at 300 K when $|\zeta_i| = 1$. This splitting is of the same order as those observed in the Raman and infrared spectra but no further conclusions can be drawn without a comparison of theoretical and experimental band shapes.

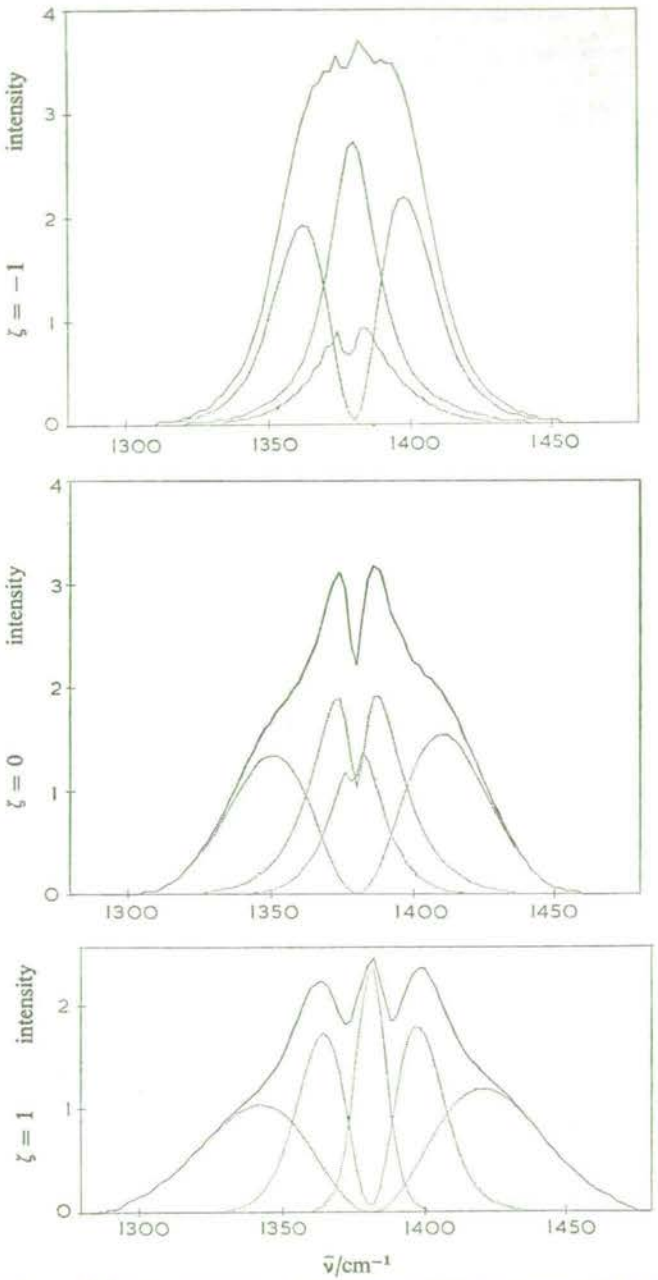

FIG. 3.—The $\Delta K = \pm 2$ Raman spectrum of the planar NO_3^- ion computed for different values of ζ. The solid line is the complete spectrum and the dashed lines comprise the Q, P and R, and O and S branches. The O and S branches are the outer bands, the Q branch the central band, and the P and R branches the inner bands for $\zeta = 1$.

The nitrate ion rotation-vibration spectrum was calculated using a general computer program written by Masri and Williams.[6] This program computes the degenerate vibration-rotation bands of symmetric top molecules in the infrared or Raman spectrum. Parameters in the program were set in accordance with the selection rules

and constants given above. In general, the rotational constants in the upper state are slightly less than the corresponding ground state values. In preliminary calculations allowed differences of up to 0.001 cm^{-1} were found to have little effect on the band shape and therefore A_1 and B_1 were set equal to A_0 and B_0 respectively in the subsequent calculations reported here. As ζ_i is unknown it was left as a variable and set at -1, $-\frac{1}{2}$, 0, $\frac{1}{2}$ and 1 in order to cover the allowed range. The maximum J value was taken to be 60, which is more than adequate at 300 K, and the band origin was set at 1380 cm^{-1}. The computer program contains a convoluting procedure whereby allowance is made for the spectrometer slit function. Spectra reported here are corrected for a spectral slit width of 5 cm^{-1} for ready comparison with experiment. Calculations were also carried out for a slit width of 3 cm^{-1} and it was found that only details associated with sharp features at the band centre were sensitive to this decrease in slit width.

Some results of the calculations are shown in fig. 2 and 3. It is pleasing to see that the infrared spectra are qualitatively similar to spectra calculated by Edgell and Moynihan in their more general study of the influence of Coriolis coupling on the shapes of perpendicular infrared bands.[7] For $\zeta = -1$, the Q branch ($\Delta K \pm 1, \Delta J = 0$) of the infrared spectrum is a delta function in the approximation used here and the apparent width arises entirely from the finite spectral slit width. It is noticeable that the Raman spectra are more complex than the infrared spectra, largely as a result of the additional O and S branches arising from the $\Delta J = \pm 2$ selection rule.

We now consider the case of a C_{3v} nitrate ion, where the nitrogen atom has been displaced out of the plane of the oxygen atoms but the 3-fold symmetry axis is retained. The moments of inertia are now

$$I_{A_0} = 3m_O r_{N-O}^2 \sin^2 \beta$$

and

$$I_{B_0} = \frac{3m_O r_{N-O}^2}{2(1+3m_O/m_N)}[2-(1-3m_O/m_N)\sin^2 \beta],$$

where β is the angle between a N—O bond direction and the figure axis. Rotational-vibrational transitions now occur between the ground state of A symmetry and the vibrational E state in accordance with the selection rules

infrared	Raman
$\Delta K = \pm 1$	$\Delta K = \pm 1, \pm 2$
$\Delta J = 0, \pm 1$	$\Delta J = 0, \pm 1, \pm 2.$

For the Raman bands, the vibrational angular momentum quantum number selection rules are $\Delta l = \pm 1$ for $\Delta K = \pm 1$ and $\Delta l = \pm 1$ for $\Delta K = \mp 2$.[8] The statistical weights are the same as for the D_{3h} ion except that the restriction to even J values for $K = 0$ no longer applies. Inversion doubling occurs in the non-planar molecule but this effect can be neglected for the purposes of the present work.

The selection rules for the infrared spectrum are the same as for the D_{3h} ion: the Raman selection rules are more complicated than before. Transitions $\Delta K = \pm 1$ and $\Delta K = \pm 2$ may both occur with intensities that are determined by the appropriate components of the polarizability tensor. For the $A_1' \rightarrow E'(D_{3h})$ transition, the non-zero elements of the polarizability tensor are $\alpha_{xx} - \alpha_{yy}$ and α_{xy}; but for the $A \rightarrow E(C_{3v})$ transition, α_{xz} and α_{yz} are also non-zero because of the additional $\Delta K = \pm 1$ selection rule. Hence the Raman intensity is given by $I(\nu) = I_{\Delta K \pm 2} + \delta I_{\Delta K = \pm 1}$, where the scaling constant δ is given by the relative magnitudes of $(\alpha_{xx}^2 = \alpha_{yy}^2 = \alpha_{xy}^2)$ and $(\alpha_{xz}^2 = \alpha_{yz}^2)$.

Polarizability tensor components are difficult to calculate from first principles and as they are not known for the NO_3^- ion δ remains an unknown quantity. However, it would be reasonable to expect that δ would be close to zero for small distortions of the molecule from D_{3h} symmetry where $\delta = 0$.

The infrared and Raman spectra for the C_{3v} ion were calculated for $\beta = 90°$, 89°, 85° and 80° under the same general conditions as for the D_{3h} ion. $I_{\Delta K=\pm 2}$ and $I_{\Delta K=\pm 1}$ were calculated separately but were not added together because of the unknown scaling factor.

The infrared and $\Delta K = \pm 2$ Raman spectra for $\beta = 90°$ were identical in form to their counterparts in the D_{3h} results, as would be expected. The C_{3v} spectra were more intense due to the changes in the statistical weights for $K = 0$ levels. There are only minor changes in the spectra when β is decreased from 90° through 89° to 80°. This is not surprising considering that the rotational constants A_0 and B_0 change only slightly, being 0.235 4 and 0.470 8 cm^{-1} respectively for $\beta = 89°$ and 0.242 7 and 0.478 7 cm^{-1} for $\beta = 80°$. The spectra decrease in intensity and there are minor changes in the bandshapes as β is reduced. However, the changes with β are small enough that fig. 2 and 3 adequately represent the C_{3v} results for $\beta \geqslant 80°$. The results obtained for the $\Delta K = \pm 1$ Raman spectra are generally similar to those found for the infrared case, except that the additional selection rule $\Delta J = \pm 2$ produces O and S branches at the extremities of the spectra given in fig. 2.

DISCUSSION

The calculations of the previous section have shown that the Raman and infrared rotational-vibrational spectra are dissimilar because of different selection rules and that the band shape is very dependent on the value of ζ. Distorting the molecule to C_{3v} symmetry makes little difference to the bands, although the Raman spectrum contains an additional component which is anticipated to be relatively weak for small distortions. This lack of sensitivity to removing certain symmetry elements from the molecule appears surprising at first but is accounted for by the fact that $B_0 \approx 2A_0$ for the distortions considered. Therefore, in the discussion that follows we need only consider the case $B_0 = 2A_0$. Changing the symmetry from D_{3h} to C_{3v} unnecessarily complicates matters.

TABLE 1.—A COMPARISON OF EXPERIMENTAL AND COMPUTED ν_3 BAND PARAMETERS FOR THE PLANAR NITRATE ION

parameter	experiment	theory			
		infrared spectrum			
ζ	—	−1	−0.5	0	0.5	1
$\tilde{\nu}_{peak}/cm^{-1}$	1347-1395	1358-1404	1360-1400	1367-1394	1372-1389	1380
$\Delta\tilde{\nu}/cm^{-1}$	48	46	40	27	17	0
		Raman spectrum			
ζ	—	−1	−0.5	0	0.5	1
$\tilde{\nu}_{peak}/cm^{-1}$	1348-1406	1382	1382	1374-1386	1370-1391	1364-1399
$\Delta\tilde{\nu}/cm^{-1}$	58	0	0	12	21	35

In comparing the computed spectra with the experimental results two essential points must be kept in mind. The first is that the ν_3 mode appears as a doublet and the ν_4 mode appears as a singlet in the experimental results. The second is that eqn (4) places definite restrictions on the values of ζ_3 and ζ_4. The object then is to compare band shapes and to find a value of ζ that fulfils the above requirements.

The pertinent parameters describing the theoretical and experimental band shapes are summarised in table 1. The experimental band centres are at 1371 and 1377 cm^{-1} in the infrared and Raman spectra respectively. For the calculations, the band origin was arbitrarily set at 1380 cm^{-1} but this is of little consequence. The computed band shapes are unaltered by a shift of origin, and the results will also apply to the 720 cm^{-1} ν_4 mode, allowing for the change in ζ. More important from a comparison point of view is the separation between peaks, $\Delta\nu$. For the infrared results, there is good agreement between theory and experiment for $\Delta\nu$ when $\zeta_3 = -1$. Furthermore, the theoretical band shape for $\zeta_4 = -\zeta_3 = 1$ is a singlet in agreement with experiment. From this point of view table 1 is misleading: an examination of fig. 2 shows that the computed bandshape does not resemble the ν_3 band for any value of ζ. A closer examination shows that the agreement between theory and experiment applies only to the $\Delta J = \pm 1$ P and R branches. A study of the Raman results is more revealing: theory and experiment do not agree for any value of ζ, nor for any branches, and neither is there agreement between $\Delta\nu$ values. The differences between the computed infrared and Raman spectra preclude any good agreement with experiment for both the D_{3h} and the C_{3v} cases.

The "free" nitrate model is not physically approachable in the condensed state due to collisional damping, but even allowing for this, the differences between the infrared and Raman spectra that arise from the selection rules would not allow good agreement with experiment. Therefore, it appears that rotational motion is not the primary cause of the splitting of the ν_3 band. Undoubtedly, rotational motion plays some role in producing the experimentally observed band shape. The computed band centres are at 1380 and 1382 cm^{-1} for the infrared and Raman spectra respectively and this is of the right sign and of the same order as that observed experimentally.

A parallel can be drawn here with the molten alkali metal nitrates, where the ν_3 band of nitrate appears as a doublet also.[9] Results of measurements of the nuclear magnetic relaxation times of the cation in molten $NaNO_3$ and $LiNO_3$ have been successfully explained in terms of a quasilattice random flight model.[10, 11] In this model a metal-nitrate species diffuses through the pseudolattice by jumping to nearest-neighbour vacancies, simultaneously undergoing nearly-free rotation. The rapid rotation occurring during the translatory jump is necessary for the existence of a quadrupole relaxation mechanism. The lifetime of the diffusing species is in the range 10^{-9} to 10^{-11} s for $NaNO_3$ [10] and this is long enough to produce observable features in the infrared and Raman spectrum. It is apparent that in the terms of the quasilattice random flight model the observed nitrate infrared and Raman band shapes are produced by a combination of two factors: perturbation of the nitrate ion by its surroundings, principally by a metal ion, and rotation of the ion.

This work indicates that the splitting of the nitrate ν_3 mode in aqueous solution most likely arises from a lowering of the symmetry due to an interaction with the local environment. The symmetry must be lower than C_{3v}. Rotational motions of the ion acting on top of this splitting then produce the observed differences in band centres between infrared and Raman spectra and are responsible for the width of the band. It would be informative to compute the rotational-vibrational bands of say a C_{2v} nitrate ion but this is a difficult calculation.

This work is the result of an initial suggestion by D. E. Irish, and his contributions through numerous discussions are gratefully acknowledged. The work was supported by the S.R.C. I thank J. T. Bulmer and D. E. Irish for providing the spectra of fig. 1.

[1] D. E. Irish and A. R. Davis, *Canad. J. Chem.*, 1968, **46**, 943.
[2] D. J. Lockwood and D. E. Irish, *Chem. Phys. Letters*, 1974, **24**, 123.
[3] D. E. Irish, *Structure of Water and Aqueous Solutions*, ed. W. A. P. Luck (Verlag Chemie and Physik Verlag, Weinheim, 1974), p. 333.
[4] G. Herzberg, *Infrared and Raman Spectra of Polyatomic Molecules* (Van Nostrand, New York, 1945)
[5] B. O. Field and C. J. Hardy, *Quart. Rev.*, 1964, **18**, 361.
[6] F. N. Masri and I. R. Williams, *Computer Phys. Comm.*, 1970, **1**, 349.
[7] W. F. Edgell and R. E. Moynihan, *J. Chem. Phys.*, 1966, **45**, 1205; see F. N. Masri and W. H. Fletcher, *J. Raman Spectr.*, 1973, **1**, 221, for a similar study of the degenerate Raman bands of symmetric top molecules.
[8] I. M. Mills, *Mol. Phys.*, 1964, **8**, 363.
[9] D. E. Irish, *Ionic Interactions: From Dilute Solution to Molten Salts*, ed. S. Petrucci (Academic Press, New York, 1971), vol. 2, p. 187.
[10] D. Harold-Smith, *J. Chem. Phys.*, 1973, **59**, 4771.
[11] D. Harold-Smith, *J. Chem. Phys.*, 1974, **60**, 1405.
[12] J. T. Bulmer, D. E. Irish, F. Grossman, G. Herriot, M. Tseng and A. J. Weerheim, to be published.

PRINTED IN GREAT BRITAIN AT
THE UNIVERSITY PRESS
ABERDEEN

J. Phys. C: Solid State Phys., Vol. 8, 1975. Printed in Great Britain.

Raman spectrum of $AgGaS_2$

D J Lockwood and H Montgomery
Department of Physics, University of Edinburgh, Edinburgh EH9 3JZ, Scotland

Received 6 June 1975

Abstract. The first- and second-order Raman spectrum of $AgGaS_2$ has been measured at room temperature. A careful analysis of the data gives phonon frequencies for the various representations at the zone centre which differ considerably from the results of two other investigations, and reasons are given why previous determinations are probably in error. The present results indicate that $AgGaS_2$ cannot be regarded as a small perturbation of a zincblende structure, but they are in accord with the predictions of a recent model calculation by Bettini. A comparison of the optic modes for $AgGaS_2$, $CuGaS_2$ and $CuAlS_2$ shows regularities which are also apparent in the analogous phosphides, and it is inferred that there is an unobserved high-frequency B_1 mode in both $CuAlS_2$ and $CdSiP_2$.

1. Introduction

There have been several recent studies of the lattice dynamics of compounds which crystallize in the chalcopyrite structure, and in particular of ternary phosphides and sulphides (Bettini 1975, Koschel *et al* 1975). Unfortunately, it is not yet possible to grow large crystals of any of these materials, and no inelastic neutron scattering work has been done so far. The available results are restricted to the zone-centre phonon frequencies derived from Raman and infrared data, although in the case of $AgGaS_2$ the elastic constants have also been measured using Brillouin scattering (Holah and Grimsditch 1975). It is found that the optic mode frequencies vary in a regular manner from compound to compound, and Bettini (1975) has given a convincing interpretation of the phosphides using force constants defined by a Keating model.

It seems likely that a similar scheme can be applied to the sulphides, though here the detailed situation is less satisfactory both from an experimental and a theoretical point of view. One of the most widely studied compounds is $AgGaS_2$, and recently two papers have appeared giving different frequencies for some of the Raman-active modes (van der Ziel *et al* 1974, Holah *et al* 1974). The data for modes with A_1 and E symmetry are in good agreement, but the data for the B_1 and B_2 modes are not; this suggests that the discrepancies arise from the measurements rather than from varying imperfections in the crystals. The sample used by Holah *et al* (1974) has now been re-examined under greatly improved experimental conditions, and the new results are presented below. We believe that the true B_1 modes have been observed for the first time, and that both the previous investigations gave erroneous values for their frequencies.

2. Experiment and results

A group theoretical analysis of the zone-centre modes of vibration in $AgGaS_2$ produces the following decomposition according to irreducible representations of space group $I\bar{4}2d$:

$$\underset{\begin{pmatrix} a & & \\ & a & \\ & & b \end{pmatrix}}{A_1} \quad \underset{\text{inactive}}{2A_2} \quad \underset{\begin{pmatrix} c & & \\ & -c & \\ & & . \end{pmatrix}}{3B_1} \quad \underset{\begin{pmatrix} . & d & \\ d & . & \\ & & . \end{pmatrix}}{4B_2(Z)} \quad \underset{\begin{pmatrix} . & & e \\ & . & \\ e & & . \end{pmatrix}}{7E(Y)}.$$

The corresponding Raman activities are indicated by the appropriate non-zero components of the polarizability tensor. Excluding acoustic modes, the Raman spectrum is therefore expected to comprise $A_1 + 3B_1 + 3B_2 + 6E$ modes.

The single crystal used for the Raman measurements was the same one used in the study by Holah *et al* (1974). The crystal was prismatic in shape, of dimension 3·5 × 2·5 × 2·5 mm, with principal faces perpendicular to the tetragonal axes and with the diagonal face perpendicular to [110]. $AgGaS_2$ exhibits {112} twinning (Korczak and Staff 1974) and on examination under polarized light the sample was seen to comprise one large domain, with a smaller domain at one end. $AgGaS_2$ is optically active (Hobden 1967, 1968) as well as being birefringent, and is unusual in that optical rotation occurs along both diad axes with opposite sense. For light at 497·4 nm, $AgGaS_2$ is optically isotropic and the optical rotation can be seen to full effect, but for wavelengths removed from this value the crystal birefringence overwhelms the optical activity (Hobden 1968). For example, at 514·5 nm the ellipticity (the ratio of minor to major axis) produced by optical activity in the presence of birefringence is only 0·034.

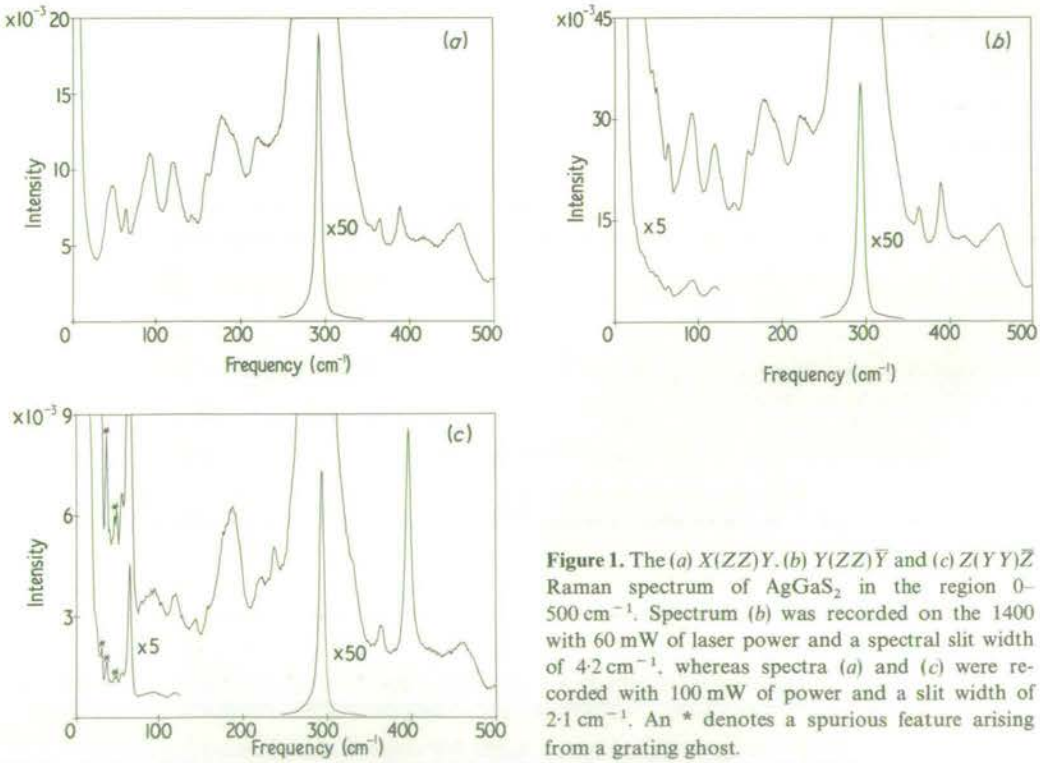

Figure 1. The (*a*) $X(ZZ)Y$, (*b*) $Y(ZZ)\bar{Y}$ and (*c*) $Z(YY)\bar{Z}$ Raman spectrum of $AgGaS_2$ in the region 0–500 cm^{-1}. Spectrum (*b*) was recorded on the 1400 with 60 mW of laser power and a spectral slit width of 4·2 cm^{-1}, whereas spectra (*a*) and (*c*) were recorded with 100 mW of power and a slit width of 2·1 cm^{-1}. An * denotes a spurious feature arising from a grating ghost.

The Raman measurements were performed at room temperature on two automated instruments: a Spex 1400 double monochromator and a Coderg T800 triple monochromator (Arthur and Lockwood 1974). Survey measurements were carried out at 476·5 nm, but all spectra reported here were obtained using 514·5 nm light from either a Spectra Physics 165 or a Coherent Radiation 52B argon laser. Spectra were recorded using the conventional 90° geometry and the back-scattering geometry, the latter being used to identify LO features. The back-scattering measurements were carried out with the crystal in an argon atmosphere in order to eliminate spectral features due to air. A goniometer mount facilitated precise positioning of the crystal in the laser beam for each orientation. The polarization of the scattered light was analysed with Polaroid film, and a polarization scrambler was placed between the analyser and spectrometer. The collection lenses used on the two instruments had apertures of $f/3$, which corresponds to a collection-cone half-angle, θ, of 9·5°. The laser beam was brought to a focus inside the crystal with an angle θ in the range 0·4 to 0·8°. The directions X, Y and Z used to denote the various polarizations refer to the crystal tetragonal axes a, b and c, respectively: a bar over the letter indicates the reverse direction, and a prime denotes directions at 45° to the principal ones in the ab plane.

The A_1-symmetry spectra are shown in figure 1 and although other peaks are obvious there is one dominant feature at 295 cm^{-1}. The $X(ZZ)Y$ and $Y(ZZ)\bar{Y}$ spectra are identical as expected, and the XX spectrum is similar to the YY one. Modes of B_1 symmetry should be seen in the XX and YY polarization and not in the ZZ polarization. Comparing figures 1(*a*) and (*b*) with figure 1(*c*) it is apparent that there are no features that could be assigned to B_1 modes with any certainty. The diagonal spectra contain comparitively strong second-order features and other peaks classified in off-diagonal polarizations. The latter case is particularly evident in figure 1(*c*).

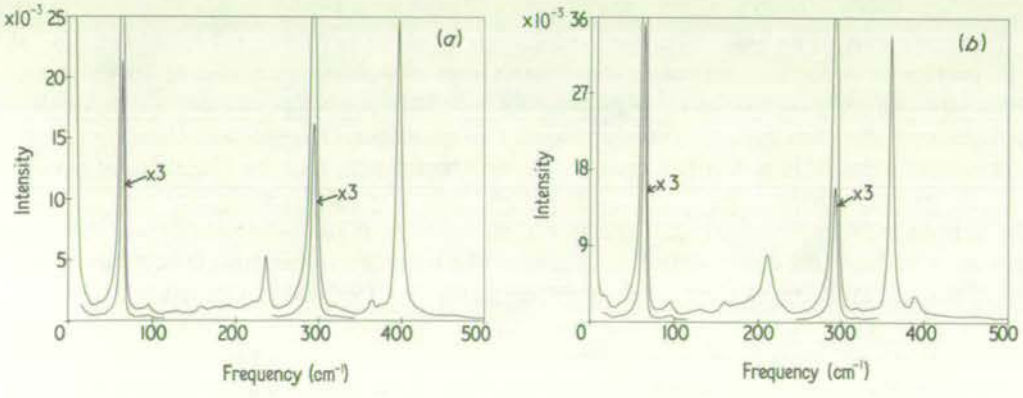

Figure 2. The (*a*) $Z(YX)\bar{Z}$ and (*b*) $X(YX)Y$ Raman spectrum of $AgGaS_2$ recorded on the 1400 with 100 mW of laser power and a slit width of 2·1 cm^{-1}.

The three modes with B_2 symmetry are shown in figure 2. B_2 modes may exhibit TO–LO splittings: figure 2(*a*) shows the LO modes and figure 2(*b*) the TO modes. The B_2 mode at 64 cm^{-1} is not split, whereas the two higher-frequency modes are split by 25·5 and 34·5 cm^{-1}, respectively. Both spectra exhibit a strong spurious peak at the A_1 mode frequency and contain other weaker features arising from modes with E symmetry.

Six E modes are expected and these can be seen in figure 3, where figure 3(*a*) shows the LO modes and figure 3(*b*) the TO modes. The band at $\sim 95\ cm^{-1}$ exhibits a low-frequency shoulder and has the same shape in both the TO and LO spectra. Therefore, the bandshape results from two E modes in close proximity rather than from any TO–LO effect. Again, the $295\ cm^{-1}$ band is strongly present, as is the $64\ cm^{-1}$ band. There is a weak feature at $18\ cm^{-1}$ but this most likely arises from second-order scattering and, in general, the off-diagonal second-order features are weak.

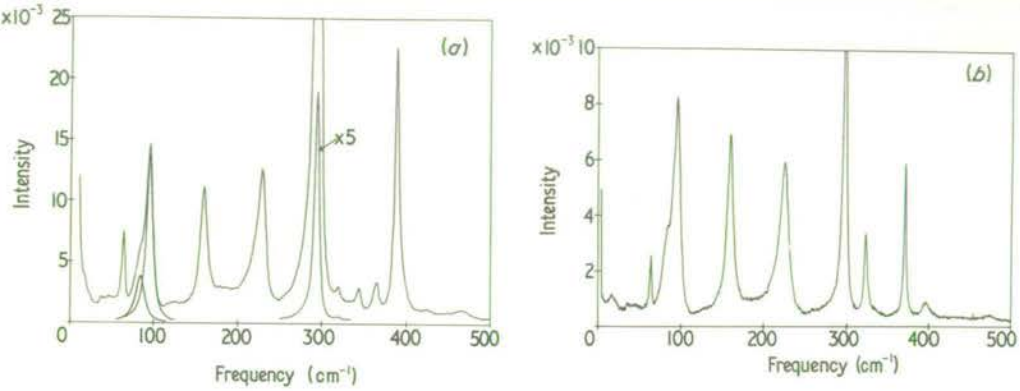

Figure 3. The (*a*) $Y(ZX)\bar{Y}$ and (*b*) $Z(YZ)Y$ Raman spectrum of $AgGaS_2$ excited with 100 mW of laser power. Spectrum (*a*) was recorded on the 1400 (slit width $2{\cdot}1\ cm^{-1}$) and spectrum (*b*) on the T800 (slit width $1{\cdot}2\ cm^{-1}$). The band at $\sim 90\ cm^{-1}$ is shown resolved into two components.

All the spectra exhibit features that arise from modes appearing in forbidden polarizations, and this has been noted in other studies (Holah *et al* 1974, van der Ziel *et al* 1974). The appearance of forbidden features can largely be explained from a study of the optical properties of $AgGaS_2$. Optical activity introduces depolarization into light-scattering measurements through rotation of plane-polarized light propagating along the optically-active axis. Fortunately, we have avoided this problem through our choice of laser wavelength, but this is not the case for some spectra reported by Holah *et al* (1974), which were recorded using laser light at 496·5 nm. Crystal birefringence can also act to depolarize Raman scattered light in certain scattering geometries and care must be taken to reduce this effect (Porto *et al* 1966). The solution to birefringence problems is to abstain from using the optic axis in experiments, but this was not possible here when the B_1, E(TO) and B_2(LO) modes were investigated. However, according to the criterion of Porto *et al* (1966), birefringence depolarization effects will be negligible in $AgGaS_2$ when $\theta \ll 4{\cdot}5°$ for 514·5 nm light propagating 2 mm along the optic axis. All spectra show some signs of depolarization effects and this is particularly so for the $Z(YY)\bar{Z}$ spectrum (figure 1(*c*)). Here, θ is 9·5° in the $\bar{Z}$ direction and birefringence effects are dominant, implying that the spectrum will contain an admixture of the $Z(YX)\bar{Z}$ spectrum. According to the formula given by Porto *et al* (1966), a value for θ of 9·5° would give a depolarization of 0·31 under the conditions used in the experiment. Comparing figures 1(*c*) and 2(*a*), it is seen that the B_2(LO) modes do appear in the YY spectrum at approximately 0·3 times their intensity in the YX spectrum. For other spectra, the depolarization effects are much smaller. For example, the depolarization ratio $I_{\text{off-diagonal}}/I_{\text{diagonal}}$ for the $295\ cm^{-1}$ band is about 0·05 for all off-diagonal polarizations (excluding the $Z(YY)\bar{Z}$ spectrum).

This is less than the expected value of ~0·3 for light propagating along the optic axis, but greater than the zero value anticipated for light directed along the X and Y axes. Therefore, the mixing of polarizations arises from some source other than birefringence acting alone, although for laser light directed along the Z axis it must be remembered that θ is not small enough for negligible birefringence effects. Scattering arising from the smaller twinned portion of the crystal and other defects in the experimental arrangement (eg slight misorientation of the crystal) are the most likely causes.

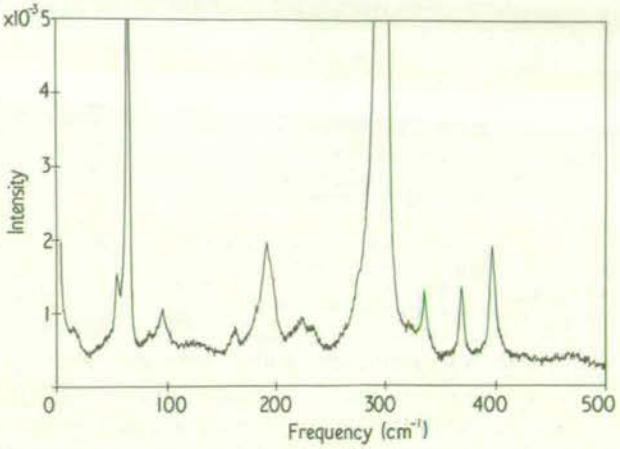

Figure 4. The $Z(Y'X')Y'$ Raman spectrum of $AgGaS_2$ recorded on the T800 with 100 mW of laser power and a slit width of 1·2 cm^{-1}.

There remains now the observation of the three B_1 modes. A scattering geometry was used in which the laser beam was directed along the optic axis and the scattered light was collected along [110]. This geometry was crucial for a successful determination of the B_1 modes, as it meant that the B_1 modes being observable in an off-diagonal polarization ($Y'X'$) were no longer obscured by the intense second-order spectrum evident in the diagonal polarizations. The B_1 modes are shown in figure 4, and are at 54, 190·5 and 333·5 cm^{-1}, respectively. The spectrum given in figure 4 contains bands arising from A_1, B_2 and E modes that are present because of imperfections in the experiment. Positive evidence for the assignment of the B_1 modes was obtained by rotating the crystal about the c axis and observing the $Z(Y''X'')Y''$ spectrum as a function of angle. According to the Raman tensors, B_1 modes are maximized in intensity when the scattered light is exactly along $Y'' = Y'$ and the B_2 modes are minimized to zero intensity. The B_1 modes decrease in intensity while the B_2 modes increase in intensity when Y'' is moved away from Y', and this is what was observed. Intensities of features arising from E modes were insensitive to this rotation.

Frequencies, linewidths (full width at half maximum) and assignments of the observed bands are given in table 1. In the case of the E modes at ~90 cm^{-1}, the band contour was least-squares fitted to a function comprising two uncoupled damped harmonic oscillators. The resulting frequency and width parameters are given in table 1. Most linewidths are of the order of 5 cm^{-1}, and therefore are resolution limited. Bands in the frequency range 190–230 cm^{-1} are considerably broader, ~13 cm^{-1}, and there must be strong anharmonic interactions in this frequency region.

As mentioned previously, the second-order spectrum of $AgGaS_2$ is weak in the

Table 1. Peak frequencies $\omega(cm^{-1})$, linewidths $\gamma(cm^{-1})$ and assignments for the Raman-active modes of $AgGaS_2$.

A_1		B_1		B_2		E	
ω	γ	ω	γ	ω	γ	ω	γ
295	5.7 ± 0.2^a	54	3.0 ± 0.2^a	64	2.9 ± 0.1^a	84.5	$14.5 \pm 3^{b,c}$
		190.5	15 ± 1^a	212	11.4 ± 0.5^a	94.5	$8.5 \pm 0.5^{b,c}$
				237.5	7.3 ± 0.3^b		
		333.5	6.0 ± 0.2^a	364	5.0 ± 0.2^a	159.5	8.6 ± 0.3^a
				398.5	7.3 ± 0.3^b	160	9.5 ± 0.5^b
						224	13.0 ± 0.4^a
						229.5	13.0 ± 0.5^b
						321.5	4.9 ± 0.2^a
						346	6.2 ± 0.3^b
						368	3.5 ± 0.2^a
						391	5.9 ± 0.3^b

[a]Spectral slit width 1·2 cm^{-1}.
[b]Spectral slit width 2·1 cm^{-1}.
[c]Curve resolved.

off-diagonal polarizations. and no significant feature was seen at frequencies above 400 cm^{-1}. This is not the case for the diagonal polarizations—strong second-order features are observable out to $\sim$800 cm^{-1}. the apparent two-phonon cut-off point. Representative spectra are shown in figure 5: the XX spectrum is identical to the YY spectrum given in figure 5(*a*). Peaks occur at 417. 460. 500. 518. 555. 591. 623. 684. 731. 754 and 773 cm^{-1}. The ZZ spectrum is remarkably similar to the YY spectrum, indicating a small anisotropy in the dispersion curves of $AgGaS_2$ for frequencies greater than about 200 cm^{-1}.

The antiresonance behaviour of the 295 cm^{-1} band intensity as observed by van der Ziel *et al* (1974) but not by Holah *et al* (1974) was qualitatively confirmed in the study.

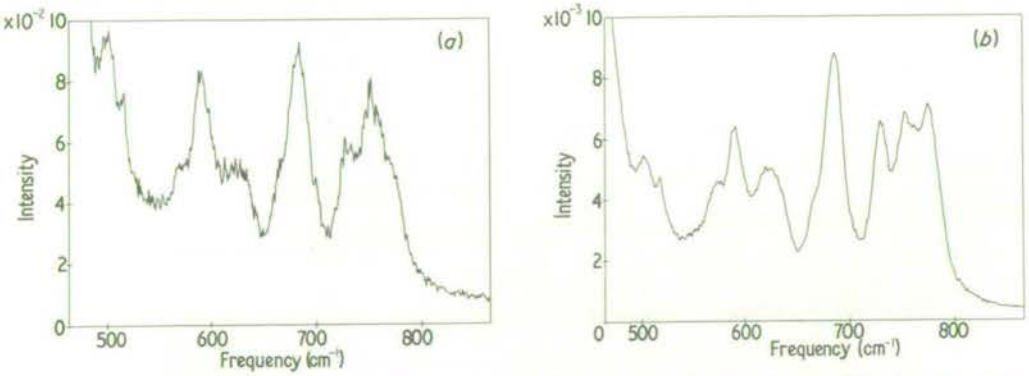

Figure 5. The (*a*) $Z(YY)\bar{Z}$ and (*b*) $Y(ZZ)\bar{Y}$ Raman spectrum of $AgGaS_2$ recorded on the 1400 with (*a*) 100 mW and (*b*) 60 mW of laser power and with a slit width of (*a*) 2·1 cm^{-1} and (*b*) 4·2 cm^{-1}.

3. Discussion

We begin by comparing these results with previous measurements on $AgGaS_2$ (see figure 6). The present measurements were made on the sample used by Holah *et al*.

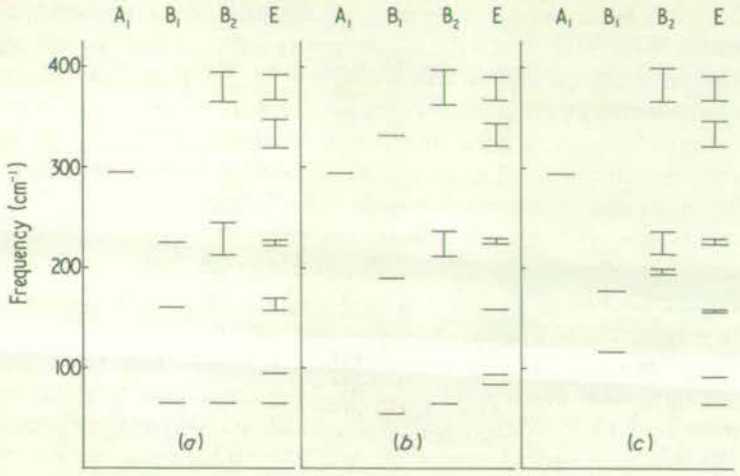

Figure 6. A comparison of the $AgGaS_2$ assignments of (*a*) Holah *et al* (1974). (*b*) the results of this work and (*c*) van der Ziel *et al* (1974).

which was different from the sample used by van der Ziel *et al*, but it is unlikely that there were serious differences in the constitutions of the two samples, as many of the measured frequencies are in good agreement. Such discrepancies as do occur probably arise from errors in measurement. All three experiments give the same value for the A_1 frequency, which is hardly surprising in view of the relatively high intensity of the A_1 peak. There is also general agreement on the E modes, except in the case of the lowest frequencies around 70 cm^{-1}. Both Holah and van der Ziel place the lowest E mode at 64 cm^{-1}, but according to the arguments of the last section this should be regarded as the strong B_2 mode which has leaked through into the scattering configuration for E modes.

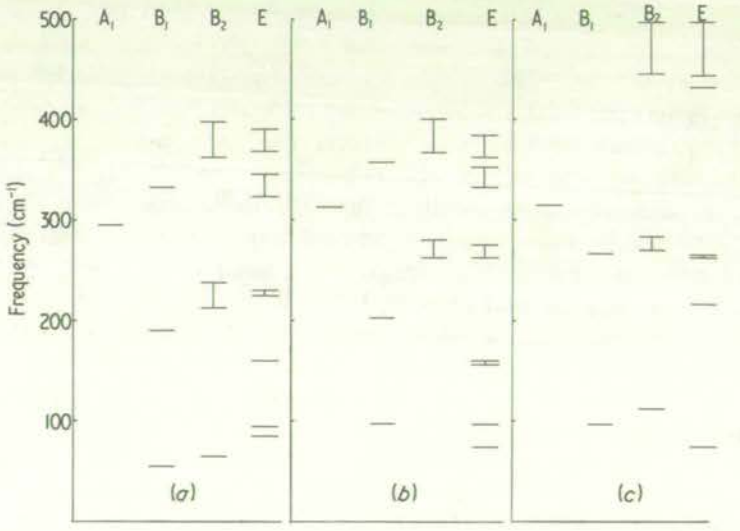

Figure 7. Phonon spectra for several chalcopyrite sulphides: (*a*) $AgGaS_2$, present results; (*b*) $CuGaS_2$, Koschel *et al* (1975); (*c*) $CuAlS_2$, Koschel *et al* (1973).

van der Ziel *et al* have made the opposite assumption, that the 64 cm^{-1} line is really an E mode which leaks partly into the B_2 geometry, but the peak heights in our measurements make this very unlikely (see figures 2 and 3). The two higher B_2 modes are given the same frequencies in all three experiments, and they are not in doubt because they have also been observed in infrared reflectance. However, there is no agreement at all between the frequencies ascribed to the B_1 modes, and our experience suggests that the genuine B_1 peaks can be observed only in the 45° geometry; the peaks observed in the earlier experiments probably arose from leak-through and second-order scattering.

In figure 7 we compare the present data on $AgGaS_2$ with the best available results on $CuGaS_2$ and $CuAlS_2$ (Koschel *et al* 1973, 1975). A number of regularities are immediately apparent, and it is gratifying to find that the present results on $AgGaS_2$ fit the general pattern much better than either of the earlier determinations. Taken as a whole, these results imply that one must abandon the argument used by many previous authors (eg Kaminow *et al* 1970, Holah *et al* 1974), which claims that the phonon spectrum of a chalcopyrite can be regarded as a fairly small perturbation of the spectrum for a zincblende material. This model cannot explain the very high intensity of the A_1 peak which is found in all these compounds; A_1 arises from a zone boundary mode in zincblende, and the Raman intensity for this mode should be much weaker than for modes which arise from the zincblende zone centre. Moreover, the perturbed zincblende model predicts that the highest B_1 mode should have nearly the same frequency as the second-highest B_2 mode, because the corresponding modes in a zincblende structure are symmetry related. This is not the case in $AgGaS_2$, nor even in $CuGaS_2$, where the atomic masses differ very little from their values in ZnS and the zincblende approximation should be at its best. Curiously, in $CuAlS_2$, where the cation masses differ widely from each other, the B_1 and B_2 frequencies appear to agree very well. However, one should note that Koschel *et al* (1973) have recorded only two of the three B_1 frequencies for $CuAlS_2$, and in their later paper (1975) they imply that the missing B_1 mode lies in the neighbourhood of 400 cm^{-1}. This conjecture would bring $CuAlS_2$ completely into line with the other sulphides and would confirm that the zincblende approximation is a poor one in all cases.

Further support for this scheme comes from Bettini's theoretical model for the phosphides (Bettini 1975). This is based on Keating's (1966) model for diamond structures, as modified by Martin (1970) to take account of zincblende materials which are partly ionic. (See Nelin (1974) for a comprehensive review of lattice dynamical models for the diamond structure.) Bettini's model treats the chalcopyrites as basically covalent materials, with strongly directional tetravalent bonds; charge transfer effects are regarded as secondary, particularly in the case of the cation with the higher valency. The only covalent forces included are the nearest-neighbour bond-stretching and bond-bending forces, and this is sufficient to give a good fit to all but the lowest phonon frequencies in a large number of phosphides. Bettini argues that non-Coulomb forces of longer range need to be included in order to fit these lower frequencies; it will also be interesting to see how well his model predicts the elastic constants, as these will no doubt soon be measured for the phosphides using Brillouin scattering (Holah and Grimsditch 1975).

If one plots the measured frequencies for $CdGeP_2$, $ZnGeP_2$ and $CdSiP_2$, one obtains a scheme remarkably similar to that shown for the sulphides in figure 7 (Bettini *et al* 1974). The main difference between the phosphides and sulphides is that the latter have larger Coulomb splittings; this suggests that the Keating–Martin model is less reliable for the sulphides, owing to their increased ionicity and the large polarizability

of the d shells in the noble metal ions (Fischer *et al* 1972). Bettini does not attempt to apply his model to the sulphides, though we feel that it can still be applied to them as a good qualitative guide. In $ZnGeP_2$, the mass difference between the cations is negligible, and one might expect its phonon spectrum to be similar to that of GaP: but according to the model, the Ge–P bond is more covalent and hence stiffer than the Zn–P bond, and this would separate the related B_1 and B_2 modes even if the two cation masses were identical. A very similar situation seems to apply to $CuGaS_2$. Now Bettini's measurements on $CdSiP_2$ are similar to Koschel's on $CuAlS_2$ in that only two of the three B_1 modes have been identified. Bettini's model predicts clearly that the missing B_1 mode in $CdSiP_2$ has a higher frequency than the two which have been observed, and this corroborates the conjecture that there is a missing B_1 mode near 400 cm^{-1} in $CuAlS_2$. It would be very interesting to use the technique of the 45° geometry to look for these high frequency B_1 modes in $CdSiP_2$ and $CuAlS_2$; in $CdSiP_2$ it might be necessary to use the back-scattering configuration $Z(X'Y')\bar{Z}$.

Finally, we summarize the qualitative information which can be gleaned from figure 7. The A_1 mode is a pure anion mode with known eigenvectors (Holah *et al* 1974) and the fact that it has almost the same frequency in all three sulphides suggests that the force constants do not vary much from compound to compound (Koschel *et al* 1975). However, these force constants deviate considerably from those found in ZnS, because the highest B_2 and E frequencies in $CuGaS_2$ are much higher than the corresponding frequencies in ZnS. On the other hand, Holah and Grimsditch (1975) find that the elastic constants of $AgGaS_2$ are actually lower than the elastic constants of ZnS; perhaps these results can be explained in terms of a strong Ga–S bond and a weak Ag–S or Cu–S bond, and elastic data on all of the sulphides would be very desirable in order to test this idea further. In $CuGaS_2$ and $AgGaS_2$ the highest B_2 and E modes have almost the same frequency, which lies well below the corresponding frequency in $CuAlS_2$. Koschel *et al* argue that in all these materials, the highest frequency modes correspond to a vibration of the trivalent cations against the anions, the monovalent cations being almost stationary; but our own opinion is that this is true only for $AgGaS_2$ and $CuAlS_2$. In $CuGaS_2$, Cu is lighter than Ga, although it has a weaker coupling to its neighbours; in the highest frequency modes it is possible for the Cu ion to have a considerable amplitude, despite the fact that the Cu mass has little effect on the mode frequency (Holah *et al* 1974). In the case of the B_2 and E modes near 230 cm^{-1}, the frequencies for $AgGaS_2$ are lower than for $CuGaS_2$, and this does indicate that both cations are contributing significantly to these modes. It is not easy to compare the modes below 100 cm^{-1}, as one of the B_2 modes in $CuGaS_2$ is missing; the distribution of modes in this frequency range seems to be rather different in the three compounds, but further measurements are needed before one can be sure that these differences are genuine, see note added in proof.

Acknowledgments

We are very grateful to Dr G D Holah for the loan of the $AgGaS_2$ crystal, and to Dr A Miller for several stimulating discussions.

Note added in proof. After submitting this paper we became aware of further work by W H Koschel and M Bettini (*Phys. Stat. Solidi* to be published). They report additional infrared and Raman measurements on a number of sulphides, and they interpret their results tentatively in terms of Bettini's model. In the case of $CuAlS_2$, it is gratifying to

learn that they have found the missing B_1 mode at 443 cm^{-1}. Their low-frequency measurements on $AgGaS_2$ agree with the present results, except in the case of the lowest E mode. They claim that the shoulder at 84·5 cm^{-1} (figure 3) is a second-order feature which disappears from the Raman spectrum when the sample is cooled to 78 K. (Unfortunately Koschel and Bettini do not present any diagrams of their Raman spectra, although they do show an infrared absorption spectrum at 78 K in which the shoulder near 84.5 cm^{-1} can still be seen.) Our own room temperature data are certainly compatible with this new assignment, and a weak line near 34 cm^{-1} is marginally visible in our spectra (see figure 3).

References

Arthur J W and Lockwood D J 1974 *J. Raman Spectrosc.* **2** 53–69
Bettini M 1975 *Phys. Stat. Solidi* (b) **69** 201–12
Bettini M, Bauhofer W, Cardona M and Nitsche R 1974 *Phys. Stat. Solidi* b **63** 641–8
Bettini M and Miller A 1974 *Phys. Stat. Solidi* b **66** 579–86
Fischer K, Bilz H, Haberkorn R and Weber W 1972 *Phys. Stat. Solidi* b **54** 285–94
Hobden M V 1967 *Nature* **216** 678
—— 1968 *Acta Crystallogr.* A **24** 676–80
Holah G D and Grimsditch M 1975 *Phys. Rev.* to be published
Holah G D, Webb J S and Montgomery H 1974 *J. Phys.* C: *Solid St. Phys.* **7** 3875–90
Kaminow I P, Buehler E and Wernick J H 1970 *Phys. Rev.* B **2** 960–6
Keating P N 1966 *Phys. Rev.* **145** 637–45
Korczak P and Staff C B 1974 *J. Crystal Growth* **24/25** 386–9
Koschel W H, Hohler V, Rauber A and Baars J 1973 *Solid St. Commun.* **13** 1011–16
Koschel W H, Sorger F and Baars J 1975 *J. Phys., Paris* to be published
Martin R M 1970 *Phys. Rev.* B **1** 4005–11
Nelin G 1974 *Phys. Rev.* **10** 4331–9
Porto S P S, Giordmaine J A and Damen T C 1966 *Phys. Rev.* **147** 608–11
van der Ziel J P, Meixner A E, Kasper H M and Ditzenberger J A 1974 *Phys. Rev.* B **9** 4286–94

16

"Light Scattering in Solids"
M. Balkanski, R.C.C. Leite & S.P.S. Porto Eds.
(Flammarion, Paris, 1975)

A RAMAN STUDY OF THE FERROELECTRIC PHASE TRANSITION IN CHROMIUM CHLORINE BORACITE

D.J. Lockwood

Physics Department, Edinburgh University, Scotland EH9 3JZ

INTRODUCTION

Boracites, $M_3B_7O_{13}X$, where M designates a divalent metal and X a halogen, are of interest because they exhibit unusual ferroelectric, magnetic, dynamical and structural properties (1). Most boracites exhibit transitions from a high temperature paraelectric cubic phase to one or more lower symmetry ferroelectric phases and some also become antiferromagnetic at low temperatures. We have undertaken a systematic Raman investigation of these phase changes, and here we report on some of the results from a study of the paraelectric-ferroelectric transition in $Cr_3B_7O_{13}Cl$.

The 'improper' ferroelectric transition occurs at 263 K in chromium chlorine boracite (Cr-Cl) (2) and involves the symmetry change $T_d^5 \rightarrow C_{2v}^5$ accompanied by a doubling of the primitive unit cell volume (1,3). Group theory predicts that the zone-centre Raman-active modes in the cubic phase transform as $4A_1 + 10E + 19F_2$ and in the orthorhombic phase as $71A_1 + 72A_2 + 71B_1 + 71B_2$. It has been proposed that the primary order parameter is associated with a doubly-degenerate zone-boundary (X point) mode of vibration in the cubic phase (4). The degenerate critical modes become homogeneous modes in the orthorhombic phase and split into $A_1 + A_2$. It is anticipated that anharmonic coupling between the A_1 soft mode and a low-frequency A_1 optic mode induces the spontaneous polarisation, P_s, as a secondary

order parameter in the ferroelectric phase (1).

EXPERIMENT AND RESULTS

The two 1-mm^3 crystals of Cr-Cl used in this study were the ones described in a previous paper (5). Raman spectra were obtained using the equipment and techniques reported earlier (5): spectra were excited with 600 mW of laser light at 488.0 nm and recorded using a spectral slit width of 3 cm^{-1} and a sampling interval of 0.5 cm^{-1}. For these low temperature studies, the Cr-Cl sample was mounted on the cold finger of an Oxford Instruments flow cryostat. A Au/Fe-chromel thermocouple mounted on the sample monitored the crystal temperature, which was controlled to within 0.1 K. The directions X, Y and Z which are used to denote the various polarisations refer to the principal cubic axes of the crystal.

The Raman spectrum of Cr-Cl was measured at temperatures in the range T_c - 50 to T_c + 50 K. Typical results for the Z(YY)X polarisation are shown in Fig. 1. Above T_c, the YY spectrum contains information about both the A_1 and E modes. The A_1 component alone can not be measured directly in any scattering geometry but the E-symmetry scattering is accessible using a crystal with faces cut perpendicular to [001], [110] and [1$\bar{1}$0] (5). One crystal had this orientation and was used to study the temperature dependence of the low-frequency E spectrum for $T > T_c$. The F_2 modes have off-diagonal polarisation. Domains are formed when the crystal enters the ferroelectric phase, and group theory indicates that there are 24 possible domain orientations although only 6 of these will affect the Raman results. Different sets of domains were formed each time the sample was taken through the transition; in the case of the spectra shown in Fig. 1, two sets of domains dominated in which P_s was either along or oppositely directed to Z or Y. Two of the orthorhombic phase unit-cell axes are at 45° to the corresponding cubic ones and the scattering tensors need to be corrected for this rotation. It turns out that the spectra given in Fig. 1 for $T < T_c$

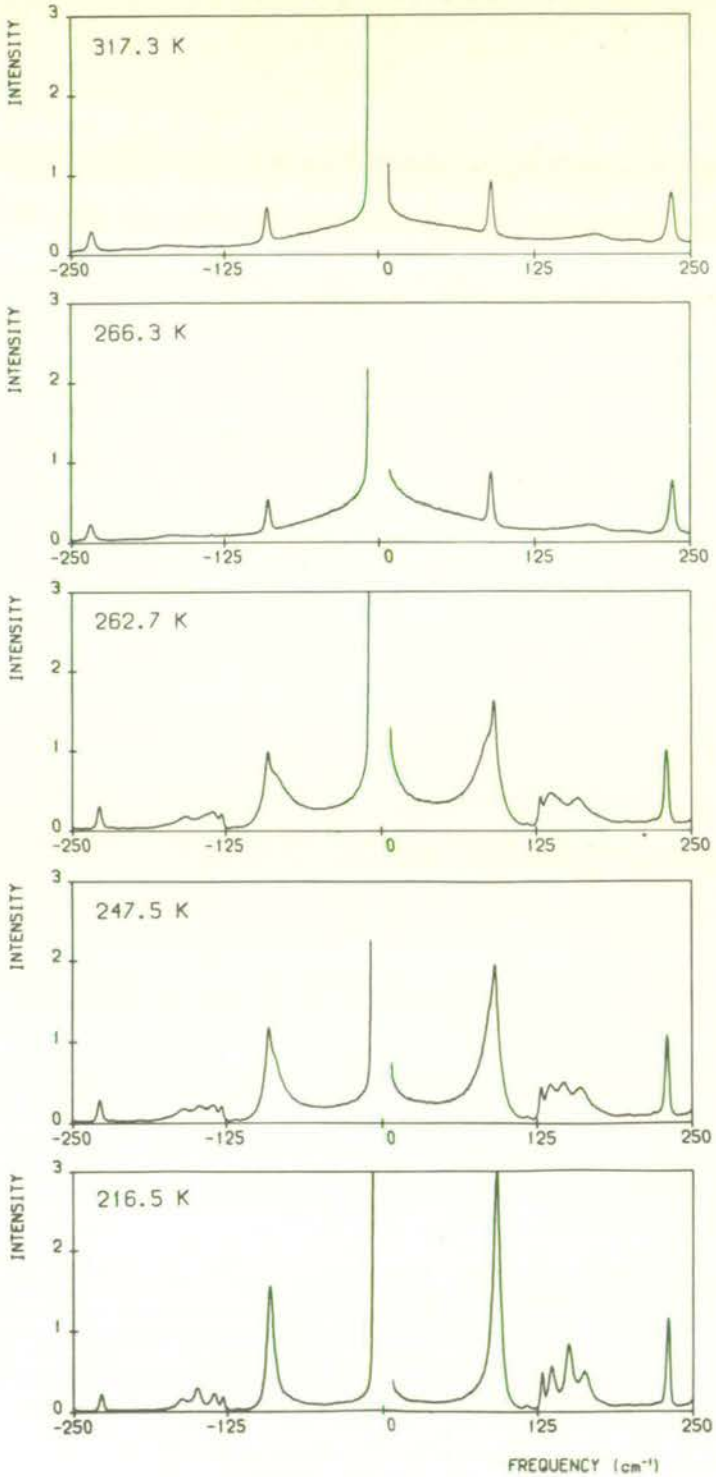

Figure 1. The low-frequency Z(YY)X Raman spectrum of Cr-Cl at temperatures above and below T_c.

show features with $A_1 + A_2$ symmetry, although it must be emphasised that some scattering from the other set of domains may be mixed into these spectra.

Above T_c, the A_1, E and F_2 modes exhibit no temperature dependence, and the odd-shaped low-frequency (0-85 cm^{-1}) feature in the F_2 spectrum (6) is only weakly temperature dependent. At T_c, there is a marked and abrupt change in the spectrum, as can be seen in Fig. 1: the F_2 low-frequency band collapses, and numerous new bands are observed in all polarisations. This confirms the first-order nature of the transition (1,4 Spectral features sharpen and some mode interaction is evident when the temperature is further lowered, but most band frequencies remain constant. Two soft modes are evident in the YY spectrum of the orthorhombic phase: the bands are at 91 and 149.5 cm^{-1} respectively for temperatures well below T_c and soften to ~85 and ~138 cm^{-1} respectively at the transition. These modes have the expected A_2/A_1 symmetry.

The temperature dependence of the wing feature in the YY spectrum has been studied in detail. An earlier study at room temperature indicated that the wing fitted equally well to either a Debye or a damped simple harmonic oscillator model (6). The Debye model was arbitrarily chosen for this study and the function $I(\omega) = S\gamma^2\omega\,[\bar{n}(\omega)+1]/(\omega^2 + \gamma^2)$ was least-square fitted to the data over the range 20-110 cm^{-1}. S is the strength of the band, γ the damping constant and $\bar{n}(\omega)$ the usual Bose-Einstein factor evaluated at frequency ω. The phonons present at higher frequencies were included in the fitting as damped harmonic oscillators, and the background, determined from the high-frequency region, was held constant at the one value for all spectra. The Debye model fitted the wing feature very well, especially for $T > T_c$: for temperatures below T_c, it was difficult to accurately account for the phonons at ~90 cm^{-1} because of the interference between modes. The resultant values for S and γ are plotted in Fig. 2. For temperatures in the range T_c - 2 to T_c + 2 K it was found that there

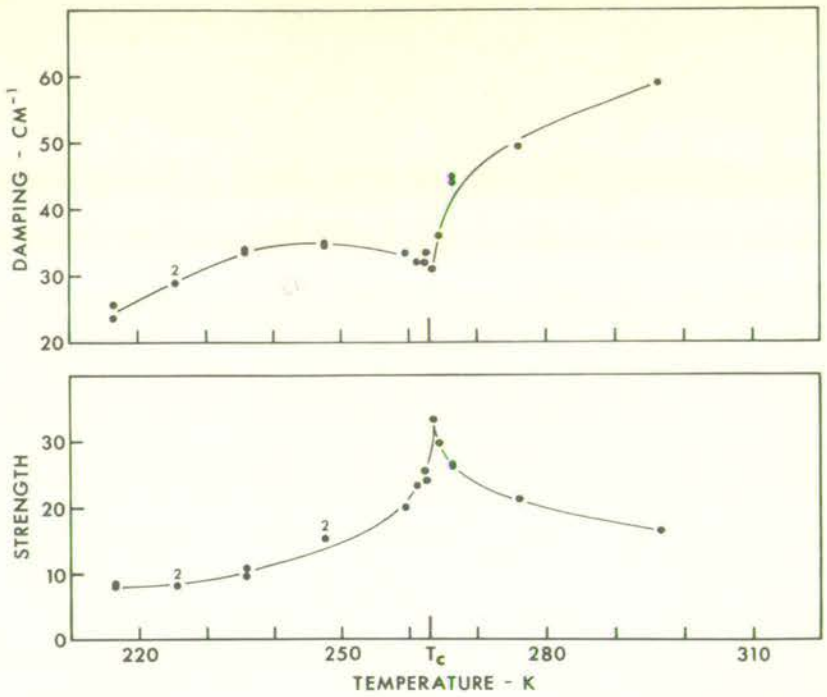

Figure 2. Temperature dependence of S and γ. The symbol 2 denotes two identical points; the lines are drawn as a guide for the eye.

was a significant increase in intensity in the YY spectrum for frequencies $< 20\ cm^{-1}$. This first showed up from the Debye-model fitting procedure, and was confirmed by an examination of the central peak intensity, which showed a marked (3X) increase in value as T_c was approached.

DISCUSSION

The spectra of Fig. 1 show that there is interference between the soft modes and other phonons, which makes it difficult to extract the temperature dependence. However, the temperature dependence of both soft modes is in qualitative agreement with theoretical predictions (7), and these results provide the first confirmation of the proposed microscopic mechanism for the cubic-orthorhombic transition(1). The presence of the wing feature could indicate some kind of dynamic disorder, or it may arise from higher-order scattering from low-frequency optic-mode branches. If the latter case were were true, then the cusp-like response found for S as a function of

temperature should be similar to the specific heat behaviour, as both properties are related to the same two-phonon Green's function. Further work is in progress to clarify the origins of the wing-type scattering.

I wish to thank Dr. H. Schmid for providing the crystals and for invaluable advice. This work was supported by the Science Research Council and the Battelle Institute, Geneva. Fig. 2 would have contained more data points but for an inopportune strike by computer operators at the Edinburgh Regional Centre!

REFERENCES

1 R.J. Nelmes, J. Phys. C, 7, 3840 (1974).

2 H. Schmid, private communication.

3 R.J. Nelmes and F.R. Thornley, J. Phys. C, 7, 3855 (1974).

4 V. Dvorak and J. Petzelt, Czech. J. Phys., B21, 1141 (1971).

5 D.J. Lockwood, J. Raman Spectrosc., 2, 555 (1974).

6 D.J. Lockwood, paper 3.27, Fourth International Conference on Raman Spectroscopy, Brunswick, Maine, (1974).

7 V. Dvorak, Czech. J. Phys., B21, 1250 (1971).

J. Phys. C: Solid State Phys., Vol. 8, 1975. Printed in Great Britain. © 1975

17

Two-magnon Raman scattering in $KMnF_3$

D J Lockwood and G J Coombs
Department of Physics, University of Edinburgh, Edinburgh EH9 3JZ, Scotland

Received 11 July 1975

Abstract. The two-magnon Raman spectrum of $KMnF_3$ has been investigated as a function of temperature, and peak position and width parameters obtained. A Green function theory developed by Balucani and Tognetti is applied to the results and accurately describes the observed temperature dependence for $T/T_N < 0{\cdot}8$. This good agreement implies that the magnetic ordering in $KMnF_3$ can be adequately represented by the cubic perovskite structure despite structural distortions and the spin canting for temperatures below 81 K. The Raman results predict a value of $4{\cdot}98 \pm 0{\cdot}07\ cm^{-1}$ for the isotropic Heisenberg exchange constant.

1. Introduction

Inelastic scattering of light from magnetic excitations has been observed in a variety of antiferromagnetic materials. In particular, the two-magnon collective excitation corresponding to a pair of spin deviations on nearest-neighbour magnetic ions on oppositely directed sublattices has proved to be the one most easily observed. Not surprisingly the majority of this work has been carried out on the simple antiferromagnets such as those with the perovskite and rutile structures typified by $RbMnF_3$ (Fleury 1968, 1970) and MnF_2 (Fleury and Loudon 1968) respectively. The interaction mechanisms for the magnetic ions with light have been considered fully by Fleury and Loudon (1968) and they estimate the total scattering of the one-magnon excitation to be less than that of the two-magnon excitation. This is in accord with the results they obtain for FeF_2. The two-magnon spectrum in $KNiF_3$ has been observed by Chinn *et al* (1971) and the one-magnon spectrum by Moch and Dugautier (1973). In all the cases cited, the two-magnon excitation at temperatures well below the transition is observed to be a prominent, decidedly asymetric peak with structure that can be shown to be a manifestation of critical points in the density of states.

$KNiF_3$ and $RbMnF_3$ are undoubtably the simplest of antiferromagnets, consisting of two oppositely-directed sublattices with the magnetic ions located on a face-centred cubic lattice. Their spin-wave spectra may be characterized by a single antiferromagnetic exchange constant between nearest neighbours and a uniform field describing the anisotropy.

$KMnF_3$ undergoes a transition to an antiferromagnetic state as the temperature is decreased below $T_N = 88{\cdot}1$ K (Cooper and Nathans 1966). Although at high temperatures the crystal structure is of the cubic perovskite form, at low temperatures there are distortions from this structure (Hidaka *et al* 1975). These effects are small, particularly for the Mn^{2+} ions, and the unit cell may be regarded as pseudo-cubic. Further, there

are deviations of the spin directions, from the edges of the pseudo-cubic cell but again they are small. The marginal nature of these departures from the ideal magnetic structure, such as that found in $RbMnF_3$, is clearly demonstrated by the neutron diffraction studies of Scatturin *et al* (1961) and Cooper and Nathans (1966), and so for the purposes of this work they may be ignored. Using inelastic neutron scattering, the one-magnon dispersion curves for $RbMnF_3$ have been determined by Windsor and Stevenson (1966) and by Saunderson *et al* (1972) and for $KMnF_3$ by Pickart *et al* (1966). The results are nearly identical; consisting of a single doubly-degenerate branch, and, as for $KNiF_3$ and $RbMnF_3$, only two parameters are needed to characterize the excitation in $KMnF_3$ (Cowley and Buyers 1972).

In this paper we report the measurement of the two-magnon Raman scattering in $KMnF_3$ at various temperatures in the magnetically ordered phase. The observation of the two-magnon spectrum in $KMnF_3$ has already been briefly reported by Popkov *et al* (1970) and they found that there was severe overlap between the two-magnon peak and phonon bands. The reasons for our further study are twofold: spectra can now be recorded under greatly improved experimental conditions and theories are now available for calculating spectra at finite temperatures. In §2 a brief description of the calculation based on these theories is given. In §3 the experimental two-magnon Raman scattering results for $KMnF_3$ are presented and experiment is compared with theory in §4.

2. Theory and Calculations

The contribution to the Raman spectrum from scattering by the two-magnon excitation is calculated on the basis of the expressions derived by Balucani and Tognetti (1973) (these authors are referred to below as BT). For a simple isotropic antiferromagnet with nearest-neighbour exchange interaction described by the Hamiltonian

$$H = J \sum_{\langle ij \rangle} S_i . S_j.$$

BT show that the two-magnon susceptibility transforming as the irreducible representation μ is given by

$$\chi^{\mu}(\omega) = \frac{G^{\mu}(\omega)}{1 - JG^{\mu}(\omega)}. \tag{2.1}$$

The two-magnon Green function of the same symmetry, G^{μ}, contains the effects of magnon interactions only insofar as they renormalize the one-magnon excitations. The expression for this quantity is

$$G^{\mu}(\omega) = -\frac{1}{N}\sum_{k} f_{\mu}^{2}(\boldsymbol{k}) \frac{2\hat{n}(\boldsymbol{k}) + 1}{\omega - 2\hat{\Omega}(\boldsymbol{k}) + i2\Gamma(\boldsymbol{k})}. \tag{2.2}$$

N is the number of unit cells, $\hat{\Omega}(\boldsymbol{k})$ and $\Gamma(\boldsymbol{k})$ are the one-magnon frequency and width, $\hat{n}(\boldsymbol{k})$ is the usual Bose–Einstein factor evaluated at this frequency and $f_{\mu}(\boldsymbol{k})$ is a factor appropriate to the irreducible representation μ. The sum is over the first Brillouin zone.

The anisotropy has been ignored. This is small, and is expected to have a negligible effect on the two-magnon spectrum.

The one-magnon frequency $\hat{\Omega}(\boldsymbol{k})$, which is renormalized due to magnon–magnon interactions, is calculated self-consistently in the Hartree–Fock approximation. This

quantity is simply related to the zero-temperature value by a multiplicative factor, α. The one-magnon width $\Gamma(\boldsymbol{k})$ is taken to be the value at the zone-boundary X point as the predominant contributions to the sum come from wavevectors in the vicinity of this point. BT develop a simple closed expression for this quantity that gives agreement with the neutron-scattering results of Saunderson *et al* (1972) for $RbMnF_3$. These expressions for the frequency and width are expected to be applicable for temperatures below, but not too close to, the Néel temperature.

Since the light interacts with deviations created on neighbouring sites, for which the exchange interaction is the strongest, it could be expected that magnon interactions would be of considerable importance in the two-magnon spectrum. This was first realised by Elliott and Thorpe (1969) who developed a theory at zero temperature. They achieve good agreement with low-temperature experimental results for $RbMnF_3$ as does Thorpe (1970) for MnF_2. The expressions of BT quoted above, reduce to theirs in the limit of zero temperature apart from a small contribution to the coupling constant in the susceptibility.

Apart from an explicit expression for the one-magnon width, identical expressions for $\chi''(\omega)$ have been obtained by Davies *et al* (1971) using diagrammatic techniques and by Natoli and Ranninger (1973) using the equation-of-motion technique. Cottam (1972) also obtains similar expressions, but with the magnon frequency calculated in the mean-field approximation and the width included phenomenologically.

BT have compared their calculations with the light-scattering results of Fleury (1970) on $RbMnF_3$ and of Chinn *et al* (1971) on $KNiF_3$. The agreement with the observed peak positions and widths is reasonable for a range of temperatures up to 0·8 T_N.

The core of the computational problem is the evaluation of the wavevector sum in the expression for the Green function (equation 2.2). In this we have followed BT and introduced the lattice Green function and converted the sum to an integral. These

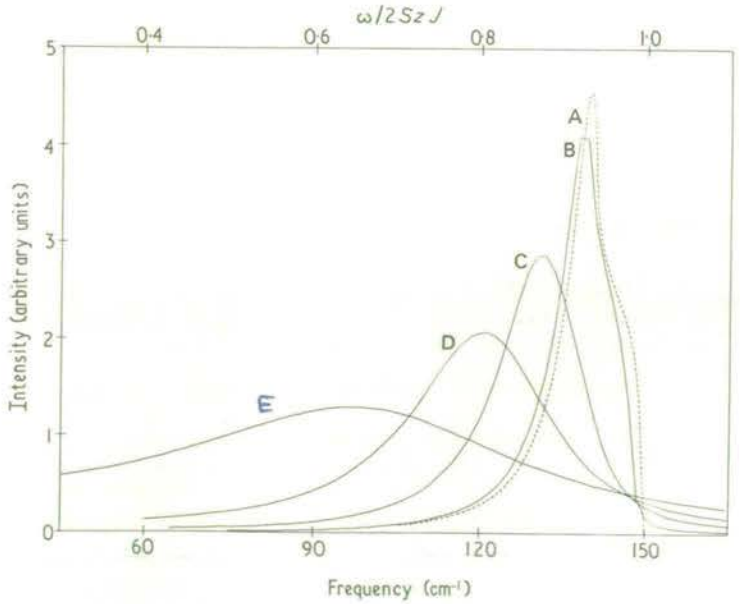

Figure 1. The computed two-magnon Raman spectrum of $KMnF_3$ at various temperatures: A, $T = 0$; B, $T = 0{\cdot}31\ T_N$; C, $T = 0{\cdot}51\ T_N$; D, $T = 0{\cdot}68\ T_N$ and E, $T = 0{\cdot}90\ T_N$. Curve A is drawn to a different intensity scale from that used for the other curves.

functions have been computed using the numerical algorithm derived by Oitmaa (1971). This algorithm gives improved accuracy compared with previous calculations (for example, Yussouf and Mahanty 1966) particularly for frequencies corresponding to excitations having wavevectors near the Brillouin zone boundary. The value of the exchange constant used was $J = 4{\cdot}98\ \mathrm{cm}^{-1}$: this choice is discussed in §3. The spin of the Mn^{2+} ion was taken as $S = \frac{5}{2}$. We have carried out the calculation only for the contribution to the susceptibility with the symmetry Γ_3^+. The other Raman-active contribution to the cross section has Γ_1^+ symmetry. It is of a non-resonant character and is believed to be unimportant (Elliott and Thorpe 1969).

The actual light-scattering cross section is related to the imaginary part of the susceptibility by the relation

$$K(\omega) = C[1 - \exp(-\hbar\omega/kT)]^{-1}\alpha^2(T)S^2[(-1/2\pi)\mathrm{Im}\chi]$$

where $\alpha(T)$ is the magnon renormalization factor evaluated at temperature T, and C is a constant. This expression has been calculated for a number of temperatures and representative results are displayed in figure 1. For the zone-temperature calculation the theory of Elliott and Thorpe (1969) was used.

3. Experiment and results

The $KMnF_3$ crystal used in this study was the one described in an earlier paper (Lockwood and Torrie 1974). The sample size was approximately $5 \times 5 \times 5\ \mathrm{mm}^3$ and was cut with faces perpendicular to the cubic-phase [001], [010] and [100] directions.

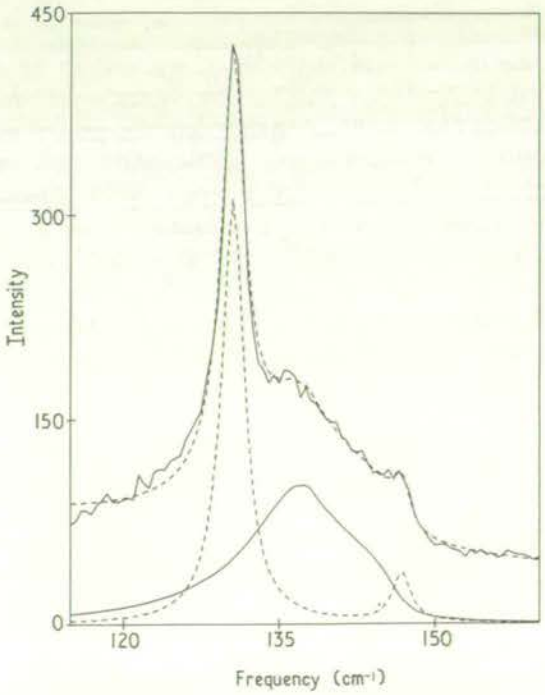

Figure 2. The Raman spectrum of $KMnF_3$ at 31·5 K recorded with a slit width of $1{\cdot}6\ \mathrm{cm}^{-1}$. The broken line is a fit of theory to experiment, with the phonon (– – – – – – –) and magnon (————————) components shown underneath.

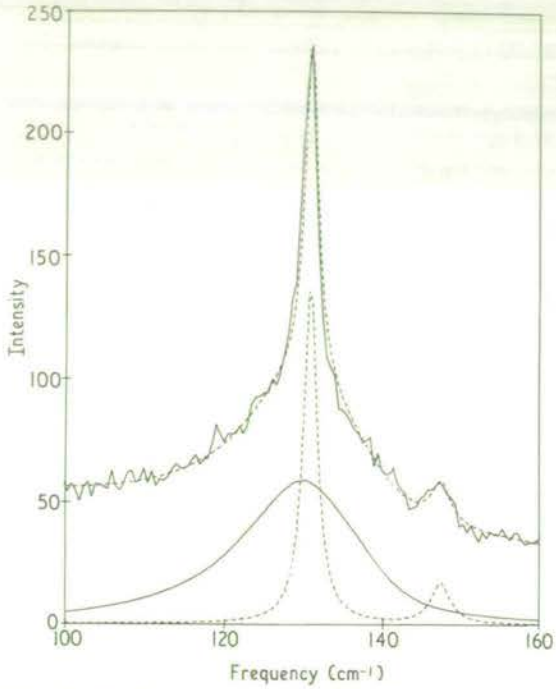

Figure 3. The Raman spectrum of $KMnF_3$ at 45 K recorded with a slit width of 1·5 cm^{-1}. The broken line is a fit of theory to experiment, with the phonon (– – – – – –) and magnon (———) components shown underneath.

The Raman spectrum was excited with 400 mW of argon laser light at 476·5 nm. Scattered light was collected at 90° to the incident beam and analysed with a Spex Ramalab double spectrometer. The photomultiplier detector pulses were processed with a digitized data collection system linked to a multichannel analyser (Arthur and Lockwood 1974) and spectra were stored on paper tape in a form suitable for direct processing on a large multi-access computer. The polarization of the scattered light was analysed with Polaroid film, and a polarization scrambler was placed between the analyser and the spectrometer.

For these low-temperature studies, the $KMnF_3$ sample was mounted on the cold finger of an Oxford Instruments flow cryostat. An Au/Fe–chromel thermocouple mounted on the sample monitored the crystal temperature, which was controlled to within 0·1 K.

Typical low-temperature results for the two-magnon Raman peak in $KMnF_3$ are given in figures 2 and 3. The spectra were recorded with diagonal polarization and show the two-magnon peak accompanied by two first-order phonon bands at 130·5 and 147 cm^{-1} (Lockwood and Torrie 1974).

As discussed earlier, $KMnF_3$ undergoes a succession of phase changes when the crystal is cooled from room temperature. The symmetry changes that occur at the structural transitions are

$$\text{cubic} \xrightarrow{(186\ \text{K})} \text{tetragonal} \xrightarrow{(91{\cdot}5\ \text{K})} \text{tetragonal} \xrightarrow{(81\ \text{K})} ?$$

The symmetry of the last phase is unknown: possibly tetragonal or orthorhombic (Hidaka *et al* 1975, Lockwood and Torrie 1974). There is no first-order Raman

spectrum in the cubic phase, but the other phases produce many first-order features (Lockwood and Torrie 1974). The presence of these phonons makes it difficult to clearly distinguish the two-magnon peak at certain temperatures. A further complication arises from the strains that can be induced when the sample is taken into the lowest-temperature phase. These strains depolarize the incident and scattered light beams so that the Raman spectra of different polarizations are mixed. This depolarization effect varied in strength, S, every time the sample was taken through the transition; S varied from 1 to 18, where $S = 1$ indicates complete depolarization. The spectra given in figures 2 and 3 were obtained when $S = 18$ and show good polarization (Lockwood and Torrie 1974).

In §2 it was noted that for an antiferromagnet with the cubic perovskite structure there are two contributions to the Raman scattering of symmetry Γ_1^+ and Γ_3^+ respectively. The spectra in figures 2 and 3 display the Γ_3^+ component. Previous work on $KNiF_3$, $RbMnF_3$ and $KMnF_3$ has shown that the Γ_1^+ Raman feature is unobservable (Chinn *et al* 1971, Fleury 1968 and Popkov *et al* 1970) in agreement with theoretical predictions (Elliott and Thorpe 1969), and, therefore, the Γ_1^+ component was not investigated. The off-diagonal Raman spectra contained no evidence for magnon peaks that could have been induced by the crystal symmetry being lower than cubic. There is a sharp feature at 136 cm^{-1} in two off-diagonal polarizations that overlaps with the two-magnon band position at low temperatures, but this is clearly a phonon band (Lockwood and Torrie 1974). From a theoretical viewpoint, no off-diagonal two-magnon peak is expected if the crystal has D_{4h} tetragonal symmetry (R A Cowley, private communication).

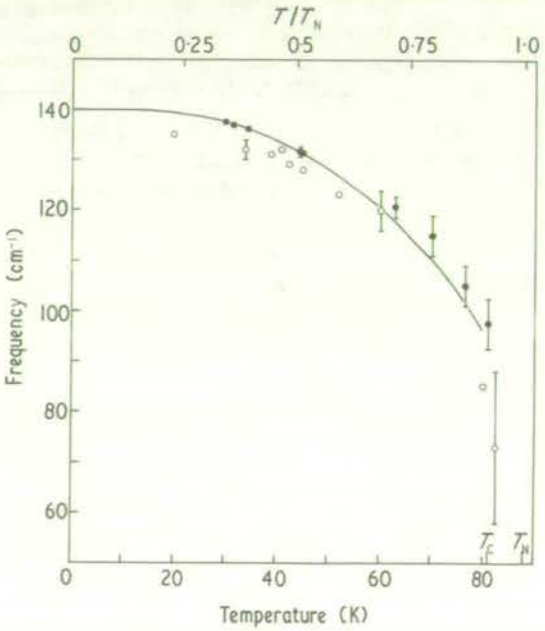

Figure 4. Experimental and theoretical two-magnon peak positions versus temperature for $KMnF_3$. The curve is the theoretical fit to the experimental points (closed circles). The experimental results of Popkov *et al* (1970) are also shown (open circles).

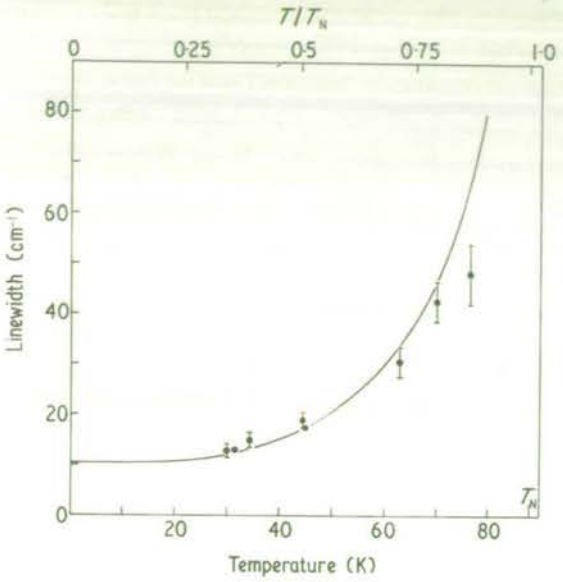

Figure 5. Theoretical curve and experimental points for the two-magnon linewidth (full width at half maximum) against temperature for $KMnF_3$.

The temperature dependence of the two-magnon band was investigated and details of peak position and full width at half maximum were extracted from the spectra after allowing for the background. The background rose sharply at lower energies and was temperature dependent. This background, together with the occurrence of the first-order phase transition at $T_C = 81$ K, made it impossible to study the two-magnon spectrum for temperatures $T > T_C$. The peak position, ω_{pk}, and width of the two-magnon band are plotted as a function of temperature in figures 4 and 5 respectively.

The data obtained for ω_{pk} as a function of temperature were extrapolated to give $\omega_{pk} = 140 \pm 2\,\text{cm}^{-1}$ at 0 K. The zero-temperature calculation for the two-magnon lineshape of Elliott and Thorpe (1969) was evaluated for different values of J and a constant relationship between ω_{pk} and the top of the two-magnon band was found. From this constant, the value of J appropriate to $\omega_{pk} = 140 \pm 2\,\text{cm}^{-1}$ was determined to be $J = 4{\cdot}984 \pm 0{\cdot}072\,\text{cm}^{-1}$.

4. Discussion

The peak frequency and width of the theoretical two-magnon bandshapes as a function of temperature are given in figures 4 and 5 for comparison with the experimental results. As can be seen, the fits are good for temperatures less than 0·8 T_N and even up to 0·9 T_N for the peak-frequency results. Theoretical and experimental values for the width diverge as T_N is approached and this is probably due to a combination of factors: the experimental two-magnon width is difficult to measure at this point because of the

wing-type background due to phonons, and the theoretical expression of Balucani and Tognetti (1973) for calculating the magnon width breaks down.

An even more critical test of the theory was performed for reduced temperatures $T/T_N < 0{\cdot}6$, where figures 4 and 5 show there is excellent agreement with experiment. The spectra given in figures 2 and 3 were least-squares fitted to a function comprising the theoretical two-magnon bandshape for that temperature and two damped simple harmonic oscillators with Bose–Einstein weighting. The background beneath the bands is sloping and was approximated to a straight line without difficulty. The parameters for the two Γ_1 phonons at 130·5 and 147 cm^{-1} were well characterized from a previous study (Lockwood and Torrie 1974) and essentially the only free parameters in the fitting were the strengths of the peaks and the constants appropriate to the background. Some allowance was made for a variation in the widths of the phonons because of the different slit widths used in the measurements: the two-magnon band is broad and did not require a slit-width correction.

Figures 2 and 3 show that the fits obtained were very good. Further confidence in the fit comes from the fact that the strength parameters of the phonons had a similar ratio in both cases.

The results of this work can now be compared with that of Popkov *et al* (1970). Their peak-frequency data are given in figure 4 and follow a similar temperature dependence to that observed here, although their points are consistently below ours. Popkov *et al* do not report on the two-magnon linewidth. It is revealing to examine the experimental spectrum given in their figure 1 recorded with a spectral slit width of 4 cm^{-1} at 20 K. This spectrum has been fitted with a zero-temperature calculation following the theory of Elliott and Thorpe (1969) and the agreement is not good. Further, their spectrum is considerably different from our spectrum recorded at 31·5 K (figure 2). It is apparent from the present work that the diagonal polarizarion spectrum of Popkov *et al* most likely contains considerable scattering intensity from phonons of other polarizations as a result of the presence of crystal strains: Popkov *et al* reported that they did not obtain complete polarization of the spectrum. This fact, coupled with the use of a wider slit width, may account for the differences between their spectra and ours. Popkov *et al* concluded from their data that the maximum magnon energy is 75 cm^{-1}, corresponding to a value of J of 5·0 cm^{-1}; but using the method described earlier, their plot of ω_{pk} against temperature indicates a value around $J = 4{\cdot}8\ cm^{-1}$.

This study of $KMnF_3$ has shown that the theory of Elliott and Thorpe (1969), extended to finite temperatures by Balucani and Tognetti (1973) and others, accurately describes the temperature dependence of the two-magnon Raman spectrum for $T/T_N < 0{\cdot}8$. The goodness of fit confirms that the perovskite cubic-symmetry picture can be used to describe the magnetic ordering in $KMnF_3$ despite the structural distortions and the spin canting for temperatures below 81 K.

The Raman results give a value of $4{\cdot}984 \pm 0{\cdot}072\ cm^{-1}$ for the isotropic exchange constant, which compares favourably with the value of 5·037 cm^{-1} determined from inelastic neutron scattering studies (Cowley and Buyers 1972).

Acknowledgments

We acknowledge helpful discussions with R A Cowley and thank D A Jones for providing the crystal. This work was supported by the Science Research Council.

References

Arthur J W and Lockwood D J 1974 *J. Raman Spectrosc.* **2** 53–69
Balucani U and Tognetti V 1973 *Phys. Rev.* B **8** 4247–57
Chinn S R, Zeiger H J and O'Connor J R 1971 *Phys. Rev.* B **3** 1709–35
Cooper M J and Nathans R 1966 *J. Appl. Phys.* **37** 1041–7
Cottam M G 1972 *J. Phys.* C: *Solid St. Phys.* **5** 1461–74
Cowley R A and Buyers W J L 1972 *Rev. Mod. Phys.* **44** 406–50
Davies R W, Chinn S R and Zeiger H J 1971 *Phys. Rev.* B **4** 992–1004
Elliott R J and Thorpe M F 1969 *J. Phys.* C: *Solid St. Phys.* **2** 1630–43
Fleury P A 1968 *Phys. Rev. Lett.* **21** 151–3
—— 1970 *J. Appl. Phys.* **41** 886–8
Fleury P A and Loudon R 1968 *Phys. Rev.* **166** 514–30
Hidaka M, Ohama N, Okazaki A, Sakashita H and Yamakawa S 1975 *Solid St. Commun.* **16** 1121–4
Lockwood D J and Torrie B H 1974 *J. Phys.* C: *Solid St. Phys.* **7** 2729–44
Moch P and Dugautier C 1973 *Proc. Int. Conf. Magnetism, Moscow*
Natoli C R and Ranninger J 1973 *J. Phys.* C: *Solid St. Phys.* **6** 345–69
Oitmaa J 1971 *Solid St. Commun.* **9** 745–8
Pickart S J, Collins M J and Windsor C G 1966 *J. Appl. Phys.* **37** 1054–5
Popkov Yu A, Fomin V I and Beznosikov B V 1970 *JETP Lett.* **11** 264–6
Saunderson D H, Windsor C G, Briggs G A, Evans M T and Hutchinson E 1972 *Proc. Symp. on Inelastic Scattering, Grenoble*
Scatturin V, Corliss L, Elliott N and Hastings J 1961 *Acta Crystallogr.* **14** 19–26
Thorpe M F 1970 *J. Appl. Phys.* **41** 892–3
Windsor C G and Stevenson R W H 1966 *Proc. Phys. Soc.* **87** 501–4
Yussouff M and Mahanty J 1966 *Proc. Phys. Soc.* **87** 689–701

Solid State Communications, Vol. 18, pp. 115–117, 1976. Pergamon Press. Printed in Great Britain

OBSERVATION OF SOFT MODES IN THE RAMAN SPECTRUM OF FERROELECTRIC $Cr_3B_7O_{13}Cl$

D.J. Lockwood

Physics Department, Edinburgh University, Edinburgh EH9 3JZ, Scotland

(*Received* 25 *July* 1975 *by R. Loudon*)

Raman spectroscopy has been used to establish the existence of two soft modes in the orthorhombic phase of the improper ferroelectric chromium chlorine boracite. The orthorhombic–cubic transition at 263 K is sharply first-order and no "soft" feature was seen in the Raman spectrum of the paraelectric phase. These results confirm the proposed microscopic mechanism for the transition.

CRYSTALS of the boracite family, $M_3B_7O_{13}X$, where M is a divalent metal and X a halogen or chalcogen, have attracted some interest because they exhibit unusual ferroelectric, magnetic and structural properties.[1] Most boracites exhibit a transition from a high temperature paraelectric cubic phase to a ferroelectric phase with orthorhombic symmetry. The symmetry change $T_d^5 \rightarrow C_{2v}^5$ is accompanied by a doubling of the primitive unit cell volume.[1,2] Boracites in the orthorhombic phase are "improper" ferroelectrics[3] – that is, the spontaneous polarisation, P_s, is not the primary order parameter. Thus boracites provide an example of a coupled phase transition where there is more than one order parameter. It has been proposed that the primary order parameter is associated with a doubly-degenerate zone-boundary(X point) mode of vibration in the cubic phase.[4] The degenerate critical modes become homogeneous modes in the orthorhombic phase and split into $A_1 + A_2$. It is anticipated that anharmonic coupling between the A_1 soft mode and a low-frequency A_1 optic mode induces P_s as a secondary order parameter in the ferroelectric phase. Dvorak[5] has suggested that in some boracites P_s arises from direct coupling to the primary order parameter while the spontaneous shear, U_s, arises largely from piezoelectric coupling to P_s. This is opposite to the behaviour in another improper ferroelectric, gadolinium molybdate (GMO), and the isomorphous compound terbium molybdate (TMO), where P_s arises from piezoelectric coupling to U_s.[6,7]

The dynamics of the ferroelectric transition in boracites have not been widely studied and the microscopic mechanism outlined above has not yet been verified. Some measurements on the far infrared spectrum of $Ni_3B_7O_{13}I$ and $Co_3B_7O_{13}I$ have been reported, but no soft mode behaviour was observed.[8] We have undertaken a systematic Raman investigation of the phase changes in boracites, and here we report on results obtained from a study of the paraelectric–ferroelectric transition in $Cr_3B_7O_{13}Cl$ (Cr–Cl). Two soft modes have been found in the ferroelectric phase, providing the first confirmation of the proposed microscopic mechanism for the cubic–orthorhombic transition.

The two 1 mm^3 crystals of Cr–Cl used in this study were the ones described in a previous paper.[9] Raman spectra were obtained using the equipment and techniques reported earlier:[9] spectra were excited with 600 mW of argon laser light at 488.0 nm and recorded using a spectral slit width of 3 cm^{-1}. The Cr–Cl sample was mounted on the cold finger of an Oxford Instruments flow cryostat; a Au/Fe–chromel thermocouple mounted on the sample monitored the crystal temperature, which was controlled to within 0.1 K. The directions X, Y and Z which are used to denote the various polarisations refer to the principal cubic axes of the crystal

The Raman spectrum of Cr–Cl was measured at

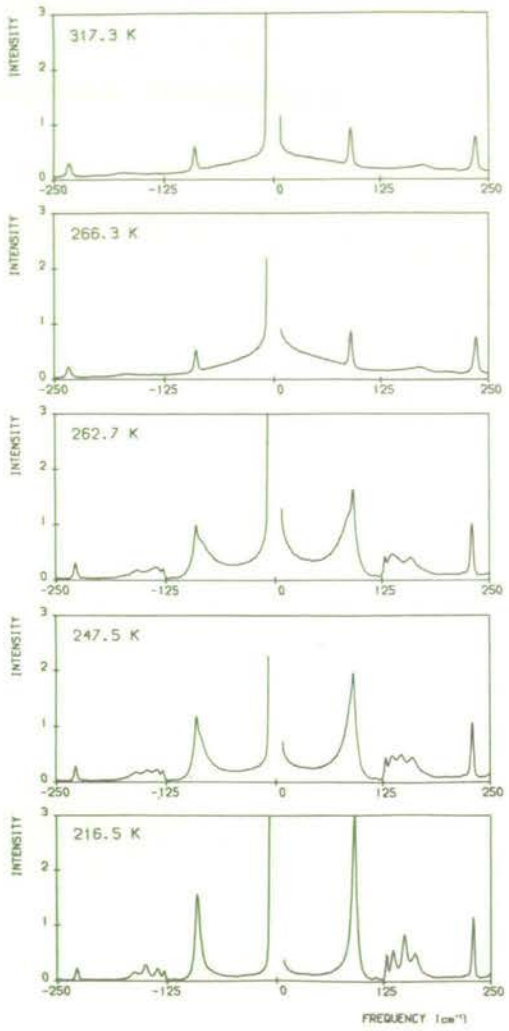

FIG. 1. The low frequency $Z(YY)X$ Raman spectrum of Cr–Cl boracite at temperatures above and below T_c.

temperatures in the range $T_c - 50$ to $T_c + 50$ K, where $T_c = 263$ K.[10] Typical results for the $Z(YY)X$ polarisation are shown in Fig. 1. The Raman-active modes in the cubic phase transform as $4A_1 + 10E + 19F_2$ and in the orthorhombic phase as $71A_1 + 72A_2 + 71B_1 + 72B_2$; Fig. 1 shows only a few of these predicted modes. Above T_c, the YY spectrum contains information about both the A_1 and E modes. The A_1 component alone can not be measured directly in any scattering geometry, but the E-symmetry scattering is accessible using a crystal with faces cut perpendicular to [001], [110] and [1$\bar{1}$0].[9] One crystal had this orientation and was used to study the temperature dependence of the E spectrum. Domains are formed when the crystal enters the ferroelectric phase, and group theory indicates that there are 24 possible domain orientations although only six of these will affect the Raman results. Different sets of domains were formed each time the sample was taken through the transition; in the case of the spectra shown in Fig. 1, two sets of domains dominated in which P_s was either along or oppositely directed to Z or Y. Two of the orthorhombic phase unit cell axes are at 45° to the corresponding cubic ones and the scattering tensors need to be corrected for this rotation. It turns out that the spectra given in Fig. 1 for $T < T_c$ show features with $A_1 + A_2$ symmetry.

Above T_c, the A_1 and E modes[9] exhibit no temperature-dependence, and this agrees with the results of the infrared measurements on Co–I.[8] At T_c, there is a marked and abrupt change in the spectrum, as can be seen in Fig. 1: numerous new bands are observed in all polarisations. This confirms the first-order nature of the ferroelectric transition in Cr–Cl, as is required by the form of the free energy.[4] Spectral features sharpen and some mode interaction is evident when the temperature is further lowered, but most band frequencies remain constant. Two soft modes are evident in the YY spectra for $T < T_c$: the bands are at 91 and 149.5 cm^{-1} respectively for temperatures well below T_c and soften to ~ 85 and ~ 138 cm^{-1} respectively at the transition. These modes have the expected A_2/A_1 symmetry, and the anisotropy in the low-temperature limit is 0.61. A wing feature present in the cubic phase A_1 spectrum[9] finally disappears at around $T_c - 50$ K.

The spectra of Fig. 1 show that there is interference between the soft modes and other phonons, which makes it difficult to extract the temperature dependence. However, the temperature dependence of both soft modes is in qualitative agreement with theoretical predictions[3] and with the results of birefringence measurements on Cr–Cl.[10] The temperature dependence of the soft modes is similar to that found for the A_1 soft mode in GMO,[11] but here the modes do not become overdamped.

These results confirm the proposed mechanism for the transition in which a doubly-degenerate zone-boundary mode softens and then becomes two distinct zone-centre modes in the ferroelectric phase. The optic mode that is responsible for P_s has not

been identified at this stage: some knowledge of the normal mode coordinates is needed, especially along the ferroelectric axis, and this is a difficult, if not impossible, problem to solve for such a complex crystal structure. The presence of the wing feature could indicate some kind of dynamic disorder, or it may arise from higher-order scattering from low-frequency optic-mode branches. Work is in progress to clarify the origins of this wing feature and to further study the dynamics of the ferroelectric phase transition in Cr–Cl and in other boracites.

Acknowledgements – I am grateful to H. Schmid for the samples of Cr–Cl boracite and for invaluable advice, to W. Cochran, R.A. Cowley and R.J. Nelmes for helpful discussions, and to F.R. Thornley for verifying the sample orientation with X-rays. This work was supported by the Science Research Council and the Battelle Institute, Geneva.

REFERENCES

1. NELMES R.J., *J. Phys. C.: Solid State Phys.* 7, 3480 (1974).
2. NELMES R.J. & THORNLEY F.R., *J. Phys. C.: Solid State Phys.* 7, 3855 (1974).
3. DVORAK V., *Czech. J. Phys.* **B21**, 1250 (1971).
4. DVORAK V & PETZELT J., *Czech. J. Phys.* **B21**, 1141 (1971).
5. DVORAK V., *J. Phys., Paris* **33** suppl. **C2**, 89 (1972).
6. PYTTE E., *Solid State Commun.* 8, 2101 (1970).
7. DORNER B., AXE J.D. & SHIRANE G., *Phys. Rev.* **B6**, 1950 (1972).
8. PETZELT J. & MAYEROVA I., *Czech. J. Phys.* **B23**, 1277 (1973).
9. LOCKWOOD D.J., *J. Raman Spectrosc.*, 2, 555 (1974).
10. SCHMID H. (private communication).
11. FLEURY P.A., *Solid State Commun.* 8, 601 (1970).

Ferroelectrics
1976, Vol. 12, pp. 113–115

THE RAMAN SPECTRUM OF LEAD GERMANATE

W. TAYLOR, D. J. LOCKWOOD, J. W. ARTHUR and T. J. HOSEA

Physics Department, University of Edinburgh, Edinburgh EH9 3JZ, Scotland

(*Received September 22, 1975*)

The complete Raman spectrum of both the ferroelectric and paraelectric phases of lead germanate ($Pb_5Ge_3O_{11}$) has been recorded for the first time. As expected from group theory, several A symmetry modes disappear at the phase transition. The absence of TO–LO splitting has been verified by forward and back scattering experiments.

A careful study has been made of the A symmetry ferroelectric soft mode which becomes overdamped at 390 K. Above this temperature the spectrum can be successfully fitted to a Debye function, yielding a relaxation time which rises to a value of 10^{-11} s near T_c.

INTRODUCTION

Lead germanate is ferroelectric at room temperature with space group $P3$.[1] Above the Curie temperature (T_c) at 178°C it becomes paraelectric with space group $P\bar{6}$ [2] gaining a mirror plane perpendicular to the c-axis as a result of a partial rotation of a GeO_4 tetrahedron and a small c-axis displacement of one of the lead atoms.

We report here the first observations of the complete Raman spectrum in both phases.

GROUP THEORY

If no simplifying assumptions are made we expect $57A + 57E$ modes in the ferroelectric phase and $30A' + 32E' + 27A'' + 25E''$ in the paraelectric phase, the A modes branching to A' and A'' (Raman inactive) and the E modes to E' and E''. Separating these modes into internal and external yields $27A + 27E$ lattice modes and $30A + 30E$ molecular modes in the ferroelectric phase.

The structure contains chains of GeO_4 tetrahedra along the c-direction with some pairs of tetrahedra linked by a common oxygen atom to form Ge_2O_7 "molecules." However, it is simplest to regard the structure as containing only GeO_4 molecules plus intervening lead atoms. In this case we have only $3A + 3E$ internal modes due to the GeO_4 in the absence of molecular field splitting, or just 6 distinct frequencies compared to the four frequencies $A_1 + E + 2F_2$ in the free state.

RESULTS

The crystal is both birefringent and optically active, the result of this being to mix the Raman tensor elements when either the incident or scattered light is parallel to the z axis. The only orientations in which mixing should be absent are those of type $x(\ )y$. The A'' and E' modes are infrared active and are therefore liable to exhibit TO–LO splitting which may be evident in the corresponding A and E modes in the ferroelectric phase.

The spectrum of most interest is $x(zz)y$ which corresponds to A_{TO} modes and includes the ferroelectric soft mode. This is shown in Figure 1a in which we see two groups of peaks—one from 0 to 500 cm^{-1} of presumably mainly lattice modes and the other from 600 to 900 cm^{-1} which is likely to contain only internal modes. The E mode spectra $x(zx)y$, $x(yz)y$ and $x(yx)y$ are not identical since different tensor elements are involved in each case. We show here only the $x(zx)y$ spectra (Figure 1c–1d)—full details of the spectra and frequencies will be published elsewhere.

In the low frequency region, modes in the A spectrum are coincident with modes in the E spectrum. This may indicate that the structure is nearly isotropic to some lattice vibrations.

The E mode spectra were expected to contain both LO and TO components but a back scattering experiment showed little evidence of this. Similarly, a forward scattering experiment, $x(zz)\bar{x}$, which should contain A_{LO} modes, gave the same spectrum as the $x(zz)y$ configuration (A_{TO}) thus confirming the absence of TO–LO splitting for these modes also.

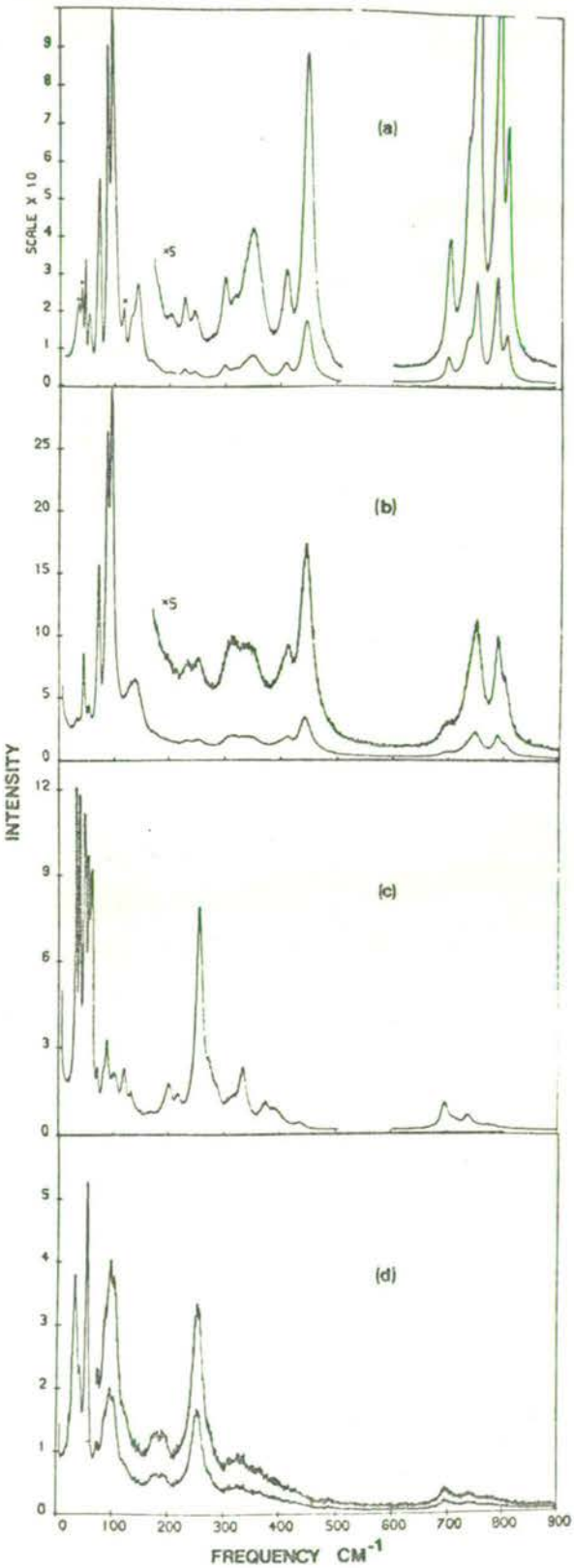

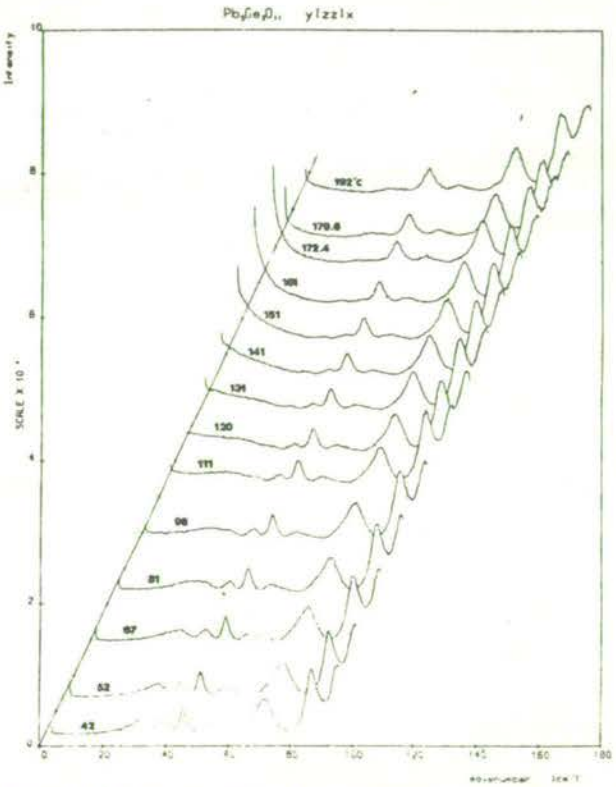

FIGURE 2 Variation of the low frequency A_{TO} spectrum with temperature.

The group of peaks around 700 to 800 cm^{-1} corresponds to some of the frequencies observed generally for XY_4 molecules such as GeO_4. The strong lines at 254 cm^{-1} in the E spectrum and 444 cm^{-1} in the A spectrum also probably belong to GeO_4. The $3A + 3E$ modes, expected for the molecule in this crystal, can be tentatively assigned to these peaks. These internal modes are not expected to change markedly on passing through the transition, and this is borne out in the observed spectra.

In the $x(zz)y$ spectra, several peaks (marked "x" in Figure 1a) disappear at the transition. This is to be expected from the group theory for those modes which become A''–Raman inactive.

The A_{TO} soft ferroelectric mode, which lies at 34 cm^{-1} in the toom temperature spectrum, shifts to lower frequency and broadens as the temperature is raised (Figure 2). At about 390 K the mode becomes overdamped and as the temperature is further

FIGURE 1 Representative spectra in the ferroelectric and paraelectric phases. (a) $x(zz)y$ below T_c–A modes. (b) $x(zz)y$ above T_c–A' modes. (c) $x(zx)y$ below T_c–E modes. (d) $x(zx)y$ above T_c–E'' modes.

raised the wing narrows and increases in intensity, reaching a maximum at T_c. Above T_c the intensity falls away more rapidly.

Ryan and Hisano[3] have attempted to fit this spectrum from 5 to 50 cm^{-1} with a simple coupled oscillator function and also with a more complicated coupled anharmonic phonon function due to Cowley and Coombs.[4] In a preliminary analysis we find that is is possible, however, to obtain a satisfactory fit over the range 4 to 75 cm^{-1} with a function consisting of uncoupled simple harmonic oscillators together with a Debye relaxation term to describe the overdamped wing. No arbitrary constraints on the parameters are required to obtain a satisfactory fit.

The value of relaxation time obtained from this procedure varies in a roughly linear fashion from 2×10^{-12} s at 414 K to 10^{-11} s near the transition. Above the transition the relaxation time falls again to about 2×10^{-12} s at 470 K. Recent neutron scattering experiments[5] indicate the presence of an unresolved quasi-elastic scattering over a wide range of temperature around T_c and of frequency less than 0.8 cm^{-1}. It seems possible that the scattering observed in the Raman spectrum is also unresolved quasi-elastic scattering near T_c. We are, therefore, currently studying the frequency region below 1 cm^{-1} by Fabry-Perot spectroscopy. We believe lead germanate to be a favourable crystal in which to observe a critical scattering peak of the kind observed in KH_2PO_4[6] which undergoes a nearly second-order ferroelectric transition.

ACKNOWLEDGMENTS

We thank H. Vass for technical assistance, the Science Research Council for financial support and the Royal Radar Establishment for samples.

REFERENCES

1. Y. Iwata, H. Koizumi, N. Koyano, I. Shibuya and N. Niizeki, *J. Phys. Soc. Japan* 35, 314 (1973).
2. Y. Iwata, N. Koyano and I. Shibuya, *J. Phys. Soc. Japan* 35, 1269 (1973).
3. J. F. Ryan and K. Hisano, *J. Phys.* C6, 566 (1973).
4. G. J. Coombs and R. A. Cowley, *J. Phys.* C6, 121 (1973).
5. R. A. Cowley and J. D. Axe, private communication.
6. N. Lagakos and H. Z. Cummins, *Phys. Rev.* B10, 1063 (1974).

Ferroelectrics
1976, Vol. 13, pp. 353–354

RAMAN SPECTRAL STUDY OF THE FERROELECTRIC PHASE TRANSITION IN BORACITES

D. J. LOCKWOOD

Physics Department, Edinburgh University, Edinburgh EH9 3JZ, Scotland

(Received September 22, 1975)

The dynamics of the cubic-to-orthorhombic ferroelectric transition in $Cr_3B_7O_{13}Cl$ have been investigated using Raman spectroscopy. Two soft modes were found in the ferroelectric phase. The integrated intensity of a wing feature in the A_1 spectrum exhibits a temperature dependence that is remarkably similar to the dielectric constant behaviour in other boracites. The Raman spectrum of single-domain orthorhombic $Mn_3B_7O_{13}Cl$ is reported for comparison purposes.

Most boracites, $M_3B_7O_{13}X$, where M is a divalent metal and X a halogen, become ferroelectric at some temperature.[1] The improper[2] first-order transition is from the high temperature phase of cubic (T_d^5) symmetry to an orthorhombic (C_{2v}^5) phase, with a concomitant doubling of the primitive unit cell volume. The primary order parameter is associated with a doubly-degenerate zone-boundary (X-point) mode of vibration in the cubic phase; this mode transforms into two separate homogeneous modes in the orthorhombic phase.[3,4]

We have measured the Raman spectrum of chromium chlorine boracite (Cr-Cl) in both phases[4-6] and of single domain Mn-Cl in the orthorhombic phase.[6] The Raman spectra were excited with 600 mW of argon laser light at 488.0 nm and the light scattered at 90° was analysed using a double monochromator. A digitized data collection system enabled direct computer processing of the results. The sample temperature was controlled to within 0.1 K for the temperature dependent studies of Cr-Cl.

The Raman-active modes in the cubic phase transform as $4A_1 + 10E + 19F_2$ and in the orthorhombic phase as $71A_1 + 72A_2 + 71B_1 + 71B_2$. All of the 33 Raman-active modes in the cubic phase have been observed for Cr-Cl, but only about one-half of the 285 modes were found in the orthorhombic phases of Cr-Cl and Mn-Cl: only a few of the modes that are simultaneously infrared active exhibit *TO-LO* splittings. The lowest-frequency modes observed in Mn-Cl were at 76 cm^{-1} in off-diagonal polarisation and at 110 cm^{-1} in diagonal polarisation: these frequencies were measured at room temperature, which is well below $T_c = 680$ K. The Raman spectrum of Cr-Cl was measured at different temperatures in the range $T_c - 50$ to $T_c + 50$ K, where $T_c = 263$ K. Above T_c, the A_1, E and F_2 modes exhibit no temperature dependence, and the odd-shaped low-frequency (0 – 85 cm^{-1}) feature in the F_2 spectrum[6] is only weakly temperature dependent. At T_c, there is a marked and abrupt change in the spectrum, confirming the first-order nature of the transition:[3] the F_2 low-frequency feature collapses and numerous new bands are observed in all polarisations. At $T_c - 50$ K, the Cr-Cl spectrum is similar in appearance to the Mn-Cl spectrum, with the lowest-frequency band at 72 cm^{-1}. Two temperature dependent modes of A_2/A_1 symmetry were found in the orthorhombic phase Cr-Cl spectrum and they are at 91 and 149.5 cm^{-1} respectively for temperatures well below T_c, softening by only a few cm^{-1} at the transition.[4] The temperature dependence of the soft modes is in qualitative agreement with theoretical predictions[2] and these results[4] provide the first confirmation of the proposed microscopic mechanism for the cubic-orthorhombic transition.[3]

The A_1 spectrum of cubic Cr-Cl exhibits a wing feature[5] that persists in the orthorhombic phase and finally disappears at around $T_c - 50$ K. The temperature dependence of the wing feature has been investigated in detail. An earlier study at room temperature indicated that the wing fitted equally well to either a Debye or a damped simple harmonic oscillator model.[6] The Debye model was arbitrarily chosen for this study and the function $I(\omega) = S\gamma^2\omega[\bar{n}(\omega) + 1]/(\omega^2 + \gamma^2)$ was least squares fitted to the data[4] over the range 20 – 110 cm^{-1}. S is the strength of the band, γ the damping constant and $\bar{n}(\omega)$ the usual Bose-Einstein factor evaluated at frequency ω. The phonons present at higher frequencies were included in the fitting as damped harmonic oscillators, and the background,

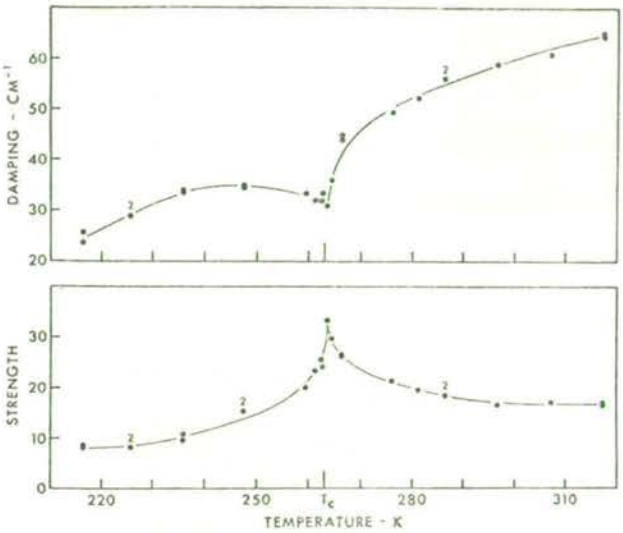

FIGURE 1 Temperature dependence of S and γ. The lines are drawn as a guide for the eye and the symbol 2 denotes two identical points.

determined from the high frequency region, was held constant at the one value for all spectra. The values obtained for S and γ are plotted in Figure 1. The Debye model fitted the wing feature very well, especially for $T > T_c$: for temperatures below T_c it was difficult to accurately account for the phonons at ~90 cm^{-1} because of the interference between modes. The integrated intensity of a Debye wing is $S\gamma\pi/2$ and this quantity is plotted in Figure 2. It is noteworthy that despite the considerable change in S and γ with temperature the integrated intensity is almost a constant for $T > T_c$.

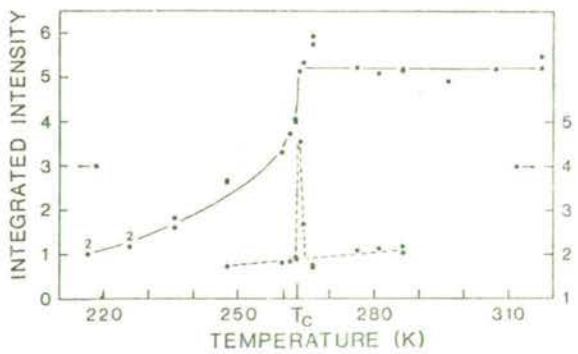

FIGURE 2 Temperature dependence of the Debye-wing integrated intensity (•) and of the central-peak integrated intensity (♦). The central-peak to Debye scale ratio is ~10^4.

For temperatures close to T_c it was found that there was a significant increase in intensity in the A_1 spectrum for frequencies < 20 cm^{-1}. This first showed up from the Debye-model fitting procedure, and was confirmed by an examination of the central peak intensity. The central peak intensity was integrated over the frequency interval -3 to $+3$ cm^{-1}, which corresponds to the complete band-pass of the spectrometer when set at zero cm^{-1} assuming an ideal triangular-shaped transfer function (the spectral slit width was 3 cm^{-1}). The results are shown in Figure 2 where it can be seen that the central peak intensity is practically temperature independent except for the sharp (2.5 x) increase in intensity for temperatures close to T_c. Ideally, the two plots in Figure 2 should be added together to give the total response at low frequencies, but the scales are such that the Debye contribution is swamped by the high central-peak intensity. (A major portion of this intensity most likely arises from stray light). It is not certain at this stage if the increase in intensity of the central peak at T_c is a real effect; it may be due to the formation of domains.

The wing feature may arise from higher-order scattering processes, or it could indicate some kind of dynamic disorder. The temperature dependence shown in Figure 2 is similar to that found for the dielectric constant in Ni-Cl, Co-Br and Co-I.[7,8] If the Debye intensity did scale with the as yet unmeasured dielectric constant of Cr-Cl then this would indicate that the wing arises predominantly from one-phonon scattering.

ACKNOWLEDGEMENTS

We wish to acknowledge helpful discussions with Dr. H. Schmid and thank him for providing the crystals. This work was supported by the Science Research Council and the Battelle Institute, Geneva.

REFERENCES

1. R. J. Nelmes, *J. Phys. C* 7, 3840 (1974).
2. V. Dvořák, *Czech. J. Phys. B* 21, 1250 (1971).
3. V. Dvořák and J. Petzelt, *Czech. J. Phys. B* 21, 1141 (1971).
4. D. J. Lockwood, *Solid State Comm.* 18, 115 (1976).
5. D. J. Lockwood, *J. Raman Spectrosc.* 2, 555 (1974).
6. D. J. Lockwood, paper 3.27, Fourth International Conference on Raman Spectroscopy, Brunswick, Maine (1974).
7. E. Ascher, H. Schmid and D. Tar. *Solid State Commun.* 2, 45 (1964).
8. F. Smutný and J. Fousek, *Phys. Stat. Sol.* 40, K13 (1970).

J. Phys. C: Solid State Phys., Vol. 9, 1976. Printed in Great Britain.

21

Lattice dynamics of the ordered vacancy compound $HgIn_2\square Te_4$

A Miller†, D J Lockwood‡, A MacKinnon† and D Weaire†
†Department of Physics, Heriot-Watt University, Edinburgh, EH14 4AS, Scotland
‡Department of Physics, University of Edinburgh, Edinburgh EH9 3JZ, Scotland

Received 30 March 1976

Abstract. $HgIn_2\square Te_4$ has a structure which may be regarded as being derived from that of zincblende by the incorporation of an ordered array of vacancies. The $k = 0$ vibrational modes of this compound have been studied using infrared reflectivity and Raman scattering measurements, the latter using Brewster-angle geometry. A semi-empirical theoretical model of the Keating type achieves a reasonable fit to the observed mode frequencies as well as the elastic constant data of Saunders and Seddon, and is used to predict dispersion relations. Qualitative features of the spectrum related to the role of the vacancy are discussed.

1. Introduction

Among the various families of tetrahedrally bonded compound semiconductors, there are some in which the crystal structure may be regarded as being derived from zincblende (or, in some cases, wurtzite) by the incorporation of an ordered array of vacancies. An example of such a compound is $HgIn_2\square Te_4$, the symbol $\square$ denoting the vacancy. Note that if the vacancy is treated as an atom of zero valence, then the Grimm–Somerfeld rule, which demands an average of four valence electrons per atom, is obeyed (Parthé 1964).

The above compound is one of a series intermediate between HgTe, in which every tetrahedral site is filled, and In_2Te_3 (or $In_2\square Te_3$), in which one in every six sites in unfilled. This series has been chosen by Saunders and Seddon (1970, 1976) for an investigation of the influence of the vacancies on various properties, including elastic constants.

We have chosen $HgIn_2\square Te_4$ for an investigation of lattice vibrational properties since it has a comparatively simple structure with seven atoms (i.e. eight tetrahedral sites) per unit cell (see figure 1). The vacancies form a body-centred tetragonal lattice. There has been some uncertainty in the past regarding the arrangement of Hg and In atoms. One possibility (Parthé 1964, Hahn *et al* 1955) may be called *defect chalcopyrite*, because of its close relationship to the chalcopyrite structure. This has symmetry $I\bar{4}$. The second possibility (Saunders and Seddon 1976) has symmetry $I\bar{4}2m$ and may be appropriately dubbed *defect stannite* to indicate its relationship to the stannite structure. Recent work on our material has firmly established the Laué group to be $4/mmm$ (F N Laird and R J Nelmes, private communication) so we believe the $I\bar{4}2m$ space group to be the correct alternative for our samples, figure 1. There is very little tetragonal compression, the axial ratio being close to its ideal value of 2·0.

We have performed infrared reflectivity and Raman scattering measurements, which, together with Saunders and Seddon's results for the elastic constants, furnish a considerable body of data which one may attempt to fit with appropriate semi-empirical models.

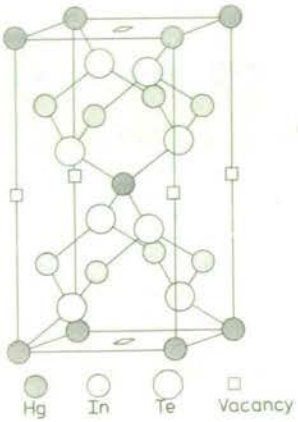

Figure 1. $HgIn_2\square Te_4$, $I\bar{4}2m$ structure.

In the only comparable previous work, that of Finkman *et al* (1975) on In_2Te_3, the attempt at analysis was in terms of the *folding* of dispersion relations appropriate to zincblende into the smaller Brillouin zone of the compound. This procedure, which has been widely used for the chalcopyrite compounds (in which there are no vacant sites), is highly questionable in the present case. It is, however, an interesting first approximation, and one of the calculations which we have performed is intended to indicate how the folded zincblende spectrum evolves when the mass and force constants associated with an ordered array of atoms are continuously reduced to zero to form a defect structure. A semi-empirical Keating model (i.e. bond bending and stretching forces only) was used. In addition, we have performed a calculation of the $\boldsymbol{k} = 0$ modes and elastic constants of $HgIn_2\square Te_4$ in the defect stannite structure, $I\bar{4}2m$. In this way, an approximate fit has been made to all of the available data using adjustable force constants.

Dispersion relations have been calculated using these force constants. While it would be difficult to investigate the dispersion relations for this particular compound by conventional neutron scattering techniques, there are closely related compounds with the $I\bar{4}2m$ and $I\bar{4}$ structures for which such a measurement should be feasible.

2. Group theory and selection rules

The $HgIn_2\square Te_4$ crystal used in this work has a body-centred tetragonal structure with the symmorphic space group $I\bar{4}2m$. There is one formula unit, i.e. 7 atoms, per unit cell, corresponding to 21 degrees of freedom. The character table for lattice vibrational modes at $\boldsymbol{k} = 0$ is given in table 1. This shows that the 18 optical modes may be associated with 5 irreducible representations in the combination $2A_1 + 1A_2 + 2B_1 + 3B_2 + 5E$. The E modes are doubly degenerate. All but the A_2 modes are Raman-active, while only the B_2 and E modes are infrared-active, having dipole moments in the z direction and in

Table 1. Character table for $k = 0$ modes of defect stannite with point group $\bar{4}2m$.

	E	C_2	$2S_4$	$2C_2'$	$2\sigma_d$	N_{opt}	N_{ac}	Activity	Symmetry
A_1	1	1	1	1	1	2		Raman	$x^2 + y^2, z^2$
A_2	1	1	1	−1	−1	1		Inactive	
B_1	1	1	−1	1	−1	2		Raman	$x^2 - y^2$
B_2	1	1	−1	−1	1	3	1	IR, Raman	z; xy
E	2	−2	0	0	0	5	1	IR, Raman	(x, y); (xz, yz)

the xy plane, respectively. This should give rise to TO–LO splittings for B_2 and E vibrational energies. The Raman tensors for the $\bar{4}2m$ point group are

$$A_1 \quad \begin{bmatrix} a & . & . \\ . & a & . \\ . & . & b \end{bmatrix} \qquad B_1 \quad \begin{bmatrix} c & . & . \\ . & -c & . \\ . & . & . \end{bmatrix} \qquad B_2\,(z) \quad \begin{bmatrix} . & d & . \\ d & . & . \\ . & . & . \end{bmatrix} \qquad E\,(x, y) \quad \begin{bmatrix} . & . & . \\ . & . & e \\ . & e & . \end{bmatrix} \quad \begin{bmatrix} . & . & e \\ . & . & . \\ e & . & . \end{bmatrix}.$$

The defect stannite structure ($I\bar{4}2m$) is closely related to the stannite ($I\bar{4}2m$), chalcopyrite ($I\bar{4}2d$) and defect chalcopyrite ($I\bar{4}$) structures. It is therefore worthwhile making some group theoretical comparisons. All four structures are derived from zincblende by an ordering of different species of atom on the cation sublattice. On the anion sublattice, identical atoms occupy all sites. All four structures are body-centred tetragonal and therefore have the same Brillouin zone, which is related to that of the corresponding zincblende structure, as shown in figure 2 for the case of the ideal axial ratio ($c/a = 2{\cdot}0$).

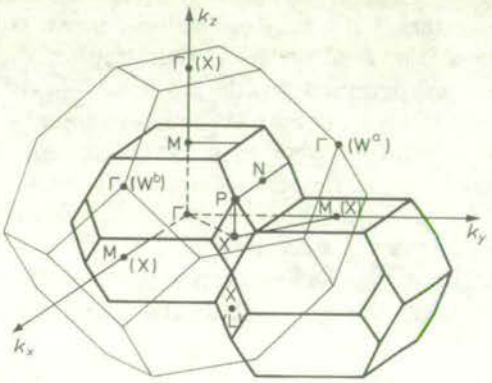

Figure 2. Face-centred cubic and body-centred tetragonal Brillouin zones for $c = 2a$. Symmetry lines are

Γ–M: $\Lambda(00\alpha)$	X–M: Y
Γ–M: $\Sigma(\alpha 00)$	X–P: W
Γ–X: $\Delta(\alpha\alpha 0)$	P–N: Q.

Face-centre cubic symmetry points are shown in parenthesis.

It can be seen that the Γ(000), X(001), $W^a(01\frac{1}{2})$ and $W^b(10\frac{1}{2})$ points of zincblende all correspond to Γ(000) of the smaller Brillouin zone. The notation of figure 2 follows Lax (1974).

Chalcopyrite and stannite structures have 8 atoms per unit cell and have the same point group, $\bar{4}2m$. There are thus 21 optical zone-centre modes. In the case of chalcopyrite, these occur in the combination $1A_1 + 2A_2 + 3B_1 + 3B_2 + 6E$ and may be individually associated with Γ-, X- and W-point phonons of zincblende if the masses and force constants are similar in both structures. In particular, X_1, X_3 and X_5 zincblende phonons have A_2, B_1 and E irreducible representations in chalcopyrite, respectively. This association, although somewhat obscured in practice by large differences in masses and force constants, has proved invaluable in the qualitative interpretation of spectra for chalcopyrite crystals (Holah *et al* 1974).

The same would be true of the quaternary stannite structure (e.g. Cu_2FeSnS_4) if the cation masses and force constants were similar. In this case the space group is symmorphic and C_2' and σ_d operations do not have a non-primitive lattice translation associated with them, as in chalcopyrite. Thus X_1, X_3 and X_5 zincblende phonons have A_1, B_2 and E irreducible representations, respectively, and the zone-centre phonons comprise $2A_1 + 1A_2 + 2B_1 + 4B_2 + 6E$.

In order to consider the effect of the reduction in the number of atoms in the defect stannite unit cell, one may imagine the I_2–II–IV–VI_4 stannite structure with the group IV atoms missing. This reduces the number of degrees of freedom by three, with the effect that a B_2 and a doubly-degenerate E mode are lost. In the case of the defect chalcopyrite structure, the removal of the atom would reduce the symmetry to $I\bar{4}$. The 18 optical zone-centre modes then comprise 3A + 5B + 5E representations, all of which are Raman-active with the B and E modes infrared-active.

3. Infrared reflectivity

A Bridgman-grown single crystal of $HgIn_2\square Te_4$ of size $10 \times 5 \times 2{\cdot}4\,mm^3$ was kindly supplied by T Seddon and G Saunders, University of Durham. It was cut with a large (100) face and a smaller (001) edge. The final surface preparation for the infrared and Raman measurements was with 1 μm diamond powder on paper backed by flat glass, and the orientation checked by the Laué x-ray back-reflection technique.

The infrared reflectivity measurements were made at room temperature on a Beckman–RIIC FS 720 interferometer in the range 40–400 cm^{-1}. The reflectance module allowed an angle of incidence of 10°; this does not introduce a significant error into the analysis, which assumed normal-incidence Fresnel equations. A grid polarizer was used to polarize the incident radiation parallel and perpendicular to the crystal *c* axis. Reflectance measurements were made from both (100) and (001) faces; the spectral resolution was 4 cm^{-1}.

Figures 3(*a*) and (*b*) show the infrared reflectivity results for radiation polarized parallel (B_2 modes) and perpendicular (E modes) to the *c* axis. Two strong oscillators can be seen in both cases; those with B_2 irreducible representations are sharper and at slightly higher energies than those with E representations.

The data was analysed by combining the Fresnel equation for reflection

$$R = \left| \frac{[\epsilon(\nu)]^{1/2} - 1}{[\epsilon(\nu)]^{1/2} + 1} \right|^2 \tag{1}$$

with an independent harmonic oscillator equation for the dielectric constant

$$\epsilon(\nu) = \epsilon'(\nu) + i\epsilon''(\nu) = \epsilon_\infty + \sum_{j=1}^{2} \frac{S_j}{\nu_j^2 - \nu^2 - i\gamma_j\nu} \tag{2}$$

in a least-squares fitting computer program (Peckham 1970). $\nu_j(\mathrm{cm}^{-1})$, $S_j(\mathrm{cm}^{-2})$ and $\gamma_j(\mathrm{cm}^{-1})$ are the resonant frequency, strength and damping factor, respectively, of the jth oscillator, and ϵ_∞ is the high-frequency dielectric constant due to electronic contributions and is also allowed to vary in the computer fitting. The calculated real and imaginary

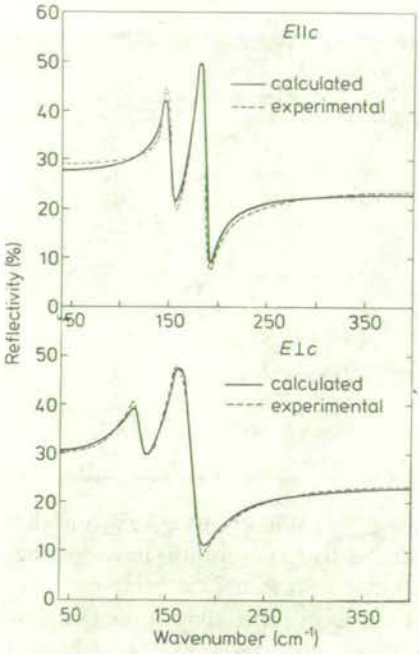

Figure 3. Infrared reflectivity for B_2 and E modes and classical oscillator dispersion fits.

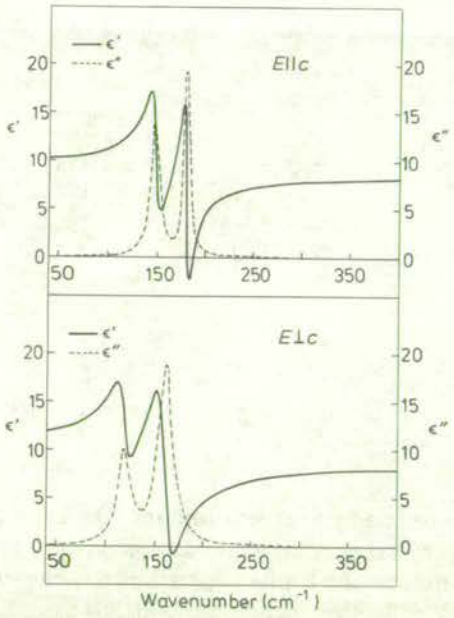

Figure 4. Calculated real and imaginary parts of the dielectric constants for B_2 and E modes.

parts of the dielectric constants are shown in figures 4(*a*) and (*b*). The maximum values of $\epsilon''(\nu)$ are close to the resonant frequency, ν_j, associated with the TO frequencies. The values of the related longitudinal optical frequencies are obtained when $\epsilon'(\nu) = 0$. Where $\epsilon'(\nu)$ does not reach zero, the minimum value is used. Table 2 gives a compilation of the infrared results for the observed B_2 and E modes. The low-frequency dielectric constants were calculated using the Lyddane–Sachs–Teller (1941) relationship.

4. Raman scattering

The Raman measurements were carried out on a Spex 1400 plus TTM triple-grating monochromator with a thermoelectrically-cooled RCA C31034A photomultiplier detector. The spectrometer and detection system were under automatic control (Arthur and Lockwood 1974) and produced the spectrum in a digital form suitable for direct

Table 2. Experimental and calculated results for $HgIn_2\square Te_4$.

Irred. rep. (§ 2)	Infrared (§ 3)				Raman (§ 4)		Calculated (§ 5)
					ν (cm^{-1})		ν (cm^{-1})
A_1 (Γ_1)	Inactive				100		99
					132		140
A_2 (Γ_2)	Inactive				Inactive		114
B_1 (Γ_3)	Inactive				~50		57
					155		158
	ν_{TO}(cm^{-1})	ν_{LO}(cm^{-1})	S(cm^{-2})	γ(cm^{-1})	ν_{TO}	ν_{LO}	ν_{TO}
	—					74	58
B_2 (Γ_4)	147	153	2.1×10^4	10·2	—	152	139
	180	184	2.2×10^4	6·6	184	189	181
$\epsilon_\infty = 8.53$							
$\epsilon_{(0)} = 9.64$							
	—					42	50
	—					61	57
E (Γ_5)	118	127	1.6×10^4	15·5	122	—	132
	160	169	5.2×10^4	18·4	162	—	160
	—	—			181	188	179
$\epsilon_\infty = 8.57$							
$\epsilon_{(0)} = 11.06$							

processing by a large computer. The band gap of $HgIn_2\square Te_4$ is at about 0·9 eV, and thus the crystal is opaque to the visible wavelengths produced by the common laser sources. Therefore, the Raman spectrum was measured in reflection. In initial experiments using back-reflection techniques, various laser lines were tried in order to determine the most suitable exciting frequency. The 488·0 and 514·5 nm lines of the argon laser were heavily absorbed by the crystal and no Raman spectrum could be observed; the He–Ne 632·8 nm laser line and the 568·2, 647·1, 676·4, 752·5 and 799·3 nm lines of the krypton laser produced a weak Raman signal. Contrary to expectation, the longer-wavelength lines of the Kr laser produced less signal than the shorter-wavelength red lines, the signal produced by the 799·3 nm line being about one-tenth of that produced by the 647·1 and 676·4 nm lines. This result indicates that there must be a dip in the absorption spectrum at around 650 nm, and accordingly the 676·4 nm line of Kr was used for the further studies reported here. The laser line was filtered using a double-prism monochromator of the Claassen *et al* (1969) type in order to eliminate plasma lines from the spectrum, and the power at the sample surface was 60 mW. At higher laser powers, ~100 mW, surface damage was produced through local heating. An argon gas jet was directed at the crystal along the line of the laser beam to help cool the crystal surface and to eliminate the Raman scattering from air. All measurements were carried out at room temperature using a spectral resolution of 3·5 cm^{-1}.

Measurements using the 180°-scattering geometry produced very weak spectra and only one Raman line could be seen: this line was at 100 cm^{-1} and had diagonal polarization. Further measurements were then carried out using the Brewster-angle technique, which maximizes the interaction between the incident light and the highly reflecting

crystal. The technique has been reviewed in detail by Beattie and Gilson (1970) and therefore only the essential points will be given here. The technique is based upon the fact that light incident on a crystal face at Brewster's angle with polarization in the plane of incidence and refraction will enter the crystal with a penetration distance of the order of the wavelength of the light before being completely absorbed. The intensity of the scattered light observed at 90° to the incident light is given by

$$I_{\parallel}^{\alpha\beta} = A[C_{\sigma\sigma}R_{\sigma\sigma} + C_{\tau\tau}R_{\tau\tau} + C_{\sigma\tau}R_{\sigma\tau}]^2 \tag{3}$$

for scattered light polarized in the plane of incidence and scattering and

$$I_{\perp}^{\alpha\beta} = A[C_{\rho\sigma}R_{\rho\sigma} + C_{\rho\tau}R_{\rho\tau}]^2 \tag{4}$$

for scattered light polarized perpendicular to the plane of incidence. The indices α, β refer to crystal directions X, Y and Z, which lie along the a, b and c axes, respectively: β labels the direction along the scattering face in the plane of incidence and α is the direction perpendicular to β, again in the plane of incidence. A is a constant, C a coefficient and R a component of the Raman tensors given in §2: σ, ρ and τ take the meanings x, y or z where appropriate. General expressions for the coefficients C have been given by Beattie and Gilson (1970) and we shall not reproduce them here. Rather, we shall give as an example the case $\alpha = Z, \beta = X$, for which $\sigma = x, \rho = y$ and $\tau = z$, and $C_{xx} = k_c/(1 + n_c^2)$, $C_{zz} = -1/(n_c + n_c^3)$, $C_{xz} = (n_c - k_c)/(n_c + n_c^3)$, $C_{yx} = n_c(1 + n_c^2)^{-1/2}$ and $C_{yz} = -(1 + n_c^2)^{-1/2}$: n_c is the ordinary refractive index for the c direction (we are ignoring the extraordinary ray) and $k_c = (n_c^4 + n_c^2 - 1)^{1/2}$. Similar expressions are readily obtained for the other cases of interest, ($\alpha = X, \beta = Y$) and ($\alpha = X, \beta = Z$).

The refractive index is related to Brewster's angle ϕ by $n = \tan\phi$, and ϕ was measured for $HgIn_2\square Te_4$ by finding the angle at which the reflected component of the 676·4 nm laser line showed a minimum intensity. The results obtained were $\phi_a = 75{\cdot}16 \pm 0{\cdot}30°$ and $\phi_c = 74{\cdot}57 \pm 0{\cdot}31°$, giving $n_a = n_b = 3{\cdot}775 \pm 0{\cdot}015$ and $n_c = 3{\cdot}622 \pm 0{\cdot}015$. Using these values for n_a and n_c, the amplitude coefficients C were calculated for various unique scattering configurations and the results are given in table 3. It must be remembered that these coefficients have to be multiplied by the corresponding Raman tensor component, and the approximate sums of such products squared, in order to obtain the scattering intensities.

Because of the high refractive index, the observed scattered light makes an angle of about 4° with the α direction within the crystal, and the direction of propagation of the

Table 3. Calculated amplitude factors for Brewster-angle scattering.

Scattering configuration	$I_{\parallel}^{ZX}$		$I_{\parallel}^{XY}$		$I_{\parallel}^{XZ}$	
Amplitude factors and symmetries	$C_{xx} = 0{\cdot}961$	$(A_1 + B_1)$	$C_{xx} = -0{\cdot}017$	$(A_1 + B_1)$	$C_{xx} = -0{\cdot}017$	$(A_1 + B_1)$
	$C_{zz} = -0{\cdot}020$	(A_1)	$C_{yy} = 0{\cdot}965$	$(A_1 + B_1)$	$C_{zz} = 0{\cdot}965$	(A_1)
	$C_{xz} = -0{\cdot}195$	(E^{TO})	$C_{yx} = -0{\cdot}190$	(B_2^{TO})	$C_{xz} = 0{\cdot}190$	(E^{LO})
Scattering configuration	$I_{\perp}^{ZX}$		$I_{\perp}^{XY}$		$I_{\perp}^{XZ}$	
Amplitude factors and symmetries	$C_{yx} = 0{\cdot}964$	(B_2^{LO})	$C_{zy} = 0{\cdot}967$	(E^{TO})	$C_{yx} = 0{\cdot}256$	(B_2^{TO})
	$C_{yz} = -0{\cdot}266$	(E^{TO})	$C_{zx} = -0{\cdot}256$	(E^{LO})	$C_{yz} = 0{\cdot}967$	(E^{TO})

phonon involved in the scattering process is at approximately 5·5° to the α direction. Allowing for the finite collection angle for the scattered light, this means that Brewster-angle scattering for this crystal is not far removed from true back scattering. The infrared-active modes are not mixed and there is a clear separation between the transverse and longitudinal waves, as is shown in table 3.

The six definitive spectra obtained from the crystal *a* and *c* faces are shown in figures 5 and 6, where one division on the intensity scale corresponds to a photomultiplier signal of 1000 counts integrated over 60 s. The dips present at about 10 cm^{-1} in the spectra of figures 6(*a*) and (*c*) result from over-occultation by the TTM; 100% transmission is attained by 18 cm^{-1}.

The $I_{\perp}$ spectra shown in figure 6 contain information about B_2- and E-mode frequencies. As table 3 shows, figure 6(*b*) contains E^{TO+LO} modes only, whereas in figures 6(*a*) and 6(*c*) the B_2^{LO} and E^{TO} modes, respectively, are the dominant features. Figure 6(*a*) shows three B_2^{LO} modes at 74, 152 and 189 cm^{-1} with an additional band at 121 cm^{-1}. This latter band corresponds closely with an E^{TO}-mode frequency, which is allowed in this polarization but may also arise from an impurity, as will be discussed later. Figures 6(*b*) and 6(*c*) show that there are E modes at 42 and 61 cm^{-1} which appear to exhibit no TO–LO splitting. There are E^{TO} modes at 122, ~162 and 181 cm^{-1}, and an E^{LO} mode at ~188 cm^{-1}; the amount of overlap between the three modes in the 100–200 cm^{-1} region makes it difficult to determine all of the frequencies. Although the B_2 and E modes appear only weakly in the Raman spectrum, the B_2^{LO} modes at 152 and 189 cm^{-1} and the E^{TO} modes at 122 and 162 cm^{-1} agree well with the infrared results (see table 2).

The $I_{\parallel}$ spectra shown in figure 5 are complex because of the variety of modes allowed in each configuration (see table 3). In each spectrum the A_1 modes are dominantly allowed, and the strongest feature at 100 cm^{-1} that was also observed in back scattering can be confidently assigned to A_1 symmetry. B_1 modes are strongly allowed in the configurations $I_{\parallel}^{ZX}$ and $I_{\parallel}^{XY}$, and the two weak bands at ~50 and 155 cm^{-1} are tentatively assigned to this symmetry; the low intensity makes it difficult to distinguish these bands, but no corresponding peaks are observed in other configurations where B_1 modes are forbidden or very weakly allowed. It should be noted that the B_1 modes in chalcopyrites, which have a similar crystal structure, are also weak and difficult to observe (Lockwood and Montgomery 1975). Figures 5(*a*) and 5(*b*) also contain peaks from E^{TO} and B_2^{TO} modes, respectively, but this is allowed according to the amplitude factors given in table 3. Figure 5(*c*) shows the $I_{\parallel}^{XZ}$ spectrum in which the $A_1(R_{zz})$ modes dominate, with a weaker contribution from the E^{LO} modes. The strong 100 cm^{-1} feature is again seen, along with E^{LO} features, and a unique sharp band is evident at 132 cm^{-1}. This latter band appears in no other spectrum, and is therefore assigned to the other A_1 mode. These results indicate that for the 100 cm^{-1} band the Raman tensor component $a \simeq b$, whereas for the 132 cm^{-1} band $b \gg a$.

A strong shoulder is observed on the high-frequency side of the 100 cm^{-1} A_1 band in all of the $I_{\parallel}$ spectra, accompanied in some cases by the E mode at ~125 cm^{-1}. It was found that when the laser power was increased to the point where surface damage occurred, this shoulder became the dominant feature in the spectrum, peaking at 120 cm^{-1} with an intensity of about twice that of the 100 cm^{-1} band. Simultaneously, two other features of lower intensity appeared at 60 and 141 cm^{-1}, respectively. The Raman spectrum of powdered TeO_2 has three principal bands at 62, 120 and 146 cm^{-1} (Pine and Dresselhaus 1971): these frequencies, and the band intensities, are a good match to the three bands seen here. Furthermore, Pine and Dresselhaus could produce the TeO_2 spectrum by melting Te with a laser beam and then allowing the sample to solidify

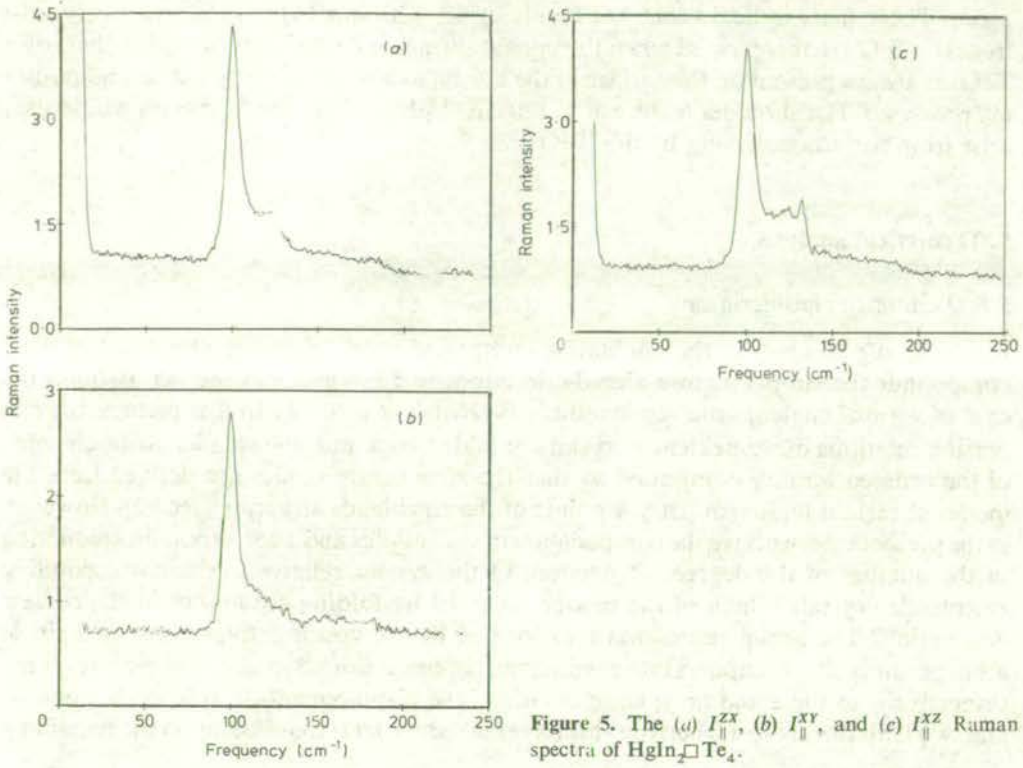

Figure 5. The (*a*) $I_{\parallel}^{ZX}$, (*b*) $I_{\parallel}^{XY}$, and (*c*) $I_{\parallel}^{XZ}$ Raman spectra of $HgIn_2\square Te_4$.

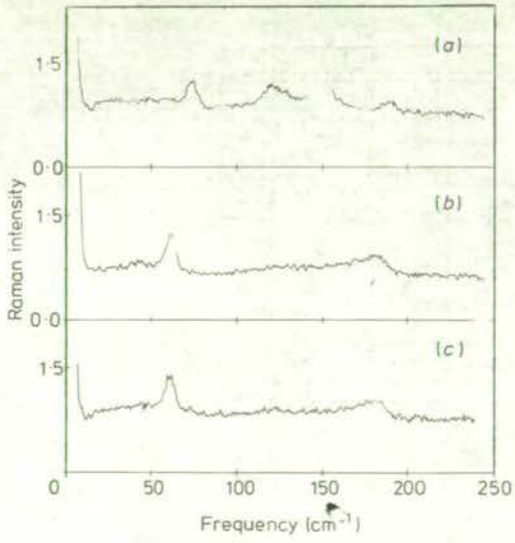

Figure 6. The (*a*) $I_{\perp}^{ZX}$, (*b*) $I_{\perp}^{XY}$, and (*c*) $I_{\perp}^{XZ}$ Raman spectra of $HgIn_2\square Te_4$.

again. These facts indicate that the bands at 60, 120 and 141 cm^{-1} most likely arise from the TeO_2 that is created when the crystal surface is heated. It is probable that some TeO_2 is always present on the surface of the crystal as a result of the grinding and polishing processes. The shoulder feature at $\sim 120\ cm^{-1}$ observed in the $I_{\parallel}$ spectra would then arise from surface scattering by this TeO_2.

5. Theoretical analysis

5.1. Qualitative considerations

It is tempting to apply to the qualitative interpretation of the lattice vibrations in these compounds the simple picture already described in § 2, which has proved useful in the case of various chalcopyrite semiconductors (Holah *et al* 1974). In this picture, the dispersion relations of a zincblende crystal are folded back into the smaller Brillouin zone of the ordered ternary compound so that the zone-centre modes are derived from the modes at certain high-symmetry $\boldsymbol{k}$ points of the zincblende structure (see § 2). However, in the present case, we have the complication of vacant sites and a corresponding reduction in the number of the degrees of freedom of the system relative to the corresponding zincblende crystal. Which of the modes obtained by folding are absent in the correct description? The group representations formed by the vector displacement of a single atom per unit cell decomposes into irreducible representations B_2 and E, which correspond, respectively, to the z and (x, y) components of the displacement. It follows that one B_2 and two E modes are lost when the atom is removed. What is the effect upon the remaining

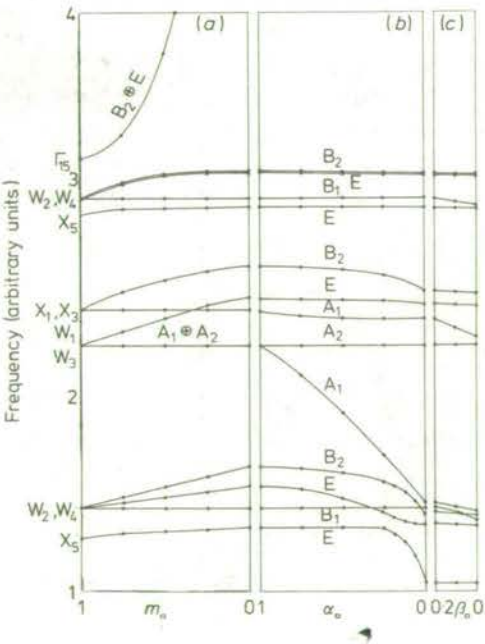

Figure 7. The 'defect diamond' calculation shows the effect of reducing (*a*) the mass on the vacancy site, (*b*) the $\alpha_{\square Te}$ central force constant and (*c*) the $\beta_{Te\square Te}$ bond-bending force constant.

modes of the large perturbation associated with the removal of one atom per cell? One aspect of this problem is illuminated by a simple argument based on the use of bond-*stretching* forces *only*. In zincblende and related semiconductors, one-third of all of the vibrational modes may be identified as those which have zero frequency in the presence of bond-stretching forces only (in zincblende itself these are the TA bands). The number of such modes is obtained by subtraction of the number of bonds per atom (which we constrain to remain constant for such a mode) from the number of degrees of freedom per atom. For an unmodified zincblende structure, the result is $3 - 2 = 1$. If a fraction f of atoms is removed, together with their associated bonds, this becomes $3(1 - f) - 2(1 - 2f) = 1 + f$. In practice, the bond-bending forces are usually small enough for this low-lying group of bands to be clearly identified. The above argument shows that while the total number of modes decreases by a fraction f, the number of these low-lying modes *increases* by the same fraction. In the case of $HgIn_2\square Te_4$ this leads us to expect (at each value of $\boldsymbol{k}$) *one* additional low-lying mode.

The symmetry of the strongly perturbed mode at $\boldsymbol{k} = 0$ may be derived from the following more detailed argument, which is capable of generalization to other cases of interest.

The modes of any structure which have non-zero frequencies in the presence of bond-stretching forces only may be obtained by using the compressions of the bonds, rather than the vector displacements of the atoms, as coordinates. The modification of the zincblende structure to form a defect structure reduces the number of these coordinates by four for each missing atom. One may decompose the group representation formed by the missing coordinates into irreducible representations. Subtraction of the representations associated with the displacement coordinates of the missing atoms themselves then isolates those representations associated with anomalous low-lying modes. In the present case we have $(A_1 + B_2 + E) - (B_2 + E) = A_1$.

The above arguments are illustrated by the calculations shown in figure 7. For simplicity, we have considered the case where one atom in eight is removed from a diamond cubic crystal to form what we shall call 'defect diamond', which is similar to the defect stannite and defect chalcopyrite structures except in that it is made up of identical atoms. We use the simple Keating (1966) model for bond-bending and bond-stretching forces,

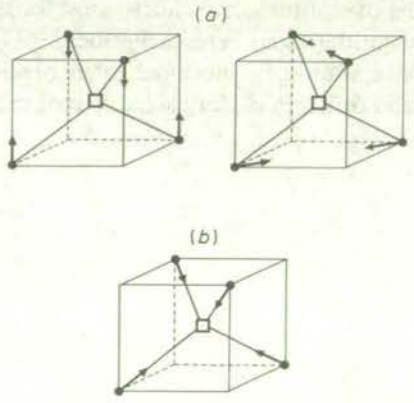

Figure 8. (*a*) The folding of zincblende dispersion relations gives two A_1 modes with displacements in the neighbourhood of the vacancy, as shown. The correct A_1 modes are linear combinations of these. (*b*) As $\alpha_{\square Te}$ is reduced, the displacements of the low-lying A_1 mode discussed in the text take the form shown.

as described in the following section. Figure 7 shows how the $k = 0$ mode frequencies vary as one atom per unit cell is 'switched off' by letting first its mass and then the force constants associated with it tend to zero. In the first stage, a B_2 and a doubly degenerate E mode are lost, as expected, but the spectrum is otherwise only slightly modified. However, when the force constants associated with the defect are cut off, the A_1 mode drops dramatically, as anticipated on the basis of the above analysis. Figure 8 shows the eigenvectors of the A_1 modes before and after the □–Te bonds are cut. It can be seen that the dropping mode primarily involves the stetching of these bonds. Note also that the frequencies of the B_1 and A_2 modes remain constant as the defect mass and defect bond-stretching force constants are taken to zero, since that part of the Hamiltonian which is being changed involves only coordinates which yield A_1, B_2 and E representations.

5.2. Keating-model fit to experimental data

A semi-empirical analysis of the experimental data of §§ 3 and 4, as well as the sound velocities measured by Saunders and Seddon (1976), has been performed using adjustable force constants of the Keating type (Keating 1966, Martin 1970). In the Keating model, the potential energy associated with a given set of atomic displacement is expressed as a sum of two terms which are sums over bonds (corresponding to central nearest-neighbour forces) and pairs of neighbouring bonds (corresponding to non-central forces), respectively.

In the case of an elemental solid, the central force term may be written

$$\tfrac{3}{4}\alpha \sum_{l,\Delta} [(\boldsymbol{u}_l - \boldsymbol{u}_{l\Delta}) \cdot \boldsymbol{r}_\Delta(l)]^2. \tag{5}$$

The summation is over all atoms l and their nearest neighbours $l\Delta$. The unit vector from the equilibrium position of atom l to that of its neighbour $l\Delta$ is $\boldsymbol{r}_\Delta(l)$ and $\boldsymbol{u}_l$ denotes the displacement of atom l.

The non-central force term is

$$\tfrac{3}{16}\beta \sum_{l,\Delta,\Delta'} [(\boldsymbol{u}_l - \boldsymbol{u}_{l\Delta}) \cdot \boldsymbol{r}_{\Delta'}(l) + (\boldsymbol{u}_l - \boldsymbol{u}_{l\Delta'}) \cdot \boldsymbol{r}_\Delta(l)]^2, \tag{6}$$

where the sum is over all atoms l and pairs of nearest neighbours $l\Delta$, $l\Delta'$.

The advantages of the Keating model over alternative short-range force schemes are marginal and, at the level of the analysis undertaken here, insignificant.

In the case of a compound, the above should be modified to incorporate different force constants α for each type of bond, and different β's for each different triad of nearest-

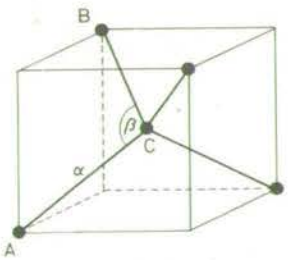

Figure 9. Notation for central (α_{AC}) and non-central (β_{ACB}) Keating model force constants given in table 4.

neighbour atoms. Figure 9 explains the notation which we have used for these various force constants.

In addition, Coulomb forces may be added in the case of a compound. We have ignored this refinement for the present, since the model already contains a considerable number of adjustable constants and is found to give a reasonable fit to the data.

The structure was assumed to be $I\bar{4}2m$, as discussed in § 1, with all atoms placed at their ideal sites (i.e. those coincident with zincblende sites) since there has not yet been an experimental determination of their exact positions.

How one is to treat the vacancy in a model of this type is not clear. The model considers the vacancy as an extra, massless atom which is dealt with in a similar manner to the electron shells in the familiar shell model for ionic solids (Woods *et al* 1960); a force matrix for cores and shells is transformed into a smaller matrix for cores only. In this case a 24 × 24 matrix (i.e. 7 atoms and one vacancy) reduces to a 21 × 21 matrix (i.e. 7 atoms only). In our initial calculations we set the □–Te bond-stretching and Te–□–Te bond-bending force constants equal to zero. However it was found difficult to obtain a satisfactory fit to the data with this restriction and we resorted to the incorporation of a □–Te force constant. This may seem paradoxical but is probably an indication of significant contributions from forces of longer range which are not built into the model.

The theoretical results shown in tables 2 and 5 were obtained with the force constants given in table 4.

As noted above. the lowest A_1 mode is of particular interest. Unfortunately, the associated A_2 mode cannot be observed in either the Raman or infrared reflectivity measurements, but it seems clear that the A_1 mode frequency in question is not lowered through the presence of the vacancy by as much as our previous argument would suggest. Indeed, this is one the reasons for the necessity of the incorporation of the □–Te force constant in the model.

Table 4. Keating model parameters required for results in table 2.

Force constant		Fitted value ($N\,m^{-1}$)
α	Hg–Te	38·9
	In–Te	21·8
	□–Te	11·8
β	In–Te–In	2·95
	In–Te–Hg	2·95
	Te–In–Te	2·95
	Te–Hg–Te	2·95
	□–Te–In	1·47
	□–Te–Hg	1·47
	Te–□–Te	0·0

Table 5. Experimental and calculated values of elastic stiffness constants (C) and bulk modulus (B) ($\times 10^{10}\,N\,m^{-2}$).

	C_{11}	C_{12}	C_{13}	C_{33}	C_{44}	C_{66}	B
Experimental	4·31	2·54	2·18	4·47	2·14	2·41	2·99
Calculated	4·2	2·88	2·9	4·4	1·18	1·21	3·35

The degree of agreement with experiment thus achieved is sufficient for present purposes—to assist in the preliminary identification and interpretation of the data. It is least satisfactory for the 147 cm^{-1} B_2 mode, the 120 cm^{-1} E mode and the C_{13}, C_{44} and C_{66} elastic constants.

Dispersion relations were calculated for various symmetry directions and are shown in figure 10.

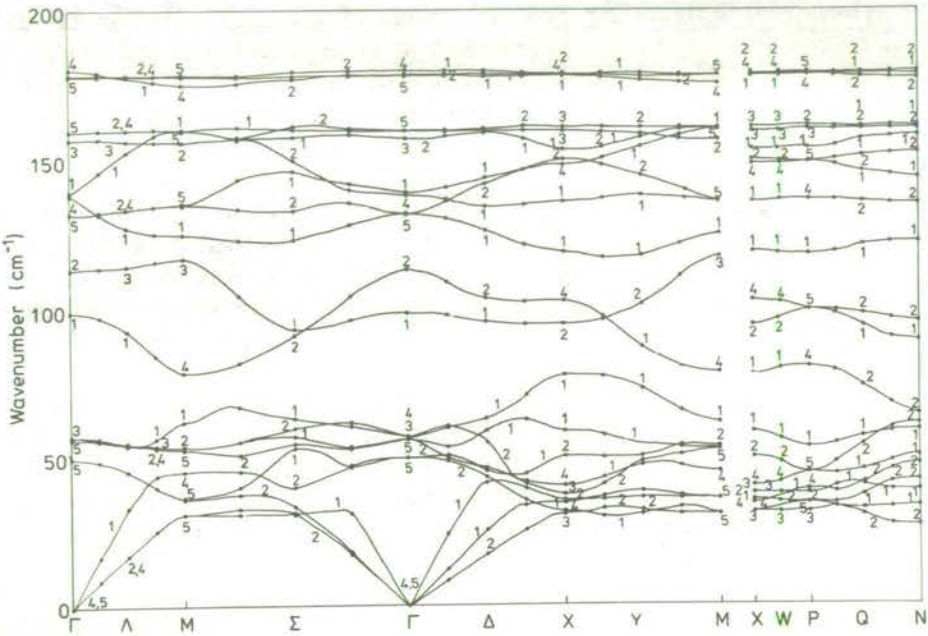

Figure 10. Phonon dispersion curves of $HgIn_2\square Te_4$ calculated using the fitted Keating model parameters.

6. Conclusions

The ordered vacancy compounds, of which $HgIn_2\square Te_4$ is a particularly simple example, pose many intriguing questions, most of them bearing on the role of the vacancies. For example, in many of these compounds, the arrangement of vacancies is disordered above a certain transition temperature. A little thought will suffice to convince the reader that this is not so straightforward a proposition as the disorder in a solid solution; in the defect case, one is dealing with a situation in which a large fraction of the cation sites are unfilled!

In addition, there is at present wide interest in the possible merits of the chalcopyrite semiconductors in various technical applications. This can be expected to widen to include the ordered vacancy compounds, some of which are in many respects similar to the chalcopyrites.

Clearly, therefore, these compounds invite further attention and it is hoped that this paper may serve to lay some of the groundwork for future investigations.

Acknowledgments

We are indebted to G Saunders for much advice and encouragement and for making available to us the crystals, grown by T Seddon and himself, upon which our measurements were performed. We wish also to thank H Vass for technical assistance in the Raman scattering work, N S J Kennedy for checking the crystal orientation and B S Wherrett for his advice on the group theoretical aspects of our investigation. This work was supported by the Science Research Council.

References

Arthur J W and Lockwood D J 1974 *J. Raman Spectrosc.* **2** 53–69
Beattie I R and Gilson T R 1970 *J. Chem. Soc.* (A) 980–6
Bettini M 1975 *Phys. Stat. Solidi* (b) **69** 201–12
Claassen H H, Selig H and Shamir J 1969 *Appl. Spectrosc.* **23** 8–12
Finkman E, Tauc J, Kershaw P and Wold A 1975 *Phys. Rev.* B **11** 3785–94
Hahn H, Frank G, Klinger W, Störger A D and Störger G 1955 *Z. Anorg. Allg. Chem.* **279** 241–70
Holah G D, Webb J S and Montgomery H 1974 *J. Phys. C: Solid St. Phys.* **7** 3875–90
Keating P N 1966 *Phys. Rev.* **145** 637–45
Lax M J 1974 *Symmetry Principles in Solid State and Molecular Physics* (New York: Wiley) p 449
Lockwood D J and Montgomery H 1975 *J. Phys. C: Solid St. Phys.* **8** 3241–50
Lyddane R H, Sachs R G and Teller E 1941 *Phys. Rev.* **59** 673–6
Martin R M 1970 *Phys. Rev.* B **1** 4005–11
Parthé E 1964 *Crystal Chemistry of Tetrahedral Structures* (New York: Gordon and Breach) pp 46–86
Peckham G 1970 *Computer J.* **13** 418
Pine A S and Dresselhaus G 1971 *Phys. Rev.* B **4** 356–71
Saunders G A and Seddon T 1970 *J. Phys. Chem. Solids* **31** 2495–504
—— 1976 *J. Phys. Chem. Solids* to be published
Woods A D B, Cochran W and Brockhouse B N 1960 *Phys. Rev.* **119** 980–99

J. Phys. C: Solid State Phys., Vol. 9, 1976. Printed in Great Britain. © 1976

Raman spectrum of $Zn_4O(BO_2)_6$

A F Murray and D J Lockwood
Department of Physics, University of Edinburgh, Edinburgh, EH9 3JZ, Scotland

Received 5 April 1976

Abstract. The first-order Raman spectrum of cubic zinc metaborate has been measured at room temperature, and the number of $q = 0$ phonon frequencies found exceeds the group theoretical prediction by one. The additional band appears as an interference feature at 122·5 cm^{-1} and is thought to be attributable to some impurity introduced during crystal growth. The results are in reasonable agreement with an earlier qualitative investigation of the infrared transmission spectrum of this material, and the reported fluorescent properties are verified. A comparison between the Raman results for zinc metaborate and those for $Cr_3B_7O_{13}Cl$ shows some correlations. A simple force-constant calculation identified four bands in each compound that can be associated with vibrations of BO_4 tetrahedra contained within the boron–oxygen framework.

1. Introduction

The crystal $Zn_4O(BO_2)_6$ is unusual in that it is one of the few anhydrous metaborates with all the boron atoms in fourfold coordination. In general, stability demands threefold coordination in anhydrous metaborates at atmospheric pressure. Crystals of basic zinc metaborate are cubic, having a bimolecular unit cell of edge length 7·48 Å. Boron and oxygen atoms are bound together to form an infinitely extended three-dimensional framework based on $(B_6O_{12})^{6-}$ rings (Smith *et al* 1964). Each boron atom is at the centre of four tetrahedrally distributed oxygen atoms, with a boron–oxygen distance of 1·52 Å and a boron–boron distance of 2·64Å. The zinc atoms lie inside irregular tetrahedra whose corners are occupied by three oxygen atoms from metaborate ions and one 'free' oxygen atom.

All the crystals thought to contain boron atoms in exclusively fourfold coordination are of the form $(MeO)_m.(B_2O_3)_n$, where Me is a divalent metal. These are $CuO.B_2O_3$ (Martinez-Ripoll *et al* 1971), $SrO.(B_2O_3)_2$ and $PbO.(B_2O_3)_2$ (Perloff and Block 1966) and $(ZnO)_4.(B_2O_3)_3$ (Smith *et al* 1964). There are, however, several materials having all boron atoms in fourfold coordination in a high-pressure phase. These are SrB_2O_4 (IV) (Dernier 1969), B_2O_3 (II) (Prewitt and Shannon 1968), HBO_2 (III) (Zachariasen 1963), $LiBO_2$ (III) (Marezio and Remeika 1966) and CaB_2O_4 (IV) (Marezio *et al* 1969). In addition, there are several compounds with mixed threefold and fourfold coordination, some of which are listed by Marezio *et al* (1969). The boracites (Nelmes 1974) are another example of this type of compound.

Apart from a qualitative examination of the infrared spectrum (Krogh-Moe 1962), there is no detailed investigation of the lattice vibrations of zinc metaborate. Here we report the Raman spectrum of this material with a view to characterizing the $q = 0$

vibrations of a crystal lattice involving a boron–oxygen framework with fourfold co-ordination. While the results are of interest in their own right, they are also of value for comparison with some current work on the lattice vibrations of boracites. The dynamics of the ferroelectric phase transition exhibited by boracites are being investigated using Raman spectroscopy, and as part of this study, the lattice vibrations of the cubic phase of $Cr_3B_7O_{13}Cl$ have been measured (Lockwood 1974, 1976). The elements common to the structures of zinc metaborate and boracite may produce common features in the Raman spectrum, which would facilitate a definite assignment.

2. Experiments and results

2.1. Group theory

A group theoretical analysis of the normal modes of vibration of the zinc metaborate structure at $q = 0$ predicts the following decomposition according to the irreducible representation of point group $\bar{4}3m$:

$$\Gamma = 3A_1 + 2A_2 + 5E + 7F_1 + 11F_2.$$

The polarizability tensors for crystals of cubic symmetry are of the form (Loudon 1964)

$$A_1 \begin{bmatrix} a & — & — \\ — & a & — \\ — & — & a \end{bmatrix} \qquad E \begin{bmatrix} b & — & — \\ — & b & — \\ — & — & -2b \end{bmatrix} \quad \text{and} \quad \begin{bmatrix} \sqrt{3}b & — & — \\ — & -\sqrt{3}b & — \\ — & — & — \end{bmatrix}$$

$$F_2 \begin{bmatrix} — & — & — \\ — & — & d \\ — & d & — \end{bmatrix}, \begin{bmatrix} — & — & d \\ — & — & — \\ d & — & — \end{bmatrix} \quad \text{and} \quad \begin{bmatrix} — & d & — \\ d & — & — \\ — & — & — \end{bmatrix}.$$

The Raman activities are indicated by the appropriate non-zero components of the polarizability tensor. Excluding acoustic modes, therefore, the Raman spectrum should comprise $3A_1 + 5E + 10F_2$ normal modes of vibration. Only modes of F_2 symmetry are infrared active.

The problem of distinguishing modes of A_1 symmetry from those of E symmetry is readily solved (Lockwood 1974). Briefly, the solution involves aligning the incident light along an axis, say x', at 45° to the cubic x and y axes, and observing the light scattered in direction y', orthogonal to x'. The E spectrum is obtained by measuring the polarizability tensor element $\alpha_{y'x'}$. A point for point subtraction of the spectrum corresponding to tensor element $\alpha_{y'x'}$ from that of α_{zz} leaves a spectrum of pure A_1 symmetry modes, provided an appropriate scaling factor is used.

2.2. Experimental details

The single crystal of $Zn_4O(BO_2)_6$ was grown by the vapour transport method (Schmid 1965) as a byproduct in the attempted growth of Zn-I-boracite, the reaction mechanism being

$$4ZnI_2(g) + 4H_2O(g) + 3B_2O_3(g \text{ or } l) = Zn_4O(BO_2)_6(s) + 8HI(g).$$

The formation of zinc metaborate instead of the boracite is a result of an insufficient quantity of ZnI_2 vapour (Schmid 1965). The crystal formed was a rhombic dodecahedron of approximate size 2 mm. The natural growth faces of the crystal were {110}, and con-

sequently faces perpendicular to the ⟨100⟩ directions were cut and polished (using 1 μm diamond powder) for use in the conventional Raman scattering measurements. Inspection of the crystal under a polarizing microscope revealed considerable growth strains, which lead to inhomogeneous optical properties. As a result, spectra of any polarization may contain additional features attributable to admixtures from spectra of other polarizations. A minor degree of mixing of spectra always occurs due to the wide collection angle of the lens used to gather the scattered light, but in this experiment the depolarization problem was more troublesome because of the strain birefringence. Adopting the approach that any spectrum is a combination of the true spectrum and small proportions of other spectra, the subtraction process described above may be used to remove unwanted modes. Provided a clear spectral feature can be used to determine a scale factor, a point for point subtraction should reveal the pure spectrum. It is, however, impossible to use this method when the spurious modes are attributable to the F_2 spectrum, due to TO–LO intensity effects.

Zinc metaborate is known to exhibit fluorescence (Terol and Otero 1961), and a broad emission band peaked at 537·2 nm was observed in survey spectra excited by the 514·5 nm radiation from an argon laser. Therefore, in order that the Raman spectrum should not be confused with the broad fluorescent background, 350 mW of 476·5 nm argon laser light was used to excite all the spectra presented here. The Raman spectrum was recorded at room temperature from both 90° and 180° scattering geometries using a Coderg T800 triple monochromator with a spectral slit width of 1·0 and 1·5 cm^{-1} for the 0–500 cm^{-1} and 500–1500 cm^{-1} frequency regions respectively. The spectrometer is connected via an interface to a PDP11 computer (Arthur and Lockwood 1974) which enables spectra to be stored in digital form. The data may be subsequently transferred to a time-sharing multi-access computer in order that the subtraction routine, along with other data handling routines (Arthur 1974, 1976) may be performed in an interactive manner.

In the following description of results, the labels X, Y refer to the [100] and [010] directions and X', Y' to the [110] and [$\bar{1}$10] directions.

2.3. The A_1 spectrum

This spectrum was isolated, as described earlier, by subtracting the $X'(Y'X')Y'$ E symmetry spectrum from the $X'(ZZ)Y'$ spectrum which contains features of both A_1 and E symmetry. These latter spectra are shown in figures 1 and 2. A first approximation to the scaling factor was found by comparing the relative intensities of the distinct E peak at 414·5 cm^{-1} in both spectra, and then adjusting the factor for complete cancellation. This led to the isolated A_1 spectrum of figure 3. The theoretical intensity scaling factors of $4b^2$ and $3b^2$ for the ZZ and $Y'X'$ spectra, respectively, indicate that cancellation should be achieved when the $Y'X'$ spectrum is multiplied by 1·33 and subtracted from the ZZ spectrum (Lockwood 1974). In fact, due to crystal and experimental imperfections, the scaling factor was found to be 1·03 ± 0·07. In figure 3, the disappearance of a mode of E symmetry is marked by an increase in the level of noise, for obvious reasons, and in places by a sharp differential feature due to a slight mismatch in the wavenumber calibration between ZZ and $Y'X'$ spectra. There are, apart from some broad second-order structure, four sharp features. One of these takes the form of a resonance interference at 122·5 cm^{-1} between a sharp peak and a broader second-order background. The peaks at 249·3 cm^{-1} and 421·9 cm^{-1} are clearly of A_1 symmetry, but the nature of the feature at 94·7 cm^{-1} is partially disguised by the proximity of E and F_2 features. The different nor-

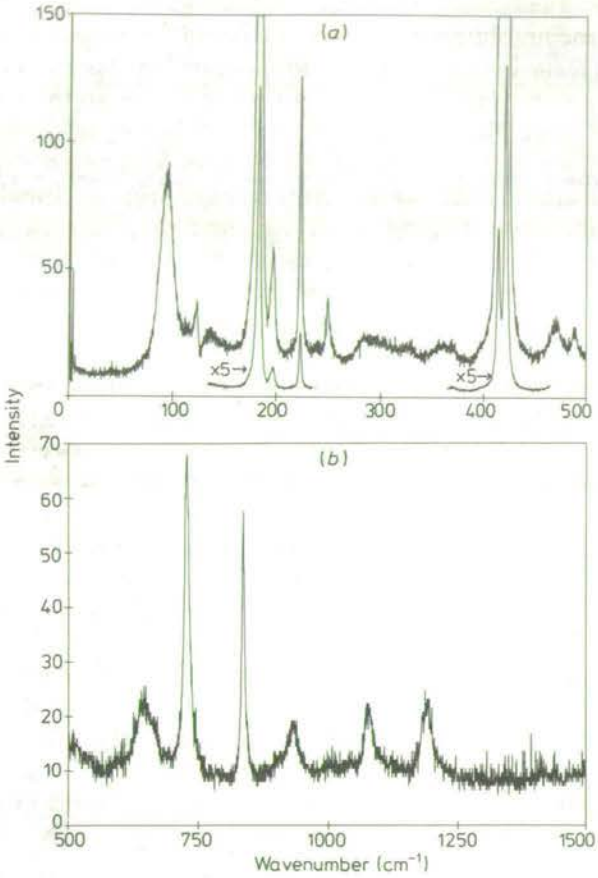

Figure 1. The $X'(ZZ)Y'$ spectrum of $Zn_4O(BO_2)_6$ in the regions 0–500 cm^{-1} and 500–1500 cm^{-1}.

mal-mode frequencies in this closely spaced trio are revealed by the use of the subtraction process and a computerized peak-finding routine (Arthur 1976), whereas visual inspection of the spectra suggests only one mode to be present. Table 1 shows all the measured frequencies, assignments, and linewidths where appropriate.

2.4. The E spectrum

From the $X'(Y'X')Y'$ spectrum of figure 2, assignments of E symmetry modes are fairly straightforward, apart from the interference feature mentioned above. F_2 symmetry modes appearing in this spectrum cannot be subtracted out due to the TO–LO intensity variations. The frequencies are tabulated in table 1.

2.5. The F_2 spectrum

Identification of modes of F_2 symmetry is complicated by splitting between the transverse

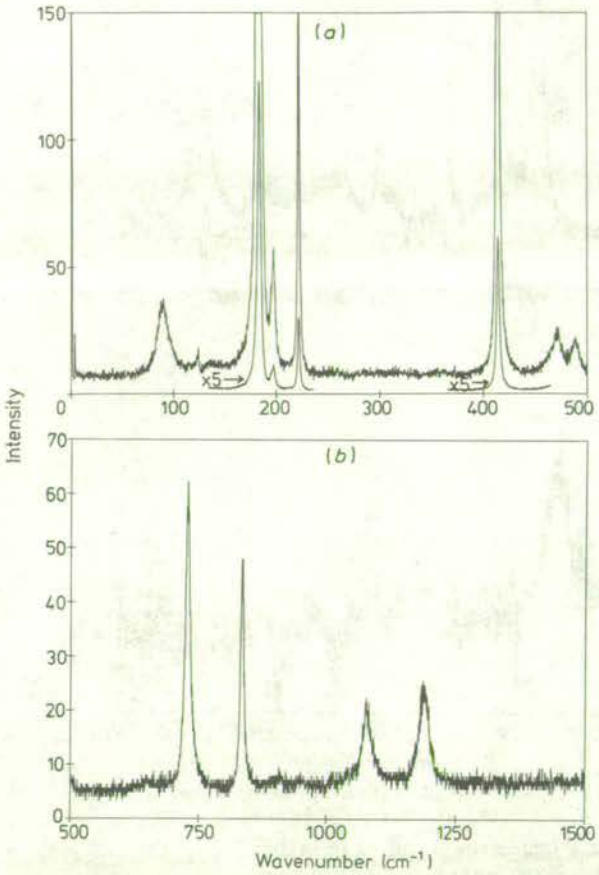

Figure 2. The $X'(Y'X')Y'$ spectrum of $Zn_4O(BO_2)_6$ in the regions 0–500 cm^{-1} and 500–1500 cm^{-1}.

and longitudinal components of some F_2 modes. The $X(YX)Y$ spectrum contains F_2 modes of transverse character only, and this spectrum is shown in figure 4. Other 90° scattering off-diagonal spectra such as $X(YZ)Y$ (see figure 5) contain both TO and LO features. In order to clarify the assignment of F_2^{LO} modes, the $X(YZ)\bar{X}$ backscattering spectrum was measured; this spectrum contains only longitudinal modes. The signal in this spectrum was weak, and the argon laser plasma lines strong, but the assignments in table 1, taken from the $X(YZ)Y$ spectrum of figure 5, were confirmed. Once again the subtraction routine was used, in this case to remove the admixture of modes of A_1 and E symmetry to give figure 5. This involved subtraction from the YZ spectrum of the ZZ and $Y'X'$ spectra with scale factors 0·045 and 0·2 respectively. This procedure reveals otherwise partially hidden spectral features of definite F_2 symmetry at 93·1 cm^{-1} and 181·6 cm^{-1}. The peak-finding computer routine again proved invaluable in detecting small wavenumber differences and very weak modes, such as the peak at 284·2 cm^{-1}.

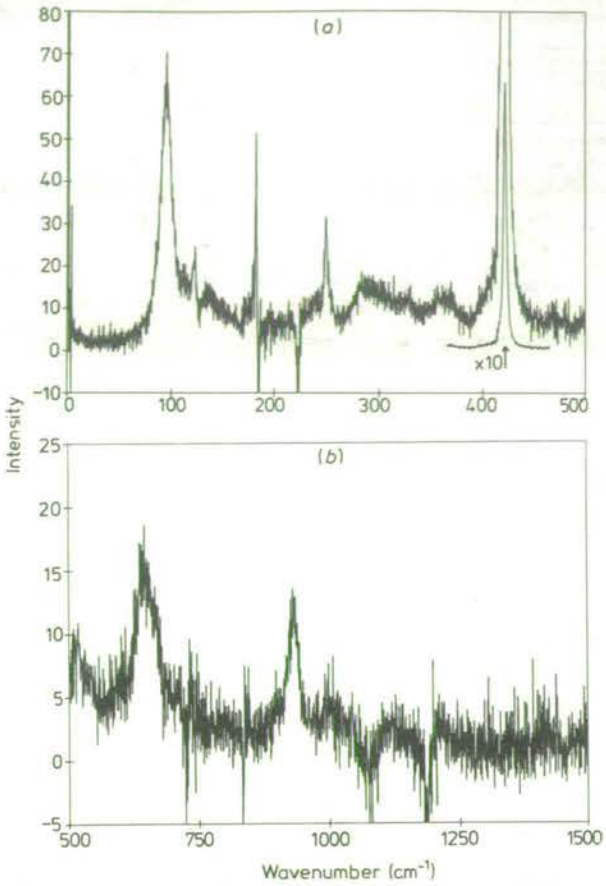

Figure 3. The A_1 spectrum of $Zn_4O(BO_2)_6$ in the regions 0–500 cm^{-1} and 500–1500 cm^{-1}.

Table 1. Peak frequencies ω (cm^{-1}), linewidths γ (cm^{-1}) and assignments for the Raman-active modes of $Zn_4O(BO_2)_6$.

A_1		E		F_2	
ω	γ	ω	γ	ω	γ
94·7	11·5 ± 1·5[a]	89·4	12 ± 1[a]	93·1	15 ± 2[a]
122·5		122·5			
249·3	3 ± 0·6[a]	183·0	4 ± 0·5[a]	181·6	4 ± 0·5[a]
421·9	3 ± 0·6[a]	414·5	3·3 ± 0·3[a]	196·7	5 ± 0·5[a]
		727·2	12·5 ± 1·5[b]	222·4	2 ± 0·5[a]
		835·9	9 ± 1·5[b]	278·0	6·5 ± 2[a]
				284·2	6·5 ± 2[a]
				471·1	14 ± 1·5[a]
				488·2	9·5 ± 1·5[a]
				653	20 ± 6[b]
				906·2	14 ± 2[b]
				1005	—[c]
				1040	—[c]
				1074·4	19 ± 1·5[b]
				1189·0	23·5 ± 1·5[b]

[a] Spectral slit width 1·0 cm^{-1}.
[b] Spectral slit width 1·5 cm^{-1}.
[c] Not sufficiently resolved for meaningful measurement.

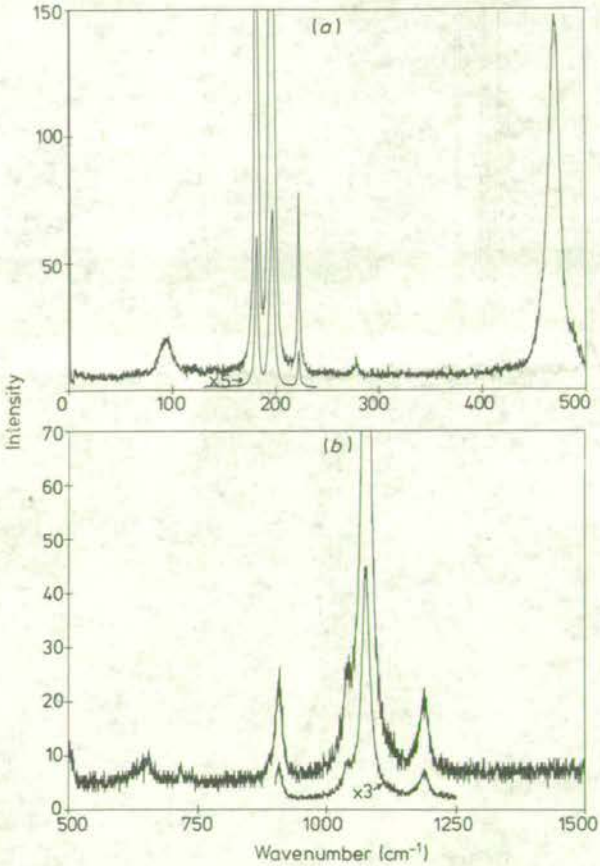

Figure 4. The $X(YX)Y$ spectrum of $Zn_4O(BO_2)_6$ in the regions 0–500 cm^{-1} and 500–1500 cm^{-1}.

3. Discussion

From the assignments in table 1 it is clear that the A_1 and E spectra are not totally in agreement with group theoretical predictions. While the F_2 spectrum contains ten distinct peaks as predicted by theory. the A_1 spectrum contains four peaks and the E spectrum contains six, both of which exceed the predicted number of modes by one. There are two possible explanations of this discrepancy. It is conceivable that the broad peak appearing in both the E and A_1 spectra (figures 2 and 3) around 90–94 cm^{-1} is spurious. This feature has been clearly resolved into three peaks of E, F_2 and A_1 symmetry at 89·4 cm^{-1}, 93·1 cm^{-1} and 94·7 cm^{-1} respectively. This near-degeneracy is quite remarkable, but these *distinct* frequencies, together with the intensities of the individual bands (figures 2, 3, 4 and 5) suggest that this is an intrinsic property. Therefore, it is anticipated that the interference feature at 122·5 cm^{-1} is the spurious mode. The intensity of this mode is comparable, and has the same frequency, in both the A_1 and E spectra.

The F_2 spectrum of figures 4 and 5 contains ten modes, allowing for splitting between transverse and longitudinal components, and should show some agreement with the infrared spectrum. The only published infrared investigation of the lattice vibrations of zinc metaborate (Krogh-Moe 1962) is very qualitative and no frequency assignments are

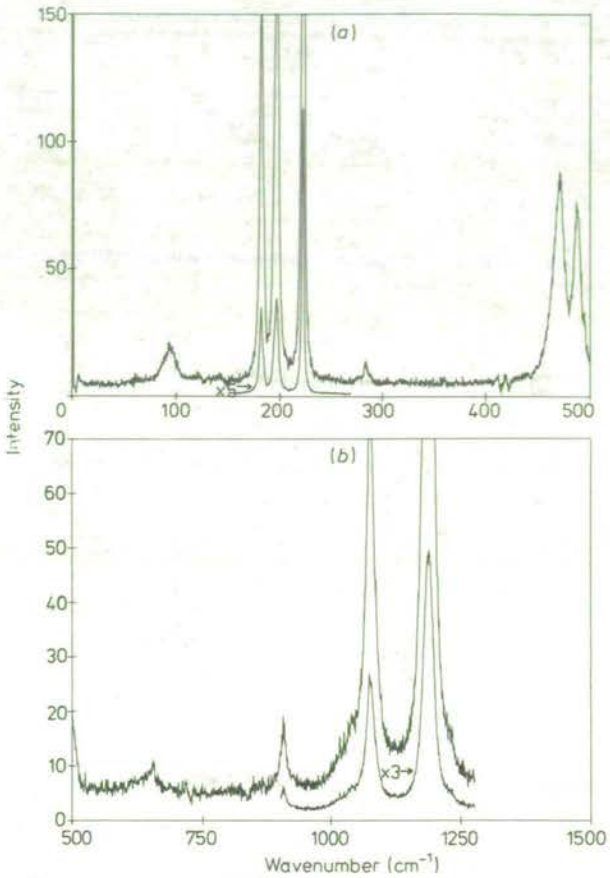

Figure 5. The $X(YZ)Y$ spectrum of $Zn_4O(BO_2)_6$ in the regions 0–500 cm^{-1} and 500–1500 cm^{-1}.

tabulated. This makes detailed comparison difficult, but measurements on the published spectrum from 670 to 5000 cm^{-1} do reveal some correlations. There are strong absorption peaks at 1040 $\pm$ 6 cm^{-1} and 1080 $\pm$ 6 cm^{-1} and a broader feature stretching from 915 cm^{-1} to 945 cm^{-1}, while there are shoulder features at 990 cm^{-1} and 1140 cm^{-1} which could correspond to longitudinal components. It seems reasonable to assume that the two sharper features correspond to the tabulated Raman frequencies of 1040 cm^{-1} and 1074·4 cm^{-1} and the broader feature to the 906·2 cm^{-1} mode, with longitudinal components where appropriate. There is, however, a strong infrared absorption at 720 cm^{-1}, which is completely absent in the Raman spectrum. This could arise from second-order absorption, or may indicate the presence of an impurity in the sample used for the infrared measurements due to the different method of preparation (crystallization from the melt of fused zinc oxide and boric acid).

It is interesting and informative to compare the observed fluorescence band at 537 nm with the luminescence data of Terol and Otero (1961). Terol and Otero observed that pure cubic zinc borate is luminescent under 253·7 nm excitation with the emission comprising a narrow band peaked at 435 nm with a weaker secondary band peaked at 535 nm. The luminescent response to 365 nm excitation was very weak. The luminescence is ascribed to trapped electrons (or positive holes) due to absences of 'free' oxygen (or zinc) atoms in the crystal structure : oxygen vacancies in the BO_4 tetrahedra are not likely because of the

high strength of the B–O framework. Activation with a small amount of Mn produces a strong green luminescence, peaked at 540 nm, under ultraviolet excitation: the Mn is divalent and is assumed to substitute for Zn. The fluorescence observed in the Raman experiments is presumed to be excited by the near-ultraviolet light characteristically produced in the argon laser plasma discharge. As noted above, low-energy excitation produces only weak luminescence in pure zinc borate. Therefore, even though there is good agreement between the peak position at 537 nm found here and the sideband at 535 nm reported by Terol and Otero, it seems unlikely that the emission is from the pure crystal, particularly as we found no evidence of the contiguous band at 435 nm. A more likely explanation, confirmed by H Schmid (1976, private communication), is the presence of some Mn in the crystal carried over as an impurity from the starting materials (see §2·2); the Mn^{2+} luminescence is strong and peaks at 540 nm, which agrees well with our observations.

Terol and Otero (1961) note that the multiple closed chains of linked $(BO_2)_6$ groups form a basket-like framework containing many cavities that are large enough to accommodate positive and negative ions. Some of these cavities are, of course, occupied by the zinc and 'free' oxygen atoms that make up the chemical formula. However, there is the possibility of other species occupying these cavities and, in particular, the growth mechanism (§2·2) suggests that HI or some other iodine species may be trapped in these sites. The presence of iodine during crystal growth could also result in I^- substituting for cavity oxygen. The spurious interference band at 122·5 cm^{-1} is, therefore, tentatively assigned to a local mode vibration of some iodine species trapped within the lattice. (The Mn ion concentration would be too small to observe an impurity mode from this ion in the absence of resonant Raman scattering.) The variation of the interference band profile with temperature and excitation frequency is being studied in an attempt to divine its origin and to obtain more information on the coupling mechanism to the phonon bath.

Any explanation of the origin of the interference feature must resolve the puzzling fact that the mode has A_1 and E symmetry.

The Raman results obtained for zinc metaborate may be compared with the $q = 0$ frequencies of chromium chlorine boracite (Lockwood 1974, 1976) with a view to determining common features arising from vibrations of the B–O framework. There are a large number of normal modes in both crystals, and some simplifications are needed to facilitate the comparison. We assume that the basic BO_4 molecular units within each crystal are independent. The vibrations of this tetrahedral molecule transform as $A_1 + E + 2F_2$, and these are considered to be internal modes in the cubic crystal. Unfortunately, the vibrational frequencies of the free BO_4^{5-} ion are unknown, and therefore no ready comparison and assignment can be made. An indirect approach was adopted. Using the known values for the vibrational frequencies of the tetrahedral ions SiO_4^{4-}, PO_4^{3-}, SO_4^{2-} and ClO_4^- as a guide, possible A_1, E and F_2 frequencies for borate were selected from the results for zinc metaborate and chromium chlorine boracite. Appropriate combinations of these frequencies were then used to obtain force constants for two different models representing the forces in tetrahedral molecules. One model assumed central forces only, and the other was the more sophisticated generalized force field model of the Urey–Bradley (1931) type. The force constants were calculated on a computer from a simultaneous least-squares fit to the four equations connecting frequencies and force constants. Different combinations from the previously selected A_1, E and F_2 frequencies were tried until the best fit was obtained. The best and most sensible fits were obtained from the same data sets for both models. These data sets are shown in table 2. The frequencies in each column are remarkably similar. Furthermore, the relative intensities show close

Table 2. Data sets for the two models (frequencies in cm^{-1}).

	$A_1(\nu_1)$	$E(\nu_2)$	$F_2(\nu_3)$	$F_2(\nu_4)$
$Zn_4O(BO_2)_6$	421	183	1075	278
$Cr_3B_7O_{13}Cl$	375	232	1160	252

agreement: the ν_1, ν_2 and ν_3 bands are strong, while the ν_4 band is weak in both cases. The force constants obtained are somewhat different from those calculated for a free molecule like SiO_4^{4-}, as can be expected. In particular, the ν_1 band in the crystal is undoubtedly much lower in frequency than one would anticipate for the free molecule. Nevertheless, it appears that frequencies at about $A_1 = 400\,cm^{-1}$, $E = 200\,cm^{-1}$, $F_2 = 1100\,cm^{-1}$ and $F_2 = 260\,cm^{-1}$ are characteristic of a B–O framework comprising or containing BO_4 tetrahedra.

Acknowledgments

We wish to thank H Schmid for considerable advice and for providing the crystal growing facilities, and H Tippmann for technical assistance in the growth of the zinc metaborate crystal. The work was supported by the Science Research Council and the Battelle Research Centre, Geneva. One of us (AFM) acknowledges the support of an SRC studentship.

References

Arthur J W 1974 *PhD thesis* University of Edinburgh
—— 1976 *J. Raman Spectrosc.* to be published
Arthur J W and Lockwood D J 1974 *J. Raman Spectrosc.* **2** 53–69
Dernier P D 1969 *Acta Crystallogr.* B **25** 1001–3
Krogh-Moe J 1962 *Z. Kristallogr.* **117** 166–70
Lockwood D J 1974 *J. Raman Spectrosc.* **2** 555–62
—— 1976 to be published
Loudon R 1964 *Adv. Phys.* **13** 423–82 (erratum **14** 621)
Marezio M and Remeika J P 1966 *J. Chem. Phys.* **44** 3348–53
Marezio M, Remeika J P and Dernier P D 1969 *Acta Crystallogr.* B **25** 965–70
Martinez-Ripoll M, Martinez-Carrera S and Garcia-Blanco S 1971 *Acta Crystallogr.* B **27** 677–81
Nelmes R J 1974 *J. Phys. C: Solid St. Phys.* **7** 3840–54
Perloff A and Block S 1966 *Acta Crystallogr.* **20** 274–9
Prewitt C T and Shannon R D 1968 *Acta Crystallogr.* B **24** 869–74
Schmid H 1965 *J. Phys. Chem. Solids* **26** 973–88
Smith P, Garcia-Blanco S and Rivoir L 1964 *Z. Kristallogr.* **119** 375–83
Terol S and Otero M J 1961 *Z. Naturf.* **16** 920–7
Urey H C and Bradley C A 1931 *Phys. Rev.* **38** 1969–78
Zachariasen W H 1963 *Acta Crystallogr.* **16** 385–9

Solid State Communications, Vol. 20, pp. 703–707, 1976. Pergamon Press. Printed in Great Britain

OBSERVATION OF A CENTRAL PEAK IN LEAD GERMANATE BY LIGHT SCATTERING

D.J. Lockwood, J.W. Arthur, W. Taylor and T.J. Hosea

Physics Department, Edinburgh University, Edinburgh EH9 3JZ, Scotland

(*Received* 7 *July* 1976; *in revised form* 5 *August* 1976 *by R.A. Cowley*)

Brillouin–Raman scattering measurements on single domain lead germanate over the temperature interval 300–455 K reveal an unresolved (less than 80 MHz) central peak. At about $T_c - 20$ K this peak begins to increase in intensity, reaching a maximum at T_c, and then falls away rapidly with increasing temperature above the transition. The central peak anomalous intensity, which is visible to the naked eye, is much larger than the intensity contributions due to phonons, including the ferroelectric soft mode, and appears to be a static effect.

THERE HAS been much recent theoretical and experimental work on the phenomenon of central peaks in the light scattering spectra of materials undergoing structural phase transitions. This work is described in the recent reviews by Cowley,[1] Nakamura[2] and Fleury[3] in which it is pointed out that in nearly all cases the width of the central peak has not been resolved.

Lead germanate, $Pb_5Ge_3O_{11}$, undergoes a phase transition from a paraelectric phase of space group $P\bar{6}$ to a ferroelectric phase of symmetry $P3$ at $T_c \simeq 450$ K.[4,5] Being a uniaxial system, the static properties of lead germanate can be expected to exhibit classical behaviour (with possible logarithmic corrections), and all evidence to date[6,7] indicates that this is the case. Previous studies of light scattering from lead germanate[8,9] have given evidence of quasielastic scattering in an unresolved regime below 5 cm^{-1} at temperatures near T_c. More recently, quasielastic ferroelectric fluctuations in lead germanate have also been observed using neutron scattering techniques.[10] As part of a new detailed investigation of light scattering in this material[11] we have examined the Brillouin and Raman spectra in this low frequency regime, extending it to a lower limit of 80 MHz.

Measurements were made on a crystal of dimension 5 × 5 × 5 mm with faces perpendicular to crystallographic axes: this crystal was cut from the same boule as one of the samples used in the neutron work of Cowley *et al.*[10] An electrical noise measurement technique[12] was used to determine $T_c = 451.7$ K. The sample was poled single domain near T_c using a 200 V/cm field applied along the [001] axis: this field was applied throughout the experiments. The spectra were excited with ~ 150 mW of 514.5 nm argon laser light and recorded in the $X(ZZ)Y$ scattering configuration, where Z refers to the ferroelectric axis. Results in the region -30 to 80 cm^{-1} were obtained on a Coderg T800 triple monochromator, with the Brillouin peaks just resolved.

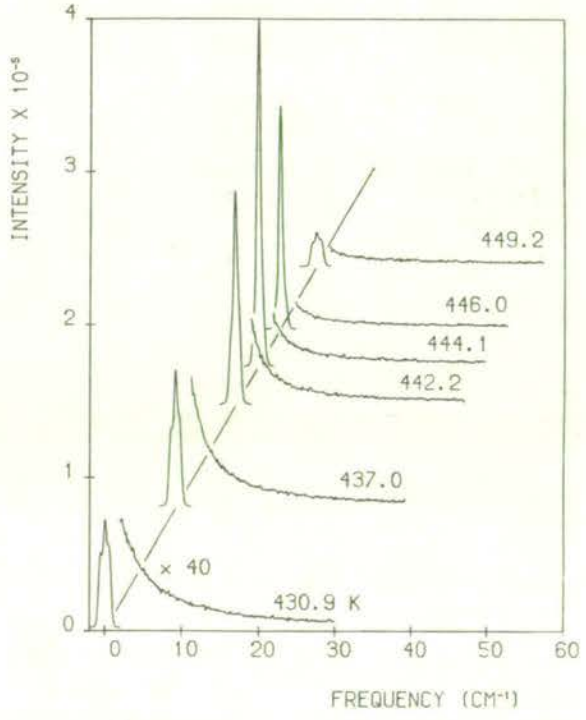

Fig. 1. The $X(ZZ)Y$ Raman spectrum of lead germanate recorded with a slit width of 0.4 cm^{-1} at various temperatures.

In the region 0 – 1 cm^{-1} a Burleigh RC40 Fabry–Perot interferometer was used in conjunction with a Spex 1400 double monochromator and third monochromator (TTM), which acted as a narrow-band filter. The use of multiple monochromating stages, together with the very high optical quality of the poled crystal, ensured that stray light response and extraneous elastic scattering were minimised. This can be seen from Figs. 1 and 2 in which, well below the transition temperature, the observed elastic component is only of the same order as that of the Brillouin. The observations reported here

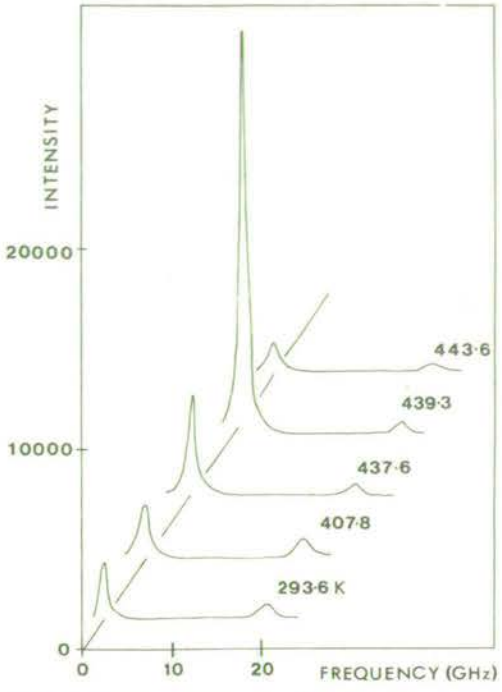

Fig. 2. The Brillouin spectrum of lead germanate recorded with a Fabry–Perot plate spacing of 3.9 mm at various temperatures.

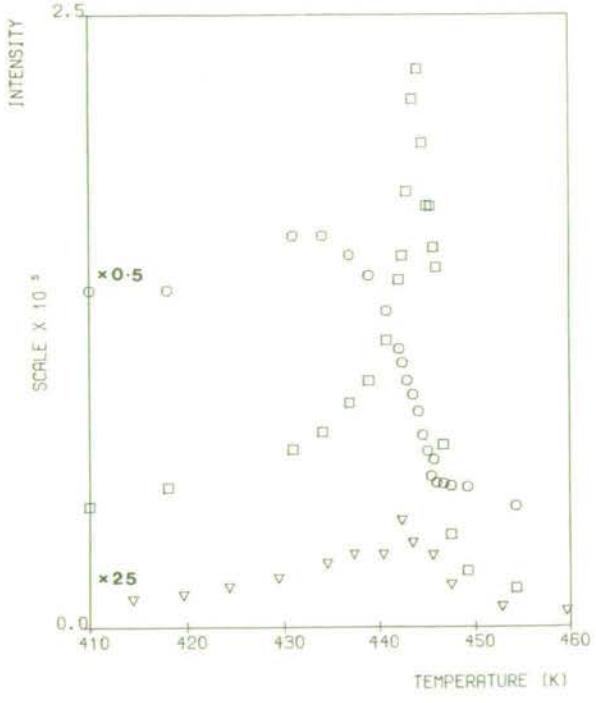

Fig. 3. The Raman intensity at 0 cm^{-1} for the central peak (□) and the phonons (▽), and the integrated intensity over all the phonons in the spectrum (○). The integrated intensity of the central peak is about 9× that of the 0 cm^{-1} peak intensity.

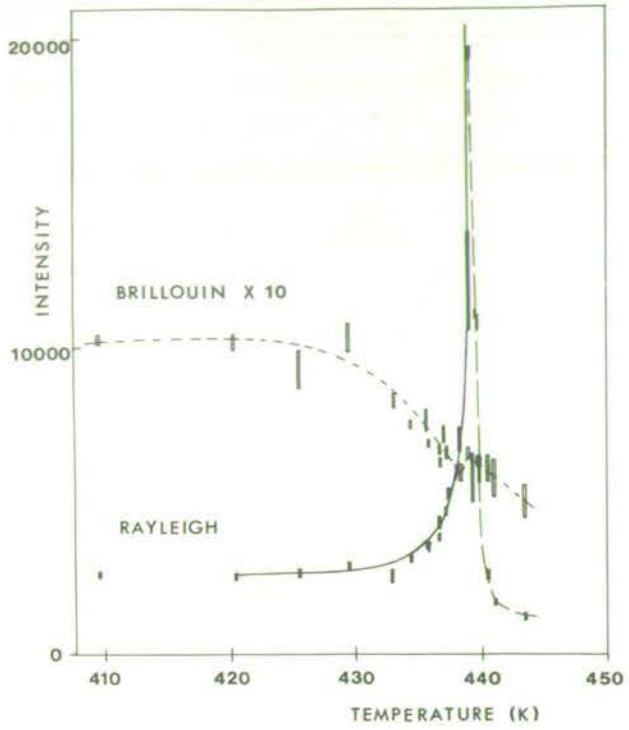

Fig. 4. The Brillouin results (plate spacing 3.9 mm) for the central peak intensity at 0 cm^{-1} (▮) and for the acoustic phonon peak intensity (▯). Note the much greater relative increase in the central peak intensity at T_c as compared with the Raman results due to the increased resolution. The solid line is of the form $[(T_c - T)^{-1} + \text{const.}]$.

would be completely obscured by the presence of a strong parasitic contribution to the intensity at $\omega = 0$.

The temperature of the sample was held stable to 0.03 K, but due to laser absorption there was a temperature differential across the illuminated region estimated at 1 K. The local laser heating also produced an apparent shift in T_c of about -9 K as measured at the crystal surface: temperatures reported in the accompanying figures are not corrected for this shift. Data were collected digitally and processed on a multi-access computer.

Results obtained earlier from 4 cm^{-1} upwards have been reported elsewhere.[11,13] The Raman results obtained here, Fig. 1, extend observation of the soft mode down to 2 cm^{-1}. The new data corroborates the existing evidence[8,13] for a quasi-elastic central component such as that described by Coombs and Cowley.[14] In the Brillouin measurements a single acoustic phonon peak is observed (Fig. 2) at 18 GHz. The Brillouin spectrum was examined with several plate separations in the range ~ 1 mm to 140 mm, with a finesse between 100 and 40.

Intensity measurements in light scattering can be difficult. With our equipment it is possible to reproduce intensities to better than 5% in any one experiment,[15] and in all the experiments reported here the intensities

measured in consecutive spectra were well correlated. However, a general decrease in intensity was observed between measurements at the lowest and highest temperatures. This is principally due to thermal effects in the silicone oil bath in which the sample was immersed, but some of the intensity behaviour may be ascribed to a decrease in the polarisability near the phase transition. We therefore produce our intensity results free of any correction.

The optic phonons in the $X(ZZ)Y$ spectrum all have A symmetry below T_c. Between room temperature and T_c there is no unusual change in the intensities of any of the phonon peaks. The general tendency is a slight increase in intensity some 10–20 K below T_c, and thereafter a rapid decrease. This behaviour is portrayed in Fig. 3 by the integrated intensity over all phonons in the spectrum defined as

$$\int_{-30}^{-2\ \mathrm{cm}^{-1}} + \int_{2}^{80\ \mathrm{cm}^{-1}} \frac{I(\omega, T)\mathrm{d}\omega}{\omega[\bar{n}(\omega, T)+1]} .$$

In the $X(ZZ)Y$ scattering geometry used here the acoustic mode propagation is along $[1, \bar{1}, 0]$, and in the high temperature phase the sole Brillouin peak observed corresponds to a true LA phonon. But in the ferroelectric phase this phonon will assume a transverse component. An order of magnitude calculation using the elastic constant data of Yamada *et al.*[16] shows that it will, however, remain almost purely longitudinal. From the lowest to highest temperatures the only major change in the spectrum of this phonon is in the intensity (see Fig. 4), which shows the same general trend as that of the optic modes. The frequency varies little, ~ 1%, and there may be some slight anomaly in frequency and intensity at the transition, although our evidence is as yet tentative. No strong coupling with the soft mode is observed: the work of Yamada *et al.*[16] indicates that the piezoelectric coupling is small.

Through the course of these experiments the central peak has been observed with resolutions varying from 13 GHz down to 80 MHz. In addition we have used photon correlation spectroscopy in the region 10 MHz to 10 Hz, with a Malvern digital autocorrelator. Finally, visual observations of the laser illuminated region were made. In all cases we observed a sharp increase in the central peak intensity at T_c. The behaviour is illustrated in Figs. 3 and 4, which give the peak intensities at 0 cm^{-1} for the Raman and Brillouin data respectively. The peak intensity begins to increase some 20 K below T_c, reaches a maximum at the transition, and then falls sharply away. Note that the central peak is much stronger than the phonons. In Fig. 3, we plot the intensity at zero frequency, due to phonons, taken from a multi-oscillator fit to Raman data from 4–75 cm^{-1} with the soft mode described by a Cowley–Coombs type response function.[13] The width of the central peak was determined to be less than 80 MHz from the Brillouin measurements, where the resolution was limited by instabilities in the laser frequency. The autocorrelation experiments produced a null result, and therefore the central peak width must be very narrow, unless it lies in the 10–80 MHz gap in our measurements. Indeed, it may be purely static in origin. Visually, the anomalous intensity appears as bright spots in the laser beam of dimension $\simeq 1\ \mu$m – a photograph of the pattern seen at T_c is given in Fig. 5(a). Away from T_c this "speckle" disappears and the laser beam appears completely smooth [see Fig. 5(b)]. A multidomain sample produces a similar but much more dense pattern of spots which remains unchanged at all temperatures below T_c. The bright spots associated with the transition are stationary and do not appear to the eye to change in size with time at a given temperature, at least over periods of several minutes. Therefore, it seems likely that the anomalous central peak intensity is static in origin, and it may arise from localised defects in the crystal. It is interesting to speculate on the possibility of a similar explanation for the unresolved central peaks observed by neutron and light scattering in other materials.

The observed temperature dependence of the central peak intensity may be explained on the basis of a static defect model where the defect introduces local departures from the homogeneity of the crystal. This influences the crystal behaviour near T_c through spatial variations in the local Curie temperature, $T_c(\mathbf{r})$. Axe *et al.*[17] have considered a static defect model dealing with variations in the local field near an impurity. This, however, leads to scattering with a temperature dependence of $(T_c - T)^{-2}$, whereas here the data are more consistent with a dependence of $(T_c - T)^{-1}$, Fig. 4. Assuming that the polarisability, α, of the crystal shows a marked dependence on $T_c - T$, the random scatter of the defect regions will produce an optical inhomogeneity throughout the sample near T_c. The scattered intensity will be of the form

$$I(\Delta\mathbf{k}) \sim \int \mathrm{e}^{i\Delta\mathbf{k}.\mathbf{r}} < \alpha\,[T_c(\mathbf{r}) - T]\ \alpha\,[T_c(0) - T] > \mathrm{d}^3 r$$

where $\Delta\mathbf{k}$ is the wavevector transfer. Taking α to be of the form $\alpha_0 + \alpha_1 (T_c - T)^{1/2}$ for $T < T_c$, and setting $T_c(\mathbf{r}) = \bar{T}_c + \delta T(\mathbf{r})$, this gives an anomalous contribution to the scattered intensity proportional to the Fourier component at $\Delta\mathbf{k}$ of

$$\frac{\alpha_1^2\ \langle \delta T(\mathbf{r}) \delta T(0) \rangle}{4(T_c - T)}$$

provided the maximum of $\delta T(\mathbf{r})$ is much less than

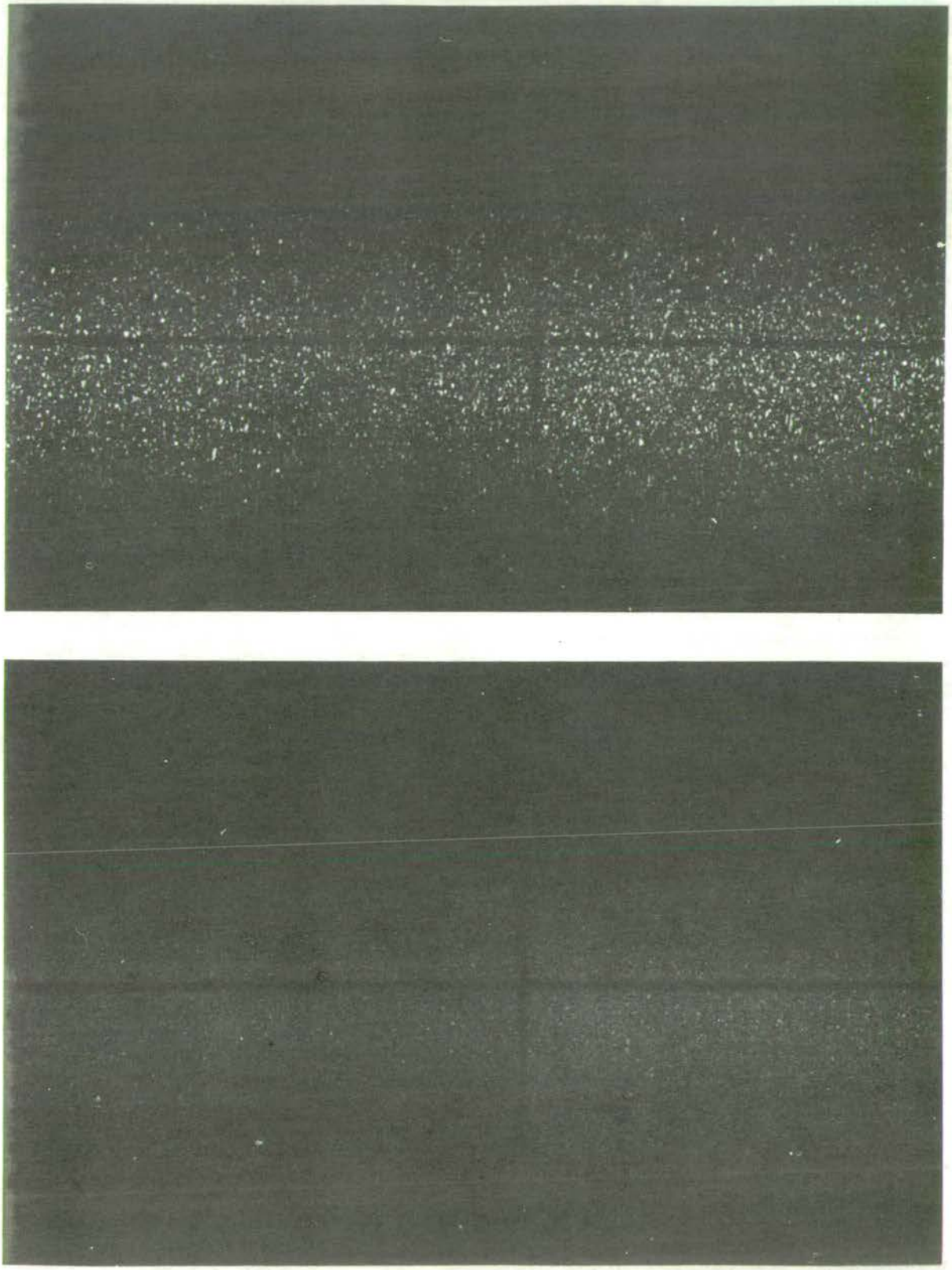

Fig. 5. Laser light scattering in lead germanate at T_c (a) and at about 5 K away from T_c (b). The photographs received identical processing. The magnification is such that the short edge dimension corresponds to 120 μm.

$T_c - T$. The central peak data shown in Fig. 4 agree reasonably well with a $(T_c - T)^{-1}$ dependence to within 1 K of the transition. This would indicate that $\delta T(\mathbf{r}) \sim$ 1 K if the model is correct. It should be noted that in a light scattering experiment Δk is restricted to small values allowing only correlations of a range $\gtrsim 0.1$ μm, say, to be observed. In a neutron scattering experiment Δk is not restricted in this way. It is, therefore, difficult to make a direct comparison between the present result and those of Cowley *et al.*[10] where the scattering is estimated to come from domain walls of size $\sim$ 10 Å.

On the other hand, a model has recently been proposed by Halperin and Varma[18] in which the distortion in a defective unit cell can hop back and forth between positions which break the symmetry in opposite senses. This model can account for the narrow central peak observed in $SrTiO_3$. The relaxation rate for such a dynamic process is expected to be very slow and might conceivably coincide with the 10–80 MHz gap in our measurements. However, Halperin and Varma[18] indicate that below T_c Rayleigh scattering from local variations in the density of impurities, as described above, can be comparable to or larger than the contribution to the central peak from their model, and this may be the case here. These authors also consider the possibility of a static impurity mechanism or "frozen" defect cell.

Acknowledgements – We are grateful to Dr. G.R. Jones for providing the crystal and thank H. Vass for technical assistance. This work was supported by the Science Research Council.

REFERENCES

1. COWLEY R.A., *Ferroelectrics* **6**, 163 (1974).
2. NAKAMURA T., *Ferroelectrics* **9**, 159 (1975).
3. FLEURY P.A., in *Light Scattering in Solids* (Edited by BALKANSKI M., LEITE R.C.C. & PORTO S.P.S.), p. 747. Flammarion, Paris (1976).
4. IWATA Y., KOIZUMI H., KOYANO N., SHIBUYA I. & NIIZEKI N., *J. Phys. Soc. Japan* **35**, 314 (1973).
5. IWATA Y., KOYANO N. & SHIBUYA I., *J. Phys. Soc. Japan* **35**, 1269 (1973).
6. NANAMATSU S., SUGIYAMA H., DOI K. & KONDO Y., *J. Phys. Soc. Japan* **31**, 616 (1971).
7. IWASAKI H., MIYAZAWA S., KOIZUMI H., SUGII K. & NIIZEKI N., *J. Appl. Phys.* **43**, 4907 (1972).
8. HISANO K. & RYAN J.F., *Solid State Commun.* **11**, 1745 (1972).
9. RYAN J.F. & HISANO K., *J. Phys. C: Solid State Phys.* **6**, 566 (1973).
10. COWLEY R.A., AXE J.D. & IIZUMI M., *Phys. Rev. Lett.* **36**, 806 (1976).
11. TAYLOR W., LOCKWOOD D.J., ARTHUR J.W. & HOSEA T.J., *Ferroelectrics* **12**, 113 (1976).
12. BROPHY J.J. & WEBB S.L., *Phys. Rev.* **128**, 584 (1962).
13. HOSEA T.J., LOCKWOOD D.J., TAYLOR W. & ARTHUR J.W. (to be published).
14. COOMBS G.J. & COWLEY R.A., *J. Phys. C: Solid State Phys.* **6**, 121 (1973).
15. LOCKWOOD D.J., *Ferroelectrics* **13**, 353 (1976).
16. YAMADA T., IWASAKI H. & NIIZEKI N., *J. Appl. Phys.* **43**, 771 (1972).
17. AXE J.D., SHAPIRO S.M., SHIRANE G. & RISTE T., in *Anharmonic Lattices, Structural Transitions and Melting* (Edited by RISTE T.) p. 23, Noordhoff, Leiden (1974).
18. HALPERIN B.I. & VARMA C.M., *Phys. Rev.* (to be published).

3 B 1707 *PHONON COUPLING IN ZINC METABORATE

A.F. MURRAY, D.J. LOCKWOOD
Physics Department, Edinburgh University, Edinburgh EH9 3JZ, Scotland

Evidence of coupling between phonon states has been reported in the Raman spectra of $BaTiO_3$[1] and quartz[2]. We have measured the room temperature Raman spectrum of $Zn_4O(BO_2)_6$ and have recorded a feature similar to that found at $175cm^{-1}$ in $BaTiO_3$. Group theory predicts that the Raman spectrum of $Zn_4O(BO_2)_6$ should contain $3A_1+5E+10F_2$ modes. These have been identified, along with an additional interference feature present in the A_1 and E spectra.[3]

The quantum mechanical formalism surrounding resonant interference (Auger processes)[4] can be summarised as follows. If a discrete one-phonon state (ϕ) is superimposed on a continuum of states $\{\psi_{E'}\}$ they may interact via anharmonic terms in the potential function to cause a perturbation of ϕ. The (perturbed) wavefunction of the coupled state ($\bar{\Psi}_E$) consists of a mixture of the discrete state wavefunction and the continuum wavefunctions. If the transition operator between initial state ψ_o and the state $\bar{\Psi}_E$ is α_{ij}, the Raman cross-section depends on the matrix element $\langle\bar{\Psi}_E|\alpha_{ij}|\psi_o\rangle$. Fano[4] has shown that the ratio of the probability of such a transition to the probability of transition to the unperturbed continuum is

$$\frac{|\langle\bar{\Psi}_E|\alpha_{ij}|\psi_o\rangle|^2}{|\langle\psi_E|\alpha_{ij}|\psi_o\rangle|^2} = \frac{(q+\varepsilon)^2}{1+\varepsilon^2} \quad \text{where } \varepsilon = \frac{E-E_r}{\pi|V_E|^2} = \frac{h(\nu-\nu_r)}{\frac{1}{2}\Gamma}$$

The width parameter V_E depends on coupling strength, and the line profile parameter q on the transition probability to a modified ϕ state. As the frequency ν of emitted photons studied is varied through ν_r, the scattering cross-section is of the form[1]

$$\sigma = \sigma_o + \sigma_1 \frac{(q+\varepsilon)^2}{1+\varepsilon^2}$$

A computerised curve fitting to this function produced the

smooth lines in the diagram, along with the tabulated optimal values of ν_r , q and Γ. In the E spectrum, an underdamped simple harmonic oscillator was fitted to the 89.4 cm^{-1} mode, and in the A_1 spectrum, to the 94.7 cm^{-1} mode. The fitted A_1 and E profiles also incorporate a heavily damped harmonic oscillator function to describe the multi-phonon background empirically. It can be inferred from the values of Γ that the Fano-type interference in the A_1 spectrum is due to a stronger coupling to the background than in the E symmetry. As for $BaTiO_3$, where again there is interference between one- and two-phonon states, the Fano model is a good fit to the data. The interference feature does, however, have mixed symmetry, and is thought to be due to some iodine species trapped as an impurity in the lattice, or to resonant Raman scattering from a manganese impurity content.[3]

1. D. Rousseau & S. Porto, Phys. Rev. Letters 20, 1354 (1968)
2. J.F. Scott, Phys. Rev. Letters 21, 907 (1968)
3. A.F. Murray & D.J. Lockwood, J. Phys. C. to be published
4. U. Fano, Phys. Rev. 124, 1866 (1961)

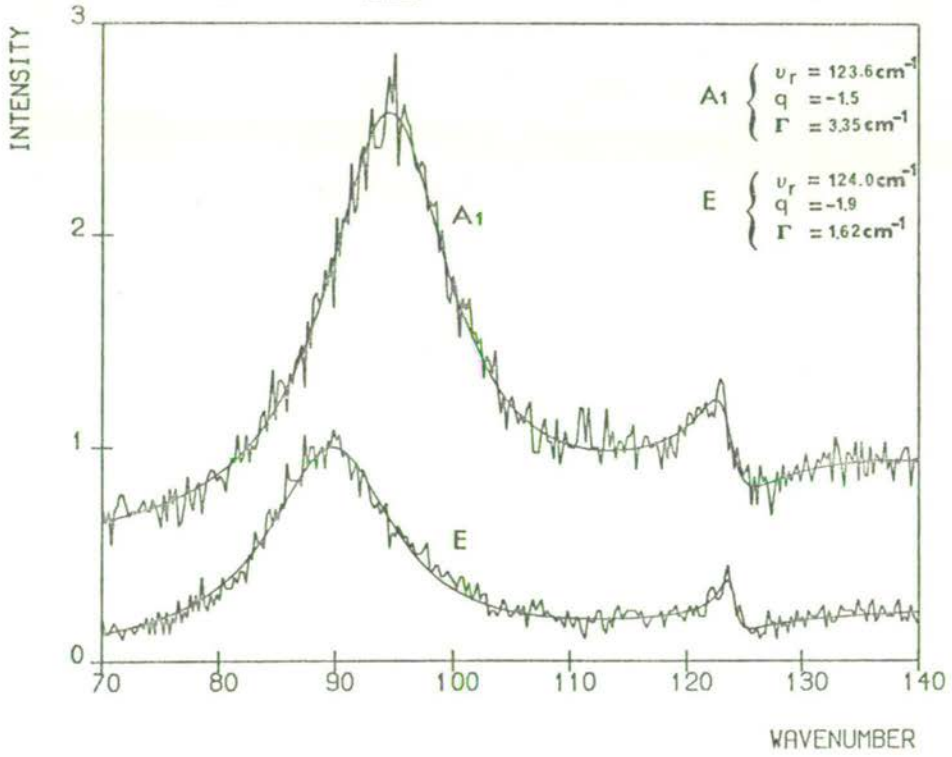

3 B 1100

ANALYSIS OF THE FERROELECTRIC SOFT MODE IN LEAD GERMANATE

T.J. HOSEA, D.J. LOCKWOOD, W. TAYLOR, J.W. ARTHUR

Physics Department, The University, Edinburgh EH9 3JZ, Scotland

Lead germanate (LG) has a paraelectric - ferroelectric phase transition at $T_c \simeq 450$ K. Earlier studies[1] of light scattering from LG have reported mode softening and unresolved quasielastic scattering below 5 cm^{-1} near T_c. Following a Raman investigation of the complete spectrum of single domain LG[2] we have re-examined the A(zz) Brillouin and Raman spectra in the low frequency region. We have fitted the Raman spectrum from 4 cm^{-1} upwards with three models for the soft mode, viz: a damped simple harmonic oscillator (DSHO), a Debye in the overdamped region, and the function due to Cowley and Coombs[3] (CC). The DSHO function used was $S\omega_o^2\Gamma^2\omega(\bar{n}+1)/[(\omega_o^2-\omega^2)^2+\omega^2\Gamma^2]$ where $\bar{n}$ is the Bose factor. In the over-damped region the damping Γ and frequency ω_o parameters were highly correlated; ω_o showed no tendency to go to zero at T_c, but remained roughly constant at about 33 cm^{-1} and instead the mode "softened" through an increase in Γ from 16 cm^{-1} at 315 K to 230 cm^{-1} at T_c. The overdamped SHO wing has a Debye-like width of ω_o^2/Γ which is plotted in Fig. 1. Virtually identical fits were obtained with the Debye model, $S\gamma^2\omega(\bar{n}+1)/(\omega^2+\gamma^2)$, where we can equate γ to ω_o^2/Γ. γ is also plotted in Fig. 1. Both models fail to fit the tail of an apparent central component evident in the lower temperature data. We obtained better fits with the more versatile CC function $S\omega_o^2\Gamma^2(1+A)\omega(\bar{n}+1)/[(\omega_o^2-\omega^2-\Gamma A/\tau)^2+\omega^2\Gamma^2(1+A)^2]$ where $\Gamma A = \delta^2\tau/(1+\omega^2\tau^2)$, δ^2 is a coupling parameter, and τ is an average phonon lifetime. At 370 K ω_o=29 cm^{-1}, Γ=15 cm^{-1}, δ^2=193 cm^{-2} and τ=0.06 cm, whereas at T_c ω_o=50, Γ=116, δ^2=1275 and τ=0.14. In the frequency region $\omega^2 << (\omega_o^2-\delta^2)/(1+\Gamma\tau)$, the additional central component has a Debye-like width of $(\omega_o^2-\delta^2)/(\omega_o^2\tau+\Gamma)$ and this is plotted in Fig. 1. At T_c, the widths produced by all models converge to ~3 cm^{-1}, corresponding to a relaxation time of 10^{-11} s. Near T_c our fitting indicates that the profile of the 'extra' CC central component, down to 4 cm^{-1}, becomes virtually indistinguish-able from that of the Debye or DSHO. However extrapolation of the different model fits indicate that the CC function has the most intense zero frequency response. This is plotted in Fig. 2. Between 300 K and T_c there is no unusual change in intensities of any of the optic phonon peaks: the behaviour is shown in Fig. 2 by the integrated intensity over all

phonons from 2 to 80 cm^{-1} with thermal weighting removed. The A(zz) acoustic mode at 18 GHz exhibits similar behaviour. The central peak was examined with resolutions varying from 13 GHz to 80 MHz, but was not resolved and in all cases we observed a sharp increase in the central peak intensity at T_c. Fig. 2 shows the peak intensity at 0 cm^{-1} for Raman data recorded with 0.4 cm^{-1} resolution. The Brillouin data which show a greater relative increase in the central peak intensity at T_c, due to the increased resolution, agree reasonably well with a $(T_c-T)^{-1}$ dependence to within 1 K of T_c. Auto-correlation measurements (10 MHz to 10 Hz) produced a null result, and therefore the central peak width must be very narrow, unless it lies in the 10-80 MHz gap. Visually, the anomalous intensity appears as stationary bright spots of dimension ≈1 μm, which disappear away from T_c. It would thus seem likely that the anomalous intensity is static in origin and indeed the $(T_c-T)^{-1}$ intensity dependence is predicted by a localised defect model. These defects introduce strains extending over a few μm which influence the "softening" in the Z direction causing a spread in the local Curie temperature predicted to be ~1 K.

1. K. Hisano and J.F. Ryan, Solid State Commun. 11, 1745 (1972).
2. W. Taylor, D. Lockwood, J. Arthur & T. Hosea, Ferroelectrics 12 in press.
3. R.A. Cowley & G.J. Coombs, J. Phys. C. 6, 143 (1973).

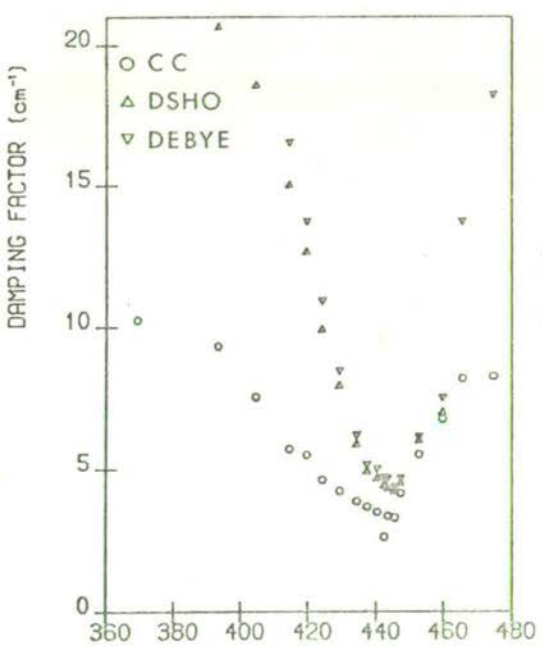

FIG 1

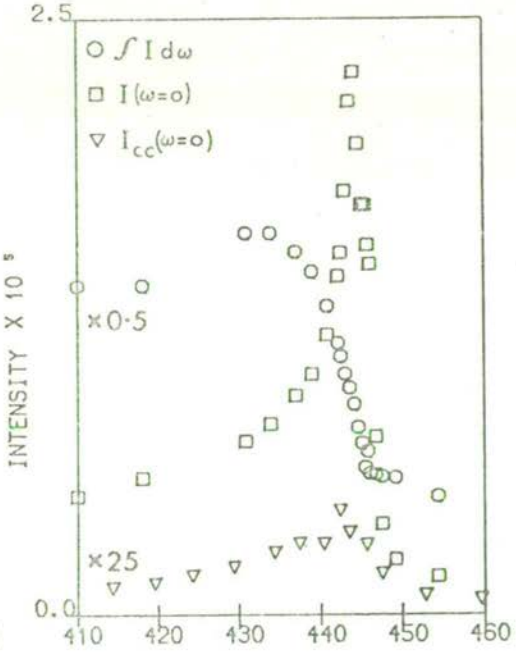

FIG 2

INVESTIGATION OF ELECTRONIC AND LATTICE PROPERTIES OF THE ORDERED VACANCY COMPOUND $HgIn_2\square Te_4$

A. MILLER, A. MacKINNON, D. WEAIRE, C.R. PIDGEON
Department of Physics, Heriot-Watt University, Edinburgh, U.K.

D.J. LOCKWOOD,
Department of Physics, University of Edinburgh, U.K.

G.A. SAUNDERS,
School of Physics, University of Bath, U.K.

Electrolytic electroreflectance and absorption measurements have been used to detect the lowest interband transitions and these have been interpreted using pseudopotential theory. Infra-red reflectivity and Raman scattering measurements have detected all allowed $k = 0$ vibrational modes. These have been interpreted with the aid of the Keating model.

1. INTRODUCTION

$HgIn_2\square Te_4$ has a tetragonal structure which may be regarded as being derived from that of zincblende by the incorporation of an ordered array of vacancies, which are necessary for the Grimm-Somerfeld rule to be obeyed. As such it is a member of a large class of "defect tetrahedral" compounds whose basic properites remain unexplored. It has a relatively simple structure with a unit cell similar to that of chalcopyrite, the subject of much recent interest, and stannite. The arrangement of cations is more closely related to that of the latter structure. One may imagine the I_2- II - IV - VI_4 stannite structure with the group IV atoms missing, and we have proposed that ittherefore be called "defect stannite".[1] The axial ratio c/a is close to the ideal value 2.0.

Previous studies of this compound have determined only the band gap [2] and elastic constants [3].

2. BAND STRUCTURE

Room temperature electroreflectance and absorption measurements have been carried out on single crystals with the light polarised parallel and perpendicular to the c-axis. The results have been interpreted using a pseudopotential

calculation [4], in the spirit of the EPM as described by Cohen and Heine [5].

The absorption coefficient with the radiation polarised E ⊥ C begins to increase sharply around 0.88eV, while this happens at 0.95eV for E ∥ c. The electrolytic electroreflectance method shows a strong peak at 0.956eV with E ⊥ c and a weaker peak at 1.09eV in both parallel and perpendicular configurations.

This may be understood using the kind of description used for the chalcopyrite compounds [6], in which the valence band structure at $\underset{\sim}{k} = 0$ is attributed to tetragonal crystal field and spin orbit contributions, as shown in Figure 1. The pseudopotential calculations also give this result. Note, however, that the crystal field parameter is much larger than that of a chalcopyrite compound of near ideal axial ratio and moreover, has the opposite sign to that found in chalcopyrites.

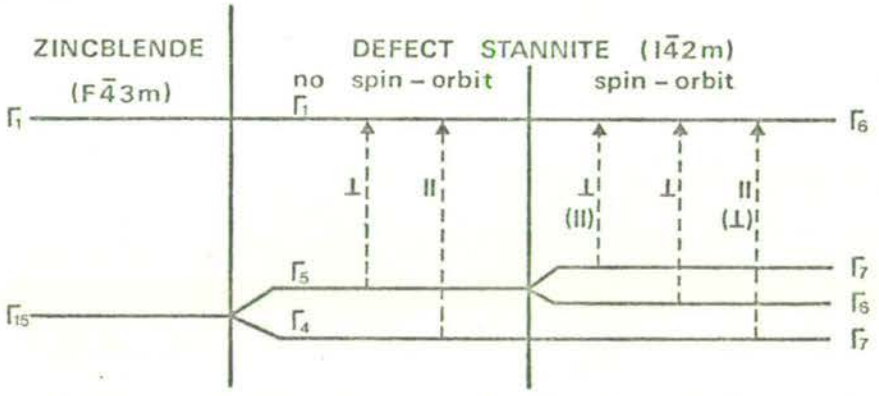

Figure 1. Valence band splitting and selection rules for $HgIn_2\square Te_4$.

3. LATTICE DYNAMICS

Infra-red reflectivity and Brewster angle Raman scattering measurements in a variety of geometries, were successful in detecting all allowed modes at $\underset{\sim}{k} = 0$ and these are listed in Table 1. Also shown are the results of a simple Keating model calculation [7] which achieves a fairly good fit to the data.

Table 1. Experimental and Theoretical results for k = 0 modes. Units: cm^{-1}.

Group Representation	IR	Raman	Calculated
$A_1(\Gamma_1)$	inactive	100 132	99 140
$A_2(\Gamma_2)$	inactive	inactive	114
$B_1(\Gamma_3)$	inactive	50 155	57 158
$B_2(\Gamma_4)$	147-153 180-184	74 -152 184-189	58 139 181
E (Γ_5)	118-127 160-169	42 61 122- 162- 181-188	50 57 132 160 179

The elastic constants data of Saunders and Seddon, from ultrasonic measurements, Table 2, are fitted fairly well by the same calculation.

Table 2. Results of Elastic Stiffness Constants (C) and Bulk Modulus (B). Units: $\times 10^{10} Nm^{-2}$.

	C_{11}	C_{12}	C_{13}	C_{33}	C_{44}	C_{66}	B
Expt.	4.31	2.54	2.18	4.47	2.14	2.41	2.99
Calc.	4.2	2.88	2.9	4.4	1.18	1.21	3.35

These results may again be analysed from the point of view which is now traditional for chalcopyrites, involving the folding of zincblende dispersion relations into the smaller Brillouin zone of the ordered structure. However the role of the vacancies must be carefully considered [1]. The effect of these is two-fold. Some modes at the top of the spectrum predicted by the folding procedure are missing and others in the middle of the spectrum are

depressed in frequency. The latter form local "breathing" modes around vacancies.

4. CONCLUSION

While we have found it useful to refer to previous work on chalcopyrites, there appear to be important differences in this case. This is particularly true of the valence band structure. In developing an explanation of the observed crystal field splitting we hope to shed light on the intriguing correlation between this splitting and tetragonal distortion which has been found for chalcopyrites and which would appear to be inapplicable to defect stannites. We believe this can be understood in terms of the effect of the ordered vacancies on the structure factors which govern the interactions responsible for the splitting.

ACKNOWLEDGEMENT

This work was supported by the Science Research Council. Contributions from A. R. Williams and R. Nelmes are gratefully acknowledged.

REFERENCES

1. A.Miller, A.MacKinnon, D.Weaire and D.J. Lockwood, J. Phys. C (Solid State Physics), to be published (1976).
2. S.L. Dahake, Brit. J. Appl. Phys 18 1340 (1967).
3. G.A. Saunders and T. Seddon, J. Phys. Chem. Solids (to be published) (1976).
4. A.R. Williams, A. Miller, A. MacKinnon and D. Weaire (to be published) (1976)
5. M.L. Cohen and V. Heine, Solid State Physics, 24 37 (1970).
6. J.L. Shay and J.H. Wernick, Ternary Chalcopyrite Semiconductors: Growth, Electronic Properties and Applications (Pergamon, Oxford 1975).
7. P.N. Keating, Phys. Rev. 145 637 (1966).

27

TWO-MAGNON RAMAN SCATTERING IN $KNi_xMn_{1-x}F_3$

G.J. COOMBS and D.J. LOCKWOOD
Physics Department, Edinburgh University, Edinburgh EH9 3JZ, Scotland

The two-magnon excitations in two single crystals of the substitutionally disordered antiferromagnet $KNi_xMn_{1-x}F_3$ with nominal concentrations $x = 0.50$ and 0.75 have been studied as a function of temperature by Raman spectroscopy. Two well-defined bands that broaden and shift to lower energy with increasing temperature were observed. A cluster model calculation is in reasonable agreement with the low-temperature results.

The advantages of antiferromagnets as examples of substitutionally disordered systems for the study of collective excitations are well known [1]. The material $KNi_xMn_{1-x}F_3$ is a particularly simple example of such a system as both constituents are antiferromagnets, with the cubic perovskite structure at high temperatures, whose magnetic-excitation spectra may be characterised by standard spin-wave theory based on the Heisenberg model with nearest-neighbour interactions. As might be expected from the large differences in the exchange constants of the two constituents, the magnon dispersion curves, as measured by neutron scattering for $x = 0.75$ [2], show two branches lying in well-separated bands both having appreciable dispersion.

We have measured the Raman spectra over a wide range of temperatures of two crystals of $KNi_xMn_{1-x}F_3$ having nominal concentrations of nickel of 0.75 and 0.50. The results at the lowest temperatures have been compared with theoretical calculations based on a simple Ising cluster model.

The crystals of $KNi_xMn_{1-x}F_3$, provided by the late D.A. Jones, were cut into cubes of approximately 5 mm edge with [100] faces. These samples were mounted in a flow cryostat and the Raman spectrum was excited with 300 mW of argon laser light at 514.5 nm with the scattered light analysed using equipment described previously [3]. The spectra reported here were recorded with $X\,(YY)\,Z$ polarization, where X, Y and Z refer to the crystal cubic axes. No magnon features were seen in the off-diagonal polarizations. The spectral resolution was 4.0 cm^{-1} at 514.5 nm.

As can be seen from the results shown in Figs. 1 and 2, there are three features in the spectra at low temperatures. The temperature dependences of the peak positions are shown in Fig. 3. On the basis of their marked temperature dependences and theoretical considerations given below, the highest frequency ($\sim$ 640 cm^{-1}) and lowest frequency ($\sim$ 420 cm^{-1}) peaks are identified as being due to two-magnon excitations on nickel–nickel pairs and manganese–nickel pairs, respectively. The weakly temperature-dependant peak in the middle, at approximately 540 cm^{-1}, is believed to be due to two-phonon scattering . A similar peak is observed in the YY spectrum of cubic $KMnF_3$ [4]. Neither the manganese–manganese two-magnon peak nor the two zone-centre one-magnon peaks were observed.

The low-temperature linewidths of the lower and upper two-magnon bands are approximately

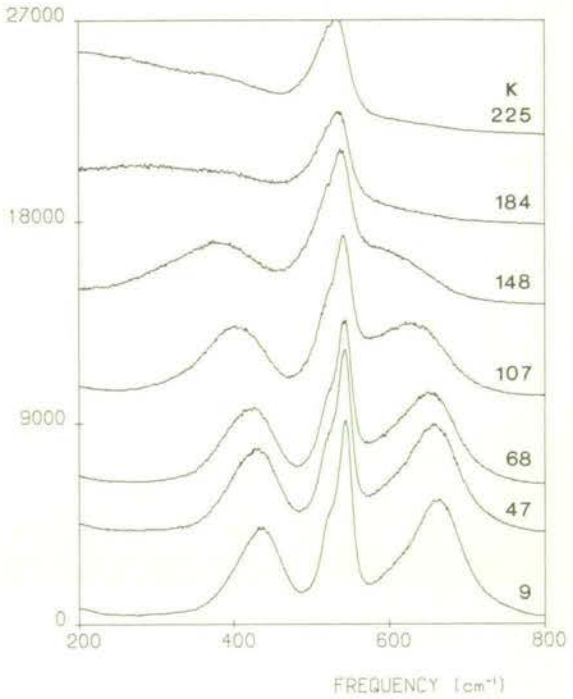

Fig. 1. Raman spectrum of $KNi_{0.75}Mn_{0.25}F_3$ recorded at various temperatures with diagonal polarization.

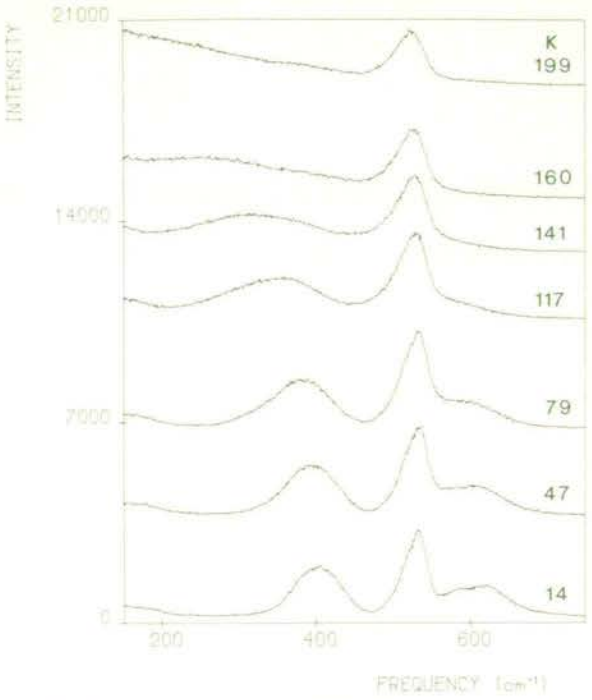

Fig. 2. Raman spectrum of $KNi_{0.5}Mn_{0.5}F_3$ recorded at various temperatures with diagonal polarization.

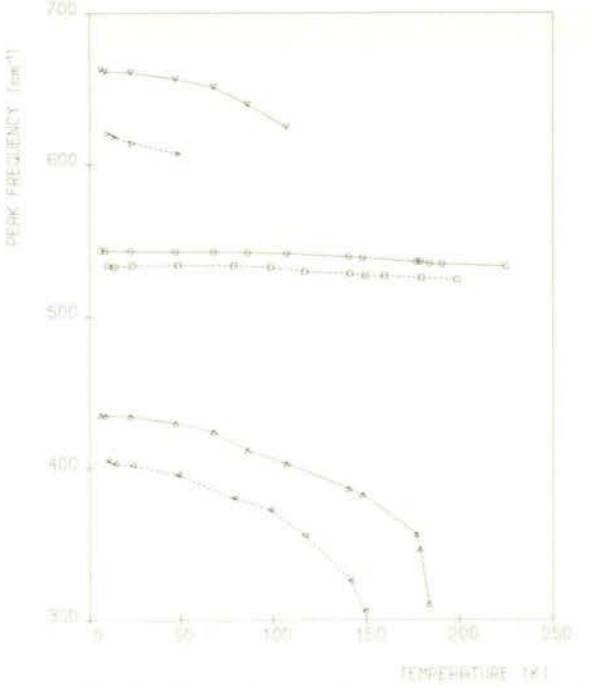

Fig. 3. Temperature dependence of the peak frequencies of the two magnon bands (∇,$\triangle$ for $x = 0.75$ and $\triangleright$,$\triangleleft$ for $x = 0.50$) and two-phonon band (0 for $x = 0.75$ and $\square$ for $x = 0.50$) in the Raman spectrum of $KNi_xMn_{1-x}F_3$.

70 and 85 cm^{-1} for both concentrations. As the temperature increases, both peaks increase in width and shift to lower frequencies until they are lost in the background. The excitations exist at temperatures well above the Néel temperatures (T_N) estimated from the nominal concentrations to be 167 and 207 K.

No structural phase transition, as found in $KMnF_3$ [4], was observed in these mixed crystals for temperatures down to about 10 K.

In an attempt to describe the results for the two-magnon scattering, we have used the Ising cluster model. This model is derived, and its limitations discussed, by Buchanan et al. [5] who apply it with some success to $Mn_xZn_{1-x}F_2$. The scattering function is given by a sum of delta functions positioned at the Ising energies of the various possible configurations of the cluster and each weighted by the probability of the occurrence of the particular configuration. We use the expressions given by Fleury and Guggenheim [6].

To facilitate the comparison of theory and experiment, the delta functions have been replaced by Lorentzians with a width arbitrarily chosen to be 15 cm^{-1}. The values of the model parameters used are taken from Cowley and Buyers [7]. The theoretical two-magnon spectrum consists of three quite distinct peaks, which may be regarded as due to excitations on nickel–nickel, nickel–manganese and manganese–manganese nearest-neighbour pairs, in order of decreasing energy. The scattering function thus obtained has been fitted to the lowest temperature spectrum for each concentration with the scattering strengths of the manganese and nickel ions taken as separately variable parameters. To take account of the two-phonon band, a harmonic oscillator response function has been used. This does not give a particularly good representation of a clearly complex peak but it should give a reasonable description of the lower part of the peak where it overlaps the magnetic scattering. A fixed, flat background has been added to the fitting function. In the fitting procedures it was found that for both crystals the agreement could be improved by reducing the concentration from the nominal value. Ultimately the values used were 0.42 and 0.57 instead of the nominal 0.50 and 0.75. Whether the fault lies with the model or the values of the nominal concentrations is

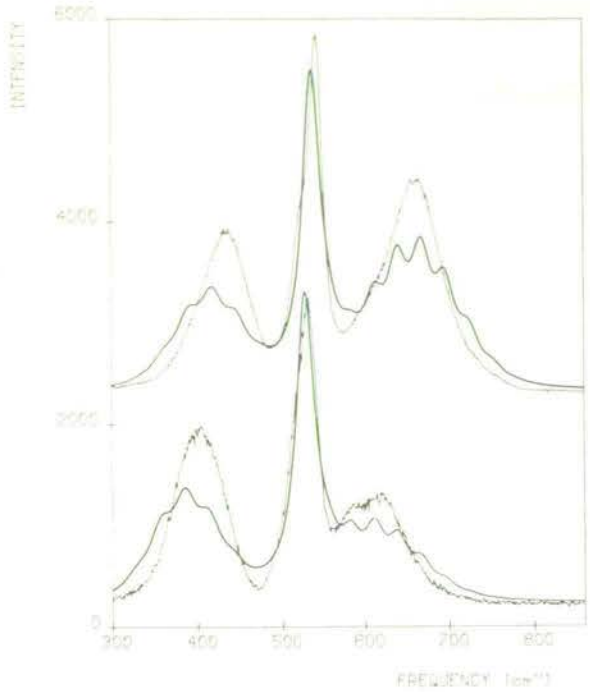

Fig. 4. Comparison of Ising cluster theory with the Raman spectra of $KNi_xMn_{1-x}F_3$. The upper spectrum is for $x = 0.75$ at a temperature of 9 K and has been divided by a factor of 5. The lower is for $x = 0.50$ at 14 K. In each case the heavy line is the theory.

unknown but the latter is suspected and it is intended to obtain accurate values of both the Néel temperatures and concentrations at some future time. The results of the fitting are shown in Fig. 4. The theoretical widths for all the two-magnon peaks may be seen to be greater than the experimental widths, which is surprising as the model includes only the effects of the disorder broadening and ignores the finite bandwidths.

References

[1] R.A. Cowley, Proc. 21st Conf. on Magnetism, Philadelphia (1975).
[2] G.J. Coombs, R.A. Cowley, D.A. Jones, G. Parisot and D. Tocchetti, Proc. 21st Conf. on Magnetism, Philadelphia (1975).
[3] D.J. Lockwood and G.J. Coombs, J. Phys. C: Solid State Phys. 8 (1975) 4062.
[4] D.J. Lockwood and B.H. Torrie, J. Phys. C: Solid State Phys. 7 (1974) 2729.
[5] M. Buchanan, W.J.L. Buyers, R.J. Elliot, R.T. Harley, W. Hayes, A.M. Perry and I.D. Saville, J. Phys. C: Solid State Phys. 5 (1972) 2011.
[6] P.A. Fleury and H.J. Guggenheim, Phys. Rev. B12 (1975) 985.
[7] R.A. Cowley and W.J.L. Buyers, Rev. Mod. Phys. 44 (1972) 406.

J. Phys. C: Solid State Phys., Vol. 10, 1977. Printed in Great Britain.

Raman spectrum of synthetic zircon ($ZrSiO_4$) and thorite ($ThSiO_4$)

R W G Syme†‡, D J Lockwood† and H J Kerr§

†Physics Department, Edinburgh University, Edinburgh EH9 3JZ, Scotland

§deceased; formerly of Physics Department, University of Canterbury, Christchurch, New Zealand

Received 27 October 1976

Abstract. The complete Raman spectra of single-crystal synthetic zircon and thorite are reported for the first time. Results are presented for thorite at 295 K and zircon at 295 and 90 K. The temperature-dependent study was essential for distinguishing between weak first-order bands and second-order features which can have narrow half-widths. The lattice vibrations in both crystals are notably harmonic. The spectra are analysed in terms of internal and lattice modes of the SiO_4^{4-} complex with some success. The crystal-field splittings for the internal modes are large. A comparison between the zircon and thorite results enables an assignment to be made of the Raman spectrum of powdered hafnon ($HfSiO_4$) reported by Nicola and Rutt.

1. Introduction

Zircon ($ZrSiO_4$) and thorite ($ThSiO_4$) are potentially suitable crystalline hosts for studying the electronic spectra of the higher valency states of rare-earth and actinide ions. They are optically transparent, readily doped with lanthanides and uranium (Chase and Osmer 1966), and provide a tetravalent site of tetragonal symmetry. For example, EPR investigations of Er^{3+}, Yb^{3+}, Gd^{3+}, Dy^{3+}, Tb^{4+} and Nb^{4+} in zircon-structure silicates have already been undertaken (see for example Hutton and Troup 1964, Hutton and Milne 1969, and Reynolds *et al* 1972). Such studies have been motivated in part by the use of Eu-doped YVO_4 (an isomorph of zircon) as a colour television phosphor. For any detailed understanding of the electronic and vibronic spectra of doped crystals it is helpful to know the lattice vibrations of the host material.

Zircon had been studied by Raman spectroscopy as early as 1939 (Hibben 1939) but no attempt was made to assign frequencies. The Raman spectrum of the SiO_4^{4-} complex in powdered $ZrSiO_4$ and $ThSiO_4$ has been examined by Griffith (1969a, b) and compared with infrared data obtained from the work of Moenke (1963). More recently, Dawson *et al* (1971) have reported on an extensive infrared and Raman study of single-crystal zircon, and Gervais *et al* (1973) have examined the temperature dependence of the infrared spectrum for the extraordinary ray of this crystal. All these works used naturally occurring crystals for their samples. A further Raman study has been carried out on powdered samples of zircon and isomorphic hafnon ($HfSiO_4$) using both natural and synthetic

‡ Permanent address: Physics Department, University of Canterbury, Christchurch, New Zealand.

material (Nicola and Rutt 1974). None of these studies produced a complete determination of the Raman spectrum for each mineral and there are inconsistencies in some of the observations and assignments.

Natural $ZrSiO_4$ and $ThSiO_4$ are frequently found in a metamict state (Pabst and Hutton 1951), i.e. an isotropic state of secondary origin, and are liable to contain various impurities (Chase and Osmer 1966, Dawson *et al* 1971). For these reasons, it was felt advisable to restrict this study to synthetic single crystals where the state of the crystal is known and there is no impurity problem. We have measured the Raman spectrum of zircon at 295 and 90 K and thorite at 295 K and have found all the first-order Raman-active modes. Special care was taken with intensity and polarization measurements and this enabled definite assignments of the vibrational frequencies to symmetry species. The assignments are discussed in terms of internal and external modes of vibration of the silicate ions and comparisons are made between the various results for zircon, thorite and hafnon. Our Raman results for zircon add to, and agree with in the main, the earlier works, but we are in disagreement with the $ThSiO_4$ results of Griffith (1969a). The differences are ascribed to differences in the crystalline form (Pabst and Hutton 1951) of the respective $ThSiO_4$ samples, and we believe this to be the first report of Raman scattering from thorite.

Unlike the other tetrahedral ions in the isoelectronic series ClO_4^-, SO_4^{2-}, PO_4^{3-} and SiO_4^{4-}, the silicate complex is not found as a separate entity in solution (Fortnum and Edwards 1956). The vibrational frequencies of the 'free' complex can only be inferred from solid state studies. It is hoped that this study of relatively simple silicate compounds† will help in the calculation of 'free' SiO_4^{4-} frequencies and force constants.

2. Group theory and selection rules

Crystals of zircon and thorite are isomorphous, with space group D_{4h}^{19} or $I4_1/amd$ (Wyckoff 1965). There are two formula units in the primitive cell and, therefore, 36 normal modes of vibration with wavevector $\boldsymbol{k} = 0$. The number of modes, N, belonging to each of the irreducible representations of D_{4h}, the point group isomorphous with the factor group, may be determined by unit-cell group analysis (Bhagavantum and Venkatarayudu 1948). The resultant decomposition of the reducible representation of the crystal vibration space is given in table 1 and agrees with that of Dawson *et al* (1971), but differs from the earlier results of Miller *et al* (1968) and Richman (1966). These latter references are concerned with the lattice vibrations of YVO_4, YPO_4 and $YbPO_4$, which are all isomorphs of zircon. The result given by Miller *et al* (1968) for the symmetry decomposition differs from that given in table 1 by an interchange of the representation labels B_1 and B_2. This difference serves to point out a common difficulty that can occur in the site-group correlation method (Hornig 1948, Winston and Halford 1949) used by Miller *et al* (1968) and Richman (1966). In the Bhagavantum method (Bhagavantum and Venkatarayudu 1948) used here, the two C_2' operations of D_{4h} were referred to the equivalent crystallographic axes a and b (or x and y, z being the axis of highest symmetry). In the correlation method, the operations of the site group and factor group must be carefully compared to obtain the correct correlation. For zircon, the SiO_4^{4-} site symmetry is D_{2d}, and for our choice of axes the correct correlation with D_{4h} symmetry is obtained when the C_2' operation in D_{2d} becomes the C_2'' operation in D_{4h}. The alternative association of the D_{2h} C_2' operation with the D_{4h} C_2' operation would require referral of the C_2'' operation of D_{4h} to the crystal-

† For an extensive study of SiO_4^{4-} vibrations in complex-structured silicates see Griffith (1969a).

lographic *a* and *b* axes. This ambiguity, inherent in the correlation method, is pointed out in an excellent review article by Fateley *et al* (1971). Miller *et al* (1968) and Richman (1966) do not explicitly state what choices they have made, but their mode decomposition and Raman tensor polarization assignments are consistent only if their *x*, *y* axes are at 45° to the crystal *a*, *b* axes. In cases where ambiguity may arise, as for D_{4h} symmetry, it is advisable to present the character table used for the group theoretical calculation and the choice of axes so that the derivation is clear.

Table 1. Character table for $k = 0$ modes of zircon with point group D_{4h}. N is the total number of modes that transform according to each irreducible representation, N_{ac} the number of acoustic modes, N_{trans} the number of translatory modes, N_{rot} the number of rotatory modes, and N_{int} the number of SiO_4^{4-} internal modes.

	E	$2C_4$	C_2	$2C_2'$	$2C_2''$	I	$2S_4$	σ_h	$2\sigma_v$	$2\sigma_d$	N	N_{ac}	N_{trans}	N_{rot}	N_{int}
A_{1g}	1	1	1	1	1	1	1	1	1	1	2	0	0	0	2
A_{2g}	1	1	1	−1	−1	1	1	1	−1	−1	1	0	0	1	0
B_{1g}	1	−1	1	1	−1	1	−1	1	1	−1	4	0	2	0	2
B_{2g}	1	−1	1	−1	1	1	−1	1	−1	1	1	0	0	0	1
E_g	2	0	−2	0	0	2	0	−2	0	0	5	0	2	1	2
A_{1u}	1	1	1	1	1	−1	−1	−1	−1	−1	1	0	0	0	1
A_{2u}	1	1	1	−1	−1	−1	−1	−1	1	1	4	1	1	0	2
B_{1u}	1	−1	1	1	−1	−1	1	−1	−1	1	1	0	0	1	0
B_{2u}	1	−1	1	−1	1	−1	1	−1	1	−1	2	0	0	0	2
E_u	2	0	−2	0	0	−2	0	2	0	0	5	1	1	1	2

In a first approximation, the 36 normal modes can be further subdivided into different types of vibrations, as well as into symmetry species. The modes can be classified into internal and external vibrations by considering the silicon–oxygen bonds to be much stronger than metal–silicate bonds. For crystals with vanadate, tungstate, phosphate and sulphate tetrahedral complexes this division according to bond strength is reasonably satisfactory. However, we will show later that this is not as good an approximation for the silicate complex. The internal modes refer to silicon–oxygen movements within the silicate complex, whereas the external modes involve lattice motions of the silicate tetrahedron as a unit. The vibrations within the complex are expected to be higher in frequency than those of the lattice because the external vibrations involve motions of the massive silicate complex. The decomposition of the internal modes (N_{int}) is given in table 1. The external modes can be further subdivided into two groups: those that involve rotatory motions of the silicate complex (N_{rot}) and those motions that are purely translatory (N_{trans}). These decompositions are also given in table 1.

Symmetry coordinates can be readily constructed for all the modes, but as detailed presentations are given by Miller *et al* (1968) and Dawson *et al* (1971) they will not be considered further here. Miller *et al* (1968) and Dawson *et al* (1971) give identical symmetry coordinates, apart from the transposed labelling of B_{1g}, B_{2g} and B_{1u}, B_{2u} representations and the two obvious labelling errors in figure 3 of Dawson *et al* (1971). The symmetry coordinates will prove to be useful for distinguishing between two or more modes of the same symmetry. For example, in the external modes two E_g modes involve movement of the metal ion, whereas the third E_g mode does not have this dependence. Therefore, changing the metal from Zr to Th should differentiate these two types of modes when the Raman frequencies are compared. However, the symmetry coordinates need

not represent the *true* normal modes of the crystal. In the cases where there is more than one mode of a given species, there is the possibility of an interaction between these modes and then the normal coordinates will be linear combinations of the appropriate symmetry coordinates.

All but one of the *gerade* modes are Raman active. The appropriate non-zero components of the Raman scattering tensor for D_{4h} irreducible representations are (Loudon 1964)

$$A_{1g}\begin{pmatrix} a & & \\ & a & \\ & & b \end{pmatrix} \quad B_{1g}\begin{pmatrix} c & & \\ & -c & \\ & & . \end{pmatrix} \quad B_{2g}\begin{pmatrix} . & d & \\ d & . & \\ & & . \end{pmatrix} \quad E_g\begin{pmatrix} . & . & e \\ . & . & . \\ e & . & . \end{pmatrix}\begin{pmatrix} . & . & e \\ . & . & . \\ e & . & . \end{pmatrix}.$$

The $A_{2u}(z)$ and $E_u(x, y)$ modes are infrared active.

3. Experiment

The crystals of zircon and thorite were provided by the Aerospace Corporation, California. The crystals, grown from lithium molybdate melts (Chase and Osmer 1966), were free of visible defects and had the tetragonal bipyramidal habit with {100} rectangular faces and {111} terminating pyramids (Reynolds *et al* 1972). Rectangular samples of dimension $6 \times 4 \times 2\,mm^3$ and $1{\cdot}0 \times 0{\cdot}7 \times 0{\cdot}5\,mm^3$ for zircon and thorite respectively, were formed by grinding such that the {100} faces were retained and with end faces normal to the c axis. The faces were then polished with 3 or 1 μm diamond powder.

The Raman spectrum was excited with a Coherent Radiation 52B argon laser operating at 514·5 nm and the 90°-scattered light was analysed using a Spex Ramalab double monochromator at a spectral resolution of $2{\cdot}2\,cm^{-1}$. For zircon the laser power used was 150 mW, while for the smaller thorite crystal the effective power (after narrow-band filtering) was increased to about 250 mW. The EMI 6256S photomultiplier detector pulses were processed with a digitized data collection system linked to a multichannel analyser (Arthur and Lockwood 1974) and the Raman spectrum was then transferred to paper tape in a form suitable for direct processing on a large computer. The polarization of the scattered light was analysed with Polaroid film, and a polarization scrambler was placed between the analyser and the spectrometer. The directions X, Y and Z that are used to denote the various polarizations refer to the crystal a, b and c axes respectively.

Raman spectra were recorded at room temperature, and for zircon further measurements were carried out at low temperatures using an Oxford Instruments CF100 flow cryostat with liquid nitrogen as the coolant. A Au/Fe–chromel thermocouple mounted on the sample monitored the crystal temperature.

4. Results

4.1. Zircon

Figure 1 shows the results for the four independent polarization components of the Raman spectrum of zircon at 90 K. In the standard notation $Z(YY)X$ indicates that the incident light is directed along the crystal Z-direction with Y-polarization and the scattered light is observed along the X-axis with Y-polarization. The recorded intensities

were found to be reproducible to within 5%. For the $Y(ZZ)X$, $Y(XY)X$ and $Y(ZY)X$ spectra the intensity scale represents actual photon counts per channel over the three second count period. The $Z(YY)X$ spectrum has been scaled to allow for the change in crystal orientation by comparison of a $Z(YZ)X$ spectrum with the $Y(ZY)X$ result. No correction has been made for the spectral response of the analysing system, but comparisons within any one frequency region are valid from spectrum to spectrum.

Some 'leak through' of forbidden bands in certain polarizations is evident in these spectra, arising from slight misorientation of the crystal and the crystal birefringence.

Table 2. Peak frequencies, linewidths and polarizations of the first-order Raman spectra of zircon and thorite. Frequencies are given to the nearest 0·5 cm^{-1} and the numbers in brackets are the half widths† of the bands $\pm 0{\cdot}1$ cm^{-1}.

$ZrSiO_4$		$ThSiO_4$		
90 K	295 K	295 K	Polarization	Symmetry species
202·5 (2·2)	202·5 (2·3)	129·5 (2·2)	XZ, YZ	E_g
216·5 (2·2)	215·5 (2·9)	126·0 (2·7)	XX, YY	B_{1g}
225·5 (2·2)	225·5 (3·3)	194·0 (3·7)	XZ, YZ	E_g
265·0 (2·2)	265·5 (2·5)	264·5 (2·5)	XY	B_{2g}
360·0 (2·3)	357·5 (4·5)	293·5 (6·9)	XZ, YZ	E_g
395·0 (3·7)	393·5 (6·0)	312·0 (3·6)	XX, YY	B_{1g}
441·5 (3·5)	439·5 (6·0)	439·5 (7·0)	XX, YY, ZZ	A_{1g}
547·0 (3·8‡)	547·0 (6·5§)	517·0 (3·7)	XZ, YZ	E_g
642·0 (3·3)	641·5 (4·7)	596·5 (4·0)	XX, YY	B_{1g}
927·0 (3·5‡)	925·5 (4·5§)	855·0 (3·6)	XZ, YZ	E_g
978·0 (2·4)	975·5 (2·8)	894·0 (3·9)	XX, YY, ZZ	A_{1g}
1012·5 (2·5)	1009·0 (3·3)	920·0 (3·3)	XX, YY	B_{1g}

† Since the spectral resolution used was 2·2 cm^{-1}, many of these half-widths are resolution limited.

‡ $\pm 0{\cdot}3$ cm^{-1}.

§ $\pm 0{\cdot}5$ cm^{-1}.

For each band the predominant polarization is, however, readily determined and the resulting symmetry-species assignments are given in table 2 together with the observed peak positions and linewidths of the first-order Raman bands at 90 and 295 K. For example, in the $Y(XY)X$ spectrum the band at 265 cm^{-1} is weaker than several other bands which are clearly 'leak through' from other polarizations. However, the complete absence of this weak band from the other three polarizations identifies it as the B_{2g} mode associated with the α_{xy} component of the Raman tensor. In cooling the crystal from room temperature to 90 K we note frequency shifts of up to 3·5 cm^{-1} and a general narrowing of band-widths (many of which are clearly resolution-limited). For the purposes of the following comparison with previous studies the room temperature results will be used.

For the bands reported by Dawson *et al* (1971) we are in general agreement with their symmetry assignments and in particular we confirm the weak 265·5 cm^{-1} band, seen only in (XY)-polarization, to be a first-order Raman band and not a laser plasma discharge line as suggested by Nicola and Rutt (1974). We have in addition been able to identify the three modes missing from the Dawson *et al* (1971) analysis—the B_{1g} mode (XX, YY) at 641·5 cm^{-1} and the two E_g modes (XZ, YZ) at 547 cm^{-1} and at 925·5 cm^{-1}. Dawson *et al* (1971) reported seeing a weak band at 547 cm^{-1} at room temperature, but claimed that

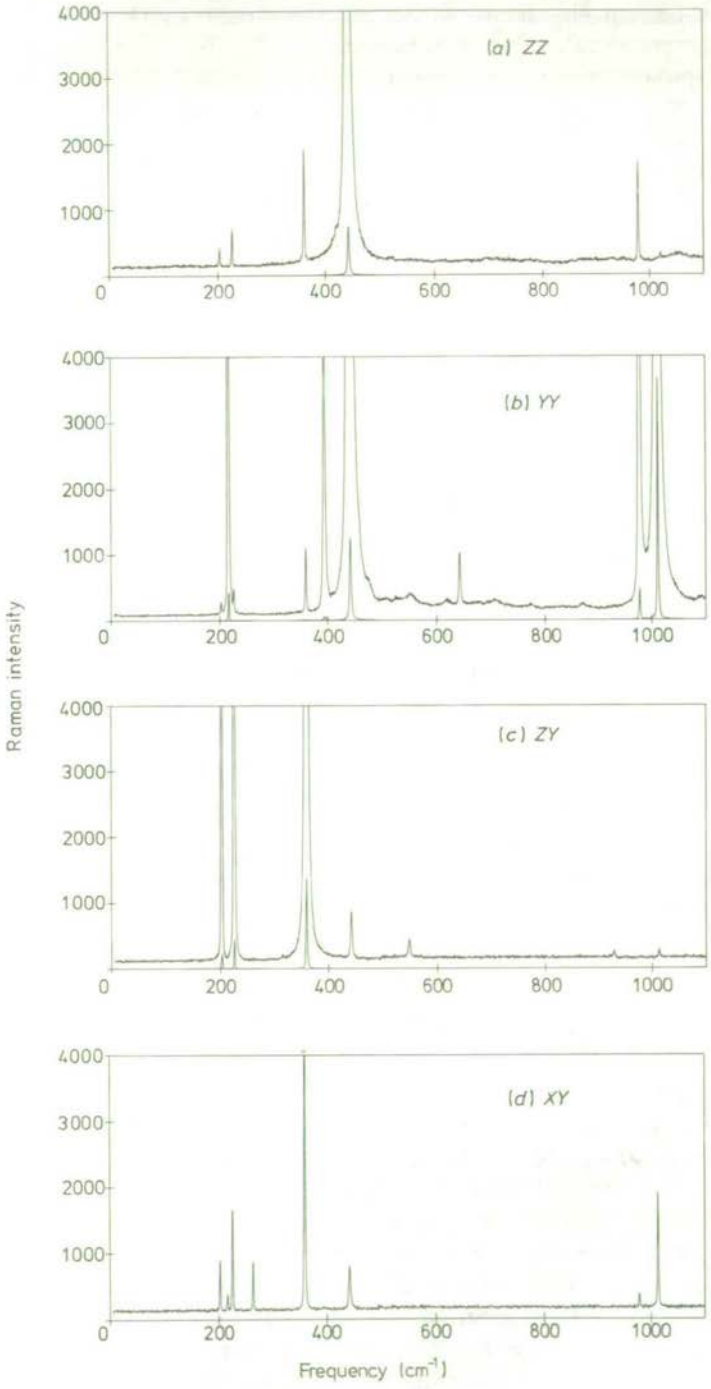

Figure 1. The polarized Raman spectrum of zircon at 90 K: (*a*) $Y(ZZ)X$; (*b*) $Z(YY)X$; (*c*) $Y(ZY)X$; (*d*) $Y(XY)X$. The strongest peaks are retraced on an intensity scale reduced by a factor of 100.

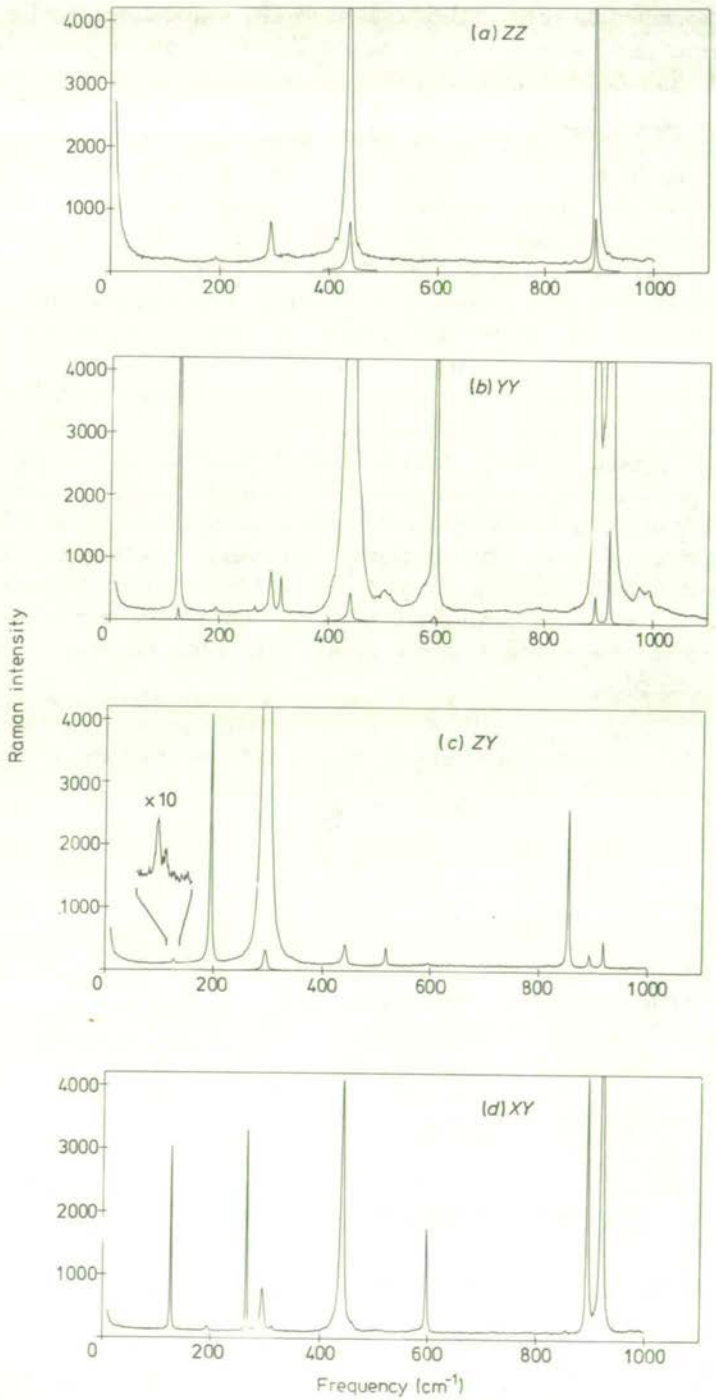

Figure 2. The polarized Raman spectrum of thorite at 295 K: (*a*) $Y(ZZ)X$; (*b*) $Z(YY)X$; (*c*) $Y(ZY)X$: (*d*) $Z(XY)X$. The strongest peaks are retraced on an intensity scale reduced by a factor of 10 for (*a*), or 100 for (*b*) and (*c*).

the band disappeared on cooling their crystal to 100 K and considered it to be a two-phonon difference band. The 547 cm^{-1} band is still very much in evidence in our measurements at 90 K, but because there is still some second-order structure present at this temperature (see particularly the $Z(YY)X$ and $Y(ZZ)X$ plots in figure 1) it was considered necessary to look carefully at the temperature dependence of these very weak bands.

For Stokes scattering the theoretical first-order Raman scattering efficiency varies as $(\bar{n} + 1)$ where $\bar{n}$ is the appropriate Bose–Einstein population factor for the corresponding phonon and temperature. For two-phonon sum or difference scattering, on the other hand, the corresponding factors are $(1 + \bar{n}_1)(1 + \bar{n}_2)$ and $(1 + \bar{n}_1)\bar{n}_2$ respectively. A comparison of intensities at 295 and 90 K should thus enable a distinction to be made between first-order bands and structure arising from higher-order scattering. In practice we cannot make a direct comparison of intensities at the two temperatures because of other changes in the experimental conditions (for example, the crystal has to be repositioned in the laser beam as the cryostat cools and contracts), but by considering the intensity of each band in question relative to that of a known first-order band in the same spectrum it is possible to avoid these difficulties. Intensities were computed by integrating over each band and subtracting out the background as obtained from adjacent regions of the spectrum. The resulting intensity ratios are compared in table 3, where the relative intensities have been scaled by the $(1 + \bar{n})$-factors appropriate for first-order scattering. Any change in this scaled intensity ratio for a given pair of lines on cooling from 295 K to 90 K would indicate departure from first-order behaviour for one (or both) of the bands being compared.

Table 3. Temperature dependence of intensities for the weak bands in zircon.

		$\frac{I(\omega_1)}{(1+\bar{n}_1)}\frac{(1+\bar{n}_2)}{I(\omega_2)} \times 10^3$	
ω_1 (cm^{-1})	ω_2 (cm^{-1})	295 K	90 K
$Y(ZY)X$ spectrum			
547·0	357·5	3·0 ± 0·2	3·1 ± 0·2
925·5	357·5	0·95 ± 0·15	1·00 ± 0·19
$Z(YY)X$ spectrum			
615	975·5	8·4 ± 0·8	2 ± 1
641·5	975·5	24 ± 1	22 ± 1
$Y(ZZ)X$ spectrum			
1019	975·5	70 ± 5	44 ± 4

From table 3 we see that within the statistical uncertainties the 547 cm^{-1}, 641·5 cm^{-1} and 925·5 cm^{-1} bands can all be confirmed as first-order rather than combination, difference or overtone structure. In the $Z(YY)X$ spectrum one can contrast the results for the 641·5 cm^{-1} band with that for the adjacent structure around 615 cm^{-1} which clearly is not first-order. Further, if the 641·5 cm^{-1} band arose, for example, from a feasible combination of the 215·5 cm^{-1} and 439·5 cm^{-1} phonons, one would expect the selected intensity ratio at 90 K to be 15 which lies well outside the range of uncertainty in the measured result of 22 ± 1.

It is of interest to note that a very weak band appearing at 1019 cm^{-1} at 295 K

(1020·5 cm^{-1} at 90 K) in the ZZ spectrum, with an intensity comparable with that of the 925·5 cm^{-1} band in the ZY spectrum, is shown not to follow a first-order temperature dependence. In this instance the narrow linewidth ($\sim$3 cm^{-1} at 90 K) compared with the other higher-order structure can be deceptive. In addition to this sharp peak, broad second-order structure is present in ZZ polarization at around 700 cm^{-1}, 850 to 950 cm^{-1} and 1050 cm^{-1}. More distinct structure persists at 90 K in the YY spectrum at 550, 620, 705, 770, 870 and 1090 cm^{-1}.

4.2. Thorite

The Raman spectrum of thorite at 295 K is presented in figure 2 and the peak positions, linewidths and symmetry assignments are summarized in table 2. Again the intensities have been scaled so that direct comparison between polarizations can be made within any given frequency region. Because of the much smaller size of the thorite crystal, the experimental conditions differed somewhat from those used for zircon by increase of the laser power and use of shorter focal length optics to focus the laser beam and to collect the scattered light. With these changes the observed photon count rates were comparable with those for zircon and, although an exact comparison cannot be made, it is estimated that the thorite intensities scale to the zircon results within an order of magnitude. The increased depolarization resulting from the change to shorter focal length optics is evident in figure 2 as an increase in polarization 'leak through', particularly in the $Z(XY)X$ spectrum, but as for zircon there is no ambiguity in the polarization of each of the twelve bands. The extremely weak band at 129·5 cm^{-1} in the $Y(ZY)X$ spectrum was located only with some difficulty and the expanded trace for this region shown in figure 2 was obtained at a higher spectral resolution and slower scan rate than the rest of the spectrum. Prominent second-order structure is evident in YY polarization at 505, 975 and 995 cm^{-1}, while there are broader peaks around 650, 720 and 790 cm^{-1} in the YY spectrum and 320, 410 and 900–1000 cm^{-1} in the ZZ spectrum.

Apart from the 264·5 cm^{-1} and 439·5 cm^{-1} bands, one notes a general shift of the peaks to lower energy (frequency) compared with the zircon results—a detailed comparison is deferred until the following section. It is of particular interest to compare the phonon frequencies observed here with the results presented by Griffith (1969a) who reported Raman-active phonons at 320, 424, 460, 976 and 1002 cm^{-1}. We see no agreement between these results and the frequencies for thorite given in table 2 and must conclude that Griffith cannot in fact have looked at thorite. Whether his results apply to huttonite, another naturally occurring form of $ThSiO_4$ (Pabst and Hutton 1951), remains open to speculation at this stage. Huttonite is a high-temperature polymorph of thorite that exists at room temperature in a metastable state. Crystals of huttonite are monoclinic, space group C_{2h}^5 (or $P2_1/n$), and thus the silicate ion will experience a different crystal field from that in thorite. Huttonite is found naturally as clear crystal fragments, while as noted in § 1 natural thorite is characteristically found in a metamict state (Pabst and Hutton 1951). X-ray diffraction measurements have confirmed that our single-crystal synthetic samples of $ThSiO_4$ are of the tetragonal thorite form. Griffith obtained his Raman frequencies from powdered samples of natural $ThSiO_4$ and it seems likely that these samples were either huttonite, or thorite in the metamict state. Griffith notes a weak Raman band at 460 cm^{-1} in both $ZrSiO_4$ and $ThSiO_4$ powders, but neither we, nor Dawson *et al*, have observed this band in the single-crystal spectra. As zircon can also occur naturally in the metamict state (Pabst and Hutton 1951), the 460 cm^{-1} band could come from the metamict silicates, or alternatively, it may arise from an impurity common to both samples studied by Griffith.

5. Discussion

In discussing the correlations between the observed Raman-active frequencies in zircon and thorite with the symmetry coordinates described by Miller *et al* (1968) and Dawson *et al* (1971) it is convenient to consider first the internal modes of the silicate complex as modified by the crystal environment. In general terms these internal modes are expected to occur at higher frequencies than the external modes which involve motion of the silicate group as a whole and the heavy metal cations. The internal modes have been assigned on the basis of results obtained from Raman measurements of other silicate groups

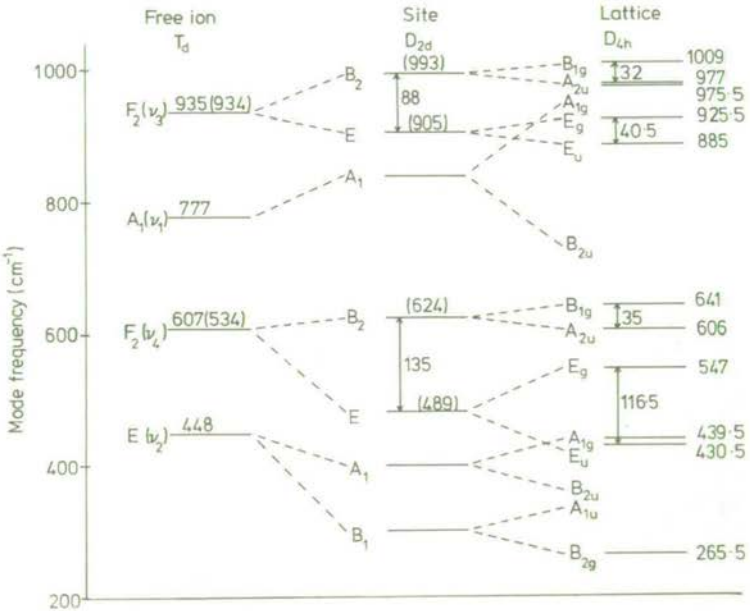

Figure 3. Correlation diagram for the internal modes of the $(SiO_4)^{4-}$ complex in zircon. The frequencies and splittings are given in wavenumbers, the sources for the data being indicated in §4 of the text. Bracketed frequencies are deduced from lattice mode data.

(Griffith 1969a, b), and from the expectation that pairs of modes arising from the $F_2(\nu_3)$ and $F_2(\nu_4)$ modes of the 'free' tetrahedral complex will be close in frequency to that of the parent mode. Our assignments are summarized in figure 3 which indicates the correlation between the free tetrahedral complex modes and the D_{4h} lattice modes via the D_{2d} site symmetry of the silicate complex in the crystal. The values given for the 'free' complex are taken from Fortnum and Edwards (1956), although these frequencies are thought to be associated with a $SiO_2(OH)_2^{2-}$ complex in solution and as such we would expect to find the ν_1 (symmetric Si–O bond stretch) mode frequency to be higher for a truly 'free' SiO_4^{4-} complex. The lattice frequencies given in figure 3 refer to zircon—our room-temperature Raman frequencies and the infrared measurements of Gervais *et al* (1973) and Dawson *et al* (1971). Gervais *et al* in their study of the A_{2u} modes obtain a value of 977 cm^{-1} for the higher A_{2u} mode in place of the 989 cm^{-1} value given by Dawson *et al* whose spectrum showed some unexplained structure in this region.

The assignments for zircon in figure 3 agree in the main with that of Dawson et *al* (1971) but our observation of the B_{1g} mode at 641·5 cm^{-1} and the E_g modes at 925·5 and 547 cm^{-1} enables a more consistent picture to be drawn. We note crystal-field splittings of 88 cm^{-1} for the $F_2(\nu_3)$ and 135 cm^{-1} for the $F_2(\nu_4)$ free silicate modes, and correlation field splittings, arising from interaction between the two silicate groups per unit cell, range from 32 to 116·5 cm^{-1}. From the splitting pattern in figure 3 we would predict the 'free' silicate F_2 frequencies to be $\nu_3 = 934{\cdot}5\ cm^{-1}$ and $\nu_4 = 534\ cm^{-1}$, but without knowledge of the inactive A_{1u} and B_{2u} modes we can say nothing further about the 'free' ν_1 and ν_2 frequencies. In the absence of any reliable infrared data for thorite (the spectrum given by Moenke (1966) is unpolarized and shows a broad absorption peaked at 1020 cm^{-1} and another at 460 cm^{-1}), we cannot give the equivalent splittings for this crystal, but comparison of the Raman frequencies between zircon and thorite (see table 2 and figure 4) suggests a similar pattern for thorite. The observed splittings indicate that the host-lattice silicate interaction and the coupling between silicate complexes is far from negligible and suggest caution in applying the internal–external mode separation. Although the lowest Raman-active internal mode which can interact with the external modes, the E_g mode at 547 cm^{-1} in zircon and 517 cm^{-1} in thorite, is well

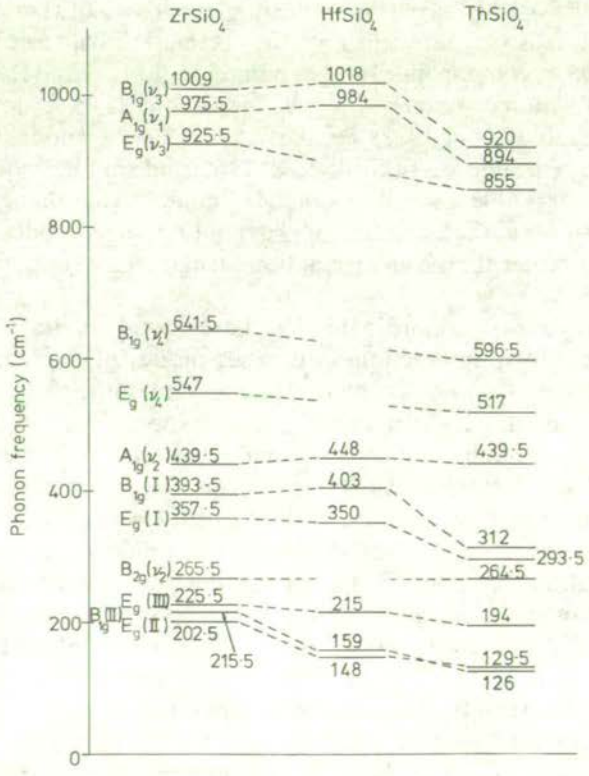

Figure 4. Comparison of frequencies of Raman-active phonons in zircon, hafnon and thorite. The hafnon frequencies are taken from Nicola and Rutt (1974). In addition to the D_{4h} symmetry labels, internal modes are labelled with the appropriate free silicate frequency (ν_i) and the external modes are distinguished by Roman numerals.

separated from the highest external E_g mode (at 357·5 cm^{-1} in zircon and 293·5 cm^{-1} in thorite), the situation is not as clearcut for the infrared-active E_u modes at 430·5, 389·5 and 287 cm^{-1} (Dawson *et al* 1971) in zircon.

In figure 4 we present a comparison of the Raman frequencies for zircon and thorite, and also include the frequencies reported by Nicola and Rutt (1974) for powdered hafnon ($HfSiO_4$). In this figure, broken lines connect bands of the same symmetry and, we consider, of the same mode character. The zircon–thorite correspondence is derived from symmetry and frequency considerations, but for hafnon we have no symmetry information and must rely on frequency and intensity in the comparison with zircon and thorite. From figures 1 and 2 we note an increase in intensity of the $A_{1g}(\nu_1)$ band relative to the $B_{1g}(\nu_3)$ band in going from zircon to thorite. The $E_g(\nu_3)$ band, although stronger in thorite than in zircon, is much weaker than the other two modes in this region and we therefore agree with the Nicola and Rutt correlation of 1018 cm^{-1} to B_{1g} and 984 cm^{-1} to A_{1g}. The assignment of the strong 448 cm^{-1} hafnon band to the $A_{1g}(\nu_2)$ internal mode is supported by the zero shift in this mode between zircon and thorite. As the other internal modes, $E_g(\nu_4)$, $B_{1g}(\nu_4)$ and B_{2g}, are weaker in zircon and thorite it is not surprising that that they were not seen in the spectrum of hafnon powder.

It is obvious from figure 4 that the internal mode frequencies are not lattice independent and this is consistent with the previous evidence from crystal-field splittings. In the tight-binding picture the $A_{1g}(\nu_1)$ symmetric stretch frequency would be independent of the lattice, but it shows a 10% variation indicating sensitivity of the Si–O bonds to the crystal environment. It is of interest to note the correlation between the frequency shifts of the $A_{1g}(\nu_1)$ mode in going from zircon to hafnon to thorite, and the corresponding changes in unit cell volumes namely 260·8 $Å^3$ for zircon, 257·5 $Å^3$ for hafnon and 322·7 $Å^3$ for thorite (Reynolds *et al* 1972). Similarly the ν_3 and ν_4 modes involve some degree of bond stretching (see figure 3 of Miller *et al* 1968) and shift in frequency accordingly. The contrasting remarkable insensitivity of the ν_2 modes to the change from zircon to thorite can be understood in that, to a first approximation, these modes involve Si–O bond angle deformation rather than a change in bond length. This supports our assignment of these modes.

The assignment of symmetry coordinates for the external modes is not obvious because there could be strong interaction with other modes of the same symmetry. As already mentioned, the B_{1g} and E_g internal modes are sufficiently separated for coupling to the external modes to be ignored in a first approximation. From table 1 we have two B_{1g} translatory modes and three E_g modes to consider. If the tight-binding approximation is valid, one of these E_g modes arises from the F_1 rotation of the silicate complex and does not involve motion of the cations (see figure 4 of Miller *et al* (1968), noting the interchange of B_{1g} and B_{2g} labels). Interaction would produce some mixing of translational and rotational character in these E_g modes. For modes involving motion of the cations the effect of the mass changes should be to produce lower frequencies as we move through the zircon–hafnon–thorite chain. The mass numbers for Zr, Hf, Th and (SiO_4) are 91·2, 178·5, 232·0 and 92·1, respectively, and we note the similarity of Zr and (SiO_4) masses in contrast to the situation for hafnon and thorite.

For zircon and thorite the symmetry, frequency and intensity comparisons suggest the correlations indicated in figure 4, where different external modes of the same symmetry are distinguished by use of Roman numerals. For hafnon, the 350 cm^{-1} (strong) and 403 cm^{-1} (weak) modes clearly correlate with the E_g(I) and B_{1g}(I) modes, respectively. The 215 cm^{-1} hafnon mode is the most intense of the low-frequency trio and by analogy with zircon and thorite is assigned to the E_g(III) mode. The relative intensities of the

E_g(II) and B_{1g}(II) modes decrease drastically in going from zircon to thorite (compare figures 1 and 2) and this suggests that the 159 cm^{-1} hafnon mode is B_{1g} and the weak 148 cm^{-1} mode is E_g. We note a relatively small shift in frequency for the E_g(III) mode across the series suggesting that this mode is predominantly rotational in character i.e. from the F_1 rotation of the silicate complex. This assignment does not agree with that of Nicola and Rutt (1974) who link the zircon 202·5 cm^{-1} and hafnon 215 cm^{-1} bands as rotatory without giving a reason for their choice.

For the B_{1g}(II) and E_g(II) modes we note a regular drop in frequency and decrease in splitting in going across the series, with a reversal of order in thorite where the splitting is small. The ratios of the three frequencies for each mode are remarkably close to the ratio of the inverse square roots of the cation masses.

$$(M_{Zr})^{-1/2}:(M_{Hf})^{-1/2}:(M_{Th})^{-1/2} = 1:0{\cdot}712:0{\cdot}626,$$

$$\omega_{Zr}:\omega_{Hf}:\omega_{Th} = \begin{cases} 1:0{\cdot}738:0{\cdot}601 & \text{for } B_{1g}\text{(II)}, \\ 1:0{\cdot}731:0{\cdot}622 & \text{for } E_g\text{(II)}. \end{cases}$$

This suggests that the B_{1g}(II) and E_g(II) modes are translatory with the motion almost entirely restricted to the cations. The actual normal coordinates for these modes would then be linear combinations of the appropriate symmetry coordinates in figure 4 of Miller *et al* (1968), such that the silicate groups provide an almost stationary matrix within which the cations oscillate. This argument assumes little change in the metal–silicate force constants for these modes. As a corollary, the B_{1g}(I) mode would involve predominantly translational motion of the silicate groups, but the E_g(I) mode could in addition have a rotational component. For zircon and hafnon the I-mode frequencies are comparable, but there is a 16–22% decrease on going to thorite implying changing force constants here. The larger splitting of the B_{1g}(I)–E_g(I) pair compared with the B_{1g}(II)–E_g(II) pair indicate a greater anisotropy for the I-modes, consistent with a silicate rather than a cation motion.

6. Conclusions

The ability to compare all the first-order Raman-active modes of zircon and thorite has been of great assistance in clarifying our understanding of these systems. The comparisons reveal that the vibrations of the silicate ion shift to lower frequency on changing from zircon to thorite, indicating a weakening of the silicon–oxygen bonding. Dawson *et al* (1971) have shown that in zircon the metal–oxygen force constant is about one-tenth that of the silicon–oxygen force constant. This fact, coupled with the large correlation field splittings and the shift in silicate frequencies on changing hosts, indicates that the internal–external model for the $\boldsymbol{k} = 0$ vibrations of zircon, hafnon and thorite must break down to some extent. Nevertheless, the model still retains the merit of providing a good basis for an understanding of the $\boldsymbol{k} = 0$ modes in these materials.

Acknowledgments

We wish to thank the Aerospace Corporation, El Segundo, California for generously

providing the synthetic zircon and thorite crystals and R J Nelmes for the x-ray diffraction measurements. This work was supported by the Science Research Council and the New Zealand Universities Research Grants Committee.

Earlier results from this study were presented at the 54th Canadian Chemical Conference, Halifax, Nova Scotia, 31 May–2 June 1971 [IKK (ZAED) 1971 abstract no. B122759].

References

Arthur J W and Lockwood D J 1974 *J. Raman Spectrosc.* **2** 53–69
Bhagavantum S and Venkatarayudu T 1948 *Theory of Groups and its Application to Physical Problems* (India: Bangalore Press)
Chase A B and Osmer J A 1966 *J. Electrochem. Soc.* **113** 198–9
Dawson P, Hargreave M M and Wilkinson G R 1971 *J. Phys. C: Solid St. Phys.* **4** 240–56
Fateley W G, McDevitt N T and Bentley F F 1971 *Appl. Spectrosc.* **25** 155–73
Fortnum D and Edwards J O 1956 *J. Inorg. Nucl. Chem.* **2** 264–5
Gervais F, Piriou B and Cabannes F 1973 *J. Phys. Chem. Solids* **34** 1785–96
Griffith W P 1969a *J. Chem. Soc.* A 1372–7
—— 1969b *Nature* **224** 264–6
Hibben J H 1939 *The Raman Effect and its Chemical Applications* (New York: Reinhold)
Hornig D F 1948 *J. Chem. Phys.* **16** 1063–76
Hutton D R and Troup G J 1964 *Br. J. Appl. Phys.* **15** 405–6
Hutton D R and Milne R J 1969 *J. Phys. C: Solid St. Phys.* **2** 2297–300
Loudon R 1964 *Adv. Phys.* **13** 423–82
Miller S A, Caspers H H and Rast H E 1968 *Phys. Rev.* **168** 964–9
Moenke H 1963 *Mineralspektren* vol 1 (Berlin: Akademie-Verlag) p 614
—— 1966 *Mineralspektren* vol 2 (Berlin: Akademie-Verlag) p 6.158
Nicola J H and Rutt H N 1974 *J. Phys. C: Solid St. Phys.* 7 1381–6
Pabst A and Hutton C O 1951 *Am. Mineralogist* **36** 60–9
Reynolds R W, Boatner L A, Finch C B, Chatelain A and Abraham M M 1972 *J. Chem. Phys.* **56** 5607–25
Richman I 1966 *J. Opt. Soc. Am.* **56** 1589–90
Winston H and Halford R S 1949 *J. Chem. Phys.* **17** 607–16
Wyckoff R W G 1965 *Crystal Structures* 2nd edn vol 3 (New York: Interscience) p 15

29

TERNARY COMPOUNDS 1977

Edited by G D Holah

1977 xiii + 325pp illustrated
240 × 159 mm casebound 0 85498 126 8 postpaid
UK £20.00 North America $38.00

This volume contains invited and contributed papers presented at the Third International Conference on Ternary Compounds which was held at Heriot-Watt University, Edinburgh from 14–15 April 1977. Among the new materials with possible technological applications, the ternary compounds have become increasingly important, and the papers presented at the conference reflect the device potential of some particular materials, as well as the inherent interest in their basic physical properties. The importance of the chalcopyrite family of ternary compounds is apparent in the proceedings, and their use in nonlinear optical devices and solar cells is thoroughly discussed. The two previous conferences on ternary compounds were held at Bath in 1973 and at Strasbourg in 1975.

The Conference Series comprises papers from important symposia and summer schools reviewing or highlighting new developments in physics and related fields. The aim is to maintain standards similar to those of the *Journals of Physics*, and so all papers are refereed before acceptance for publication. Now running to over thirty volumes, the series is an established and respected vehicle for publication of proceedings.

Orders from the United States, Canada and Mexico should be sent to

American Institute of Physics
Dept B/N
335 East 45th Street
New York, NY 10017
USA

Orders from all other countries should be sent to

Physics Trust Publications
Blackhorse Road
Letchworth
Herts SG6 1HN
England

Published by
The Institute of Physics
Bristol and London

Institute of Physics Conference Series number **35**

Raman spectrum of $AgGaS_2$ revisited: temperature dependence of the degenerate modes

D J Lockwood
Physics Department, Edinburgh University, Edinburgh EH9 3JZ, Scotland

Abstract. The Raman and infrared spectrum of $AgGaS_2$ has been examined independently by several research groups and a consistent assignment of the zone-centre lattice frequencies has now been established with the exception of the low-frequency E modes. For these modes, room-temperature Raman measurements have shown a doublet at 85 and 95 cm^{-1} and some very weak broad structure peaked at 18 and 38 cm^{-1}. We have remeasured the E mode Raman spectrum as a function of temperature, and have analysed the intensities of observed bands. Allowing for the thermal population factor, the temperature dependence of intensities of established E modes at 95, 160, 222 (TO) and 233 (LO) cm^{-1} exhibit first-order behaviour. Relative to these modes, the 18 and 85 cm^{-1} bands increase in intensity with increasing temperature. A detailed intensity analysis shows that the strong 85 cm^{-1} band is a summation band of second order arising from modes of energy around 43 cm^{-1}. At low temperatures (about 140 K), there is a well defined band at 35 cm^{-1} and it appears to be first order, although the band intensity is not well correlated with the intensities of other first-order E modes because of strong anharmonic interactions with the two-phonon continuum. Details of the temperature dependence of the frequencies and damping of the modes are presented.

1. Introduction

The lattice dynamics of ternary compounds which crystallize in the chalcopyrite structure have recently attracted considerable attention. The most widely studied compounds are the ternary phosphides and sulphides, where the phonon frequencies have been calculated using an extended Keating model (Bettini 1975, Koschel and Bettini 1975) and a rigid-ion model (Poplavnoi and Tyuterev 1975a, b, c). The theoretical results are compared with zone-centre phonon frequencies derived from Raman and infrared data.

The zone-centre lattice vibrations of $AgGaS_2$ have been investigated in great detail experimentally by infrared and Raman spectroscopy (Holah *et al* 1974, Van der Ziel *et al* 1974, Lockwood and Montgomery 1975, Koschel and Bettini 1975) and also by Brillouin scattering (Holah and Grimsditch 1975), and the higher-mode frequencies are readily predicted by a Keating-model calculation (Koschel and Bettini 1975). A consistent assignment of the zone-centre lattice frequencies has now been established with the exception of the low-frequency E modes. For these modes, room-temperature Raman measurements (Lockwood and Montgomery 1975) have shown a doublet at 85 and 95 cm^{-1} and some very weak broad structure peaked at 18 and 38 cm^{-1}, whereas

at lower temperatures Koschel and Bettini (1975) report that marked relative intensity changes occur for these bands. Low-temperature infrared spectra (Koschel and Bettini 1975) show intense bands at 85 and 95 cm^{-1}, and a weak band at 34 cm^{-1}. In view of the aforementioned work on the lattice dynamics of $A^{I}B^{III}S_2$ chalcopyrites, and to aid computations of the lower-mode frequencies using improved models, it is important to determine which of the low-frequency E bands are first order in character.

We report here new measurements of the E mode Raman spectrum, and give an analysis of the temperature dependence of the observed bands.

2. Experiment

The crystal of $AgGaS_2$ used for this experiment was the one used in an earlier study (Lockwood and Montgomery 1975). The Raman measurements were performed on a Spex Ramalab double spectrometer with an EMI 6256S photomultiplier detector. The spectrometer and detection system were under automatic control (Arthur and Lockwood 1974) and produced the spectrum in a digital form suitable for direct processing by a large computer. Spectra were excited with 100 mW of 514·5 nm light from a Coherent Radiation 52B argon laser, and the 90° scattered light was recorded at a spectral resolution of 2·8 cm^{-1}. The polarization of the scattered light was analysed with Polaroid film, and a polarization scrambler was placed between the analyser and the spectrometer. For the low-temperature measurements the sample was placed in an Oxford Instruments CF100 flow cryostat. The sample temperature was monitored with a Au–Fe/chromel thermocouple and could be controlled to within 0·1 K.

The directions X, Y and Z used to denote the various polarizations refer to the crystal tetragonal axes *a*, *b* and *c*, respectively.

3. Results

The temperature dependence of the low-frequency E modes can be seen from the spectra given in figure 1. Because the 514·5 nm laser line lies at the absorption edge in $AgGaS_2$, the relative intensities of given Raman bands decreased with increasing temperature as a result of the temperature shift of the absorption edge. Accordingly, the spectra given in figure 1 have been normalized with reference to the lowest temperature data by comparing integrated intensities of distinct peaks and allowing for the Bose population factor. The band at 64 cm^{-1}† that can be seen in figure 1 is a strong B_2 mode that is forbidden in this polarization but appears as a result of the optical properties of $AgGaS_2$ coupled with experimental imperfections (Lockwood and Montgomery 1975). Note that the intensity of this forbidden band does not scale with the intensity of other strong peaks.

The temperature dependence of peaks shown in figure 1 was investigated in detail by a least-squares fitting of each peak to a damped simple harmonic oscillator response function in the form $I(\omega)\omega[\bar{n}(\omega, T) + 1] + C$, where

$$I(\omega) = \frac{S\omega_0^2\gamma^2}{(\omega^2 - \omega_0^2)^2 + \omega^2\gamma^2} .$$

†Unless otherwise indicated, peak frequencies quoted in the text are the room-temperature values.

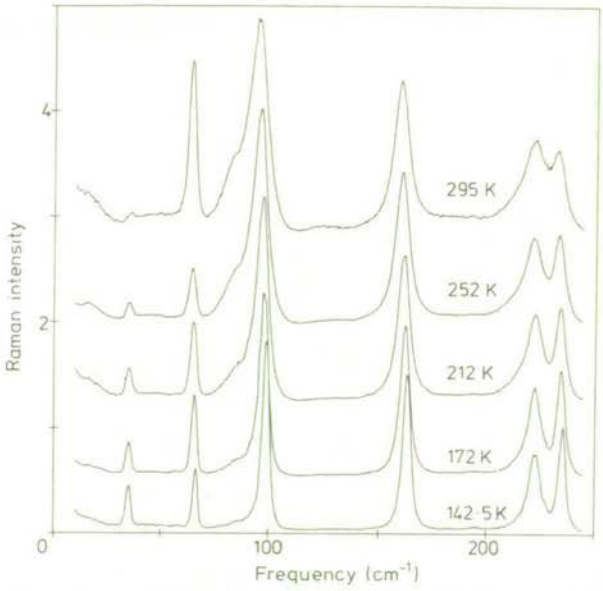

Figure 1. The X(ZY)Z Raman spectrum of $AgGaS_2$ recorded at various temperatures. For this polarization both E^{TO} and E^{LO} modes are allowed.

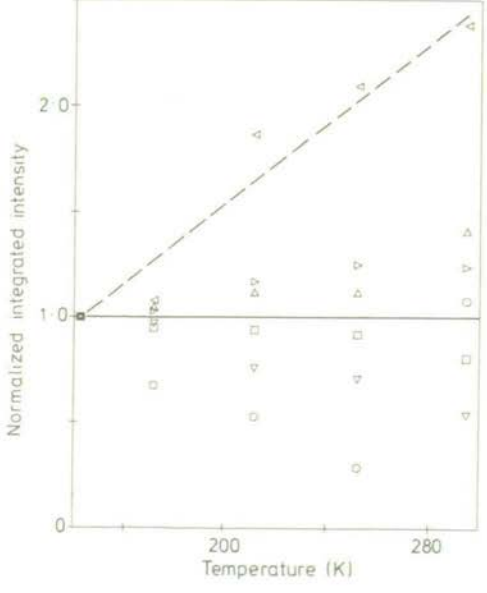

Figure 2. The temperature dependence of the integrated intensity of bands shown in figure 1. The symbols denote data for band 1 (○), band 3 (◁), band 4 (▷), band 5 (□), band 6 (△) and band 7 (▽) as identified by frequency in table 1.

Table 1. Frequency (ω_0) and damping (γ) parameters obtained from classical oscillator fits to the spectra shown in figure 1. ω_0 and γ are given in cm^{-1}.

Temperature (K)	Band 1		Band 2		Band 3		Band 4		Band 5		Band 6		Band 7	
	ω_0	γ	ω_0	γ	ω_0	γ	ω_0	γ	ω_0	γ	ω_0	γ	ω_0	γ
142·5	35·3	2·4	66·5	2·0	87·3	24·1	98·9	3·2	163·1	4·2	222·4	7·6	235·2	3·4
172	35·4	2·6	65·8	2·4	87·6	18·8	97·8	4·2	162·1	5·3	222·1	8·8	234·6	4·0
212	35·4	2·9	65·3	2·9	87·7	19·0	96·9	5·5	161·4	6·6	222·0	11·8	234·3	4·7
252	35·5	3·2	64·8	3·4	86·5	17·0	95·9	6·7	160·6	7·6	221·2	13·9	233·7	5·6
295	38·2	13·2	64·3	3·5	85·6	17·0	95·2	8·3	160·1	8·1	221·7	18·3	233·3	6·6

S, ω_0 and γ are the oscillator strength, frequency and damping constant, respectively, C is a constant background and $\bar{n}(\omega, T)$ is the thermal population factor for Bosons evaluated at frequency ω and temperature T. Peaks that are close in frequency were fitted simultaneously. The integrated intensity of the damped simple harmonic oscillator

$$\int_0^\infty I(\omega)\mathrm{d}\omega = S\gamma\pi/2$$

and this quantity, normalized to unity at $T = 142{\cdot}5$ K, is plotted as a function of temperature for each of the peaks in figure 2. The intensity of the 64 cm^{-1} band is not plotted in figure 2 for the reasons given above. The frequencies of the fitted bands decrease monatonically as the temperature increases as can be seen from the data of table 1. The 295 K fitted frequencies given in this table may differ from the simple *peak* values reported earlier (Lockwood and Montgomery 1975) because of overlap of bands. Other E modes in $AgGaS_2$ not shown in figure 1 behave similarly, with peak frequencies of 325·6, 337·6, 371·4 and 398·4 cm^{-1} at 142·5 K decreasing to 322, 333·1, 367·9 and 394·4 cm^{-1}, respectively, at 295 K. In the same way, the intense A_1 mode decreases from 298·0 to 294·7 cm^{-1} and the weak B_1 modes from 58·1 and 194·3 cm^{-1} to 54 and 190·5 cm^{-1}, respectively, over the same temperature range. The damping constant data given in table 1 show a much greater temperature dependence than the frequencies and to aid ready comparison in later discussion these results are presented in figure 3.

4. Discussion

The integrated intensity data of figure 1 can be used to determine the order of the scattering process that produced a particular peak (Syme *et al* 1977). First-order Raman bands have a temperature dependence governed by the $\omega[\bar{n}(\omega, T) + 1]$ factor, and as

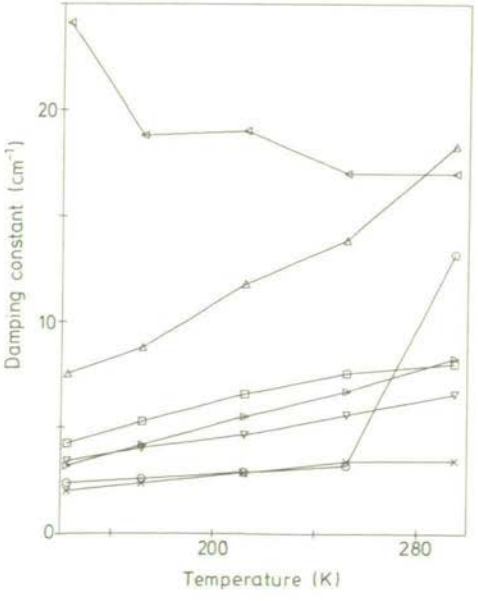

Figure 3. The temperature dependence of the damping constant (γ) of bands shown in figure 1. The symbols have the same meaning as for figure 2 with the addition of data for band 2 (X).

this factor has been removed in the fitting procedure first-order band intensities in figure 1 will be independent of temperature. Despite the increasing spread in the data with increasing temperature, which arises from the increasing multiplicative normalization factor acting on a constant statistical distribution of initial intensities, it can be seen from figure 2 that the bands at 95, 160, 222(TO) and 233 (LO) cm^{-1} are clearly first-orde in character with intensities distributed about the horizontal line at unity. This is the expected result. However, it is apparent from figure 2 that the 85 cm^{-1} band has an intensity which rises with increasing temperature and it can not, therefore, be a first-order band. Other evidence for this conclusion comes from the damping constant data for this band (table 1 and figure 3): the damping constant *decreases* with increasing temperature contrary to the normal behaviour of first-order bands. The 18 cm^{-1} band does not exhibit first-order character either (see figure 1) and this leaves the 38 cm^{-1} band as the only possibility for the remaining first-order E mode. At low temperatures (about 140 K), this latter band is well defined and has shifted to 35 cm^{-1}, but when the temperature is increased the intensity of this band decreases markedly (figure 1) and is not well correlated with the intensities of other first-order bands (figure 2). The other band parameters ω_0 and γ increase anomalously when the temperature is increased from 252 to 295 K (see table 1 and figure 3). Nevertheless, it appears that the 38 cm^{-1} band is first-order in character, and the unusual high-temperature behaviour most likely arises because of strong anharmonic interactions with the underlying two-phonon continuum. Further evidence of this nature will be presented shortly.

For two-phonon Raman scattering, the Bose population factor is $[\bar{n}(\omega_1, T) + 1] \times [\bar{n}(\omega_2, T) + 1]$ for summation bands and $[\bar{n}(\omega_1, T) + 1]\bar{n}(\omega_2, T)$ for difference bands arising from phonons of frequency ω_1 and ω_2. Any analysis of the temperature dependence of the integrated intensity of the 85 cm^{-1} band in terms of these factors must also take account of group theoretical selection rules. The cross product of the symmetry species of the two phonons combining to produce the 85 cm^{-1} band must contain the zone-centre E representation. The combining phonons are allowed to come from anywhere in the Brillouin zone provided that their wavevectors are equal and opposite. For $AgGaS_2$, only the zone-centre frequencies are known, and for these modes the allowed combinations are $E \times A_1$, $E \times A_2$, $E \times B_1$ and $E \times B_2$. Koschel and Bettini (1975) tentatively ascribe the 85 cm^{-1} band to a two-phonon difference line. From table 1 of Lockwood and Montgomery (1975) it can be seen that the nearest allowed difference combination is 321·5 (E) − 237·5 (B_2) = 84 (E) cm^{-1}. However, this combination does not predict the observed temperature dependence of the intensity. For example the integrated intensity ratio I(142·5 K)/I(295 K) = 0·59 for the 85 cm^{-1} band with Bose weighting factor $[\bar{n}(321{\cdot}5\ cm^{-1}, T) + 1]\bar{n}(237{\cdot}5\ cm^{-1}, T)$ removed. Other difference combinations are disallowed for the same reason. On the other hand, there is one allowed summation band 38(E) + 54 (B_1) = 92 (E) cm^{-1} which is close in frequency to 85 cm^{-1}. The ratio I(142·5 K)/I(295 K) = 0·96 with Bose weighting removed and this is very close to the desired value of unity. Infrared intensities of summation bands are governed by a $[1 + \bar{n}(\omega_1, T) + \bar{n}(\omega_2, T)]$ Bose factor, and for the summation band of 38 + 54 cm^{-1} the observed intensity will fall by only 1/3·7 in going from 295 to 77 K. In the Raman spectrum the corresponding factor is 1/8·9. These predicted intensity changes agree with the results of Koschel and Bettini (1975) who reported that the 85 cm^{-1} band had low intensity in the Raman spectrum at 78 K but still had considerable

intensity in the infrared spectrum at that temperature. Therefore, the 85 cm^{-1} band likely arises from a summation of the 54 (B_1) and 38 (E) cm^{-1} bands at wavevectors close to the Brillouin zone centre. It is probable then that there is an interaction between the 38 cm^{-1}, 85 cm^{-1} and 95 cm^{-1} E bands, especially at higher temperatures, which would affect the 38 cm^{-1} band parameters.

In earlier measurements it was noted that there are strong anharmonic interactions in the frequency range 190–230 cm^{-1} (Lockwood and Montgomery 1975). The temperature dependence and magnitude of the damping parameter for the 222 cm^{-1} band (table 1 and figure 3) confirm this conclusion.

5. Conclusions

The Raman measurements reported here show that bands at 38 cm^{-1} and 95 cm^{-1} are the two lowest fundamental E modes of $AgGaS_2$. This corrects an earlier erroneous conclusion (Lockwood and Montgomery 1975), where a band at 85 cm^{-1} was taken to be the lowest E mode, and verifies the initial assignment of Koschel and Bettini (1975). The 85 cm^{-1} band is a summation band of second order arising from modes of energy around. 43 cm^{-1} at wavevectors close to the zone centre.

References

Arthur J W and Lockwood D J 1974 *J. Raman Spectrosc.* 2 53–69
Bettini M 1975 *Phys. Stat. Solidi* b69 201–12
Holah G D and Grimsditch M 1975 *J. Physique* 36 C3 185–8
Holah G D, Webb J S and Montgomery H 1974 *J. Phys. C: Solid St. Phys.* 7 3875–90
Koschel W H and Bettini M 1975 *Phys. Stat. Solidi* b72 729–37
Lockwood D J and Montgomery H 1975 *J. Phys. C: Solid St. Phys.* 8 3241–50
Poplavnoi A S and Tyuterev V G 1975a *Fiz. Tverd. Tela* 17 313–6
—— 1975b *Fiz. Tverd. Tela* 17 1055–60
—— 1975c *J. Physique* 36 C3 169–76
Syme R W G, Lockwood D J and Kerr H J 1977 *J. Phys. C: Solid St. Phys.* 10 1335–48
Van der Ziel J P, Meixner A E, Kasper H M and Ditzenberger J A 1974 *Phys. Rev.* B9 4286–94

30

TERNARY COMPOUNDS 1977

Edited by G D Holah

977 xiii + 325pp illustrated
40 × 159 mm casebound 0 85498 126 8 postpaid
JK £20.00 North America $38.00

This volume contains invited and contributed papers presented at the Third International Conference on Ternary Compounds which was held at Heriot-Watt University, Edinburgh from 14–15 April 1977. Among the new materials with possible technological applications, the ternary compounds have become increasingly important, and the papers presented at the conference reflect the device potential of some particular materials, as well as the inherent interest in their basic physical properties. The importance of the chalcopyrite family of ternary compounds is apparent in the proceedings, and their use in nonlinear optical devices and solar cells is thoroughly discussed. The two previous conferences on ternary compounds were held at Bath in 1973 and at Strasbourg in 1975.

The Conference Series comprises papers from important symposia and summer schools reviewing or highlighting new developments in physics and related fields. The aim is to maintain standards similar to those of the *Journals of Physics*, and so all papers are refereed before acceptance for publication. Now running to over thirty volumes, the series is an established and respected vehicle for publication of proceedings.

Orders from the United States, Canada and Mexico should be sent to

American Institute of Physics
Dept B/N
335 East 45th Street
New York, NY 10017
USA

Orders from all other countries should be sent to

Physics Trust Publications
Blackhorse Road
Letchworth
Herts SG6 1HN
England

Published by
The Institute of Physics
Bristol and London

Institute of Physics Conference Series number **35**

Structure and lattice dynamics of the complex ordered-vacancy compound $Hg_3In_2\square Te_6$

A MacKinnon† §, A Miller†. D J Lockwood‡, G Ross† and G D Holah†
†Department of Physics, Heriot-Watt University, Edinburgh EH14 4AS, Scotland
‡Department of Physics, University of Edinburgh, Edinburgh EH9 3JZ, Scotland

Abstract. $Hg_3In_2\square Te_6$ has a structure which may be regarded as being derived from that of zincblende by the incorporation of an ordered array of vacancies. It has space group $P\bar{4}3m$ with lattice parameter 18·870 ± 0·003 Å, that is 3 × 3 × 3 zincblende cubes or 108 primitive zincblende unit cells, of which 18 contain vacancies.

Infrared reflectivity and Raman-scattering measurements were made and analysed qualitatively in terms of the properties of breathing modes about the vacancies. The model is generalized to predict the properties of other ordered-vacancy compounds.

1. Introduction

$Hg_3In_2\square Te_6$ is one of a series of compounds, intermediate between HgTe and $In_2\square Te_3$, which have structures which can be regarded as being derived from that of zincblende by the incorporation of an ordered array of vacancies. The results of lattice dynamical investigations have been reported for $HgIn_2\square Te_4$ (Miller *et al* 1976) and for $In_2\square Te_3$ (Finkman *et al* 1973, 1975). In addition, studies of elastic constants have been carried out for several members of the series by Saunders and Seddon (1970, 1971, 1976).

Maynell *et al* (1970) observed that the room-temperature structure of $Hg_3In_2\square Te_6$ is cubic with lattice parameter 18·870 ± 0·003 Å and point group either $\bar{4}3m$, $m3m$, or 432. Laue back-reflection photographs demonstrate that it is a zincblende superlattice comprising 3 × 3 × 3 zincblende cubes. Of the above point groups, only $\bar{4}3m$ is a subgroup of zincblende. Therefore the space group must be $F\bar{4}3m$, $I\bar{4}3m$, $P\bar{4}3m$ or $P\bar{4}3n$, of which only $P\bar{4}3m$ is compatible with a zincblende basis; $I\bar{4}3m$ and $P\bar{4}3n$ involve translations to the body centre of a zincblende cube, while $F\bar{4}3m$ requires a non-integer number of formula units. The space group must therefore be $P\bar{4}3m$, comprising 198 atoms and 18 vacancies per cell.

Clearly the most important detail that must be determined is the position of the vacancies. By considering how the sites of the zincblende basis transform under the operations of this space group, the atomic sites can be divided into sets which must contain identical atoms. Using this, together with the condition that no atom may have more than one vacancy as its nearest neighbour, the possible distributions of vacancies can be reduced to two (MacKinnon 1977). Although this assumption seems reasonable,

§Present address: Institut für Physik, Universität Dortmund, 4600 Dortmund, Federal Republic of Germany.

it must be noted that it cannot be valid for $III_2\square VI_3$ compounds, like $In_2\square Te_3$, since the proportion of vacant sites is too high. The possible vacancy positions are given in table 1.

The only simple constraint that might help in determining the positions of the Hg and In atoms is that the average valency of the nearest neighbours of a given atom should be the same as in the parent zincblende compound. In the case of $Hg_3In_2\square Te_6$ this would imply only two possible environments for the Te atoms, that is, (Hg,Hg,Hg,Hg) and (Hg,In,In,□). However, checking this assumption with the tables of identical positions shows it to be incompatible with the known symmetry.

Table 1. Possible vacancy positions.

Case 1	Case 2
(0,0,0)	(2,0,0)
(2,0,0)	($\bar{2}$,0,0)
($\bar{2}$,0,0)	(0,2,0)
(0,2,0)	(0,$\bar{2}$,0)
(0,$\bar{2}$,0)	(0,0,2)
(0,0,2)	(0,0,$\bar{2}$)
(0,0,$\bar{2}$)	(2,2,0)
(2,2,2)	(2,$\bar{2}$,0)
(2,$\bar{2}$,$\bar{2}$)	($\bar{2}$,2,0)
($\bar{2}$,2,$\bar{2}$)	($\bar{2}$,$\bar{2}$,0)
($\bar{2}$,$\bar{2}$,2)	(0,2,2)
($\bar{2}$,2,2)	(0,2,$\bar{2}$)
($\bar{2}$,$\bar{2}$,$\bar{2}$)	(0,$\bar{2}$,2)
(2,2,$\bar{2}$)	(0,$\bar{2}$,$\bar{2}$)
(2,$\bar{2}$,2)	(2,0,2)
(0,3,3)	(2,0,$\bar{2}$)
(3,0,3)	($\bar{2}$,0,2)
(3,3,0)	($\bar{2}$,0,$\bar{2}$)

These positions are expressed in units such that the basis vectors of simple zincblende are (1,1,0), (1,0,1) and (0,1,1).

It has been shown (McCartney 1971) that in the related compound $Hg_5In_2\square Te_8$ the Hg and In atoms are randomly distributed while the vacancies are ordered. There is also some evidence of this from an x-ray analysis of $HgIn_2\square Te_4$ (F N Laird and R J Nelmes, private communication) for which the structure appears to depend on the method of preparation. For this reason and because the dominant feature of the structure is the vacancies, no attempt has been made to determine the Hg and In distributions.

2. Infrared reflectivity

A Bridgman-grown single crystal of $Hg_3In_2\square Te_6$ of size 5 × 4 × 3 mm^3 was kindly supplied by G Saunders of the University of Bath. It was cut with (110) and (100) faces and oriented by Laue back reflection. The final surface preparation for the infrared and Raman measurements was with 0·25 μm diamond powder on paper backed by flat glass.

The infrared reflectivity measurements were made at room temperature on a Beckman-RIIC FS 720 interferometer in the range 40–500 cm^{-1}, on the (110) face.

The reflectance module allowed an angle of incidence of 10°; this does not introduce a significant error into the analysis, which assumed normal-incidence Fresnel equations. The spectral resolution was 4 cm^{-1}.

Figure 1 shows the infrared reflectivity results. Five broad bands can be seen. The data was analysed by combining a Kramers–Krönig analysis of the reflectivity

$$\theta(\omega_0) = \frac{\omega_0}{\pi} \int_0^\infty \frac{\ln[R(\omega)]\,d\omega}{\omega^2 - \omega_0^2} \tag{1}$$

with the Fresnel equation for reflection:

$$R^{1/2} \exp(i\theta) = \frac{[\epsilon(\omega)]^{1/2} - 1}{[\epsilon(\omega)]^{1/2} + 1}. \tag{2}$$

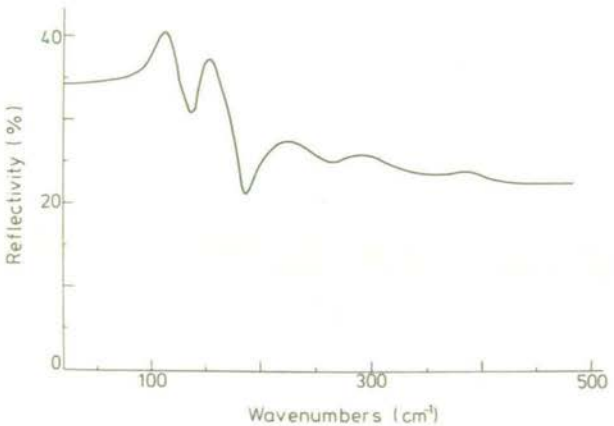

Figure 1. Measured infrared reflectivity of $Hg_3In_2\square Te_6$.

The Kramers–Krönig analysis presents some difficulty as the structure in the spectrum clearly extends to both higher and lower frequencies than have been measured. Existing computer programs for carrying out such an analysis assume implicitly that there is no structure in the spectrum outside the measured range. Such an assumption is clearly

Table 2. Resonant frequency, strength and damping factor of peaks in infrared reflectivity (figures 1 and 2). The first column gives an interpretation in terms of multiphonon coupling.

Peak	Frequency (cm^{-1})	Strength ($\times 10^4$ cm^{-2})	Damping (cm^{-1})
A	118	1·5	25
B	158	2·2	30
2A	238	3·6	82
2B	304	5·1	106
2A+B	395	4·0	84

not valid in our case, so an alternative strategy has been adopted. The reflectivity is assumed to be constant outside the measured range and this constant is chosen to minimize the variance of $\theta(\omega)$ at the ends. This technique applies in this case because the peaks in the spectrum are very broad and $\theta(\omega)$ is a slowly varying function, whereas, using a more conventional extrapolation of $R(\omega)$, $\theta(\omega)$ would be forced to zero very rapidly at the ends, thereby introducing a structural feature not present in the data.

The real and imaginary parts of the dielectric constant as calculated by the above method are shown in figure 2. To each of the peaks in $\epsilon''(\omega)$ a Lorentzian has been fitted and classical harmonic oscillator parameters derived. These are shown in table 2.

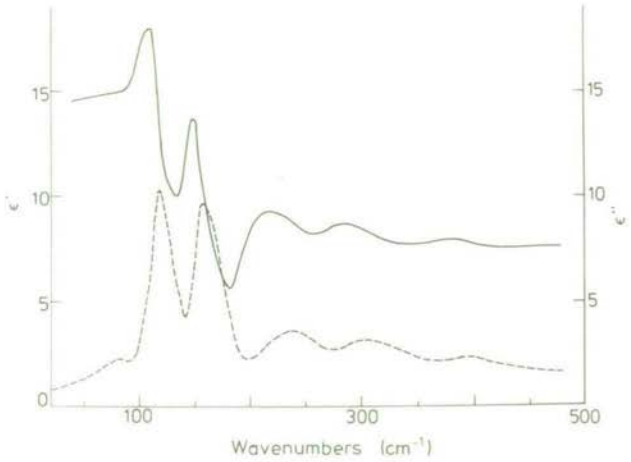

Figure 2. Calculated real and imaginary parts of the dielectric constants of $Hg_3In_2Te_6$. Full line: ϵ'; broken line: ϵ''.

3. Raman scattering

The band gap of $Hg_3In_2\square Te_6$ is at about 0·75 eV and therefore the Raman measurements were carried out using the Brewster-angle technique. This technique has been successfully applied to $HgIn_2\square Te_4$ and full details of the method are given in Miller *et al* (1976).

The room-temperature Raman spectrum was excited by a coherent radiation 52B argon laser operating at 514·5 nm and the 90° scattered light from the (100) face was analysed using a Spex Ramalab double monochromator at a spectral resolution of 3·5 cm^{-1}. The laser power used was 20 mW, and the beam was slightly defocused to prevent the sample from overheating and thereby avoiding surface damage of the kind noted for $HgIn_2\square Te_4$ (Miller *et al* 1976). An argon gas jet was directed at the sample along the line of the laser beam to help cool the crystal surface and to eliminate the Raman scattering from the air.

The EMI 6256S photomultiplier detector pulses were processed with a digitized data collection system linked to a multichannel analyser (Arthur and Lockwood 1974). The polarization of the scattered light was analysed with Polaroid film, and a polarization scrambler was placed between the analyser and the spectrometer.

For a cubic material, all Raman-active modes can be measured from two polarizations, $I_{\parallel}$ and $I_{\perp}$, using the notation given in Miller *et al* (1976). The $I_{\parallel}$ spectrum contains A_1 and E modes predominantly, and the $I_{\perp}$ spectrum contains T_2 modes (table 4). The results obtained from the Raman measurements are shown in figures 3(*a*) and (*b*). Figure 3(*a*), the $I_{\parallel}$ spectrum, shows features at around 120 cm^{-1} superimposed on an intense sloping background caused by stray light within the monochromator. Peaks are apparent at 107, 115, 119 and 122 cm^{-1}, and a shoulder at approximately 140 cm^{-1}, with a much weaker feature at 155 cm^{-1}. The $I_{\perp}$ spectrum in figure 3(*b*) shows four very weak broad bands at 78, 90, 121 and 139 cm^{-1}, and a shoulder at approximately 185 cm^{-1}.

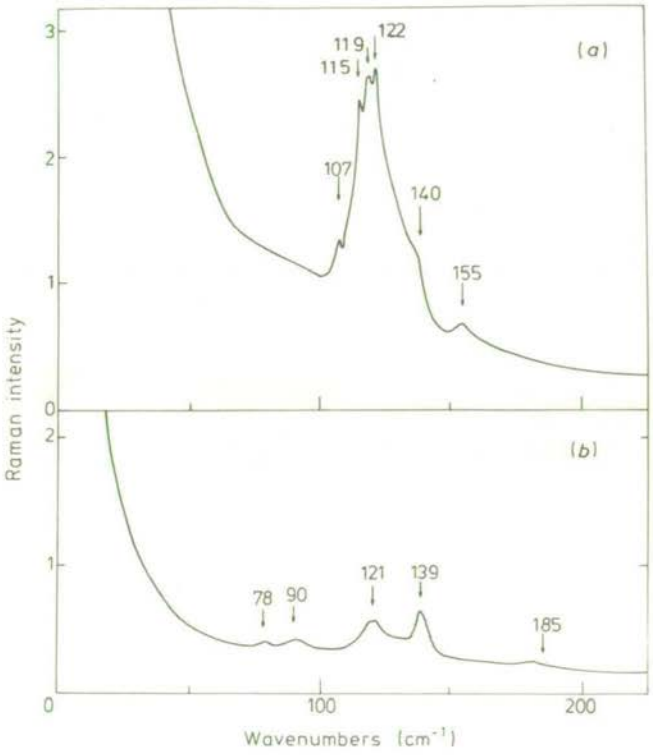

Figure 3. (*a*) $I_{\parallel}$, (*b*) $I_{\perp}$ Raman spectra of $Hg_3In_2\square Te_6$.

As for $HgIn_2\square Te_4$ (Miller *et al* 1976), the high refractive index of $Hg_3In_2\square Te_6$ implies that Brewster-angle scattering is effectively back-scattering, and the phonon in this case is travelling close to the [100] direction. Therefore for the infrared-active T_2 modes only the longitudinal waves are being studied and the bands at 78, 90, 121 and 139 cm^{-1} correspond to T_2 LO phonons. These bands are broad and could conceivably comprise several overlapping bands (cf. infrared).

For the modes of figure 3(*a*) we can not distinguish between those of A_1 and E symmetry. Further experiments under greatly improved experimental conditions are in progress.

4. Theoretical analysis

4.1. Infrared

It is tempting to apply the simple picture which has proved useful in the case of various chalcopyrite semiconductors (Holah *et al* 1974), to this compound for a qualitative interpretation of the results. In this picture, the dispersion relations of a zincblende crystal are folded back into the smaller Brillouin zone of the ordered ternary compound so that the zone-centre modes are derived from the modes at certain high-symmetry **k** points of the zincblende structure.

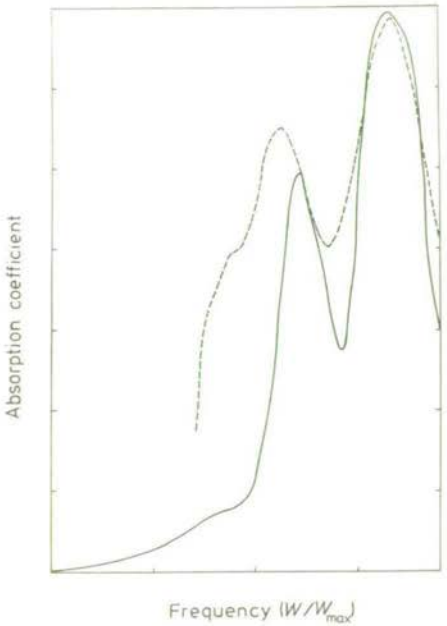

Figure 4. Absorption coefficient of $Hg_3In_2\square Te_6$ and of amorphous germanium. Full line: $Hg_3In_2\square Te_6$; broken line: α-Ge.

In the present case the unit cell is so large that a much simpler comparison is possible. Figure 4 shows the absorption coefficient of $Hg_3In_2\square Te_6$, derived from the Kramers–Krönig analysis of the reflectivity data, superimposed on an infrared absorption measurement of amorphous germanium (Lurio and Brodsky 1972). The curves are scaled by the frequency of the highest mode of $HgIn_2\square Te_4$ (Miller *et al* 1976) and crystalline Ge respectively. The comparison is successful because $Hg_3In_2\square Te_4$ samples have 108 points in the zincblende Brillouin zone, which is a fair approximation to an integration over the whole zone. In addition, the vacancies introduce significant distortions to the basic zincblende structure of a type which gives the local environment of the cations statistical variations not unlike those in a tetrahedrally bonded continuous random network. The peaks above 200 cm^{-1} will be considered later.

4.2. Raman

In discussing the lattice dynamics of $HgIn_2\square Te_4$, Miller *et al* (1976) suggest that the properties are strongly influenced by breathing modes about the vacancies. Their

Raman-scattering results tend to confirm this. Their spectra contain several peaks, but one at about 100 cm^{-1} is about two orders of magnitude stronger than the others. This peak can be identified as due to a breathing mode about the vacancy. The term 'breathing mode' refers to a motion in which the anions (Te) surrounding a vacancy move towards the vacancy simultaneously.

It can be demonstrated (MacKinnon *et al* 1977) that in the top valence bands of a tetrahedral ordered-vacancy compound the electrons are predominantly localized on the vacant site. Clearly the energy of such bands must be very sensitive to the detailed configuration of the anions surrounding the vacancy. In particular, displacement of the anions in a breathing mode is expected to induce considerable periodic variations of the energies of these bands. This, of course, must result in a similar large variation in the electronic contribution to the dielectric constant, resulting in strong Raman scattering from such a mode.

The Raman measurements (figure 3) show strong features near 120 cm^{-1} for the $I_{\parallel}$ configuration, which can be assigned to breathing modes of A_1 and E symmetries, and weaker features in the $I_{\perp}$ configuration. This is largely what one would expect on the basis of the above argument.

4.3. Group theory

In a compound like $Hg_3In_2\square Te_6$, whose unit cell contains several vacancies, the symmetries of the breathing modes can be determined by a simple rule: *'The irreducible representations of the breathing modes are the same as those determined by performing the group operations on spherically symmetric basis functions situated on the vacant sites.'*

Therefore, in a compound with only one vacancy per unit cell, strong Raman scattering will be seen from modes with the identity representation (A_1). This is confirmed by the results of Miller *et al* (1976) for $HgIn_2\square Te_4$.

Table 3. Summary of group theory of $Hg_3In_2\square Te_6$ showing the numbers of irreducible representations of various types.

	Case 1					Case 2				
	A_1	A_2	E	T_1	T_2	A_1	A_2	E	T_1	T_2
Zincblende	34	17	51	73	92	34	17	51	73	92
Lost	3	—	3	5	10	3	1	4	6	8
$Hg_3In_2\square Te_6$	31	17	48	68	82	31	16	47	67	84
Acoustic	—	—	—	—	1	—	—	—	—	1
Optic	31	17	48	68	81	31	16	47	67	83
Breathing	5	—	2	—	3	2	—	2	1	3

A full group theoretical analysis of the structure of $Hg_3In_2\square Te_6$ is given in MacKinnon (1977) and the important results are summarized in table 3 for both the possible vacancy configurations. One important point must however be made; it is not adequate, in a detailed comparison of the irreducible representations of the Γ point of an ordered-vacancy compound with those of various points of zincblende, simply to 'fold back' the

zincblende bands and determine the resulting representations using compatibility relations (Finkman and Tauc 1973, Finkman *et al* 1975). The total number of degrees of freedom is reduced by three for every vacancy created. The symmetries of the lost mode can be determined by the following rule: *'The irreducible representations of the lost modes are the same as those determined by performing the group operations on x, y and z displacement basis functions situated on the vacant sites.'*

This rule is, of course, similar to that for the breathing modes. This result is given in table 3.

Table 4. Character table for $Hg_3In_2\square Te_6$ at the Γ point ($\bar{4}3m$) (Lax 1974).

	E	$8C_3$	$3C_{2x}$	$6S_{4z}$	$6\sigma_{xy}$	Activity	Symmetry
$A_1(\Gamma_1)$	1	1	1	1	1	Raman	$x^2+y^2+z^2$
$A_2(\Gamma_2)$	1	1	1	−1	−1	—	
$E\ (\Gamma_{12})$	2	−1	2	0	0	Raman	$x^2-y^2, x^2+y^2-2z^2$
$T_1(\Gamma_{25})$	3	0	−1	1	−1	—	
$T_2(\Gamma_{15})$	3	0	−1	−1	1	IR, Raman	$(x,y,z);(xy,yz,zx)$

Table 4 shows the character table for the point group $\bar{4}3m$. It is difficult to distinguish the two structures from Raman-scattering results since the $T_1(\Gamma_{25})$ modes are Raman inactive and that is the only representation with breathing modes present in one structure but not in the other.

4.4. Multiphonon process

In a system where Raman scattering is strong one would anticipate significant effects attributable to two-phonon processes. Both effects require large third-order terms in the potential. Since the highest mode in $HgIn_2\square Te_4$ is at 189 cm^{-1}, the peaks above 200 cm^{-1} in figures 1 and 2 can be attributed to two- and three-phonon reflectivity (table 2). It is unusual for multiphonon effects to be observed in reflectivity measurements, but this simply serves to confirm the existence of a mechanism for the enhancement of such processes such as proposed in § 4.2. Anharmonic effects have been reported in other similar materials, such as $Ag_2Hg\square I_4$ (Kasper and Browall 1975).

Selection rules for two-phonon effects can be derived by considering which products of irreducible representations from points in **k** space satisfying $\mathbf{k}_1 + \mathbf{k}_2 = 0$ contain the representation Γ_{15}. A fuller study of these selection rules is given in MacKinnon (1977).

However, since we expect the anharmonicity due to breathing modes to be strongest near the zone centre, it is worthwhile to reproduce the results for the Γ point. Table 5 shows the representations of the products of the representations, while table 6 gives the

Table 5. Product representations of the point group $\bar{4}3m$.

A_1	A_2	E	T_1	T_2
A_2	A_1	E	T_2	T_1
E	E	A_1+A_2+E	T_1+T_2	T_1+T_2
T_1	T_2	T_1+T_2	$A_1+E+T_1+T_2$	$A_2+E+T_1+T_2$
T_2	T_1	T_1+T_2	$A_2+E+T_1+T_2$	$A_1+E+T_1+T_2$

combinations of two breathing-mode phonons that can be observed in reflection. It should be noted that no such combinations exist for $HgIn_2\square Te_4$ and no multiphonon reflectivity is observed.

Table 6. Infrared-active two-phonon combinations involving breathing modes.

	Case 1					Case 2				
	A_1	A_2	E	T_1	T_2	A_1	A_2	E	T_1	T_2
A_1	–	–	–	–	*	–	–	–	–	*
A_2	–	–	–	–	–	–	–	–	–	–
E	–	–	–	–	*	–	–	–	*	*
T_1	–	–	–	–	–	–	–	*	*	*
T_2	*	–	*	–	*	*	–	*	*	*

5. Conclusion

The ordered-vacancy compounds of which $Hg_3In_2\square Te_6$ is a particularly complex example, pose many intriguing questions, most of them bearing on the role of the vacancies. Our measurements do not uniquely determine the distribution of the vacancies, but it has been demonstrated that breathing modes centred on the vacancies give rise to enhanced Raman scattering and other anharmonic effects.

There is at present wide interest in the possible merits of the chalcopyrite semiconductors in various technical applications. This can be expected to widen to include the ordered-vacancy compounds, some of which are in many respects similar to chalcopyrites.

Clearly, therefore, these compounds invite further attention, especially regarding nonlinear optical properties. It is hoped that this paper may serve to lay some of the groundwork for future investigations.

Acknowledgments

We are indebted to G A Saunders for making available to us the crystals, grown by T Seddon and himself, upon which our measurements were performed, and for much advice and encouragement, and to H Vass for technical assistance in the Raman-scattering work. We wish to thank D Weaire, P G Harper and B S Wherrett for many useful discussions on the theoretical aspects of our investigation. This work was supported by the Science Research Council.

References

Arthur J W and Lockwood D J 1974 *J. Raman Spectrosc.* 2 53–69
Finkman E, Tauc J, Kershaw R and Wold A 1975 *Phys. Rev.* **B11** 3785–94
Holah G D, Webb J S and Montgomery H 1974 *J. Phys. C: Solid St. Phys.* 7 3875–90
Holah G D, Webb J S and Montgomery H 1974 *J. Phys. C: Solid St. Phys.* 7 3875–90
Kasper J S and Browall K W 1975 *J. Solid St. Chem.* 13 49–56
Lax M J 1974 *Symmetry Principles in Solid State and Molecular Physics* (New York: Wiley)
Lurio A and Brodsky M H 1972 *Bull. Am. Phys. Soc.* 17 322
—— 1977 unpublished
McCartney H 1971 *PhD Thesis* University College, London
MacKinnon A 1977 *PhD Thesis* Heriot-Watt University, Edinburgh

MacKinnon A, Miller A and Ross G 1977 this volume
Maynell C A, Saunders G A and Seddon T 1970 *Phys. Lett.* 31A 338–9
Miller A, Lockwood D J, MacKinnon A and Weaire D L 1976 *J. Phys. C: Solid St. Phys.* 9 2997–3011
Miller A, MacKinnon A, Weaire D L, Pidgeon C R, Lockwood D J and Saunders G A 1976 *Proc. Int. Conf. on Physics of Semiconductors, Rome* p 509
Saunders G A and Seddon T 1970 *J. Phys. Chem. Solids* 31 2495–504
—— 1971 *Phys. Lett.* 34A 443–4
—— 1976 *J. Phys. Chem. Solids* 37 873–82

Solid State Communications, Pergamon Press. Printed in Great Britain

RAMAN SCATTERING FROM MAGNONS IN $CoCl_2$ AND $FeCl_2$

D. J. Lockwood

Physics Department, Edinburgh University, Edinburgh EH9 3JZ, Scotland

I.W. Johnstone

Physics Department, University of Nottingham, Nottingham NG7 2RD, England

and

G. Mischler and P. Carrara

Laboratoire de Physique des Solides, Associé au CNRS, 31077 Toulouse Cédex, France

(*Received* 17 *August* 1977 *by C.W. McCombie*)

One-magnon Raman scattering has been observed in the metamagnets $CoCl_2$ and $FeCl_2$. The $k = 0$ magnon energies are $16 \pm 1\,cm^{-1}$ at 21 K and $16.4 \pm 0.4\,cm^{-1}$ at 12 K, respectively and these values are in good agreement with previous AFMR and neutron scattering results. A search for two-magnon scattering in both compounds was unsuccessful, largely because of masking from nearby first-order phonons and a weak temperature dependent broad band at $140\,cm^{-1}$ in $CoCl_2$, which is assigned to two-phonon scattering from acoustic phonons.

UNTIL NOW, observation of inelastic light scattering from magnetic excitations has been largely restricted to the simple antiferromagnets such as MnF_2 and $KMnF_3$ which have the rutile and perovskite structure, respectively. In this paper we report the first observation of Raman scattering by magnons in the layered transition metal dihalides, $CoCl_2$ and $FeCl_2$. These crystals are isomorphic with the $CdCl_2$ structure (space group D^5_{3d}) and form an ordered magnetic lattice consisting of hexagonal sheets of ferromagnetically aligned moments. Since adjacent planes have oppositely directed moments the overall structure is antiferromagnetic. The exchange interaction is extremely anisotropic with the interlayer $J \ll$ intralayer J, hence the lattice can be ferromagnetically saturated by relatively small external magnetic fields applied parallel and perpendicular to the c axis for $FeCl_2$ (easy-axis) and $CoCl_2$ (easy-plane), respectively. For these reasons, and since both compounds become antiferromagnetic at readily accessible temperatures ($T_N = 24.7$ K for $CoCl_2$ and 23.5 K for $FeCl_2$), their lattice dynamics and magnetic properties have attracted continuing interest for some years. This interest has centred on inelastic neutron scattering and AFMR experiments which have yielded magnon energies for both crystals and the results are summarised in Table 1. In contrast, Raman scattering has been previously restricted to $CoCl_2$ alone [3, 4] although results are now available for both the paramagnetic and antiferromagnetic phases of $FeCl_2$ and $FeBr_2$ for the phonons and electronic levels within the $(^5D)^5T_{2g}$ manifold. These latter measurements will be discussed in a forthcoming publication.

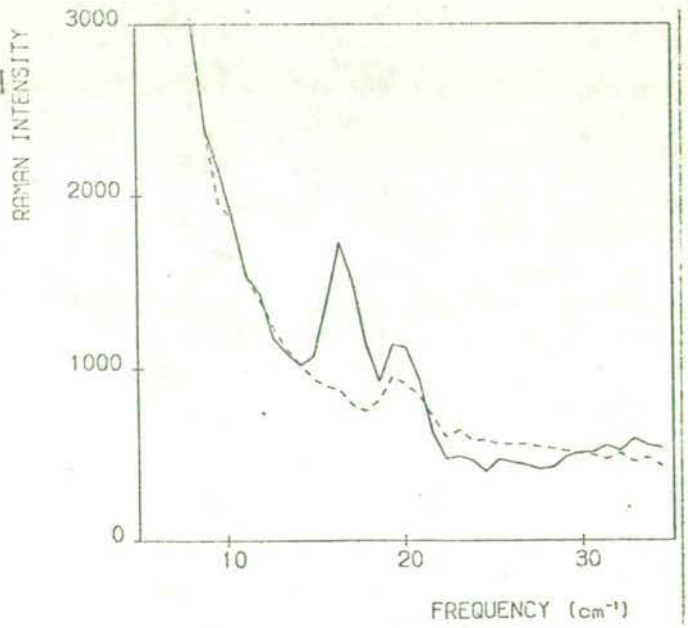

Fig. 1. The low frequency Raman spectrum of $FeCl_2$ recorded at 12 K (solid line) and 30 K (dashed line) with a spectral resolution of $1.8\,cm^{-1}$ and using 70 mW of laser light at 647.1 nm.

The crystals of $CoCl_2$ and $FeCl_2$, grown by the Bridgeman method [4], were cleaved perpendicular to the c-axis just prior to mounting in a Thor 500 Varistat cryostat where the sample is immersed in the coolant.

Table 1. Comparison of previous and present results for the magnon energy (cm^{-1}) at k = 0 and in zero magnetic field in $FeCl_2$ and $CoCl_2$. The corresponding temperatures (K) are given in brackets

	Raman scattering	AFMR	Neutron scattering
$FeCl_2$	16.4 ± 0.4(12)	16.5 ± 0.3(4.2)[10] 16.2(12)[10]* 16.7 ± 0.2(4.2)[11] 16.51 ± 0.06(1.2)[12] 16(4.2)[13]	17.2 ± 0.4(5)[7] 16.1(12)[7]* 16.7 ± 0.3(4)[14]
$CoCl_2$	16 ± 1(21)	19.3 ± 0.4(4.2)[10] 16(21)[10]* 19.0 ± 0.2(4.2)[15] 18.7(4.2)[16]	16.1(4.5)[8]

* Estimated from the temperature dependence of the magnon energy.

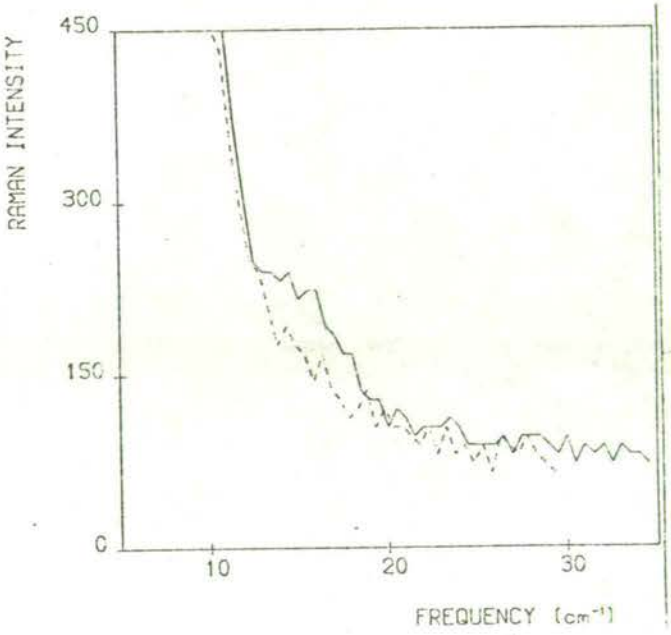

Fig. 2. The low frequency Raman spectrum of $CoCl_2$ recorded at 21 K (solid line) and 37 K (dashed line) with a spectral resolution of 2.7 cm^{-1} and using 100 mW laser light at 476.5 nm.

The Raman spectrum of deep purple $CoCl_2$ and brown $FeCl_2$ was excited with approximately 100 mW of argon laser light at 476.5 nm and krypton laser light at 647.1 nm respectively. The laser beam was focussed onto the cleaved face at grazing incidence with the plane of polarisation parallel to this face. The 90° scattered light was analysed with a Coderg T800 triple grating spectrometer and detected with a RCA C31034A photomultiplier. Because of depolarization effects associated with surface scattering no polarisation analysis was attempted. Spectral data were collected automatically under computer control [5] and the sample temperature was monitored with a Au/Fe–chromel thermocouple placed at the crystal surface

Typical low temperature spectra are given in Fig. 1 and 2 for $FeCl_2$ and $CoCl_2$, respectively. The peaks at 16 ± 1 cm^{-1} and 16.4 ± 0.4 cm^{-1} are assigned to be due to one-magnon scattering because they renormalise to zero frequency and intensity with increasing temperature and vanish from temperatures in excess of T_N. The small peak at 19.4 cm^{-1} in Fig. 1 is a krypton plasma line. These frequencies may be compared with the data from other experiments, list in Table 1. It is anticipated that the energies as measured by Raman scattering will show small discrepancies from those measured at 4 K using the AFMR technique reflecting the difference in sample temperatures for the two experiments. However, a direct comparison may be made using the known temperature dependence of the respective magnon energies. The actual crystal surface temperature was obtained by estimating the laser heating from a comparison of the observed and known Neèl temperatures and correcting all temperatures by adding the difference between the two (~ 9 K). The observed T_N was noted when the spectra showed that a sharp change in the electronic properties of the crystal had occured [4]. As can be seen from Table 1 the temperature adjusted magnon energies obtained by the various technicques compare very well.

Because one- and two-magnon scattering of comparable intensity has been observed in FeF_2 [6] a search was made for scattering due to magnon pairs. Two-magnon scattering arises from pairs of magnons with equal and oppositely directed wavevector from throughout the Brillouin zone. However, experiments on perovskite and rutile crystals have shown that most Raman intensity comes from spin pairs at the zone boundary [1, 2]. For the case of $FeCl_2$ the zone boundary energy of the in-plane spin wave is

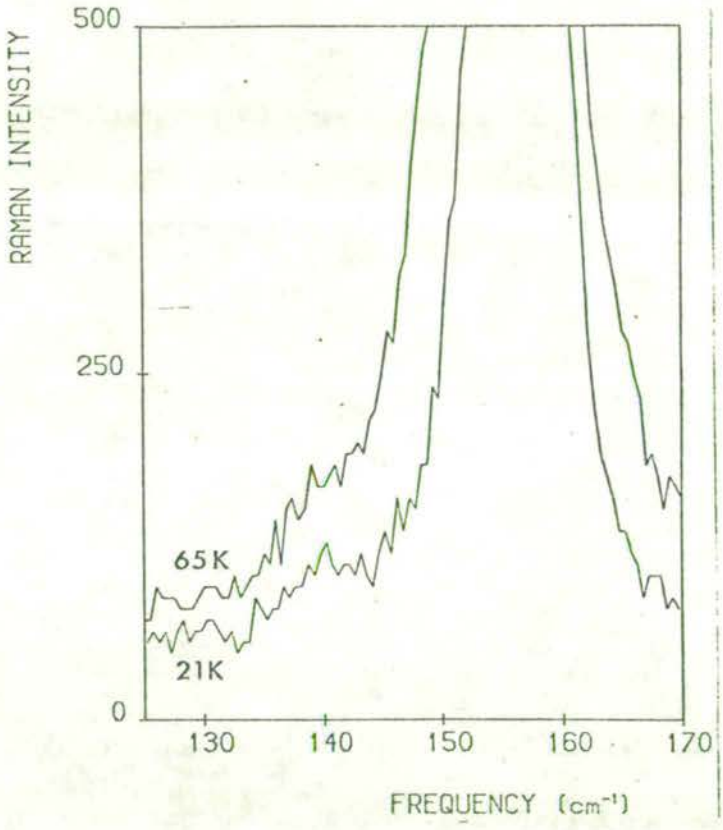

Fig. 3. The 150 cm^{-1} region of the Raman spectrum of $CoCl_2$ recorded at temperatures below and well above T_N = 25 K. Experimental conditions were the same as those given in Fig. 2. The intense peak at about 157 cm^{-1} is the E_g phonon [3].

54 cm^{-1} [7] which predicts two-magnon scattering in the vicinity of 108 cm^{-1}. Since none was observed, two-magnon scattering in $FeCl_2$ is weak compared with the one-magnon scattering, and therefore it may also be obscured by the low energy wing of the E_g phonon at 149 cm^{-1}. In $CoCl_2$ a broad band was observed at 140 cm^{-1} (Fig. 3), which is close to twice the zone boundary magnon energy of 78 cm^{-1} [8]. However, the band intensity increases with temperature (see Fig. 3) and remains relatively constant in frequency. This is inconsistent with expected two-magnon behaviour. Hence, we assign the band to be two-phonon in character and propose that the scattering arises from phonons on the Σ_1[100] acoustic branch near the zone boundary. The Σ_1 zone boundary energy is 73 cm^{-1} at room temperature [9] giving a two-phonon overtone energy of 146 cm^{-1}. Further, it is likely that the intense E_g phonon at 157 cm^{-1} (21 K) completely masks the two-magnon band.

Acknowledgements – We are grateful to G.D. Jones for providing the crystals, to the Royal Society of London and the Centre National de la Recherche Scientifique for a visit to Edinburgh under the European Science Exchange Programme (G.M.), and to the S.R.C. for a Research Fellowship (I.W.J.).

REFERENCES

1. FLEURY P.A. & LOUDON R., *Phys. Rev* **166**, 514 (1968).
2. LOCKWOOD D.J. & COOMBS G.J., *J. Phys C: Solid State Phys.* 8, 4062 (1975).
3. CHRISTIE J.H. & LOCKWOOD D.J., *Light Scattering in Solids*, (Edited by M. Balkanski), p. 145. Flammarion, Paris (1971).

4. CHRISTIE J.H., JOHNSTONE I.W., JONES G.D. & ZDANSKY K., *Phys. Rev.* B12, 4656 (1975).
5. ARTHUR J.W. & LOCKWOOD D.J., *J. Raman Spectrosc.* 2, 53 (1974).
6. FLEURY P.A., PORTO S.P.S., CHEESEMAN L.E. & GUGGENHEIM H.J., *Phys. Rev. Lett.* 17, 84 (1966).
7. BIRGENEAU R.J., YELON W.B. COHEN E. & MAKOWSKY J., *Phys. Rev.* B5, 2607 (1972).
8. HUTCHINGS M.T., *J. Phys. C. Solid State Phys.* 6, 3143 (1973).
9. CARRARA P., REDOULES J.P., ESCRIBE C. & ZIEBECK K.R.A., *Solid State Commun.* 21, 929 (1977).
10. JACOBS I.S., ROBERTS S. & LAWRENCE P.E., *J. Appl. Phys.* 36, 1197 (1965).
11. JOHNSON K.C. & SIEVERS A.J., *Phys. Rev.* B7, 1081 (1973).
12. PETITGRAND D. & MEYER P., *J. Phys.* 37, 1417 (1976).
13. FERT A.R., LEOTIN J., OUSSET J.C., BERTRAND D., CARRARA P. & ASKENAZY S., *Solid State Commun.* 18, 327 (1976).
14. VETTIER C. & YELON W.B., *Phys. Rev.* B11, 4700 (1975),
15. JACOBS I.S., ROBERTS S. & SILVERSTEIN S.D., *J. Appl. Phys.* 39, 816 (1968).
16. MAGARIÑO J., TUCHENDLER J., FERT A.R. & GELARD J. (to be published).

The Raman spectrum of tin-tetraiodide : temperature and pressure measurements and lattice dynamical calculations

by

I.U. Heilmann*

Research Establishment, Risø, Roskilde, Denmark.

D.J. Lockwood and G.S. Pawley

Physics Department, Edinburgh University, Scotland.

Abstract

Tin-tetraiodide was chosen for a temperature and pressure dependent lattice-dynamical study because of its pronounced anharmonic properties. The variation of the Raman spectrum with temperature from 100 K to 298 K has been measured using a single crystal specimen. The temperature dependence of the mode frequencies and linewidths are given together with symmetry assignments. Further measurements were made at room temperature using a powdered sample under pressure, showing considerable variation in internal as well as external modes. Isochoric and isobaric temperature shifts, relative pressure shifts and Grüneisen parameters are obtained from this data.

The group theory for this system is presented. Our analysis was

---

* Also at

Physics Laboratory 1, University of Copenhagen.

confirmed by extensive lattice dynamical calculations, first using a model in which the molecules were assumed to be rigid units, and then using a model which gave the internal modes as well as the lattice modes. The pressure variation was also calculated using both models. The first model gave good agreement with the measured lattice mode frequencies, but insufficient mode splitting was found with the second model, showing that the simple atom-atom potential used for the intermolecular forces is not adequate for a detailed description of the molecular interaction.

Introduction

The molecular crystal tin tetraiodide SnI_4 has recently been subjected to investigations of its dynamical properties, with particular emphasis on the influence of temperature and pressure (Heilmann 1977). For various reasons SnI_4 is a well-suited object for such kinds of study. Firstly the substance is strongly anharmonic with a high thermal expansivity and a large compressibility, properties which favour the effects of varying the temperature and the external pressure on the substance. Secondly, the material has favourable spectroscopic properties, allowing a variety of experimental techniques to be applied. Thus, both elements Sn and I have isotopes (^{119}Sn, ^{127}I and ^{129}I) with transitions suitable for Mössbauer studies.

SnI_4 is a convenient almost exclusively coherent scatterer of thermal neutrons. Inelastic (one-phonon) as well as elastic neutron scattering on single crystals has been carried out. Neutron diffraction data was used for a number of structure refinement procedures in order to obtain precise atomic positions in the unit cell and in particular in order to test the models of thermal vibrations applied in current crystallography.

The crystal structure of SnI_4 is relatively simple (see next section) and can be visualised in terms of a slight deviation from an 'ideal' structure consisting of a face-centred cubic lattice of iodine atoms with tin atoms in one eighth of the tetrahedral interstices. The point group of the crystal ($m\bar{3}$) has an inversion centre, with the result that half of the zone-centre modes are Raman-active only, but not all of the other odd-parity modes are infrared-active.

All modes of the isolated SnI_4 molecule are Raman active. The frequencies were determined by Stammreich et al. (1956)

and later by Pistorius and Haarhoff (1959), both measured on the molecules in organic solutions. Dawson (1975) has measured the Raman spectrum of a single crystalline SnI_4 sample and observed three lattice modes and five internal modes. However, no polarisation analysis of the spectra and consequent detailed group theoretical assignment of the modes were carried out in this work. Recently, the temperature and pressure dependence of the Raman spectrum of powdered SnI_4 was investigated by Peercy et al. (1975). These authors found a strong temperature and pressure dependence of the modes, in particular for the lattice modes. The difference of the pressure dependence of the modes was used to separate these into external and internal modes but no definite symmetry assignments were possible because of the lack of polarisation data.

In the present work we have measured the polarised Raman spectra of oriented single crystals of SnI_4 at temperatures between 100 K and 295 K. It has been possible to isolate spectra containing modes of a single representation thus allowing a detailed comparison with group theoretical predictions. The pressure dependence between 1 bar and 4.2 kbar of the Raman spectrum of powdered SnI_4 was measured at room-temperature. The results agree well with those found by Peercy et al. (1975). Using the results obtained from the single-crystal samples it was possible to assign the bands of the powder spectrum to the appropriate representations. Lattice dynamical calculations assuming molecular rigidity as well as one allowing the molecules to deform have been carried out for various external pressures, and the results are compared with the experimentally found mode frequencies.

2. Crystal structure and group theory

The crystal structure of SnI_4 is cubic Pa3, with eight molecules in the unit cell. This is the same space group as used by N_2, CO_2, C_2H_2, all of which have four molecules in the cell, each molecule being positioned on a centre of symmetry and aligned along a (111) direction. The SnI_4 structure can therefore be considered as pairs of tetrahedral molecules related by the symmetry centres each arranged with one tetrahedral 3-fold axis along the common (111) direction and each with a vertex on this axis directed away from the symmetry centre. Such a pair of molecules then has two degrees of freedom more than a single N_2 molecule consistent with the space group symmetry, namely translations away (or towards) the symmetry centre and rotations about the (111) axis in such a way as to preserve the symmetry centre. These two degrees of freedom plus the cubic unit cell length are the only three parameters which can vary with pressure or temperature, provided that the molecule itself is not distorted. A stereoscopic view of the crystal structure is given in figure 1.

In the free state any molecule with five atoms will have $3 \times 5 - 6 = 9$ modes of vibration. For tetrahedral SnI_4 these modes are distributed in three different representations: $A_1 + E + 2F_2$ hereafter labelled simply $A + E + 2F$. As A and E occur only once the associated eigenvectors are uniquely determined, but this is not the case for the F-modes. The problems this causes are discussed in section 5. In the crystalline state the 8 molecules in the primitive unit cell give $3 \times 5 \times 8$ modes for every possible phonon wave-vector. In the present study we are interested only in the modes at the Γ-point where there are six representations, A_g, E_g, F_g, A_u, E_u, F_u.

The correlation between the free molecule modes and the crystal modes is given in table 1. For

the purpose of enumeration the translation and the rotation of the free molecule can be regarded as two more occurrences of F, giving (for 8 molecules) by a factor group analysis

$$8(A + E + 4F) \rightarrow 5A_g + 5E_g + 15F_g + 5A_u + 5E_u + 15F_u$$

Of these 50 normal modes, the 25 gerade modes are Raman active and the 12 F_u modes are infrared active, not including the acoustic modes. The symmetry coordinates for one molecule are given in Figure 2, from which the symmetry coordinates of the crystal as a whole are derived using the phase factors between the eight molecules in the unit cell.

The frequencies of the free molecule modes measured by Pistorius and Haarhoff (1959) are

		(cm^{-1})	(symmetry)
ν_1	=	149	A^1
ν_2	=	47	E^2
ν_3	=	216	F^3
ν_4	=	63	F^4

The superscripts 1 to 4 are introduced here to show the correspondence with a particular mode. This is found convenient when considering the crystal modes (see table 2), as superscripts are then given for these modes in order to show the correlation with the free molecule modes. With this scheme the lattice modes appear with no superscript as these are correlated with the translations and rotations of the free molecule.

Our group-theoretical result differs from that of Dawson (1976) and of Peercy et al. (1975), both of whom used the molecular site symmetry procedure. Our result was confirmed by a full lattice-dynamical calculation in which the full symmetry of the structure is input data and all possible lattice modes are calculated. This was done to high precision so that all degeneracies could be found unambiguously. The error Dawson and Peercy et al. made was in applying the site group correlation method to a case where the symmetry is too high for this method to be valid. There is no unique way of

close examination of the effect of group operations on the molecules.

3. Experiment

3.1 Single crystal Raman spectra.

Single crystals of SnI_4 were grown from the melt using the Bridgman technique. The starting material was SnI_4 powder doubly recrystallised from $CHC\ell_3$. The resulting boules of single crystal SnI_4 were oriented by means of X-ray Laue photographs and were then cut to form cubes of about $5 \times 5 \times 5$ mm^3 using a 0.2 mm steel-thread saw coated with $A\ell_2O_3$ powder suspended in paraffin. One crystal was cut with {100} faces and another was cut with four {110} faces and two {100} faces. The crystal faces were polished with 6 μm diamond suspended in silicone oil on the back surface of photographic paper, followed by 1 μm diamond powder in silicone oil on a wax lap.

The single-crystal Raman spectrum was excited with 50 mW of 647.1 nm light from a Spectra Physics 165 krypton laser, and the 90°-scattered light was analysed using a Coderg T800 triple monochromator at a spectral resolution of 0.65 cm^{-1}. The RCA C31034A photomultiplier detector pulses were processed with a digitized data collection system and the whole operation of recording the Raman spectrum was controlled automatically by a time-shared PDP-11 computer (Arthur and Lockwood 1974). The computer-stored data was then transferred to a large multi-access computer for further processing. The polarization of the scattered light was analysed with Polaroid film, and a polarization scrambler was placed between the analyser and the spectrometer. The directions X,Y and Z that are used to denote the various polarizations refer to the crystal a, b and c axes respectively. A prime denotes axes at 45° to the principal axes in the a-b plane i.e. along [110] directions.

Raman spectra were recorded at room temperature, and at low temperatures using a Thor Cryogenics 500 Varistat where the gaseous nitrogen coolant is in direct contact with the sample. A Au/Fe - chromel thermocouple

mounted on the sample monitored the crystal temperature.

3.2 Powder Raman spectra under pressure.

The pressure dependence of the SnI_4 Raman spectrum was investigated at room temperature. The diamond pressure cell used for the present experiments was constructed for the purpose of Mössbauer absorption measurements. It is an improved version of that used by Heilmann and Olsen (1977) and has been used for more thorough measurements of the pressure and temperature dependence of the ^{119}Sn-Mössbauer absorption in SnI_4 (Heilmann and Olsen, 1977, to be published). Figure 3 shows two cross-sections of the pressure cell, (A) is a steel chamber and (B) denotes the two steel anvils, in which the diamond pistons (D) are embedded. The powdered sample (S) is between the diamond pistons. (C) is screws in (B) emerging into a slit in (A) preventing the anvils (B) rotating but allowing the left anvil to translate along the axis of the cell. The pressure force is applied to the anvils through a stack of circular steel springs (E) which can be compressed by the screw (F). Each spring has a well defined (almost linear) characteristic, published by the manufacturer (Mubea, Denmark). By arranging the springs in parallel and/or in series the resulting characteristic and/or displacement can be increased. Thus, knowing the pitch of the screw (F), a known force can be applied to the pistons by turning (F) a certain amount, provided that all friction effects can be ignored. In order to diminish the friction, the springs, the screw and the inside of the chamber were lubricated with Molekote high pressure grease. The area of the diamond pistons being 6 mm^2, the arrangement of the springs as shown in fig. 3 thus gave an obtainable pressure range of 0 to 4.7 kbar.

Raman spectra of powdered SnI_4 were recorded in the 180°-scattering geometry using a laser power of 100 mW and a spectral resolution of 1.1 cm^{-1}. A separate measurement without the sample showed that the

pressure cell produced a negligible background signal.

4. Results and assignments

Typical high and low temperature Raman spectra are shown in figures 4 and 5. For a cubic crystal, the X(ZZ)Y and X(ZX)Y spectra should contain only $A_g + E_g$ and F_g modes, respectively, while the X'(Y'X')Y' should contain the E_g modes alone (Lockwood, 1974). In fact, on close examination it can be seen that there is a mixing of polarisations, with strong bands of one polarisation appearing weakly in forbidden polarisations. This situation often occurs because of experimental imperfections such as misalignment of crystal axes or the wide collection angles used in the optics, which act to destroy the purity of the polarisation. But with computer recorded data this defect is easily overcome. Knowing that any spectrum is a combination of the true spectrum and small proportions of other spectra, then provided a clear spectral feature can be used to determine a scale factor, a scaled point-for-point subtraction of one spectrum from another should reveal the pure spectrum. This process is readily carried out using a multi-access computer on-line and has already been successfully applied by Murray and Lockwood (1976) to another cubic crystal $Zn_4O(BO_2)_6$. The subtraction of spurious features was carried out for the lowest-temperature data and the resulting spectra are shown in figure 6. Note that as was found for $Zn_4O(BO_2)_6$, many previously hidden features are now revealed. The pure A_g spectrum has been revealed by subtracting an appropriately scaled X'(Y'X')Y' spectrum from the X'(ZZ)Y' spectrum as well as removing the spurious F_g component. The frequencies of peaks in the spectra were determined using a computerised peak-finding routine (Arthur, 1976). The temperature dependence of frequencies and widths and the assignments of observed bands are given in table 2. These results are much more comprehensive than those published by earlier workers.

In section 2, it was predicted that there should be $5A_g$, $5E_g$ and $15F_g$

modes observable in the Raman spectrum. All E_g modes have been found, and all but one of the A_g modes. The missing A_g mode is predicted to be at about 215 cm^{-1} but is presumably too weak to be observed especially with the increased noise in this frequency region due to the subtraction of F_g modes (see figure 6). Some F_g modes are close in frequency and almost overlap. In order to ascertain the mode frequencies, the 100 K spectrum in these regions has been least squares fitted by computer to a function comprising two or more damped simple harmonic oscillators. In the lattice region where six F_g modes are expected, only four oscillators were needed to reproduce the observed band shape adequately, as can be seen in figure 7(a), and the other 2 modes are presumed to be unobservably weak. In the 54 cm^{-1} region two F_g internal modes are expected, and two oscillators were needed to reproduce the observed bandshape (figure 7(b)) but because of the noise resulting from the earlier subtraction of an E_g mode in this region the second oscillator parameters have a larger error. Three modes are predicted in the 60-70 cm^{-1} region and although two modes are obvious, a third weak oscillator was required to reproduce the observed complex band shape (figure 7(c)). Note that the F_g bands at ~ 65 and ~ 215 cm^{-1} are identical in shape, apart from different frequency separations, as would be expected from the group theory. Previous workers had assumed only two bands existed in these two regions both from their spectra and their group theory (see section 2). Band parameters obtained from these fits are given in table 2.

Typical room-temperature Raman spectra obtained from powdered SnI_4 at various pressures are shown in figure 8. The atmospheric pressure spectrum is similar to that reported by Peercy et al. (1975). Comparison with the single crystal spectra of figures 4,5 and 6 shows that the Raman spectra of the powder contains much less information. Nevertheless, the pressure dependence of several lattice and internal modes could be readily determined and the band frequency and width parameters as a function of pressure are given in table 3. The single crystal work

enables the definite symmetry assignments given in the table. Note that apart from the ~ 150 cm^{-1} A_g mode, all mode peak intensities decrease with increasing pressure (see figure 8).

5. Temperature and pressure effects

Our SnI_4 Raman data show a considerable temperature and pressure variation of the frequencies as was found by Peercy et al. (1975). This variation is particularly pronounced for the external modes. Moreover the bandwidths are strongly temperature dependent, and become reduced by ~ 60% in both external and internal peaks on going from room temperature to 100 K. These effects are all manifestations of substantial anharmonic terms in the intermolecular potentials.

The lattice dynamical calculation is necessarily based on the harmonic approximation of infinitely small vibrational displacements and is therefore unable to account for anharmonic effects like thermal expansion. As an approximation one often uses the quasiharmonic model, which allows for a dependence of the mode frequencies on the specific volume. As the frequencies in this model depend solely on the specific volume, measurements of frequencies as functions of both temperature and pressure - as in the present case - provide a direct test on the validity of the quasiharmonic model. If we consider a mode-frequency in general to be a function of volume and temperature, $\omega = \omega(V,T)$, the following relation obtains,

$$\left(\frac{\partial\omega}{\partial T}\right)_V = \left(\frac{\partial\omega}{\partial T}\right)_P + 3\alpha B \left(\frac{\partial\omega}{\partial P}\right)_T \qquad (5.1)$$

where α is the linear thermal expansion coefficient and B is the bulk modulus ($B = K^{-1}$, K being the compressibility). Clearly, the quasiharmonic approximation is equivalent to putting the isochoric (explicit anharmonic) shift $(\partial\omega/\partial T)_V$ equal to zero. The value of α in the temperature interval 4 K to 400 K was determined in the recent neutron work on SnI_4 (Heilmann, to be published) giving $\alpha = 79(2) \times 10^{-6}\ K^{-1}$ at room-temperature.

The compressibility at atmospheric pressure is determined by Peercy et al.(1975) to be $K = 20.1 \times 10^{-3}$ kbar^{-1}, compared with our value $K = 18(2) \times 10^{-3}$ kbar^{-1}. The relative pressure shifts $(\partial \ln\omega/\partial P)_T$ with estimated errors at room temperature and atmospheric pressure are summarised in table 4, column a, together with the values obtained by Peercy et al., column b. Also listed are the values obtained from the molecular rigid-body lattice dynamical calculations, column c. The corresponding mode Grüneisen parameters γ are also shown. Furthermore table 4 gives the temperature shifts $(\partial \ln\omega/\partial T)_p$ of the mode frequencies (at atmospheric pressure and room temperature) with estimated errors, compared with the values of Peercy et al.. A reasonably good agreement is found between the two sets of experimental values (a & b) and the calculated values (c). The last columns of table 4 contain the isochoric temperature shifts $(\partial \ln\omega/\partial T)_V$ found by means of eq(5.1) and the values of α and K stated above. While Peercy et al. report relatively small values (without errors), we find large values for the external modes and the lowest internal mode, although the errors are considerable. In obtaining these values Peercy et al. used the value $\beta = 156 \times 10^{-6}$ K^{-1} for the volume thermal expansivity which is much smaller than the value we have measured, $3\alpha = 237(6) \times 10^{-6}$ K^{-1}. In contrast to Peercy et al. we therefore conclude that the quasiharmonic model does not seem to be adequate in the description of the temperature dependence of at least some of the external zone centre modes.

It can be seen from fig.9 that the pressure dependence of the internal modes shows a slight increase from linearity at increasing pressures which we think is just significant. As Peercy et al. found a linear dependence throughout this range of pressure, we hope to make further measurements at higher pressures to resolve this discrepancy. The greater pressure dependence of the external mode frequencies over the internal mode frequencies is consistent with the observation by Lynch and Drickamer (1966) that the molecular separation is more sensitive to pressure changes than is the molecular distortion.

and the sublimation energy, E_s. Appropriate for room-temperature we obtained the following

Assumed		Found	
a	= 12.27 Å	A	= 6691.6 kcal mol^{-1} $Å^{-6}$
α	= 2.5 $Å^{-1}$	B	= 41196.0 kcal mol^{-1}
E_s	= 16.00 kcal mol^{-1}		

In doing this we inserted into the program the 'ideal' structure, mentioned in the introduction. The program then allowed the molecules to shift along and rotate about the three-fold axes, obeying the crystal symmetry as well as shifting the cell parameter a, until a static equilibrium configuration was obtained. The model structure thus found was sufficiently close to the real structure to justify the lattice dynamical calculations. As the most thorough determination of measured frequencies of the lattice modes was obtained at 100 K another set of parameters A and B was found in an analogous way, assuming the unit cell parameter a = 12.12 Å at 100 K:

Assumed		Found	
a	= 12.12 Å	A	= 7659 kcal mol^{-1} $Å^{-6}$
α	= 2.5 $Å^{-1}$	B	= 43106.9 kcal mol^{-1}
E_s	= 16.1238 kcal mol^{-1}		

The calculated Γ-mode frequencies at 100 K are listed together with the observed values in the two first columns of table 5. Apart from one of the F_g-modes and the high A_g-mode which are calculated too low, the agreement is seen to be fairly good.

In addition, the molecular rigid-body lattice dynamics calculations were carried out at elevated pressures, using the procedure described by Pawley and Mika (1974). Using the parameter set A, B, α appropriate for room-temperature, calculations were performed at atmospheric pressure and 4.2 kbar. The results are shown in table 5 together with the experimentally found values. The calculated pressure shifts are in reasonably good agreement with observations, as is also seen from table 4 (column c), although the

shift of the high A_g mode is calculated too low.

The potential parameters A, B and α used in the calculations presented here were found in a rather heuristic manner. However, the calculated acoustic phonon dispersion relations agree within 15% with those obtained from the inelastic neutron studies (Heilmann 1977). We are now working on a computer procedure for fitting the set of parameters A, B, α to the set of observed phonon frequencies of modes throughout the Brillouin zone.

6.2 Born von-Kármán model

In all the theoretical calculations just discussed, the separation approximation* has been used. However it is clear from the experimental results that there is not a large separation in the frequencies of the internal and the external modes of SnI_4. Therefore it is of interest to calculate the lattice dynamics for the case where the molecules are allowed to deform. Such a calculation was first done by Pawley and Cyvin (1970) for naphthalene, and their procedure is used here. The requirements for such a calculation are an internal force field for the molecule and an intermolecular potential function. The latter is furnished by the atom-atom interaction used in the rigid molecule calculations.

The internal force field of the molecule is such as to give rise to the four frequencies ν_1, ν_2, ν_3, ν_4 mentioned in section 2. If the eigenvectors for these four modes were known exactly, then the force field could be reconstructed without any assumptions. Unfortunately two of the frequencies belong to the F representation, and there would appear to be no reliable analysis of XY_4 molecules in the literature which would furnish eigenvectors for ν_3 and ν_4. It is possible to write down two orthogonal sets of symmetry coordinates for the F representation, and this leads to the essentially two-dimensional problem of finding the orthogonal linear combinations to give the eigenvectors for ν_3 and ν_4. When this is achieved the internal force field follows immediately.

Herzberg (1945) suggests some symmetry coordinates, and these have continued in use (see Cracknell, 1968) although better coordinates are available. Figure 10 shows just one of the three figures necessary to depict these triply degenerate modes, the black arrows show a motion which involves the central atom, whereas the white arrows show a motion of the outer atoms only. These patterns of motion have been associated

* In this assumption the internal modes and the external modes are assumed to be well separated in frequency.

by Herzberg and Cracknell with the higher and lower frequencies respectively, but they do not sufficiently emphasise that this result is an approximation. For SnI_4 it is rather a poor approximation. The logic behind this choice would appear to be that the low frequency mode is one of bond bending, but when the combination of the two motions shown is found such that the lengths A^oB^o = AB, this is far from being approximately the 'white arrow' motion. As symmetry coordinates we therefore choose the definition given by Cyvin (1968), and make the assumption that the pure bond-bending symmetry coordinate is the normal coordinate for ν_4. This assumption is supported by the results of Basile et al. (1973) who have studied the force fields for 146 tetrahedral molecules. These authors conclude that the bond-bending character of the ν_4-mode of tetrahalides becomes more predominant as the mass of the halogen increases.

The full Born-von Kármán calculation is now straightforward, albeit rather large. The internal molecular force field is generated, and the 15×15 matrix is expressed in orthogonal coordinates. The roots of this matrix are the modes corresponding to A+E+2F plus the six zero roots for translation and rotation. Eight copies of this matrix are individually oriented for the eight molecules in the unit cell, and are placed down the diagonal of a 120×120 matrix. The atom-atom interactions are added to the body of this matrix, which, on solving, gives 60 gerade and 60 ungerade modes for the Γ-point. For convenience and speed the large matrix was factored into gerade and ungerade parts as modes of non-zero wave-vectors were not required.

The calculated frequencies of all the Γ-point modes are given in table 6. A further calculation was done to investigate the effect of hydrostatic pressure on these modes of vibration, and these results are also given in table 6. Apart from the eigenvector approximation discussed above, there is another approximation made in these calculations which might have a small effect on the results. Any such lattice dynamical calculation must necessarily be made for a system in stable equilibrium, and this condition has been rigorously applied for the rigid-body calculations

discussed earlier. The structure corresponding to the equilibria at zero and at 3.8 kbar pressure was used as the starting point for the full calculation, but as bending of the molecule was then introduced, a new term in the potential energy was consequently neglected. The justification for this is that the internal force field contains by its very nature no anharmonic terms, and the anharmonic variation in the intermolecular potential due to a slight deformation of the molecule can be considered negligible.

This calculation gives three types of result, an internal mode frequency shift, its symmetry splitting and its pressure variation. On all these accounts the average calculated variation is significantly less than that observed. . It is clear that, although the 6-exp interaction works well for the rigid-body motion, it does not adequately account for the detailed interaction. Consequently there must be an important interaction neglected in this work. This could very well be a coulombic interaction between local dipole moments generated by the short range forces when molecules approach each other closely. The inclusion of such 'shell model' interactions has been suggested by Luty and Pawley (1974) and by Pawley and Leech (1977), and is being implemented.

Acknowledgment

The authors greatly acknowledge assistance from Dr. G.B. Jensen in orienting and cutting the crystals. We wish to thank Dr. O. Fauerskov-Nielsen and Dr. R. Berg for performing preliminary Raman-experiments on SnI_4 and Hugh Vass for technical assistance in polishing the crystals. One of us (I.U.H.) is grateful to the Research Establishment Risø for financial support to go to Edinburgh.

References

Arthur, J.W., (1976), J. Raman Spectrosc., 5, 9-19.

Arthur, J.W. and Lockwood, D.J., (1974), J. Raman Spectrosc., 2, 53-69.

Basile, L.J., Ferraro, J.R., La Bonville, P. and Wall, M.C., (1973), Coordination Chemistry Reviews 11, pp.21-69.

Cracknell, A.P.C., (1968), Applied Group Theory, Pergamon Press, Oxford.

Cyvin, S.J., (1968), Molecular vibrations and mean square amplitudes (p.122) Universitetsforlaget, Norway.

Dawson, P., (1975), Spectrochimica Acta, 31A, 1101-2.

Heilmann, I.U. (1977) Ph.D. Thesis, University of Copenhagen.

Heilmann, I.U. and Olsen, B., (1977), J. Phys. C., 10, 1175-80

Herzberg, G. (1945), Infrared and Raman Spectra of Polyatomic Molecules, Van Nostrand, New York.

Kitaigorodskii, A.I., (1966), J. Chim. Phys., 63, 6-14

Lockwood, D.J., (1974), J. Raman Spectrosc., 2, 555-62.

Luty, T., and Pawley, G.S., (1974), Phys. Stat. Sol. B66, 309-19.

Lynch, R.W. and Drickamer, H.G., (1966), J. Chem. Phys., 45, 1020-30

Murray, A.F. and Lockwood, D.J., (1976), J. Phys. C., 9, 3691-700.

Pawley, G.S., (1967), Phys. Stat. Sol., 20, 347-60.

Pawley, G.S., (1972), Phys. Stat. Sol., B49, 475-88.

Pawley, G.S. and Cyvin, S.J., (1970), J. Chem. Phys. 52, 4073-7.

Pawley, G.S. and Leech, J.W., (1977), J. Phys. C., 10, 2527-46.

Pawley, G.S. and Mika, K., (1974), Phys. Stat. Sol., B66, 679-86.

Peercy, P.S., Samara, G.A. and Morosin, B., (1975), J. Phys. Chem. Solids, 36, 1123-8.

References (continued)

Pistorius, C.W.F.T. and Haarhoff, P.C., (1959), Z. Phys. Chem. (N.F.), 19, 202- 5.

Rinaldi, R.P. and Pawley, G.S., (1975), J. Phys. C., 8, 599-616.

Stammreich, H., Forneris, R. and Tavares, Y. (1956), J. Chem. Phys., 25, 1278-9.

Figure captions

*

Figure 1 Stereoscopic view of the crystal structure of SnI_4.

Figure 2 The five symmetry coordinates for the A_g and A_u crystal modes. (a) and (b) are external mode motions, whereas (c), (d) and (e) are internal mode motions. Only one of the eight molecules in the unit cell is shown, the other molecules vibrate with displacements either in or out of phase with the motions shown, depending on the parity. (a) and (b) could be represented as pure translation and pure rotation, but the combination shown corresponds closer to the actual motion in the lattice modes.

Figure 3 The diamond-window pressure cell. The various parts of the cell are described in the text.

Figure 4(a) The X(ZZ)Y Raman spectrum of SnI_4 recorded at 298 K (upper trace) and 112 K (lower trace).

Figure 4(b) The X(ZX)Y Raman spectrum of SnI_4 recorded at 298 K (upper trace) and 112 K (lower trace).

Figure 5 The X'(Y'X')Y' Raman spectrum of SnI_4 recorded at 298 K (upper trace) and 100 K (lower trace).

Figure 6 The pure A_g(a), E_g(b) and F_g(c) Raman spectra of SnI_4 derived from data recorded at 100 K.

Figure 7(a) The low frequency F_g lattice spectrum recorded at 100 K fitted with four damped harmonic oscillators (dashed curve).

Figure 7(b) The lowest frequency F_g internal modes (100 K spectrum) fitted with two damped harmonic oscillators.

Figure 7(c) Low frequency F_g internal modes (100 K spectrum) fitted with three damped harmonic oscillators.

See p20

Figure 8 Pressure dependence of the Raman spectrum of powdered SnI_4 at room temperature. The pressures are 0.001, 2.0 and 4.2 kbar for the lower, middle and upper traces, respectively. The sharp features marked with an asterisk are Kr plasma lines.

Figure 9 Pressure dependence of (a) internal and (b) lattice mode frequencies of SnI_4 at room temperature. Frequencies are determined within $\pm$ 0.2 cm^{-1}. Estimated errors in the pressure are $\pm$ 0.2 kbar.

Figure 10 The triply degenerate F_g,F_u modes. The solid arrows show displacements in the symmetry coordinate usually associated with the higher frequency. The other symmetry coordinate, in which the central atom does not move, is shown by the unfilled arrows. A linear combination is possible such that A^oB^o = AB and there is no stretching of the bonds. We use this as the eigenvector for F^4, the mode of lower frequency. The orthogonal F^3 eigenvector involves motion of the iodine atoms along (111) directions and the tin atoms along (001). Orthogonality in displacement space is not required.

---

* Stereoscopic pairs must be reproduced with a separation between the corresponding parts about 5mm less than the average eye separation. A figure with the wrong separation is worse than useless.

Tables

1. Correlation between the free molecule representations and the Γ-point crystal representations.

2. Peak frequencies ν and line widths γ (FWHM), in cm^{-1}, and assignments for bands in the Raman spectrum of SnI_4 as a function of temperature. The superscripts on the symmetry labels refer to the corresponding free molecule vibration (see section 2). Frequencies are determined within ± 0.1 cm^{-1}.

3. Pressure dependence of peak frequences $\nu(cm^{-1})$ and linewidths $\gamma(cm^{-1})$ for bands in the room temperature Raman spectrum of powdered SnI_4.

4. Room temperature values for the frequencies and their logarithmic temperature and pressure derivatives of various Raman active modes in SnI_4. a) refers to experimental values found in the present work, b) refers to values found by Peercy et al. (1975) and c) refers to the results of the molecular rigid body lattice dynamical calculation. The derivatives are calculated at zero pressure.

5. Observed and calculated frequencies (cm^{-1}) of external Γ-modes in SnI_4. The calculated values result from the molecular rigid-body lattice dynamics calculation.

6. Calculated frequencies (cm^{-1}) of all the crystal modes for zero wave-vector at zero and 3.8 kbar pressure, as at room temperature.

FREE MOLECULE	CRYSTAL
A	$A_g + F_g + A_u + F_u$
E	$E_g + 2F_g + E_u + 2F_u$
F	$A_g + E_g + 3F_g + A_u + E_u + 3F_u$

Table 1 Correlation between the free molecule representations and the Γ-point crystal representations.

Table 2 Peak frequencies ν and line widths γ (FWHM), in cm^{-1}, and assignments for bands in the Raman spectrum of SnI_4 as a function of temperature.

The superscripts on symmetry labels refer to the corresponding free molecule vibration (see section 2). Frequencies are determined within ±0.1 cm^{-1}.

Symmetry Assignment	E_g	F_g	F_g	F_g	A_g	F_g	E_g		F_g	A_g		F_g	F_g^2	F_g^2	E_g^2		E_g^4	F_g^4	F_g^4	A_g^4	F_g^4	A_g^1		F_g^1	F_g^3	F_g^3	E_g^3	F_g^3	A_g^3
Temperature (K)	ν	ν	ν	ν	ν	ν	ν	γ	ν	ν	γ	ν	ν	ν	ν	γ	ν	ν	ν	ν	ν	ν	γ	ν	ν	ν	ν	ν	ν
100.0	25.4	23.9	26.1	-	27.0	29.0	29.9	1.0	34.6	39.3	1.1	-	52.8	54.0	54.2	1.8	65.2	63.6	66.0	70.5	68.0	148.4	1.3	148.0	210.3	216.5	213	220.7	~ 216
111.5	25.3	23.8	-	-	-	-	29.8	1.0	34.4	39.2	1.3	-	-	-	54.2	2.0	-	63.6	66.0	-	-	148.3	1.4	-	210.2	216.5	-	220.7	-
119.0	25.1	23.8	-	-	-	-	29.6	1.1	34.2	39.0	1.4	-	-	-	54.0	2.1	-	63.6	65.9	-	-	148.3	1.5	-	210.0	216.4	-	220.6	-
146.0	24.9	23.5	-	-	-	-	29.3	1.2	33.9	38.7	1.5	-	-	-	53.8	2.5	-	63.7	65.9	-	-	148.1	1.8	-	209.8	216.3	-	220.6	-
179.5	24.5	23.1	-	-	-	-	28.9	1.3	33.5	38.2	1.8	-	-	-	53.4	3.1	-	63.6	65.7	-	-	147.5	2.2	-	209.4	216.1	-	220.3	-
199.8	24.3	23.0	-	-	-	-	28.6	1.4	33.1	37.8	2.0	-	-	-	53.3	3.5	-	63.7	65.7	-	-	147.3	2.4	-	209.1	215.8	-	219.9	-
221.5	24.0	22.7	-	-	-	-	28.3	1.5	32.7	37.5	2.2	-	-	-	53.1	3.8	-	63.6	65.6	-	-	147.2	2.6	-	208.8	215.5	-	-	-
239.4	23.9	-	-	-	-	-	28.1	1.6	32.5	37.2	2.1	-	-	-	53.1	4.1	-	63.8	65.6	-	-	147.0	2.8	-	208.7	215.5	-	219.6	-
261.0	23.6	-	-	-	-	-	27.8	1.6	32.2	36.8	2.7	-	-	-	53.0	4.5	-	63.9	65.5	-	-	146.8	3.1	-	208.3	215.2	-	-	-
280.0	23.4	-	-	-	-	-	27.6	1.8	31.9	36.5	2.4	-	-	-	52.8	5.0	-	-	65.5	-	-	146.6	3.3	-	208.3	215.0	-	-	-
298.0	23.2	-	-	-	-	-	27.4	2.0	31.6	36.2	3.0	-	-	-	52.6	5.0	-	-	65.4	-	-	146.5	3.4	-	208.0	214.8	-	-	-

Pressure (kbar)	LATTICE MODES					INTERNAL MODES								
	E_g	E_g		A_g		E_g^2		F_g^4	A_g^1		F_g^3	F_g^3		
	ν	ν	γ	ν	γ	ν	γ	ν	ν	γ	ν	ν		
0.001	23.6	27.5	2.1	36.3	3.0	52.6	6.0	65.4	147.0	3.6	208.4	215.1		
1.1	25.2	29.4	2.3	39.4	3.1	54.2	5.7	66.0	147.4	3.6	208.8	215.2		
2.0	25.5	30.0	2.4	40.2	3.0	54.7	5.5	66.2	147.5	3.6	208.9	215.3		
2.8	25.8	30.8	2.7	41.5	3.0	55.5	5.7	66.7	147.9	3.7	209.2	215.3		
3.6	26.6	31.8	3.3	43.3	3.0	56.4	6.0	67.1	148.2	3.6	209.4	215.6		
4.2	27.2	32.6	4.2	44.3	3.5	57.7	6.0	67.8	148.8	3.9	210.0	215.9		

Table 3

Pressure dependence of peak frequencies ν (cm^{-1}) and linewidths γ (cm^{-1}) for bands in the room temperature Raman spectrum of powdered SnI_4.

Mode	ω (cm^{-1})	$(\partial \ln\omega/\partial p)_T$ ($kbar^{-1}$)			γ			$(\partial \ln\omega/\partial T)_p$ ($10^{-5}K^{-1}$)		$(\partial \ln\omega/\partial T)_V$ ($10^{-5}K^{-1}$)	
		a	b	c	a	b	c	a	b	a	b
F_g	22	-	-	.050	-	-	2.7	-45(7)	-	-	-
E_g	23.2	.051(9)	.063	.053	2.5(5)	3.1	2.8	-48(5)	-50.7	+12(15)	-1.8
E_g	27.4	.054(7)	.065	.050	2.7(3)	3.2	2.7	-46(4)	-47.4	+17(12)	+3.0
F_g	31.6	-	-	.055	-	-	2.9	-48(3)	-	-	-
A_g	36.2	.063(6)	.054	.053	3.1(3)	2.7	2.8	-43(3)	-40.9	+31(10)	+0.9
E_g^2	52.6	.021(4)	.016	-	1.0(2)	.8	-	-15(2)	-13.0	+10(7)	-0.5
F_g^4	64	-	-	-	-	-	-	+3(2)	-	-	-
F_g^4	65.4	.007(3)	.0067	-	.3(2)	.3	-	-5(1)	-9.2	+3(4)	-3.9
A_g^1	146.5	.002(1)	.0028	-	.10(5)	.1	-	-6.6(6)	-5.5	-4(2)	-3.3
F_g^3	208.0	.0015(8)	.0018	-	.07(4)	.1	-	-5.6(5)	-2.7	-4(2)	-1.3
F_g^3	214.8	.0005(5)	.0016	-	.02(2)	.1	-	-4.0(5)	-3.8	-3(2)	-2.5
F_g^3	219	-	-	-	-	-	-	-3.6(5)	-	-	-

Table 4 Room temperature values for the frequencies and their logarithmic temperature and pressure derivatives of various Raman active modes in SnI_4 . a) refers to experimental values found in the present work, b) refers to values found by Peercy et al. (1975) and c) refers to the results of the molecular rigid body lattice dynamical calculation.
The derivatives are calculated at zero pressure.

Mode	100 K	1 bar	298 K	1 bar	298 K	4.2 kbar
	obs	calc	obs	calc	obs	calc
F_g	23.9	24.0	-	21.33	-	25.00
E_g	25.4	24.4	23.2	21.27	27.2	25.83
F_g	26.1	25.73	-	22.67	-	27.33
F_g	29.0	26.10	-	23.43	-	27.43
A_g	27.0	30.47	-	27.03	-	32.47
E_g	29.9	31.70	27.4	28.13	32.6	33.47
F_g	-	32.53	-	28.90	-	34.73
F_g	34.6	34.40	31.6	30.53	-	36.80
A_g	39.3	36.17	36.2	32.20	44.3	38.67
F_g	-	38.10	-	33.53	-	40.63

Table 5 Observed and calculated frequencies (cm^{-1}) of external Γ-modes in SnI_4. The calculated values result from the molecular rigid-body lattice dynamics calculation.

	MODE	PRESSURE (kbar)		MODE	PRESSURE (kbar)	
		0.0	3.8		0.0	3.8
INTERNAL FREE MOLECULE MODE	E_g	21.01	23.17	F_u	0.0	0.0
	F_g	21.76	23.75	A_u	18.58	20.54
	F_g	22.44	24.37	F_u	21.05	23.15
	F_g	23.64	25.81	E_u	23.41	25.48
	A_g	25.53	27.77	F_u	25.71	28.08
	F_g	27.30	29.62	E_u	28.37	30.79
	E_g	27.75	30.27	F_u	29.78	32.71
	F_g	29.23	31.91	A_u	30.85	33.68
	A_g	32.52	35.75	F_u	31.99	35.20
	F_g	33.60	37.10	F_u	33.08	36.45
47 E^2	F_g^2	51.74	52.91	F_u^2	54.70	56.20
	F_g^2	54.75	56.36	E_u^2	56.33	58.39
	E_g^2	55.39	56.86	F_u^2	61.15	63.66
63 F^4	E_g^4	66.17	67.10	F_u^4	65.29	65.88
	F_g^4	66.47	67.26	F_u^4	66.11	66.78
	F_g^4	68.21	69.36	A_u^4	66.37	67.23
	A_g^4	71.16	72.97	F_u^4	67.81	68.93
	F_g^4	71.25	73.04	E_u^4	68.33	69.51
149 A^1	A_g^1	150.41	150.68	A_u^1	150.41	150.69
	F_g^1	150.52	150.88	F_u^1	150.46	150.78
216 F^3	F_g^3	216.49	216.61	F_u^3	216.48	216.59
	F_g^3	216.51	216.64	A_u^3	216.49	216.61
	E_g^3	216.52	216.66	F_u^3	216.52	216.65
	F_g^3	216.57	216.72	E_u^3	216.55	216.70
	A_g^3	216.59	216.75	F_u^3	216.61	216.78

Table 6. Calculated frequencies (cm^{-1}) of all the crystal modes for zero wave-vector at zero and 3,8 kbar pressure, as at room

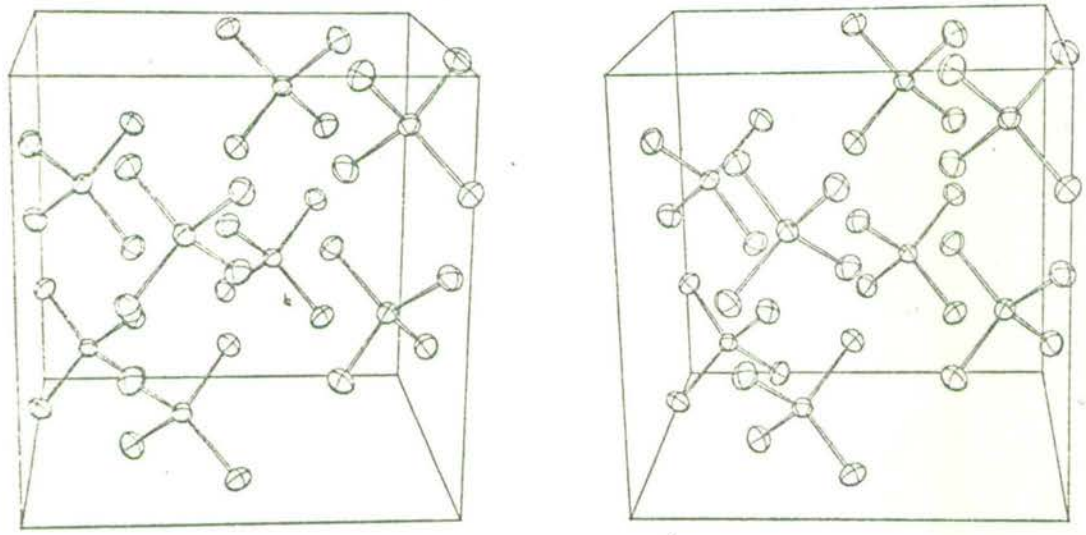

Fig 1

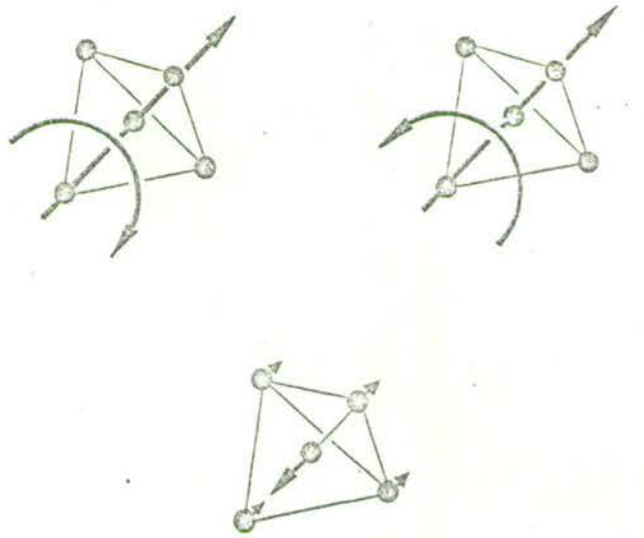

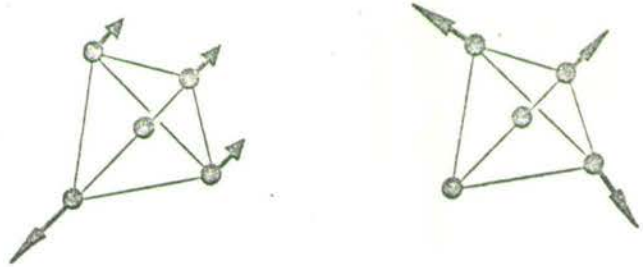

(a) (b) (c) (d) (e)

Figure 2

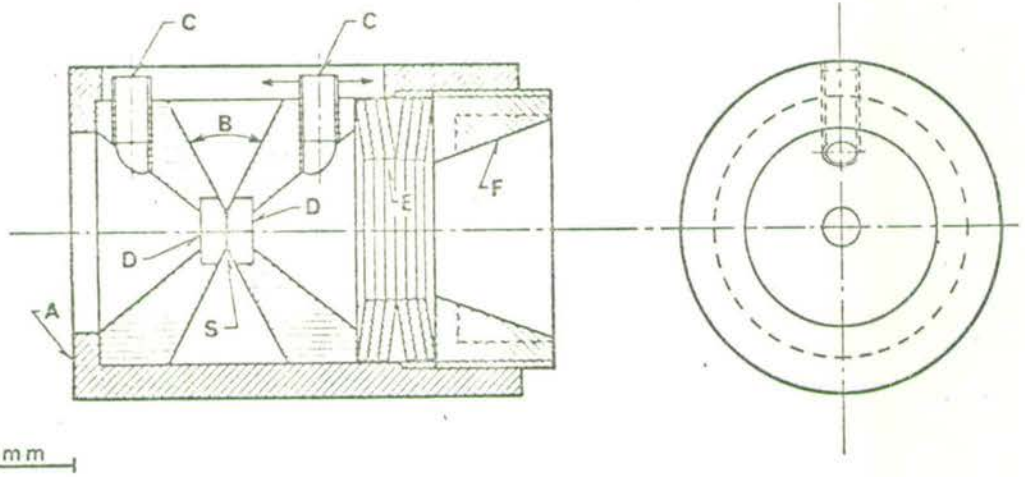

Fig 3

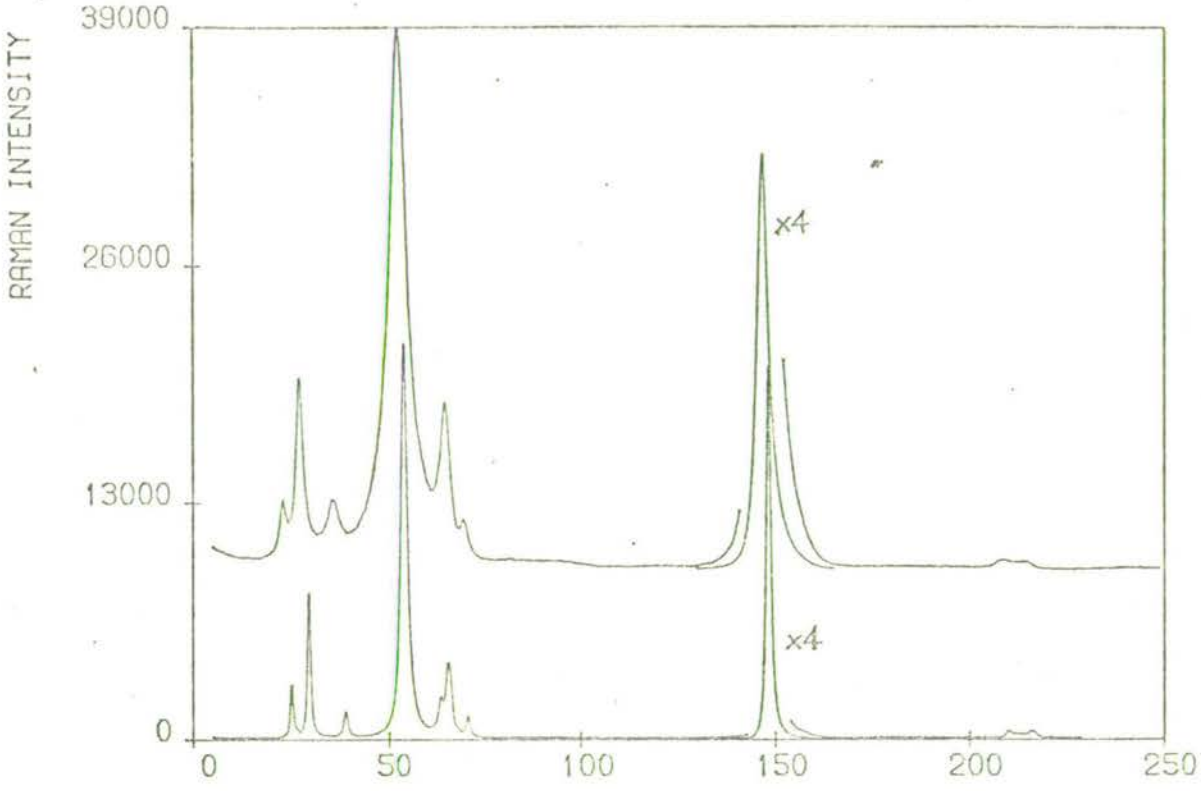
RAMAN INTENSITY
39000
26000
13000
0
x4
x4
0
50
100
150
200
250
FREQUENCY (cm⁻¹)

Fig 4 (a)

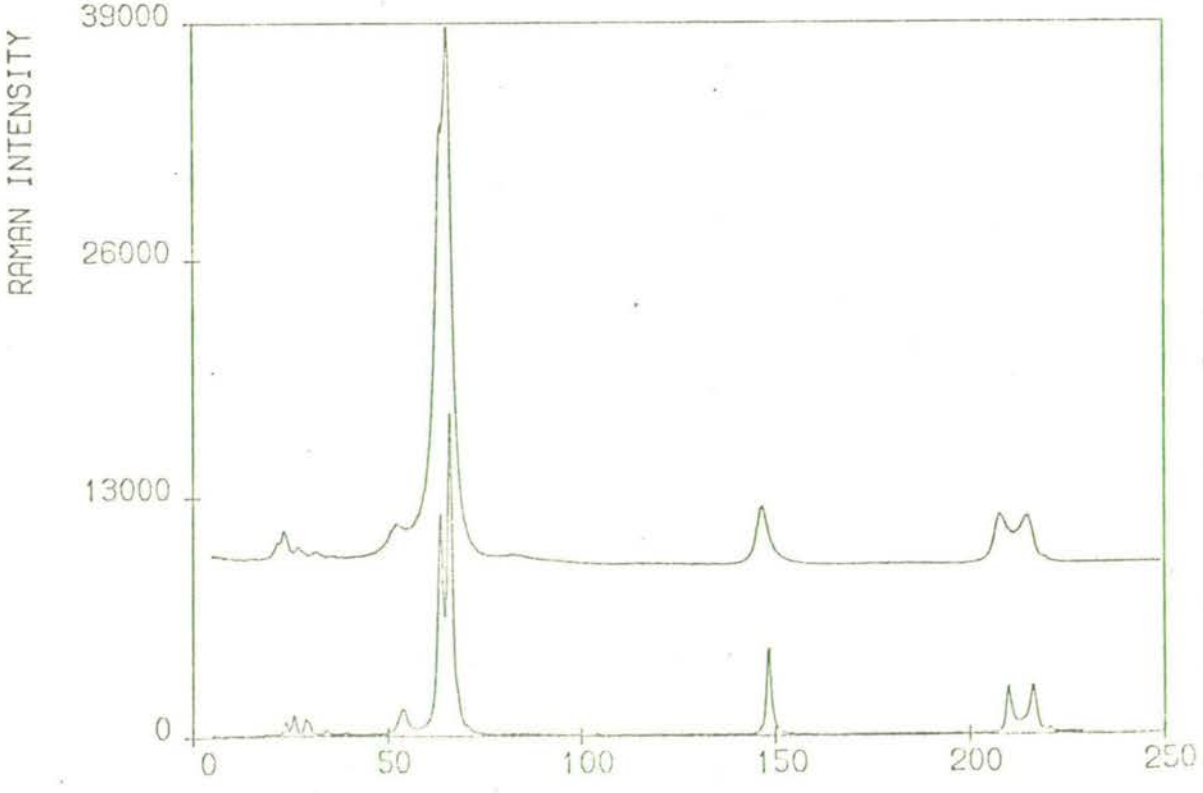
RAMAN INTENSITY
39000
26000
13000
0
0
50
100
150
200
250
FREQUENCY (cm⁻¹)

Fig 4 (b)

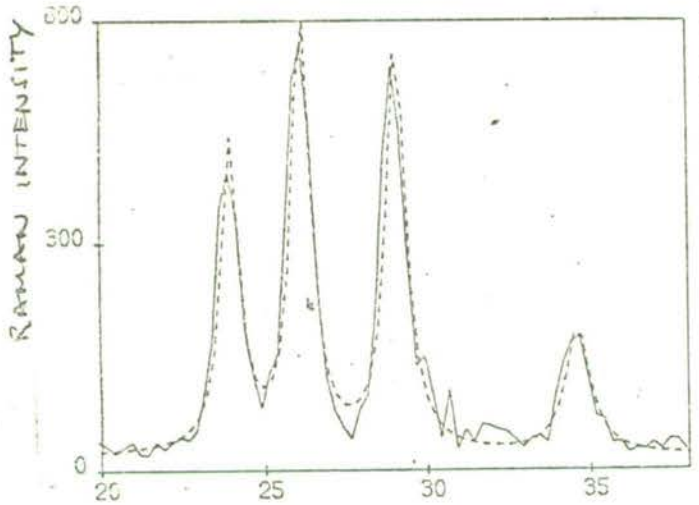

Fig 7(a)

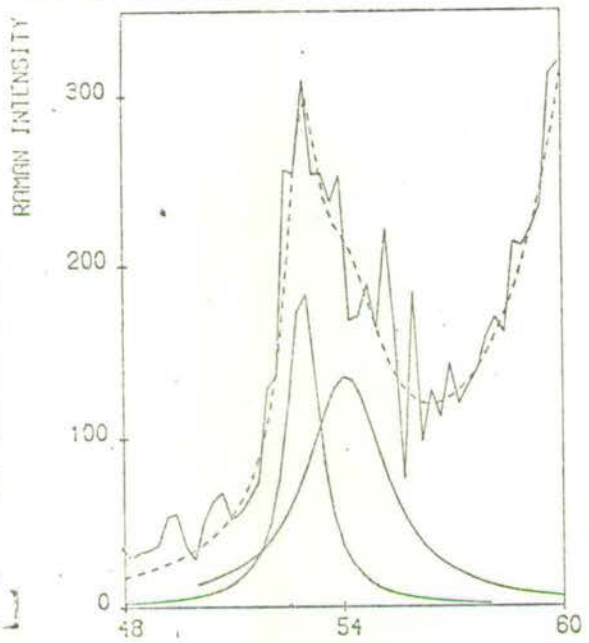

Fig 7 (b)

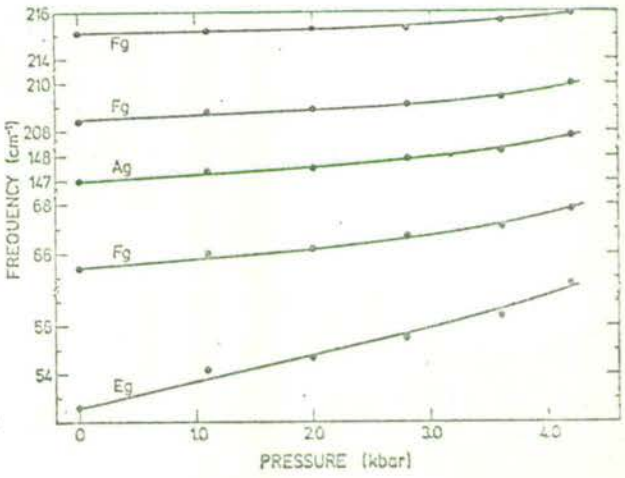

Fig 9(a)

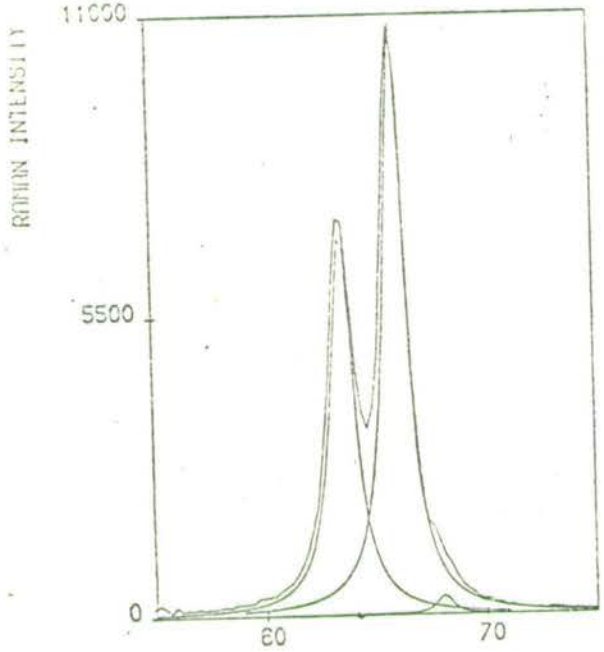

Fig 7(c)

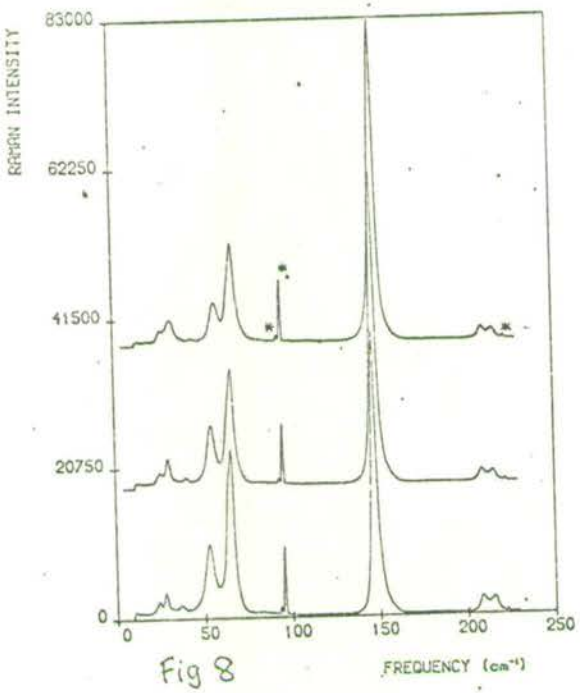

Fig 8

Fig 9(b)

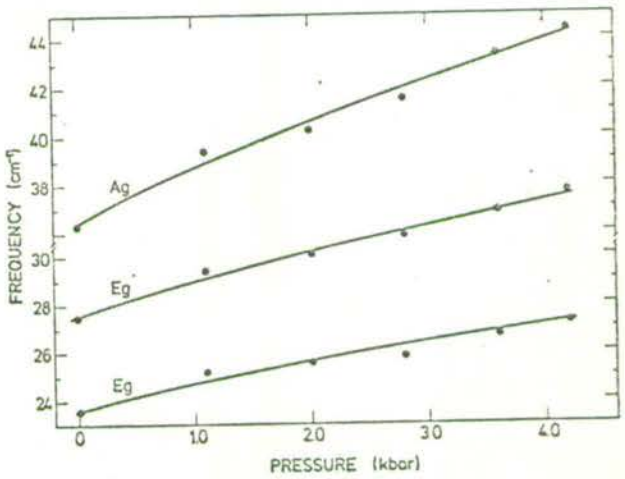

J. Phys. C: Solid State Phys., Vol. 10, 1977. Printed in Great Britain. © 1977

Phonon coupling in $Zn_4O(BO_2)_6$ studied by Raman spectroscopy

A F Murray and D J Lockwood
Department of Physics, University of Edinburgh, Edinburgh EH9 3JZ, Scotland

Received 9 August 1977, in final form 5 September 1977

Abstract. The Raman spectrum of cubic zinc metaborate contains an interference feature at 122·5 cm^{-1} in both the A_1 and E symmetries. The lineshape is analysed using models involving either the interaction between a one-phonon state and a continuum of multi-phonon states, or anharmonic coupling between one-phonon states. Both models describe the results adequately, but the former is preferred on theoretical grounds.

1. Introduction

Evidence of strong coupling between phonon excitations in solids has been reported in numerous materials such as $BaTiO_3$ (Rousseau and Porto 1968), quartz (Scott 1968) and $AlPO_4$ (Scott 1970). Coupling is most commonly observed when a soft mode associated with a phase transition overlaps in frequency another phonon of the same symmetry as a result of a change in pressure or temperature. Resonant interference has only rarely been observed (e.g. SiO_2 and $AlPO_4$). We have measured the room temperature Raman spectrum of cubic zinc metaborate and have recorded an interference feature of this type at 122·5 cm^{-1}. We describe in this paper the analysis of the resultant Raman cross-section in terms of two distinct models.

The first model, outlined in section two, was developed by Fano (1961) to describe the phase shifts in atomic state wavefunctions, and the corresponding excitation spectra, due to the configuration interaction between a discrete state and a continuum of states (or a number of continua). This interaction produces asymmetric peaks in the continuous absorption spectra of atomic or molecular systems. We have used this formalism to describe the Raman spectral lineshape due to interaction between a well defined phonon and a broad second or higher-order background.

The second model involves coupling, via anharmonic terms in the crystal Hamiltonian, of two phonons. This predicts a lineshape similar to that observed in $Zn_4O(BO_2)_6$ when the lifetime of one of the phonons is much greater than that of the other (see for instance Cowley 1966). The details of this model are outlined in section three.

We compare the results of two different applications of the Fabo model, involving different assumptions, and the application of the coupled oscilator mode, in §4.

2. The Fano model

Strictly, this model describes the lineshape due to a discrete state which decays only into

the continuum. This means that the configuration interaction is wholly responsible for the finite lifetime of the state.

If we represent the discrete state by $|p\rangle$, the continuum states by $\{|\psi_E\rangle\}$, and the perturbed wavefunction of eigenvalue E by $|\phi_E\rangle$, we wish to study $\sigma_1(E)$. the scattering cross section for transitions from initial state $|i\rangle$ to final state $|\phi_E\rangle$, which for a transition operator component α_{xy}, is proportional to $|\langle\phi_E|\alpha_{xy}|i\rangle|^2$. With the following definitions in terms of total Hamiltonian H,

$$H|p\rangle = E_p|p\rangle, \tag{2.1}$$

$$\langle\psi_E|H|p\rangle = V_E, \tag{2.2}$$

$$\langle\psi_{E'}|H|\psi_{E''}\rangle = E'\delta(E' - E''), \tag{2.3}$$

It can be shown that:

$$|\langle\phi_E|\alpha_{xy}|i\rangle|^2 = |\langle\psi_E|\alpha_{xy}|i\rangle|^2\left(\frac{\langle\tilde{p}|\alpha_{xy}|i\rangle}{\pi V_E^*\langle\psi_E|\alpha_{xy}|i\rangle} + \frac{E - E_0}{\pi|V_E|^2}\right)^2\left[1 + \left(\frac{E - E_0}{\pi|V_E|^2}\right)^2\right]^{-1}, \tag{2.4}$$

where:

$$|\tilde{p}\rangle = |p\rangle + P\int V_{E'}|\psi_{E'}\rangle/(E - E')\,dE',$$

$$E_0 = E_p + P\int|V_{E'}|^2/(E - E')\,dE'$$

and P denotes 'principal part'.

Writing:

$$q = \frac{\langle\tilde{p}|\alpha_{xy}|i\rangle}{\pi V_E^*\langle\psi_E|\alpha_{xy}|i\rangle} \tag{2.7}$$

and

$$\frac{E - E_0}{\pi|V_E|^2} = \frac{\omega - \omega_0}{\frac{1}{2}\Gamma}. \tag{2.8}$$

The cross section (σ_1) for scattering to the perturbed state of energy E in terms of the cross section (σ_0) for scattering to the unperturbed state $|\psi_E\rangle$ is given by:

$$\sigma_1(\omega) = \sigma_0(\omega)\left(q + \frac{\omega - \omega_0}{\frac{1}{2}\Gamma}\right)^2\left[1 + \left(\frac{\omega - \omega_0}{\frac{1}{2}\Gamma}\right)^2\right]^{-1}. \tag{2.9}$$

Some of the family of curves defined by this function are plotted in figure 1. Fano (1961) has shown that when more than one continuum of states is present, the scattering cross section may be written as:

$$\sigma(\omega) = \sigma_1(\omega) + \sigma_2(\omega), \tag{2.10}$$

where $\sigma_2(\omega)$ corresponds to the underlying noninteracting continuum, and $\sigma_0(\omega)$ is redefined as one linear combination of the continua.

3. Coupled modes

The application of one phonon Green function techniques to the analysis of coupling

between optical phonons is now commonplace (e.g. Cowley 1966, Scott 1971). Only the briefest survey need be given here to define the notation used.

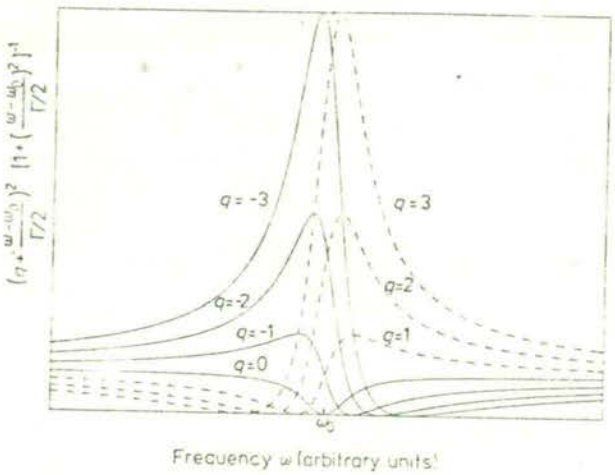

Figure 1. Shape of function 2·9 for different values of q

The cross section for light scattering from optical phonons may be written:

$$\sigma(\omega) = (\bar{n}(\omega) + 1) \sum_{i,j=1}^{N} S_i S_j \operatorname{Im}(G_{ij}(\omega)), \tag{3.1}$$

where $\bar{n}(\omega) + 1$ is the Bose population factor, $G_{ij}(\omega)$ the one phonon Green function matrix, and S_i, S_j may be loosely termed the scattering strengths of the uncoupled modes. They include the polarisability tensor elements, the input field strength, ω^2, and other constant factors. It can be shown that the inverse of $G(\omega)$ in the case of two modes (a and b), coupled by anharmonic terms in the crystal Hamiltonian, may be written:

$$G^{-1}(\omega) = \begin{pmatrix} \omega_a^2 - \omega^2 + i\omega\Gamma_a & \Delta + i\gamma\omega \\ \Delta + i\gamma\omega & \omega_b^2 - \omega^2 + i\omega\Gamma_b \end{pmatrix}. \tag{3.2}$$

By choice of a suitable unitary transformation, either the real or imaginary part of $G^{-1}(\omega)$ may be diagonalised, corresponding to purely imaginary or real coupling respectively. If the other oscillator parameters are redefined suitably, the cross section is unaffected by this transformation. The distinction between real and imaginary coupling only becomes apparent when a soft mode is involved, so we may arbitrarily choose imaginary coupling in this case. Inversion of $G^{-1}(\omega)$ leads to a complicated function in which the parameters of oscillators a and b may not be decoupled, and there is an anti-resonance dip between ω_a and ω_b when $\Gamma_b \gg \Gamma_a$. This function corresponds to coupling between one-phonon states, and therefore differs in concept from the Fano model.

4. Comparison with experiment

Three functions were used to perform a computerised least squares fit to the observed room temperature A_1 and E spectra of zinc metaborate (Murray and Lockwood 1976).

These are as follows.

Coupled modes

A lineshape of the form 3.1 with $N = 3$ and $G_{23}^{-1} = G_{13}^{-1} = 0$ corresponds to two coupled modes and one uncoupled mode. A flat continuous background must be included to account for noninteracting continua and the photomultiplier dark current. If ω_c, Γ_c are the resonant frequency and linewidth of the uncoupled mode, table 1 summarises the results of this analysis.

Table 1. Coupled oscillator parameters

	ω_a (cm^{-1})	Γ_a (cm^{-1})	ω_b (cm^{-1})	Γ_b (cm^{-1})	γ	ω_c (cm^{-1})	Γ_c (cm^{-1})
A_1	124·4	4·3	143·1	73·6	12·4	94·9	11·8
E	123·8	1·8	163·8	103·2	7·2	90·2	12·2

The resulting functions, along with the experimental results, are presented in figure 2. The fine detail of this description in the vicinity of the resonance feature is represented by the broken line in the inset to figure 2.

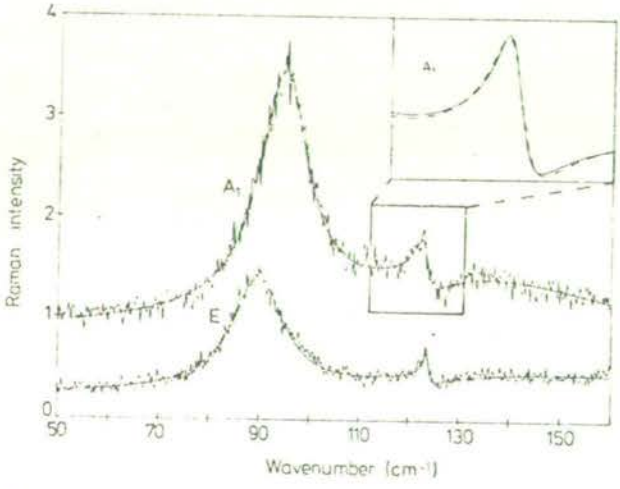

Figure 2. Experimental and theoretical forms for the room temperature A_1 and E spectra of $Zn_4O(BO_2)_6$ in the frequency region 50 cm^{-1}–160 cm^{-1}.

4.2. Fano interference

If Fano interference between a discrete state and a featureless continuum of states is assumed, a diagonal 2×2 Green function must be included to describe the noninteracting modes, and an additive constant, again to account for the noninteracting continua and the dark current. This model involves the same number of variable parameters as 4.1. If ω_b, Γ_b, ω_c, Γ_c are the noninteracting oscillator parameters, the fitted results are given by table 2.

The parameters describing the noninteracting modes are in good agreement with those of table 1, although they now describe uncoupled excitations. The fitted spectrum obtained

is indistinguishable from that of §4.1 to the scale of the large graph in figure 2, but the detail is shown in the inset as a full curve.

Table 2. Fano model parameters.

	q	ω_0 (cm^{-1})	Γ (cm^{-1})	ω_b (cm^{-1})	Γ_b (cm^{-1})	ω_c (cm^{-1})	Γ_c (cm^{-1})
A_1	−1·59	123·5	3·0	141·5	63·4	95·0	12·0
E	−2·26	123·9	1·49	163·2	101·6	90·2	12·3

4.3. Modified Fano interference

Following the reasoning of Rousseau and Porto (1968), an analysis was attempted involving Fano interference with $\sigma_0(\omega)$ in 2.10 represented by an oscillator function and $\sigma_1(\omega)$ by a constant, with a single uncoupled oscillator to describe the 95 cm^{-1} mode. This led to values of $q = -0{\cdot}5$, $\omega_0 = 125{\cdot}0$ cm^{-1} and $\Gamma = 1{\cdot}2$ cm^{-1} for the A_1 spectrum, corresponding to figure 3. Convergence proved impossible in the case of E symmetry.

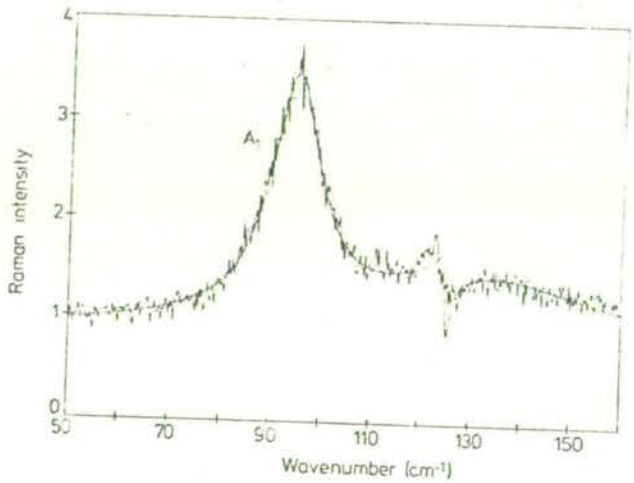

Figure 3. Experimental and theoretical forms for the A_1 spectrum of $Zn_4OO(BO_2)_6$ in the frequency region 50 cm^{-1}–160 cm^{-1}, using the model described in §4.3.

5. Conclusion

Firstly, function 4.3 may be dismissed as an inadequate description of this phenomenon in the case of zinc metaborate. The function involves fewer variable parameters. The results obtained from functions 4.1 and 4.2 are almost indistinguishable in figure 2. The goodness of fit test indicates that the Fano description is as good as the coupled mode description in the E symmetry, and less than one per cent better in the A_1 case. This is hardly significant. Physically the Fano model would appear to be the more suitable, as the coupled oscillator analysis involves assuming that the broad background peak is first order. This would contradict the group theoretical prediction (Murray and Lockwood 1976). For this reason, we believe the Fano description to be more significant, although the experiment is not accurate enough to discriminate between the two theories.

A study of the temperature dependence of this feature revealed little change in the spectral lineshape as far ar 130 K, with no evidence of decoupling.

Acknowledgment

AFM thanks the SRC for the award of a Research Studentship.

References

Cowley R A 1966 *Phonons in Perfect Lattices and Lattices with Point Imperfections* ed Stevenson R W H (Edinburgh: Oliver and Boyd) pp 170–207
Fano U 1961 *Phys. Rev.* **124** 1866–78
Murray A F and Lockwood D J 1976 *J. Phys. C: Solid St. Phys.* **9** 3691–700
Rousseau D L and Porto S P S 1968 *Phys. Rev. Lett.* **20** 1345–57
Scott J F 1968 *Phys. Rev. Lett.* **21** 907–10
—— 1970 *Phys. Rev. Lett.* **24** 1107–10
—— 1971 *Light Scattering in Solids* ed Balkanski M (Paris: Flammarion) pp 387–92

RAMAN SPECTRAL STUDY OF CUBIC NICKEL-IODINE BORACITE

A.F. Murray and D.J. Lockwood

Physics Department, University of Edinburgh,
Edinburgh, EH9 3JZ, Scotland.

The Raman spectrum of cubic nickel-iodine boracite is reported for temperatures between 88 and 295 K. Anomalies in the temperature dependance of E and A_1 symmetry modes at 128 K are interpreted as being related to anomalies in the structural, magnetic, and electrical properties of this material. A 20 cm^{-1} softening of a broad E symmetry mode is also noted. The 88 to 295 K results for this system are all characteristic of a material with a cubic space group.

Nickel iodine boracite, $Ni_3B_7O_{13}I$ (Ni - I), has a first order transition from a high temperature paraelectric cubic phase to an orthorhombic improper ferroelectric phase at T_c = 64 K, at which temperature Ni - I also becomes weakly ferromagnetic.[1] Both the dielectric constant and magnetic susceptibility exhibit a broad maximum at around 125 K [1], while the lattice constant increases anomalously by about 0.1%.[2] Apart from a tentative suggestion that this behaviour may be due to short-range magnetic ordering associated with localised structural ordering[1], the microscopic origin of this phenomenon is not understood.

We have studied the Raman spectrum of Ni - I using the same single [100] growth sector B^{11} enriched sample examined in reference 3. With 400 mW of 647.1 nm krypton laser light aligned along the [$\bar{0}$01] crystal axis the Raman scattering along the [$\bar{1}$10] axis was analysed in all polarisations. The sample temperature was varied between 88 K and 295 K by use of a nitrogen vapour flow cryostat, and the scattered light dispersed by a Spex 1400 double monochromator (295 K) and a Coderg T800 triple monochromator (88 K - 210 K) with a spectral slit width of 2.5 cm^{-1} in both cases.

The room temperature Raman spectra are presented in Figure 1. E and F_2 symmetry modes are active in the Z(Y'X')Y' and Z(Y'Z)Y' polarisations respectively, where X',Y',Z refer to the crystal [110], [$\bar{1}$10], [001] directions. Allowing that the F_2 spectrum is relatively weak, the A_1 spectrum is isolated by subtracting the Z(Y'X')Y' spectrum from the Z(X'X')Y' spectrum [4]. The results between 88 K and room temperature are consistent with a cubic crystal space group throughout this temperature range, in agreement with X-ray results at 77 K and room temperature[3,5], and are also consistent with a structure containing BO_4 groups.[4] The low frequency F_2 and A_1 symmetry line profiles are characteristic of a cubic boracite[6] but the expected A_1 wing is far less well-defined, and the low frequency A_1 and E symmetry modes more heavily damped than their counterparts in the spectra of other boracites (e.g. Cu - Cℓ, Cr - Cℓ).

Part of the work concerning the temperature variation of the Raman spectra is illustrated in Figures 2 and 3. In Figure 2 the peak position of one of the higher frequency E modes is plotted as a function of temperature, from experiments performed at different times and in different polarisations. The black circles represent Z(Y'X')Y' results and the open circles, Z(X'X')Y' spectra. The triangles and squares illustrate later experiments in Z(Y'X')Y' geometry, with temperature increasing and decreasing respectively. From these results it is clear that the natural frequency rises with decreasing temperature, dropping anomalously at about 128 K. This effect became

less pronounced as the sample 'deteriorated' after several temperature cycles, but was characteristic of all the high frequency E modes. The linewidths of these bands show the opposite behaviour, decreasing with falling temperature and increasing at 128 K. In contrast, the broad 170 cm^{-1} E mode frequency decreases with temperature, increasing anomalously at 128 K as shown in Figure 3. There is no corresponding linewidth anomaly for this mode in the given temperature range. The frequencies and linewidths for this feature are taken from a computerised least squares fitting of an anharmonically damped oscillator lineshape over the region 30 - 240 cm^{-1}. Examples of fitted A_1, E and F_2 spectra are shown in Figure 1. The broad A_1 peak at 166 cm^{-1} exhibits a similar, if less dramatic, temperature variation. No significant temperature variation can be attributed to the very weak F_2 spectrum.

From these results it is apparent that there is some disturbance of the structure at around 128 K, but there is no spectroscopic evidence for either a structural transition, or long range antiferromagnetic ordering. These results are in accord with the suggestion of short range magnetic ordering giving rise to the susceptibility maximum. The softening of the heavily damped E mode is unlike the results in Cr - Cℓ and Cu - Cℓ, and suggests that the 64 K transition differs from the usual boracite behaviour. The low frequency modes are mostly related to vibrations involving motion of the nickel and iodine ions. Softening of these modes would therefore indicate a repositioning of one or more of these ions. Such displacements must, however, retain the overall cubic symmetry, as verified in reference 2. At all temperatures in our study of Ni - I, the Raman spectrum indicates that the system is cubic.

We acknowledge the support of the S.R.C. (A.F.M.) and U.S. Army Research and Development Group (Europe) (D.J.L.).

REFERENCES

1. See the review by NELMES, R.J., J. Phys. C. 7, 3840 (1974).
2. WILL, G., and MORCHE, H., J. Phys. C. 10, 1389 (1977).
3. THORNLEY, F.R., KENNEDY, N.S.J., and NELMES, R.J., J. Phys. C. 9, 681 (1976).
4. MURRAY, A.F., and LOCKWOOD, D.J., J. Phys. C. 9, 3691 (1976).
5. NELMES, R.J., and THORNLEY, F.R., J. Phys. C. 9, 665 (1976).
6. LOCKWOOD, D.J., Ferroelectrics 13, 353 (1976).

FIGURE CAPTIONS

Figure 1. The room temperature Raman spectrum of Ni - I.

Figure 2. Temperature dependence of an E mode peak frequency.

Figure 3. Temperature dependence of the broad E mode natural frequency.

Please note

Figure 1 is designed to be reproduced at full-page width, and Figures 2 and 3 at single column width.

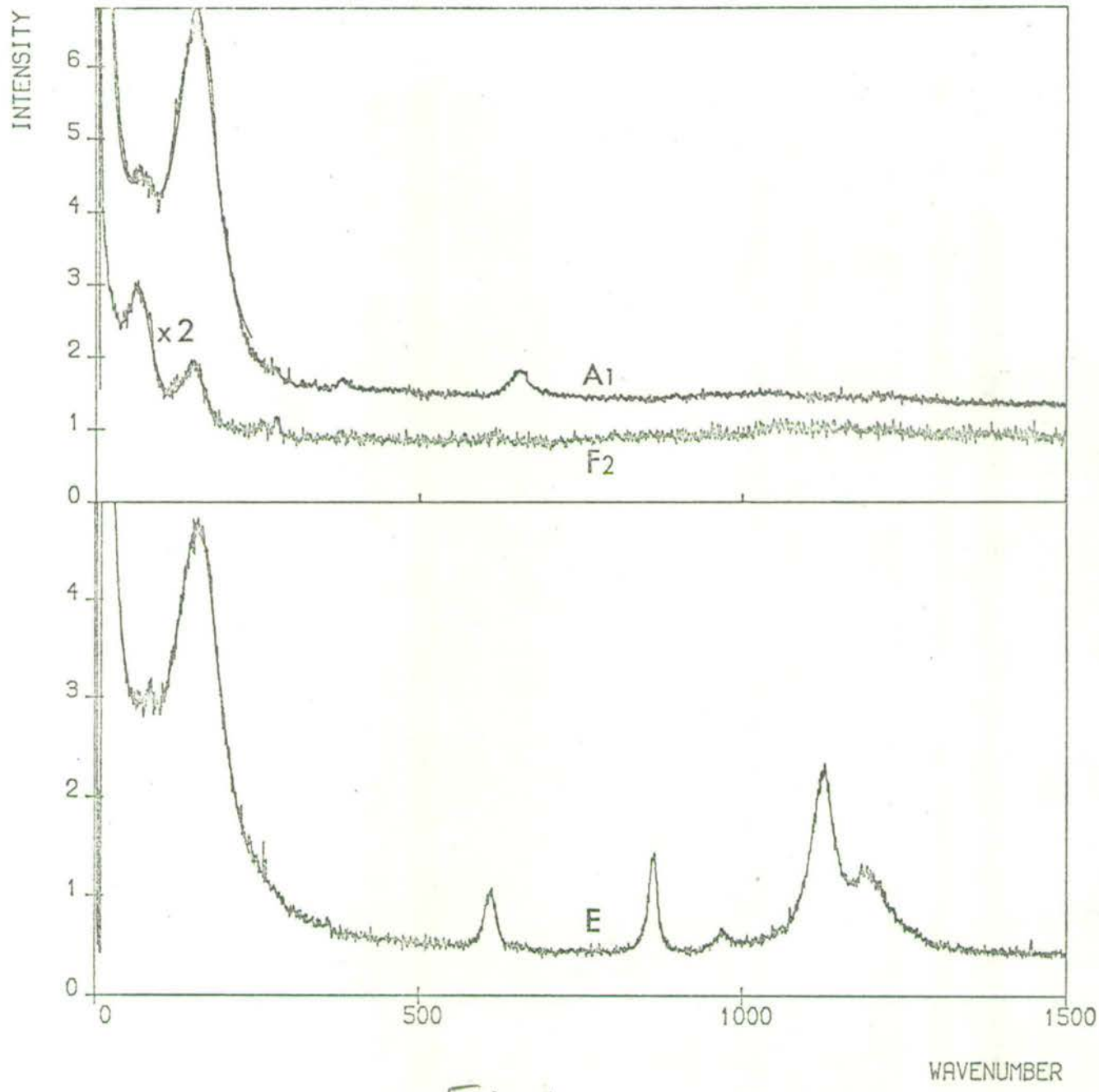
INTENSITY
6
5
4
3
2
1
0
x 2
A1
F2
4
3
2
1
0
E
0
500
1000
1500
WAVENUMBER

Fig. 1

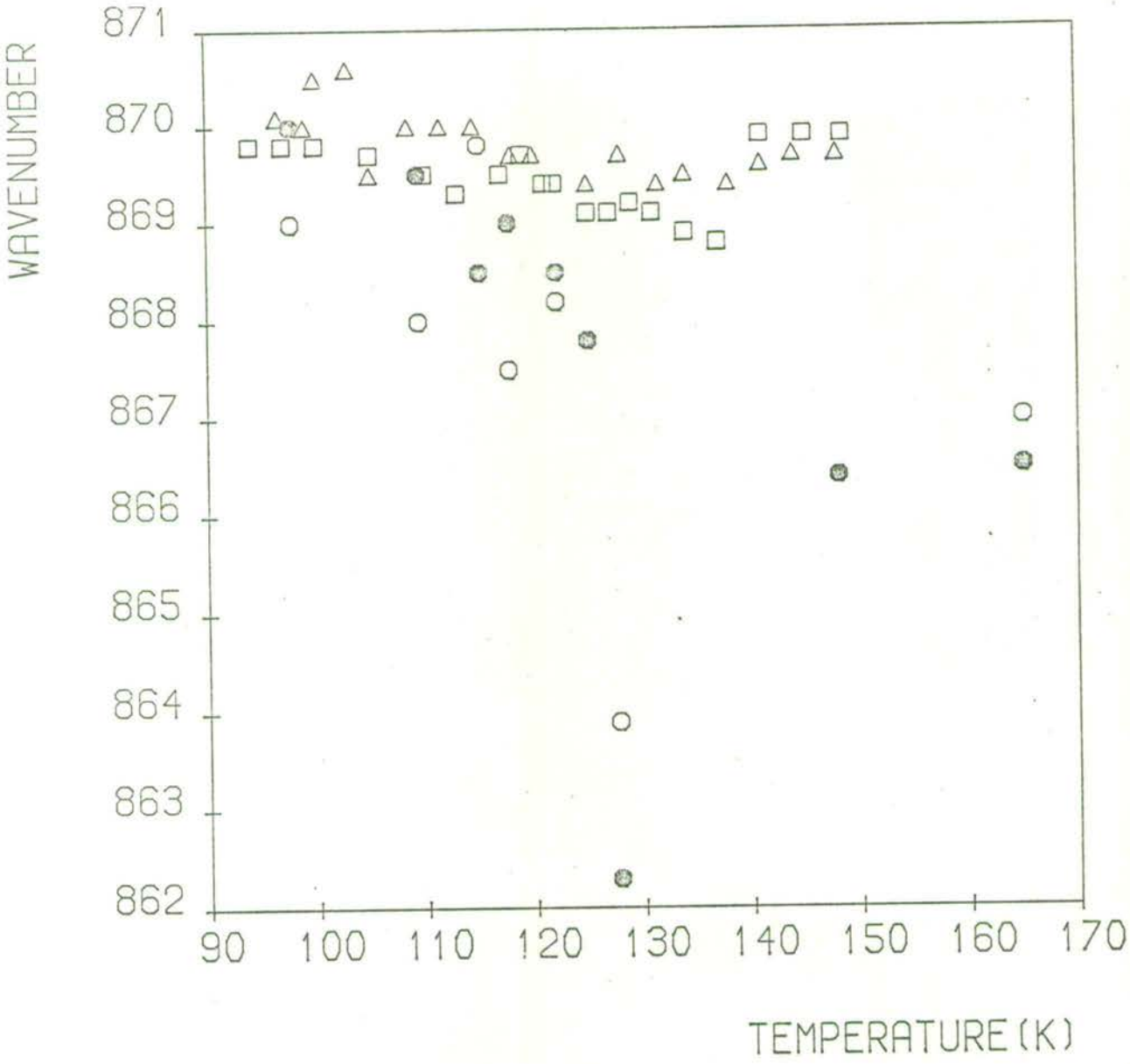
WAVENUMBER
871
870
869
868
867
866
865
864
863
862
90
100
110
120
130
140
150
160
170
TEMPERATURE (K)

Fig. 2

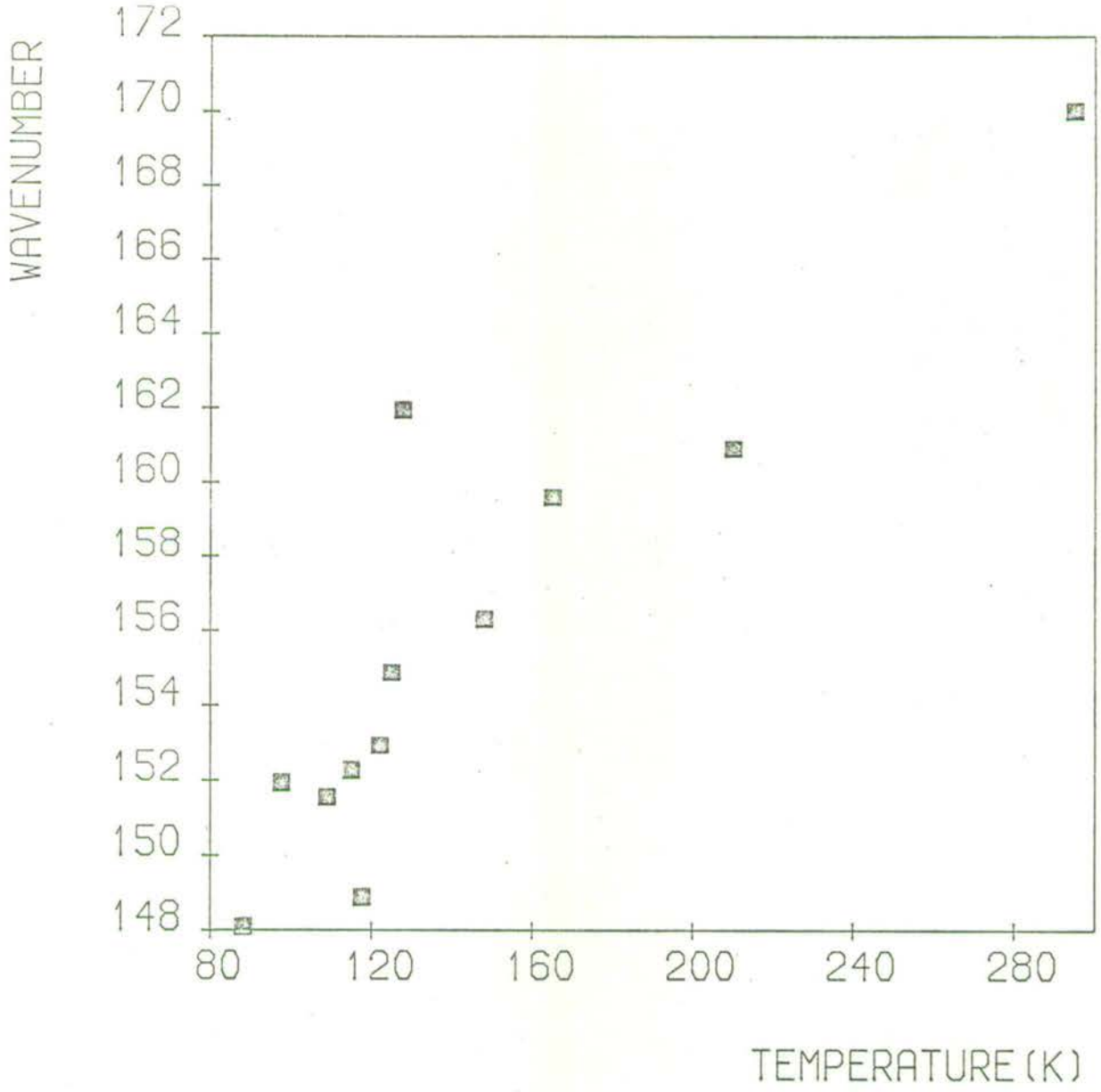
WAVENUMBER
172
170
168
166
164
162
160
158
156
154
152
150
148
80
120
160
200
240
280
TEMPERATURE (K)

Fig. 3

DYNAMICS OF THE MOLECULAR SOLID SnI_4

I.U. Heilmann

Risø National Laboratory, DK-4000 Roskilde, Denmark

N.B. Olsen

Roskilde Universitets Center, Denmark

D.J. Lockwood, G.A. Mackenzie and G.S. Pawley

University of Edinburgh, Scotland

The dynamics of the molecular solid SnI_4 has been investigated with special emphasis on the temperature- and pressure dependence. Several experimental techniques such as inelastic neutron scattering, Raman-scattering and Mössbauer absorption were applied. The eigenfrequencies of SnI_4, especially the external ones, exhibit pronounced anharmonic temperature and pressure shifts. The rigid-body lattice dynamics model of Pawley[1] was applied to the system, and at a given temperature the calculated eigenfrequencies and their pressure shifts are in reasonable agreement with observations. The measurement of both temperature and pressure shifts of some Raman active zone-centre modes allowed a determination of the isochoric temperature shifts $(\partial\omega/\partial T)_V$, which proved to be significant. In contrast to this, the temperature and pressure dependence of the ^{119}Sn Mössbauer absorption intensity seems to be uniquely determined by the specific volume solely.

The molecular crystal tin tetraiodide, SnI_4, is an extremely compressible substance with a large thermal expansion, thus exhibiting bulk properties indicative of soft, anharmonic intermolecular forces. The structure is cubic, $Pa\bar{3}$, with eight tetrahedral SnI_4-molecules in the primitive cell, and the material has favourable spectroscopic properties, allowing a variety of experimental techniques to be applied. In the present work we have investigated the dynamics of SnI_4 with particular emphasis on the temperature and pressure dependence, using inelastic neutron scattering, Raman scattering and Mössbauer absorption.

Figure 1 shows the cubic unit cell as determined from a recent structure refinement[2]. The structure can be visualized in terms of a slight deviation from an "ideal" structure consisting of a face-centered cubic lattice of iodine-atoms with tin atoms in one eighth of the interstices. The molecules are arranged in pairs related by the symmetry centres, with one tetrahedral 3-fold axis along the common (111)-direction and each with a vertex on this axis directed away from the symmetry centre. Two parameters, ℓ and ψ, describing the translation along and rotation about the crystal 3-fold axes of the molecules, respectively, plus the cubic unit cell length, a, are thus allowed to vary without breaking the space group symmetry, provided that the molecule itself is not distorted.

We have applied to the present system the rigid-body molecular lattice dynamical model of Pawley[1]. The interaction between molecules is approximated by the sum of interatomic interactions, using the "6-exp"-potential

$$V(r) = -\frac{A}{r^6} + Be^{-\alpha r} \qquad 1$$

where r is the distance between atoms in different molecules, and A, B and α are constants depending on the species of the interacting atoms. A considerable simplification is obtained by assuming that the Sn-Sn and Sn-I interactions

have the same parameters as I-I interactions. This is acceptable because Sn atoms are shielded by I atoms, whereupon the I-I interaction will dominate. With this assumption we can then follow Kinaldi and Pawley[3] and obtain values of A and B for a given α, assuming the unit cell size and the sublimation energy, E_s. Appropriate for room temperature we obtained the following

Assumed:		Found:	
a	= 12.27 Å	A = 6691.6	kcal mol^{-1}Å^{-6}
α	= 2.5 Å^{-1}	B = 41196.0	kcal mol^{-1}
E_s	= 16 kcal mol^{-1}		

In doing this we inserted into the program the "ideal" structure and the program then varied ℓ, ψ and a until a static equilibrium configuration was obtained. The model-structure thus found was sufficiently close to the real structure to justify the lattice dynamical calculations.

Each of the eight molecules in the unit cell having six external degrees of freedom, the dynamical matrix becomes a 48×48 matrix, making the computation and analysis of results rather lengthy. Figure 2 shows the calculated dispersion relations of molecular rigid-body modes in the Σ-direction, $\vec{q} = (\xi,\xi,0)$. By inspection of the symmetry properties of the eigenvector components, two irreducible representations Σ_1 and Σ_2 were revealed, one (Σ_1) preserving the glide mirror plane parallel to $\vec{q}$, and one (Σ_2) breaking it. Likewise, at the Γ-point, 4 non-degenerate, 4 doubly degenerate and 12 triply degenerate modes were calculated, divided into an equal number of g- and u-modes. These results agree with group theoretical predictions (the little group of $\vec{q}$ being m and m3 for Σ and Γ, respectively). At the zone-boundary point M, twelve 4-fold degenerate modes were calculated. Calculations were carried out in the other high symmetry directions, Δ and Λ, as well, giving results in accordance with group theoretical predictions. The fraction L of librational energy of the total energy of a mode is included in figure 2 in the following way: solid curves denote $0 < L < 0.33$, dashed curves $0.33 < L < 0.67$ and dotted curves denote $0.67 < L < 1.00$.

per unit cell. The features discussed here stand out clearly in the calculated dispersion relations (figure 2): Optical modes of predominantly translational character are found in continuation of the acoustic branches. This feature was utilized in the interpretation of the Mössbauer-results (see later).

Polarised Raman-spectra of a polished, oriented single crystal were measured at different temperatures between 100 K and 300 K. By means of a subtraction technique, the pure A_g-, E_g- and F_g-spectra at 100 K were revealed and excellent agreement was found between observations and group theoretical predictions[4]. In addition, the pressure-dependence (0 - 4.2 kbar) of the Raman-powder spectrum was measured at room-temperature using a diamond-window pressure cell, constructed for Mössbauer-absorption purposes. The single-crystal measurements allowed for an assignment of the observable bands in the powder spectrum, including three external modes. Room temperature values of the observed external and two internal modes at 1 bar and at 4.2 kbar are shown in table 1, together with calculated values. The

Table 1. Observed and calculated mode frequencies and temperature derivatives of some Raman active modes in SnI_4.

Mode	Frequency (cm^{-1}), 295K				$\left(\frac{\partial \ln \omega}{\partial T}\right)_P$	$\left(\frac{\partial \ln \omega}{\partial T}\right)_V$
	1 bar		4.2 kbar		($10^{-5} K^{-1}$)	
	obs	cal	obs	cal	obs	obs
F_g^{ex}	22.7	21.33	-	25.00	-55.7	-
E_g^{ex}	23.2	21.27	27.2	25.83	-45.8	+8.9
E_g^{ex}	27.4	28.13	32.6	33.47	-44.3	+15.2
F_g^{ex}	31.6	30.53	-	36.80	-48.1	-
A_g^{ex}	36.2	32.20	44.3	38.67	-44.3	+27.1
E_g^{in}	52.6	-	57.7	-	-14.5	+10.5
A_g^{in}	147.0	-	148.8	-	-6.8	-4.4

lattice dynamics calculations at applied pressure were carried out as described by Pawley and Mika[5]. It is seen that the external modes exhibit a very pronounced pressure dependence and that the calculated pressure shifts are in reasonably good agreement with observations. Likewise, the observed temperature depen-

dence of the external modes (at atmospheric pressure) is strong, as also listed $((\partial \ell n\omega/\partial T)_P)$ in the table. From the measured temperature and pressure shifts of the band-frequencies we can calculate the isochoric (pure-temperature) shifts of the frequencies, through the relation

$$\left(\frac{\partial \ell n\omega}{\partial T}\right)_V = \left(\frac{\partial \ell n\omega}{\partial T}\right)_P + \beta/K \left(\frac{\partial \ell n\omega}{\partial P}\right)_T \qquad 2$$

where β and K are the volume thermal expansivity and compressibility, respectively. In the quasi-harmonic approximation the term $(\partial \ell n\omega/\partial T)_V$ is neglected. The values in the last column of the table are obtained from (2) by inserting $\beta = 237(5)\cdot 10^{-6}\ K^{-1}$ (at 295 K)[6] and $K = 20.1\cdot 10^{-3}$ kbar^{-1} [7]. It is seen that the isochoric shifts are of the same order of magnitude as the isobaric shifts and that therefore the quasi-harmonic model does not seem to be adequate in the description of the temperature- and pressure dependence of the zone-centre modes.

The pronounced temperature- and pressure dependence of the external modes in SnI_4 is reflected in the temperature- and pressure dependence of the Mössbauer absorption spectra of SnI_4. Fig. 4 shows the logarithm of the intensity of the ^{119}Sn absorption line in SnI_4 as function of temperature. The points of curve a, b and c were measured at 1 bar, 2.1 kbar and 4.2 kbar, respectively, using a diamond-window pressure cell (open circles). Particular care was taken to ensure a small absorber-thickness, so that $\ell n(\Delta I/I_\infty) \propto -2W$, where 2W is the Debye-Waller factor of the absorbing nuclei (Sn). Some conspicuous features can be seen from fig. 4. At a given pressure the temperature dependence of $\ell n(\Delta I/I_\infty)$ for $T > \sim 170$ K exhibits an anomalous deviation from the straight line low-temperature behaviour (the dashed lines). Secondly, the absorption intensity exhibits an unusually pronounced pressure dependence. These effects must be ascribed to the strong temperature and pressure dependence of the external modes, as it can be shown that the contribution to the mean-square displacement $\langle x^2 \rangle_{Sn}$ of the Sn-atom from

the internal modes almost can be ignored[8]. The linear low-temperature behaviour of ℓnI versus T can be successfully interpreted by assuming a gaussian Debye-Waller factor, $2W = \kappa^2 \langle x^2 \rangle_{Sn}$ and a Debye-distribution for all external modes, implying that

$$\langle x^2 \rangle_{Sn} = \frac{3\hbar^2 T}{M_{mol} k_B \theta^2} \quad \text{for } T \gtrsim \theta \qquad 3$$

where θ is a cut-off frequency for external modes and M_{mol} is the molecular mass. This apparently crude approximation is supported by the observed continuation of the acoustic phonon dispersions into optical, predominantly translational external modes. These "pseudo-acoustic" translational modes are exactly those which contribute critically to $\langle x^2 \rangle_{Sn}$, since the Sn-atom is located in the molecular centre of mass. From the observed slope of ℓnI versus T at 1 bar (figure 4) one obtains from (3) $\theta = 52 \pm 2$ K (~ 36 cm^{-1}). This value is in good agreement with the highest zone-centre mode at ~ 120 K, $A_g \sim 39$ cm^{-1}, found in the Raman work. Similarly, we may derive the value of θ at 2.1 kbar and 4.2 kbar, thus obtaining $\theta = 60 \pm 2$ K (~ 42 cm^{-1}) at 4.2 kbar. This pressure shift is seen to agree well with the observed pressure shift of the high A_g^{ex}-mode (measured at room temperature, see table 1). At higher temperatures the isobaric temperature reductions of the external mode-frequencies cause the ℓnI vs. T curves to deviate from linearity. Because of the fact that the isochoric (explicit anharmonic) temperature shifts $(\partial \ell n \omega / \partial T)_V$ at room temperature of external zone-centre modes proved to be significant (see table 1), it is dubious whether the gaussian (harmonic) Debye-Waller factor $2W = \kappa^2 \langle x^2 \rangle_{Sn}$ can be applied in the high-temperature range. However, it seems as if the temperature and pressure dependence of the Mössbauer-data may be adequately interpreted in terms of a quasi-harmonic model, implying that the Debye-Waller factor 2W is determined by the specific volume solely. From the recently determined thermal expansivity and the known compressibility at room temperature one finds that the relative volume increment $\Delta V/V = 3.7\%$ in going from 100

K to 295 K at 1 bar is compensated by an external pressure of 2.1 kbar. From figure 4 it is seen that the 2.1 kbar curve (b) intersects the low-temperature continuation of the 1 bar curve at about room temperature. This indicates that the temperature dependence of the Mössbauer absorption of a sample clamped at 100 K at 1 bar would be linear. This suggests that the isochoric shifts $(\partial \ell n \omega / \partial T)_V$ of most of the modes contributing to $\langle x^2 \rangle_{Sn}$ are small, in contrast to what was observed for the zone-centre modes.

A more detailed analysis of the presented Mössbauer data is being carried out.

REFERENCES

1. PAWLEY, G.S., phys. stat. sol. (b) 49, 475 (1972).
2. HEILMANN, I.U., HAZELL, R. and LARSEN, F.K., to be published.
3. RINALDI, R.P. and PAWLEY, G.S., J. Phys. C. 8, 599 (1975).
4. HEILMANN, I.U., LOCKWOOD, D.J. and PAWLEY, G.S., submitted to J. Phys. C. (1977).
5. PAWLEY, G.S. and MIKA, K., phys. stat. sol. (b) 66, 679 (1974).
6. HEILMANN, I.U., Ph.D. Thesis, University of Copenhagen (1977).
7. PEERCY, P.S., SAMARA, G.S. and MOROSIN, B., J. Phys. Chem. Sol. 36, 1123 (1975).
8. HEILMANN, I.U. and OLSEN, N.B., J. Phys. C. 10, 1775 (1977).

Figure Captions

Figure 1. The cubic unit cell of SnI_4.

Figure 2. Phonon dispersion relations for wavevectors $\vec{q} = (\xi,\xi,0)$ in SnI_4 resulting from the molecular rigid-body lattice dynamical model.

Figure 3. Observed room-temperature phonon frequencies in SnI_4 for wavevectors $\vec{q} = (\xi,0,0)$ (a), $\vec{q} = (\xi,\xi,0)$ (b) and (c) and $\vec{q} = (\xi,\xi,\xi)$ (d). The scattering vector $\vec{K}$ for filled and open circles is indicated above and below, respectively. The dotted lines result from the molecular rigid-body lattice dynamical calculations.

Figure 4. The logarithm of the ^{119}Sn Mössbauer absorption intensity in SnI_4 versus temperature at atmospheric pressure (a), 2.1 kbar (b) and 4.2 kbar (c).

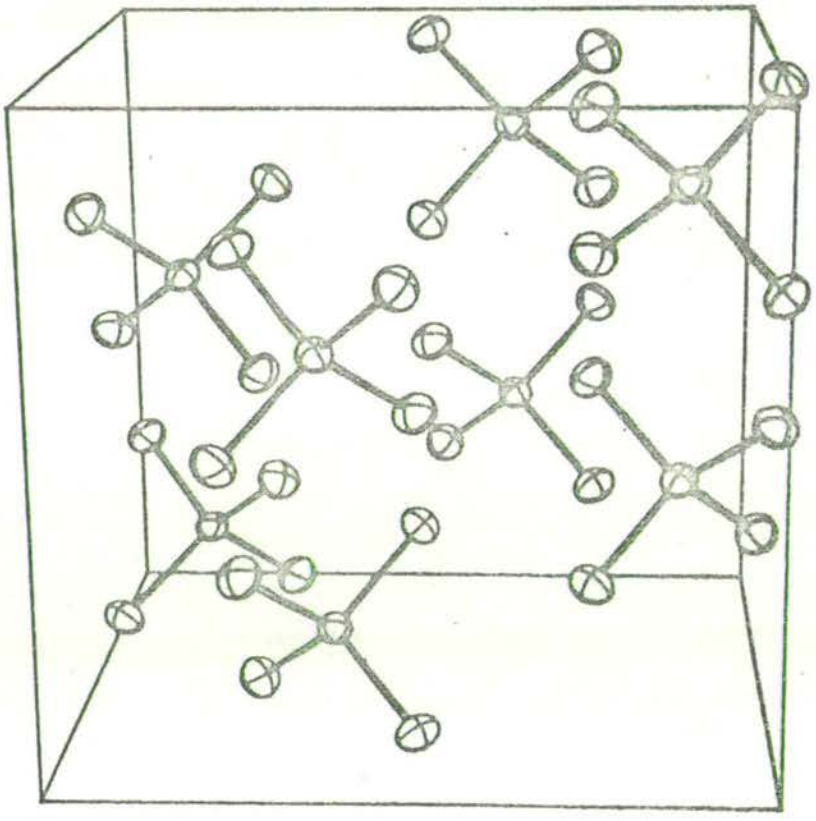

Fig. 1

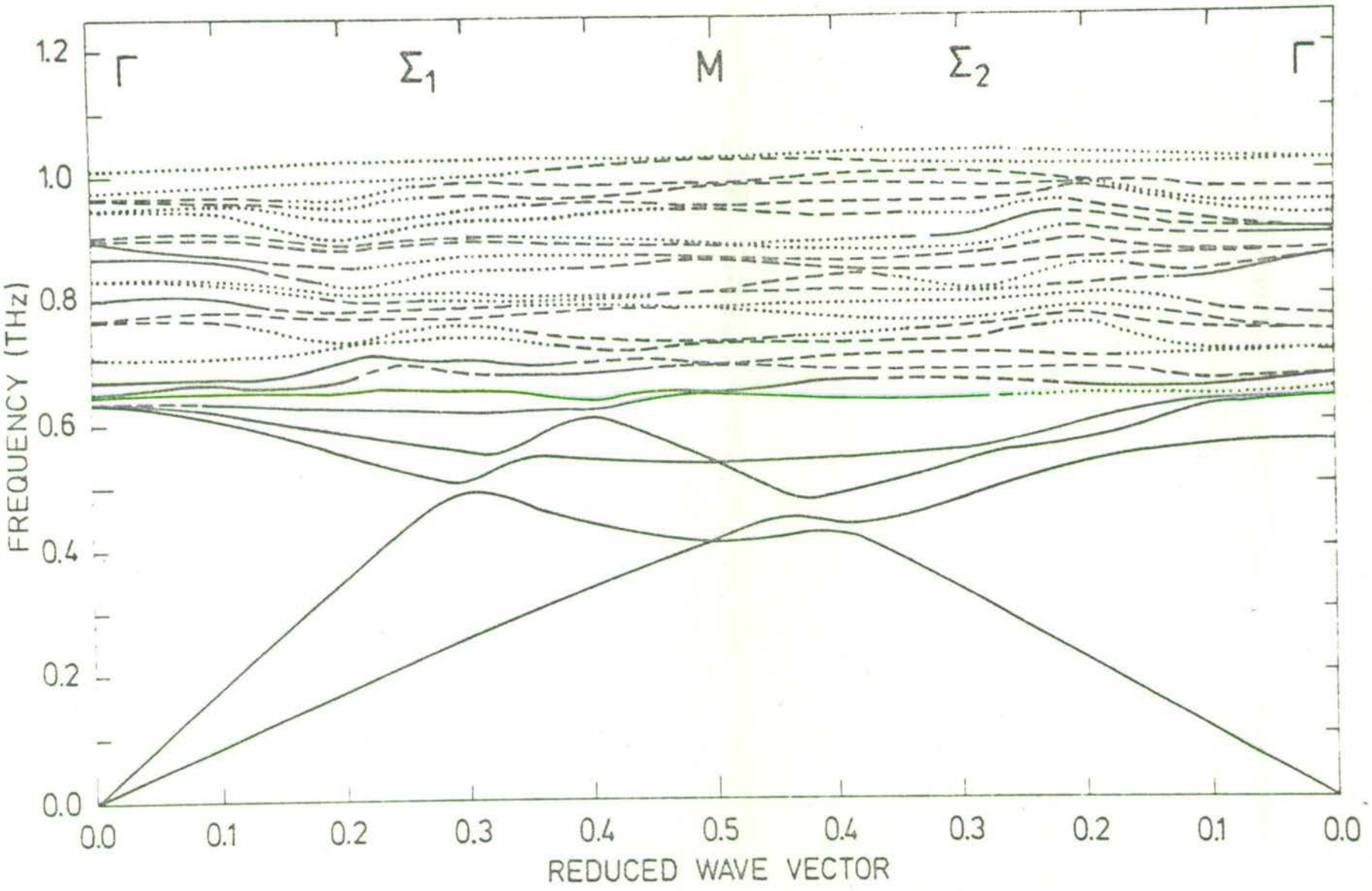
Γ
Σ1
M
Σ2
Γ
1.2
1.0
0.8
0.6
0.4
0.2
0.0
FREQUENCY (THz)
0.0
0.1
0.2
0.3
0.4
0.5
0.4
0.3
0.2
0.1
0.0
REDUCED WAVE VECTOR

Fig. 2

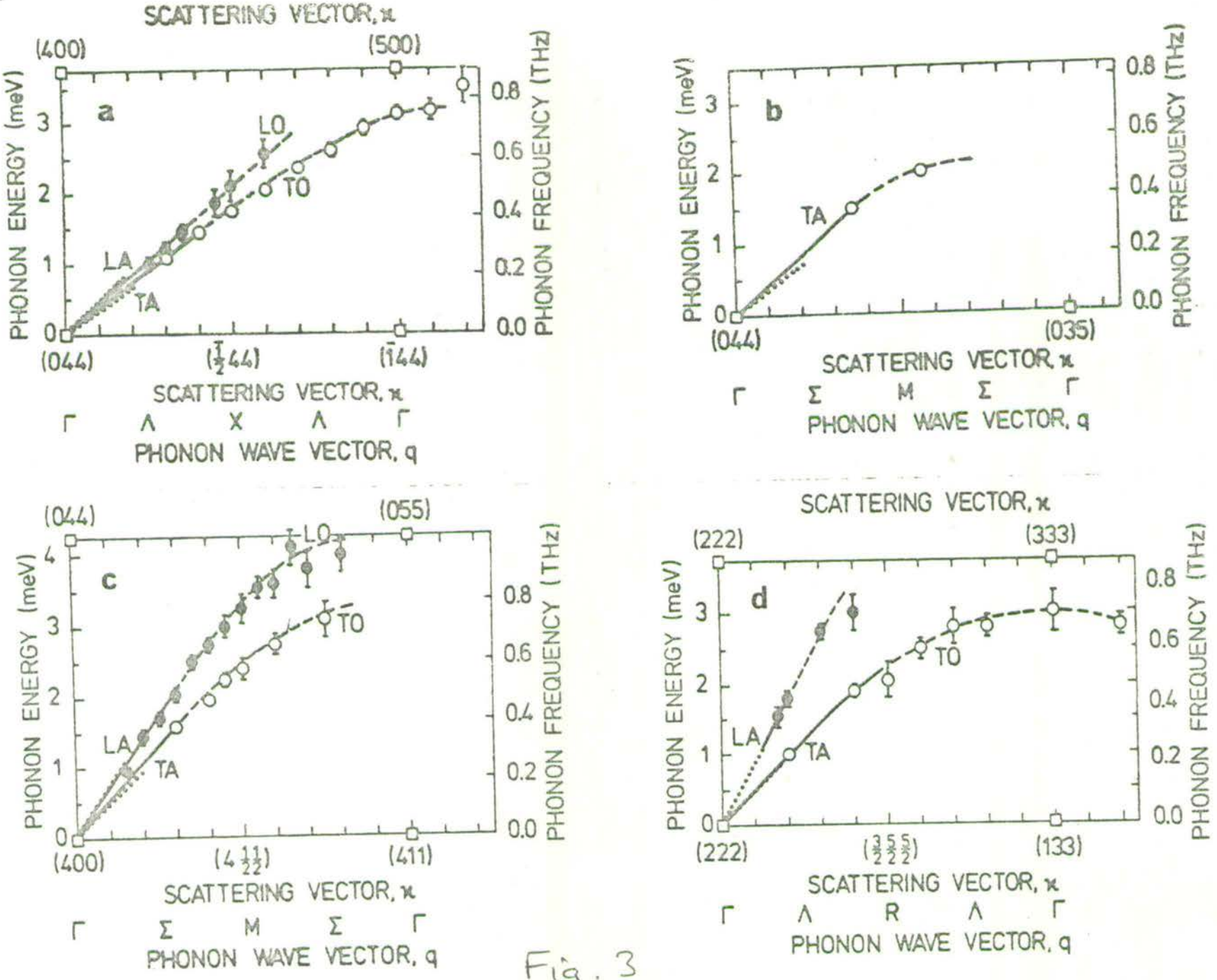
SCATTERING VECTOR, x
(400)
(500)
a
LO
TO
LA
TA
PHONON ENERGY (meV)
PHONON FREQUENCY (THz)
(044)
(½44)
(144)
SCATTERING VECTOR, x
Γ Λ X Λ Γ
PHONON WAVE VECTOR, q
b
TA
(044)
(035)
SCATTERING VECTOR, x
Γ Σ M Σ Γ
PHONON WAVE VECTOR, q
(044)
(055)
c
LO
TO
LA
TA
(400)
(4 11/22)
(411)
SCATTERING VECTOR, x
Γ Σ M Σ Γ
PHONON WAVE VECTOR, q
SCATTERING VECTOR, x
(222)
(333)
d
LA
TA
TO
(222)
(3/2 5/2 5/2)
(133)
SCATTERING VECTOR, x
Γ Λ R Λ Γ
PHONON WAVE VECTOR, q

Fig. 3

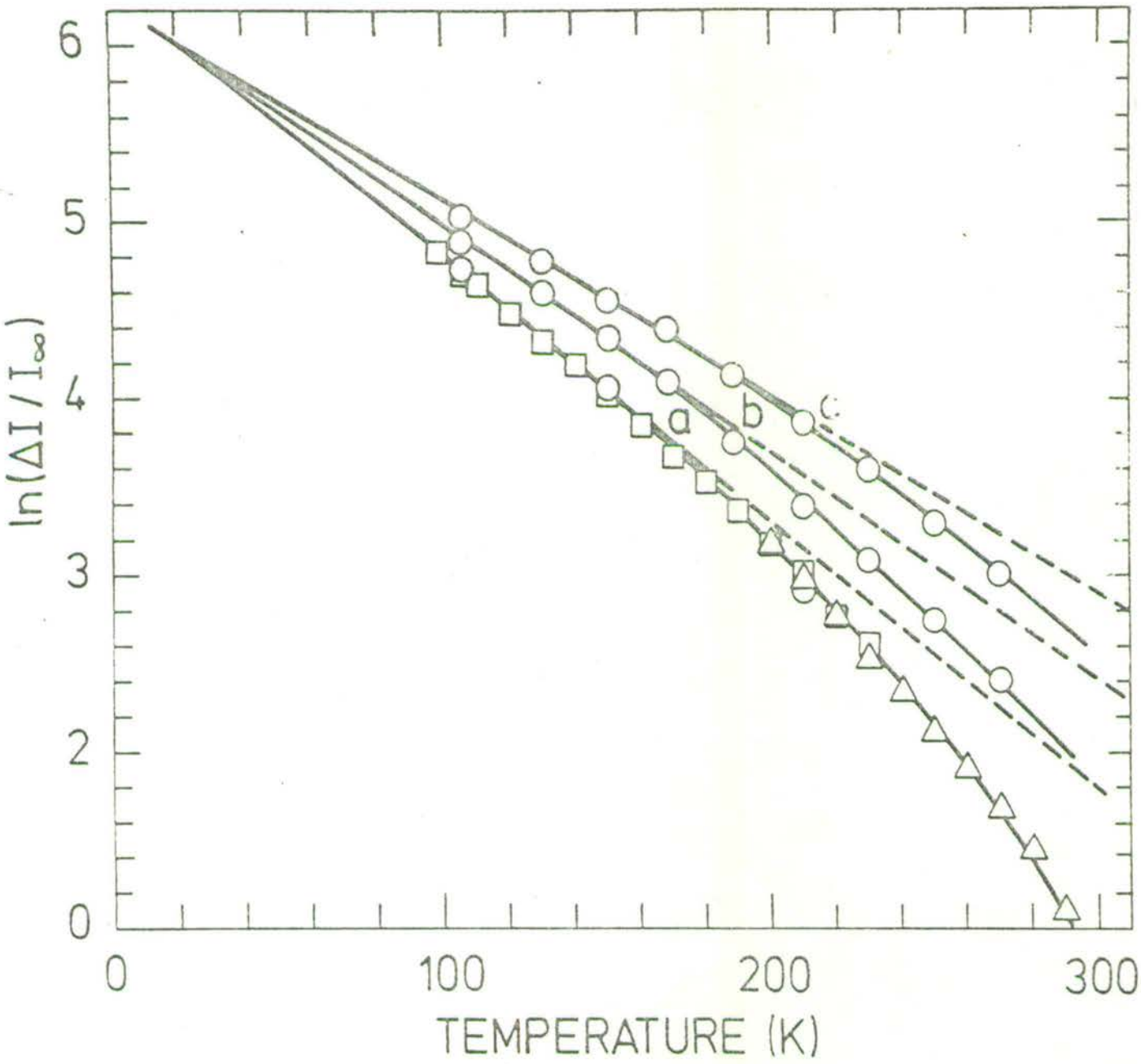

Fig. 4

RAMAN STUDY OF THE FERROELECTRIC PHASE TRANSITION IN COPPER-CHLORINE BORACITE

D.J. Lockwood and R.W.G. Syme†

Physics Department, Edinburgh University,

Edinburgh EH9 3JZ, Scotland.

Abstract

The dynamics of the improper ferroelectric transition in $Cu_3B_7O_{13}Cl$ have been investigated using Raman spectroscopy. Details are presented of the cubic phase spectrum and of two soft modes found in the orthorhombic ferroelectric phase. Comparisons are made with results from earlier Raman measurements on $Cr_3B_7O_{13}Cl$.

† Permanent address : Physics Department,
University of Canterbury,
Christchurch, New Zealand.

Most boracites, $M_3B_7O_{13}X$ where M is a divalent metal and X a halogen or chalcogen, exhibit a first-order cell-doubling transition from a high temperature paraelectric cubic phase (T_d^5) to a ferroelectric phase with orthorhombic symmetry (C_{2v}^5).[1] In copper chlorine boracite (Cu-Cℓ), this improper transition is one of the most nearly continuous of all the boracites and therefore of the most interest with regard to the critical properties of improper ferroelectrics. In order to investigate the dynamics of the ferroelectric transition we have measured the Raman spectrum of Cu-Cℓ at various temperatures above and below T_c = 365 K.

The light-blue coloured Cu-Cℓ crystal used in this study was grown by the vapour transport method.[2] The ends of the needle-shaped crystal were cut off to yield a 1 × 1.3 × 3 mm^3 cuboid with $\{100\}_{cubic}$ faces, which were polished with 1μ diamond powder. Raman spectra were excited with up to 400 mW of argon laser light at 488.0 nm, and the 90° scattered light was analysed using a Coderg triple monochromator at 2.6 cm^{-1} resolution. A computer controlled data collection system enabled direct computer processing of the results.

The Raman active modes in the cubic phase transform as $4A_1 + 10E + 19F_2$ and in the orthorhombic phase as $71A_1 + 72A_2 + 71B_1 + 71B_2$. Representative spectra of the cubic phase recorded at 550 K are shown in Figure 1, and after separating the A_1 and E spectra[3] peaks can be assigned to A_1 [~133, ~199, 385, 665, 909 and 1065 cm^{-1}, where the last two peaks are probably second order], E [82.5, 239, 386, 408, 466, 746, 913, 991, 1066 and 1155 cm^{-1}] and F_2[~40, ~145, 198, 222, 264-283, 385, 452-457, ~580, ~615, ~645, ~675, 809, ~890, 961, 1054-1100 and 1167-1240 cm^{-1}, where TO-LO pairs are hyphenated] symmetry. Above T_c, the Raman

results are typical of a cubic boracite with a wing feature in the A_1 spectrum and an odd-shaped low frequency (0 - 100 cm^{-1}) feature in the F_2 spectrum.[3,4] The A_1, E and F_2 modes exhibit no unusual temperature dependence, and the spectral features are similar to those found in Cr-Cℓ.[3-5] Modes are observed at 385(A_1), 239(E), 1167(F_2) and 264(F_2) cm^{-1} that are characteristic of a B-O framework containing BO_4 tetrahedra.[6]

At T_c, there is a marked change in the spectrum : numerous new bands appear in all polarizations, and about 1/3 of the 285 allowed modes were found. The onset of new spectral features is not as abrupt as for Cr-Cℓ[5] consistent with a weaker first-order transition. Spectral features sharpen and grow in intensity when the temperature is further lowered, but most band frequencies remain nearly constant. Two soft modes of A_2 and A_1 symmetry are evident for $T<T_c$: the bands are at 67 and 136 cm^{-1} respectively for temperatures around T_c - 50 K, and soften to ~ 60 and ~ 130 cm^{-1} respectively at the transition (see Figure 2). This closely parallels the soft mode behaviour in Cr-Cℓ[5] except that for Cu-Cℓ the modes have lower frequencies at T_c (indicative of a more nearly continuous transition) and are more heavily damped. The heavier damping at T_c in Cu-Cℓ, indicative of higher anharmonicity, correlates with the appreciably higher anharmonic thermal motion of the Cℓ atom in cubic Cu-Cℓ compared with Cr-Cℓ[7] and with the more pronounced X-ray diffuse scattering in Cu-Cℓ compared with Cr-Cℓ.[8]

We thank H. Schmid and H. Tippmann for consultations and technical advice and acknowledge the support of the Science Research Council, the Battelle Research Centre, Geneva, and the U.S. Army Research and Development Group (Europe).

REFERENCES

1. See review by R.J. Nelmes, J. Phys. C 7, 3840 (1974).

2. H. Schmid, J. Phys. Chem. Solids 26, 973 (1965).

3. D.J. Lockwood, J. Raman Spectrosc. 2, 555 (1974).

4. D.J. Lockwood, Ferroelectrics 13, 353 (1976).

5. D.J. Lockwood, Solid State Comm. 18, 115 (1976).

6. A.F. Murray and D.J. Lockwood, J. Phys. C 9, 3691 (1976).

7. F.R. Thornley, R.J. Nelmes and N.S.J. Kennedy, Ferroelectrics 13, 357 (1976).

8. P. Felix, M. Lambert, R. Comes and H. Schmid, Ferroelectrics 7, 131 (1974).

FIGURE CAPTIONS

Figure 1. The (a) A_1 + E and (b) F_2^{TO} Raman spectra of cubic Cu-Cℓ recorded at 550 K.

Figure 2. The low-frequency diagonal-polarization Raman spectrum of orthorhombic Cu-Cℓ at temperatures close to, and well below T_c.

Please note

Figure 1 has been designed for reproduction at full-page width and Figure 2 for single column width.

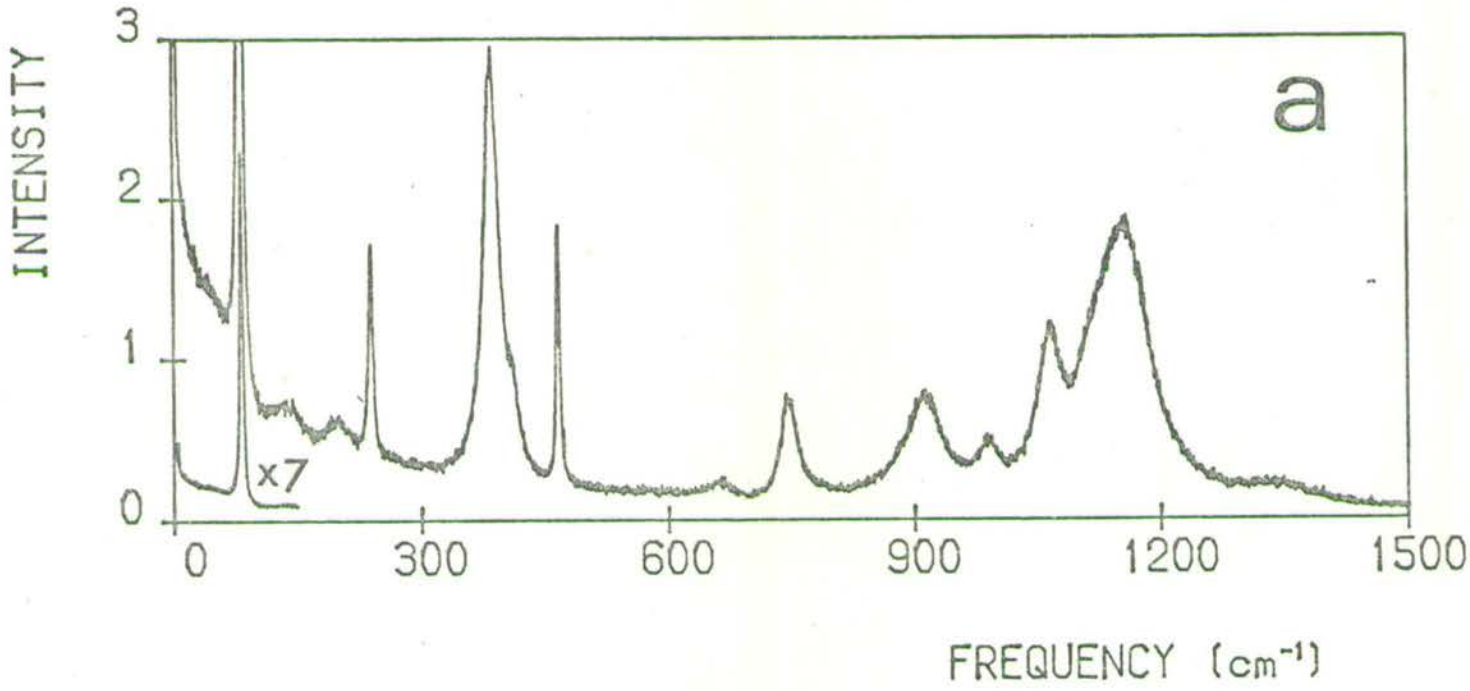

FIGURE 1(a). LOCKWOOD & SYME

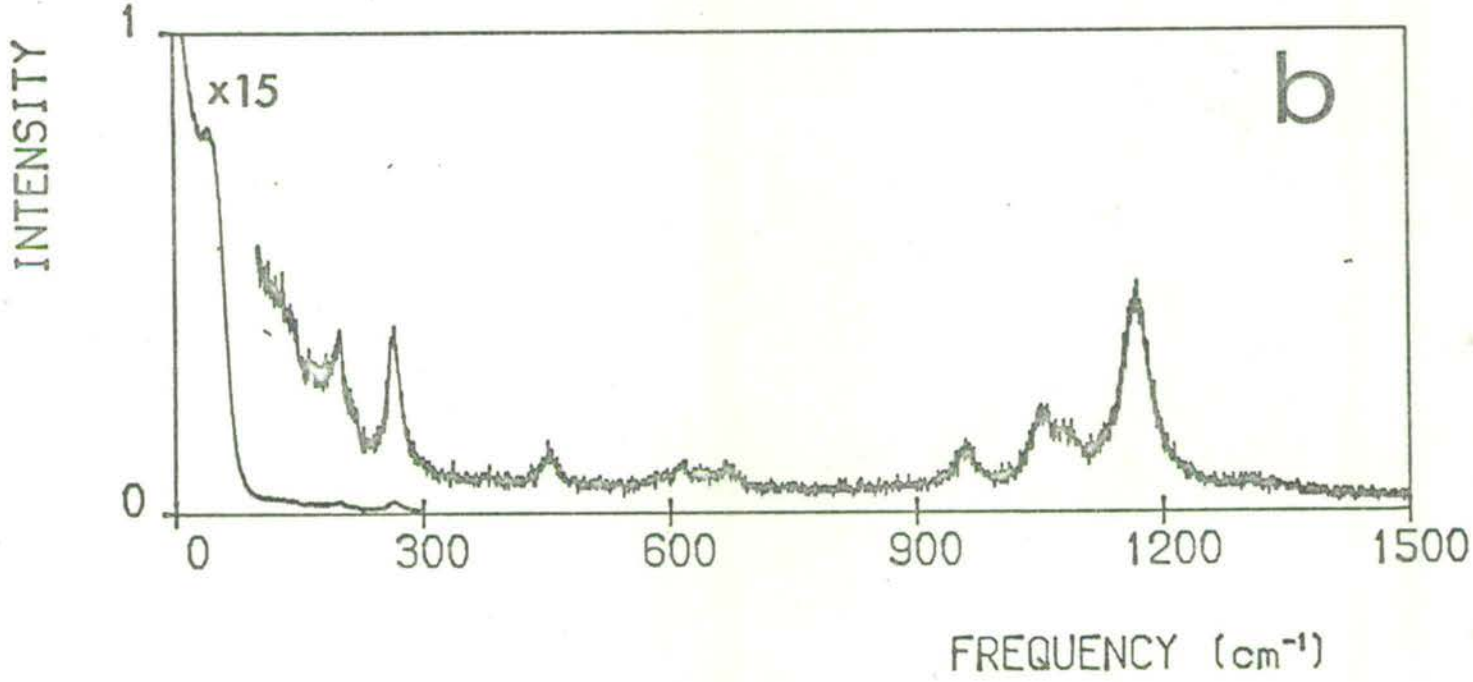

FIGURE 1(b). LOCKWOOD + SYME

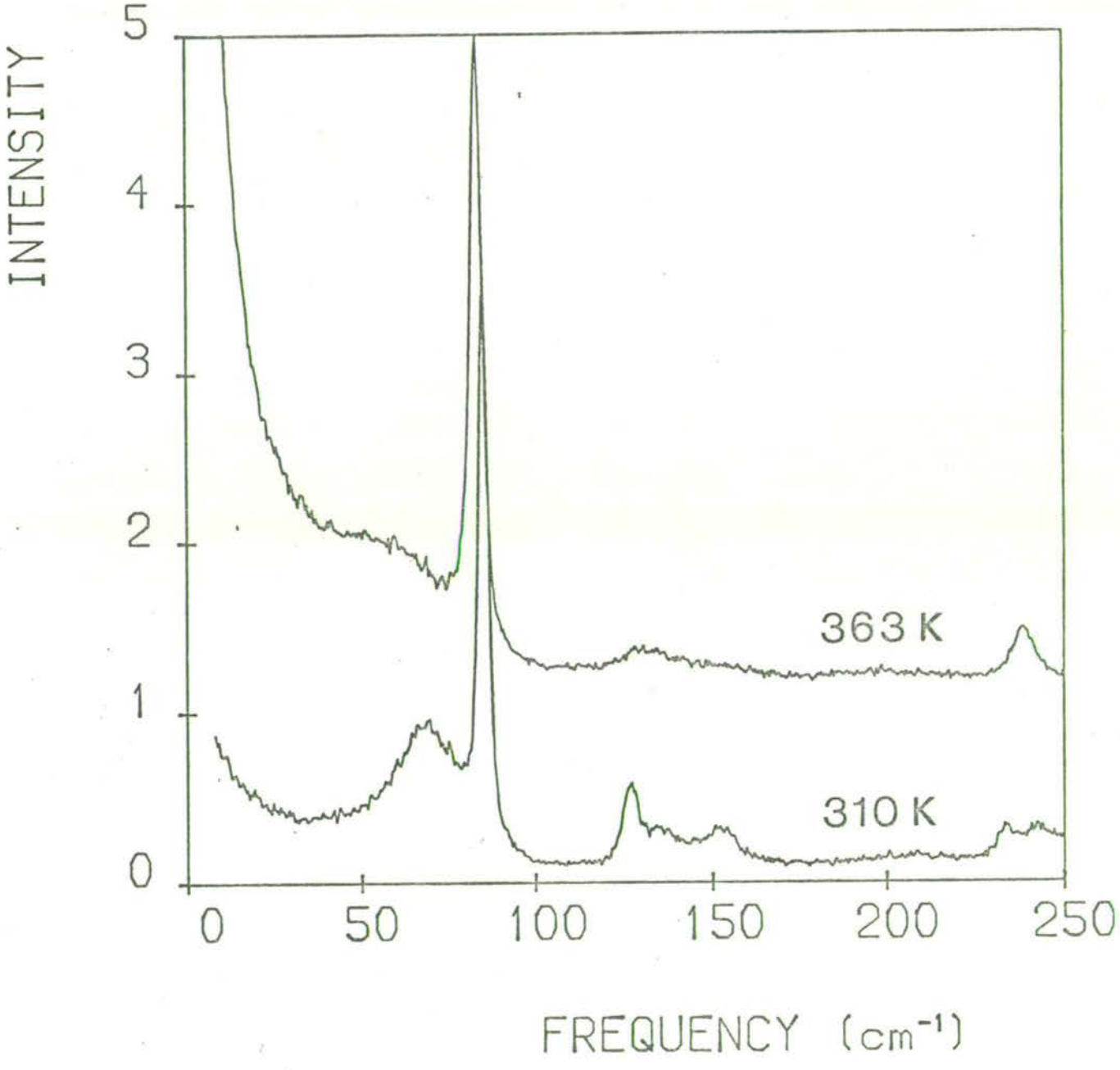

FIG. 2. LOCKWOOD & SYME

LATTICE DYNAMICS OF NICKEL-IODINE BORACITE

D.J. LOCKWOOD and A.F. MURRAY

Physics Department, Edinburgh University,

Edinburgh EH9 3JZ, Scotland

Abstract

The dynamics of the ferroelectric phase transition at T_c = 68 K in $Ni_3B_7O_{13}I$ have been investigated using inelastic light scattering. Apart from an anomaly at 128 K, most spectral features exhibit no abrupt change with decreasing temperature, and unexpectedly few new bands appear for $T < T_c$. The observed softening of a low frequency E mode in advance of, and subsequent to the ferroelectric transition is also at variance with normal boracite behaviour and suggests the presence of a further phase transition. The Raman spectra indicate cubic symmetry for $T > T_c$, and any deviation from this symmetry below T_c must be small.

As temperature is varied from 295 K to 68 K, the high frequency modes rise in frequency with an anomaly at 128 K (see Figure 2a), associated with irregularities in the magnetic, dielectric and structural properties.[6] Below the transition the spectrum does not alter radically, although the observed bands sharpen rapidly just above 68 K, the only 'new' features being two weak bands around 1100 cm^{-1} (see Figure 1). The temperature dependence of the fitted frequency of the 863 cm^{-1} band (Figure 2a) exhibits a marked kink at roughly 68 K. The broad, low frequency E symmetry mode softens from 170 cm^{-1} as temperature decreases (Figure 2b), with an anomalous rise in natural frequency ω_o at 128 K, followed by a sharper drop to 134 cm^{-1} at 68 K. This mode subsequently continues to soften! The damping constant Γ decreases smoothly, if not linearly, with decreasing temperature (Figure 2b). There is no linewidth anomaly at 128 K for this phonon.

From these results it is apparent that there is very little change in the composition of the spectrum at T_c, and only minor alterations to the phonon frequencies and lifetimes, suggesting a near second order transition. This may be contrasted with the strongly first order nature of the corresponding transition in Cr-Cl.[7] Similarly, the non-appearance of many new bands may be set against the plethora of features appearing below T_c in the orthorhombic phases of Cr-Cl [5,7] and Mn-Cl.[5] The marked softening of the low frequency E mode is completely different to the lack of temperature variation of the corresponding features in the cubic Cr-Cl and Cu-Cl boracite spectra. The low frequency modes are mostly associated with vibrations involving motion of the nickel and iodine ions, so the softening would indicate some repositioning of these ions, and would seem to foreshadow some further/

further transition at a lower temperature. Any such repositioning must, however, retain cubic symmetry for $T > T_c$. We do not yet have enough data to determine the symmetry of the ferroelectric phase, but the existing results suggest that any deviation from cubic symmetry is slight. Further work is in progress to elucidate the behaviour close to the transition.

We thank H. Schmid for helpful discussions and acknowledge the financial support of the S.R.C. (AFM) and the U.S. Army Research and Development Group (Europe) (DJL).

References

1. H. Schmid, Growth of Crystals 7, 25 (1969).

2. F.R. Thornley, N.S.J. Kennedy and R.J. Nelmes, J. Phys. C 9, 681 (1976).

3. A.F. Murray and D.J. Lockwood, J. Phys. C 9, 3691 (1976).

4. R.J. Nelmes and F.R. Thornley, J. Phys. C 9, 665 (1976).

5. D.J. Lockwood, Ferroelectrics 13, 353 (1976).

6. A.F. Murray and D.J. Lockwood, paper 4B.04, International Conference on Lattice Dynamics, Paris, France (1977).

7. D.J. Lockwood, Solid State Commun. 18, 115 (1976).

Figure Captions

Figure 1. The $Z(X'X')Y'$ spectrum of Ni-I.

Figure 2. (a) Temperature variation of the natural frequency of an E mode.

(b) Temperature variation of the natural frequency ω_o (squares) and damping constant Γ (triangles) of the low frequency E mode.

Please Note

Figure 1 is designed to be reproduced at full-page width.

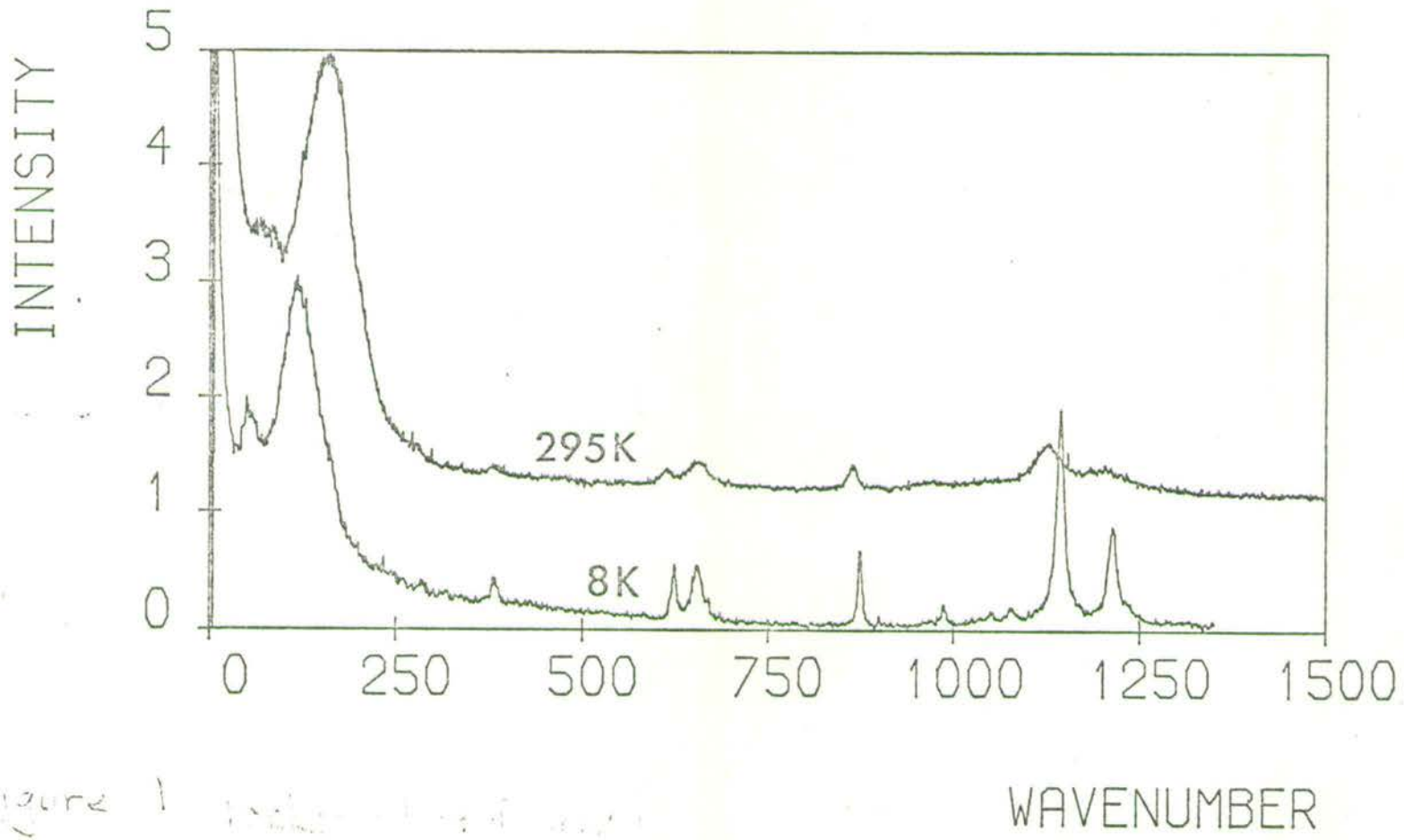

Figure 1

Fig. 1

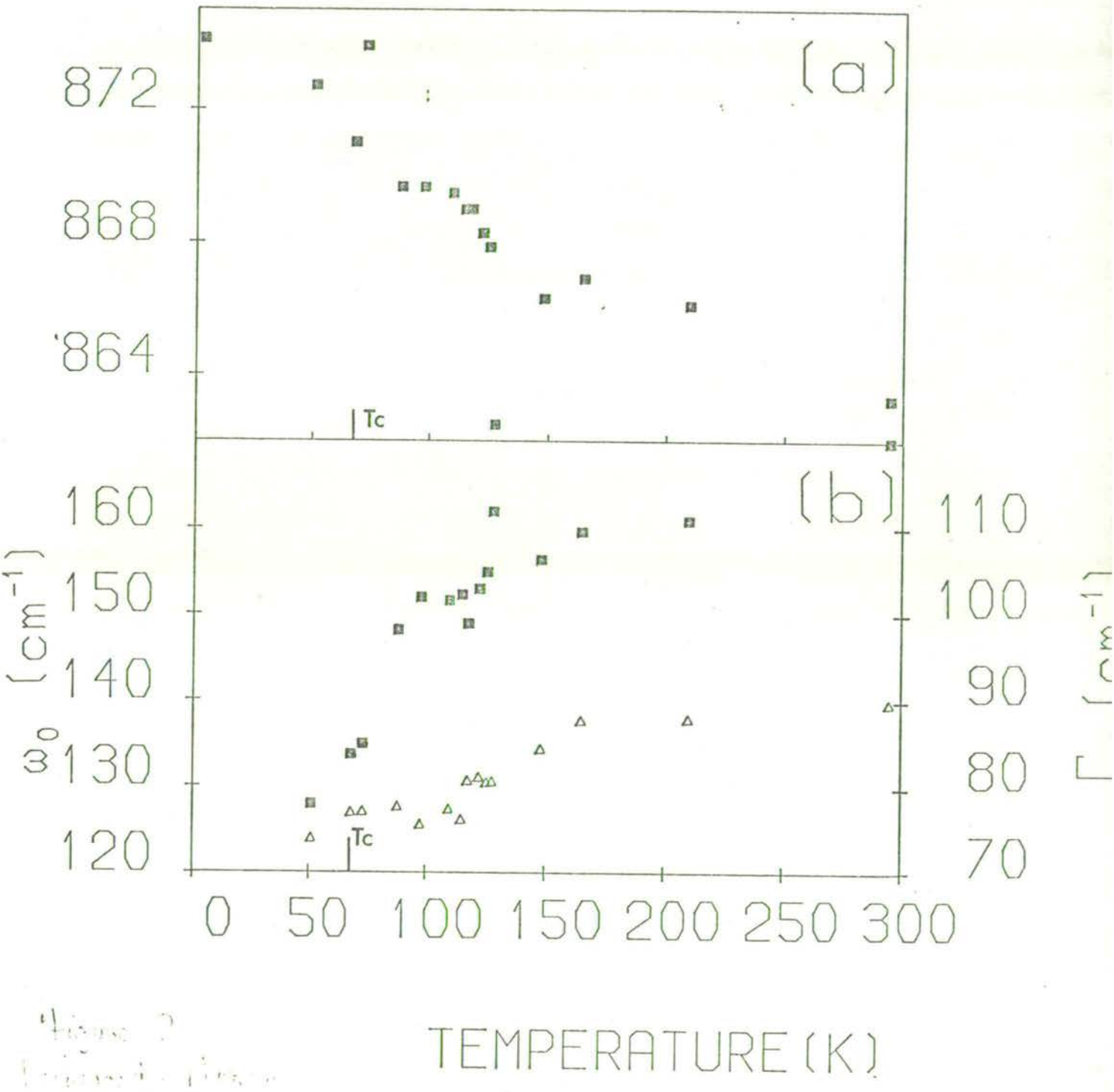
(a)
872
868
864
Tc
(b)
160
150
140
130
120
110
100
90
80
70
Tc
ω_o (cm^{-1})
Γ (cm^{-1})
0 50 100 150 200 250 300
TEMPERATURE (K)

Fig. 2

THE RAMAN SPECTRUM OF PURE AND BARIUM DOPED LEAD GERMANATE

T.J. HOSEA, W. TAYLOR and D.J. LOCKWOOD
Physics Department, University of Edinburgh, Edinburgh EH9 3JZ, Scotland.

ABSTRACT

Observations of the Raman spectra of $Pb_{5-X}Ba_XGe_3O_{11}$ show that for $0 < X \lesssim 0.4$ while there are small changes in relative intensities and increased broadening of all the modes, the frequencies and number of both the lattice and internal modes do not appear to be substantially altered in comparison to those of the pure material. The temperature dependence of the ferroelectric soft A-mode however is dramatically affected, even for small X and this is accompanied by a much reduced transition temperature.

INTRODUCTION

The Raman spectra of pure lead germanate $Pb_5Ge_3O_{11}$ have been studied in some detail[1] with much attention focussed on the behaviour of the A-symmetry ferroelectric soft mode[1,2]. More recently our studies of the very low frequency region of a poled single domain crystal have revealed the presence of a critical central peak[3] but we have found no evidence of the dynamic component reported by Fleury[4].

In this paper we describe the effects on the Raman spectra of replacing a small fraction of the lead atoms by barium.

RESULTS

Two samples of $Pb_{5-X}Ba_XGe_3O_{11}$ were studied and the results compared to those of the pure material. The Curie temperatures were determined from capacitance measurements as 450.5 ± 0.5 K, 358.5 ± 1 K and 319 ± 2 K, and from the results of Watton et al.[6] which relate X to T_c, this gave values for X = 0, 0.28, 0.33 respectively. Since the dielectric anomaly observed at the phase transition becomes progressively broader and weaker for increased doping, the associated uncertainties in our measurements of T_c also increase. This suggests a more diffuse phase transition for the doped material.

Group theory predicts 27 A-symmetry lattice modes and 30 A-symmetry internal modes[1(d)]. For X = 0 at 110 K we observe at least 30 peaks in the x(zz)y orientation in the region 0 to 500 cm^{-1} in addition to 5 modes (probably associated with internal vibrations of the GeO_4 molecular group) between 650 and 850 cm^{-1}. The effect of doping is to broaden the modes so much that even at 110 K we observe only 22 modes between 0 and 500 cm^{-1} and 5 modes between 650 and 850 cm^{-1}.

It is evident from the representative spectra in figure 1 that the dominant effect of the doping on the spectra is that of an overall broadening of all the modes. The spectra for X = 0.33 exhibit only slightly greater broadening than the spectra for X = 0.28. A few peaks in this region were fitted with damped oscillator functions and the results indicate that in comparison to X = 0 there are small relative intensity changes of the peaks, and their natural frequencies change only by a few wavenumbers. These modes are not all broadened equally, but their damping constants range from 1.3 to 3.3 times those of the equivalent modes in the pure material. These effects all increase with increasing X.

The lattice spectra in other orientations and the higher frequency (650-850 cm^{-1}) internal modes are similarly affected by the Ba doping. Since we see no evidence of extra peaks or pronounced changes in the natural frequencies, it seems that the concentrations are too low to determine whether a one-mode or two-mode type of mixed crystal behaviour is operative.

The spectra in figure 2 show that the soft mode peak frequencies decrease and become overdamped, narrowing critically as T_c is approached for both X = 0 and X = 0.28.

In the pure material at 110 K we observe four modes 'A', 'B', 'C' and 'D' at about 30, 37, 43 and 46 cm^{-1} respectively. At 110 K, C is the 'soft-mode' but as the temperature increases there is an interaction with mode B which takes over as the soft mode. It becomes critically damped at $\sim$ 390 K, about 60 K below T_c, but heavy damping above 315 K masks any possible interaction with mode A. Above 390 K, fitting has shown[2] that the inverse width and height of the overdamped wing maximize at T_c. This wing persists weakly above the transition.

For X = 0.28 at 110 K, the soft mode is not easily identified because of overall broadening of the spectrum but above 190 K the soft mode feature is clearly visible. Critical damping occurs at about 298 K = T_c - 60 K for this material. The relative intensity of the low frequency response near T_c, however, is much weaker for the doped material and the overdamped wing falls away less rapidly above T_c. The sample with X = 0.33 shows a similar behaviour but becomes overdamped at 260 K $\simeq$ T_c - 60 K and has an even weaker low frequency response near T_c. This behaviour is in keeping with our observations of the diffuse nature of the dielectric 'anomaly' around T_c for the doped material.

An analysis of the respective soft modes near their critical damping temperatures indicates that at any one temperature the damping parameter, in comparison to the pure material, is 50% larger for X = 0.28 and 90% for X = 0.33. The addition of these small concentrations of barium (5.6% and 6.6%) has also caused a pronounced lowering of the transition temperatures (by 92 K and 131 K respectively), apparently saturating at 8% doping with $T_c \simeq 250$ K[6]. Equivalent doping concentrations in crystals in which the germanium is partially replaced by silicon,[5,7] produce a proportionately smaller decrease in T_c.

Our results suggest that the Pb atoms are thus much more directly involved in the soft mode motion than the Ge atoms.

ACKNOWLEGEMENTS

We are grateful to H. Vass for technical assistance, the Science Research Council and the U.S. Army Research Office for financial support and Dr. G.R. Jones, R.R.E. Malvern who supplied the samples.

REFERENCES

1. (a) K. Hisano and J.F. Ryan, Solid State Comm. 11, 119, (1972).
(b) J.F. Ryan and K. Hisano, J. Phys. C6, 566, (1973).
(c) G. Burns and B.A. Scott, Phys. Lett. A39, 177, (1972).
(d) W. Taylor, D.J. Lockwood, J.W. Arthur and T.J. Hosea, Ferroelectrics 12, 113, (1976).
(e) W. Müller-Lierheim, T. Suski and H.H. Otto, Phys. Stat. Sol.(b) 80, 31 (1977).
2. T.J. Hosea, D.J. Lockwood, W. Taylor and J.W. Arthur, Proc. 5th Raman Conf. p.610 (Freiburg 1976).
3. D.J. Lockwood, J.W. Arthur, W. Taylor and T.J. Hosea, Solid State Comm., 20, 703, (1976).
4. P.A. Fleury and K.B. Lyons, Phys. Rev. Lett. 37, 1088, (1976).
5. H. Iwasaki, S. Miyazawa, H. Koizumi, K. Sugii and N. Niizeki, H. Appl. Phys., 43, 4907, (1972).
6. R. Watton, C. Smith and G.R. Jones, Ferroelectrics 14, 719, (1976).
7. W. Gebhardt and W. Müller-Lierheim, Proc. Int. Conf. on Lattice Dynamics (Paris 1977).

Figure 1: Part of the x(zz)y Raman spectra at 111 K for $Pb_{5-X}Ba_XGe_3O_{11}$ with X = 0 and 0.28.

Figure 2: Temperature dependence of the low frequency x(zz)y Raman spectra of $Pb_{5-X}Ba_XGe_3O_{11}$ showing behaviour of the soft mode for both X = 0 and X = 0.28.

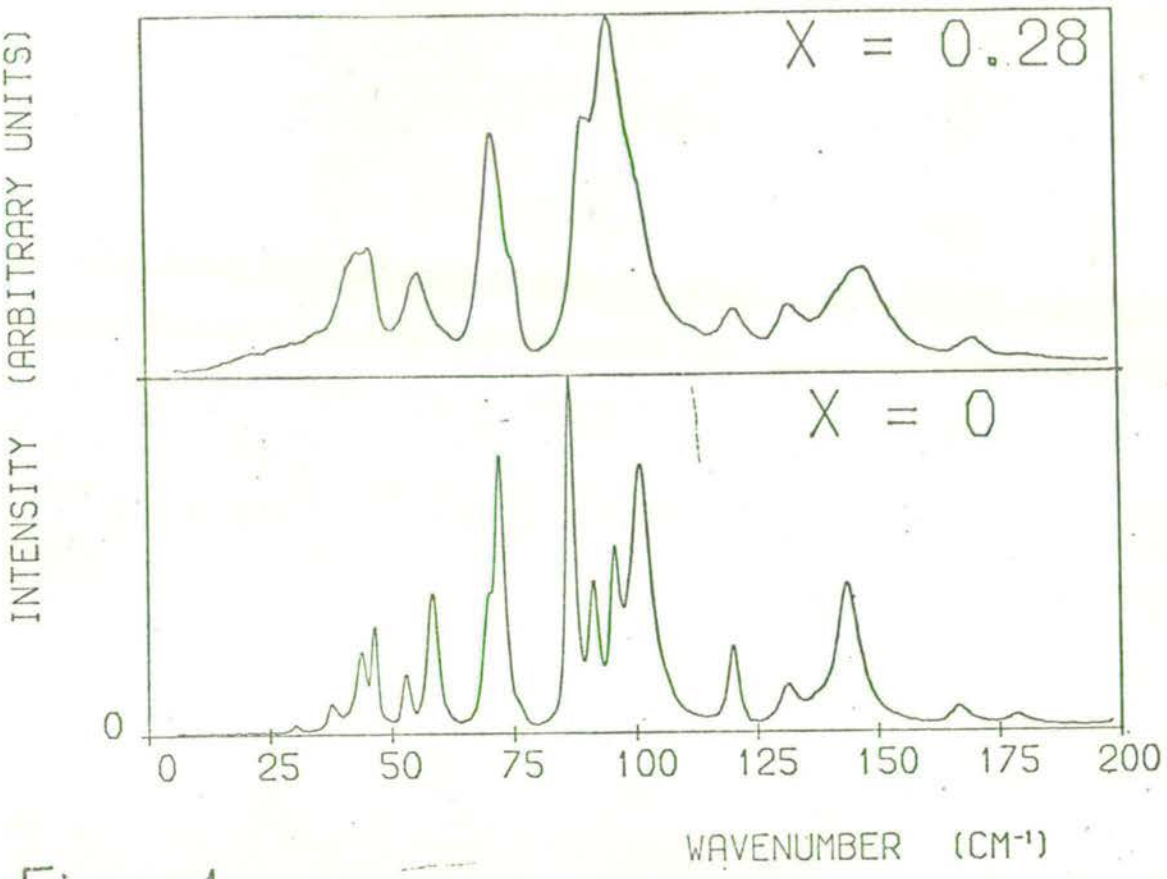
X = 0.28
X = 0
INTENSITY (ARBITRARY UNITS)
0
0 25 50 75 100 125 150 175 200
WAVENUMBER (CM⁻¹)

Figure 1

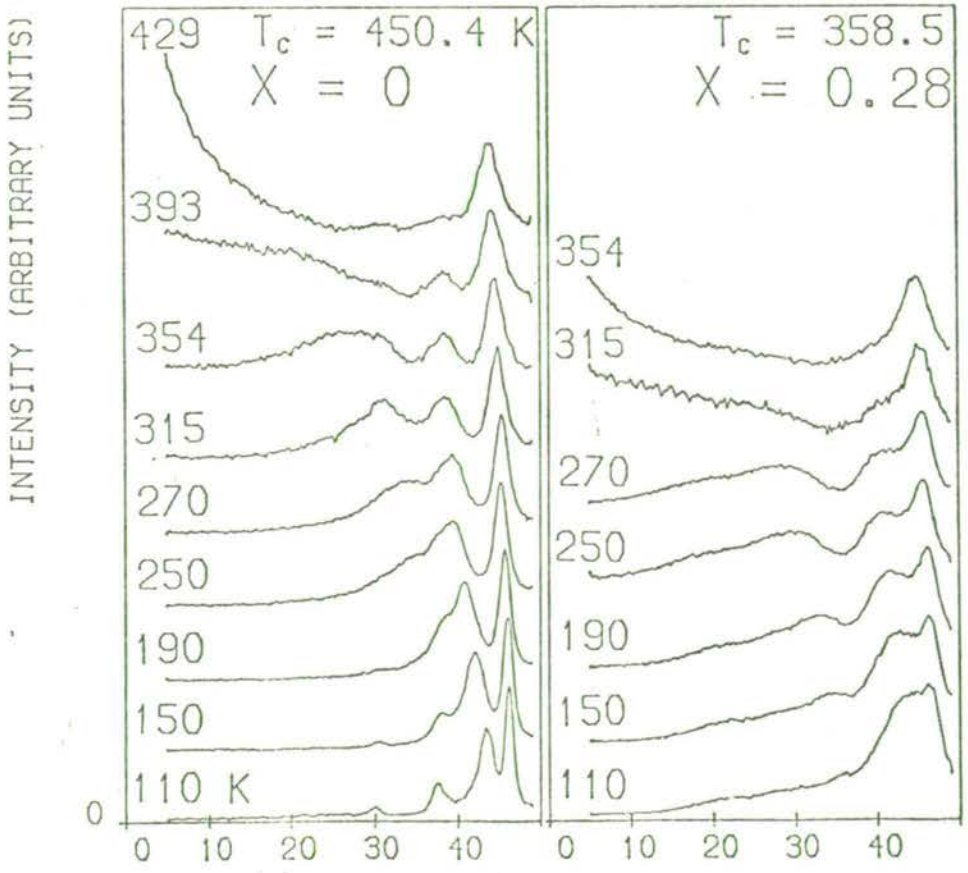
INTENSITY (ARBITRARY UNITS)
429 T_c = 450.4 K
X = 0
393
354
315
270
250
190
150
110 K
0
0 10 20 30 40
T_c = 358.5
X = 0.28
354
315
270
250
190
150
110
0 10 20 30 40

Raman Spectrum of the Orthorhombic Phase of the Improper Ferroelectric Manganese-Chlorine Boracite

D.J. Lockwood

Physics Department, Edinburgh University,
Edinburgh EH9 3JZ, Scotland.

Abstract

Boracites are of interest because they exhibit unusual ferroelectric, magnetic, dynamical and structural properties. Most boracites exhibit a transition from a high temperature paraelectric cubic phase to an orthorhombic ferroelectric phase, and in $Mn_3B_7O_{13}Cl$ this improper ferroelectric transition occurs at T_c = 680 K. The Raman spectrum of a small single-domain sample of $Mn_3B_7O_{13}Cl$ has been measured at room temperature in order to characterise the lattice dynamics of the orthorhombic phase of boracites. Polarisation studies, which yielded results for all but the α_{zz} component of the Raman tensor, enabled an assignment of mode symmetries. The Raman spectrum of orthorhombic $Mn_3B_7O_{13}Cl$ is complicated, and about 180 of the 288 modes at $\underline{k}$ = 0 have been observed. Modes at high frequency are assigned to vibrations of the B-O framework whilst low frequency modes (<200 cm^{-1}) arise predominantly from vibrations involving metal and halogen atoms.

Short Title

Raman Spectrum of Orthorhombic $Mn_3B_7O_{13}Cl$

1. Introduction

Boracites, $M_3B_7O_{13}X$ (M-X) where M is a divalent metal and X a halogen or chalcogen, are of interest because they exhibit unusual ferroelectric, magnetic, dynamical and structural properties.[1] In general, boracites will undergo at some temperature a transition from a high temperature paraelectric phase of cubic symmetry to a ferroelectric orthorhombic phase. This transition is classed as <u>improper</u>[2] because the spontaneous polarisation is not the primary order parameter. For boracites, the spontaneous polarisation is a secondary order parameter arising from coupling between between optic modes in the ferroelectric phase. This behaviour may be contrasted with that of another class of improper ferroelectrics typified by terbium molybdate, where the spontaneous polarisation arises indirectly through coupling between acoustic and optic modes.[3]

Improper ferroelectrics have attracted wide attention because of their unusual nature and many physical properties of boracites have been studied.[1] Until recently, however, very little was known about the lattice dynamics of these compounds. Raman studies of the cubic phase and cubic-to-orthorhombic transition in Cr-Cℓ[4-6] , Cu-Cℓ[7] and Ni-I[8] have been reported. Soft modes have been observed in Raman scattering from ferroelectric Cr-Cℓ[5] and Cu-Cℓ[7] confirming the proposed microscopic mechanism for the transition[9] whereby the primary order parameter is associated with a doubly-degenerate zone boundary (X point) mode of vibration in the cubic phase. The softening of this mode results in a first order transition to the orthorhombic phase where the degenerate critical modes split and become homogenous modes observable in Raman scattering. In both of these experiments the samples were multidomain in the orthorhombic phase making a complete spectral data analysis difficult. As part of an ongoing project to investigate the dynamics of the improper ferroelectric transition in boracites, and to assist the assignment of modes observed in the orthorhombic spectrum of Cr-Cℓ and Cu-Cℓ, we present here the results of a Raman

study of a single domain sample of orthorhombic Mn-Cℓ. In Mn-Cℓ, the improper ferroelectric transition occurs at T_c = 680 K.

2. Group Theory

The paraelectric phase of boracites has space group symmetry $F\bar{4}3c$ (T_d^5), with two formula units in the primitive cell.[1] A factor group analysis of the 144 normal modes at $\underline{k}$ = 0 gives the following symmetry reduction

$$\Gamma_{144} = 4A_1 + 6A_2 + 10E + 18F_1 + 20F_2 \ , \tag{1}$$

where the symmetry labels are taken from the T_d character table of Ref. 10. In the improper ferroelectric phase the crystal space group is $Pca2_1$ (C_{2v}^5), with four formula units in the primitive cell.[1] The 288 zone centre normal modes now transform as

$$\Gamma_{288} = 72A_1 + 72A_2 + 72B_1 + 72B_2 \tag{2}$$

according to the irreducible representations of point group C_{2v}.[10] The correlation table for the zone centre modes is given in Table 1 and this indicates that the 144 cubic-phase modes become

$$\Gamma_{144} = 34A_1 + 34A_2 + 38B_1 + 38B_2 \tag{3}$$

in the orthorhombic phase. The remaining 144 modes arise from the Brillouin zone X point of the cubic phase which has become a reciprocal lattice point in the ferroelectric phase. All the zone centre modes are Raman active with Raman tensors

$$A_1 \begin{pmatrix} a & & \\ & b & \\ & & c \end{pmatrix} \qquad A_2 \begin{pmatrix} \cdot & d & \\ d & \cdot & \\ & & \cdot \end{pmatrix} \qquad B_1 \begin{pmatrix} \cdot & & e \\ & \cdot & \\ e & & \cdot \end{pmatrix} \qquad B_2 \begin{pmatrix} \cdot & & \\ & \cdot & f \\ & f & \cdot \end{pmatrix}$$

and $A_1(z)$, $B_1(x)$ and $B_2(y)$ are also infrared active. Excluding acoustic

modes, the Raman spectrum of orthorhombic Mn-Cℓ is therefore expected to comprise $71A_1 + 72A_2 + 71B_1 + 71B_2$ modes.

3. Experiment

The Mn-Cℓ crystal used in this experiment was grown by the vapour transport method[11] at the Battelle Research Centre, Geneva. The plate-like crystal contained a single-domain section occurring naturally as a result of growth conditions, and this section was exposed by grinding to yield a cuboid sample of area ~ 0,8 × 0,3 mm^2 and 135 μm thick. Final surface preparation was a polishing with 1 μm diamond powder on the rear surface of photographic paper backed by flat glass. The sample had previously been examined by X-ray diffraction using the Laue back reflection technique and this provided enough information to determine the pseudo-cubic (pc) directions. The crystal was ground in such a way that the plate end faces were perpendicular to $\langle 110 \rangle_{pc}$ with the plate faces perpendicular to $[001]_{pc}$.

Unfortunately, the X-ray diffraction results were not good enough to enable a unique determination of the orthorhombic axes, and optical studies in polarised light were used to obtain this information. Birefringence measurements proved that the sample was single domain with the spontaneous polarisation perpendicular to the plane of the plate i.e. along $[001]_{pc}$. At 297 K, the birefringence in the plane of the plate was $\Delta n = n_\gamma - n_\alpha = 0.016$ in both yellow (589 nm) and green (546 nm) light. The two optic axes of this biaxial crystal are in the plane of the plate (i.e. perpendicular to $[001]_{pc}$) and are close to $\langle 100 \rangle_{pc}$ directions. By comparison with other boracites, and in particular Ni-Cℓ, where the relationship between extinction directions and orthorhombic axes is known,[12] the orthorhombic a and b axes were associated with extinction directions γ and α, respectively. The orthorhombic c axis, the ferroelectric axis, is parallel to the spontaneous polarisation and therefore must lie along

$[001]_{pc}$. Thus the sample had faces perpendicular to the orthorhombic a, b and c axes.

The Raman spectrum was recorded in the range 0-2000 cm^{-1} at 300 K using the conventional 90^{o} scattering geometry. The spectrum was excited with 600 mW of argon laser (Coherent Radiation 52B) light at 488.0 nm and analysed with a Spex Ramalab double monochromator. The experiment was repeated with 800 mW of argon laser radiation at 514.5 nm in order to distinguish laser plasma lines from Raman lines. A spectral slit width of 2.2 cm^{-1} was used for all measurements. The polarisation of the scattered light was analysed with Polaroid film and a polarisation scrambler was placed between the analyser and the spectrometer. The detector was a Centronic P4249B photomultiplier. A "hard-wired" logic system[13] was used to control the experiment and to produce the spectrum in digital form suitable for subsequent computer analysis.

The directions X, Y, Z that are used to denote the various polarisations of the scattered light refer to the crystal a, b, c axes, respectively. If subsequent X-ray diffraction studies coupled with birefringence measurements prove that the above inference of crystal axes is incorrect, then X and Y are interchanged, and the B_1 and B_2 symmetry assignments given in the next section will have to be interchanged. The α_{xx} and α_{yy} polarisability tensor components of A_1 symmetry will also be interchanged.

4. Results and Discussion

Spectra recorded at room temperature in various polarisations are given in Figures 1 and 2. Complete sets of four polarised spectra were obtained for two different orientations of the sample, and as each off-diagonal component gave similar results for both cases only the unique spectra are presented in the figures. Despite the biaxial nature of this

crystal, there is very little, if any depolarisation of the scattered light, as can be seen from Figures 1 and 2. This is partly because the laser light was directed along the crystal c(Z) axis, perpendicular to the optic axes. Unfortunately, it proved difficult to obtain spectra with (ZZ) polarisation because the sample was so thin. For this polarisation the incident and scattered light must pass along directions orthogonal to the c axis i.e. in the plane of the plate, where the crystal was only 0.1 mm thick.

The spectra show numerous peaks and subsidiary structure. A complete analysis of the mode frequencies is a difficult and time consuming task for such a complicated spectrum. Hence Table 2 lists frequencies of prominent peaks only as found from a computer analysis of the data using a peak finding routine.[14] In this way, about 180 modes have been found in five polarisations. For the A_1 modes, symmetry allows Raman tensor components $\alpha_{xx} = a$, $\alpha_{yy} = b$ and $\alpha_{zz} = c$ to assume unequal values and therefore some spectral features may have low, or zero intensity in one or more diagonal polarisations. In Table 2, there are few coincidences in frequency for peaks observed in (XX) and (YY) polarisations, and certainly there are no intensity correlations, as is consistent with the orthorhombic symmetry. Therefore, it seems likely that the (ZZ) spectrum will contain other A_1 modes unobserved in (XX) or (YY) polarisation, perhaps as many as 30. But even if this, and the number of peaks not found by the computer search, is allowed for, the number of modes observed in the Raman spectrum is considerably less than the 285 predicted by group theory.

A further complication that must be considered is the possibility of TO-LO splittings for the infrared active modes. However, only a few modes exhibit observable TO-LO splittings in the cubic phase of boracites[6,7,15]. Therefore, even though the A_1, B_1 and B_2 modes are dipolar, it is

anticipated that very few of the peaks observed in Raman spectra of these symmetries are to be assigned to TO-LO pairs. The scattering geometries used for the spectra displayed in Figures 1 and 2 dictate that for the B_1 and B_2 modes only TO phonons are observed. In the other off-diagonal B_1 and B_2 polarisations, viz. Z(XZ)X and Z(YZ)Y, respectively, the phonons observed have mixed transverse-longitudinal character. As noted earlier, these polarisations give results similar to the corresponding spectra shown in Figures 1 and 2, with the exception of bands in the 1100-cm^{-1} region. This confirms that TO-LO splittings are small for most, but not all the modes. Modes in the 1100-cm^{-1} region of cubic-phase boracites exhibit large (~ 60 cm^{-1}) TO-LO splittings[7,8], and similar splittings are indicated for orthorhombic Mn-Cℓ from the present results. The A_1 spectra of figures 1 and 2 comprise modes of mixed TO-LO character.

A full lattice dynamical calculation for orthorhombic Mn-Cℓ is extremely difficult because there is such a large number of normal modes. Nevertheless, some general observations are possible. A previous study of cubic compounds possessing a boron-oxygen framework[16] has shown that there are vibrational frequencies which are characteristic of BO_4 groups, and these are listed in Table 3. From the correlations of Table 1 it is apparent that the cubic-phase degeneracies are removed in the orthorhombic phase, and indeed this is what is found. Table 3 compares predicted and observed frequencies with good agreement. It is worth noting at this point that atom displacements from cubic-phase positions in orthorhombic boracites are extremely small.[1] The boracite boron-oxygen framework is complicated, containing BO_4, OBO_3 and OB_4 units[1], and therefore other modes at similar frequencies can be expected in all polarisations, as has been observed (see Figures 1 and 2 and Table 2). Thus most high frequency modes can be assigned to vibrations of the B-O framework. Raman studies of Cℓ and I boracites[6-8] have shown

that modes at low frequency (< 250 cm^{-1}) are sensitive to substitution of both metal and, in particular, halogen, indicating that these modes derive from vibrations involving these atoms. The high frequency modes are relatively unaffected by these substitutions in agreement with the structural observation that the B-O cage varies little with different metals and halogens.[1,17] Thus the modes in Table 2 of frequencies < 200 cm^{-1} likely arise from lattice modes involving motions of the Mn and Cℓ ions. These low frequency modes are notably sharp at room temperature, in contrast to heavy damping observed in this region in the cubic phase spectrum of other boracites.[6-8] Also notable is the absence of a wing feature of A_1 symmetry indicative that the disorder found in cubic boracites[6] has vanished for Mn-Cℓ at temperatures well below T_c.

It is noticeable that there is no very low frequency mode in the Raman spectrum of Mn-Cℓ. Such a mode could be expected in a material exhibiting soft modes at a displacive phase transition. The lowest observed mode is at 76 cm^{-1} and has A_2 symmetry. This behaviour appears to be characteristic of the orthorhombic phase of boracites. In Cr-Cℓ and Cu-Cℓ, the lowest band frequencies are at 91 and 67 cm^{-1}, respectively, for $T << T_c$, again in A_2 symmetry.[5,7] For these boracites this A_2 band is one of the soft modes, and therefore the 76 cm^{-1} band of Mn-Cℓ is likely to exhibit soft mode behaviour near T_c. The A_1 soft mode is at 149.5 cm^{-1} and 136 cm^{-1} in Cr-Cℓ and Cu-Cℓ, respectively, for $T << T_c$[5,7]: it is not obvious where the corresponding A_1 mode occurs Mn-Cℓ. It may be either the 141 cm^{-1} (XX) band or the 137 cm^{-1} (YY) band, but is more likely to be found in the as yet unmeasured (ZZ) spectrum. The strong first-order nature of the improper ferroelectric transition in boracites precludes the appearance of any mode at low frequency in the orthorhombic phase: mode softening is typically only 10 cm^{-1} before the transition

occurs.[5,7] The abruptness of the transition also makes it difficult to use Raman spectroscopy to follow cubic phase modes through into the orthorhombic phase.

6. Conclusion

It can be expected that a crystal having numerous normal modes at $\underline{k} = 0$ will produce a complicated Raman spectrum. For boracites, degeneracies in the cubic phase reduce the number of mode frequencies to manageable proportions, but in the ferroelectric phase the low symmetry removes this advantage. And so the observed Raman spectrum of orthorhombic Mn-Cℓ comprises a large number of modes, too many to be dealt with by a conventional lattice dynamics calculation. The general characteristics of the orthorhombic boracite spectrum, as contrasted with the cubic phase spectrum, are numerous sharp bands, with no features below about 60 cm^{-1} and a complete absence of Debye-like wings for temperatures well below T_c.

This work on Mn-Cℓ could be extended by further measurements to determine the α_{zz} polarisability tensor component of the Raman spectrum and the various TO/LO components of polar modes. However, the dynamics of boracites are so complex that such work would not greatly assist our understanding of these materials. At this stage, the most valuable information about the dynamics of the ferroelectric transition will come from studies of any temperature dependent features in the Raman spectrum.

Acknowledgements

Thanks are due to H. Schmid for many illuminating discussions about the properties of boracites, to J.-P. Rivera for providing the Mn-Cℓ crystal, to H. Tippmann for technical advice on crystal preparation,

Reference Pub/3/4/IJPAP/RE-12/77

Footnote to be added to the manuscript "Raman Spectrum of the Orthorhombic Phase of the Improper Ferroelectric Manganese-Chlorine Boracite" by D.J. Lockwood.

Recent studies[18,19] have shown that the orthorhombic a, b and c axes, as defined by the standard setting ($Pca2_1$) for the crystal space group, are associated with the extinction directions α, γ and β, respectively, for Mn-Cl and Ni-Cl. This means that the changes noted in the last paragraph of Section 3 must be applied to Section 4.

Additional References

18. Rivera, J.-P., University of Geneva, (private communication).

19. Schmid, H. and Tippmann, H., Ferroelectrics, (in press).

References

1. Nelmes, R.J., J. Phys. C: Solid State Phys., 7 (1974), 3840.
2. Dvorak, V., Ferroelectrics, 7 (1974), 1.
3. Dorner, B., Axe, J.D. and Shirane, G., Phys. Rev., B6 (1972), 1950.
4. Lockwood, D.J., J. Raman Spectrosc., 2 (1974), 555.
5. Lockwood, D.J., Solid State Commun., 18 (1976), 115.
6. Lockwood, D.J., Ferroelectrics, 13 (1976), 353.
7. Lockwood, D.J. and Syme, R.W.G., Ferroelectrics, (in press).
8. Lockwood, D.J. and Murray, A.F., Ferroelectrics, (in press).
9. Dvorak, V. and Petzelt, J., Czech. J. Phys., B21 (1971), 1141.
10. Wilson, E.B., Decius, J.C. and Cross, P.C., Molecular Vibrations (McGraw-Hill, New York), 1955.
11. Schmid, H., J. Phys. Chem. Solids, 26 (1965), 973.
12. Schmid, H., (private communication).
13. Arthur, J.W. and Lockwood, D.J., J. Raman Spectrosc., 2 (1974), 53.
14. Arthur, J.W., J. Raman Spectrosc., 5 (1976), 9.
15. Petzelt, J. and Mayerova, I., Czech J. Phys., B23 (1973), 1277.
16. Murray, A.F. and Lockwood, D.J., J. Phys. C: Solid State Phys., 9 (1976), 3691.
17. Nelmes, R.J. and Thornley, F.R., J. Phys. C: Solid State Phys., 7 (1974), 3855.

Table 1. Correlation table for irreducible representations of point groups T_d and C_{2V}.

Point Group	Irreducible Representation				
T_d	A_1	A_2	E	F_1	F_2
C_{2V}	A_1	A_2	A_1+A_2	$A_2+B_1+B_2$	$A_1+B_1+B_2$

Table 2

Frequencies (cm^{-1}) and assignments of peaks in the Raman spectrum of Mn-Cℓ at 300 K (T_c = 680 K).

(XX)	(YY)	(XY)	(YZ)	(ZX)
A_1	A_1	A_2	B_2	B_1
		76		
110		91	97	
119		113		
141	137	143	144	
163	162		154	150
	187		175	159
195	197	193	216	184
215	210	226	228	202
236	239	238	237	227
258	252	250	254	252
	267	264		268
	279		278	
306		302	316	299
	338	339	338	330
354	354	354	354	351
				364
	382	384	385	
400	398	398		400
422	414	414	435	
436	435	450	448	427
475	474		469	468
507	504		490	508
541	538	534	520	545
558	557	556	547	
596	595	599	596	598
613	612		616	
638				
657	655	656	655	657
717	706	715	683	697
754	755	745	704	718
772	772	771	771	
791	797		793	791
834	832	833	832	
849		856		
869	876		867	870
919	901	907	900	915
939	945	925	942	940
959		938	959	959
1026	1023	1037	1038	1049
1077	1074	1070	1075	
1129	1126	1147	1126	1145
1202	1203		1200	1343
1349	1361	1343	1366	1398
1400	1402	1392	1401	1427

Table 3

Assignments of modes to BO_4 vibrations.

Typical cubic phase frequencies (cm^{-1}) and symmetry.[16]	Observed orthorhombic Mn-Cℓ frequencies (cm^{-1}) possessing the expected symmetry.
400 (A_1)	354,400,436 (A_1)
200 (E)	195,215,236 (A_1) : 193,226,238 (A_2)
1100 (F_2)	1077,1129 (A_1) : 1145 (B_1) : 1075,1126 (B_2)
260 (F_2)	258 (A_1) : 252 (B_1) : 254 (B_2)

Figure Captions

Figure 1. The (a) Z(XX)Y, (b) Z(YY)X, (c) Z(YX)Y, (d) Z(YZ)X and (e) Z(XZ)Y Raman spectrum of Mn-Cℓ recorded at 300 K from 0-500 cm^{-1} using 514.5 nm radiation. The weak sharp structure at low frequency (< 120 cm^{-1}) arises from Raman scattering by air.

Figure 2. The (a) Z(XX)Y, (b) Z(YY)X, (c) Z(YX)Y, (d) Z(YZ)X and (e) Z(XZ)Y Raman spectrum of Mn-Cℓ recorded at 300 K from 500-1500 cm^{-1} using 514.5 nm radiation. Asterisks denote laser plasma lines.

z(xx)y
14

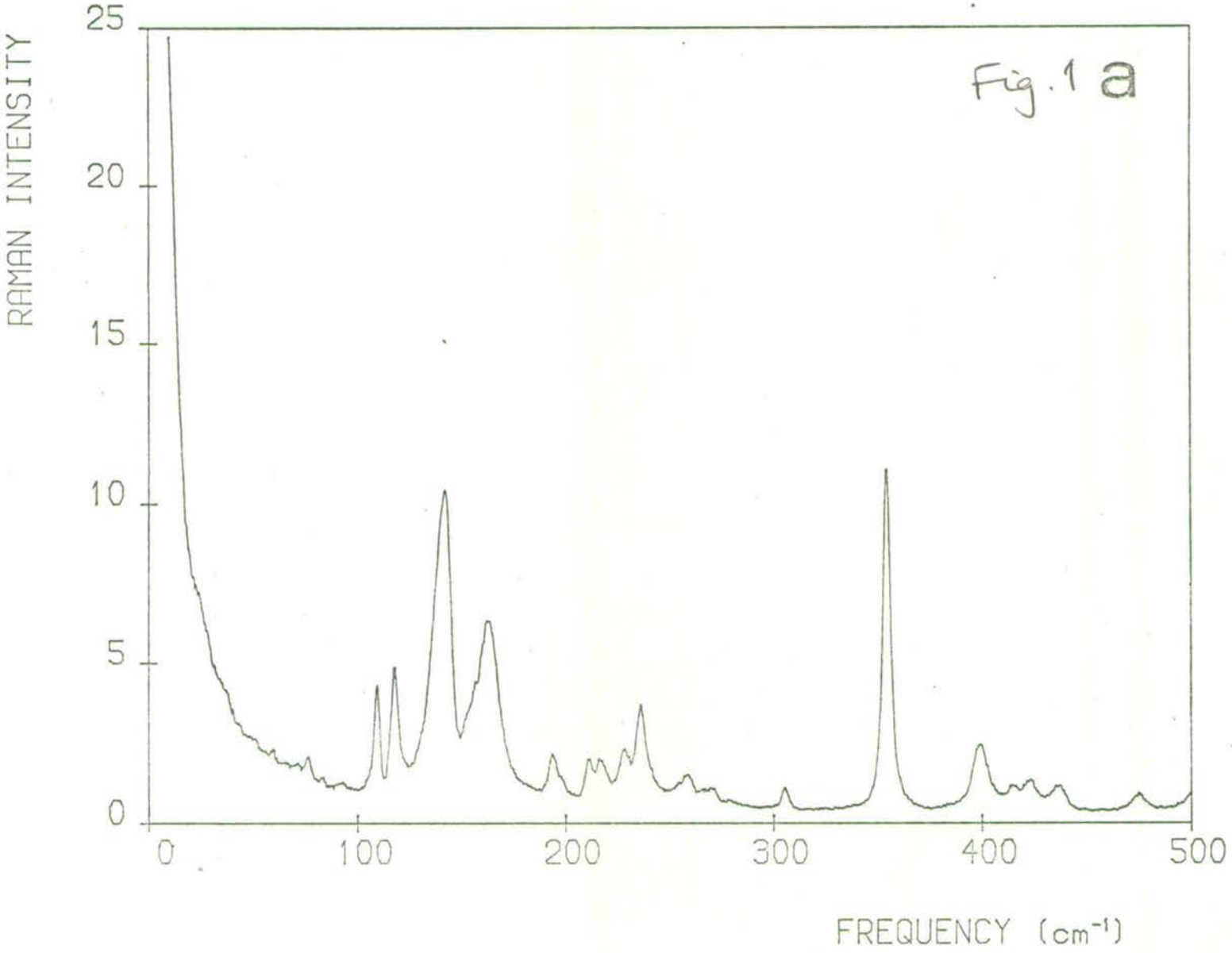

Figure 1 (a) Backward

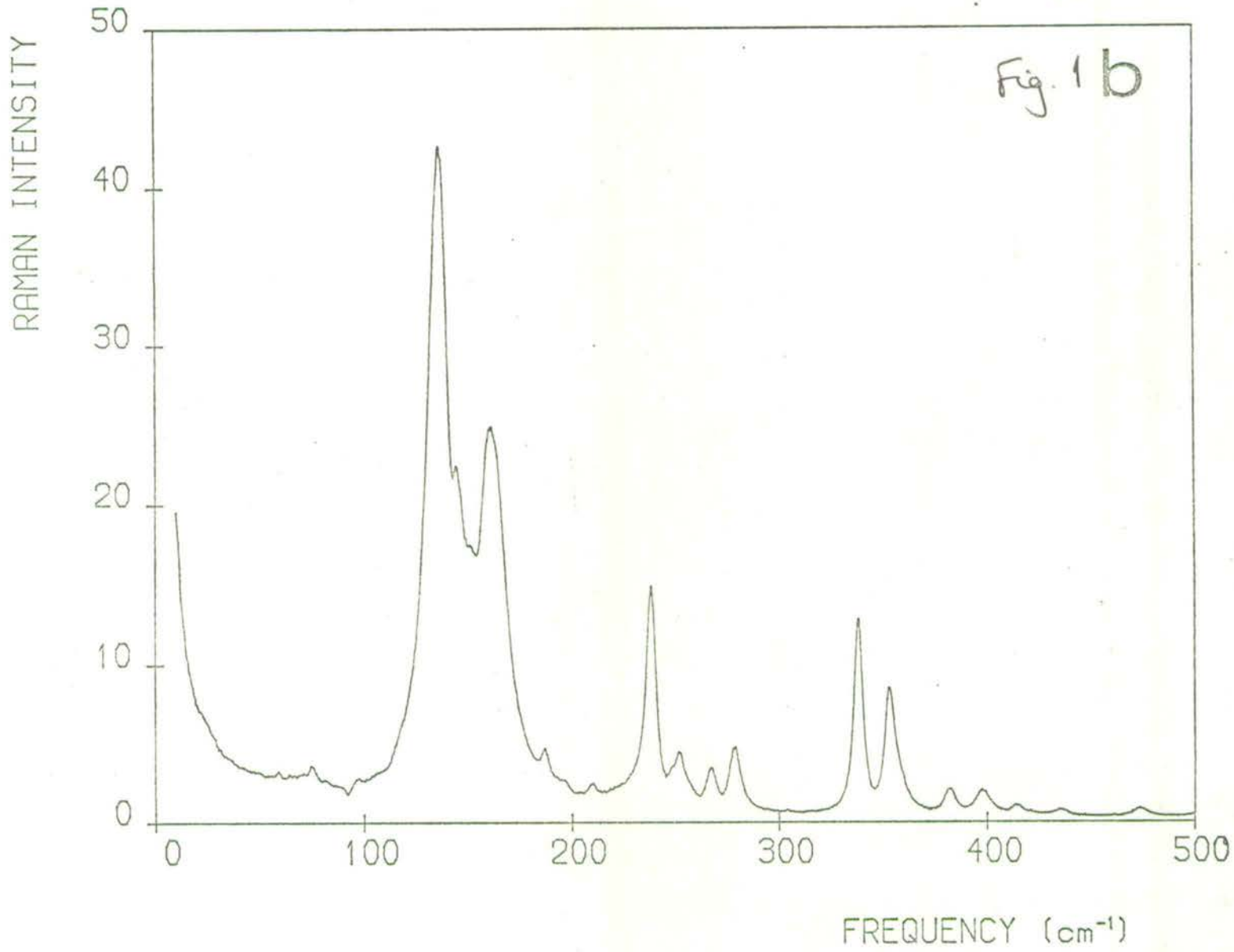

Figure 1(b) Lockwood

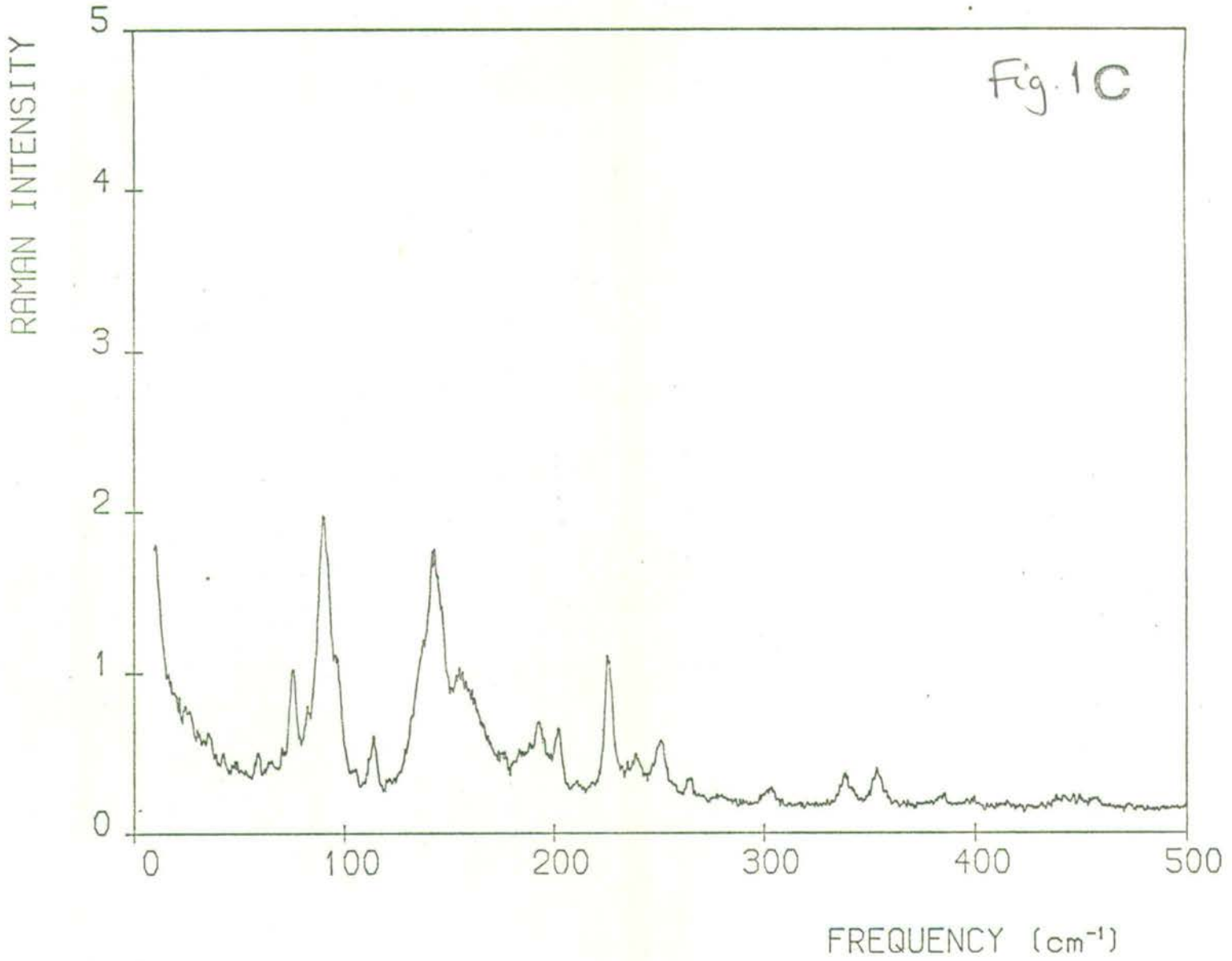

Fig. 1C

Figure 1(c) Laboured

z(x/z)x

3b

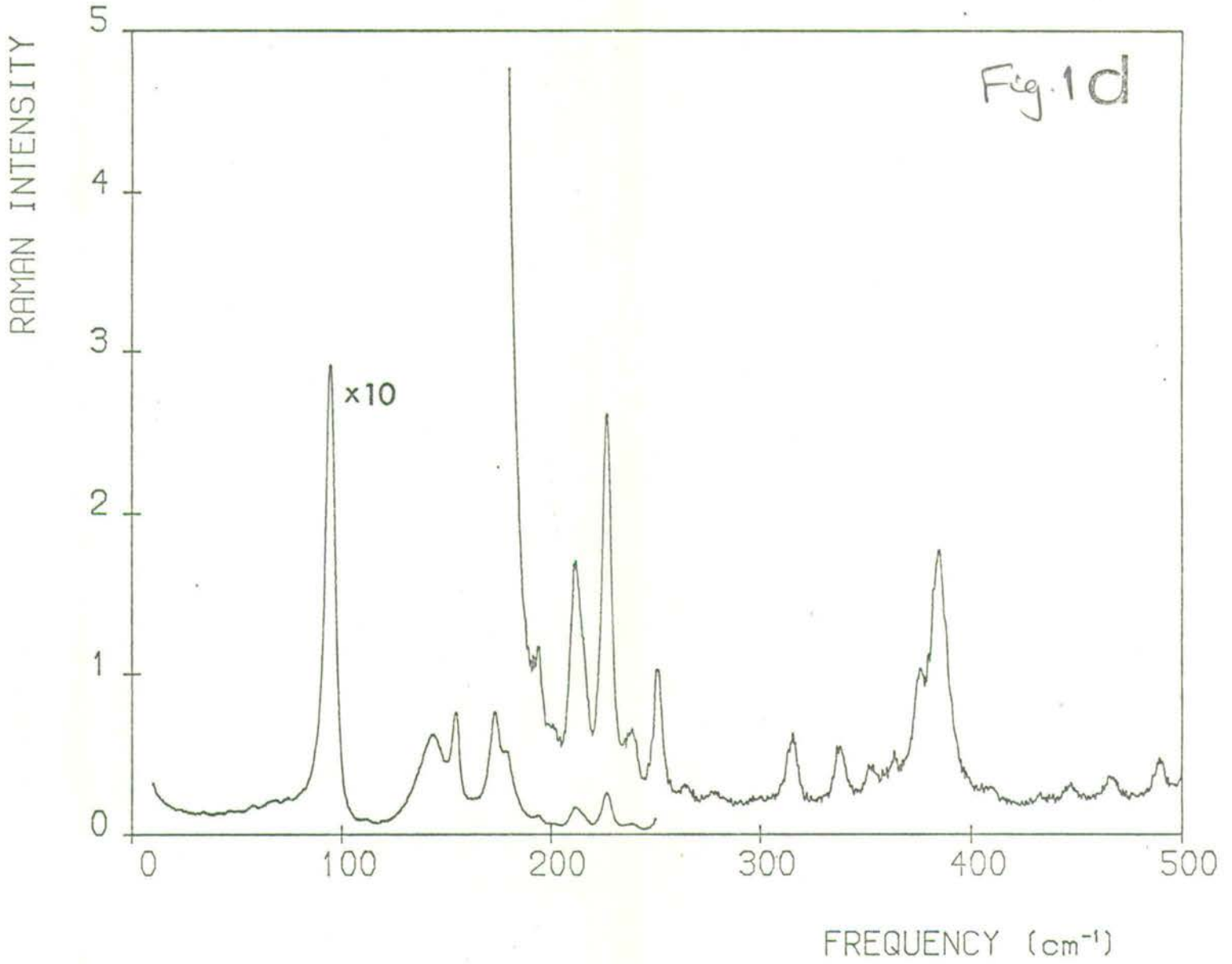

Figure 1(d) Lockwood

z(xz)y

17

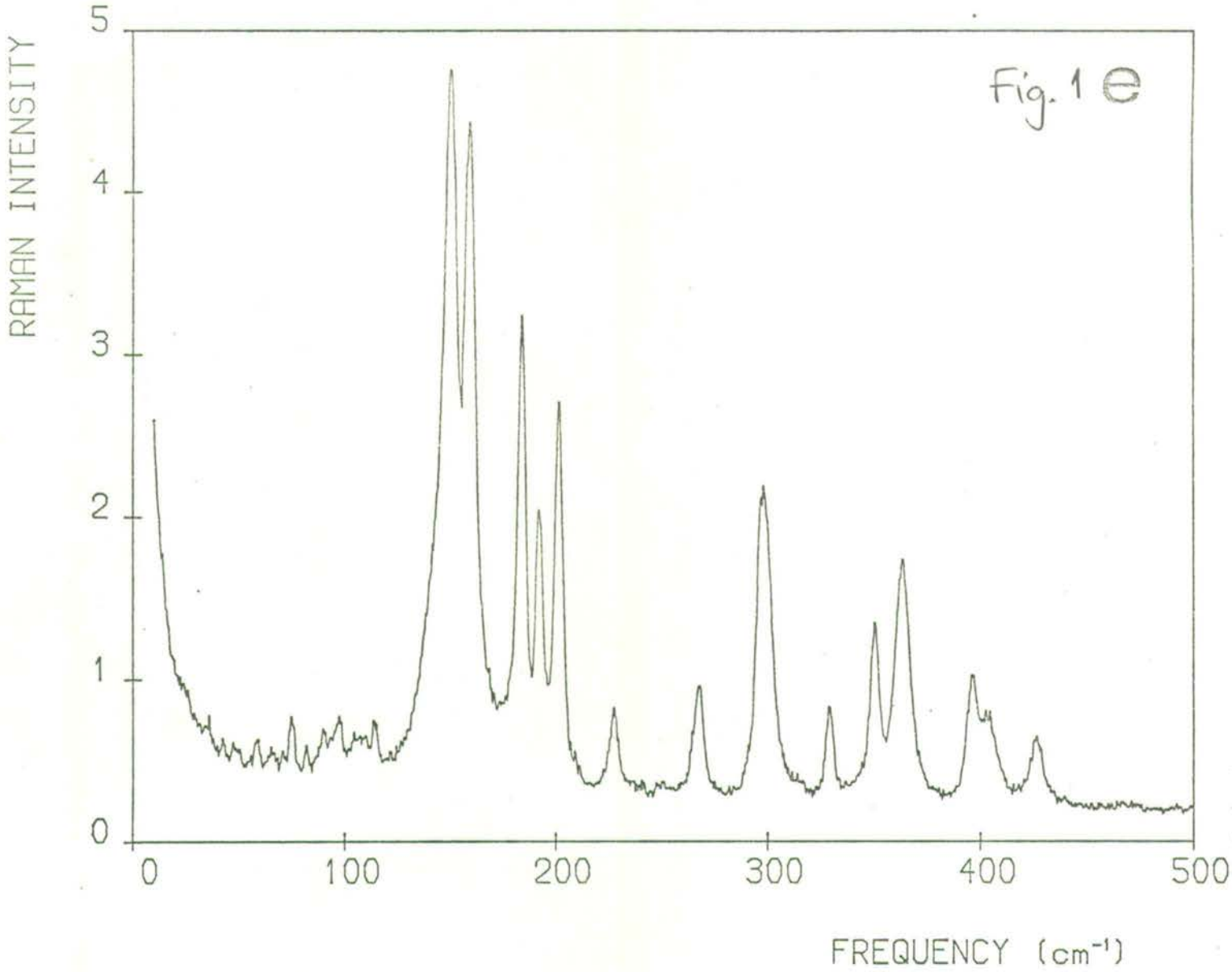

Fig. 1 e

Figure 1(e)

2 (xx) y

15, 16

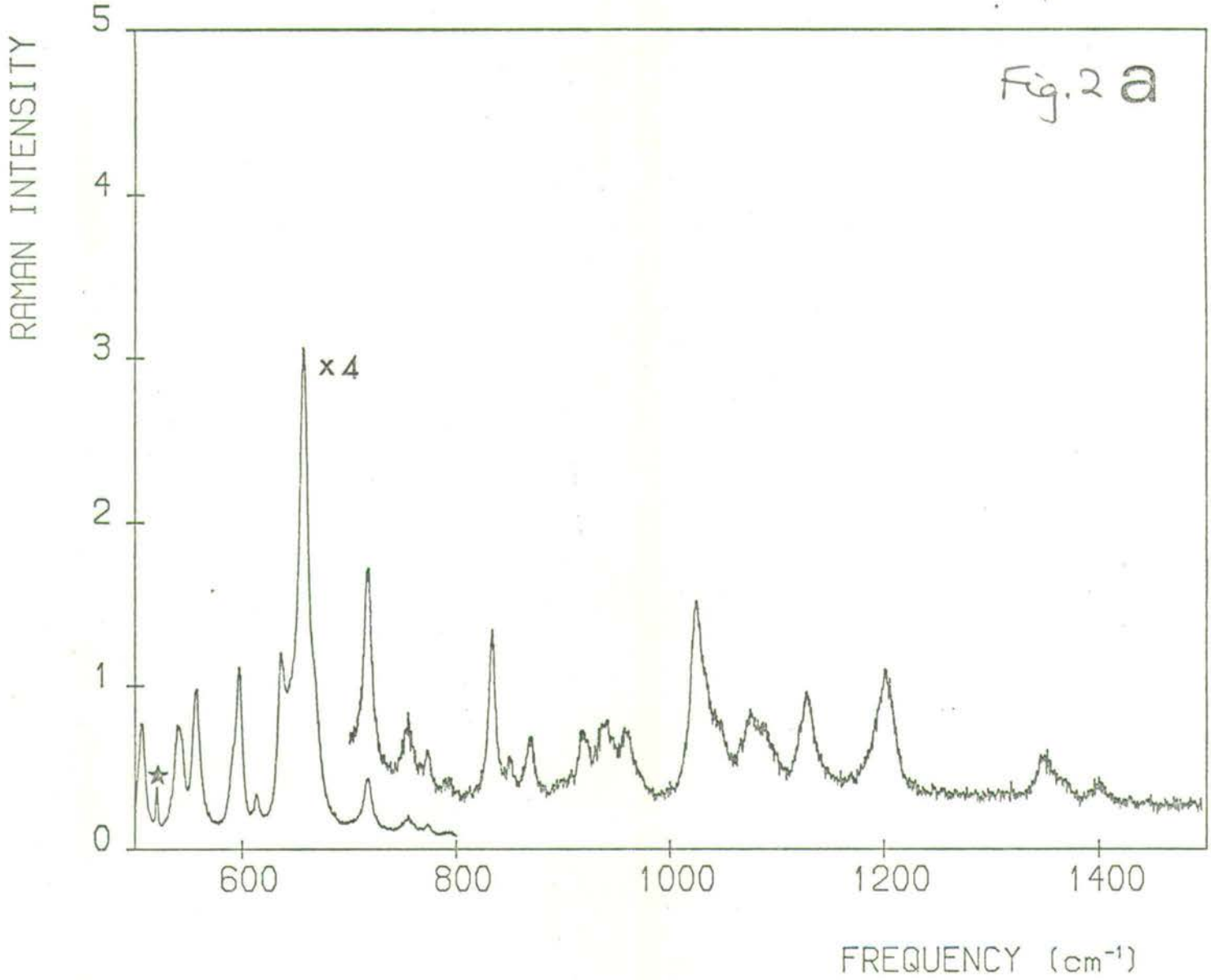

Fig. 2a

Figure 2(a) Lockwood

2(YY)X

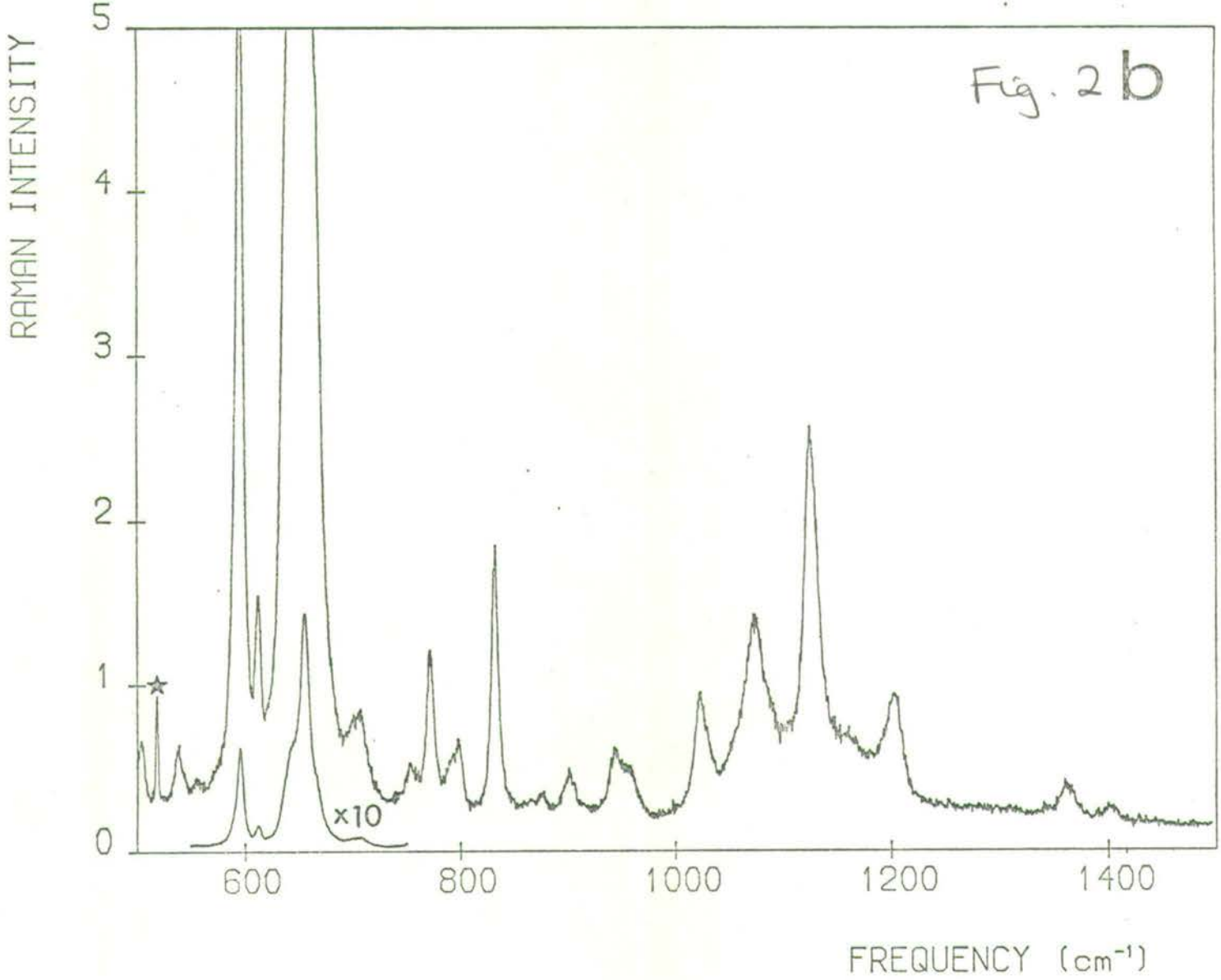

Figure 2 (b) Backward

z(yx)y
24, 25

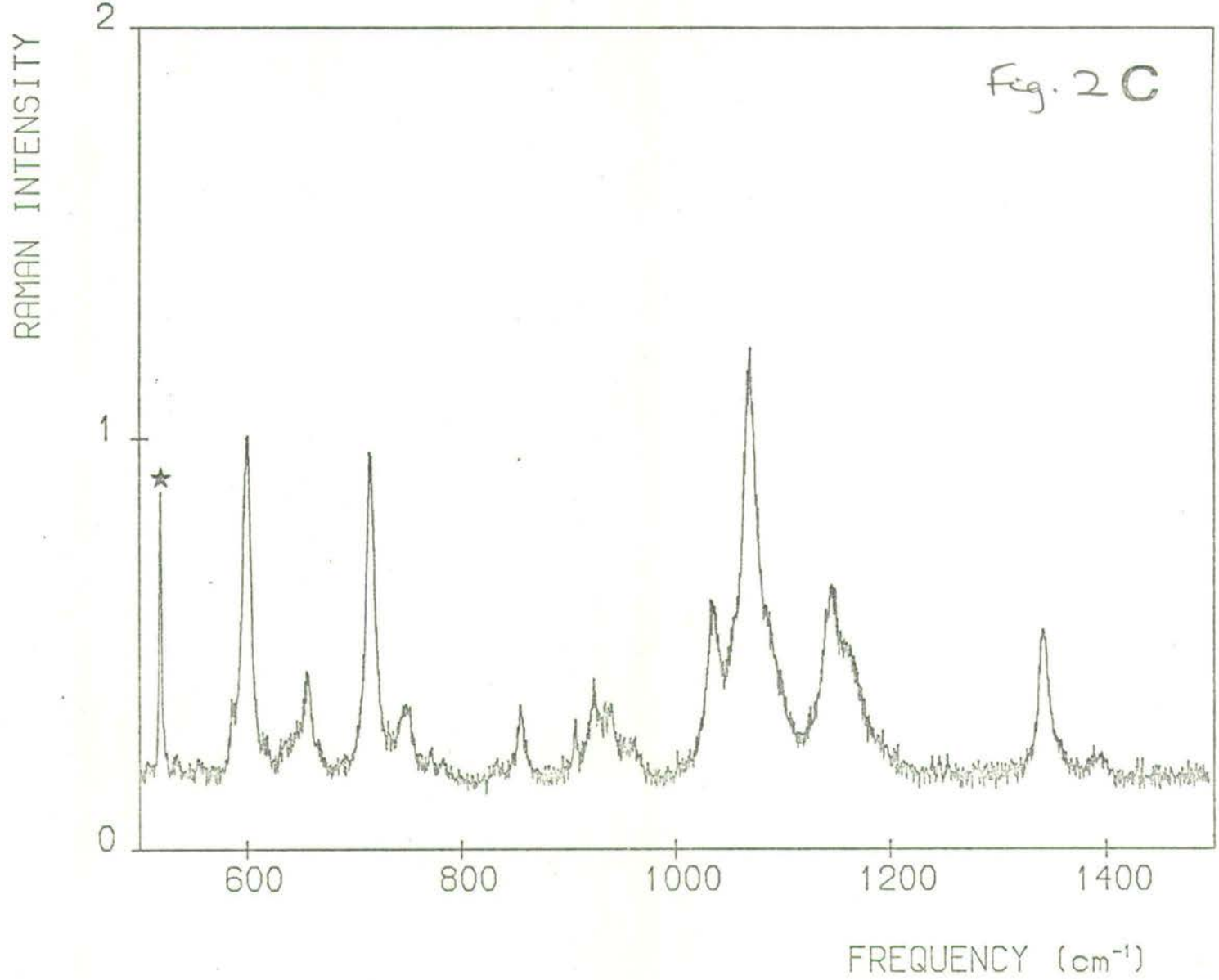

Fig. 2C

Figure 2(c) backward

-z(yz)x

39,42

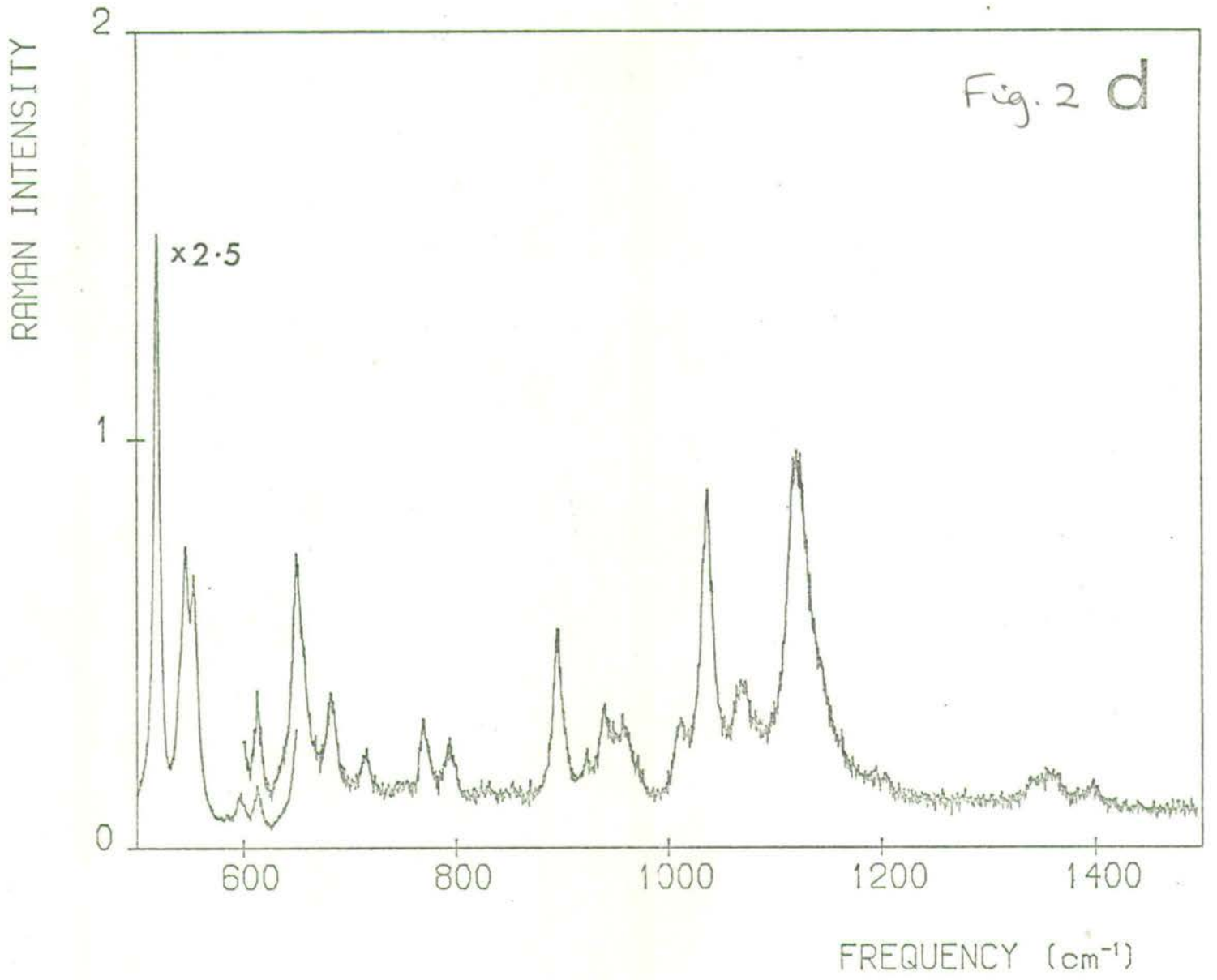

Fig. 2 d

Figure 2(d) Lorbwood

z(x2)y

13, 19

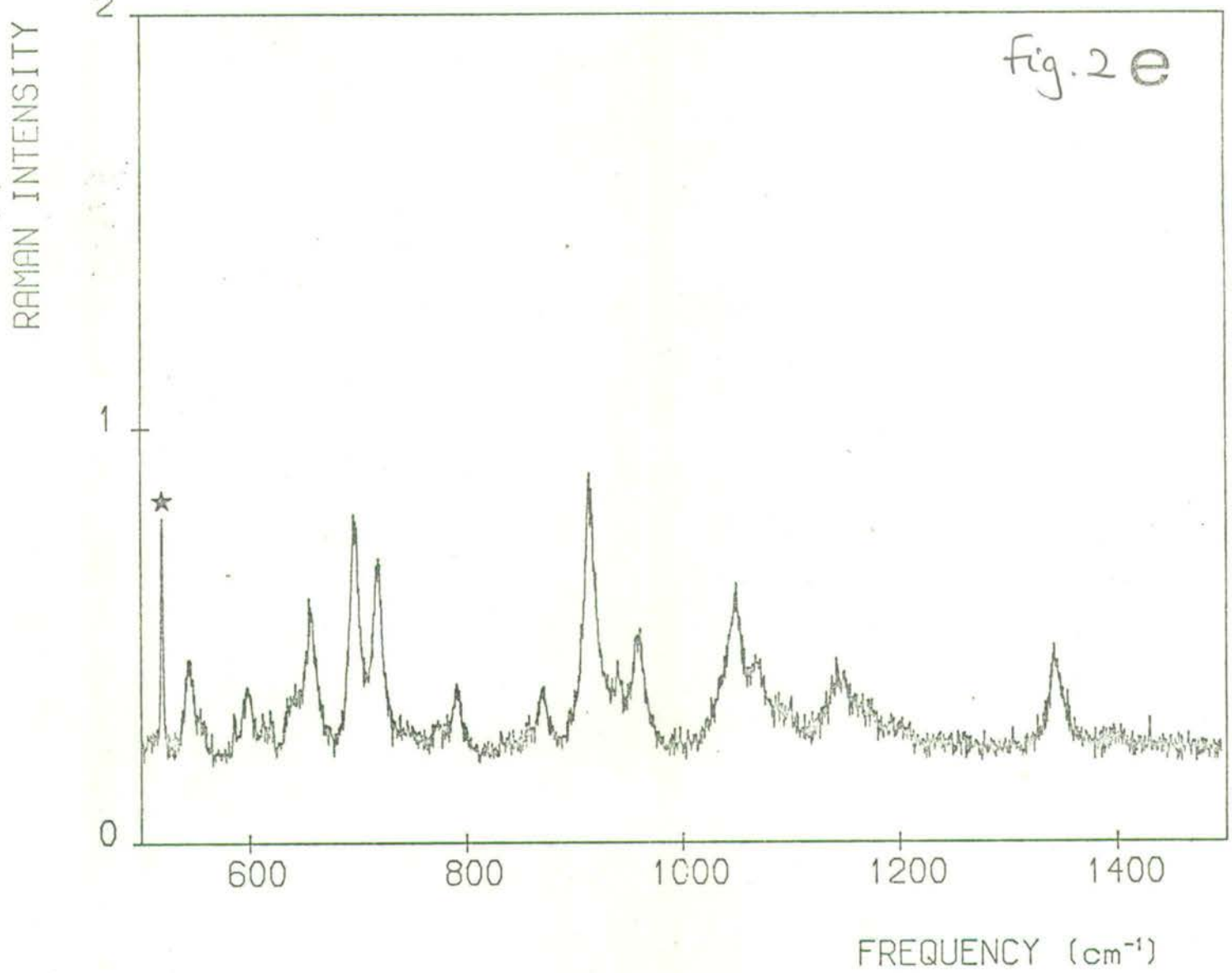

Figure 2 (e) Lockwood

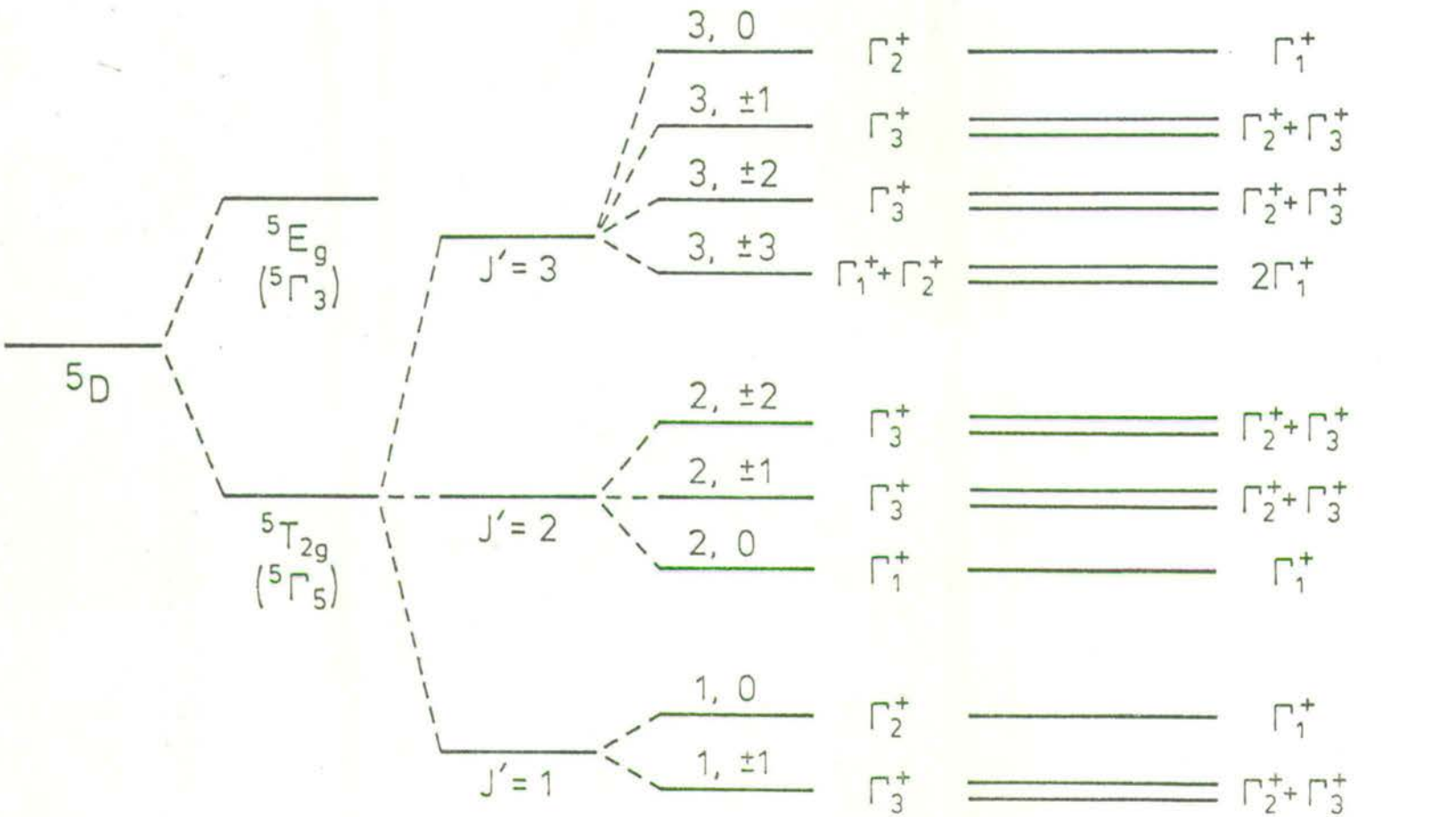

Free ion

Cubic field

L . S ($l' = 1$) S is effective $J' = l' + S$

Trigonal field (J, Jz)

Symmetry in paramagnetic phase (D_{3d} point group)

Symmetry in molecular field approx. (C_{3i} point group H||z)

Selection rules for $T > T_N$

$\Gamma_3^+ \times \Gamma_1^+ = \Gamma_3^+$

$\Gamma_3^+ \times \Gamma_2^+ = \Gamma_3^+$

$\Gamma_3^+ \times \Gamma_3^+ = \Gamma_1^+ + \Gamma_2^+ + \Gamma_3^+$

Hot bands:

$\Gamma_2^+ \times \Gamma_1^+ = \Gamma_2^+$

$\Gamma_2^+ \times \Gamma_2^+ = \Gamma_1^+$

$\Gamma_2^+ \times \Gamma_3^+ = \Gamma_3^+$

Raman tensors

$\Gamma_1^+ \begin{pmatrix} a & & \\ & a & \\ & & b \end{pmatrix}$

$\Gamma_2^+ \begin{pmatrix} \cdot & -c & \\ c & \cdot & \\ & & \cdot \end{pmatrix}$

$\Gamma_3^+ \begin{pmatrix} d & d & -e \\ d & -d & e \\ -f & f & \cdot \end{pmatrix}$

O.K.

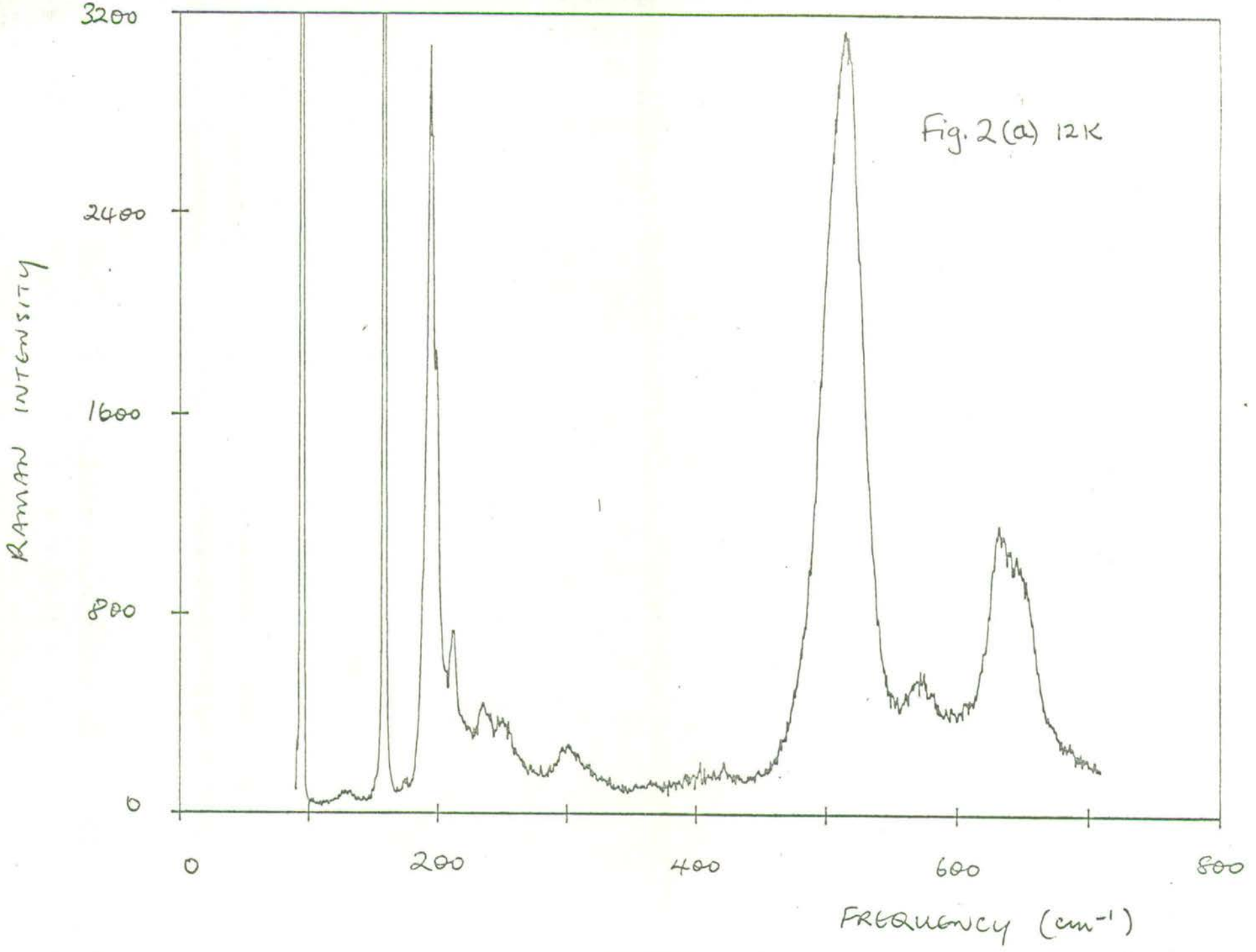
3200
2400
1600
800
0
RAMAN INTENSITY
0
200
400
600
800
FREQUENCY (cm⁻¹)
Fig. 2(a) 12K

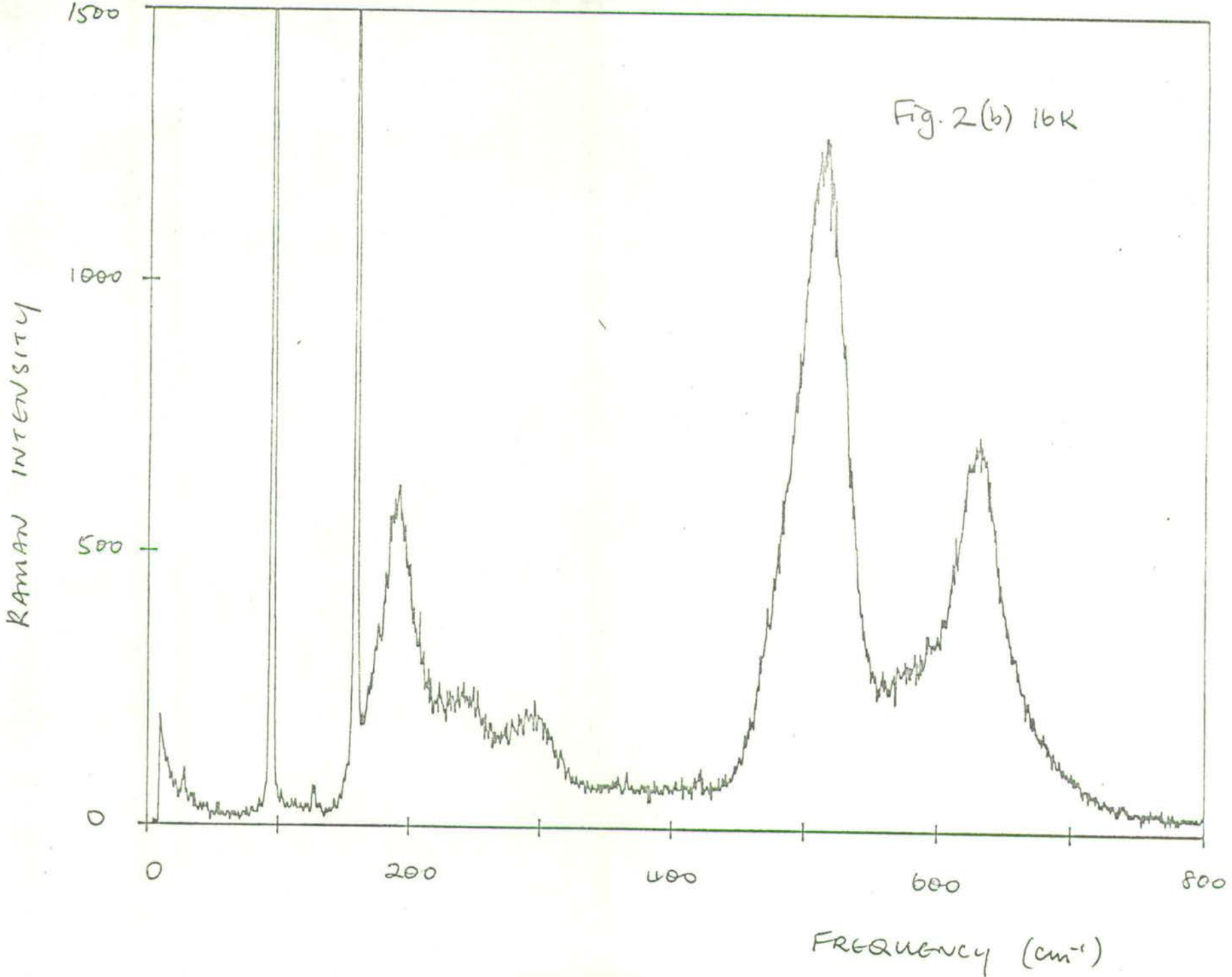
Fig. 2(b) 16K
1500
1000
500
0
RAMAN INTENSITY
0
200
400
600
800
FREQUENCY (cm⁻¹)

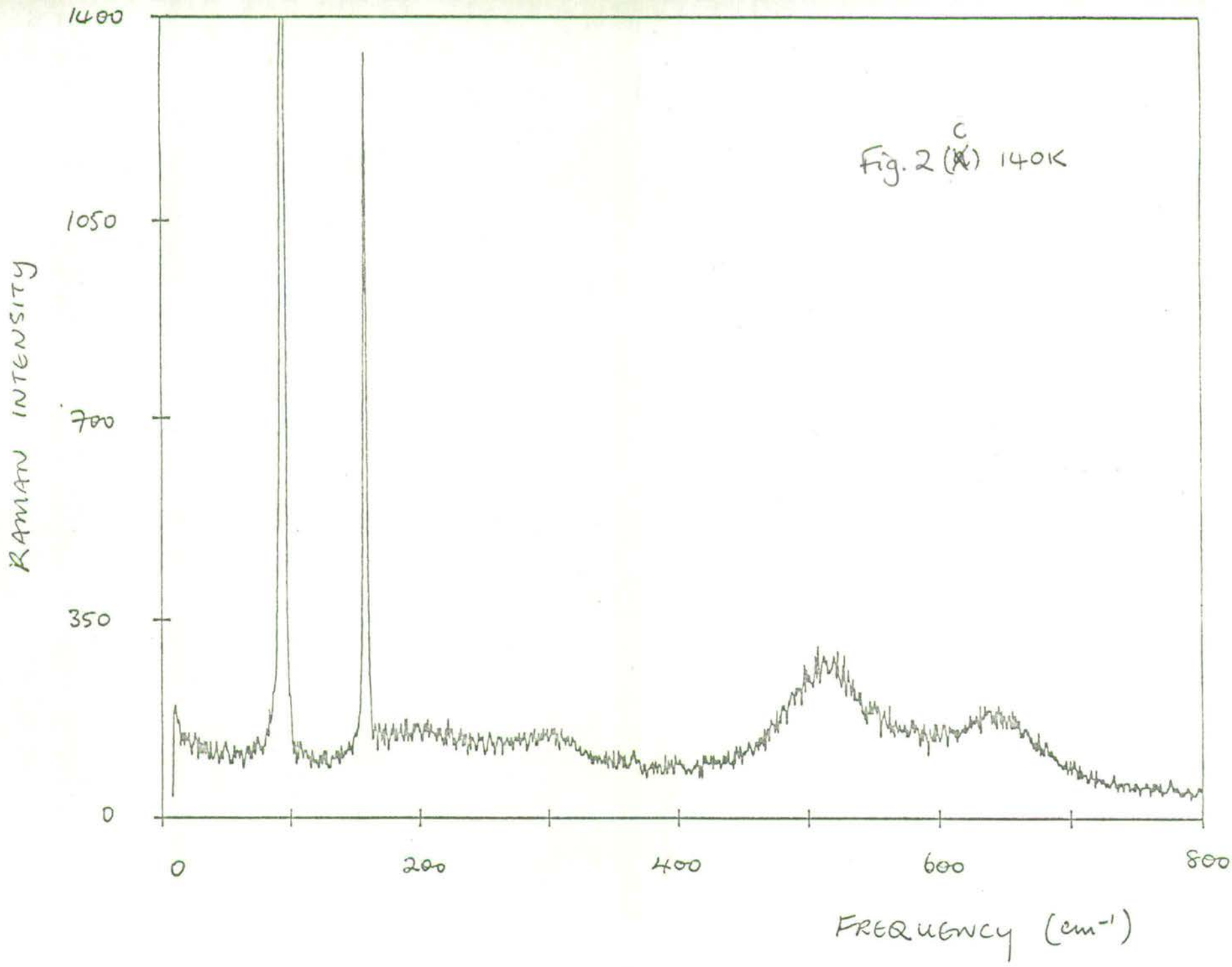
1400
1050
700
350
0
RAMAN INTENSITY
0
200
400
600
800
FREQUENCY (cm⁻¹)

Fig. 2 (C) 140K

Fig. 3

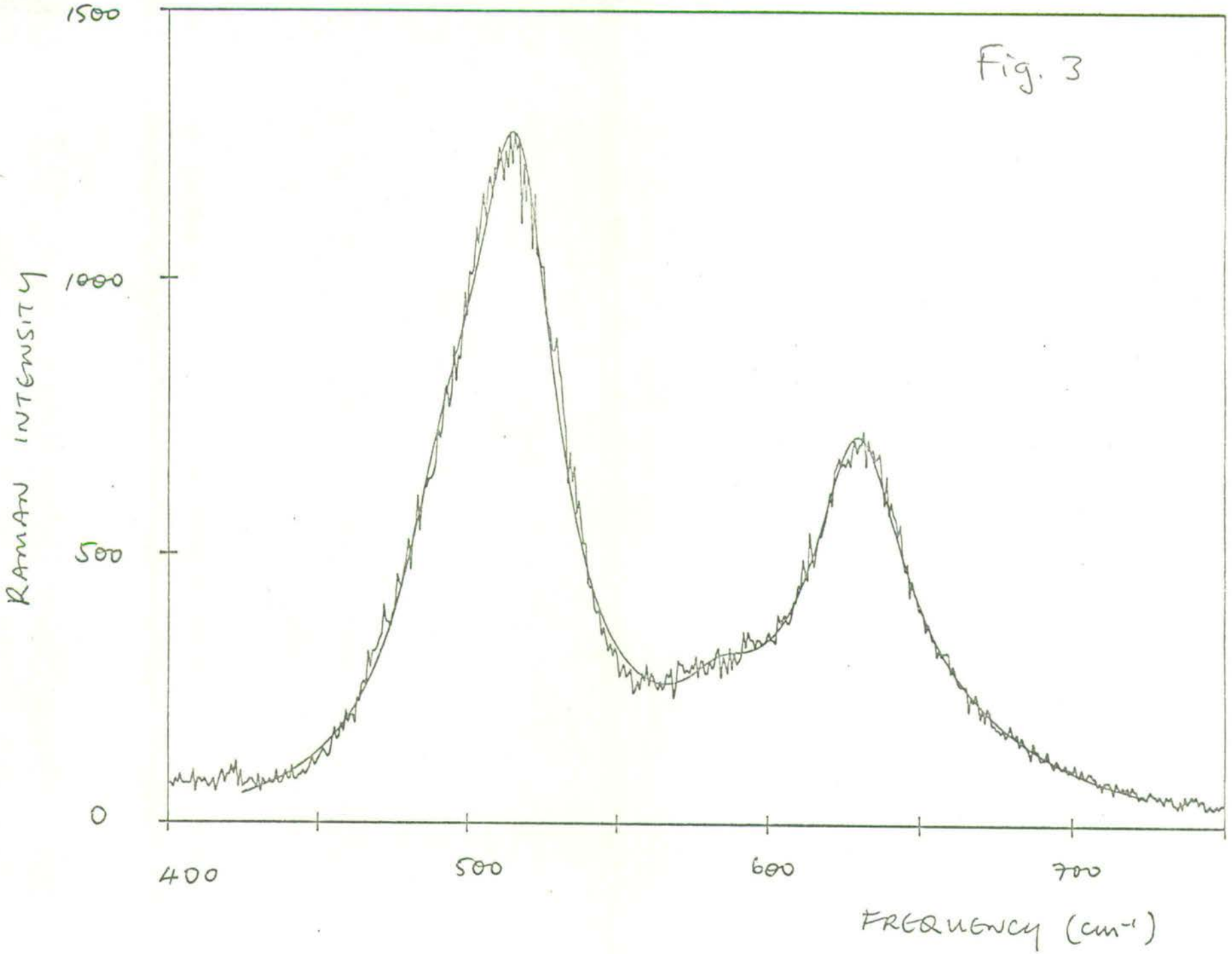
1500
1000
500
0
RAMAN INTENSITY
400
500
600
700
FREQUENCY (cm⁻¹)

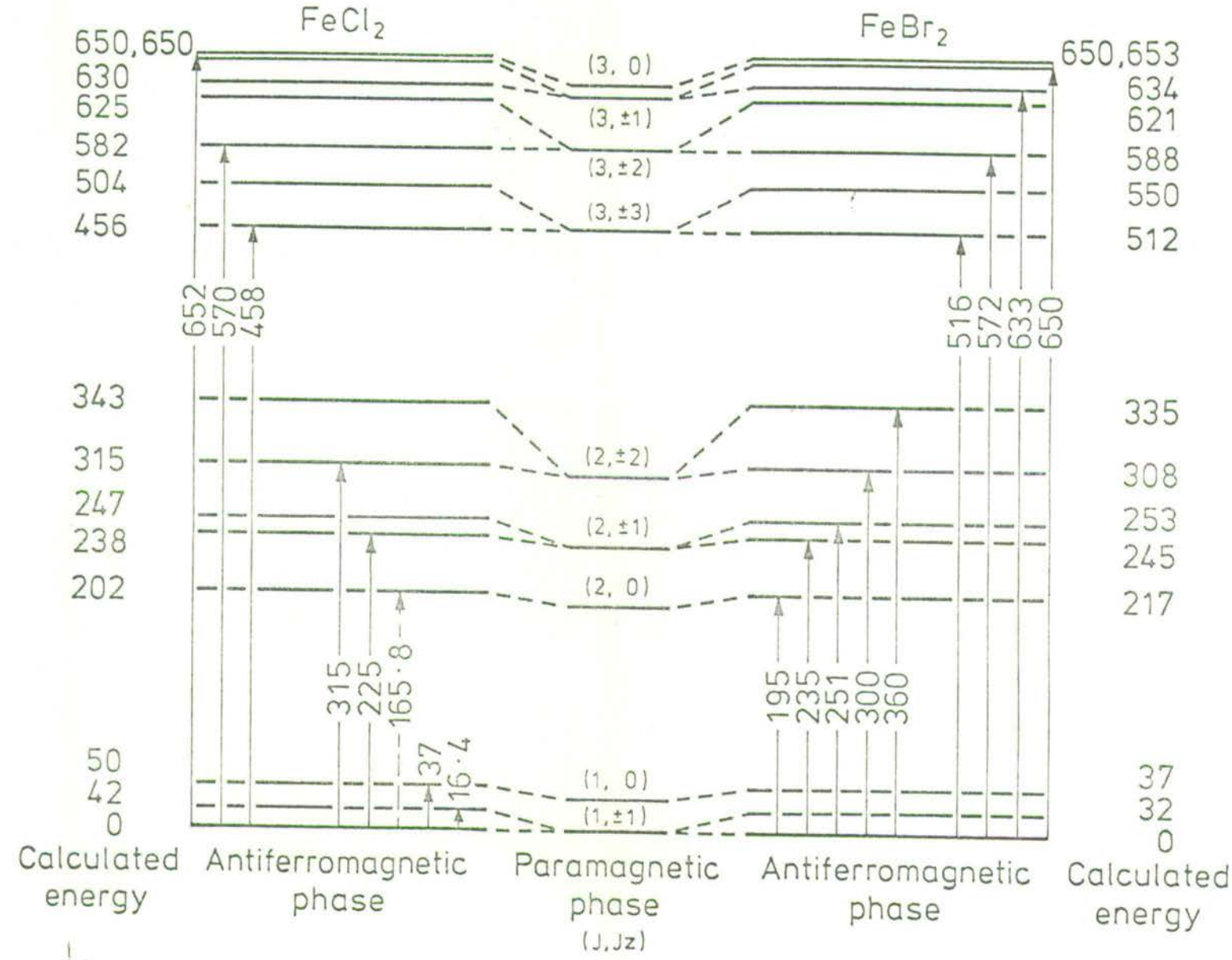
FeCl2
FeBr2
650,650
630
625
582
504
456
650,653
634
621
588
550
512
(3, 0)
(3, ±1)
(3, ±2)
(3, ±3)
652
570
458
516
572
633
650
343
315
247
238
202
335
308
253
245
217
(2, ±2)
(2, ±1)
(2, 0)
315
225
165·8
37
16·4
195
235
251
300
360
50
42
0
37
32
0
(1, 0)
(1, ±1)
Calculated energy
Antiferromagnetic phase
Paramagnetic phase
(J, Jz)
Antiferromagnetic phase
Calculated energy

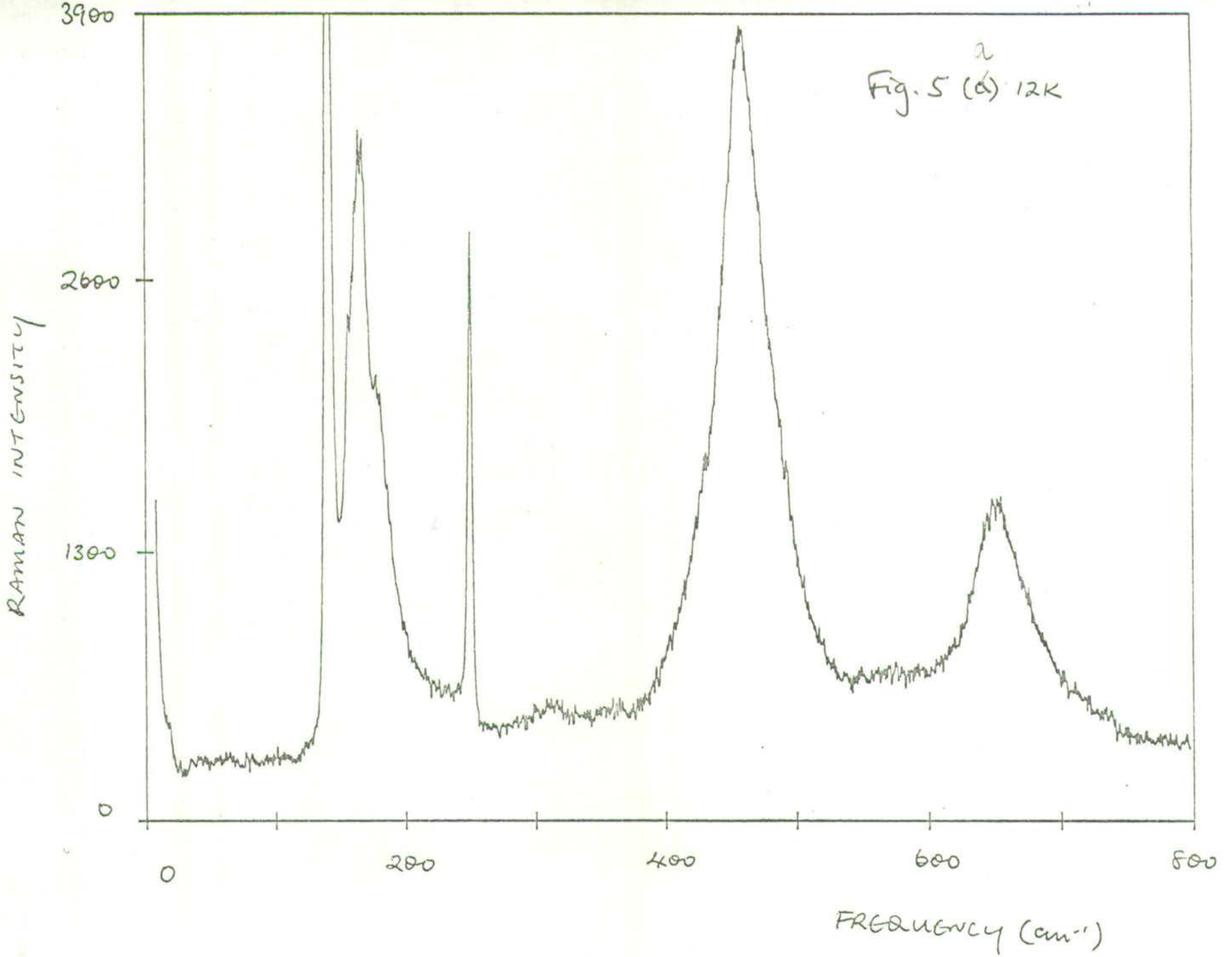
Fig. 5 (a) 12K
3900
2600
1300
0
RAMAN INTENSITY
0
200
400
600
800
FREQUENCY (cm⁻¹)

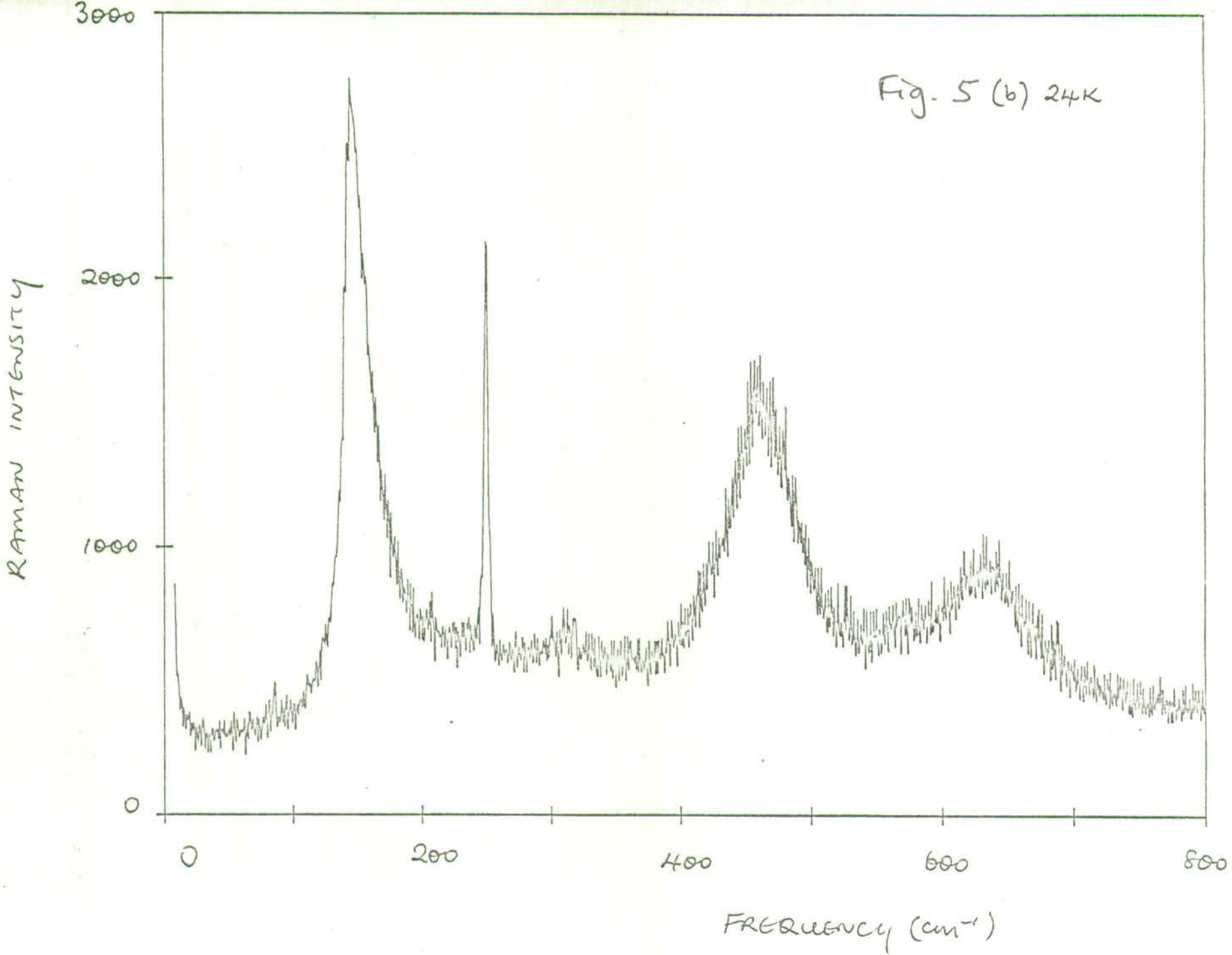
Fig. 5 (b) 24K
RAMAN INTENSITY
3000
2000
1000
0
0
200
400
600
800
FREQUENCY (cm⁻¹)

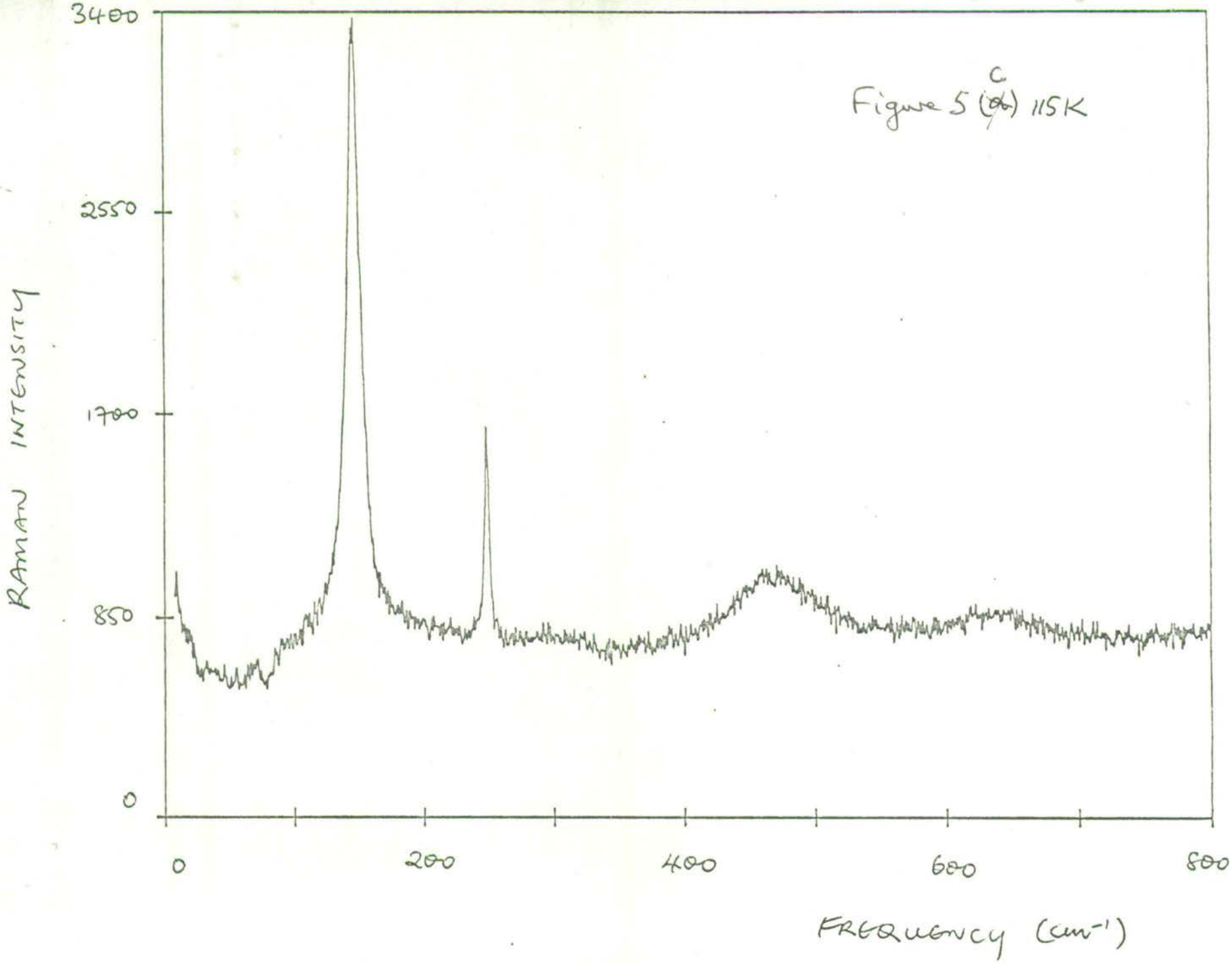

Figure 5 (c) 115K

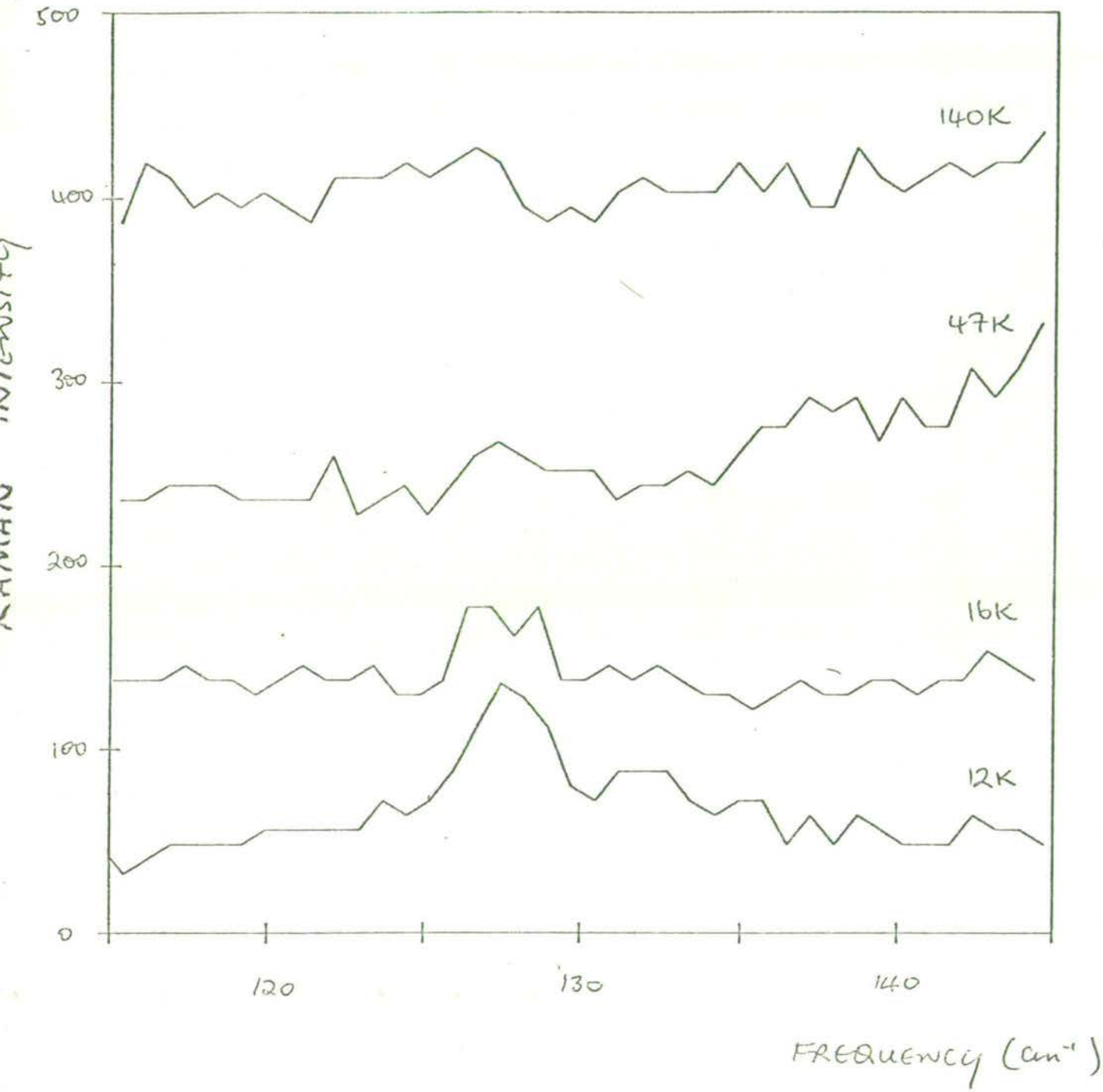
500
400
300
200
100
0
140K
47K
16K
12K
120
130
140
FREQUENCY (cm⁻¹)

Figure 6

Raman spectrum of the puzzling paraelectric phase of nickel-iodine boracite

A.F. Murray and D.J. Lockwood

Physics Department, University of Edinburgh,
Edinburgh EH9 3JZ, Scotland.

Abstract

The Raman spectrum of $Ni_3B_7O_{13}I$ is reported and the number of $q = 0$ phonon frequencies observed is compared with the group theoretical prediction. Anomalies in the temperature dependence of phonon lifetimes and frequencies are correlated with abnormalities in the dielectric, magnetic and structural properties at $\simeq$ 130 K. The Raman spectra at temperatures from 88 K to 300 K indicate cubic symmetry. The static and temperature dependant structure of the Raman spectra are compared and contrasted with their counterparts for other boracites. It is concluded that $Ni_3B_7O_{13}I$ is unique among boracites in many ways, at least in its cubic phase.

Short title:

Raman spectrum of paraelectric $Ni_3B_7O_{13}I$

1. Introduction

Nickel iodine boracite, $Ni_3B_7O_{13}I$ (Ni - I) undergoes an improper first order transition from a high temperature paraelectric phase of cubic symmetry (T_d^5) to a ferroelectric phase at $T_c \simeq 68$ K, with a concomitant onset of weak antiferromagnetic ordering (Schmid 1969, Nelmes 1974, Lockwood et al. 1977). The existence of ferroelectric and ferromagnetic transitions is a characteristic of the boracite family (Nelmes 1974), that is, those compounds of the form $M_3B_7O_{13}X$, where M represents a divalent metal, and X a halogen or chalcogen. Of the halogen boracites studied so far by various techniques, only Ni - I has been found to exhibit a simultaneous ferroelectric/magnetic transition.

Ni-I is particularly interesting, however, for reasons additional to the usual boracite improper and therefore 'coupled' phase transition, involving more than one order parameter (Nelmes 1974). These are the existence of 'growth sectors', with the attendant optical anisotropy (Schmid 1969), and the anomalous dielectric, magnetic and structural properties of the cubic phase at $T \simeq 130$ K. These anomalies, illustrated in figure 1, comprise broad maxima in the magnetic and dielectric susceptibilities. (Ascher et al. 1966) and an increase of about 0.1% in the lattice constant (Will and Morche 1977).

The light scattering study reported in this paper is concerned with the cubic phase, as a first step in understanding the dynamics of this interesting compound. It could be anticipated that some manifestation of the abnormalities in the magnetoelectric and structural properties should occur in the Raman spectrum. Such an expectation is reinforced by the existence of a broad minimum at about 120 K, with a broad maximum at about 150 K, in the elastic compliance (Lockwood et al. 1977) and a similar result from shear mode measurements of the elastic coefficient C_{44} (Rehwald 1977). The phenomenon of growth sectors should present

no difficulties under the experimental conditions described below, involving a single growth sector.

An infrared study of Ni - I at 300 K and 100 K (Petzelt and Mayerová 1973) provides a useful basis for comparison of F_2 scattering properties. Also, the published Raman spectra of the paraelectric phases of Cr-Cℓ (Lockwood 1976) and Cu-Cℓ (Lockwood and Syme 1977) may be collated with their counterparts for Ni - I, with a view to identifying equivalent bands.

While the structure of the ferroelectric phase of Ni - I is not clear, the paraelectric phase has been shown to be cubic from a full structural analysis at room temperature and 77 K, by X-ray (Nelmes and Thornley 1976) and neutron (Thornley et al. 1976) diffraction respectively, and from powder diffraction studies of the lattice constant over the range 77 K to 300 K (Will and Morche 1977).

in both instruments. The scattered light was analysed with Polaroid film followed by a polarisation scrambler. The spectrometers were automatically controlled and data collected digitally (Arthur and Lockwood 1974, Arthur and Murray 1977). Temperature control was achieved by use of a Thor nitrogen vapour flow cryostat with a chromel vs. gold-iron thermocouple for temperature measurement. The laser beam was positioned as close as possible to the sample surface to maximise heat dissipation, but $\simeq$ 5 K of laser heating was still detected at the thermocouple. This would seem to suggest that the temperature at the beam position was a few degrees higher than that measured by the thermocouple.

3. Results

A group theoretical analysis of the zone centre normal modes of the Ni - I structure predicts the following decomposition according to the irreducible representations of point group $\bar{4}3m$

$$\Gamma = 4A_1 + 6A_2 + 10E + 18F_1 + 20F_2$$

of which, excluding acoustic modes, $4A_1 + 10E + 19F_2$ should be Raman-active and $19F_2$ infrared active.

The form of the Raman tensors (Loudon 1964) means that the Z(Y'Z)Y' spectrum contains modes of F_2 symmetry (figure 2a), the Z(Y'X')Y' spectrum, modes of E symmetry (figure 2b), and the Z(X'X')Y' spectrum modes of $A_1 + E + F_2$ symmetry (figure 2c). Subtraction of the spectrum of figure 2b from that of figure 2c with a suitable choice of scale factor reveals the $A_1 + F_2$ spectrum (Murray and Lockwood 1976), (figure 2d). As the F_2 scattering is roughly ten times weaker than the $A_1 + E$ scattering, we have ignored its contribution to figure 2d. Subtraction is in this case quite impossible, no suitable 'scaling mode' being present. The resultant spectra are described below.

3.1 The A_1 spectrum

This spectrum exhibits a Debye-like wing feature, common to all boracites (Lockwood 1976, Lockwood and Syme 1977) but less pronounced in this case, its influence on the cross section being negligible beyond $\simeq$ 100 cm^{-1}. There is a broad feature centred on $\simeq$ 154 cm^{-1} with an indistinct but non-negligible broad feature peaking at 100 cm^{-1}. Over the rest of the frequency range studied only two further discrete peaks are visible at 378 cm^{-1} and 655 cm^{-1}, with some structure in the 900 - 1400 cm^{-1} range.

3.2 The E spectrum

This spectrum resembles the A_1 spectrum in the region 0-300 cm^{-1},

having a similar Debye-like wing, with broad modes peaking at 160 and 84 cm^{-1}. There are, in addition, three discrete, isolated bands and a pair of high frequency modes, characteristic of a cubic boracite.

3.3 The F_2 spectrum

The scattering of F_2 symmetry is very weak. Again, a narrow Debye wing feature is present, with an oddly shaped scattering profile below 200 cm^{-1}, comprising apparently two bands, plus two very weak bands at 255 cm^{-1} and 280 cm^{-1}. It is impossible to decide at this stage whether the broad structure around 600 cm^{-1} and 1000-1200 cm^{-1} is a result of some superposition of weak first order bands or of second or higher order. The Z(Y'Z)Y' spectrum contains TO and LO features, the Z(X'Z)Y' spectrum differing only in the absence of LO modes.

In table 1 the frequencies and linewidths (where appropriate) are presented for Ni - I at room temperature, along with the results of the infrared investigation at 300 K (Petzelt and Mayerová 1973).

In figures 3 and 4 we present a selection of spectra of E and A_1 symmetries respectively, recorded at various temperatures. From a visual scrutiny of these figures it is apparent that no change in the composition of the spectrum occurs as the temperature is varied from 295 K to 88 K. The only obvious modification to the scattering cross section is a sharpening of the peaks. A computer fitting procedure proved essential in order that the true behaviour of the Raman spectrum as a function of temperature could be explored. The F_2 spectrum was studied over the region 0-300 cm^{-1} at temperatures between 88 K and 300 K but the signal-attenuating effects of cryostat windows rendered the results too weak for detailed analysis.

4. Analysis of results

As mentioned in §3, a computer least squares fitting procedure was used to investigate the temperature variation of the Raman spectra. Discussion of this procedure benefits from a segregation of the spectra into low frequency (0-300 cm^{-1}) and high frequency (300-1400 cm^{-1}) regions.

4.1 The high frequency spectra

The peaks in the high frequency spectra may each be represented by the response function

$$G(\omega) = \frac{S\Gamma\omega}{(\omega_o^2 - \omega^2)^2 + \Gamma^2\omega^2}$$

where ω_o represents the resonant frequency, Γ the damping constant and S the oscillator strength. Incorporating the appropriate thermal weighting factor, the parameters ω_o and Γ for several E modes and the 655 cm^{-1} A_1 mode were obtained. These are presented in figures 5 and 6 respectively.

4.2 The low frequency spectra

The model response function in this case proves more problematic. Firstly, a Debye-like wing feature with response function

$$G(\omega) = \frac{S\omega}{\omega^2 + \gamma^2}$$

must be added to two functions of the form presented in §4.1, where S is again a strength parameter and γ a width. The resultant function, when fitted to the observed data, produced the fitted profiles represented by the smooth curves in figure 7 and the parameters for the E and A_1 spectra presented in figures 8 and 9.

Secondly, if coupling is presumed to occur between the low frequency modes, an inverse response function having matrix form

$$g^{-1}(\omega) = \begin{bmatrix} \omega_1^2 - \omega^2 + i\Gamma_1\omega & i\gamma\omega \\ i\gamma\omega & \omega_2^2 - \omega^2 + i\Gamma_2\omega \end{bmatrix}$$

must be postulated, having a response function given by

$$G(\omega) = \sum_{i,j} S_i S_j g_{ij}(\omega) .$$

The motivation for such an ansatz comes from the poor agreement between the observed and calculated lineshapes in the A_1 and F_2 symmetries (figures 7a and c). In fact, coupling did not improve the fitted description of the data and, in some cases, produced considerably poorer fits.

5. Discussion

5.1 Classification of room temperature modes

From table 1 it is evident that, while the correct number of A_1 symmetry bands are present, there is a dearth of both E and F_2 peaks. There are seven E peaks clearly visible along with, we suspect, a very weak feature around 360 cm^{-1} (see discussion below). This is a shortfall of two upon the predicted ten E modes. The most serious deficiency occurs in the F_2 symmetry, where only four peaks are found, the bracketed pair in table 1 being a TO-LO pair. This assertion is confirmed by comparison with the infrared results which also indicate that the 0-300 cm^{-1} spectrum is far more complex than it appears at first sight. This would account for the peculiar low frequency line profile in figure 2a.

Some clue as to the whereabouts of 'missing' bands can be gained from a comparison of the BO_4 molecular vibration frequencies obtained by fitting a generalised force field model for XY_4 molecules (Urey and Bradley 1931) to the vibrational frequencies of $Zn_4O(BO_2)_6$ and Cr-Cℓ (Murray and Lockwood 1976). These frequencies should be relatively insensitive to change of halogen or metal in the boracite formula, as such a change does not drastically disturb the B-O framework (Nelmes 1974, Nelmes and Thornley 1974). Comparison with Cr-Cℓ and $Zn_4O(BO_2)_6$ results suggest that the 378 $cm^{-1}(A_1)$ and 255 $cm^{-1}(F_2)$ modes can be associated with B-O framework vibrations. Furthermore, the existence of vibrations at frequencies around 300 $cm^{-1}(E)$ and 1100 $cm^{-1}(F_2)$ is suggested by this comparison. This would reinforce the presence of an E band at about 360 cm^{-1} and support the notion that the structure around 1100 cm^{-1} alluded to in §3.3 contains first order peaks. The comparable modes in Cr-Cℓ are at 375 $cm^{-1}(A_1)$, 232 $cm^{-1}(E)$ and 1160 cm^{-1}, 252 $cm^{-1}(F_2)$ (Murray and Lockwood 1976) and in Cu-Cℓ at 385 $cm^{-1}(A_1)$, 239 $cm^{-1}(E)$ and 1167 cm^{-1}, 264 $cm^{-1}(F_2)$ (Lockwood and Syme 1977). The insensitivity to metal substitution is clearly demonstrated.

The low frequency modes in all spectra are more heavily damped than their counterparts in Cr-Cℓ and Cu-Cℓ, particularly in the E symmetry, where the damping is roughly ten times greater for Ni - I. The lowering of frequencies from Cr-Cℓ and Cu-Cℓ to Ni - I produces a low frequency total cross section of great complexity, which may contribute to the shortening of the phonon lifetimes, and consequently higher damping. The frequency lowering also confirms that these vibrations are largely attributable to motions of the metal and halogen ions, in particular the latter.

The A_1 Debye wing is considerably narrower than in Cr-Cℓ and Cu-Cℓ, where the wing was conjectured as being due to disorder (Lockwood 1976). X-ray studies have shown that this disorder, if extant, is due only to the Cℓ ion, being most obvious in Cu-Cℓ, and corresponds to an uncorrelated displacement of the halogen ions along the [111] axes. The Raman results for Ni - I suggest that any disorder is much less than in Cℓ boracites, in accord with the room temperature X-ray results (Nelmes and Thornley 1974, 1976, Kennedy 1977). In addition, the Ni - I spectra contain a Debye wing in the E and F_2 symmetries, suggesting that the disorder lacks definite symmetry, and is consequently more homogeneous than in Cℓ boracites, where no such wing was observed.

From the fitted spectra in figure 7 it is apparent that the A and F_2 low frequency spectra are not adequately described by the model of §4.2. In the case of F_2 symmetry this is undoubtedly due to the complexity of the low frequency F_2 lineshape revealed by the infrared results (Petzelt and Mayerová 1973). Inspection of the two mode fit of figure 7a suggests, in fact, the presence of at least four bands. In the A_1 spectrum, where the numbers of observed and predicted modes agree, such an explanation is not valid. As the coupled mode analysis described in §4.2 did not improve the fits, the additional structure must be due to the small admixture of F_2 modes introduced by the form of the Raman tensors.

5.2 Temperature dependence of the modes

The normal behaviour of the parameters ω_o and Γ as temperature is decreased consists of a steady rise in ω_o with a drop in Γ, as the lattice contracts and anharmonic effects reduce. From figure 5 it can be seen that this behaviour is interrupted by an anomalous decrease in ω_o and increase in Γ for the high frequency E modes around 128 K. In figure 6, a similar effect is observed for the 655 cm^{-1} A_1 feature, although its proximity to the 611.5 cm^{-1} E mode made fitting less exact. This unusual phenomenon suggests that, in agreement with the X-ray work of Will and Marche (1977), the unit cell dimension expands and contracts again over the interesting temperature region. The calibration of the Raman spectra can be verified by studying the laser frequency, the krypton emission lines, and the duplication of E-symmetry peaks in the Z(X'X')Y' and Z(Y'X')Y' spectra.

The low frequency modes behave even more oddly. Figures 8 and 9 reveal frequency ω_o falling with decreasing temperature, with an anomalous rise at 128 K, and damping Γ decreasing more or less smoothly with decreasing temperature. Again, the parameters for the A_1 symmetry mode are more scattered due to the subtraction process, and are possibly somewhat unreliable due to the underlying F_2 component. Firstly, however, it can be gleaned from figures 8 and 9 that some disturbance in the lattice occurs at around 128 K. Secondly, the $\simeq$ 20 cm^{-1}(E) and $\simeq$ 15 cm^{-1}(A_1) mode softenings are completely uncharacteristic of boracite behaviour. This can be seen from the Cr-Cℓ and Cu-Cℓ spectra where only the A_1 Debye wing has strong temperature dependence, the other modes behaving normally. Such a softening is usually precursive to a displacive phase transition. Since the low frequency modes can be attributed largely to motions of the Ni and I atoms as described in §5.1, a transition to a phase with these atoms repositioned seems likely at some low temperature.

6. Conclusion

The Raman spectrum of Ni - I displays reasonable agreement with group theoretical predictions, considering the highly absorptive nature of the material, and indicates a cubic space group from 88 K to 300 K. The anomaly in the frequencies and linewidths of the Raman bands must be associated with the irregularities in the magnetic and dielectric properties. It is also consistent with the expansion of the lattice at around this temperature. The dielectric response is especially related to the F_2 modes and no useful predictions concerning dielectric variations can be obtained from our weak F_2 spectra. Such information should, however, result from an exhaustive infrared study of cubic Ni - I.

The interesting dynamic changes occur in the low frequency boracite spectra. This region for Ni - I contains many modes, and the complex interactions required to explain the observed temperature dependence cannot be determined from the Raman spectra alone.

Work is in progress to further investigate both the unusual A_1 and E mode softening and the dynamics of the ferroelectric transition.

7. Acknowledgements

We are grateful to Dr. H. Schmid for invaluable discussions on the physical properties of boracites and to Dr. R.J. Nelmes for discussions on structural aspects of Ni - I. This work was supported by the SRC (AFM), the Battelle Research Centre, Geneva, and the U.S. Army Research and Development Group (Europe) (DJL).

References

Arthur J W and Lockwood D J 1974 J. Raman Spectrosc. 2 53-69

Arthur J W and Murray A F 1977 to be published

Ascher E, Rieder H, Schmid H and Stössel H 1966 J. App. Phys. 37 1404-5

Dormann E 1970 J. Phys. Chem. Solids 31 199-214

Kennedy N S J 1977 PhD thesis University of Edinburgh

Lockwood D J 1976 Ferroelectrics 13 353-4

Lockwood D J, Rivera J-P and Schmid H 1977 to be published

Lockwood D J and Syme R W G 1977 Ferroelectrics to be published

Loudon R 1964 Adv. Phys. 13 423-82 (erratum 14 621)

Murray A F and Lockwood D J 1976 J. Phys. C: Solid St. Phys. 9 3691-700

Nelmes R J 1974 J. Phys. C: Solid St. Phys. 7 3840-54

Nelmes R J and Thornley F R T 1976 J. Phys. C: Solid St. Phys. 9 655-80

Nelmes R J and Thornley F R T 1974 J. Phys. C: Solid St. Phys. 7 3855-74

Petzelt J and Mayerová I 1973 Czech. J. Phys. B23 1277-80

Rehwald W 1977 private communication

Schmid H 1965 J. Phys. Chem. Solids 26 973-88

Schmid H 1969 Growth of Crystals 7 25-52 (New York Consultants Bureau)

Thornley F R T, Kennedy N S J and Nelmes R J 1976 J. Phys. C: Solid St. Phys. 9 681-92

Urey H C and Bradley C A 1931 Phys. Rev. 38 1969-78

Will G and Morche H 1977 J. Phys. C: Solid St. Phys. 10 1389-94

Table 1

Resonant frequencies $\omega_o(cm^{-1})$, damping parameters $\Gamma(cm^{-1})$ and assignments for the Raman active modes and frequencies for the infrared active modes (Petzelt and Mayerová 1973) of Ni - I.

A_1		E		F_2		F_2 (infrared)	
ω_o	Γ	ω_o	Γ	ω_o	Γ	ω_o^{TO}	ω_o^{LO}
81.5	61	84.5	35	74.5	48	42	42
163.5	76	170.0	90	152.5	42	54	70
378.0[a]	18[a]	611.5	20	255.0	b	89	91
655.0	30	863.5	15	280.0	b	112	114
		943.0	36			135	136
		1125.5	43			168	168
		1199.5	74			195	198
						224	226
						258	286
						308	308
						320	322

All ω_o and Γ are from computer fits except:

[a] Measured from spectrum

[b] Measured from spectrum and too weak for assignment of Γ

Figure Captions

Figure 1. Temperature dependence of the dielectric (ε) and magnetic (χ_g) susceptibilities (Ascher et al. 1966) and the lattice constant (a_o) (Will and Morche 1977) of Ni - I in the cubic phase.

Figure 2. The room temperature Raman spectra of Ni - I in the different scattering geometries

a) Z(Y'Z)Y' , F_2 modes

b) Z(Y'X')Y' , E modes

c) Z(X'X')Y' , $A_1 + E + F_2$ modes

d) Subtracted spectrum (see § 3), $A_1 + F_2$ modes

Figure 3. The E symmetry Raman spectrum of Ni - I at different temperatures.

Figure 4. The A_1 (+ F_2) symmetry Raman spectrum of Ni - I at different temperatures.

Figure 5. Temperature variation of the resonant frequency ω_o (squares) and damping Γ (triangles) of some E symmetry modes of Ni - I. The lines are intended merely as a guide to the eye.

Figure 6. Temperature variation of the resonant frequency ω_o (squares) and damping Γ (triangles) of the 655.0 cm^{-1} A_1 symmetry mode.

Figure 7. The low frequency spectra of Ni - I with theoretical fits (smooth lines) in terms of two oscillators plus a Debye-like wing: /

Figure 7 a) F_2 symmetry.

b) E symmetry.

c) A_1 (+ F_2) symmetry.

Figure 8. Temperature variation of the resonant frequency ω_o (squares) and damping Γ (triangles) of the 170.0 cm^{-1} E symmetry mode. The lines are intended merely as a guide to the eye.

Figure 9. Temperature variation of the resonant frequency ω_o (squares) and the damping Γ (triangles) of the 163.5 cm^{-1} A_1 symmetry mode.

Figure 1

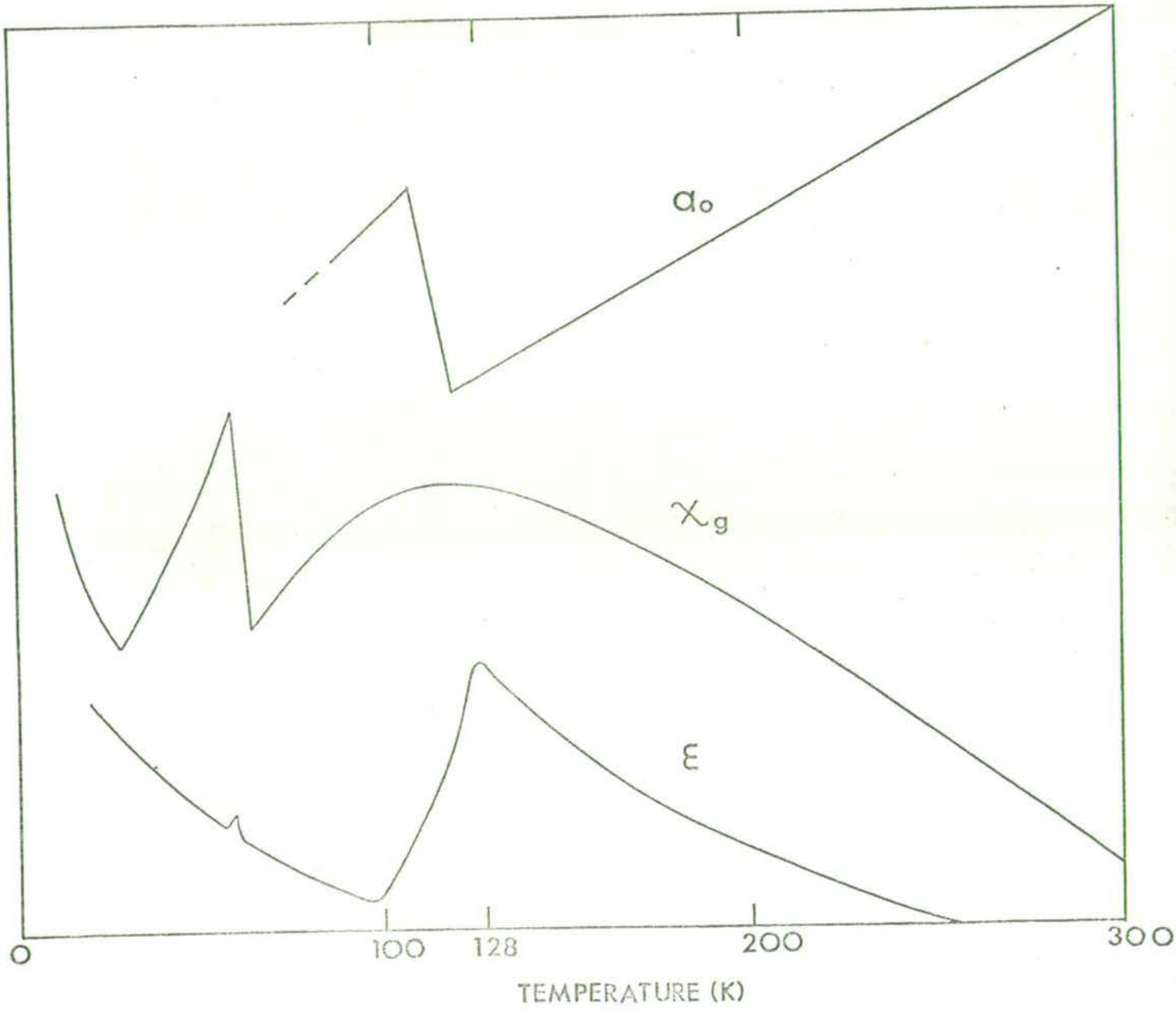

Figure 2

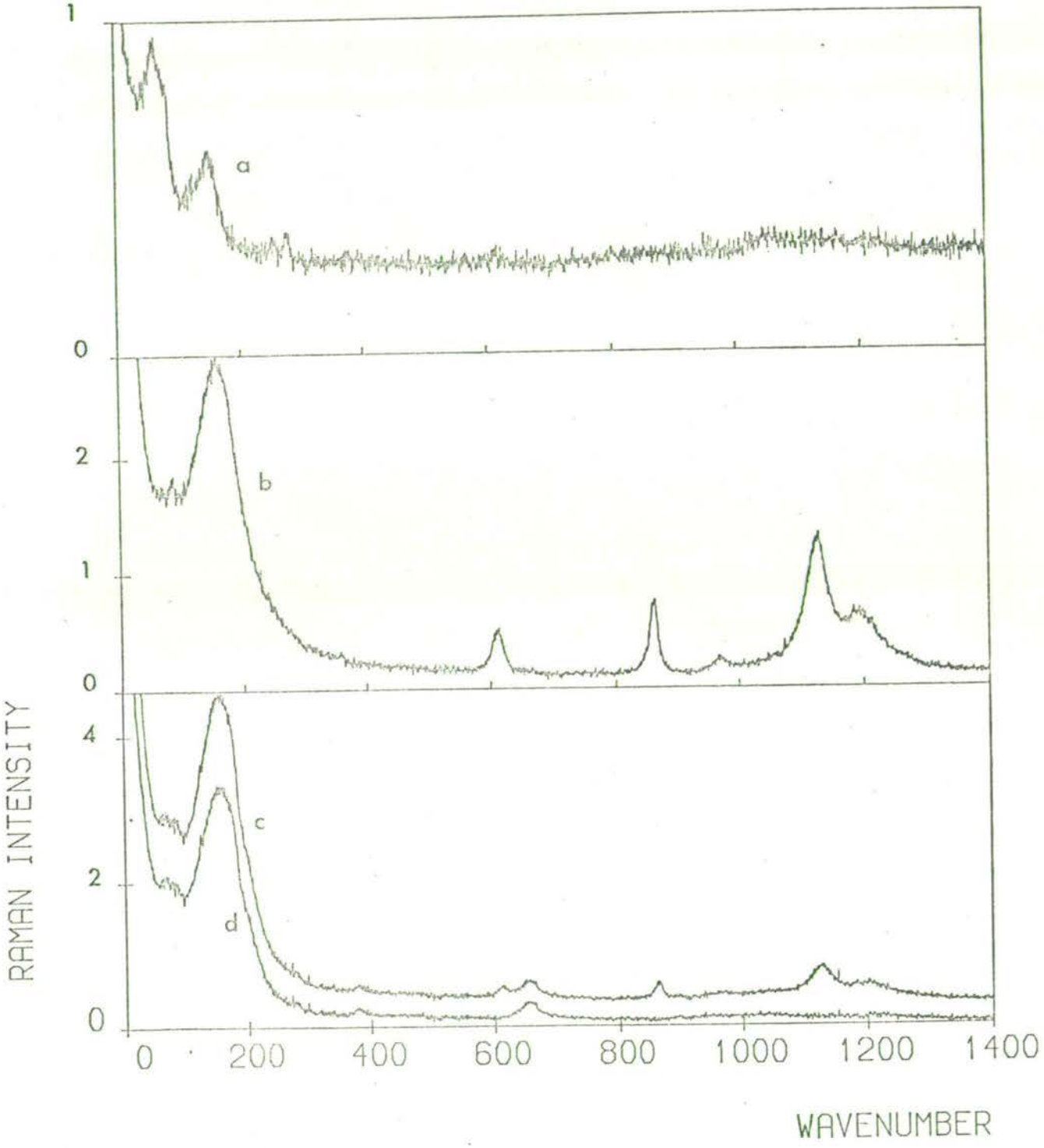
1
a
0
2
b
1
0
4
c
2
d
0
RAMAN INTENSITY
0
200
400
600
800
1000
1200
1400
WAVENUMBER

Figure 3

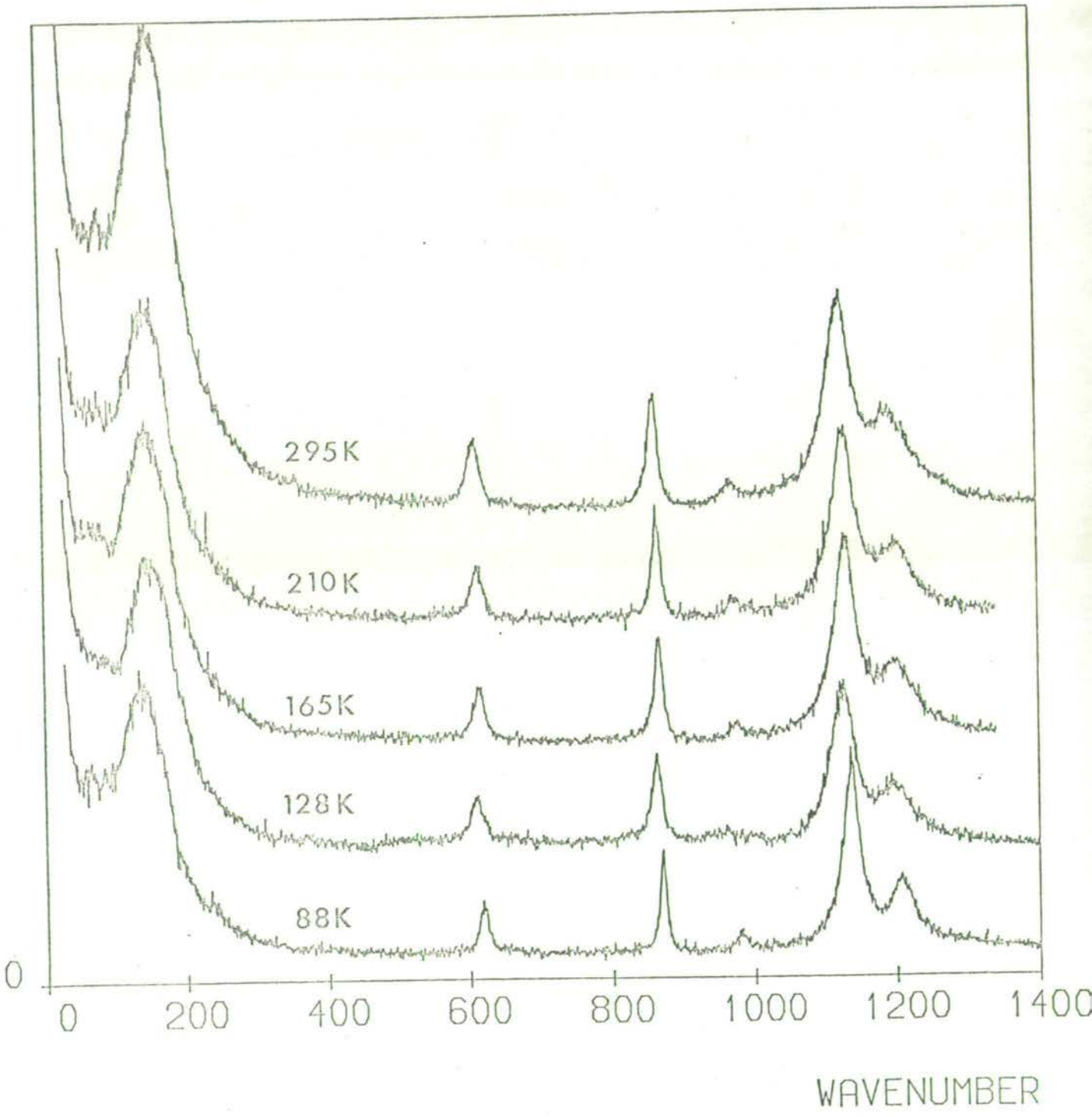
295K
210K
165K
128K
88K
0
0
200
400
600
800
1000
1200
1400
WAVENUMBER

Figure 4

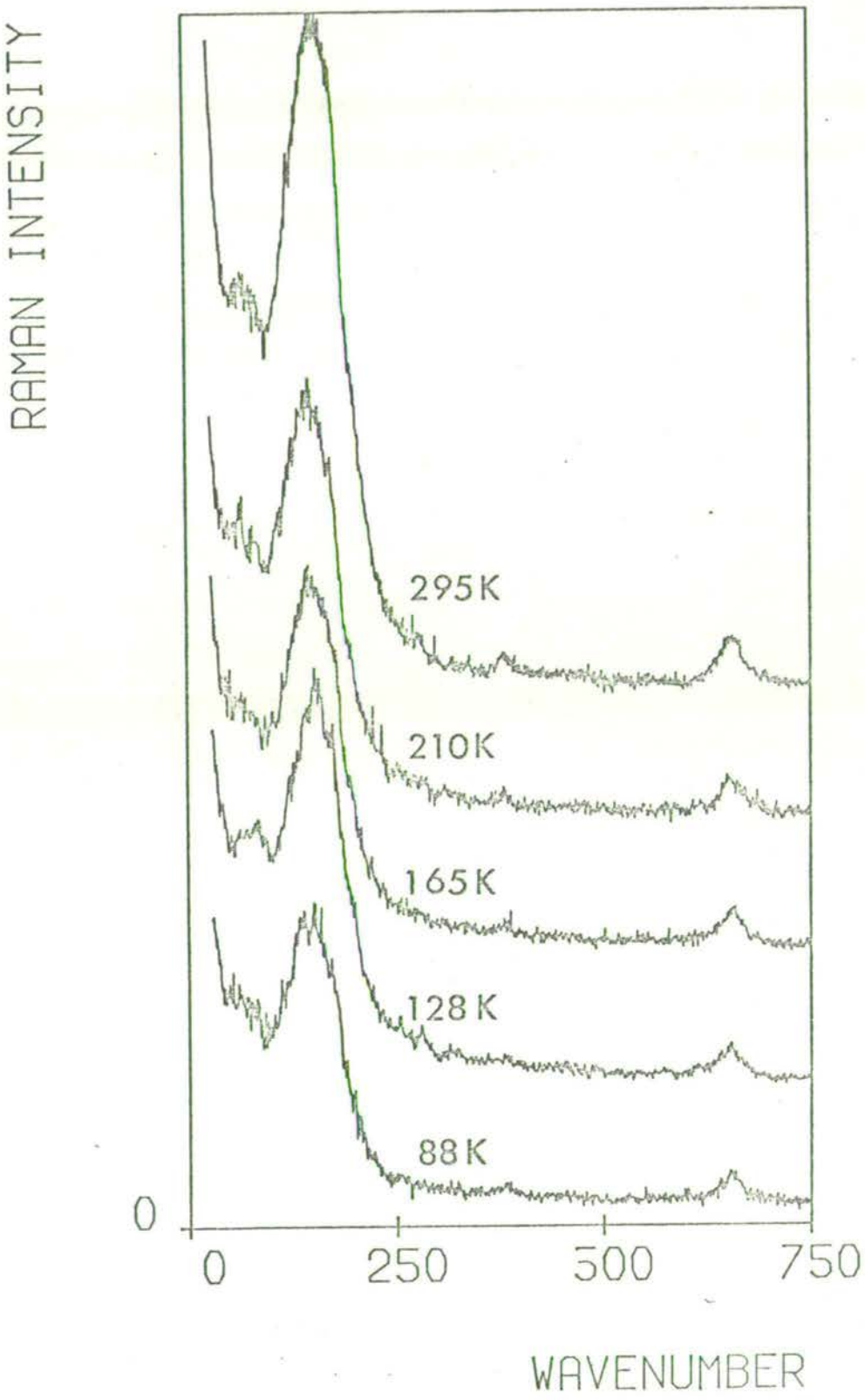
RAMAN INTENSITY
295K
210K
165K
128K
88K
0
0
250
500
750
WAVENUMBER

Figure 5

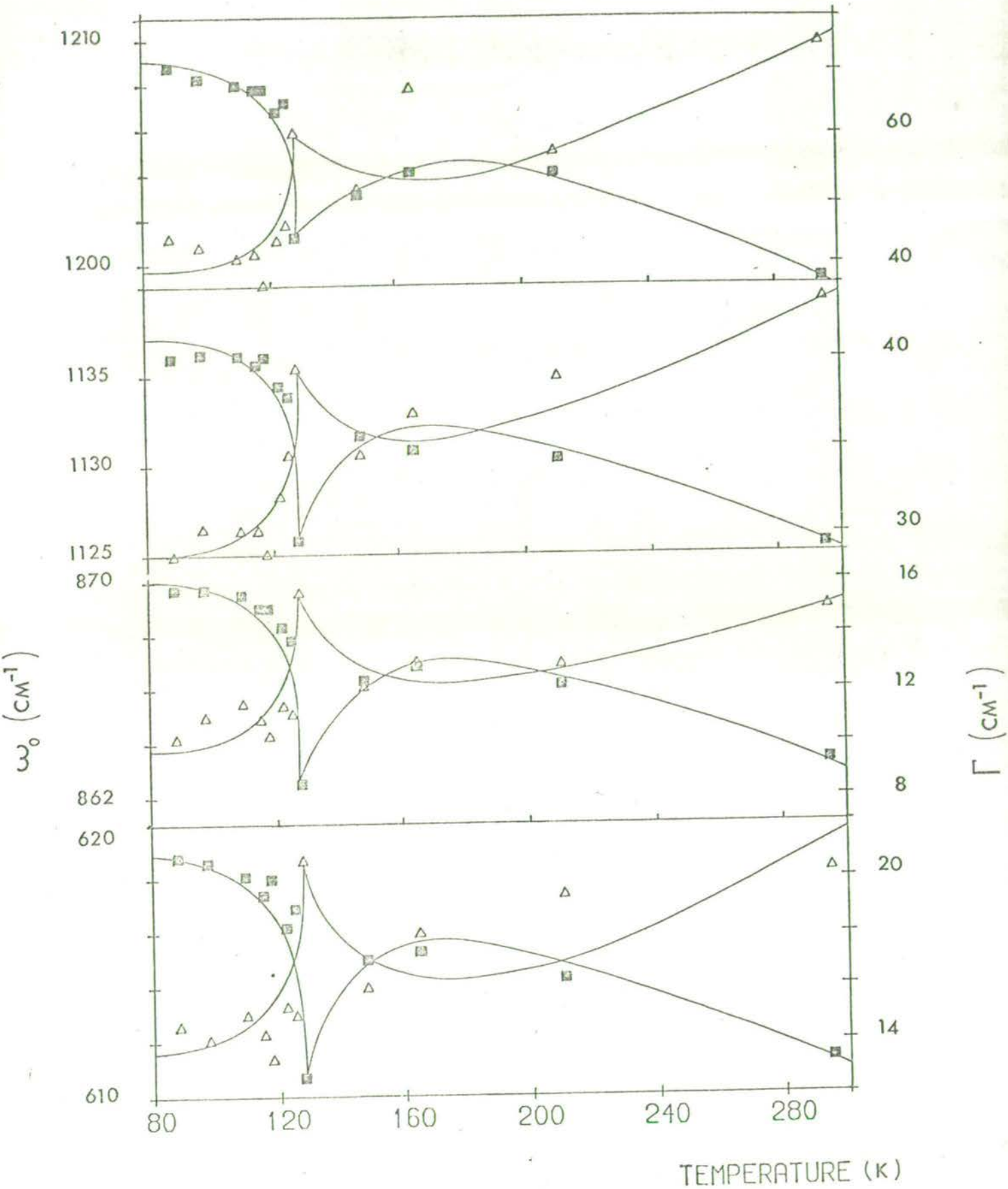
1210
1200
1135
1130
1125
870
862
620
610
60
40
40
30
16
12
8
20
14
80
120
160
200
240
280
TEMPERATURE (K)
ω₀ (CM⁻¹)
Γ (CM⁻¹)

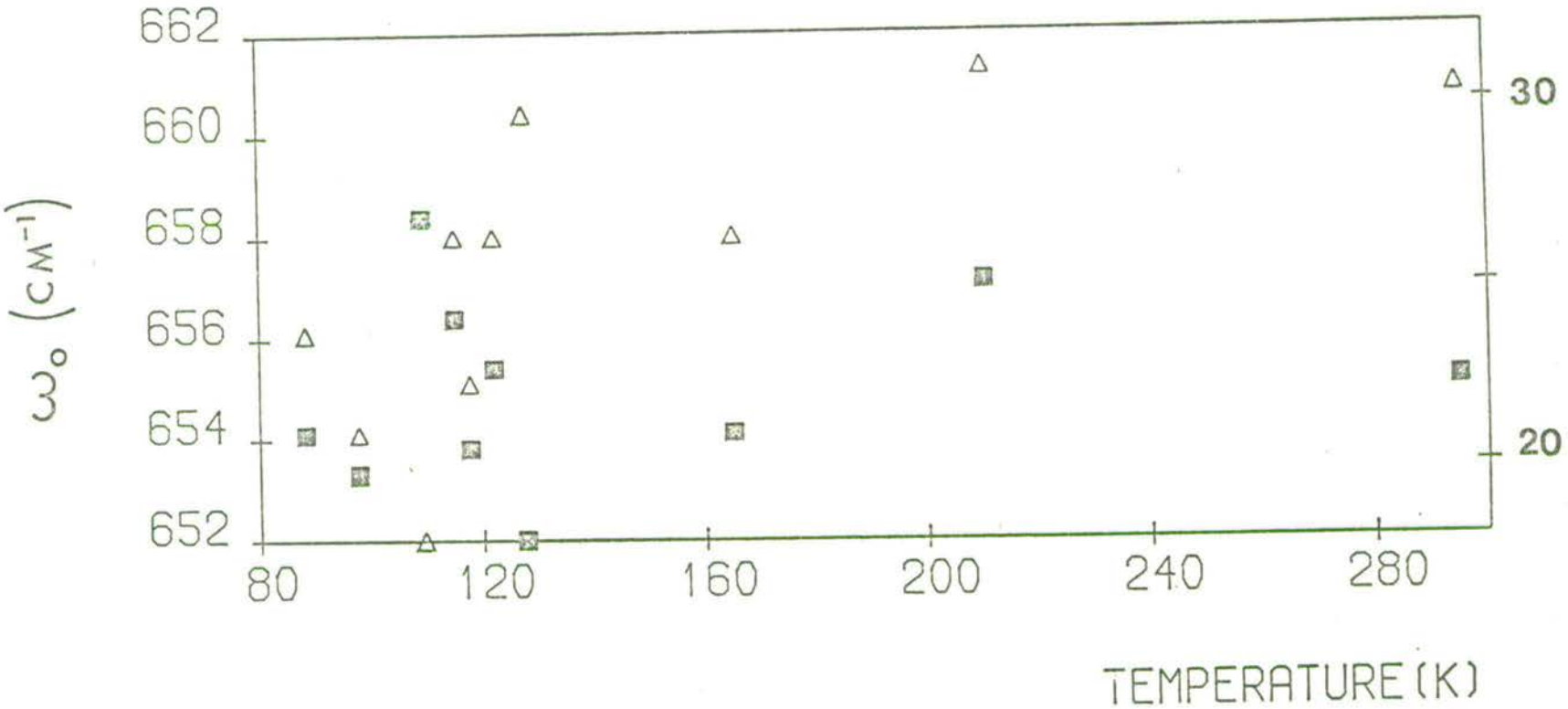
662
660
658
656
654
652
80
120
160
200
240
280
30
20
ω_o (CM^{-1})
Γ (CM^{-1})
TEMPERATURE (K)

Figure 4

Figure 8

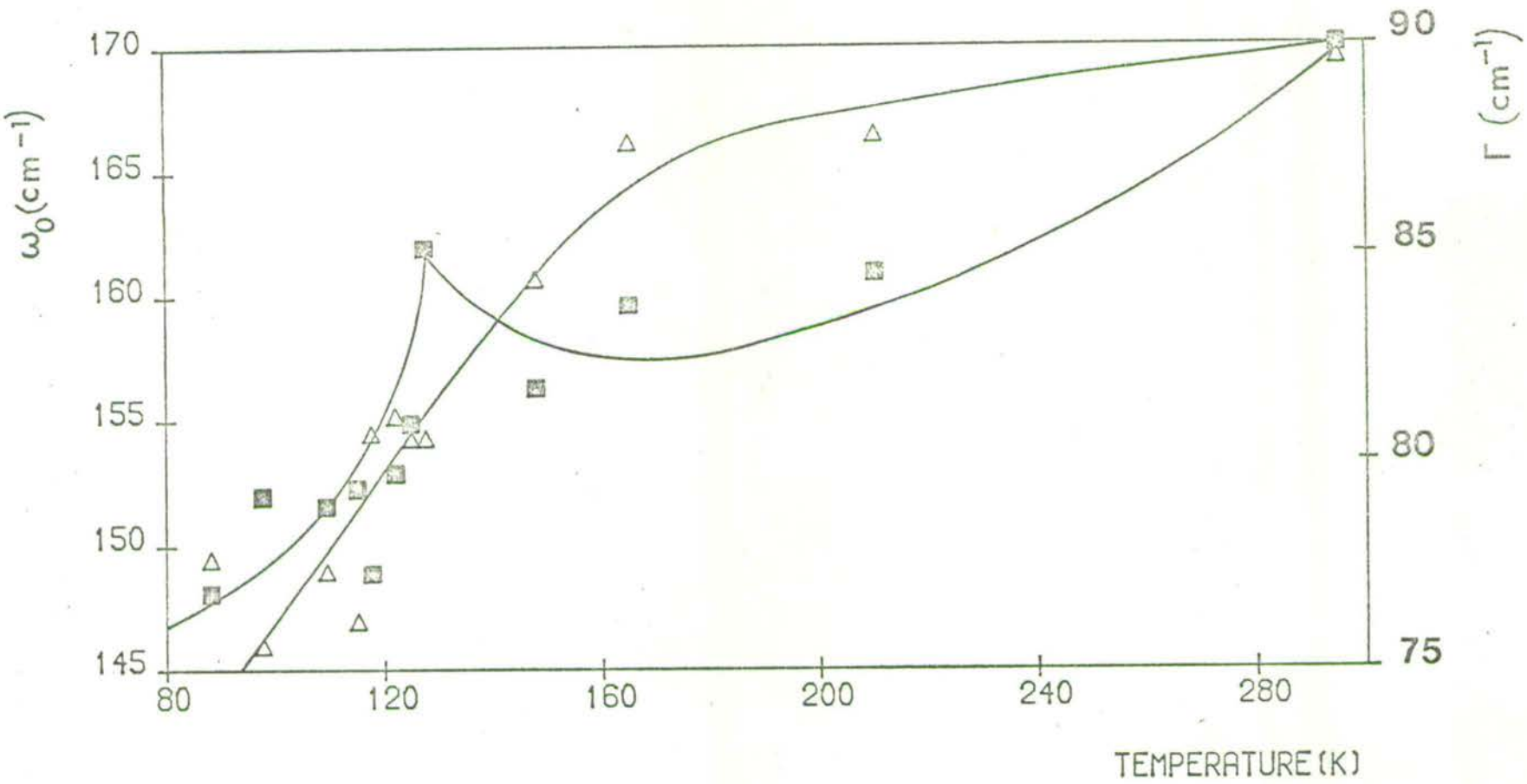
170
165
160
155
150
145
$\omega_0(cm^{-1})$
90
85
80
75
$\Gamma\ (cm^{-1})$
80
120
160
200
240
280
TEMPERATURE (K)

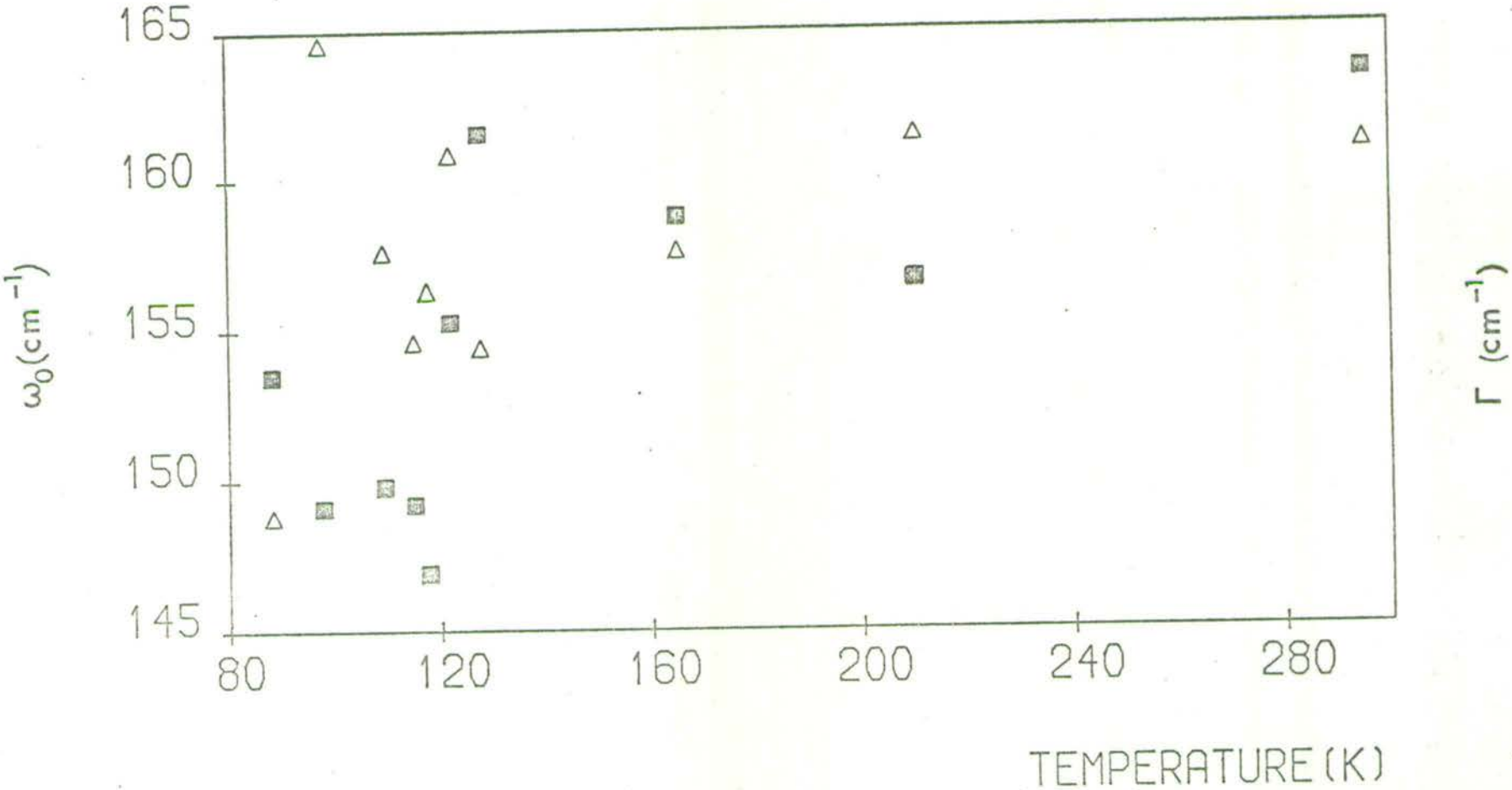
165
160
155
150
145
$\omega_0(cm^{-1})$
80
120
160
200
240
280
TEMPERATURE (K)
$\Gamma\ (cm^{-1})$

Figure 9.

TEMPERATURE-DEPENDENT ELECTRON-PHONON COUPLING IN $FeCl_2$ OBSERVED BY RAMAN SCATTERING

I. W. JOHNSTONE, D. J. LOCKWOOD* and G. MISCHLER†

Department of Physics, University of Nottingham, University Park, Nottingham NG7 2RD, England

*Department of Physics, Edinburgh University, Edinburgh EH9 3JZ, Scotland

†Laboratoire de Physique des Solides, Associé au CNRS, 31077 Toulouse Cédex, France.

ABSTRACT: Strong coupling between an electronic transition in the $^5T_{2g}(^5D)$ manifold of Fe^{2+} ions in $FeCl_2$ and the E_g phonons in this material has been observed by light scattering. The Raman spectrum is temperature dependent and shows a marked change at the antiferromagnetic ordering temperature. Above T_N, the spectrum contains a symmetric band which becomes asymmetric on the high energy shoulder when the temperature is lowered. Just below T_N the band comprises two sharp features accompanied by a third broad band. Well below T_N the sharp features have coalesced. A simple model is presented which successfully accounts for the observed temperature dependence of the band-position,-width, and structure.

Short Title: Electron-Phonon Coupling in $FeCl_2$.

"Inspec" Classification Numbers: 78.30, 75.30

1. INTRODUCTION

Since all ferrous compounds have significant orbital contributions to their magnetic moments and a corresponding complexity of low-lying electronic energy levels, they have the potential to display strong electron-phonon interactions. The most commonly observed of these are magnetoelastic in character and in $FeCl_2$, the magnon-phonon interaction has been widely studied. The first observations of magnon-phonon effects were by Laurence and Petigrand (1973), who interpreted an anomaly in the thermal conductivity of antiferromagnetic $FeCl_2$ as arising from coupling between the TA(ξ00) phonon branch and the magnons. Using their results, Lovesey (1974) determined the repulsion between the acoustic phonon and magnon branches at the 'cross-over' point. Subsequently, Cracknell (1974) group-theoretically determined the selection rules for magnon-phonon interactions in $FeCl_2$ and verified that the coupling predicted by Laurence and Petigrand (1973) was symmetry allowed.

Earlier, in a neutron-scattering study of the antiferromagnetic properties of $FeCl_2$, Birgenau et al. (1972) observed magnetic excitations at energies of 17 and 21 MeV, at 5 K. The structure of the spectra for various $\underline{k}$ values was complicated, but they were able to deduce from their temperature-dependent study that the 17 MeV band did not have purely magnetic, but mixed exciton-phonon character.

Now, as a result of a light scattering study from phonons and electronic excitations in $FeCl_2$ (Johnstone et al. 1978), we have obtained detailed information on this strong electron-phonon coupled mode near 150 cm^{-1} (for $\underline{k}$ = 0 phonons). The Raman results presented in Section 3 indicate that the spectrum has a marked temperature

dependence, a behaviour which is readily described in terms of the simple model presented in Section 4.

2. EXPERIMENT

The dark yellow-brown colour of $FeCl_2$ necessitates surface scattering experiments. Samples were prepared in a dry box by cleaving sections along planes perpendicular to the crystal c-axis from boules grown by the Stockbarger method. The quality of the crystal surface determines the quality of the Raman spectrum and so care was taken to prepare a plane surface, free from undulations and scratches, by carefully peeling away a final, thin crystal layer. Freshly prepared samples were immediately mounted in a Thor 500 flow cryostat, where the sample is cooled by direct contact with the refrigerant. A chromel/gold-iron thermocouple mounted on the crystal surface was used to monitor the sample temperature.

Weak spin-forbidden optical transitions occur in $FeCl_2$ at 11850, 14850 and 18150 cm^{-1} (Freeman 1968). In order to minimize laser heating of the sample, and to maximize the scattered light intensity, the Raman spectrum was excited with $\sim$ 100 mW of 647.1 nm (15433 cm^{-1}) radiation from a Spectra Physics 165 Krypton laser. Other commonly used Krypton (e.g. 676.4 nm or 14784 cm^{-1}) and argon laser lines were too heavily absorbed while the blue/green lines also produced intense fluorescence.

The laser light was directed along the c-face of the crystal with polarization in the plane of incidence. In this grazing incidence configuration, the scattered light is largely depolarized and therefore, no polarization measurements were attempted. The 90° scattered light was dispersed with a Coderg T800 triple monochromator having a spectral

resolution of 1.8 cm^{-1} and the Raman signal detected with an RCA C31034A photomultiplier. Data collection was carried out automatically under computer control (Arthur and Lockwood 1974).

3. RESULTS

Representative spectra, recorded at temperatures above and below T_N (23.5 K) and covering the frequency range of interest are given in Figure 1. A sharp feature can be seen at $\sim$ 250 cm^{-1} and a broad band at $\sim$ 145 cm^{-1}. This latter feature has a most peculiar temperature dependence, exhibiting a marked change at T_N. Well below T_N, the spectrum comprises a very sharp peak at 141.1 cm^{-1} accompanied by a broad band at 165.8 cm^{-1}. As the temperature is raised the sharp band splits and the broad band decreases in energy until at T_N all features are superimposed. Just above T_N the band shape remains markedly asymmetric. Simultaneously there are marked relative intensity changes compared with the band near 250 cm^{-1}. It is difficult to obtain a width for such a complex band shape. However, at 12 K both sharp features are resolution-limited in width. Peak frequencies found at various temperatures are listed in Table I, including details of the structure found for $T < T_N$. The temperatures given in Table I have been corrected for localized laser heating of the order of 10 K by comparing the observed T_N with the known value of 23.5 K, since the conspicuous changes in the electronic spectra that occur at T_N are an excellent indicator of the transition.

Crystals with the $CdCl_2$ structure possess two Raman-active normal modes at $\underline{k} = 0$ of $A_{1g}(\Gamma_1^+)$ and $E_g(\Gamma_3^+)$ symmetry, respectively. (Lockwood 1973). Raman studies of $CdCl_2$, $MnCl_2$ and $CoCl_2$ have

shown that typical frequencies for these phonons are 235 cm^{-1} (A_{1g}) and 145 cm^{-1} (E_g). (Lockwood 1973). Comparison with the results listed in Table I indicates that the sharp peak at 246 cm^{-1} (277. K) is the A_{1g} phonon of $FeCl_2$. The temperature dependence of this band, both in frequency and damping, is characteristically phonon-like, and supports this assignment. It could be anticipated that the remaining band at 144 cm^{-1} (277 K) is the other, E_g, phonon, because it has the expected frequency. However, the temperature dependence of the width and shape of this band is highly irregular. Transitions between crystal-field states of Fe^{2+} can occur in this frequency region, and comparison with the Raman spectrum of a similar material, $FeBr_2$ (Johnstone et al. 1978), shows that this is indeed the case. Furthermore, energy level calculations for the $^5T_{2g}(^5D)$ manifold of Fe^{2+} in $FeCl_2$ (Johnstone et al. 1978) predict an electronic transition near 150 cm^{-1}. Therefore, there is close proximity of electronic and phonon energy levels at $\sim$ 150 cm^{-1} with the consequent possibility of effects due to strong symmetry allowed electron-phonon coupling. In the next section we develop a theory of the coupling that predicts the observed temperature dependence.

4. THEORY

The energies of coupled electron-phonon excitations may be derived using a Hamiltonian of the form:

$$\mathcal{H} = \mathcal{H}_o^{ph(1)} + \mathcal{H}_o^{ph(2)} + \mathcal{H}_o^{el} + \mathcal{H}_{int}^{(1)} + \mathcal{H}_{int}^{(2)} \qquad (4.1)$$

where $\mathcal{H}_o^{el}$, $\mathcal{H}_o^{ph(1)}$ and $\mathcal{H}_o^{ph(2)}$ describe the unperturbed energies of the

electron, non-resonant, and resonant phonons respectively. The electron-phonon interaction has two parts; namely $\mathscr{H}_{int}^{(1)}$, the non-resonant interaction with the phonons which gives rise to Jahn-Teller effects, and $\mathscr{H}_{int}^{(2)}$ describing any resonant interaction. This latter term becomes important in the rare case when the phonon energy $\hbar\Omega_o$ equals the energy $\hbar\omega_o$ of a particular electronic transition. As can be seen in Figure 2, when this occurs the levels $|e,0,0>$, $|g,0,1>$ and $|g,1,0>$ coincide. Any coupling between them is then particularly effective and gives rise to splittings with mixed electron-resonant-phonon eigenstates.

For Fe^{2+} ions the energies of $\mathscr{H}_o^{el}$ are those of the d^6 configuration. In particular, the cations in $FeCl_2$ are located at inversion centres of D_{3d} symmetry and experience a static crystal-field which has a 1% trigonal distortion from cubic (Carrara 1968). The combined action of this and the spin-orbit coupling, on the $^5T_{2g}(^5D)$ cubic ground term gives rise to the energy level scheme in Figure 3. The energies of transitions have been calculated by Johnstone et al. (1978) using a model for which it was necessary to include a dynamic Jahn-Teller interaction in the Hamiltonian to obtain good agreement with experiment. That is, $\mathscr{H} = \mathscr{H}_o^{ph} + \mathscr{H}_o^{el} + \mathscr{H}_{int}^{(1)}$. Strictly then, all the states are already vibronic in character but for simplicity we will continue to refer to them as being electronic.

The unperturbed energies of the doubly-degenerate resonant E_g phonons may be represented as an harmonic oscillator so that its energies may be represented by the Hamiltonian:

$$\mathscr{H}_o^{ph(2)} = \hbar\Omega_o(a_\theta^\dagger a_\theta + a_\varepsilon^\dagger a_\varepsilon) \qquad (4.2)$$

neglecting the zero-point energies, and where the $a_\theta^\dagger, a_\theta$ ... are the phonon creation and annihilation operators.

The symmetries of the wavefunctions for the coupled electronic-resonant phonon system are obtained from the product representations of the phonon and electronic states of interest as follows (see Figure 3):

$$\Gamma_1^{+ph} \times \Gamma_3^{+el} = \Gamma_3^+$$

$$\Gamma_1^{+ph} \times \Gamma_1^{+el} = \Gamma_1^+$$

$$\Gamma_3^{+ph} \times \Gamma_3^{+el} = \Gamma_1^+ + \Gamma_2^+ + \Gamma_3^+$$

which are in turn, linear combinations of states of the form $|n_\theta n_\varepsilon \Gamma_k^{+el}\rangle$ where n_θ, n_ε denote the harmonic oscillator occupation numbers for the doubly-degenerate E_g phonons and Γ_k^{+el} $(k = 1,2,3\theta,3\varepsilon)$ the symmetry of the particular electronic state.

The electronic-resonant phonon interaction is written as:

$$\mathscr{H}_{int}^{(2)} = V\left[E_\theta(a_\theta^\dagger + a_\theta) + E_\varepsilon(a_\varepsilon^\dagger + a_\varepsilon)\right] \tag{4.3}$$

where E_θ, E_ε are electronic orbital operators with the following non-zero matrix elements:

$$\langle\Gamma_1^{+el}|E_\theta|\Gamma_{3\theta}^{+el}\rangle = \langle\Gamma_1^{+el}|E_\varepsilon|\Gamma_{3\varepsilon}^{+el}\rangle = 1$$

and which transform as the θ and ε representations respectively, while V is the strength of the interaction. Since the interaction has Γ_1^+ symmetry it follows that only the two Γ_1^+ states will be mixed by the

interaction while those of Γ_2^+, Γ_3^+ symmetry will remain unperturbed. The full Hamiltonian $\mathcal{H}$ has eigenvalues and eigenstates:

$$\Gamma_1^{+(2)}: E = \tfrac{1}{2}\hbar(\Omega_o+\omega_o) + \sqrt{2V^2 + \frac{\hbar^2}{4}(\Omega - \omega_o)^2} \quad \cos\rho|\text{oo}\Gamma_1^+\rangle + \sin\rho|x\rangle$$

$$\Gamma_2^+, \Gamma_3^{+(2)}: E = \hbar\Omega_o \qquad |\text{1o}\Gamma_{3\varepsilon}^+\rangle \quad \frac{1}{\sqrt{2}}\{|\text{1o}\Gamma_{3\theta}^+\rangle - |\text{o1}\Gamma_{3\varepsilon}^+\rangle\} \quad |\text{o1}\Gamma_{3\theta}^+\rangle$$

$$\Gamma_1^{+(1)}: E = \tfrac{1}{2}\hbar(\Omega_o + \omega_o) - \sqrt{2V^2 + \frac{\hbar^2}{4}(\Omega - \omega_o)^2} \quad \cos\rho|x\rangle - \sin\rho|\text{oo}\Gamma_1^+\rangle$$

$$\Gamma_3^{+(1)}: E = 0 \qquad |\text{oo}\Gamma_{3\theta}^+\rangle \quad |\text{oo}\Gamma_{3\varepsilon}^+\rangle$$

where $|x\rangle = \frac{1}{\sqrt{2}}\{|\text{1o}\Gamma_{3\theta}^+\rangle + |\text{o1}\Gamma_{3\varepsilon}^+\rangle\}$ and $\tan 2\rho = -2\sqrt{2}V/\hbar(\omega_o - \Omega)$. They are given again in Figure 4 for V = 5 cm^{-1}.

A single electronic transition $\hbar\omega_o$ near 150 cm^{-1} would be expected to split under $\mathcal{H}_{int}^{(2)}$ into three delta functions, the central peak being associated with the $\Gamma_2^+, \Gamma_3^{+(2)}$ phonons and the pair to higher and lower energy with the $\Gamma_1^{+(2)}$ and $\Gamma_1^{+(1)}$ modes respectively. In reality both the unperturbed phonons and electronic states have finite line widths. The electronic transitions in $FeCl_2$ to higher energy typically have linewidths of 30 to 40 cm^{-1} (Johnstone et al. 1978). Contributions to their linewidths come from the coupling of the electronic d^6 states to the lattice via a dynamic Jahn-Teller interaction (i.e. $\mathcal{H}_{int}^{(1)}$), inhomogeneous broadening due to local strains, spin-spin and dipolar interactions between adjacent Fe^{2+} ions. Furthermore, hot band transitions from the $|1o\rangle$ state (Figure 3), which will be significantly populated above 10 K, give unresolved structure on the low frequency

shoulders of all bands. Hence, we represent the electronic transitions as a Gaussian distribution of frequencies peaked at ω_o, with a half-width of 30 cm^{-1} and intensity I, and the unperturbed phonon transition as due to classical oscillators with a half-width of 3 cm^{-1} and intensity I'. The linewidths and intensities of the $\Gamma_1^{+(1)}$ and $\Gamma_1^{+(2)}$ coupled modes, together with the strength of the interaction V will be regarded as adjustable parameters.

The envelope of the coupled mode spectrum is obtained by mapping the Gaussian at $\hbar\omega_o$ onto the solutions of $E(\omega_o)$ for the $\Gamma_1^{+(1)}$ and $\Gamma_1^{+(2)}$ modes and then adding algebraically the central peak intensity due to the Γ_2^+, $\Gamma_3^{+(2)}$ states. The temperature dependence of the band is then explained in terms of the effects on the convoluted envelope by a shift of $\hbar\omega_o$ to higher energy. Thus, for $\hbar\omega_o = \hbar\Omega_c =$ 146 ~~145.4~~ cm^{-1} measured at 162 K we obtain, ignoring the Bose weighting factor, a smooth, symmetric band shape which is consistent with experiment. Just above T_N the band becomes asymmetric which correlates with a small positive shift in $\hbar\omega_o$ produced by the effect of short-range order between neighbouring ferrous ions. On cooling to T_N the crystal becomes antiferromagnetically ordered and the new energies of the shifted and split $|JJ_Z>$ states may be estimated with a molecular field approximation, assuming little dispersion of the higher frequency bands. Such a calculation (Johnstone et al. 1978) fitted to experiment at 12 K predicts a +24 cm^{-1} shift to higher energy for the $|20>$ level. If the convolution is repeated in an analogous manner for $\hbar\omega_o$ = 163 ~~171~~ and $\hbar\Omega$ = 14~~1~~ 102 cm^{-1} (12 K) one obtains the band shape in Figure 5 where the relative intensities of the contributions from each mode have been weighted to agree with experiment. The model successfully predicts a sharp, closely-split doublet to the low energy side of a broad, slightly asymmetric band. The doublet splitting

and the relative displacement of the two bands is a measure of the repulsion energy of the coupled modes and the temperature of the crystal. Between T_N and 0 K, the renormalization of the exciton shifts the effective frequency $\hbar\omega_o$ to higher energy which produces an asymptotic reduction in the splitting of the $\Gamma_1^{+(1)}$ and $\Gamma_2^+, \Gamma_3^{+(2)}$ modes. A rapid increase of intensity of this sharp band is consistent with the final merging of the two while the broad band near 170 cm^{-1} will continue to shift to higher energy. This predicted temperature dependence is clearly reproduced in Figure 5 for a temperature independent repulsion energy, V, at the cross-over point equal to 5 cm^{-1}.

5. CONCLUSIONS

The complexities in the 150 cm^{-1} region of the energy spectrum of $FeCl_2$ alluded to, but unexplained in the work of Birgenau et al. (1972), have been successfully attributed to electron-phonon coupling between accidentally degenerate states of the two systems levels. The simple model of Section 4 accounts for the observed band frequency, width and structure at all temperatures. However, this model is partly phenomenological because the band intensity, frequency and damping are treated as adjustable parameters. It is easy to estimate frequency parameters from the data, but accurate values for intensity and damping constants can only be obtained with difficulty from a deconvolution of the spectral line shape.

A more sophisticated analysis of these results taking into account whole crystal states when considering the electron-phonon coupling for $T < T_N$ is being undertaken. It will also consider possible intensity and line width mechanisms since an understanding of the intensity would

be of great interest in regard to the role of the dynamic Jahn-Teller effect.

ACKNOWLEDGEMENTS

We wish to thank Professor K. W. H. Stevens for his critical reading of this manuscript and to acknowledge useful discussions with Drs. C. A. Bates and J. R. Fletcher. We also thank Dr. G. D. Jones and Mr. R. Ritchie of the University of Canterbury, New Zealand for providing the $FeCl_2$ crystal. This work was supported by the SRC (IWJ), the DHHS (DJL) and the Royal Society and CNRS through the award of a European Exchange Programme visit to Edinburgh (GM).

TABLE I. Temperature dependence of peak frequencies (± 0.4 cm^{-1}) of the A_{1g} phonon and coupled electronic-resonant phonon band in the Raman spectrum of $FeCl_2$

TEMPERATURE (K)	ELECTRONIC-RESONANT PHONON BAND (cm^{-1})			A_{1g} PHONON (cm^{-1})
12	165.8		141.1	250.1
16	163.8	141.5	139.9	249.9
22	154.0	142.9	140.8	249.7
24			146.0	249.7
37			148.7	249.6
50			149.1	249.5
69			148.2	249.1
105			146.3	248.7
144			145.7	248.3
162			145.4	248.1
189			144.9	247.8
277			143.9	246.2

REFERENCES

Arthur, J. W. and Lockwood, D. J., 1974, J. Raman Spectrosc., 2, 53-69.

Birgenau, R. J., Yelon, W. B., Cohen, E. and Makovsky, J., 1972, Phys. Rev. B 5, 2607-15.

Carrara, P., 1968, These Universite Paris IX, France.

Cracknell, A. P., 1974, J. Phys. C: Solid State Phys., 7, 4323-34.

Freeman, T. E., 1968, M.Sc. Thesis, University of Canterbury, New Zealand.

Johnstone, I. W., Lockwood, D. J. and Mischler, G., 1978, to be published.

Laurence, G. and Petitgrand, D., 1973, Phys. Rev. B, 8, 2130-38.

Lockwood, D. J., 1973, J. Opt. Soc. Am., 63, 374-82.

Lovesey, S. W., 1974, J. Phys. C: Solid State Phys., 7, 2049-59.

FIGURE CAPTIONS

FIGURE 1. The Raman spectrum (50-300 cm^{-1}) of $FeCl_2$ recorded at various temperatures: (a) 277 K, (b) 162 K, (c) 105 K, (d) 50 K, (e) 24 K, (f) 22 K, (g) 16 K and (h) 12 K.

FIGURE 2. Energy-level scheme for a generalized electron-phonon coupled system.

FIGURE 3. Ground state energy-level splittings for Fe^{2+} in $FeCl_2$ and $FeBr_2$ including those for purely electronic and electronic-resonant phonon coupled systems.

FIGURE 4. Derivation of the observed band shape (A) for the coupled electron-resonant phonon modes near 150 cm^{-1} from the mapping of a Gaussian distribution (B) of electron frequencies at $\hbar\omega_o$ onto the solutions of $\mathscr{H}$ (Equation 4.1).

FIGURE 5. Computed electronic-resonant phonon Raman spectrum for various temperatures where the contributions from the $\Gamma_1^{+(1)}$ (ooo), $\Gamma_{2,3}^{+}$ (—), $\Gamma_1^{+(2)}$ (•••) components are shown beneath. Figures 5-a,b,c,d,e were computed with $\hbar\omega_o$ and $\hbar\Omega_o$ (cm^{-1}) = 146,146; 146,149; 143,150; 142,155; and 142,163 and should be compared with Figures 1-b,e,f,g and h respectively.

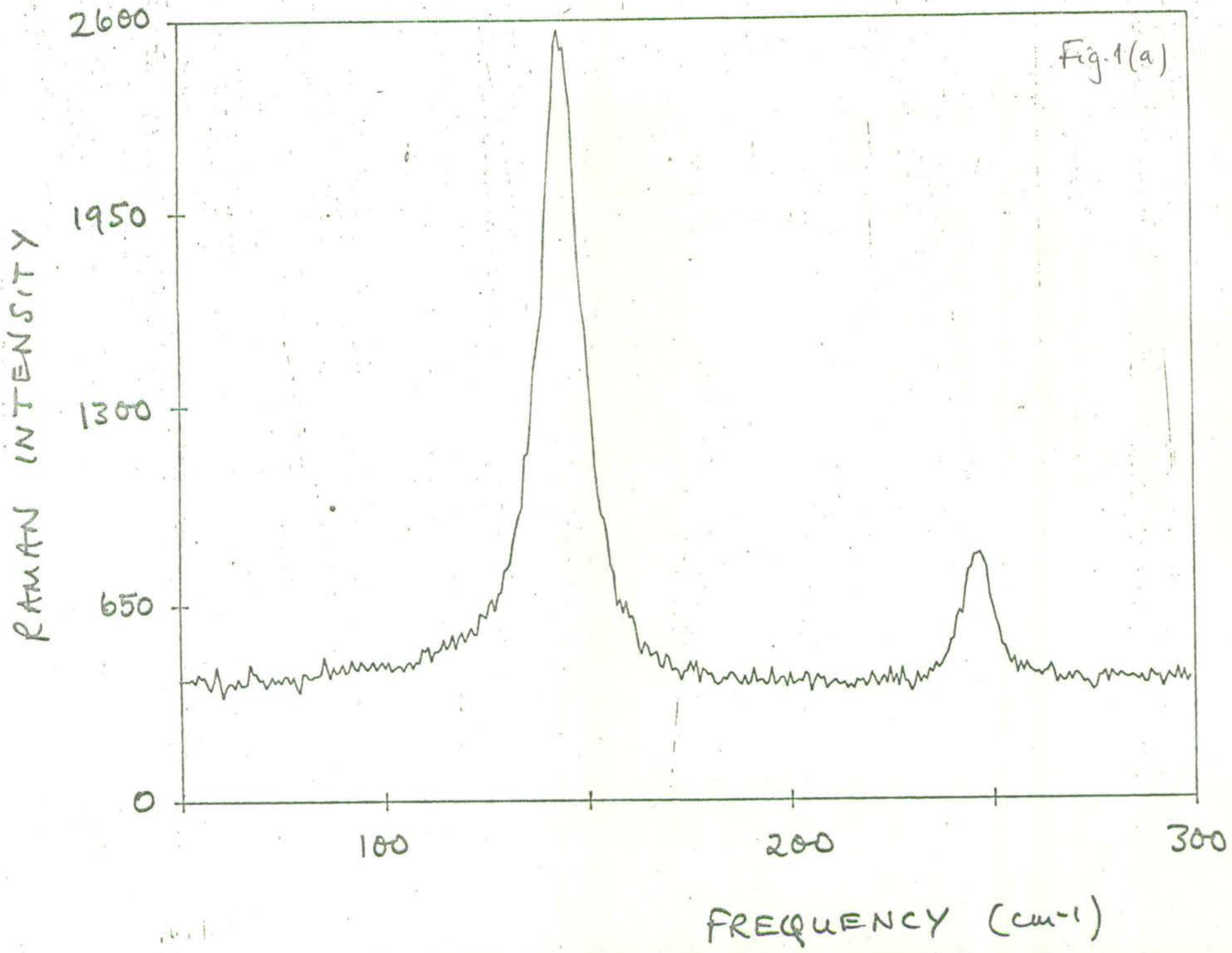
Fig. 1(a)
2600
1950
1300
650
0
RAMAN INTENSITY
100
200
300
FREQUENCY (cm⁻¹)

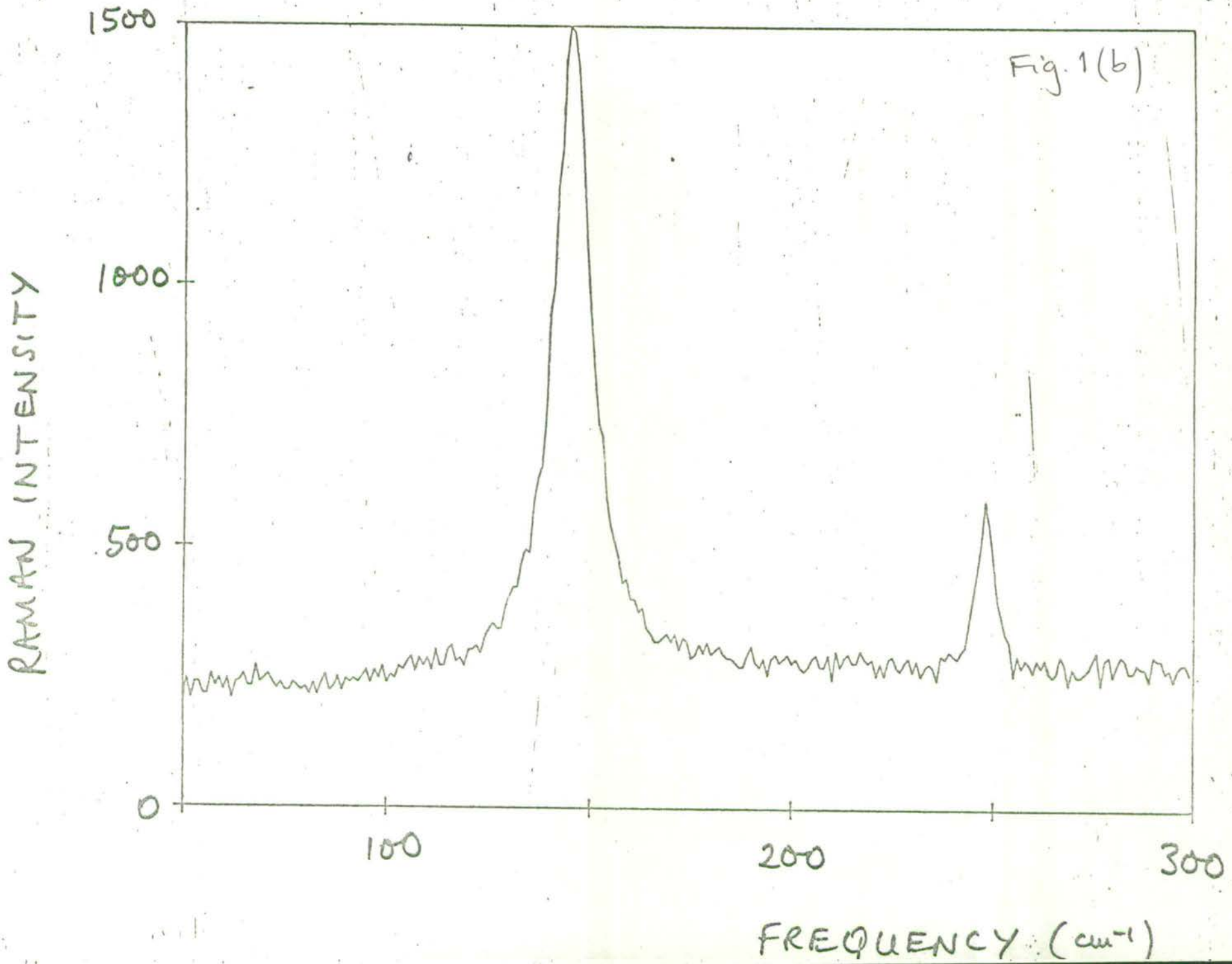
Fig. 1(b)
1500
1000
500
0
RAMAN INTENSITY
100
200
300
FREQUENCY (cm⁻¹)

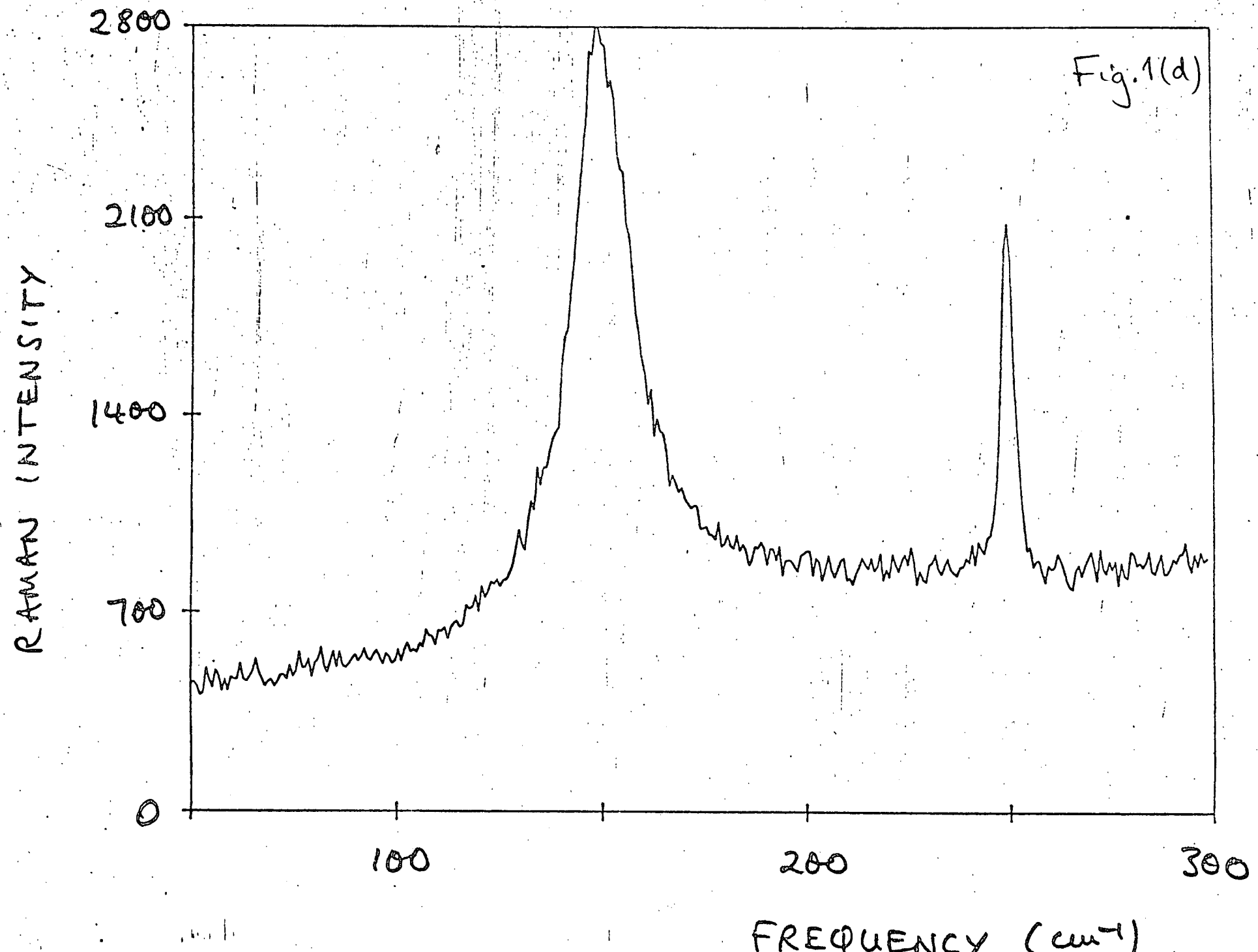
Fig. 1(d)
2800
2100
1400
700
0
RAMAN INTENSITY
100
200
300
FREQUENCY (cm⁻¹)

H_2 (105 K)

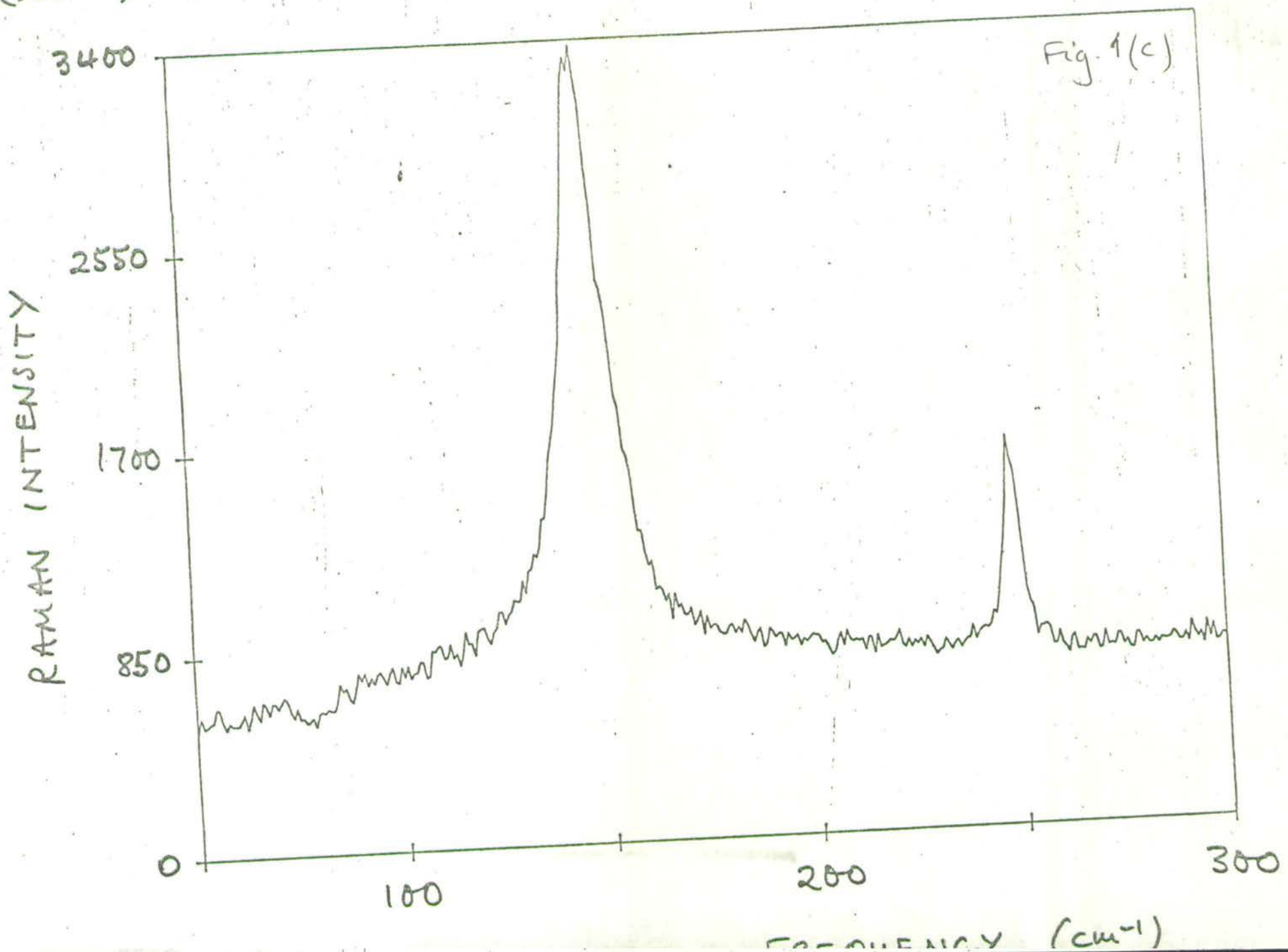
Fig. 1(c)
3400
2550
1700
850
0
RAMAN INTENSITY
100
200
300
FREQUENCY (cm⁻¹)

$FeCl_2$ (2H)

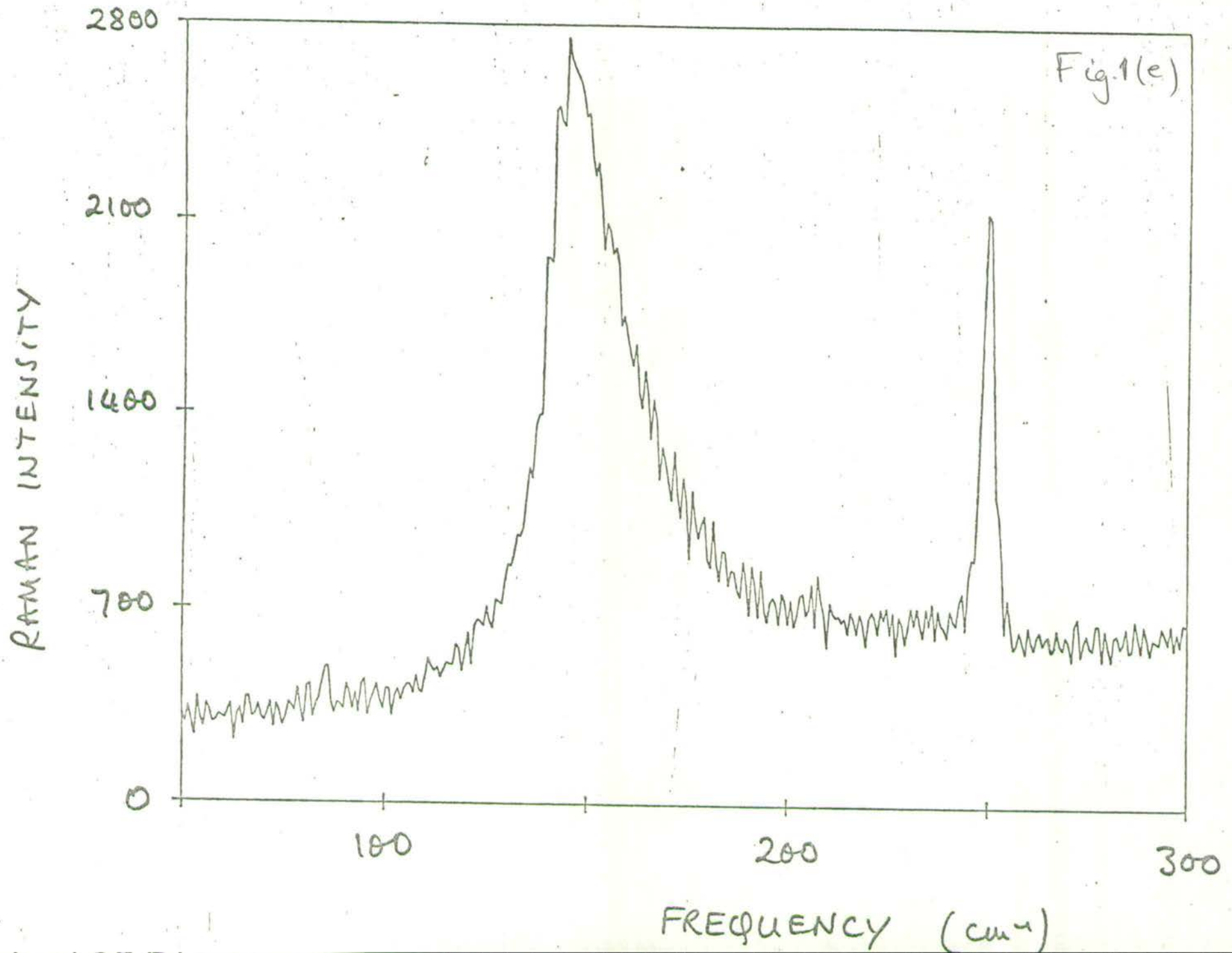

Fig. 1(e)

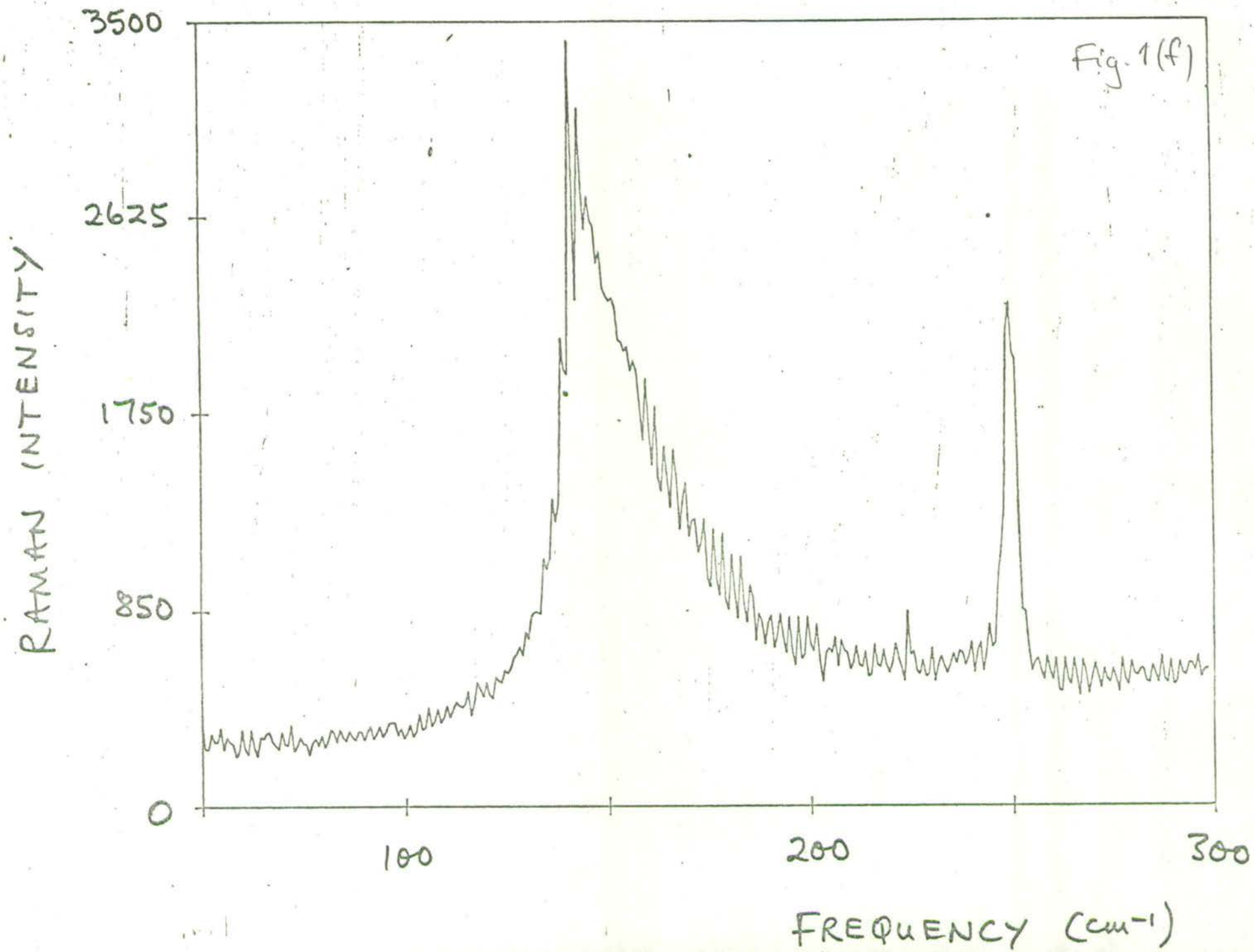
Fig. 1(f)
3500
2625
1750
850
0
RAMAN INTENSITY
100
200
300
FREQUENCY (cm⁻¹)

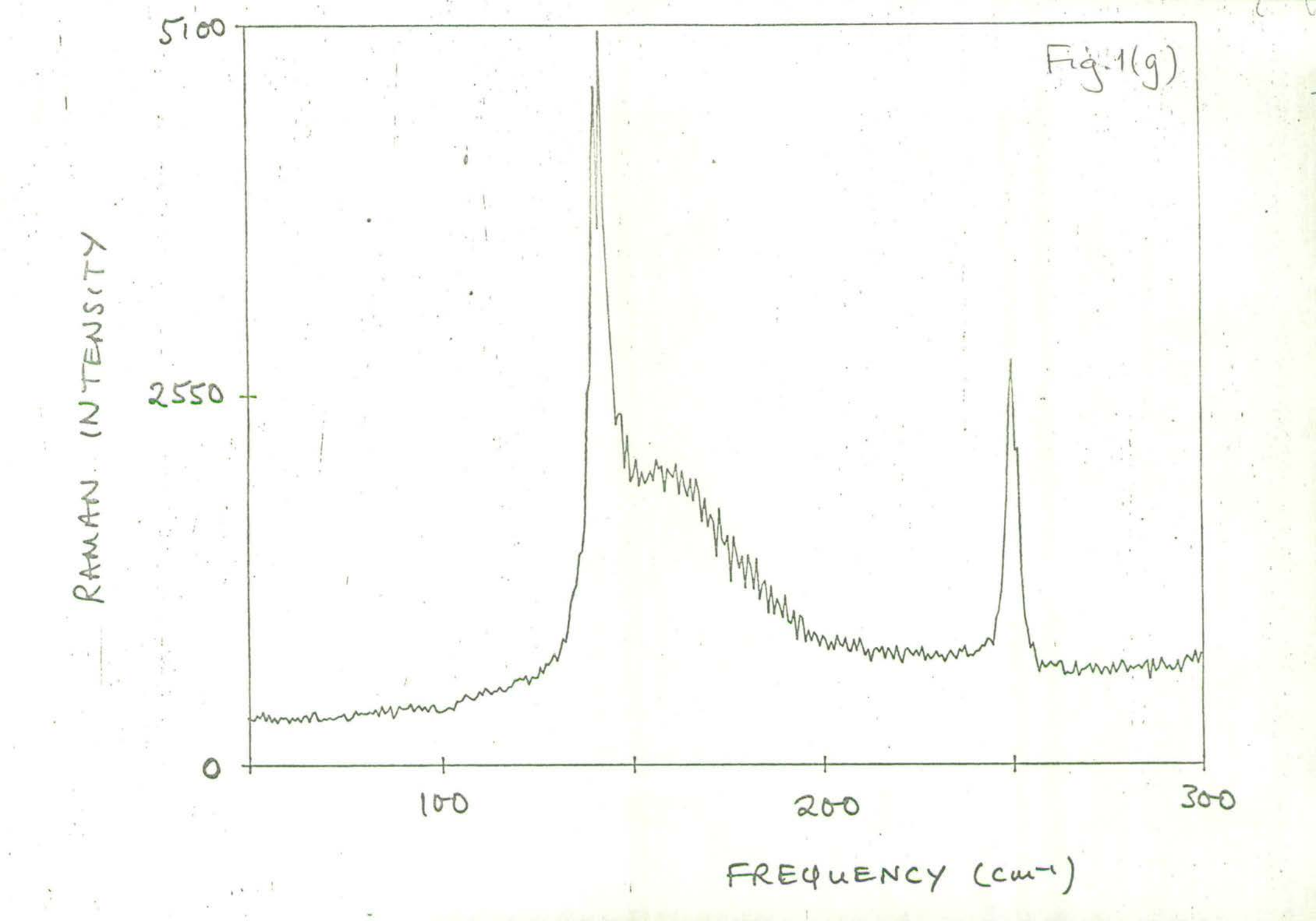
Fig. 1(g)
5100
2550
0
RAMAN INTENSITY
100
200
300
FREQUENCY (cm⁻¹)

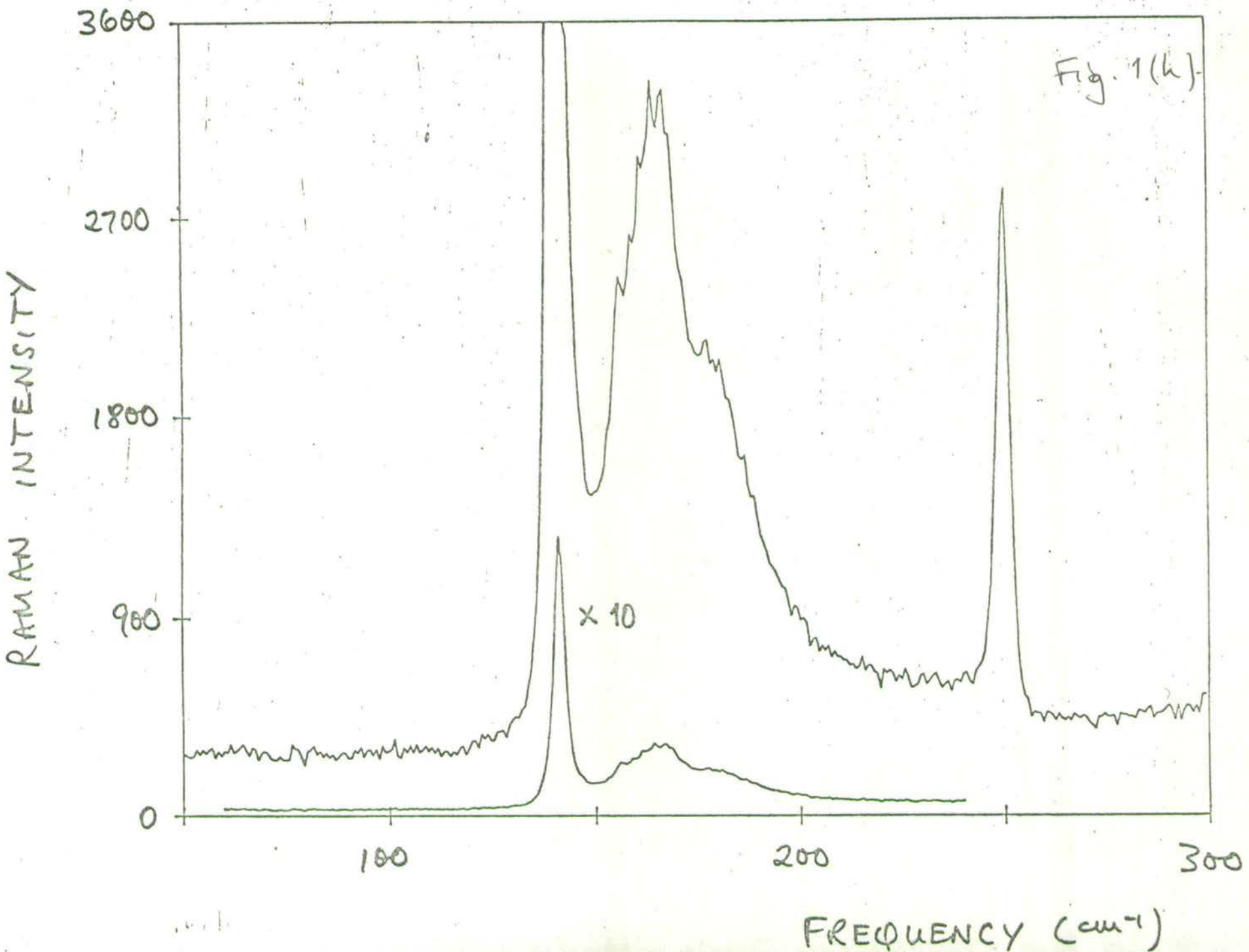
3600
2700
1800
900
0
RAMAN INTENSITY
× 10
100
200
300
FREQUENCY (cm⁻¹)

Fig. 1(h)

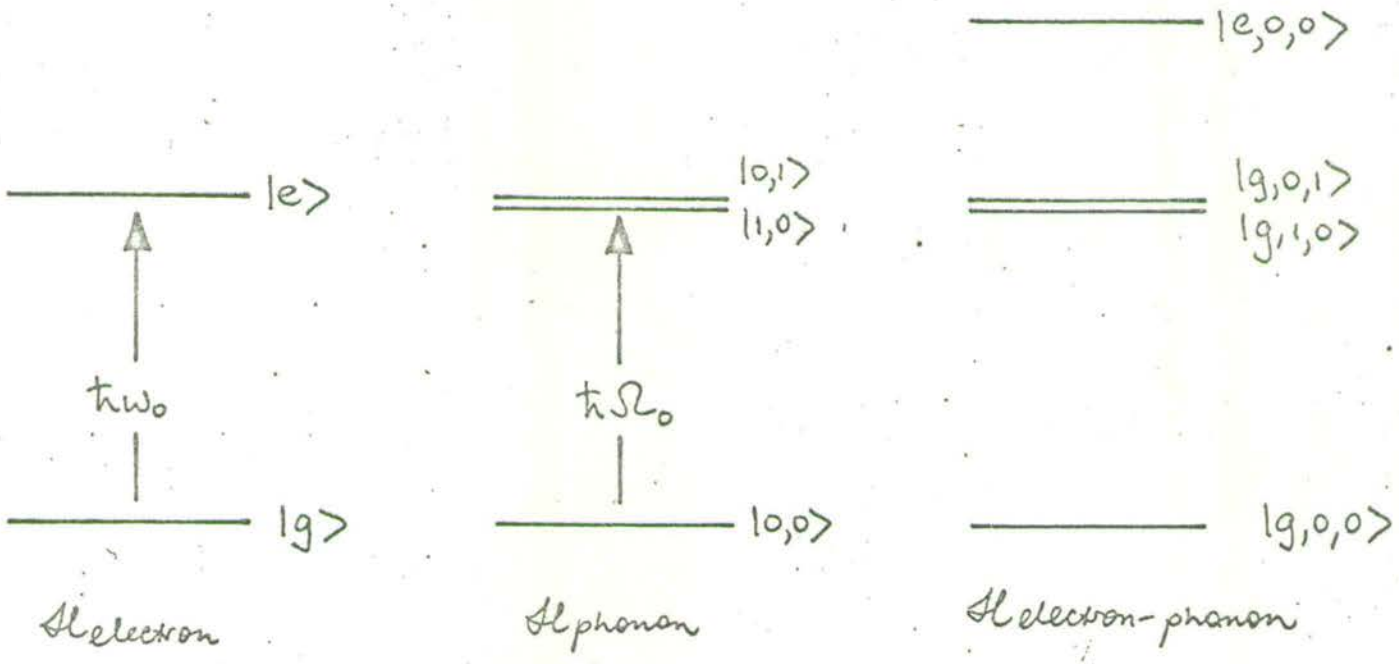
|e,0,0>
|e>
|0,1>
|1,0>
|g,0,1>
|g,1,0>
ħω₀
ħΩ₀
|g>
|0,0>
|g,0,0>
ħ electron
ħ phonon
ħ electron-phonon

Figure 2

Johnston et al

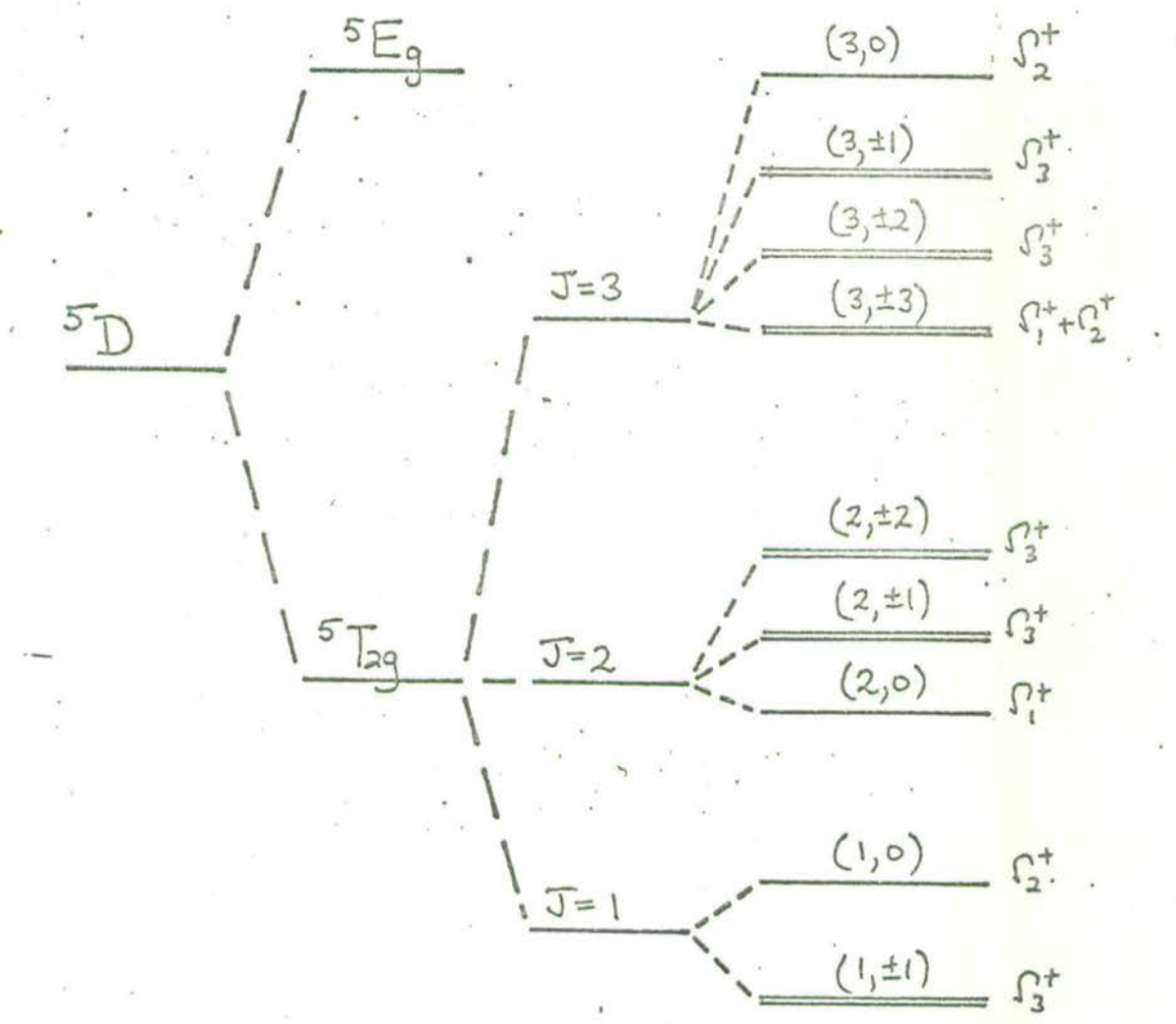

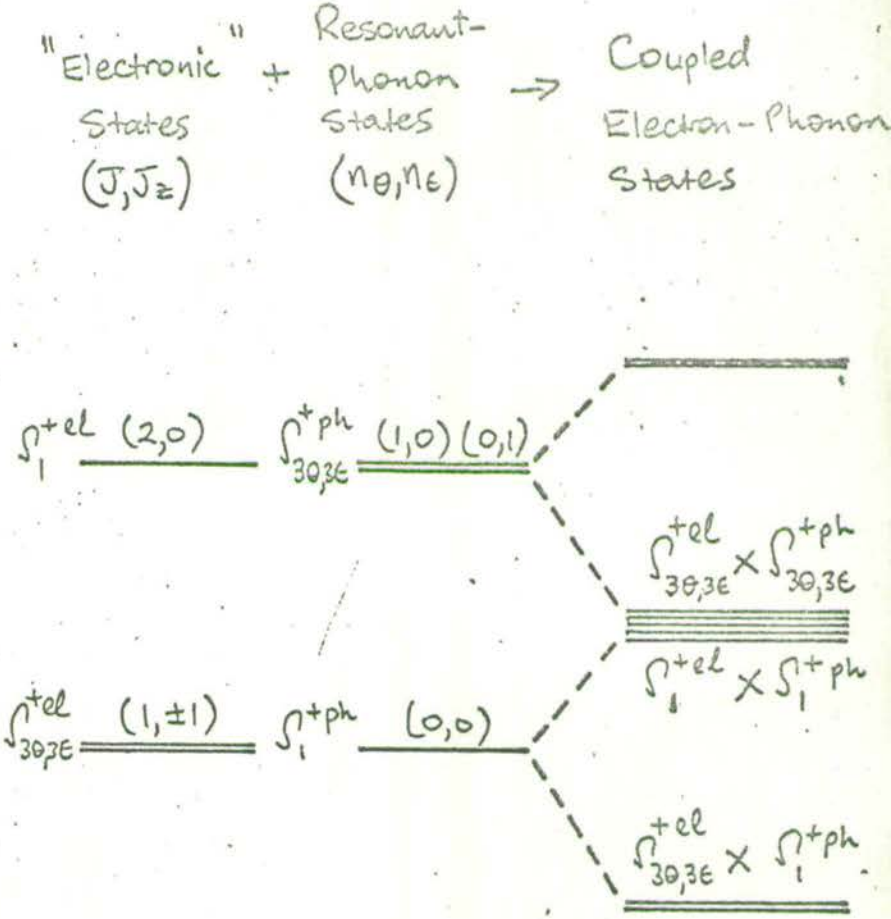

Figure 3

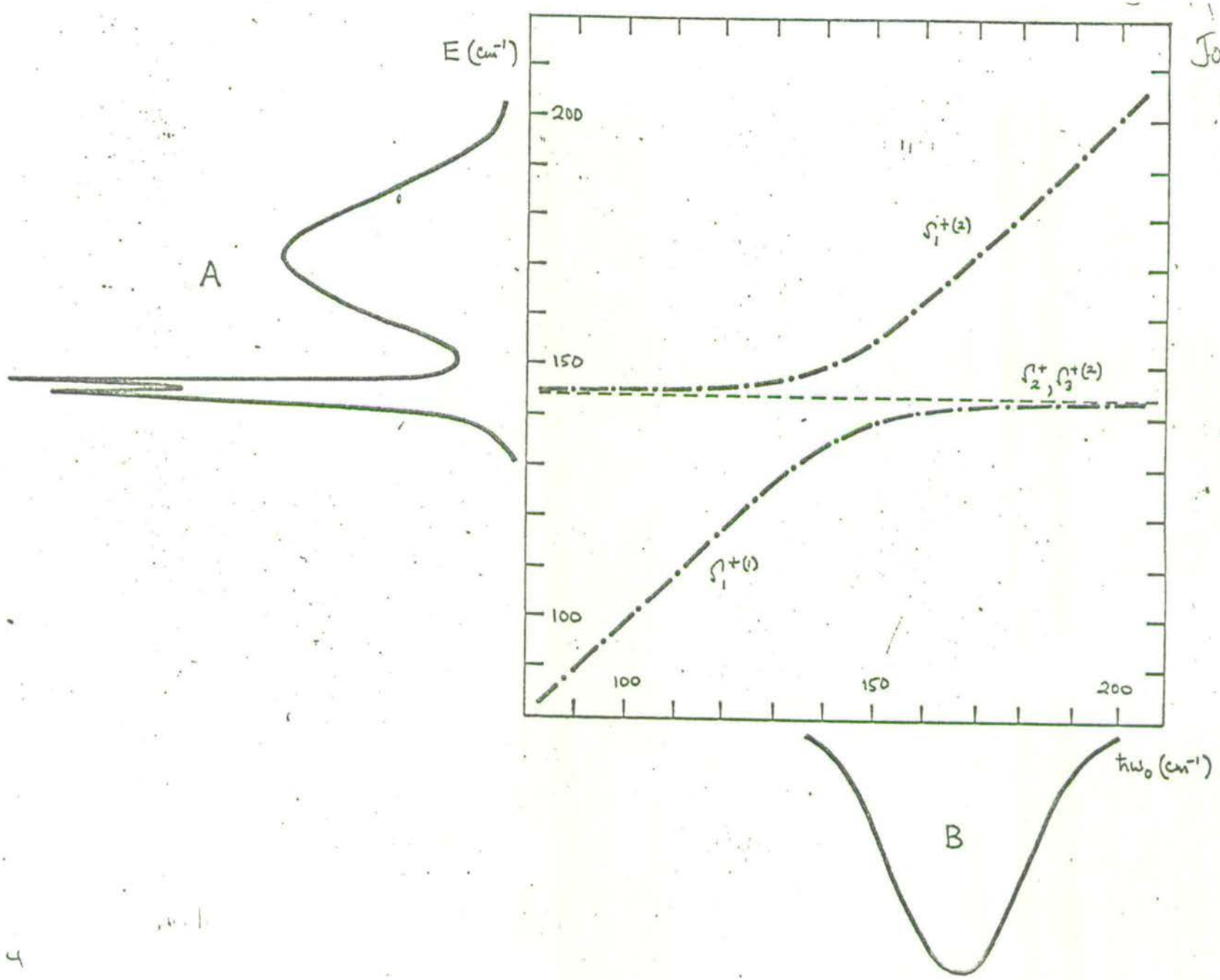

Figure 4

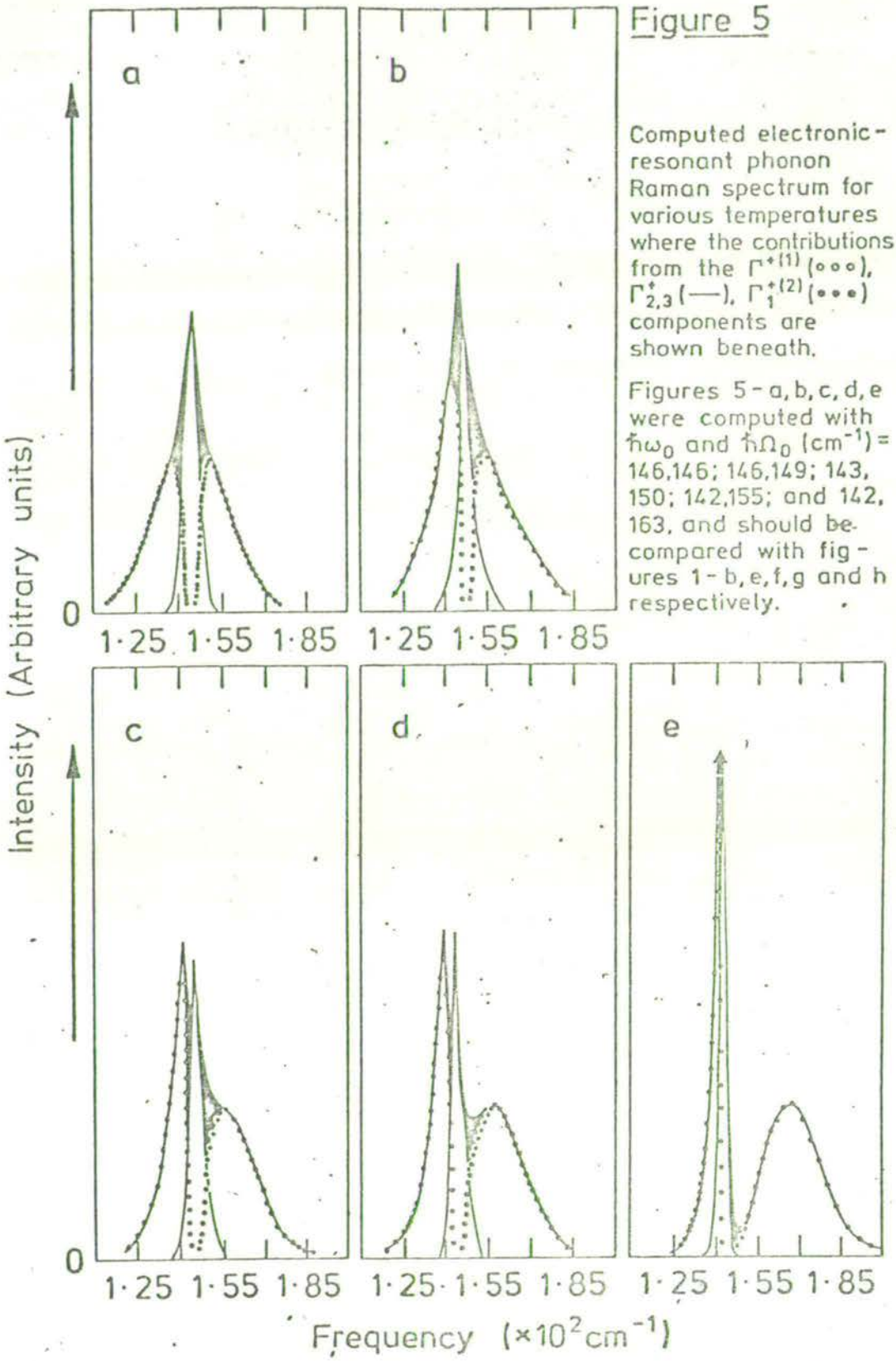

Figure 5

Computed electronic-resonant phonon Raman spectrum for various temperatures where the contributions from the $\Gamma^{+(1)}$ (ooo), $\Gamma^{+}_{2,3}$ (—), $\Gamma^{+(2)}_{1}$ (•••) components are shown beneath.

Figures 5-a, b, c, d, e were computed with $\hbar\omega_0$ and $\hbar\Omega_0$ (cm^{-1}) = 146,146; 146,149; 143, 150; 142,155; and 142, 163, and should be compared with figures 1-b, e, f, g and h respectively.

EXAMPLES OF A DYNAMIC JAHN-TELLER SYSTEM: RAMAN SCATTERING FROM ELECTRONIC EXCITATIONS AND PHONONS IN PARAMAGNETIC AND ANTIFERROMAGNETIC $FeCl_2$ AND $FeBr_2$

I. W. JOHNSTONE, D. J. LOCKWOOD* and G. MISCHLER**

Department of Physics, University of Nottingham, University Park, Nottingham NG7 2RD, England

*Department of Physics, University of Edinburgh, Edinburgh EH8 3JZ, Scotland

**Laboratoire de Physique des Solides, Associe au CNRS, 31077 Toulouse Cedex, France

ABSTRACT: Raman spectra of $FeCl_2$ and $FeBr_2$ have been measured above and below their Neel temperature within an energy range of 0 to 900 cm^{-1}. Spectral features due to scattering from phonons and electronic excitations are analyzed and assigned to symmetry species. A dynamic Jahn-Teller calculation using a full-lattice model has been extended, for the first time, to describe all levels within the $^5T_{2g}(^5D)$ manifold and gives the best, and an accurate description of the observed electronic transitions. Justification for the use of this model comes from the good agreement between calculated and experimentally determined groundstate g values and its successful extension through a molecular-field calculation to predict the energies of transitions observed in the antiferromagnetically ordered crystal. The results of this work indicate that even though the dynamic Jahn-Teller effect is weak, it nevertheless plays an important role in $FeCl_2$ and $FeBr_2$. A weak temperature-dependent band at 127.7 cm^{-1} in the spectrum of $FeBr_2$ is assigned to second-order scattering from a magnon-phonon combination mode.

Short Title: Raman Scattering in $FeCl_2$ and $FeBr_2$.

Classification Numbers: 78.30, 75.30K, 71.70C

1. INTRODUCTION

Electronic Raman scattering studies of iron-group transition metal ion compounds has a brief history. The first studies focussed on cobaltous compounds: Co^{2+} in $CdCl_2$ (Lockwood 1969, and Christie and Lockwood 1971), $CoCl_2$ (Christie and Lockwood 1971), CoF_2 (MacFarlane 1970) and $Co(NH_4)_2SO_4.6H_2O$ (Azima et al. 1970). Since then, there have been many studies of the same compounds, but in greater detail, as for example Christie et al. (1975). These, together with compounds containing iron (II) are the only divalent ions of this series to be widely examined. The reason for this emphasis is simple - transition metal compounds are highly coloured and the blue/green argon laser lines were ideally suited for Co^{2+} studies. More recently, high-power krypton lasers have become available and their red lines have enabled investigation of Fe^{2+} systems. Of all the many iron (II) compounds that have been studied, e.g. FeF_2 (Fleury et al. 1966), FeF_3 (Shepherd 1973a,b, and Meixner et al. 1973) and $FeCl_2.2H_2O$ (Kinne et al. 1975, and Graf and Schaack 1976), surprisingly, only one case of Raman scattering from electronic levels has been reported. This was for $FeCO_3$ (Popkov et al. 1973 and Lyons et al. 1976) in which there is an electronic transition at 438 cm^{-1} when measured at temperatures below the Neel temperature T_N. It increases by $\sim$ 20 cm^{-1} in energy at the transition. All other work has concentrated exclusively on the spectra due to magnons and phonons. To date there have been no Raman investigations of the optical phonons and low-lying electronic transitions in the interesting materials $FeCl_2$ and $FeBr_2$ although light scattering from magnons in $FeCl_2$ has recently been reported (Lockwood et al. 1978).

Anhydrous $FeCl_2$ and $FeBr_2$, which have the $CdCl_2$ and CdI_2 structure respectively, are worthy of study for many reasons. In layered compounds of these kinds each ferrous ion in the X^--Fe^{2+}-X^- sandwiched layers is surrounded by an almost octahedral arrangement of anions and has D_{3d} site symmetry. Below the Neel temperature, (23.5 K for $FeCl_2$, 14.2 K for $FeBr_2$), the Fe^{2+} spins within any one layer align ferromagnetically with a strong anisotropy confining them to the trigonal axis while the antiparallel spins of successive layers are weakly coupled to give an overall antiferromagnetic structure. At low temperatures, the application of a small magnetic field, applied parallel to the trigonal axis, can induce a transition from the antiferromagnetic state to a ferromagnetic ione. Hence, these materials simulate a two-dimensional ferromagnet and are known as metamagnets. The magnetic properties of $FeCl_2$ and $FeBr_2$ have been exhaustively studied. Measurements of magnon dispersion using neutron-scattering, of magnetization, specific heat, parallel and perpendicular susceptibilities, and H_c, the critical field, have all been reported (see, for example, for $FeCl_2$: Wilkinson et al. 1959, Jacobs and Lawrence 1967, Carrara 1968, Birgenau et al. 1972, and Bertrand et al. 1974, and for $FeBr_2$: Jacobs and Lawrence 1964, Fert et al. 1973, and Yelon and Vettier 1975). These measurements provide information about electronic excitations of frequency necessarily restricted to $\lesssim$ 30 cm^{-1}. Only Mossbauer measurements (Ono et al. 1964 and Fujita et al. 1969) have been able to give some information on the higher electronic excitations within the $^5T_{2g}$ (^5D) manifold. All these results are in good agreement with the above model of the antiferromagnetic ordering where the two-dimensional character is more prominent in $FeCl_2$ than in $FeBr_2$.

Apart from these magnetic studies, the acoustic phonon dispersion curves of $FeCl_2$ have been measured at room temperature by neutron scattering (Yelon et al. 1974). Neutron scattering experiments have also revealed two electronic excitations near 136 and 168 cm^{-1} in $FeCl_2$ (Hautecher et al. 1962 and Birgenau et al. 1972), but nothing is known from experiment about the phonons and low-energy electronic states of $FeBr_2$.

FeX_2 compounds are also of interest as examples of dynamic Jahn-Teller systems. Evidence of this in $FeCl_2$, from the observation of a temperature-dependent splitting in the absorption band due to the spin-allowed $^5T_{2g} \rightarrow {}^5E$ transition near 7000 cm^{-1}, has already been reported (Jones 1967 and Freeman and Jones 1969). Furthermore, $FeCl_2$ exhibits interesting magnon-phonon coupling (Lawrence and Petigrand 1973, Lovesey 1974, and Cracknell 1974) together with strong resonant coupling between a particular electronic transition and the E_g optical phonon as reported by Johnstone et al. (1978).

It is obvious from this review that there is a real paucity of data in the energy range 30 to 1000 cm^{-1} for both $FeCl_2$ and $FeBr_2$ and indeed, all ferrous compounds. We report here the results of the first Raman studies of phonons and electronic excitations in these compounds and covering the region 0 to 900 cm^{-1} at various temperatures above and below T_N.

2. EXPERIMENT

Samples for the Raman experiments were prepared by cleaving sections from single crystals grown by the Stockbarger method.

Details of the preparation necessary for surface-scattering from these brown-coloured materials are given by Johnstone et al. (1978). The samples were mounted in a Thor 500 cryostat where there is direct contact with the coolant gas. An Au-Fe/chromel thermocouple, mounted on the sample surface, was used to monitor the crystal temperature.

Raman spectra were excited with approximately 100 mW of 647.1 nm krypton laser light, this line proving suitable for both $FeCl_2$ and $FeBr_2$ by avoiding weak absorption bands (Johnstone et al. 1978) and at the same time allowing for the possibility of resonance enhancement. The laser beam was directed along the surface of the sample at grazing incidence with the 90° scattered light being collected along the crystal c-axis direction. A Coderg T800 triple monochromator, operating at a spectral resolution of 1.8 cm^{-1}, was used to analyze the scattered light which in turn was detected with an RCA C31034A photomultiplier. Each spectrum was recorded automatically in digital form under 'on-line' computer control (Arthur and Lockwood 1974) and was subsequently analyzed on a large, multi-access computer. No polarization measurements were attempted because the scattered light was largely depolarized.

Preliminary experiments revealed a laser-excited fluorescence emitted by all samples. In all cases the fluorescence intensity was both time and temperature dependent: the intensity diminished with increasing time under laser irradiation and with decreasing temperature. For the $FeBr_2$ crystal grown by Legrand in France this fluorescence was not a problem but the $FeCl_2$ crystal from the same source proved unusable for a detailed Raman study. Instead, an $FeCl_2$ sample grown by Ritchie of Canterbury University, New Zealand, was used for all measurements reported here, although the

fluorescence even in this case was never negligible.

3. ENERGY LEVEL SCHEME AND SELECTION RULES

An energy level scheme appropriate to Fe^{2+} ions in FeX_2 compounds has been discussed in some detail by Ono et al. (1964) and Alben (1969). The free ion ^5D ($3d^6$) term of the ferrous ion is split by the cubic component of the crystal field so that the orbital triplet $^5T_{2g}$ is lowest. Since the spin-orbit coupling and residual trigonal component of the crystal field are much smaller than the cubic crystal field the $^5T_{2g}$ orbital triplet may be treated as having an effective angular momentum $\ell' = 1$ and spin $S = 2$. The combined action of these perturbations is to produce three multiplets for $J' = 1$, 2, and 3 (where $J' = \ell' + S$) with the triplet lowest and separated from the quintuplet by some 200 cm^{-1}. The level diagram is given in Figure 1 and shows the 15 states (of the split $^5T_{2g}$ term) have either Γ_1^+, Γ_2^+ or Γ_3^+ representations of the D_{3d} point group with the exception of the (3, ±3) level which is accidentally degenerate. The selection rules governing the occurrence of Raman active transitions between such levels may be derived from the symmetry properties of the relevant Raman scattering tensors. Thus, for example, $\Gamma_3^+ \rightarrow \Gamma_1^+, \Gamma_2^+$ transitions are absent in α_{ZZ} polarization as can be seen from the selection rules and Raman tensors given in Figure 1. In fact all transitions are Raman active, noting that the Γ_2^+ tensor is purely antisymmetric.

Below T_N the point symmetry of the Fe^{2+} ion is reduced to C_{3i} and the shifted and split states may be described within the molecular-field approximation. The Γ_3^+ levels split into Γ_2^+ and

Γ_3^+ states while the singly degenerate Γ_1^+ and Γ_2^+ states now have Γ_1^+ symmetry as also shown in Figure 1.

A factor group analysis for both crystals predicts two $\underset{\sim}{k} = 0$ Raman active phonons having $\Gamma_1^+(A_{1g})$ and $\Gamma_3^+(E_g)$ representations under D_{3d} point symmetry.

4. RESULTS

4.1 $FeBr_2$

Representative Raman spectrum of $FeBr_2$, recorded at temperatures above and below T_N = 14.2K) are presented in Figure 2. All the spectra show two narrow intense bands whose frequencies of 94.5 and 158 cm^{-1} do not vary within experimental error (± 0.5 cm^{-1}) for a temperature range of 140K to 12K (Table 1). They do however, sharpen appreciably on cooling and are resolution limited at 12K. This behaviour characterises them as phonons, two of which are expected. Two groups of broad lines are observed at frequencies grouped around 250 and 600 cm^{-1}, respectively, and are assigned to electronic transitions. These bands sharpen, show small shifts in position due to contraction of the lattice, and grow appreciably in intensity as the temperature is lowered, with dramatic changes at T_N.

Above T_N, the first group of bands comprises three peaks at 192, 244 and 296 cm^{-1} whereas the second has peaks at 512, 585 and 631 cm^{-1}. In order to obtain accurate frequencies for the model calculations in Section 5, all the bands in the spectrum recorded at 16K were fitted to a number of damped harmonic oscillators having intensity of the form:

$$I(\omega) = [\bar{n}(\omega) + 1] S\omega_o^2\gamma^2 / [(\omega^2 - \omega_o^2)^2 + \gamma^2\omega^2] \qquad (4.1)$$

In the above expression, $\bar{n}(\omega)$ is the usual Bose population factor evaluated at frequency ω, S is the strength, ω_o the resonant frequency, and γ the

damping of the oscillator. The fitting was performed using a computerised least-squares procedure, allowing for Poisson noise in the data. An attempt to fit the 8-60 cm^{-1} region with a single oscillator produced a non-physical result, and, therefore, any band in this region is considerably weaker than other electronic bands to higher energy. The three peaks in the 250 cm^{-1} region were adequately represented by three oscillators whose defining parameters are given in Table II. However, the shoulder to low frequency and surmounted by the 158 cm^{-1} phonon could not be fitted by an additional oscillator due to the presence of this phonon. The 600 cm^{-1} region was first fitted with three oscillators giving a reasonable result, but further fitting with four and then five oscillators significantly improved the fit, the five oscillator model giving a very good description as can be seen in Figure 3. Parameters obtained from this last fitting are also given in Table II.

Below T_N, the band structure is much more complex as can be seen on comparison of spectra recorded at 12 and 16K. Peak frequencies for prominent bands are given in Figure 4.

4.2 $FeCl_2$

Raman spectra of $FeCl_2$ were recorded at various temperatures above and below T_N (= 23.5K) and some results are presented in Figure 5. Although the spectra are similar in form to those obtained for $FeBr_2$ analagous lines are much broader. This, coupled with the unusual band structure near 150 cm^{-1} makes identification of distinct peaks for some spectral features more difficult. Again, at 12K there are two sharp and intense lines due to scattering from phonons but with shifted energies of 141 and 250 cm^{-1} in this crystal. The band structure near 150 cm^{-1} has a complicated temperature dependence which has been explained in terms of strong electron-resonant phonon coupling (Johnstone et al 1978). On the band's high frequency shoulder

there are two further weak bands at approximately 216 and 310 cm^{-1} ($T > T_N$). These are assigned as electronic in origin, as are the bands at approximately 460, 570 and 635 cm^{-1}. All these features show little shift on cooling to T_N, but do sharpen and grow in intensity. Bands in the 24K spectrum were least squares fitted to harmonic oscillators with success in the high energy region 400-600 cm^{-1} but gave no reliable fitting of the group to lower energy. Hence, the energies of these levels were estimated from the spectra directly and necessarily have large experimental uncertainties. Parameters describing the fitting obtained are listed in Table III and indicate that if five bands are present in the 400-600 cm^{-1} region the upper two have very similar energies.

The effect of antiferromagnetic ordering is apparent from the spectra given in Figure 5. Some bands shift markedly whereas all bands sharpen and grow dramatically in intensity on cooling to a base temperature of 12K. Peak frequencies for these bands are listed in Figure 4.

A peculiar, critical intensity phenomenon was observed in spectra recorded within the range of $T = T_N \pm 8K$. For these temperatures alone, as can be seen in Figure 1 of Johnstone et al 1978 and Figure 5 of this work, the intensity of scattered light has a cyclic modulation whose amplitude is independent of Raman signal. The amplitude is however, clearly temperature dependent as can be seen in the high frequency end of the 16K spectrum of Figure 1 where the temperature was allowed to rise.

5. ENERGY LEVEL CALCULATIONS

5.1 THREE POSSIBLE MODELS

The starting point for all our electronic energy level calculations is to assume that the $^5T_{2g}$ orbital ground state of an Fe^{2+} ion placed in an octahedral crystal field may be described by an effective orbital angular momentum $\ell' = 1$ and spin $S = 2$ (Bates 1971). First-order perturbation effects of spin-orbit coupling and the trigonal component of the crystal field are then easily derived using a Hamiltonian of the form:

$$\tilde{\mathcal{H}}^{(1)} = \tilde{\mathcal{H}}_{SO} + \tilde{\mathcal{H}}_{trig}$$

$$= -\lambda \underset{\sim}{\ell}.\underset{\sim}{S} + V(\ell_z^2 - \tfrac{2}{3}) \qquad (5.1)$$

where $V = \langle \ell_z = \pm 1 | \mathcal{H}_{trig} | \ell_z = \pm 1 \rangle$ and λ is the free-ion spin-orbit coupling constant ($= 114\ cm^{-1}$). This yields the energy level scheme in Figure 1.

Additional contributions to an effective Hamiltonian come from matrix elements of these same perturbations when evaluated between the ground triplet and excited electronic states. The closest of these excited states is some $7000\ cm^{-1}$ higher in energy and labelled ^5E_g. For coupling to second order the Hamiltonian is:

$$\tilde{\mathcal{H}}^{(2)} = \tilde{\mathcal{H}}^{(1)} + \tilde{\mathcal{H}}_{SO-SO} + \tilde{\mathcal{H}}_{trig-SO} + \tilde{\mathcal{H}}_{trig-trig} \qquad (5.2)$$

where the subscripts indicate which perturbations are involved and

$$\tilde{\mathcal{H}}_{SO-SO} = -\frac{2\lambda^2}{\Delta}\left[\underset{\sim}{\ell}.\underset{\sim}{S} + (\underset{\sim}{\ell}.\underset{\sim}{S})^2 - 2(E_\theta^{\ell} E_\theta^{S} + E_\varepsilon^{\ell} E_\varepsilon^{S})\right]$$

their main results, details of which are outlined more fully in a recent review by Bates (1977). The effective Hamiltonian describing the trigonal crystal field and spin orbit coupling perturbations to second order is given as:

$$\tilde{\mathcal{H}}^{(3)} = \tilde{\mathcal{H}}_{SO} + \tilde{\mathcal{H}}_{eff\text{-}trig} + \tilde{\mathcal{H}}^{(2JT)}_{trig\text{-}SO} + \tilde{\mathcal{H}}^{(2JT)}_{SO\text{-}SO} + \tilde{\mathcal{H}}^{(2JT)}_{trig\text{-}trig} \qquad (5.3)$$

where

$$\tilde{\mathcal{H}}_{SO} = -\gamma\lambda \underset{\sim}{\ell}.\underset{\sim}{S}$$

$$\tilde{\mathcal{H}}_{eff\text{-}trig} = \gamma\{V - (\delta\alpha)^2\Delta - \delta E_{JT}(\delta\alpha)^2\}(\ell_z^2 - \tfrac{2}{3})$$

$$\tilde{\mathcal{H}}^{(2JT)}_{trig\text{-}SO} = \lambda F_a V\{(\underset{\sim}{\ell}.\underset{\sim}{S})(\ell_z^2 - \tfrac{2}{3}) + (\ell_z^2 - \tfrac{2}{3})(\underset{\sim}{\ell}.\underset{\sim}{S})\}$$

$$\tilde{\mathcal{H}}^{(2JT)}_{SO\text{-}SO} = \lambda^2\left[F_a(\underset{\sim}{\ell}.\underset{\sim}{S})^2 + \tfrac{2}{3}(F_b - F_a)\{S(S+1) + E^{\ell}_{\theta}E^{S}_{\theta} + E^{\ell}_{\epsilon}E^{S}_{\epsilon}\}\right]$$

$$\tilde{\mathcal{H}}^{(2JT)}_{trig\text{-}trig} = -\tfrac{1}{3}V^2\{\tfrac{2}{3}F_b - F_a(\ell_z^2 - \tfrac{2}{3})\}$$

γ, F_a, F_b are the Jahn-Teller reduction factors, E_{JT} is the Jahn-Teller stabilization energy, $\delta = 0 \rightarrow \frac{5}{2}$, and the other terms are as defined in equations (5.1) and (5.2). The superscript '2JT' in the above expressions indicates a second-order Jahn-Teller term while the subscripts indicate which perturbations are involved as before. Second-order contributions from $E - T_2$ admixtures are assumed to be unimportant and are therefore omitted.

Matrix elements of all these operators are most conveniently evaluated using a $|J'J'_z\rangle$ basis, where $J' = \ell' + S$, for the $^5D(T_2)$ ground manifold since $\underset{\sim}{\ell}.\underset{\sim}{S}$ is diagonal within these states. Details of this have been given by Bates (1977) and we follow him in omitting the constant terms

in $\tilde{\mathcal{H}}^{(2JT)}_{SO-SO}$ and $\tilde{\mathcal{H}}^{(2JT)}_{trig-trig}$ together with the second and third terms in $\tilde{\mathcal{H}}_{eff-trig}$ since they are relatively small when compared to V.

The expressions used in the calculation of the ground state g values were those quoted by Bates and Steggles (1975) in their equations 3.9 and 3.10.

5.2 DISCUSSION OF PARAMETERS

A Data General Company Nova 1220 computer was used to perform the numerical diagonalisation of the three Hamiltonians $\tilde{\mathcal{H}}^{(1)}$, $\tilde{\mathcal{H}}^{(2)}$ and $\tilde{\mathcal{H}}^{(3)}$. The energies of observed electronic Raman transitions were then fitted using an iterative procedure in which the appropriate parameters of Υ, F_a, F_b, λ, $\delta\alpha$, and V were adjusted until the root mean square deviation of the calculated from experimental values was a minimum. This in turn was taken as an indication of the quality of fit. From a comparison of the results given in Table IV, the 'full-lattice' Jahn-Teller model is clearly the most appropriate to describe the low-lying energy levels of both $FeBr_2$ and $FeCl_2$. The results of diagonalising $\tilde{\mathcal{H}}^{(2)}$ show that second-order contributions from the ^5E states are unimportant and even degrade the quality of the fit. The Jahn-Teller interaction is probably more important since the interaction involves coupling to the lattice phonons and not distant electronic excited states.

Our computer calculations give λ close to the free ion value of $-114\ cm^{-1}$ and so there is little covalency reduction, while the trigonal parameters V and $\delta\alpha$ have the expected order of magnitude for these compounds (Christie et al 1975). The strength of the Jahn-Teller interaction is weak compared to that noted for Fe^{2+} in Al_2O_3 (Bates and Steggles 1974): the Ham reduction factor is ~ 0.9, compared with 0.2, while F_a and F_b are reduced by one-tenth. As expected, the relations between the first and second-order reduction parameters as given by the

'cluster' model are not obeyed. From the best fit calculations for $FeBr_2$ ($FeCl_2$) we obtain $\gamma = 9.4047 \times 10^{-1}$ (9.13125×10^{-1}), $F_a = 1.4325 \times 10^{-4}$ (3.175×10^{-4}) and $F_b = 7.000 \times 10^{-4}$ (1.1025×10^{-3}) whereas in the 'cluster' model if $\gamma = 0.9$ then $f_a = (F_a h\nu) = 0.0785$ and $f_b = (F_b h\nu) = 0.2$ where ν is the frequency of the coupled mode. This gives $F_a/F_b = 0.3925$ which is not found. A value of ν has been estimated for $FeCl_2$ from the temperature dependent splitting of the optical absorption band due to the $^5T_2 \rightarrow {}^5E$ transition, observed by Freeman and Jones (1969). They obtain an effective frequency of 89 cm^{-1} to describe the lattice-phonon-continuum's contribution to the splitting.

In the case of both $FeBr_2$ and $FeCl_2$ the g values for the ground state $J' = 1$ manifold have been determined using a variety of techniques and the set of parameters obtained could be tested by comparing these g values with the calculated splitting factors for these parameters. These are shown in Table V where the two sets of values agree within experimental error.

5.3 THE MOLECULAR FIELD MODEL

Below T_N, the Raman spectra of the two crystals show splittings and shifts of the single ion levels due to the exchange interactions between the Fe^{2+} ions. As a further test of the model Hamiltonian $\tilde{\mathcal{H}}^{(3)}$ we attempt to predict these new frequencies within a molecular field approximation. This is attempted with the knowledge that while such a model is adequate for describing the higher energy excitons, where dispersion is vanishingly small, this theory does not account for the levels to lower energy where spin correlation effects are important.

To the terms in $\tilde{\mathcal{H}}^{(3)}$ we add the molecular field interaction $\tilde{\mathcal{H}}_{MF}$, appropriate for an easy-axis antiferromagnet and having the form:

$$\tilde{\mathcal{H}}_{MF} = \frac{2}{3}\left[J_1 \langle S_z^{\alpha} \rangle_o + J_2 \langle S_z^{\beta} \rangle_o\right] S_z \qquad (5.4)$$

where J_1 and J_2 are the intralayer ferromagnetic and interlayer antiferromagnetic exchange parameters respectively while $\langle S_z^{\alpha} \rangle_o = -\langle S_z^{\beta} \rangle_o = -1$ are the zero-temperature, zero magnetic field expectation values of S_z for the ground state of the Fe^{2+} ion on the two sublattices α and β. Hence, the expression for $\tilde{\mathscr{H}}_{MF}$ reduces to:

$$\tilde{\mathscr{H}}_{MF} = \frac{2}{3}(J_1 - J_2)S_z \qquad (5.5)$$

For $(J_1 - J_2)$ equal to 14.5 cm^{-1} ($FeBr_2$) and 18.5 cm^{-1} ($FeCl_2$) the energy levels obtained are given in Figure 4 and are in good overall agreement with experiment, especially for the most clearly resolved peaks. The particular values of $(J_1 - J_2)$ used may be compared with those obtained from other techniques, but, as can be seen in Table VI, there is a wide disparity between previous results.

The magnon energies are calculated to be 32 and 42 cm^{-1} for $FeBr_2$ and $FeCl_2$ respectively whereas these levels have been observed directly at 17.3 cm^{-1} (Fert et al 1976) and 16.4 cm^{-1} (Lockwood et al 1978). This expected discrepancy can be attributed to the use of an isotropic exchange Hamiltonian, appropriate for a spin = $\frac{1}{2}$ level, for calculating the energy levels of an orbital triplet. As this approach ignores dipolar interactions and orbital contributions to the exchange any more precise description of the system would need to take account of these effects and preferably consider collective excitations of whole crystal states as well.

6. DISCUSSION

6.1 PHONON SPECTRA

All the Raman spectra showed two narrow and intense lines below 250 cm^{-1} due to scattering from $\underset{\sim}{k} = 0$ phonons. Although the $FeBr_2$ and $CdBr_2$ structures are slightly different we compare their phonon spectra in order to make definite assignments. From the results given by Lockwood (1973) and Johnstone (1975) we can see that the features at 158.5 and 94.5 cm^{-1} (12K) have energies consistent with them being assigned to A_{1g} and E_g normal modes respectively. A similar comparison for the two features at 250 and 141 cm^{-1} (12K) in $FeCl_2$ with those at 233 and 131 cm^{-1} (300K) for $CdCl_2$ confirms that these are the A_{1g} and E_g modes also although the latter assignment is complicated by the electron-resonant phonon coupling noted earlier.

6.2 ELECTRONIC BANDS

As can be seen from a comparison of Figures 2 and 4 together with Table IV the electronic Raman spectrum of these two crystals are very similar with the levels grouped together in the same overall pattern while the model used to calculate their energies employs very similar parameters in both cases. However, there are small differences. The peaks in the $FeBr_2$ spectra are better resolved than for $FeCl_2$ which is consistent with previous comparisons of results obtained for $CoBr_2/CoCl_2$ and $CdBr_2(Co^{2+})/CdCl_2(Co^{2+})$ crystal systems. Also, the $\underset{\sim}{k} = 0$ phonon peaks have lower energies than are observed for $FeCl_2$ which explains the absence of resonant electron-phonon coupling in the bromide.

The widths of all lines are large compared to those generally observed in dilute crystal systems (Figure 3, Christie et al 1975) and principal contributions to these are assumed to come from inhomogeneous broadening due to local strains, spin-spin and dipolar interactions between adjacent

Fe^{2+} ions, and possibly from the coupling of the electronic states to the lattice via the dynamic Jahn-Teller effect. In addition to these mechanisms, there is a low frequency shoulder to each of the main lines. This produces a marked asymmetry of lineshape which grows with increasing temperature and may be easily observed in the 12-100K range. In particular, when fitting a series of oscillators to the $J' = 3$ manifold of levels (Section 4.1) this shoulder proved to be due to a band approximately 23 cm^{-1} (25 cm^{-1}) below the main peak at 516.6 (464) cm^{-1} in $FeBr_2$ ($FeCl_2$) which suggests that each is due to a transition from the thermally populated $|1,0\rangle$ state. We therefore assign energies of 23 and 25 cm^{-1} to the first electronic states in $FeBr_2$ and $FeCl_2$. This is in agreement with the predictions of the full-lattice Jahn-Teller model and the results of a closer examination of the low-frequency spectrum of $FeCl_2$ in which we find ~~two~~ a very weak, broad band$ at 28 cm^{-1} (30K) ~~and 37 cm^{-1} (12K)~~ which shifts to 37 cm^{-1} (12K) ~~where the latter is the former, only shifted~~ upon the onset of antiferromagnetic ordering (Figure 1, Lockwood et al 1977). Below T_N, there is the added possibility of hot band transitions from the magnon and so for all temperatures, all bands are expected to show asymmetric broadening, which is what is observed.

Another point of interest is that the asymmetry is clearly most marked for the more intense transitions; namely those between $|1,0\rangle \rightarrow |2,0\rangle$ and $|1,0\rangle \rightarrow |3,\pm3\rangle$ states. The selection rules for all hot band transitions (Figure 1) predict that transitions from Γ_2^+ to Γ_1^+ states have Γ_2^+ symmetry and are associated with the antisymmetric Raman tensor whereas all other transitions, except that between $|1,0\rangle \rightarrow |3,\pm3\rangle$ have Γ_3^+ symmetry. Hence, the hot band transitions can be expected to have differing intensities by reason of selection rules alone. If we ignore the small Jahn-Teller induced splitting of the accidentally degenerate $|3,\pm3\rangle$ states then hot band transitions to this level will have either Γ_1^+ or Γ_2^+ symmetry, which may account for its intense nature. Experimentally we see the $|1,0\rangle \rightarrow |3,\pm3\rangle$

transition as stronger than the $|1,0\rangle \rightarrow |2,0\rangle$ transition while the others are very weak and could not be fitted when included in the oscillator fits for the bands. Therefore, the differences in intensity of the hot band transitions are consistent with selection rules although naturally, determination of relative intensities can only be obtained from a calculation of the individual elements in the appropriate scattering tensors.

The only unexplained aspect of the results is the extreme range of intensity for the individual transitions and their differing temperature dependence. Some of the temperature dependent intensity behaviour is most probably due to changes in the position of optical absorption bands. These will sharpen and shift with lowering temperature, thereby affecting the Raman scattering cross-section for each transition and the possibility of resonance enhancement. However, we cannot explain why the $|1, \pm1\rangle \rightarrow |1,0\rangle$ transition is so weak compared with all others and the reason for the large variation in intensity of the transitions to the levels comprising the $J' = 2$ and $J' = 3$ manifolds. Even though group theory can predict that all transitions are Raman allowed, as is observed, any further description of the system must await a detailed calculation of the Raman scattering cross-sections, especially in regard to the dynamic Jahn-Teller effect.

The oscillations in scattered light intensity observed for $FeCl_2$ near T_N remain partially unexplained. The amplitude of the modulation is independent of Raman signal and is, therefore, most likely caused by some critical scattering phenomenon throughout the visible region of the electromagnetic spectrum thereby affecting the virtual electronic states in the Raman process. Such critical behaviour has already been observed in $FeCl_2$. Robbins and Day (1973) have reported a time-dependent oscillation in their photomultiplier-indicated-light-level when studying the absorbance due to critical scattering near 4260 Å. They also found that the oscillations occurred only for temperatures approaching T_N, but in their experiment, only within a small range of magnetic field near

12 kOe as well. These two independent experiments then, certainly preclude the possibility that the oscillations are caused by a spurious instrumental effect. We suggest that the observed behaviour in both experiments is related to the formation of domains bounding differing magnetic phases within the one crystal. In the optical absorption experiment the domains define antiferromagnetic and ferromagnetic regions of the sample for fields very close to the metamagnetic transition value of 10.5 kOe (4.2K) whilst in our experiments the domains are present in the mixed antiferromagnetic/paramagnetic phase near T_N in the absence of any external magnetic field. Since the mechanism by which these domains interact with light remains uncertain we are currently undertaking more measurements of the optical phenomenon associated with this unusual type of magnetic ordering.

7. MAGNON-PHONON MODE IN $FeBr_2$

Weak temperature-dependent structure can be seen in the 130 cm^{-1} region of the Raman spectrum of $FeBr_2$. Spectra recorded at various temperatures, above and below T_N, are displayed in Figure 6. A sharp feature superimposed on a broad band can be seen at 127.7 cm^{-1} (12K). As the temperature is raised this decreases in intensity and shifts to slightly lower energy (e.g. 127.2 cm^{-1} at 16K). The band has largely disappeared by 47K and certainly vanished by 140K.

All first-order scattering due to phonons and electronic excitations have been identified in $FeBr_2$ and so this peak at 127.7 cm^{-1} must be associated with higher order scattering. However, it cannot be a difference band nor a phonon combination band, as the temperature dependence of the band intensity is opposite to that expected for these processes.

The 127.7 cm^{-1} band is assigned to a combination of the E_g phonon and magnon at wavevectors near the zone boundary. The dispersion of the E_g

phonon is not known but lattice dynamics calculations indicate that the $q = (00\xi)$ dispersion is small for layered MX_2 compounds (Pasternak 1976) and therefore the zone-centre frequency of 94.3 cm^{-1} (12K) can be assumed for the zone boundary value. From neutron scattering studies the zone boundary magnon energy is known to be 45 cm^{-1} at 5K (Yelon and Vettier 1975). The summation band is therefore expected to occur at 139 cm^{-1}, in reasonable agreement with observation. Further evidence for this assignment comes from the band's temperature dependence. The E_g phonon shifts only slightly in frequency as the temperature is raised to 140K (Table I) whereas the zone-centre magnon renormalises to zero energy at T_N. However, in some materials the zone boundary excitations decrease in frequency more slowly than this (e.g. CoF_2, R A Cowley et al 1973) and can still be observed above T_N in second-order Raman scattering (e.g. Chinn et al 1971) because only short-range spin correlations are important. Therefore, the 127.7 cm^{-1} combination band is predicted to decrease only slowly in frequency when the temperature is raised above OK and decrease in intensity as the spin excitations are damped out. For temperatures well in excess of T_N the band should vanish which, as can be seen in Figure 6, is what is observed.

8. CONCLUSIONS

All the paramagnetic and antiferromagnetic energy levels of the lowest cubic field multiplet of the Fe^{2+} ion have been determined. (Second order Raman scattering from a magnon-phonon combination band has also been identified). Above T_N the levels have been successfully fitted using a model including a weak dynamic Jahn-Teller interaction while the antiferromagnetically ordered state has been described using molecular field theory. Although the strength of the Jahn-Teller interaction is weak, when compared to that found for $Al_2O_3:Fe^{2+}$ for example, it is nevertheless significant

and demonstrates that an effect which would have previously been neglected, absorbed into effective parameters, or masked in a higher-order calculation can no longer be considered in this way. In particular, it is interesting to note that for this case the usual higher-order crystal-field calculation is unsuccessful. Further vindication of the multimode dynamic Jahn-Teller model comes from the successful prediction of observed ground state g-values and the energy of the first excited state of the $^5T_{2g}(^5D)$ energy level scheme.

Previous data, with which to test a full lattice Jahn-Teller model, has come from acoustic paramagnetic resonance (APR) and electric-field induced EPR measurements (see for example Bates and Steggles 1975). Hence, past studies have been necessarily restricted to developing a description of levels within 20 cm^{-1} of the ground state. This work has provided the first stringent test of the theory and the extension of its use to describe all 15 states of the $^5T_{2g}(^5D)$ manifold has been very successful, certainly justifying the use of a multi-mode (full lattice) model in future analyses of the spectra of Fe^{2+} ions. Its success has also prompted us to use an analagous model in the analysis of the Raman spectrum of Co^{2+} ions in $CoBr_2$ and $CoCl_2$ which will be reported in a forthcoming publication.

ACKNOWLEDGEMENTS

We wish to thank Professor K W H Stevens for his critical reading of this manuscript and to acknowledge useful discussions with Drs C A Bates and J R Fletcher. We would also like to thank Dr G D Jones and Mr R Ritchie of the University of Canterbury, New Zealand, for the $FeCl_2$ crystal. This work was supported by the SRC (IWJ), the DHSS (DJL) and the Royal Society and CNRS through the award of a European Exchange Programme visit to Edinburgh (GM).

REFERENCES

Abou-Ghantous M, Bates C A, Chandler P E and Stevens K W H, 1974a, J Phys C: Solid St Phys 7, 309-24.

Abou-Ghantous M, Bates C A and Stevens K W H, 1974b, J Phys C: Solid St Phys 7, 325-38.

Alben R, 1969, J Phys Soc Japan 26, 261-78.

Arthur J W and Lockwood D J, 1974, J Raman Spectrosc 2, 53-69.

Azima A, Grunberg P, Hoff J, Koningstein J A and Preudhomme J, 1970, Chem Phys Letters 7, 565-67.

Bates C A, 1977, Physics Reports, to be published.

Bates C A and Steggles P, 1975, J Phys C: Solid St Phys 8, 2283-99.

Bertrand Y, Fert A R and Gelard J, 1974, J Physique 35, 385-391.

Birgenau R J, Yelon Y B, Cohen E and Makovsky J, 1972, Phys Rev B 5, 2607-15.

Carrara P, 1968, Doctoral Thesis, Universite Paris IX, France.

Chinn S R, Zeiger H J and O'Connor J R, 1971, Phys Rev B 3, 1709-35.

Christie J H, Johnstone I W, Jones G D and Zdansky K, 1975, Phys Rev B 12, 4656-65.

Christie J H and Lockwood D J, 1971, Chem Phys Letters 8, 120-22.

Cowley R A, Buyers W J L, Martel P and Stevenson R W H, 1973, J Phys C: Solid St Phys 6, 2997-3019.

Cracknell A P, 1974, J Phys C: Solid St Phys 7, 4323-34.

Fert A R, Carrara P, Lanusse M C, Mischler G and Redoules J P, 1973, J Phys Chem Solids 34, 223-30.

Fleury P A, Porto S P S, Cheesman L E and Guggenheim , 1966, Phys Rev Letters 17, 84-7.

Freeman T E and Jones G D, 1969, Phys Rev 182, 411-5.

Fujita T, Ho A and Ono K, 1969, J Phys Soc Japan 27, 1143-49.

Graf L and Schaak G, 1976, Z Physik B 24, 83-9.

Ham F S, 1965, Phys Rev 138 A 1727-40.

Hautecher S, Konstatinovic J, Cribier D and Jacrot B, 1962, Compt Rend 254, 1026-28.

Jacobs I S and Lawrence P E, 1964, J Appl Phys 35, 996-7.

Jacobs I S and Lawrence P E, 1967, Phys Rev 164, 866-78.

1975,
Johnstone I W, Doctoral Thesis, University of Canterbury, New Zealand.

Johnstone I W, Lockwood D J and Mischler G, 1978, J Phys C: Solid St Phys, to be published.

Jones G D, 1967, Phys Rev 155, 259-61.

Kinne R W, O'Sullivan W J, Ryan J F and Scott J F, 1975, Phys Rev B 11, 1960-

Laurence G and Petitgrand D, 1973, Phys Rev B 8, 2130-8.

Lockwood D J, 1971, Light Scattering Spectra of Solids, ed G B Wright (Springer, New York) 75-84.

Lockwood D J, 1973, J Opt Soc Am 63, 374-82

Lockwood D J and Christie J H, 1971, Chem Phys Letters 9, 559-63.

Lockwood D J, Johnstone I W, Mischler G and Carrara P, 1978, Solid St Comm, to be published.

Lovesey S W, 1974, J Phys C: Solid St Phys 7, 2049-59.

Lyons K B, Carter H L and Fleury P A, 1976, Light Scattering in Solids, ed M Balkansky (Flammarion, Paris) 244-8.

Macfarlane R M, 1970, Phys Rev Letters 25, 1454-57.

Meixner A E, Dietz R E and Rousseau D L, 1973, Phys Rev B 7, 3134-41.

Ono K, Ho A and Rujita T, 1964, J Phys Soc Japan 19, 2119-26.

Pasternak A, 1976, J Phys C: Solid St Phys 9, 2987-95.

Popkov K A, Enemenko V V, Fomin V I and Mokhir A P (1973) Soviet Phys Solid St 14, 1985-89.

Robbins D J and Day P, 1973, Chem Phys Lett 19, 529-31.

Shepherd I W, 1973a, Phys Lett 43A, 305-6.

Shepherd I W, 1973b, Phys Lett 45A, 297-8.

Shepherd I W, 1971, J Appl Phys 42, 1482-3.

Stephens P J, 1969, J Chem Phys 51, 1995-2005.

Stephens P J and Lowe-Pariseau M, 1968, Phys Rev 171, 322-35.

Sturge M D, 1967, Solid St Phys 20, 91-211 (New York: Academic Press).

Wilkinson M, Cable J W, Wollan E O and Koehler W C, 1959, Phys Rev 113, 497-507.

Yelon Y B, Scherm R and Vettier C, 1974, Solid St Comm 15, 391-4.

Yelon Y B and Vettier C, 1975, J Phys C: Solid St Phys 8, 2760-68.

FIGURE CAPTIONS

Figure 1: Energy-level scheme for the $^5T_{2g}$ (^5D) term of an Fe^{2+} ion in both a purely trigonal and trigonal + exchange field. Selection rules describing observed transitions from the Γ_3^+ ground state and Γ_2^+ first excited state are given in the inset, together with the appropriate Raman scattering tensors.

Figure 2: Raman spectra of $FeBr_2$ recorded at (a) 12K, (b) 16K, and (c) 140K between 0 and 800 cm^{-1}. The off-scale intensities of the first order phonons near 94.5 and 158 cm^{-1} are: (a) 11008, 7136; (b) 6288, 3400; and (c) 2736, 1330 counts respectively.

Figure 3: The five harmonic oscillator band fit (———) to the 16K Raman spectrum of $FeBr_2$ in the 425-725 cm^{-1} region obtained using equation (4.2). (See also Table II).

Figure 4: Calculated and experimentally determined energy levels within the $^5T_{2g}$ (^5D) term for an Fe^{2+} ion in antiferromagnetically ordered $FeBr_2$ and $FeCl_2$.

Figure 5: Raman spectrum of $FeCl_2$ recorded at (a) 12K, (b) 24K, and (c) 115K between 0 and 800 cm^{-1}. The off-scale intensity of the peak near 140 cm^{-1} in spectrum (a) is 12656 counts.

Figure 6: Raman spectrum of $FeBr_2$ recorded between 110 and 150 cm^{-1} for various temperatures above and below T_N (= 14.2K) and showing the assigned magnon-phonon combination band.

TABLE II: Parameters obtained from a fit of three (five) harmonic oscillators to the 175-350 cm^{-1} (425-725 cm^{-1}) regions of the $FeBr_2$ Raman spectrum recorded at 16K.

Strength S	Resonance Frequency ω_o (cm^{-1})	Damping Constant γ (cm^{-1})
2.71	191.5	30.0
0.57	243.7	45.7
0.45	295.9	37.8
0.84	493.9	40.6
2.07	516.6	34.4
0.14	584.4	28.7
0.78	630.3	34.9
0.34	637.0	106.7

TABLE III: Parameters obtained from a fit of four and five harmonic oscillators to the 380-750 cm^{-1} region of the $FeCl_2$ Raman spectrum recorded at 24K.

Strength S	Resonance Frequency ω_o (cm^{-1})	Damping Constant γ (cm^{-1})
0.25	438.7	157.6
2.25	464.0	63.5
0.19	568.3	37.3
0.78	635.6	83.4
0.25	438.2	171.0
2.26	463.9	63.4
0.19	568.4	37.1
0.55	635.2	73.9
0.25	637.4	114.3

TABLE IV: Calculated and experimentally determined energies for the electronic levels within the $^5T_{2g}$ (^5D) ground term for $T > T_N$. All measurements and parameters are in units of wave numbers (cm^{-1}).

	Assignment (J, J_z)	Calculated $\tilde{\mathcal{H}}(1)$	Calculated $\tilde{\mathcal{H}}(2)$	Calculated $\tilde{\mathcal{H}}(3)$	Experimental
	(1,±1)	0	0	0	0
	(1,0)	17.6	24.5	20.8	23†
	(2,0)	187.6	182.6	200.4	191.5
	(2,±1)	213.0	208.4	232.5	243.7
	(2,±2)	277.9	279.8	305.4	295.9
$FeBr_2$ (T=16K)	(3,±3)	525.6	518.9	511.3	516.6
		525.6	523.1	512.8	
	(3,±2)	601.0	611.1	588.8	584.4
	(3,±1)	628.0	622.7	625.1	630.3
	(3,0)	635.9	634.7	637.0	637.0
RMS Deviation		15.1	20.4	6.5	
Parameters γ		1.0	1.0	9.4047×10^{-1}	
F_a		0	0	1.4325×10^{-4}	
F_b		0	0	7.0000×10^{-4}	
λ		-1.1242×10^{2}	$-1.13.7\times10^{2}$	-1.1261×10^{2}	
V		-1.695×10^{2}	-1.5237×10^{2}	-2.0232×10^{2}	
$(\delta\alpha)$		0	-2.3000×10^{2}	0	
	(1,±1)	0	0	0	0
	(1,0)	24.0	31.9	31.3	25†,28
	(2,0)	161.5	158.8	179.2	*
	(2,±1)	194.3	194.8	221.1	216
	(2,±2)	271.4	276.8	307.6	310
$FeCl_2$ (T=24K)	(3,±3)	472.2	473.3	457.6	464.0
		472.2	475.3	458.9	
	(3,±2)	589.4	603.1	583.4	568.3
	(3,±1)	620.8	620.4	617.9	635.2
	(3,0)	629.7	629.4	629.0	637.4
RMS Deviation		19.5	21.9	7.4	
Parameters γ		1.0	1.0	9.1312×10^{-1}	
F_a		0	0	3.175×10^{-4}	
F_b		0	0	1.1025×10^{-3}	
λ		-1.0358×10^{2}	-1.0412×10^{2}	-1.0132×10^{2}	
V		-2.271×10^{2}	-2.0519×10^{2}	-2.9594×10^{2}	
$(\delta\alpha)$		0	-2.5875×10^{2}	0	

† inferred from the harmonic oscillator analysis of J' = 3 band

* electron-resonant phonon coupled mode (Johnstone et al 1978).

TABLE V: Calculated and experimentally determined ground state g-values for $FeCl_2$ and $FeBr_2$

g Component	$FeCl_2$ Experiment	$FeCl_2$ Theory	$FeBr_2$ Experiment	$FeBr_2$ Theory
$g_{\|\|}$	4.1 ±0.1[a]	4.43	3.9 ±0.1[a]	4.24
	4.3 ±0.1[b]		4.05±0.2[f]	
	4.5 ±0.7[c]		4.4 ±0.7[c]	
$g_{\perp}$	3.25[d]	3.08	3.24[d]	3.27

a - Carrara (1968)

b - Jacobs and Lawrence (1967)

c - Wilkinson et al (1959)

d - A calculated value obtained from magnetic susceptibility measurements (Bertrand et al 1974)

e - Fert et al (1973)

f - Jacobs and Lawrence (1964)

TABLE VI: Summary of values (cm^{-1}) for the isotropic ferromagnetic (J_1) and antiferromagnetic (J_2) exchange parameters appropriate for $FeCl_2$ and $FeBr_2$.

$FeCl_2$				$FeBr_2$			
J_1	J_2	(J_1-J_2)		J_1	J_2	(J_1-J_2)	
		16.4	a			7.0	g
15.6	-2.1		b,c	4.4	-5.28±0.14		c,h
15.75	-1.58		d	26±4	-5.1 ±0.5		j
40±3	-2.0±0.7		e				
		18.5	f			14.5	f

a - Ono K et al (1964)
b - Carrara P (1968)
c - Bertrand Y et al (1974)
d - Alben R (1969)
e - Birgenau R J et al (1972)
f - this work
g - Fujita T et al (1969)
h - Fert A R et al (1973)
j - Yelon Y B et al (1975)